内部センシングに基づく
柔軟物のリアリティベースモデリングに
関する研究

研究課題番号 17206024

平成17年度～平成19年度 科学研究費補助金
(基盤研究(A)(2)) 研究成果報告書

平成20年3月

研究代表者　　平井　慎一

(立命館大学 理工学部 教授)

内部センシングに基づく
柔軟物のリアリティベースモデリングに
関する研究

研究課題番号 17206024

平成17年度～平成19年度 科学研究費補助金
(基盤研究(A)(2)) 研究成果報告書

平成20年3月

研究代表者　　平井　慎一

(立命館大学 理工学部 教授)

Reality-based Modeling of Deformable Soft Objects via Internal Sensing

Project Number 17206024

From April 2005 to March 2008
Report for the Research Project
Grant in Aid for Scientific Research (A)(2)
by the Ministry of Education, Culture, Sports,
Science and Technology of Japan

March 2008

Head investigator Shinichi Hirai

(Professor, Faculty of Science and Engineering,

Ritsumeikan University)

平成17年度～平成19年度 科学研究費補助金
(基盤研究(A)(2)) 研究成果報告書

課題番号　17206024
研究課題　内部センシングに基づく
柔軟物のリアリティベースモデリングに関する研究

研究組織
研究代表者: 平井 慎一 (立命館大学 理工学部 教授)
研究分担者: 田中 弘美 (立命館大学 情報理工学部 教授)
研究分担者: 鳥山 寿之 (立命館大学 理工学部 教授)
研究分担者: 登尾 啓史 (大阪電気通信大学 総合情報学部 教授)
研究分担者: 喜多 泰代 (産業技術総合研究所
情報技術研究部門 主任研究員)

交付決定額 (金額単位: 千円)

	直接経費	間接経費	合計
平成17年度	13,400	4,020	17,420
平成18年度	13,800	4,140	17,940
平成19年度	9,600	2,880	12,480
総計	36,800	11,040	47,840

まえがき

本研究の目的は，生体組織や臓器，食品素材に代表される柔軟物のモデリングを，柔軟物内部の直接センシングを通して行い，リアリティベースモデリング (Reality-Based Modeling) の基盤技術を確立することである．近年，手術シミュレーションにおける臓器のモデリング，デジタルヒューマンに代表される人体の筋骨格モデリング，食品工学における食品素材の力学的モデリング等において，複雑な力学的特性を有する柔軟物のモデリングが必要とされている．このような柔軟物では，非一様な力学特性を示すことが多い．従来の同定手法では，力学特性が一様であることを前提とし，柔軟物から切り出した試験片の力学特性を計測し，それを全体の力学特性であると見なしていた．非一様な柔軟物，特に生体組織に対してこのような手法を適用することは難しい．そこで本研究では，マイクロメカニカルセンサと三次元イメージング技術を融合して，柔軟物の内部挙動を計測し，計測結果をベースにするモデリング技法を開拓する．

第 1 章では，柔軟体の MR 画像から内部変形場を推定する手法を確立する．変形前の MR ボリューム画像と変形後の MR ボリューム画像から，内部変形場を推定する．MR ボリューム画像の特徴は，1) 変形前と変形後で位置や姿勢が異なる，2) 変形前と変形後で特徴点が変化する，という点にある．本報告では生体組織を対象に，1) 骨等の変形が少ない部分を用いて変形前と変形後の MR ボリューム画像をレジストレーションする手法，2) 双方向のマッチングを通して特徴点の対応を探索する手法を提案する (成果　論文 [1], 論文 [4], 口頭発表 [2])．本手法により，MR ボリューム画像から内部の変形を推定することができる．

第 2 章では，超音波画像による柔軟物の内部変形計測について述べる．超音波画像は，動的な変形を計測できるという特質を持っており，粘性特性の推定など MR 画像を用いた推定とは異なる特性の推定を可能にする．本章では，超音波画像による柔軟物の内部変形計測を実験的に評価し，動的な有限要素シミュレーションと比較した．(成果　論文 [12], 口頭発表 [5])

第 3 章では，内部変形計測により非均一な弾性特性を同定する手法を確立する．弾性特性を始めとする力学特性を推定するためには，変位や変形の計測とともに，力

や圧力の計測が必要である．MR 画像による内部変形計測により，柔軟物内部の変形を計測することができるが，従来のロードセル等は磁性体を含むため MR 環境下で使うことができない．MR コンパティブルな力覚センサが開発されているが，使用条件の制約や測定点の少なさなど非一様な力学特性の同定には課題が残る．そこで本章では，力学的特性が既知の物体で力学的特性が未知の対象物体を変形させ，双方の内部変形を計測することにより，対象物体の未知の力学的特性を推定する手法を提案し，シミュレーションと実験によりその有効性を検証する (成果　論文 [5], 口頭発表 [1], 口頭発表 [3], 口頭発表 [4], 口頭発表 [7], 口頭発表 [9])．まず，弾性パラメータの同定手法として，逐次同定法と一括同定法を提案し，各手法の同定精度をシミュレーションを通して評価する．次に，MRI による内部変形計測手法について述べる．さらに，CT によるファントムの内部変形計測の結果を用いて，各手法を実験的に評価する．

第 4 章では，適応的なモデリング手法について述べる．柔軟物の変形モデルにおいて，メッシュを細かくするとモデルの表現力と精度は向上するが，計算時間を多く要する．メッシュが粗いと計算時間は短縮できるが，モデルの表現力と精度が低下する．モデルの精度と計算時間を両立させるためには，一様なメッシュではなく，必要に応じてメッシュの粗密を変化させる適応的なモデリング手法が望まれる．モデルの粗密を制御するために操作中の力学量を評価し，メッシュの粗密を適応的に変化させるアダプティブメッシュが提案されている (成果　論文 [13], 口頭発表 [10])．アダプティブメッシュでは，力学量の変化が大きい部分ではメッシュを細かく，変化が小さい部分ではメッシュを粗くする．アダプティブメッシュの構成法とその評価について述べる．また，階層的なメッシュにより，モデルの表現力と計算時間を両立させることができる (成果　論文 [2], 論文 [7], 論文 [8])．階層的なメッシュ表現では，表面と内部で粗密が異なるメッシュを採用し，モデルの表現力と計算時間を両立させる．階層的なメッシュ表現の構成法とその評価，特に力の再現性について述べる．柔軟物の変形には，位相が保たれる形状変化と切断や合併のような位相変化がある．アダプティブメッシュは，柔軟物の位相変化を表現することができる (成果　論文 [9], 論文 [10])．この手法では，切断に伴い各ノードに作用する力を評価し，その評価を基にメッシュ構造の位相を変化させる．切断モデルの構成法とその評価について述べる．

第 5 章では，動的モデルのアクティブ虚血ダイナミクスへの応用とマンモグラフィーへの応用を述べる．アクティブ虚血ダイナミクスへの応用に関しては，動的なレオロジー変形シミュレーションと実験結果とを比較し，評価した．またマンモグラフィーへの応用に関しては，マンモグラフィーとパーティクルモデルによる計算結果とを比較し，評価する．さらに，ファントムの撮影結果との比較を通して，パーティク

ルモデルの精度を検証する (成果　論文 [6]).

第 6 章では，マイクロフォースセンサによる柔軟物内部の力計測について述べる．MEMS 技術に基づき製作されたマイクロフォースセンサを柔軟物体の内部に埋め込み，センサの特性を実験的に評価する．クロストークの少ない計測値が得られること，柔軟物体を押す方向に対応する力を検出できることが示されている (成果　論文 [3], 論文 [11], 口頭発表 [6], 口頭発表 [8], 口頭発表 [11]).

また，本研究課題の成果は，柔軟指操作 (論文 [14]) や間接同時位置決め (論文 [15]) に応用されている．生体組織は非一様な力学特性を示すことが多く，本報告の手法は有効であると考える．また，ポリマーアクチュエータやゲルアクチュエータ等の人工筋肉では，パラメータが大きくばらつき，また時間とともに変化する．このような系のモデリングと同定に関しては，本報告の手法が基礎となると考える．

本報告では主として非一様な弾性特性の推定を対象とした．弾性特性は，静的な計測により同定することができるため MRI による内部変形計測が有効であった．粘性等の動的な特性は，センシングの手法が限られていることもあり未開拓の部分が多い．これは次の課題としたい．また，本報告の成果を基礎として，人が物体を把持しているときや道具を操作しているときの手指の内部変形が計測できる可能性がある．これにより，人の巧みさが力学的なリアリティを持って解明できるのではないかと考える．これに関しても今後の検討課題としたい．

論文

[1] Penglin Zhang, Shinichi Hirai, and Kazumi Endo, *A Feature Matching-based Approach to Deformation Fields Measurement from MR Images of Non-rigid Object*, Int. J. of Innovative Computing, Information and Control, acceptted for publication, 2008.

[2] 井川 武思, 登尾 啓史, "階層レオロジー MSD モデルの形状精度と計算時間について", VR 医学, Vol. 6, No. 1, 修正後掲載予定, 2008.

[3] 井上 貴浩, 藤井 郁夫, 平井 慎一, Qiang Wang, Dzung Viet Dao, 杉山 進, "マイクロフォース・モーメントセンサ埋め込み型柔軟指先の製作と圧縮実験による評価", 日本機械学会論文誌 C 編, Vol. 73, No. 736, pp.3228–3233, 2007.

[4] Penglin Zhang, Shinichi Hirai, Kazumi Endo, and Shigerhiro Morikawa, *Local Deformation Measurement of Biological Tissues Based on Feature Tracking of 3D MR Volumetric Images*, 2007 IEEE/ICME Int. Conf. on Complex Medical Engineering (CME2007), Beijing, May 23–25, 2007.

[5] Penglin Zhang, Shinichi Hirai, and Kazumi Endo, *A Method for Non-rigid 3D Deformation Fields Measurement: Application to Human Calf MR Volumetric Images*, Workshop on Modeling, Identification, and Control of Deformable Soft Objects, IEEE/RSJ Int. Conf. on Intelligent Robots and Systems, San Diego, U.S.A., November, 2007.

[6] Yasuyo Kita, Shinichi Tokumoto, and Shinichi Hirai, *On Compression Model for Integrative Analysis of Different View Breast Xrays*, Workshop on Modeling, Identification, and Control of Deformable Soft Objects, IEEE/RSJ Int. Conf. on Intelligent Robots and Systems, San Diego, U.S.A., November, 2007.

[7] Takeshi Ikawa and Hiroshi Noborio, *On the Precision and Efficiency of Hierarchical Rheology MSD Model*, Proc. of the IEEE/RSJ International Conference on Intelligent Robots and Systems, pp.376–383, 2007.

[8] Haruyuki Yoshida, Fumiaki Ujibe, Hiroshi Noborio, *Force/Shape Reappearance of MSD Rheology Model Calibrated by Force/Shape Sequence*, Proc. of the 17th Int. Conf. on Artificial Reality and Telexistence, pp.121–128, 2007.

[9] Huynh Quang Huy Viet, Takahiro Kamada, Yasufumi Takama, and Hiromi T. Tanaka, *An Adaptive 3D Surface Mesh Cutting Algorithm for Deformable Objects*, 情報処理学会「画像の認識・理解シンポジウム (MIRU'06)」論文集, pp.1359–1364, July, 2006.

[10] Huynh Quang Huy Viet, Takahiro Kamada, Yasufumi Takama, and Hiromi T. Tanaka, *A Virtual Surface Cutting Operation Using Mesh Refinement Method*, Proc. 20th Int. Congress and Exhibition Osaka, International Jornal of Conputer Assisted Radiology and Surgery (CARS06), pp.150–152, June, 2006.

[11] Ikuo Fujii, Takahiro Inoue, Dzung Viet Dao, Susumu Sugiyama, and Shinichi Hirai, *Tactile Perception Using Micro Force/Moment Sensor Embedded in Soft Fingertip*, Proc. IEEE Sensors, pp.558–562, Daegu, Korea, October, 2006.

[12] Junji Muramatsu, Takashi Ikuta, Shinichi Hirai, and Shigehiro Morikawa, *Validation of FE Deformation Models using Ultrasonic and MR Images*, Proc. 9th IEEE Int. Conf. on Control, Automation, Robotics and Vision, pp.1091–1096, Singapore, December, 2006.

[13] Hiromi T. Tanaka, Yoshinori Tsujino, Takahiro Kamada, and Hyung Quang Huy Viet, *Bisection Refiniment Based Real-Time Adaptive Mesh Model for Deformation and Cutting of Soft Object*, Proc. 9th IEEE Int. Conf. on Control, Automation, Robotics and Vision, pp.1103–1110, Singapore, December, 2006.

[14] Takahiro Inoue and Shinichi Hirai, *Local Minimum of Elastic Potential Energy on Hemispherical Soft Fingertip*, Proc. IEEE Int. Conf. on Robotics and Automation, pp.2319–2324, Barcelona, April, 2005.

[15] Mizuho Shibata and Shinichi Hirai, *Stability Analysis for Dynamic Control on Contact with Soft Interface in Continuous-discrete Time System*, Proc. IEEE/RSJ Int. Conf. on Intelligent Robots and Systems, pp.1628–1633, Edmonton, Canada, August, 2005.

口頭発表

[1] 遠藤和美, 村松潤治, 平井慎一, 柔軟物の内部変形計測による FE モデルの力学パラメータ同定, ロボティクス・メカトロニクス'07 講演会予稿集 CD-ROM, 2007.

[2] Penglin Zhang, Shinichi Hirai, and Kazumi Endo, *A Feature Tracking-based Approach for Local Deformation Fields Measurement of Biological Tissue from MR Volumes*, 3rd Joint Workshop on Machine Perception and Robotics (MPR2007), Kusatsu, November, 2007.

[3] Kazumi Endo, Penglin Zhang, Shinichi Hirai, and Shinichi Tokumoto, *Identification of Nonuniform Physical Parameters through Measurement of Inner Deformation*, 3rd Joint Workshop on Machine Perception and Robotics (MPR2007), Kusatsu, November, 2007

[4] 遠藤和美, 張鵬林, 平井慎一, 徳本真一, 柔軟物の内部変形計測による非一様 FE モデルのパラメータ同定法の検証, 計測自動制御学会システムインテグレーション部門学術講演会, pp.1170–1171, 2007.

[5] 活田崇至, 村松潤治, 早見信一郎, 森川茂廣, 平井慎一, 田中弘美, 超音波画像と MRI を用いた内部計測による柔軟物の FE モデルの検証, ロボティクスシンポジア予稿集, pp.544–549, 2006.

[6] 藤井郁夫, 井上貴浩, 平井慎一, Dzung Viet Dao, 杉山進, MEMS フォースセンサを用いたソフトフィンガ型触覚デバイスの開発と接触実験, ロボティクス・メカトロニクス'06 講演会予稿集 CD-ROM, 2006.

[7] 徳本真一, 平井慎一, CT スキャナを用いたパラメータ同定のための柔軟物の内部変形計測, 計測自動制御学会システムインテグレーション部門学術講演会, pp.73–74, 2006.

[8] 藤井郁夫, 井上貴浩, Dzung Viet Dao, 杉山進, 平井慎一, マイクロフォース・モーメントセンサ内蔵ソフトフィンガの開発と接触実験, 計測自動制御学会システムインテグレーション部門学術講演会, pp.488–489, 2006.

[9] 遠藤和美, 張鵬林, 村松潤治, 平井慎一, 森川茂廣, MRI ボリュームデータにおける 3 次元ブロックマッチングを用いた FE モデルパラメータの同定, 計測自動制御学会システムインテグレーション部門学術講演会, pp.1036–1037, 2006.

[10] Yoshinori Tsujino, Huynh Quang Huy Viet, and Hiromi T. Tanaka, *A Real-Time Dynamic Adaptive Deformable Mesh Model for Soft Objects Based on Bisection Refinement and Binary Simplification Algoritms*, 2nd Joint Workshop on Machine Perception and Robotics, Fukuoka, November 2006.

[11] 藤井郁夫, 井上貴浩, Dzung Viet Dao, 杉山進, 平井慎一, マイクロフォース・モーメントセンサを内蔵した半球型ソフトフィンガの静的接触実験, 計測自動制御学会システムインテグレーション部門学術講演会, pp.1123–1124, 2005.

目 次

第1章　柔軟体のMR画像からの内部変形場の推定

1.1　緒言

Since its initial use for human imaging over 20 years ago, magnetic resonance imaging (MRI) has become a widely used clinical imaging modality [3]. MRI has increasingly employed in biomedical applications. As one of research branches in MR image processing, interior deformation fields measurement is very important for physical parameters estimation. The purpose of this paper is to develop a valid approach for measurement the dense deformation fields of non-rigid and non-uniform object. The input data of this procedure is MR images before and after deformation.

Though there has been significant growth on deformation fields measurement from medical MR images, most works have been done are mainly focus on non-rigid registration approaches. Especially, many proposed approaches are based on elastic deformable model[2-10]. Generally, the deformable models can be classified in two basic categories: parametric and geometric deformable models [7]. Parametric deformable models, also called snakes, was first proposed by Kass, Witkin and Terzopoulos in 1987 [13]. Parametric deformable models represent curves and surfaces explicitly in their parametric forms during deformation. Usually, it must formulate an energy function for a deformable contour in order to find a parameterized curve that minimizes the weighted sum of internal energy and potential energy. Different from parametric deformable models, geometric deformable models are based on curve evolution theory and the level set method, representing curves and surfaces implicitly as a level set of a higher-dimensional scalar function. Their parameterizations are computed only after complete deformation, this allowing topological adaptivity to be easily accommodated [14]. In deformable models, the motion fields of deformable contour or surface can be regarded as the deformation fields.

Though the deformable models undergo a significant development, and are widely used in image segmentation, non-rigid registration and deformation fields measure-

ment, they still have some limitations. Typically, for parametric approach, the difference between the initial model and the desired object boundary will directly affect the final result. Moreover, it has difficulty dealing with topological adaptation such as splitting or merging model parts, a useful property for recovering either multiple objects or an object with unknown topology. Although geometric approach can address the topological adaptation using curve evolution theory, it may generate shapes that have inconsistent topology with respect to the actual object, when applied to noisy images with significant boundary gaps [14]. Furthermore, the most important issue of deformable models in deformation fields measurement is that they cannot deal with the interior deformation fields measurement.

In this paper, we propose a feature matching-based approach to measure sparse local deformation fields from MR images of non-rigid non-uniform biological tissues. By means of linear interpolation, the interior dense deformation fields at different regions of an object are interpolated using local deformation fields on the nodes of an irregular Dealunay triangle net. In this case, certain numbers of high curvature feature points (also called points of interest) in the initial and deformed MR volumetric images are first pre-extracted to form two feature points sets. Then, we apply the proposed feature matching method into the two feature points sets in order to find feature pairs homologous each other. The local deformation fields are computed from the obtained homologous feature point pairs.

This paper is organised as follows. Section 2 gives overview of the proposed approach. Section 3 describes interior deformation fields measurement from MR images. Section 4 presents examples and the results of preliminary experiments. The final section presents our discussion and conclusions.

1.2 内部変形場の推定法の原理

The pipeline of our approach is shown in Figure 1.1. At the initial phase, Harris operator [15] is used to automatically extract high curvature points of interest from the initial and deformed MR images as references features. The purpose of *absolute orientation* is to find the geometric relationship between deformed MR image and the initial one. Many approaches have been reported to address this problem. For example, a mutual information based non-rigid registration approach [21] was proposed to find geometric transformation parameters in order to align two medical images. In this paper, we use an unit quaternion method [16][17] to find the solution

of the transformation parameters of two systems: rotation matrix $\mathcal{R}$ and translation vector τ. This mainly comes from: *1)* there is a rigid region (bone) in experiment data; *2)* we have already extracted rigid feature points around bone, which are useful for finding geometric transform parameters by means of unit quaternion approach.

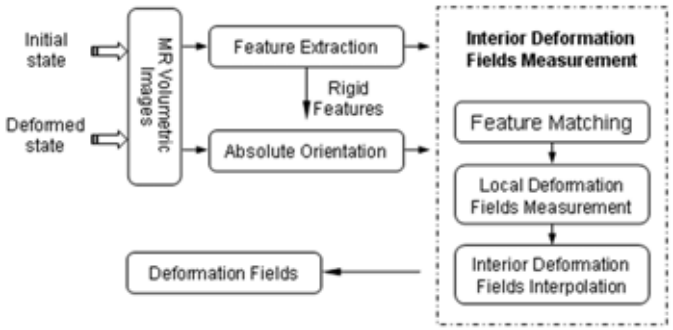

図 1.1: Pipeline of the proposed approach

Before obtaining the dense deformation fields, we must track the precise corresponding position in the deformed MR image for a given feature point of interest in the initial MR image. In this paper, we propose a *correlation score* based robust algorithm to obtain homologous point pairs.

The obtained point matches are used to measure the local deformation fields at the corresponding location under a global coordinate system. Subsequently, in order to calculate the dense deformation fields, we propose to infer the interior dense deformation fields using sparse local deformation fields at the nodes of Dealunay triangles.

Finally, the reverse movement of selected check points is used to evaluate the reliability of obtained dense deformation fields. When the check points in the deformed image can move back to their original position in the initial image, it implies that the obtained deformation fields is reliable and accurate.

1.3 MR画像における内部変形の計測

This section presents how to measure interior deformation of non-rigid non-uniform object by means of the proposed approach. Concisely, we first try to obtain a potential matches set (PMS) through a robust feature matching algorithm (two steps feature matching algorithm). Whereafter, interior deformation is calculated using interpolation algorithm in Delaunnay triangles.

1.3.1 特徴点のマッチング

A) First matching. Let $\mathbf{x} = [x \quad y]^{\mathbf{T}}$ be the coordinates of an MR image, $\mathbf{p_1}$ be feature point in the initial MR image, and $\mathbf{p_2}$ be the projection of $\mathbf{p_1}$ in the deformed MR image. Then, the position of $\mathbf{p_2}$ can be calculated using affine transformation with rotation matrix $\boldsymbol{\mathcal{R}}$ and translation vector $\boldsymbol{\tau}$ as follows:

$$\mathbf{x}_{\mathbf{p_2}} = \boldsymbol{\mathcal{R}}\mathbf{x}_{\mathbf{p_1}} + \boldsymbol{\tau}, \tag{1.1}$$

where $\mathbf{x}_{\mathbf{p_1}} = [x_1, y_1]^{\mathrm{T}}$ and $\mathbf{x}_{\mathbf{p_2}} = [x_2, y_2]^{\mathrm{T}}$ are coordinates of point $\mathbf{p_1}$ and $\mathbf{p_2}$, respectively.

Let us introduce the following rectangular region for matching:

$$\mathcal{C}_m = \{\mathbf{x} = [x \quad y]^{\mathbf{T}} | x \in [-m, m],\ y \in [-n, n]\}. \tag{1.2}$$

The size of this region is given by $|\mathbf{C}_m| = (2m+1)(2n+1)$. Let $g(\mathbf{x})$ and $g'(\mathbf{x})$ be the intensity of the initial and deformed MR images at position $\mathbf{x}$. Let $\bar{g}_{\mathbf{p_1}}$ and $\bar{g}'_{\mathbf{p_2}}$ be the means of intensity in the rectangular region $\mathbf{C}_m$ around $\mathbf{p_1}$ in the initial image and $\mathbf{p_2}$ in the deformed image:

$$\bar{g}_{\mathbf{p_1}} = \frac{1}{|\mathcal{C}_m|} \sum_{\mathbf{x} \in \mathcal{C}_m} g(\mathbf{p}_1 + \mathbf{x}),\ \bar{g}'_{\mathbf{p_2}} = \frac{1}{|\mathcal{C}_m|} \sum_{\mathbf{x} \in \mathcal{C}_m} g'(\mathbf{p_2} + \mathbf{x}), \tag{1.3}$$

Let $\sigma(g_{\mathbf{p_1}})$ and $\sigma(g_{\mathbf{p_2}})$ be the standard derivation of the rectangular region $\mathbf{C}_m$ around $\mathbf{p_1}$ in the initial image and $\mathbf{p_2}$ in the deformed image, respectively. The correlation score between feature points $\mathbf{p_1}$ and $\mathbf{p_2}$ can be calculated using match regions around them, which is given by

$$cs(\mathbf{p_1}, \mathbf{p_2}) = \frac{\sum_{\mathbf{x} \in \mathcal{C}_m} (g(\mathbf{p}_1 + \mathbf{x}) - \bar{g}_{\mathbf{p_1}})(g'(\mathbf{p}_2 + \mathbf{x}) - \bar{g}'_{\mathbf{p_2}})}{|\mathcal{C}_m| \sigma(g_{\mathbf{p_1}}) \times \sigma(g_{\mathbf{p_2}})} \tag{1.4}$$

Through first matching stage, a point matches set with many-to-many relationships is obtained. Namely, a point in the initial MR image may be paired not less than one points (we called candidate matches) in the deformed MR image, and vice versa. Therefore, the first matching based on correlation score only is rough and insufficient. To disambiguate the matches and obtain potential matches set (PMS), relaxation technique is introduced in the following section. Here, pair $(\mathbf{p_1}, \mathbf{p_2})$ be regarded as a potential match if and only if $\mathbf{p_2}$ is the best candidate match of $\mathbf{p_1}$, and $\mathbf{p_1}$ also is the best candidate match of $\mathbf{p_2}$.

B) Relaxation labeling. The idea of relaxation technique is to use iterated local context updates to achieve a globally consistent result [18]. One of the key issues of relaxation algorithm is to design a valid cost function in order to control the convergence rate. Let $SM(\mathbf{p_1}_i, \mathbf{p_2}_j)$ be the strength of match $(\mathbf{p_1}_i, \mathbf{p_2}_j)$. Cost function $\boldsymbol{\varepsilon}$ is given by the average of strength of match (SM) as follows:

$$\boldsymbol{\varepsilon} = \frac{1}{N_t} \sum_{i,j=1}^{N_t} SM(\mathbf{p_1}_i, \mathbf{p_2}_j) \tag{1.5}$$

where N_t is the total number of matches in PMS, $\mathbf{p_1}_i$ represents the i-th point in the initial image, and $\mathbf{p_2}_j$ represents the j-th candidate match of $\mathbf{p_1}_i$.

Let $\mathcal{N}(\mathbf{p_1}_i)$ and $\mathcal{N}(\mathbf{p_2}_j)$ be the neighbors of point $\mathbf{p_1}_i$ and $\mathbf{p_2}_j$ within a circle, respectively. We expect many potential matches $(\mathbf{n_1}_k, \mathbf{n_2}_l)$ if and only if $(\mathbf{p_1}_i, \mathbf{p_2}_j)$ is a potential match, where $\mathbf{n_1}_k \in \mathcal{N}(\mathbf{p_1}_i)$ and $\mathbf{n_2}_l \in \mathcal{N}(\mathbf{p_2}_j)$. Otherwise, we expect only a few, or even none at all. Then, referring to the strength of match function proposed in [19], we define the SM function between $\mathbf{p_1}_i$ and $\mathbf{p_2}_j$ as:

$$SM(\mathbf{p_1}_i, \mathbf{p_2}_j) = cs(\mathbf{p_1}_i, \mathbf{p_2}_j) + \sum cs(\mathbf{n_1}_k, \mathbf{n_2}_l) \cdot e^{-\mathcal{J}(\mathbf{p_1}_i, \mathbf{p_2}_j; \mathbf{n_1}_k, \mathbf{n_2}_l)} \tag{1.6}$$

where the sum is computed over all $\mathbf{n_1}_k \in \mathcal{N}(\mathbf{p_1}_i)$ and $\mathbf{n_2}_l \in \mathcal{N}(\mathbf{p_2}_j)$.

Theoretically, if $(\mathbf{p_1}_i, \mathbf{p_2}_j)$ is a potential match, and that $(\mathbf{n_1}_k, \mathbf{n_2}_l)$ with $\mathbf{n_1}_k \in \mathcal{N}(\mathbf{p_1}_i)$ and $\mathbf{n_2}_l \in \mathcal{N}(\mathbf{p_2}_j)$ also is a potential match, then the following two are satisfied: *1)* the distance between $\mathbf{n_1}_k$ and $\mathbf{p_1}_i$ in the initial image should close or even equal to the distance between $\mathbf{n_2}_l$ and $\mathbf{p_2}_j$ in the deformed image, and *2)* the deformation direction of $\mathbf{p_1}_i$ should close or even identical to the deformation direction of $\mathbf{n_1}_k$, due to they are in a local region. Taking account of the above two in SM function, let us introduce the relative distance difference and direction constraint.

Let $d(\mathbf{p_1}_i, \mathbf{n_1}_k)$ be Euclidean distance between $\mathbf{p_1}_i$ and $\mathbf{n_1}_k$ in the initial image, $d(\mathbf{p_2}_j, \mathbf{n_2}_l)$ be Euclidean distance between $\mathbf{p_2}_j$ and $\mathbf{n_2}_l$ in the deformed image. According to [20], the relative distance difference $dist(\mathbf{p_1}_i, \mathbf{p_2}_j; \mathbf{n_1}_k, \mathbf{n_2}_l)$ between $d(\mathbf{p_1}_i, \mathbf{n_1}_k)$ and $d(\mathbf{p_2}_j, \mathbf{n_2}_l)$ is given by

$$dist(\mathbf{p_1}_i, \mathbf{p_2}_j; \mathbf{n_1}_k, \mathbf{n_2}_l) = 1 + \frac{2|d(\mathbf{p_1}_i, \mathbf{n_1}_k) - d(\mathbf{p_2}_j, \mathbf{n_2}_l)|}{d(\mathbf{p_1}_i, \mathbf{n_1}_k) + d(\mathbf{p_2}_j, \mathbf{n_2}_l)}. \tag{1.7}$$

Moreover, let notation $\overrightarrow{\mathbf{p_1}_i\mathbf{p_2}_j}$ be the vector from $\mathbf{p_1}_i$ to its corresponding position $\mathbf{p_2}_j$, $\overrightarrow{\mathbf{n_1}_k\mathbf{n_2}_l}$ be the vector form $\mathbf{n_1}_k$ to its corresponding position $\mathbf{n_2}_l$, and

$\mathcal{O}(\overrightarrow{\mathbf{p_{1}}_i\mathbf{p_2}_j}, \overrightarrow{\mathbf{n_{1}}_k\mathbf{n_2}_l})$ be the angle between vector $\overrightarrow{\mathbf{p_{1}}_i\mathbf{p_2}_j}$ and $\overrightarrow{\mathbf{n_{1}}_k\mathbf{n_2}_l}$. Then, the $\mathcal{O}(\overrightarrow{\mathbf{p_{1}}_i\mathbf{p_2}_j}, \overrightarrow{\mathbf{n_{1}}_k\mathbf{n_2}_l})$ is given by

$$\mathcal{O}(\overrightarrow{\mathbf{p_{1}}_i\mathbf{p_2}_j}, \overrightarrow{\mathbf{n_{1}}_k\mathbf{n_2}_l}) = 1 + \frac{1}{1+\cos\theta} \tag{1.8}$$

where θ represents the angle between vector $\overrightarrow{\mathbf{p_{1}}_i\mathbf{p_2}_j}$ and $\overrightarrow{\mathbf{n_{1}}_k\mathbf{n_2}_l}$.

So far, we have already obtained the relative distance difference factor $dist(\cdot)$ and deformation direction factor $\mathcal{O}(\cdot)$, the term $\mathcal{J}(\mathbf{n_{1}}_k, \mathbf{n_2}_l)$ in SM function (1.6) is then defined as

$$\mathcal{J}(\mathbf{p_{1}}_i, \mathbf{p_2}_j; \mathbf{n_{1}}_k, \mathbf{n_2}_l) = \mathcal{O}(\overrightarrow{\mathbf{p_{1}}_i\mathbf{p_2}_j}, \overrightarrow{\mathbf{n_{1}}_k\mathbf{n_2}_l}) \cdot dist(\mathbf{p_{1}}_i, \mathbf{p_2}_j; \mathbf{n_{1}}_k, \mathbf{n_2}_l). \tag{1.9}$$

It is noting that comparison with the similar SM function in [19]. This paper introduces the local deformation direction information to improve the robustness of SM function, especially, in the non-uniform heterogeneous object. Because the deformation direction are different in different regions, pairs' deformation direction close to the direction of candidate match must obtain larger weight for candidate match's SM computation, and vice versa. For example, in Figure 1.2, pairs $(\mathbf{n_{1}}_2, \mathbf{n_2}_2)$ and $(\mathbf{n_{1}}_3, \mathbf{n_2}_3)$ must obtain lower weight than the others in $SM(\mathbf{p_{1}}_i, \mathbf{p_2}_j)$ computation, since the deformation direction of these two pairs is opposite to that of the candidate match $(\mathbf{p_{1}}_i, \mathbf{p_2}_j)$.

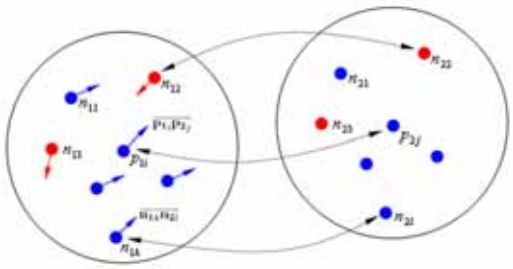

図 1.2: Pairs within neighbors of candidate match $(\mathbf{p_{1}}_i, \mathbf{p_2}_j)$

In this paper, we use the same relaxation labeling implementation procedure introduced in [17]. The result of performing the above feature matching algorithm is that a PMS is obtained, which will be used to measure local sparse deformation fields and to infer the dense interior deformation fields of a non-uniform object.

1.3.2 変形場の推定

We propose a Delaunay triangle based linear interpolation approach to obtain the dense deformation fields of an image. First, we use feature points in the initial (or deformed) MR image and obtain corresponding feature points in the PMS to construct Dealunay triangle net. The deformation fields of pixels inside a triangle are computed using the deformation fields of the triangle's nodes.

Let m be the number of triangles, $j = 0, 1, \cdots, m-1$ be the index of triangles, $k = 1, 2, 3$ be the node number of a triangle and $\mathcal{D}_{j,k}$ be displacement vector of the k-th node of triangle j. Then, $\mathcal{D}_{j,k}$ is given by

$$\mathcal{D}_{j,k} = \boldsymbol{\mathcal{R}}\mathbf{x}_{j,k} + \boldsymbol{\tau} - \mathbf{x}'_{j,k}, \tag{1.10}$$

where $\mathbf{x}_{j,k} = [x,\ y]^{\mathbf{T}}$ be the position of the k-th node of triangle j in the initial image, which corresponds the position vector in the deformed MR image $\mathbf{x}'_{j,k} = [x',\ y']^{\mathbf{T}}$. Let us define function w_k on triangle $\Delta(j)$. Assume that the area of the triangle is positive. Let $\mathbf{p}_i$ be an arbitrary point within the triangle $\Delta(j)$. The ratio between areas of $\Delta(\mathbf{p}_i, \mathbf{p}_{\bar{k}})$ and $\Delta(j)$ determines the function:

$$w_k = \frac{\Delta(\mathbf{p}_i, \mathbf{p}_{\bar{k}})}{\Delta(j)} \tag{1.11}$$

where $\Delta(\mathbf{p}_i, \mathbf{p}_{\bar{k}})$ represents the triangle consists of point $\mathbf{p}_i$ and two nodes except the k-th node of the triangle $\Delta(j)$. The displacement vector $\mathcal{D}_j$ of the pixels within triangle $\Delta(j)$ is given by

$$\mathcal{D}_j = \sum_{k=1}^{3} w_k \mathcal{D}_{j,k}. \tag{1.12}$$

1.4 実験結果

Several practical examples were designed to demonstrate the capabilities of the proposed approach. First, we applied the proposed approach to the MR images sampled from a volunteer's calf using an MRI scanner at different times and different status (initial and deformed). In both cases, FOV was 20×20 cm, and the slice gap was 2 mm. In this example, we selected two slices sampled at same location before and after deformation (Figure 1.3) as the input data and performed the proposed feature matching approach on them. To compare with the similar feature matching algorithm, we also applied the robust feature matching (RFM) algorithm proposed

7

表 1.1: Error of the checking points (NOTE: TPA, the proposed approach; FPS, feature points; ITs, iteration times; T, cost time in seconds.)

	FPS in initial	FPS in deformed	α	matches in PMS	ITs	T
TPA	200	240	\	72	101	5
RFM	200	240	10	63	101	5

by Chen [19] to the same data under same experiment conditions. Table 1.1 shows the numeric result of feature points matching using two approaches.

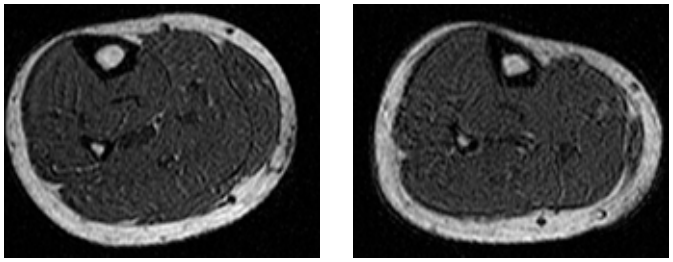

図 1.3: Input data of the exmaple (Left: Initial slice. Right:Deformed slice)

Table 1.1 indicates that the proposed approach can obtain more matches than RFM under the same conditions, in spite of it cost more time than RFM. The later results (Fig.1.5 and Table 1.2) show that the proposed approach has higher accuracy than RFM.

Secondly, to obtain the dense deformation fields, we calculated the sparse deformation fields correspond to the matches obtained previously using two approaches. Then, we constructed the irregular Delaunay triangle net, and performed the proposed linear interpolation approach to obtain the dense deformation fields. Figure 1.4 shows the delaunay triangle net and the dense deformation fields overlaid on the deformed slice. The delaunay triangle net was constructed using feature points obtained PMS. The deformation fields are obtained using the two set of sparse deformation fields introduced above. In Figure 1.4, the green color correspond to small deformation area, and yellow color correspond to the large deformation area.

Finally, to evaluate the reliability and precision of the estimated deformation field, we selected 10 obvious points (Figure 1.5(a)) which can be observed easily. Then, performing reverse movement using the invert deformation fields of obtained deformation fields on these check points, we observe if they can move back to the initial position in the initial slice. Figure 1.5(b) and (c) illustrate the movement result of

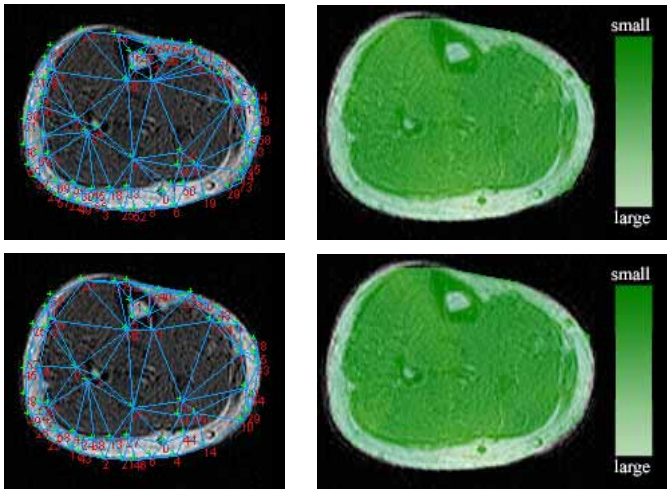

図 1.4: Inferred deformation fields (Left: Irregular Delaunay triangles. Right: Dense deformation fields overlaid on deformed slice. Top: result of the proposed approach. Down: result of RFM)

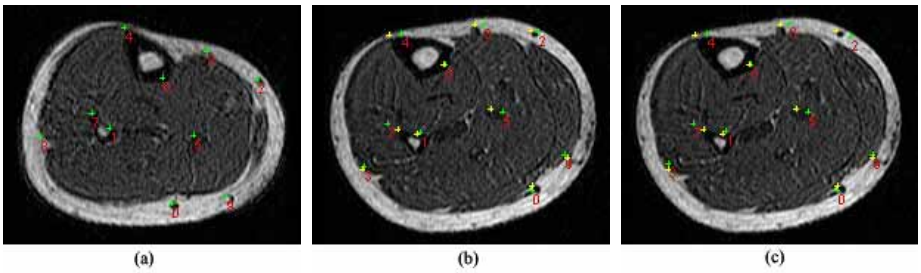

図 1.5: Deformation fields evaluation ((a) initial position of check points in deformed slice. (b) the reverse movement result using the deformation fields obtained by the proposed approach. (c) reverse movement result using the deformation fields obtained by RFM; Yellow cross, the original position of check points. Green cross, the reverse movement result of check points using dense deformation fields)

10 check points. In Figure 1.5(b) and (c), yellow cross illustrate the original position of check points, and green one illustrate the projections of reverse movement result of the check points in the deformed MR slice. As shown in Figure 1.4, most of the check points can go back to their original position in the two approaches, implying that the estimated deformation field is reliable. To evaluate the accuracy, the distance between the location of a check point after performing reverse movement and its actually original location is used to measure the error of the check point. Accordingly, the root mean square error (RMSE) of these check points also are computed to evaluate the accuracy of obtained deformation. Table 1.2 gives the error of selected 10 check points and RMSE, respectively. In Table 1.2, there are only two check points (4, 5 and 7) whose error over 0.2 in the proposed approach, but, there are four check points (2, 4, 5 and 7) whose error over 0.2 in RFM approach, this illustrate the deformation fields obtained using the proposed approach more reliable than that obtained using RFM. Moreover, the RMSE in Table 1.2 also reveals that there is evident improvement in the proposed approach compare to RFM approach.

表 1.2: Error of the checking points (NOTE: TPA, the proposed approach; EPi, error of the i-th point; the unit in the table is cm, $1cm \approx 30$ pixels)

	EP0	EP1	EP2	EP3	EP4	EP5	EP6	EP7	EP8	EP9	RMSE
TPA	0.105	0.074	0.170	0.100	0.242	0.242	0.000	0.314	0.199	0.120	0.396
RFM	0.105	0.074	0.328	0.167	0.242	0.242	0.000	0.314	0.170	0.100	0.417

1.5 結言

We proposed a feature matching-based approach to measure the deformation field from MR images. The proposed approach uses matched feature point pairs to measure the local deformation, then interpolates the deformation field of every pixel via the deformation field of nodes of Dealunay triangles constructed using the corresponding points. The preliminary experiment results reveal that the proposed approach is effective. Advantages of the proposed approach include:

1). Comparison with the existed non-rigid registration approach, the proposed approach can be use in both image registration and deformation measurement areas.

2). Comparison with deformable models which used in the deformation measurement, the proposed featuring matching-based approach can measure deformation not only on the contour of object, but also in the inner of object.

3). The feature matching based approach for deformation measurement does not need the initial contour of an object. This is independent of the shape of the initial contour.

4). The proposed approach is more suitable for dense deformation fields measurement of non-rigid non-uniform object, due to take into account the local deformation direction information.

However, limitations need to be further addressed include:

1). The accuracy of deformation fields depends on the number of feature pairs in PMS, sparse feature pairs usually lower the accuracy of deformation fields. Therefore,the proposed approach will not suitable for those data which cannot extract enough feature points.

2). False matches appeared in the PMS will affect the accuracy and reliable of obtained deformation fields. Therefore, good method needs to be proposed to remove false matches.

3D Feature extraction and matching

3D Feature extraction In the paper, we extend the 2D Harris corner operator to form a 3D operator for extracting 3D feature points (also called FPs). The extended operator was given by

$$\mathbf{M} = \begin{pmatrix} I_x^2 & I_xI_y & I_xI_z \\ I_xI_y & I_y^2 & I_yI_z \\ I_xI_z & I_yI_z & I_z^2 \end{pmatrix}, \; R_F = \frac{det(\mathbf{M})}{trace(\mathbf{M})}. \tag{1.13}$$

where k is an empirical constant, $det(\mathbf{M})$ and $trace(\mathbf{M})$ are the determinant and trace of the matrix $\mathbf{M}$, respectively. R_F serve as a response function of each voxel, if R_F of a voxel exceeds a given threshold, then the voxel may be a FP.

Correlation Score-based matching and iteration relaxation The basic idea of us is to perform similarity matching between feature point set (FPS) in the initial volume and FPS in the deformed volume based on correlation score. The result is that we obtain a many-to-many match set. Next, we define an energy function (Eq.1.14) to disambiguate matches iteratively.

$$\boldsymbol{\varepsilon} = \frac{1}{N}\sum_{i,j=1}^{N} SM(\mathbf{p_1}_i, \mathbf{p_2}_j) \tag{1.14}$$

where N is the total number of matched pairs in a potential matches set (PMS) at time t, $SM(\mathbf{p_1}_i, \mathbf{p_2}_j)$ defines the strength of match between $\mathbf{p_1}_i$ and $\mathbf{p_2}_j$.

Residual based SM For FPs in the initial volume, to find their corresponding feature points in the deformed volume, we develop a function named strength of matching (SM) to express the possibility of matching between two point sets. Let $\mathcal{N}(\mathbf{p_1}_i)$ and $\mathcal{N}(\mathbf{p_2}_j)$ be, respectively, the neighbors of $\mathbf{p_1}_i$ and $\mathbf{p_2}_j$, then we have

$$SM(\mathbf{p_1}_i, \mathbf{p_2}_j) = cs(\mathbf{p_1}_i, \mathbf{p_2}_j) + \alpha \sum_{k,l=1}^{s} \frac{cs(\mathbf{n_1}_k, \mathbf{n_2}_l) \cdot \eta(\mathbf{n_1}_k, \mathbf{n_2}_l)}{1 + diff(\mathbf{p_1}_i, \mathbf{p_2}_j; \mathbf{n_1}_k, \mathbf{n_2}_l)} \tag{1.15}$$

where s represents the total number of the potential matches in $\mathcal{N}(\mathbf{p_1}_i)$ and $\mathcal{N}(\mathbf{p_2}_j)$, balancing parameter α used to balance the weight during iteration, the contribution ratio of each potential matches $(\mathbf{n_1}_k, \mathbf{n_2}_l)$ is given by residual factor $\eta(\mathbf{n_1}_k, \mathbf{n_2}_l)$ and relative distance difference $diff(\mathbf{p_1}_i, \mathbf{p_2}_j; \mathbf{n_1}_k, \mathbf{n_2}_l)$. Where into, $\eta(\mathbf{n_1}_k, \mathbf{n_2}_l)$ can be

defined using *Gibbs distribution* of gray error (or residual) between points in a potential pair. Namely,

$$\eta(\mathbf{n_{1}}_k, \mathbf{n_{2}}_l) = \frac{1}{\mathcal{Z}(\mathbf{n_{1}}_k, \mathbf{n_{2}}_l)} \cdot \mathbf{exp}^{-\lambda \cdot \boldsymbol{\zeta}(\mathbf{n_{1}}_k, \mathbf{n_{2}}_l)} \tag{1.16}$$

where the notation $\boldsymbol{\zeta}(\mathbf{n_{1}}_k, \mathbf{n_{2}}_l)$ and $\mathcal{Z}(\mathbf{n_{1}}_k, \mathbf{n_{2}}_l)$ respectively represents the sum of gray error and its partition function (or normalizing constant) of the pair $(\mathbf{n_{1}}_k, \mathbf{n_{2}}_l)$. They are, respectively, given by

$$\boldsymbol{\zeta}(\mathbf{n_{1}}_k, \mathbf{n_{2}}_l) = \sum_{\mathbf{x}_{\mathbf{n_{1}}_k} \in \mathcal{N}} \mid g_{\mathbf{n_{1}}_k}(\mathbf{x}_{\mathbf{n_{1}}_k}) - g'_{\mathbf{n_{2}}_l}(\mathbf{x}_{\mathbf{n_{1}}_k}, \boldsymbol{\mathcal{R}}) \mid \tag{1.17}$$

$$\mathcal{Z}(\mathbf{n_{1}}_k, \mathbf{n_{2}}_l) = \sum_{k,l=1}^{s} \mathbf{exp}^{-\lambda \cdot \boldsymbol{\zeta}(\mathbf{n_{1}}_k, \mathbf{n_{2}}_l)} \tag{1.18}$$

In addition, $diff(\mathbf{p_{1}}_i, \mathbf{p_{2}}_j; \mathbf{n_{1}}_k, \mathbf{n_{2}}_l)$ is given by

$$diff(\mathbf{p_{1}}_i, \mathbf{p_{2}}_j; \mathbf{n_{1}}_k, \mathbf{n_{2}}_l) = \frac{d(\mathbf{p_{1}}_i, \mathbf{n_{1}}_k) - d(\mathbf{p_{2}}_j, \mathbf{n_{2}}_l)}{dist(\mathbf{p_{1}}_i, \mathbf{p_{2}}_j; \mathbf{n_{1}}_k, \mathbf{n_{2}}_l)} \tag{1.19}$$

where $dist(\mathbf{p_{1}}_i, \mathbf{p_{2}}_j; \mathbf{n_{1}}_k, \mathbf{n_{2}}_l)$ is the average distance between two pairs ($\mathbf{p}_s$, $\mathbf{n}_s$). Let us define the Euclidean distance between the pair of points $\mathbf{p}_s$ and $\mathbf{n}_s$ as

$$d(\mathbf{p}_s, \mathbf{n}_s) = \|\mathbf{p}_s - \mathbf{n}_s\|. \tag{1.20}$$

We then have

$$dist(\mathbf{p_{1}}_i, \mathbf{p_{2}}_j; \mathbf{n_{1}}_k, \mathbf{n_{2}}_l) = \frac{d(\mathbf{p_{1}}_i, \mathbf{n_{1}}_k) + d(\mathbf{p_{2}}_j, \mathbf{n_{2}}_l)}{2}. \tag{1.21}$$

Fig.1.6 shows the local deformation fields obtained using the approach in this section.

The experiment shows that the accuracy of matching is low. This because the gray error (or residual) between two points represents the similar property with the correlation score.

Direction-based SM Let $A^{\mathbf{n}\to\mathbf{n}'}_{\mathbf{p}\to\mathbf{p}'}$ be the angle between deformation fields $\mathbf{p} \to \mathbf{p}'$ and $\mathbf{n} \to \mathbf{n}'$, then, $A^{\mathbf{n}\to\mathbf{n}'}_{\mathbf{p}\to\mathbf{p}'}$ takes 0, 1, 2 or 3 corresponding to zero degrees, lower than 90 degrees, equal to 90 degrees and higher than 90 degrees, respectively. Normalizing the angle, we then have the direction constraint factor $\mathcal{O}(\cdot)$ of a potential match in $SM(\mathbf{p}, \mathbf{p}')$ as:

$$\mathcal{O}(\mathbf{n},\ \mathbf{n}') = A^{\mathbf{n}\to\mathbf{n}'}_{\mathbf{p}\to\mathbf{p}'}/3. \tag{1.22}$$

13

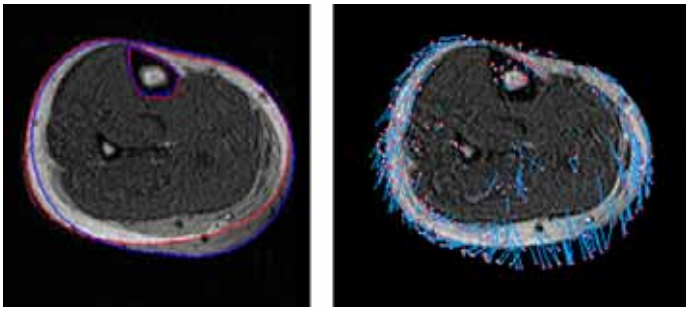

(a)Deformed slice overlaid on the initial slice (b)The projection of 3D deformation field on 2D plane

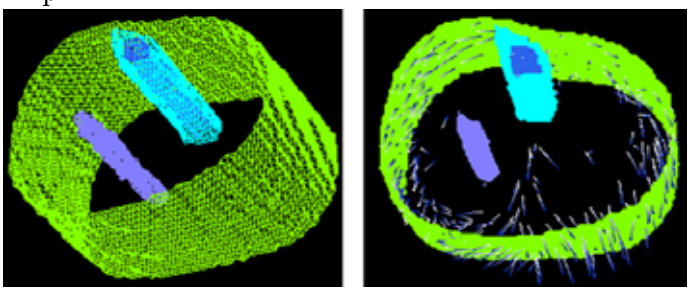

(c)Mesh model (d)3D local deformation field

図 1.6: Original MR volumetric image

Thus, we define a SM function with direction constraint as:

$$SM(\mathbf{p}_i, \mathbf{p}'_j) = cs(\mathbf{p}_i, \mathbf{p}'_j) + \alpha \sum_{k=1}^{s} cs(\mathbf{n}_k, \mathbf{n}'_k) \cdot w_{(\mathbf{n}_k,\ \mathbf{n}'_k)} \tag{1.23}$$

where $w_{(\mathbf{n}_k,\ \mathbf{n}'_k)}$ integrates the direction consistency and relative distance of potential matches $(\mathbf{n},\ \mathbf{n}')$ within $\mathcal{N}(\mathbf{p}_i, \mathbf{p}'_j)$, which is given by

$$w_{(\mathbf{n}_k,\ \mathbf{n}'_k)} = \exp(-\mathcal{J}_k), \quad k = 1,\ 2, \cdots, n \tag{1.24}$$

with notation

$$\mathcal{J}_k = \begin{cases} diff(\mathbf{p}_i, \mathbf{p}'_j; \mathbf{n}_k, \mathbf{n}'_k) & \text{if } \mathcal{O}(\mathbf{n}_k,\ \mathbf{n}'_k) = 0 \\ \mathcal{O}(\mathbf{n}_k,\ \mathbf{n}'_k) \cdot diff(\mathbf{p}_i, \mathbf{p}'_j; \mathbf{n}_k, \mathbf{n}'_k) & \text{otherwise} \end{cases}$$

where $diff(\cdot)$ represents the relative distance between $\mathbf{n}_k \Leftrightarrow \mathbf{p}_i$ and $\mathbf{n}'_k \Leftrightarrow \mathbf{p}'_j$.

14

Interior Deformation Fields Measurement

This section introduce how to obtain the interior dense deformation fields using the potential matches obtained in the stage of matching. The concise idea of us is: (1) use point matches in the PMS to measure the local displacement correspond to the location where point lies in. (2) use the points in the PMS to reconstruct irregular FE model of non-rigid object. (3) use the local displacement to infer the dense deformation fields in a tetrahedron.

Sparse local deformation fields measurement Let $\mathcal{D}$ be the displacement of a voxel before and after movement, $\mathbf{x}_1 = (x_1,\ y_1,\ z_1)$ and $\mathbf{x}_2 = (x_2,\ y_2,\ z_2)$ be the coordinate of the voxel in the initial and final MR volumetric image, respectively. Then, the displacement of a voxel is defined using the Euclidean distance between the voxel and its homologous point (Eq.1.25).

$$\mathcal{D} = \|\mathcal{R}(\mathbf{x}_1) - \mathbf{x}_2\| \tag{1.25}$$

where $\mathcal{R}(\cdot)$ represents the rotation transformation between the initial and the final MR volumetric images.

Here, we note that the translation transformation between two volumes isn't considered in the Eq.(1.25). This is because the translation between the initial and final MR volumetric image never affects the deformation of a nonrigid object. Thus, we don't have to consider translation but the rotation.

Through the above computation, we yield a displacement vector $\mathbf{u}_i = [dx,\ dy,\ dz]^{\mathbf{T}}$ at each FEM node within the model. Displacement $\mathbf{u}_i$ on a tetrahedron node will be used to approximate the displacement of a voxel inside the tetrahedron.

Finite Element Model Reconstruction To obtain interior dense deformation using finite element model (FEM), the finite element (FE) model of a non-rigid object need to be reconstructed using irregular tetrahedra. Since the model will be used to approximate the interior deformation fields, we use FPs in the PMS as the node of an FE model, then, use the extension Delaunay triangulation algorithm to form the irregular tetrahedron model. For instance, Fig.1.7 shows a FE model of part human calf.

Inferring Interior Dense Deformation Fields To obtain the inner dense deformation fields, we propose a piecewise linear approximation based on a 3D finite

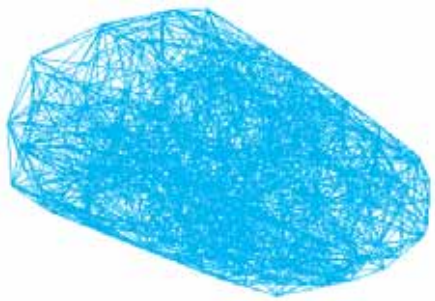

図 1.7: Irregular tetrahedron model of part of human calf

element method. For a tetrahedron $\diamondsuit P_i P_j P_k P_l$ within the model, let P_i be a nodal point of the tetrahedron, and $[x_i, y_i, z_i]^{\mathsf{T}}$ be coordinates of point P_i. Then, the signed volume of tetrahedron $\diamondsuit P_i P_j P_k P_l$ is given by

$$\diamondsuit P_i P_j P_k P_l = \frac{1}{3!} \begin{vmatrix} x_i & y_i & z_i & 1 \\ x_j & y_j & z_j & 1 \\ x_k & y_k & z_k & 1 \\ x_l & y_l & z_l & 1 \end{vmatrix} \tag{1.26}$$

Thus, for a volume voxel P at $\mathbf{x} = (x, y, z)$ lying anywhere within an arbitrary tetrahedron $\diamondsuit P_i P_j P_k P_l$ of the model, its displacement may be approximated by weighting the finite element's node displacements $\mathbf{u}_i$ by their shape function

$$\mathbf{u}(\mathbf{x}) = \sum_{n=1}^{4} \mathbf{u}_n N_n \tag{1.27}$$

where N_i is the shape function of nodal $n = (i, j, k, l)$, which is given by

$$N_n = \frac{\diamondsuit P P_j P_k P_l}{\diamondsuit P_i P_j P_k P_l}, \tag{1.28}$$

Hence, approximation displacements for all voxels $\mathbf{x}_i$ in the volume are obtained.

Experiments and Results

Some practical examples were designed to demonstrate the capabilities of the proposed approach.

In experiments, all MR volumetric images were sampled from one volunteer's calf using an MR scanner under initial and deformed cases. The initial and deformed

data were sampled from the same location of the volunteer's calf. Both the initial and deformed MR volumetric images were of FOV 20×20 cm and slice gaps of 2 mm. To ensure the sufficient resolution along the z-axis, we performed linear interpolation between each two initial slices. As a result, we obtained $256 \times 256 \times 57$ voxels of initial and deformed MR volumetric images respectively. Figure 1.8 illustrates the volume visualization result of the data used in the experiments.

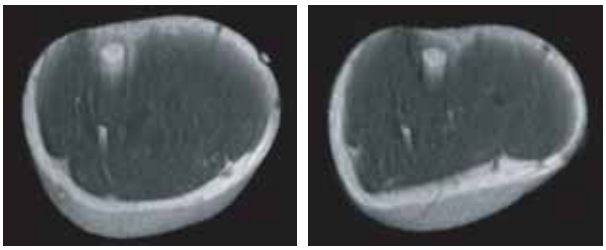

図 1.8: Original volumes used in the experiment (left: initial volume, right: deformed volume)

To indicate the validity of the proposed approache, we compared our feature matching algorithm with the homologous approach suggested in [19]. All the experimental results presented below are based on the PMS obtained using these two feature matching approaches. Table 1.3 show the results obtained using different feature matching methods. Figure 1.9 shows the local sparse displacement of each FEM node.

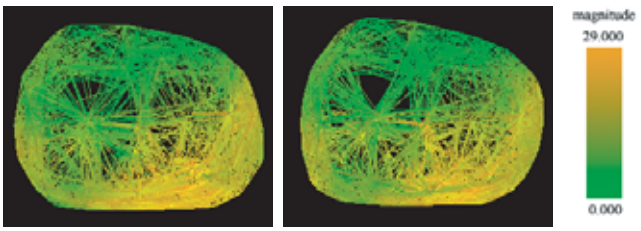

図 1.9: Displacement of an FEM node (Left: PMS obtained using the proposed method, there are 4344 tetrahedra in total; Right:PMS obtained using the method proposed in [19], there are 4798 tetrahedra in total)

Figure 1.10 illustrates the visualization result of dense deformation fields. Here, the dense deformation vector fields are first computed using the above linear approximation approach by our own software, then, it is saved into a file as MetaImage

表 1.3: Comparison result for different feature matching approaches

Approaches	PNs in IV	PNs in FV	PMS	Tetrahedrons	RMS
this paper	1000	5000	771	4344	26.00
RPFM	1000	5000	827	4798	26.35

(PNs: Point numbers;IV: Initial volume; FV: Deformed volume; RFM: Robust point feature matching, proposed by G.Q. Chen in 2001.)

format and visualized in free software Paraview. To facilitate observation of the inner deformation of different regions, only 30000 vectors are shown in the figure.

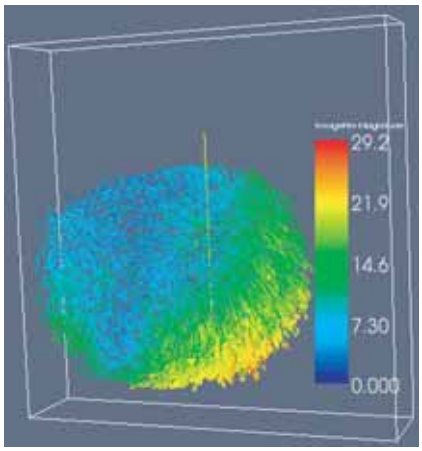

図 1.10: Dense deformation fields (Deformation magnitudes are mapped using rainbow color coding, with dark blue corresponding to 0-pixel, and dark red corresponding to 30-pixels deformation magnitude.)

To evaluate the accuracy of the deformation fields, the evaluation approach suggested in [22] is used in our experiment. That approach uses the root mean squared (RMS) of residual differences (Eq. 1.29) to evaluate the quality of the registration result using deformation fields.

$$\mathbf{E_{RMS}} = \sqrt{\frac{1}{N}\sum_{\mathbf{x}\in\Omega}(I_a(\mathbf{x}) - I_r(\mathbf{x}))^2} \tag{1.29}$$

In implementation, we deform the initial volume to obtain a computation deformation volume using measured dense deformation fields. Thereafter, an RMS algorithm

is applied between the actual deformed volume and two computation results. Table 1.10 gives the comparison results. It is noted that, due to rotation and translation transformation along the z-axis, after resampling, some slices are out of the boundary of z. Thus, in this experiment, slices from 10 to 50 are used to compute $\mathbf{E_{RMS}}$.

19

A Method for Non-rigid 3D Deformation Fields Measurement: Application to Human Calf MR Volumetric Images

Penglin Zhang, Shinichi Hirai and Kazumi Endo

Abstract— **This work is concerned with inner deformation fields measurement of non-rigid non-uniform objects from 3D Magnetic Resonance (MR) volumetric images. In order to obtain dense deformation fields of non-uniform objects, an improved robust feature matching algorithm is presented and used to obtain a matching feature point set which is the foundation of sparse local deformation fields measurement. Inner dense deformation fields can then be inferred using a linear approximate approach in an irregular tetrahedra finite element model. To test the validity of this proposed method, some experiments were designed and conducted for this paper.**

I. INTRODUCTION

Since its initial use for human imaging over 20 years ago, magnetic resonance imaging (MRI) has become a widely used clinical imaging modality [1]. MRI is being increasingly employed in biomedical applications. Accordingly, MR image processing techniques have become a central issue in biomedical applications. However, most studies over the past decades have focused on MR image segmentation, registration and reconstruction, with biological tissue deformation measurement and physical parameter estimation being investigated in only a few studies.

With an ever increasing application of biomedical imaging, it is becoming more important for computer-assisted clinical diagnosis, surgery simulation and operation planning to acquire knowledge regarding the motion and deformation of biological tissue. In addition, there is much focus on the physical characteristics of tissues. In the past decade, there has been much research involving deformation measurements from MR volumetric images using elastic deformable models [2] [3] [4]. In general, deformable models can be classified into two categories: parametric and geometric active models [5]. The parametric active contours, also called snakes, were first introduced by Kass, Witkin and Terzopoulos in 1987 [6]. They were widely used in deformation estimation, segmentation, motion tracking and registration of biomedical images. Later, many researchers expanded and developed their own approaches based on this work. Lang et al. [7], Cho et al. [3] and Matuszewski et al. [2] proposed estimating the deformation of the object based on the parametric active contours. Their general idea of parametric active contours is to first define an energy function in which the local minimum is obtained at the boundary of the object, and then to try to minimise the designed function to deform a given initial contour toward the boundary of the object to obtain deformation fields of the object.

The geometric active model was first proposed by Caselles et al. [8]. Malladi et al. [9], Caselles [10] and Chenoune et al. [5] developed different aspects of this method, but their geometric partial differential equations were proposed by Caselles et al. [8]. They used the propagation of curves and surfaces for boundary detection and motion tracking.

Although the deformable model algorithm has undergone significant development, some problems still remain. The energy model of parametric active contours is not capable of handling changes in the topology of the evolving contours when direct implementations are performed, and special, often heuristic, topology handling procedures must be used [10]. The geometric active contours do not work well for objects that have poor contrast. That is, when the object boundary is indistinct or has gaps, the contours tend to leak through the boundary [11]. In addition, it is difficult to characterise the global shape of an object with the geometric active contour algorithm.

To avoid the problems associated with the deformable model algorithm, we propose a feature tracking-based approach first to measure sparse local deformation of a non uniform non-rigid object from biomedical MR volumetric images. In our method, we automatically extract the high curvature feature points (also called points of interest) from the initial MR volumetric image, then, use the proposed matching approach to obtain their homologous positions in the final MR volumetric image. Finally, the dense deformation fields of the nonrigid non-uniform object are computed using a linear approximation approach.

This paper is organised as follows. Section 2 describes feature extraction and matching. Section 3 introduces inference of the dense deformation fields using the FF Method. Section 4 presents examples and the results of experiments. Section 5 presents a conclusion regarding the proposed approach.

II. FEATURE EXTRACTION AND MATCHING

A feature point is one of the most important factors in the present application. It is often used in various areas related to measurements based on computer vision. In this paper, the feature point matching based approach is used to obtain sparse local deformation fields of a nonrigid non-uniform object. Briefly, we first extract a certain number of feature points from the initial MR volumetric image and then match their homologous points in the final MR volumetric

Penglin Zhang is with the Faculty of Science and Engineering / School of Remote Sensing and Information Engineering, University of Ritsumeikan / University of Wuhan, 525-8577 Kusatsu, Japan zpl@se.ritsumei.ac.jp

Shinichi Hirai and Kazumi Endo are with the Faculty of Science and Engineering, Robotics, University of Ritsumeikan, 525-8577 Kusatsu, Japan hirai@se.ritsumei.ac.jp

image. The displacements corresponding to feature points are thus measured using their positions in the initial and final volumetric images, respectively. Here, high curvature points and edge points in the MR volumetric image are defined as feature points (FPS).

A. Feature Extraction

In order to automatically pre-extract a certain number of FPS, we extend the 2D Harris operator [12] to form a 3D operator. We thus obtain an auto-correlation matrix $\mathbf{M}$ of 3D operator, which is given by

$$\mathbf{G} \otimes \mathbf{M} = \mathbf{G} \otimes \begin{pmatrix} I_x^2 & I_x I_y & I_x I_z \\ I_x I_y & I_y^2 & I_y I_z \\ I_x I_z & I_y I_z & I_z^2 \end{pmatrix} \quad (1)$$

with eigenvector $\lambda = [\lambda_1, \lambda_2, \lambda_3]$. Where I_x, I_y and I_z are computed by convolving the image with a gradient template along the $x-$, $y-$ and $z-$axes. The Gaussian template $\mathbf{G}$ reduces the influence of noise. Since the eigenvector λ represents the principle curvature along $x-$, $y-$ and $z-$axes, we define response function R_F as

$$R_F = det(\mathbf{M}) - k * (trace(\mathbf{M}))^2 \quad (2)$$

where k is an empirical constant ($k = 0.04\ to\ 0.06$ from Harris's suggestion), $det(\mathbf{M})$ and $trace(\mathbf{M})$ are the determinant and trace of the matrix $\mathbf{M}$, respectively. Voxels whose R_F exceeds a given threshold will be regarded as FPS. From Eq.(2), we find that the selected empirical constant k affects the matching result. Thus, to avoid the influence of an improper k, in implementation, the response function also can be defined as

$$R_F = \frac{det(\mathbf{M})}{trace(\mathbf{M})}. \quad (3)$$

B. Feature Matching

Feature matching is the foundation of our approach. The outcome may determine the accuracy of later obtained deformation fields. Our feature matching method consists of two steps: First, we perform an initial matching process using a correlation score between two cube regions around a point pair. Next, the relaxation technique is used to disambiguate matches and to obtain a potential match set (PMS). In fact, this idea is similar to the method proposed by [13] and [14]. Namely, use of a homologous algorithm.

Here, we do not describe the initial matching process as the correlation tool is a very popular algorithm used in various areas. In the course of relaxation, the cost function is defined as the average of strength of matches (SM), see [13]. The SM of a pair depends on its own correlation score $cs(\cdot)$ and the influence factor of potential matches within its neighborhood. The influence factor of potential matches includes the correlation score, residual and relative distance.

However, in later practice, we note that direction consistency of deformation fields corresponding to potential matches within the neighborhood of a given match $m(\mathbf{p}, \mathbf{p}')$ would be more important for $SM(\mathbf{p}, \mathbf{p}')$ than its residual. This is mainly because the residual is likely to be affected by noise, whereas direction will not. Moreover, in spite of the direction of deformation fields (DODF) of non-rigid non-uniform objects being inconsistent, they are usually consistent within a local region. Therefore, if $m(\mathbf{p}_i, \mathbf{p}'_j)$ is a potential match, then its corresponding DODF must be consistent with the DODF corresponding to the potential matches within its neighborhood. In other words, if match $m(\mathbf{p}, \mathbf{p}')$ is a good match, we expect to see more potential matches within its neighborhood $\mathcal{N}(\mathbf{p}, \mathbf{p}')$, whose corresponding DODF are consistent. On the contrary, we expect to see only a few such matches, or even none at all, in their neighborhood.

Based on this idea, different to the pre-existing work, in this paper, we use DODF corresponding to feature point matches as a constraint to improve the robustness of the point matching algorithm, especially when it is used for a non-rigid non-uniform object. In this way, we yield

$$SM(\mathbf{p}_i, \mathbf{p}'_j) = cs(\mathbf{p}_i, \mathbf{p}'_j) + \alpha \sum_{k=1}^{s} cs(\mathbf{n}_k, \mathbf{n}'_k) \cdot w_{(\mathbf{n}_k,\ \mathbf{n}'_k)} \quad (4)$$

where $w_{(\mathbf{n}_k,\ \mathbf{n}'_k)}$ integrates the direction consistency and relative distance of potential matches $(\mathbf{n},\ \mathbf{n}')$ within $\mathcal{N}(\mathbf{p}_i, \mathbf{p}'_j)$, which is given by

$$w_{(\mathbf{n}_k,\ \mathbf{n}'_k)} = \exp(-\mathcal{J}_k), \quad k = 1,\ 2, \cdots, n \quad (5)$$

with notation

$$\mathcal{J}_k = \begin{cases} diff(\mathbf{p}_i, \mathbf{p}'_j; \mathbf{n}_k, \mathbf{n}'_k) & \text{if } \mathcal{O}(\mathbf{n}_k,\ \mathbf{n}'_k) = 0 \\ \mathcal{O}(\mathbf{n}_k,\ \mathbf{n}'_k) \cdot diff(\mathbf{p}_i, \mathbf{p}'_j; \mathbf{n}_k, \mathbf{n}'_k) & \text{otherwise} \end{cases}$$

where $diff(\cdot)$ represents the relative distance between $\mathbf{n}_k \Leftrightarrow \mathbf{p}_i$ and $\mathbf{n}'_k \Leftrightarrow \mathbf{p}'_j$, and $\mathcal{O}(\cdot)$ represents the constraint of the direction of potential matches. Let start position of a deformation field be the origin of Cartesian space, then, its direction can be approximated to 8 states in 2D case or 26 states in 3D case, respectively, as shown in Figure 1.

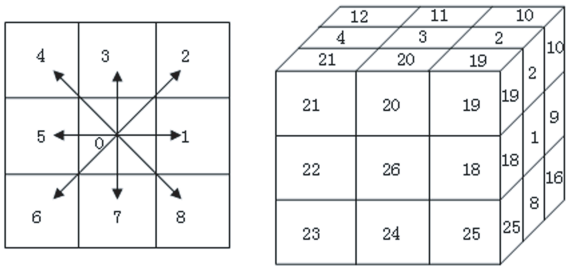

Fig. 1. The direction of deformation field (left: 2D case, right: 3D case)

Let notation $\phi_{\mathbf{p}\to\mathbf{p}'}$ be the DODF corresponding to the deformation $\mathbf{p} \to \mathbf{p}'$, then we have

$$\phi_{\mathbf{p}\to\mathbf{p}'} = \{\alpha \mid \alpha = 1,\ 2,\ 3\ , ...,\ 26\} \quad (6)$$

where notation $\mathbf{p} \to \mathbf{p}'$ represents the deformation caused by $\mathbf{p}$ moving to $\mathbf{p}'$.

Furthermore, let $A^{\mathbf{n}\to\mathbf{n}'}_{\mathbf{p}\to\mathbf{p}'}$ be the angle between $\mathbf{p} \to \mathbf{p}'$ and $\mathbf{n} \to \mathbf{n}'$, and $A^{\mathbf{n}\to\mathbf{n}'}_{\mathbf{p}\to\mathbf{p}'}$ takes 0, 1, 2 or 3 corresponding

to zero degrees, lower than 90 degrees, equal to 90 degrees and higher than 90 degrees, respectively, Then, the direction constraint factor $\mathcal{O}(\cdot)$ of a potential match in $SM(\mathbf{p}, \mathbf{p}')$ computation is defined as

$$\mathcal{O}(\mathbf{n},\ \mathbf{n}') = A^{\mathbf{n}\to\mathbf{n}'}_{\mathbf{p}\to\mathbf{p}'}/3. \tag{7}$$

The result of performing the above feature matching algorithm is that a PMS is obtained, which will be used to measure local sparse deformation fields and to infer the dense interior deformation fields of a non-uniform object.

III. Inferring Dense Deformation Fields Using the FE Method

In order to obtain dense interior deformation fields, an approximation approach using an FE model will be considered in this paper.

A. FE Modeling

As the first step of obtaining dense deformation fields, a finite element (FE) model of an object should be built using irregular tetrahedra. Here, since the model will be used to approximate the interior deformation fields, we use FPS from the PMS as the input in an FE model. The irregular tetrahedron algorithm used in FE modeling actually is an extension of the Delaunay triangulation irregular network (TIN) in 3D case, in brief it is given by the following pseudo code.

Begin

$N \leftarrow$ *the number of FPS in the initial volume*;
$j \leftarrow 0$; // The number of formed tetrahedrons.
Empty the **Triangle_List**; // List of triangles which consist of tetrahedrons.
for$(i = 0$ *to* $N)$
  Searching 3 FPS $\Rightarrow$ *first triangle*; //The triangle //must satisfy the properties of Delaunay TIN.
for$(i = 0$ *to* $N)$
{
  if (*The points satisfy the* **D_properties**) Then
  {
    Form first tetrahedron;
    Triangle_List $\leftarrow$ *three new triangles*;
    $j \leftarrow j + 1$;
  }
}
while (**Triangle_List** *isn't empty*)
{
  Pop a triangle from Triangle_List;
  for$(i = 0$ *to* $N)$
  {
    if(*The points satisfy the* **D_properties**) Then
    {
      Form a new tetrahedron;
      if (*triangles are not in the Triangle_List*);
        Triangle_List $\leftarrow$ *triangles*;
      $j \leftarrow j + 1$;
    }
}

End.

The notation **D_properties**, represents properties which must be satisfied in the course of modeling a tetrahedron by using a point and a triangle. These properties include: (1) The circum-sphere of a tetrahedron formed by the point and triangle must be empty. In other words, it must not contain other nodes apart from the four nodes of the formed tetrahedron. (2) The distance from a circum-sphere center to the triangle must be the minimum of all circum-spheres which may be constructed using the triangle and points.

Figure 2 illustrates the irregular tetrahedra FE model of part of a human calf.

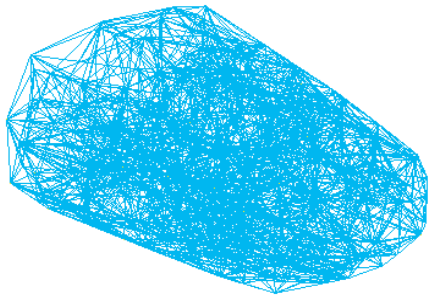

Fig. 2. Irregular tetrahedron model of part of human calf

B. Sparse local displacement measurement

Let $\mathcal{D}$ be the displacement of a voxel before and after movement, $\mathbf{x}_1 = (x_1,\ y_1,\ z_1)$ and $\mathbf{x}_2 = (x_2,\ y_2,\ z_2)$ be the coordinate of the voxel in the initial and final MR volumetric image, respectively. Then, the displacement of a voxel is defined using the Euclidean distance between the voxel and its homologous point (Eq.8).

$$\mathcal{D} = \|\mathcal{R}(\mathbf{x}_1) - \mathbf{x}_2\| \tag{8}$$

where $\mathcal{R}(\cdot)$ represents the rotation transformation between the initial and the final MR volumetric images. In this paper, $\mathcal{R}(\cdot)$ is calculated using the unit quaternion proposed by Horn [15].

Here, we note that the translation transformation between two volumes isn't considered in the Eq.(8). This is because the translation between the initial and final MR volumetric image never affects the deformation of a nonrigid object. Thus, we don't have to consider translation but the rotation.

Through the above computation, we yield a displacement vector $\mathbf{u}_i = [dx,\ dy,\ dz]^{\mathbf{T}}$ at each FEM node within the model. Displacement $\mathbf{u}_i$ on a tetrahedron node will be used to approximate the displacement of a voxel inside the tetrahedron.

C. FE displacement

To obtain the inner dense deformation fields, we propose a piecewise linear approximation based on a 3D finite element method.

For a tetrahedron $\diamondsuit P_iP_jP_kP_l$ within the model, let P_i be a nodal point of the tetrahedron, and $[x_i, y_i, z_i]^{\mathsf{T}}$ be coordinates of point P_i. Then, the signed volume of tetrahedron $\diamondsuit P_iP_jP_kP_l$ is given by

$$\diamondsuit P_iP_jP_kP_l = \frac{1}{3!}\begin{vmatrix} x_i & y_i & z_i & 1 \\ x_j & y_j & z_j & 1 \\ x_k & y_k & z_k & 1 \\ x_l & y_l & z_l & 1 \end{vmatrix} \tag{9}$$

Thus, for a volume voxel P at $\mathbf{x} = (x, y, z)$ lying anywhere within an arbitrary tetrahedron $\diamondsuit P_iP_jP_kP_l$ of the model, its displacement may be approximated by weighting the finite element's node displacements $\mathbf{u}_i$ by their shape function

$$\mathbf{u}(\mathbf{x}) = \sum_{n=1}^{4} \mathbf{u}_n N_n \tag{10}$$

where N_i is the shape function of nodal $n = (i, j, k, l)$, which is given by

$$N_n = \frac{\diamondsuit P P_jP_kP_l}{\diamondsuit P_iP_jP_kP_l}, \tag{11}$$

Hence, approximation displacements for all voxels $\mathbf{x}_i$ in the volume are obtained.

IV. Experiments and Results

Some practical examples were designed to demonstrate the capabilities of the proposed approach. All experiments were carried out using our own software developed using Visual C++, which runs on Microsoft Windows XP. And all experimental results described below were obtained on a Dell PC with a 2.80 GHz Intel Pentium D CPU and 1 GB of RAM.

In experiments, all MR volumetric images were sampled from one volunteer's calf using an MR scanner under initial and deformed cases. The initial and deformed data were sampled from the same location of the volunteer's calf. Both the initial and deformed MR volumetric images were of FOV 20×20 cm and slice gaps of 2 mm. To ensure the sufficient resolution along the z-axis, we performed linear interpolation between each two initial slices. As a result, we obtained $256 \times 256 \times 57$ voxels of initial and deformed MR volumetric images respectively. Figure 3 illustrates the volume visualization result of the data used in the experiments.

Since feature matching plays a key role in the proposed method, we compared our feature matching algorithm with the homologous approach suggested by George.Q.Chen in [14]. All the experimental results presented below are based on the PMS obtained using these two feature matching approaches.

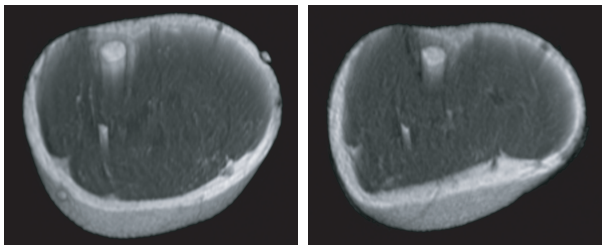

Fig. 3. Original volumes used in the experiment (left: initial volume, right: deformed volume)

Feature matching is the first phase of deformation fields measurement. In this phase, the size of a match cube is set as $9 \times 9 \times 3$ pixels. Whereas, the size of a search cube is dynamic varies depending on the distance of the feature point far from the moment center of the slice which the feature point lies on. The initial size of a search cube is set as $17 \times 17 \times 3$ voxels. Table I show the results obtained using different feature matching methods.

After obtaining PMS, a finite element model of a nonrigid object is reconstructed accordingly, and the displacements of all nodes in the model are also computed by using approaches introduced in section III. Figure 4 shows the displacement of each FEM node.

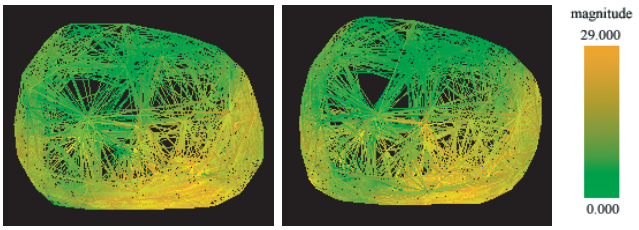

Fig. 4. Displacement of an FEM node (Left: PMS obtained using the proposed method, there are 4344 tetrahedra in total; Right:PMS obtained using the method proposed in [14], there are 4798 tetrahedra in total)

Figure 5 illustrates the visualization result of dense deformation fields. Here, the dense deformation vector fields are first computed using the above linear approximation approach by our own software, then, it is saved into a file as MetaImage format and visualized in free software Paraview. To facilitate observation of the inner deformation of different regions, only 30000 vectors are shown in the figure.

To evaluate the accuracy of the deformation fields, the evaluation approach suggested in [16] is used in our experiment. That approach uses the root mean squared (RMS) of residual differences (Eq. 12) to evaluate the quality of the

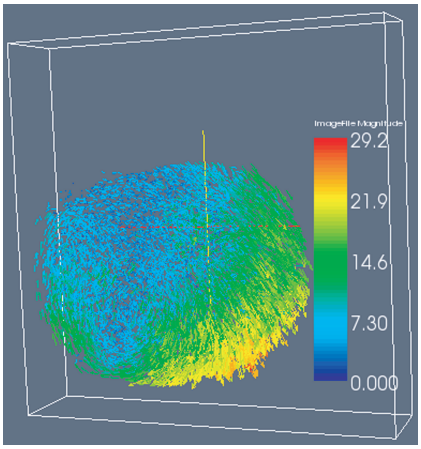

Fig. 5. Dense deformation fields (Deformation magnitudes are mapped using rainbow color coding, with dark blue corresponding to 0 mm, and dark red corresponding to 30-mm deformation magnitude.)

registration result using deformation fields.

$$\mathbf{E_{RMS}} = \sqrt{\frac{1}{N}\sum_{\mathbf{x}\in\Omega}(I_a(\mathbf{x}) - I_r(\mathbf{x}))^2} \qquad (12)$$

In implementation, we deform the initial volume to obtain a computation deformation volume using measured dense deformation fields. Thereafter, an RMS algorithm is applied between the actual deformed volume and two computation results. Table I gives the comparison results. It is noted that, due to rotation and translation transformation along the z-axis, after resampling, some slices are out of the boundary of z. Thus, in this experiment, slices from 10 to 50 are used to compute $\mathbf{E_{RMS}}$.

Finally, to observe if the deformation fields are valid or not, Figure 6 presents images of the calf part actual deformation slices, computation slices and the differences between them. The computation slices were re-sampled results of the initial volume dependent on the measured dense deformation fields.

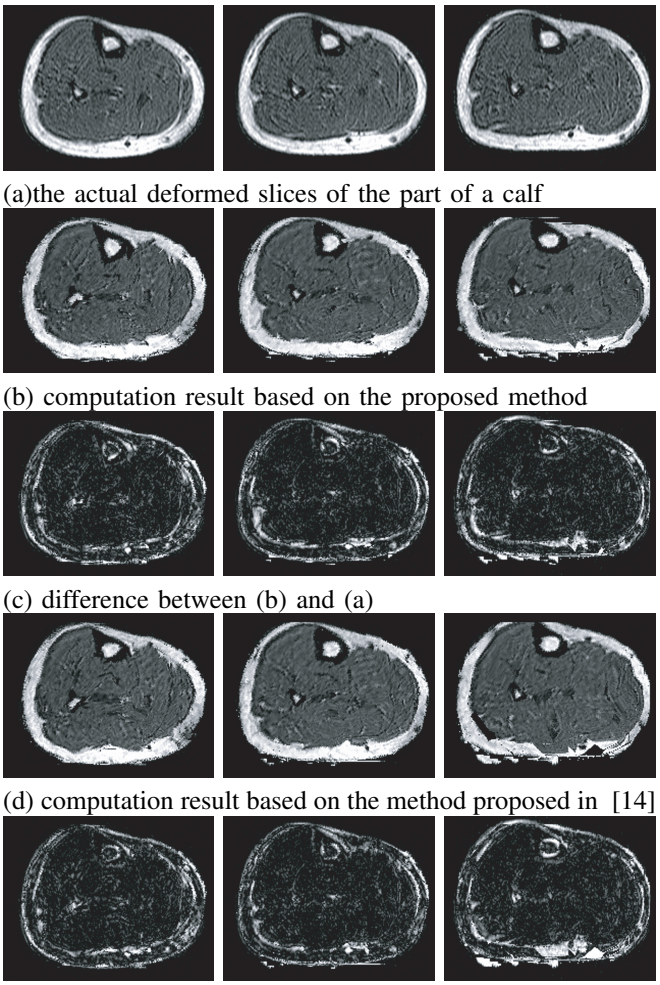

(a)the actual deformed slices of the part of a calf

(b) computation result based on the proposed method

(c) difference between (b) and (a)

(d) computation result based on the method proposed in [14]

(e) difference between (d) and (a)

Fig. 6. Resample and Difference (From left to right, slice numbers are 15, 30 and 45, respectively)

V. CONCLUSIONS AND FUTURE WORK

A. Conclusions

This paper proposed a feature match based approach to measure the deformation fields of a non-uniform nonrigid object from 3D MR volumetric images. Main contributions include:

(1) Presentation of a new approach in feature matching based deformation fields measurement from MR volumetric images. Different from many registration approaches currently used to measure deformation fields, this paper proposed inferring dense deformation fields dependent on the sparse local deformation fields corresponding to the feature points in the MR volumetric image. The advantages include:(a)The computation cost of finite feature points is lower than that of voxel-by-voxel as used by most registration approaches. (b)The proposed approach is noise insensitive compared with traditional registration approaches.

(2) Improvement to the robustness of a feature matching algorithm for a nonrigid non-uniform object, local direction consistency and relative distance are introduced into the feature matching algorithm as constraints, making the algorithm more suitable for application to nonrigid objects than originally proposed in [13] and [14].

Our preliminary experimental results shown in section IV

TABLE I

COMPARISON RESULT FOR DIFFERENT FEATURE MATCHING APPROACHES

Approaches	Point Numbers in IV	Point Numbers in FV	Potential Matches	Tetrahedra	RMS
Approach in this paper	1000	5000	771	4344	26.004284253441
Approach in [14]	1000	5000	827	4798	26.351873220353

(IV: Initial volume; FV: Deformed volume.)

reveal that the improved feature matching method is efficient. Moreover, the differences between the actual slices and the computation slices (Figure 6) indicate that we can deform the initial volume to the deformation volume using obtained deformation fields. It further reveals that the deformation fields are valid.

Further improvement includes applying the proposed approach to other data-sets in order to further test the robustness of this method.

B. Future Works

Physical parameters estimation is our final goal. Thus our next work should be to estimate the physical parameters of non-rigid non-uniform objects based on the Finite Element Model (FEM) shown in Eq. (13).

$$\mathbf{f} = \mathbf{kd} \tag{13}$$

where vector $\mathbf{f}$ represents the force acting on the FEM nodes, $\mathbf{k}$ represents the stiffness matrix which depends on the physical parameters of the object, and $\mathbf{d}$ is the displacement vector corresponding to the FEM nodes.

It is obvious that the deformation fields obtained using the approach presented in this paper will act as the input for physical parameters estimation.

VI. ACKNOWLEDGMENTS

The authors gratefully acknowledge the contribution of rheology research group.

REFERENCES

[1] S. J. Riederer, "Current technical development of magnetic resonance imaging," *ENGINEERING IN MEDICINE AND BIOLOGY. IEEE.*, vol. 19, no. 5, pp. 34–41, 2000.

[2] B. J. Matuszewski, J. K. Shen, and L. K. Shark, "Estimation of internal body deformations using an elastic registration technique," *Proceedings of the International Conference on Medical Information Visualisation-BioMedical Visualisation*, pp. 15–20, 2006.

[3] J. Cho and P. J. Benkeser, "Elastically deformable model-based motion-tracking of left ventricle," *Proceedings of the 26th Annual International Conference of the IEEE EMBS*, vol. 1, no. 3, pp. 1925–1928, 2004.

[4] X. Papademetris, A. J. Sinusas, D. P. Dione, R. T. Constable, and J. S. Duncan, "Estimation of 3-d left ventricular deformation from medical images using biomechanical models," *Transactions on Medical Imaging. IEEE*, vol. 21, no. 7, pp. 786– 800, July 2002.

[5] Y. Chenoune, E. Delechelle, E. Petit, T. Goissen, J. Garot, and A. Rahmouni, "Segmentation of cardiac cine-mr images and myocardial deformation assessment using level set methods," *Computerized Medical Imaging and Graphics*, vol. 29, no. 8, pp. 607–616, Dec. 2005.

[6] M. Kass and A. Witkin, "Snakes: active contours models," *International Journal of Computer Vision*, vol. 1, no. 4, pp. 321–331, Jan. 1987.

[7] J. Lang, D. K. Pai, and R. J. Woodham, "Robotic acquisition of deformable models," in *Proc. ICRA '02*, vol. 1, 2002, pp. 933 – 938.

[8] V. Caselles, F. Catte, T. Coll, and F. Dibos, "A geometric model for active contours in image processing," *Numerische Mathematik*, vol. 66, no. 1, pp. 1–31, Dec. 1993.

[9] R. Malladi, J. A. Sethian, and B. C. Vemuri, "Shape modeling with front propagation: a level set approach," *Transactions on Pattern Analysis and Machine Intelligence. IEEE*, vol. 17, no. 2, pp. 158–175, Feb. 1995.

[10] V. Caselles, "Geometric models for active contours," *Image Processing. Proceedings. International Conference on*, vol. 3, pp. 9–12, Oct. 1995.

[11] F. Huang and J. Su, "Face contour detection using geometric active contours," *Proceedings of the 4th World Congress on Intelligent Control and Automation*, June 2002.

[12] C. Harris and M. Stephens, "A combined corner and edge detector," *Proceedings of The Fourth Alvey Vision Conference*, pp. 147–151, 1988.

[13] P. L. Zhang, S. Hirai, K. Endo, and S. Morikawa, "Local deforamtion measurement of biological tissues based on feature tracking of 3d mr volumetric images," *2007 IEEE/ICME International Conference on Complex Medical Engineering*, May 2007.

[14] G. Q. Chen, "Robust point feature matching in projective space," *Computer Vision and Pattern Recognition, 2001. CVPR 2001*, vol. 1, pp. 717–722, 2001.

[15] B. K. Horn, "Closed form solution of absolute orientation using unit quaternions," *Optical Society of America A: Optics, Image Science, and Vision*, vol. 4, no. 4, pp. 629–642, 1987.

[16] P. Rogelj, S. Kovacic, and J. C. Gee, "Validation of a non-rigid registration algorithm for multi-modal data," *Medical Imaging 2002: Image Processing*, pp. 299–307, 2002.

Local Deformation Measurement of Biological Tissues Based on Feature Tracking of 3D MR Volumetric Images

Penglin Zhang[1,2], Shinichi Hirai[1], Kazumi Endo[1] and Shigerhiro Morikawa[3]
[1]Dept. of Robotics, Faculty of Science and Engineering, Ritsumeikan University
[2]School of Remote sensing and Information Engineering, Wuhan University
[3]Shiga University of Medical Science
Kusatsu, Shiga 525-8577, Japan

***Abstract*—Being able to measure deformations precisely in tissue by magnetic resonance (MR) imaging is very useful for many medical imaging applications. While a variety of different algorithms have been formulated for this purpose, few are based on tracking features in the images. Here, we propose an approach of automatically extracting feature points and matching them to measure local deformation as seen in 3D MR volumetric images. Ccorrelation scores (cs) are given to pairs of high curvature points in a 3D cubic region to ensure that they are well matched. Those with scores above a given threshold are considered as candidate points. The strength of matching of the candidate points are evaluated using an iterative energy function, and then the well matched points are used to estimate the deformation.The approach was very effective when applied to actual MR volumetric images of a person's calf.**

I. Introduction

Pre-estimating deformation or motion of biological tissues is often required for computer-assisted medical applications, such as clinical diagnosis, surgery simulation, operation planning, and evaluation of physical characteristics of biological tissues, which are becoming increasingly more common. Images can be obtained in three dimensions (3D) using magnetic resonance (MR), computer tomography(CT), ultrasonic (US) scans, all of which are non-invasive. Magnetic resonance imaging (MRI) is particular good for estimating deformation of tissue because it affords superb anatomic images with excellent spatial resolution and contrast between soft tissues.

Estimations of deformation from MR volumetric images are mainly based on elastic deformation models [1]-[3], which can be classified into either parametric or geometric active models [4]. In the former, parametric active contours, also called snakes, were first introduced by Kass et al. in 1987 [5], and subsequently used by Lang et al. [6], Cho et al. [2] and Matuszewski et al. [1] to estimate deformation of soft objects. Its general idea is to try to minimise the designed function to deform a given initial contour toward the boundary of the object to obtain the object's deformation. The geometric active model was first proposed by Caselles et al. [7], and developed by Malladi et al. [8], Caselles [9] and Chenoune et al. [4]. In the geometric active model, propagation of curves and surfaces are used to detect boundaries and track motion.

Moreover, much work has also been done on MRI tagging technique for measuring deformation. The MRI tagging method was proposed by Zerhouni [11], and has been subsequently developed: Amini et al. [12] introduced a coupled B-snake grids and constrained thin-plate splines to analyze 2D tissue deformations; Wang et al. [14] proposed using subspace approximation techniques to compute motion fields and introduced a spline technique to reconstruct dense displacement fields; Chen et al.[28] introduced an approach for tracking the tags; and Huang et al.[13] introduced an environment to fit and track volumetric tagged MRI data by a 4D deformable B-spline model. In all these MRI tagging methods, a set of radio-frequency (RF) pulses are used to make trackable tags in thin slices perpendicular to the imaging plane [12].

Although the algorithms used to measure the deformations have been much improved in recent years, some problems still remain. The parametric active model cannot handle changes in the topology of the evolving contours when implementations of deformation made are performed directly, and special, often heuristic, topology handling procedures must be used [9]. In the geometric active model, when contrast is poor and boundaries are not clear or continuous in the images, the contours tend to leak through the boundary [10]. The tagged images must have a regular grid pattern in the imaging plane, and if the number of tagged points is low the accuracy of the measurements will be poor.

Herein, we propose an approach based on matching point features to measure local deformation of biological tissues from MR volumetric images. Briefly, we extract enough points of high curvature (also called points of interest) automatically in MR volumetric images taken before and after deformation of the tissue, which hereafter we refer to as initial and

deformed images, and then compare their relative positions. We describe the approach in Section 2 and give examples and preliminary experimental results in Section 3. In the final section, we present a discussion and conclusions.

II. METHOD

Our approach consists of three steps: registration, point feature matching and deformation measurement.

A. Registration

Registration is determination of the absolute orientation of one data set with respect to another [25]. Its application to MR images has been well studied [17]- [23]. Registration is usually applied to non-rigid objects using either a voxel-based or a feature-based method [23]. In [23]. In the former method, optimized transformation is performed to maximize the difference in intensity in regions where the intensity would otherwise be similar in the initial and deformed images. The latter method uses information from different identifiable structures of the object.

In the present study, we use a registration technique to find the movement of two coordinate systems in initial and deformed MR volumetric images of a volunteer's calf (Figure 1). We select features, considered rigid, around the bone (Figure 2a) in the initial image and compare them with their corresponding features in the deformed image to obtain rotation matrix $\boldsymbol{\mathcal{R}}$ and translation vector $\boldsymbol{\tau}$.

Denoting the position vector in the initial and deformed volumetric images as $\mathbf{x_i}$ and $\mathbf{x_d}$, respectively, and consideration their geometric movement, we have affine transformation

$$\mathbf{x_d} = \boldsymbol{\mathcal{R}}\mathbf{x_i} + \boldsymbol{\tau}. \tag{1}$$

$\boldsymbol{\mathcal{R}}$ and $\boldsymbol{\tau}$ can be estimated using a set of rigid features. Using the quaternion q_0, q_x, q_y and q_z (Horn [24]) in the rotation matrix $\boldsymbol{\mathcal{R}}$, we can obtain equation (2) with the constraint $q_0^2 + q_x^2 + q_y^2 + q_z^2 = 1$.

$$\boldsymbol{\mathcal{R}} = \begin{pmatrix} q_0^2+q_x^2-q_y^2-q_z^2 & 2(q_xq_y-q_0q_z) & 2(q_xq_z+q_0q_y) \\ 2(q_yq_x+q_0q_z) & q_0^2-q_x^2+q_y^2-q_z^2 & 2(q_yq_z-q_0q_x) \\ 2(q_zq_x-q_0q_y) & 2(q_zq_y+q_0q_x) & q_0^2-q_x^2-q_y^2+q_z^2 \end{pmatrix} \tag{2}$$

Let n be the number of selected rigid features, and $\mathbf{x_i}_k$ $(k = 1, 2, ..., n)$ be their position vectors in the initial volumetric image and $\mathbf{x_d}_k$ $(k = 1, 2, ..., n)$ be their corresponding the position vectors in the deformed volumetric image. Let $\bar{\mathbf{x_i}}$ and $\bar{\mathbf{x_d}}$ represent their centroids in the initial and deformed images, respectively. We can write

$$\bar{\mathbf{x_i}} = \frac{1}{n}\sum_{k=1}^{n}\mathbf{x_i}_k, \quad \bar{\mathbf{x_d}} = \frac{1}{n}\sum_{k=1}^{n}\mathbf{x_d}_k. \tag{3}$$

To find the rotation, let us denote the new coordinates as

$$\mathbf{x'_i}_k = \mathbf{x_i}_k - \bar{\mathbf{x_i}}, \quad \mathbf{x'_d}_k = \mathbf{x_d}_k - \bar{\mathbf{x_d}}. \tag{4}$$

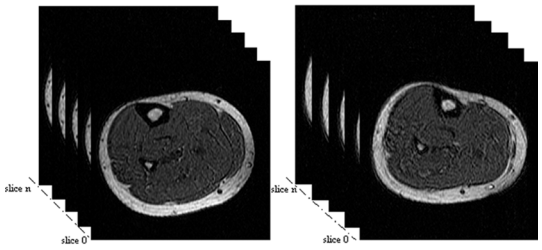

(a)Initial MR slices (b)Final MR slices

Fig. 1. Original MR volumetric image

We then introduce a 3×3 matrix $\mathbb{M}$ computed by the sums of cross products of coordinates measured in the initial volumetric image and those measured in the deformed volumetric image.

$$\mathbb{M} = \sum_{k=1}^{n}\mathbf{x'_i}_k\mathbf{x'_d}_k^{\mathbf{T}} \tag{5}$$

According to Horn [24], the above matrix contains all the information required to solve the least-squares problem for rotation.

Note that the 3×3 matrix $\boldsymbol{\mathcal{A}} = \mathbb{M} - \mathbb{M}^{\mathbf{T}}$ is skewed symmetric, implying that multiplying matrix $\boldsymbol{\mathcal{A}}$ and a 3-dimensional vector will give the outer product of vector $\boldsymbol{\delta}$ and the vector. Letting $\boldsymbol{\mathcal{A}}_{i,j}$ be the $(i,j) - th$ element of matrix $\boldsymbol{\mathcal{A}}$, vector δ is given by

$$\boldsymbol{\delta} = [\boldsymbol{\mathcal{A}}_{2,3} \quad \boldsymbol{\mathcal{A}}_{3,1} \quad \boldsymbol{\mathcal{A}}_{1,2}]^{\mathbf{T}} \tag{6}$$

Let us introduce a new 4×4 real symmetric matrix:

$$\boldsymbol{\mathcal{B}} = \left(\begin{array}{c|c} trace(\mathbb{M}) & \delta^{\mathbf{T}} \\ \hline \delta & \mathbb{M} + \mathbb{M}^{\mathbf{T}} - trace(\mathbb{M})\mathbf{E} \end{array}\right) \tag{7}$$

where $trace(\mathbb{M})$ is the trace of matrix $\mathbb{M}$, and $\mathbf{E}$ is a 3×3 unit matrix.

It can be shown that the unit quaternion $\mathbf{q} = [q_0, q_x, q_y, q_z]$ is the eigenvector corresponding to the largest positive eigenvalue of matrix $\boldsymbol{\mathcal{B}}$ [24][25]. This implies that rotation matrix $\boldsymbol{\mathcal{R}}$ can be estimated. The translation vector $\boldsymbol{\tau}$ is computed as

$$\boldsymbol{\tau} = \boldsymbol{\mathcal{R}}\bar{\mathbf{x_i}} - \bar{\mathbf{x_d}}. \tag{8}$$

Figures 2b and 2c show the results of registering a 2D and a 3D image, respectively. The blue and orange contours represent the surfaces in the initial and deformed images, respectively.

B. Point feature matching

Point feature matching is central to our approach. First, we compute a correlation score[26][27] between two cubic regions around a feature point in initial and deformed volumetric images, and then disambiguate matches through a relaxation labeling technique.

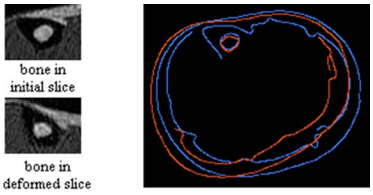

(a) bone region in initial (upper) and final (bottom) MR slices (b) overlaid result of registered 2D contours

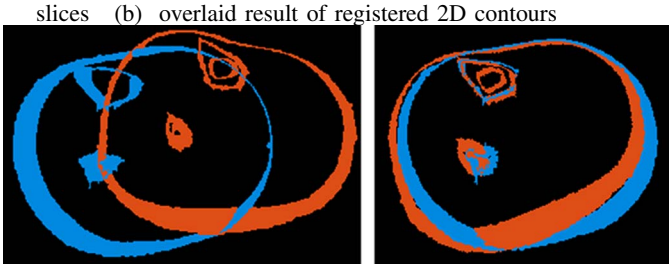

(c) unregistered and (d) registered 3D surface model

Fig. 2. Original MR volumetric image

1) First matching through correlation score: Given a high curvature point $\mathbf{p_1}$ pre-extracted from the initial MR volumetric image using a Harris operator [31], we first compute its projection point $\mathbf{p_2}$ in the deformed volumetric image using equation (1). We then select a match cubic region of size $(2m+1)\times(2n+1)\times(2h+1)$ and search the cubic region of size $(2u+1)\times(2v+1)\times(2w+1)$ around $\mathbf{p_1}$ and $\mathbf{p_2}$. The search cube size reflects a pre-estimation of maximum deformation. The match and search cubic regions can be described as

$$\mathcal{C}_m = \{\mathbf{x} = [x \;\; y \;\; z]^{\mathbf{T}} | \; x \in [-m, m],\; y \in [-n, n],\; z \in [-h, h]\}, \tag{9}$$

$$\mathcal{C}_s = \{\mathbf{x} = [x \;\; y \;\; z]^{\mathbf{T}} | \; x \in [-u, u],\; y \in [-v, v],\; z \in [-w, w]\}. \tag{10}$$

Let $g_{(\mathbf{x})}$ and $g'_{(\mathbf{x})}$ be the voxel value of the initial and deformed volumetric images at point $\mathbf{x}$. The correlation score between two match cubic regions around voxel $\mathbf{p_1}$ in the initial volumetric image and voxel $\mathbf{p_2}_j$ (high curvature points within the search cube around $\mathbf{p_2}$) in the deformed volumetric image is defined by

$$cs(\mathbf{p_1}, \mathbf{p_2}_j) = \frac{\sum_{\mathbf{x}\in\mathcal{C}_m}(g_{(\mathbf{p_1}+\mathbf{x})} - \bar{g}_{(\mathbf{p_1})})(g'_{(\mathbf{p_1}+\mathbf{x})} - \bar{g}'_{(\mathbf{p_2}_j)})}{|\mathcal{C}_m|\sqrt{\sigma^2(g_{\mathbf{p_1}}) \times \sigma^2(g_{\mathbf{p_2}_j})}} \tag{11}$$

where

$$|\mathbf{C}_m| = (2m+1)(2n+1)(2h+1),$$

$$\bar{g}_{\mathbf{p_1}} = \frac{1}{|\mathcal{C}_m|}\sum_{\mathbf{x}\in\mathcal{C}_m} g_{(\mathbf{p_1}+\mathbf{x})},\;\; \bar{g}'_{\mathbf{p_2}_j} = \frac{1}{|\mathcal{C}_m|}\sum_{\mathbf{x}\in\mathcal{C}_m} g'_{(\mathbf{p_2}_j+\mathbf{x})}.$$

Here, $\sigma(g_{\mathbf{p}})$ is the standard derivation of MR volumetric image $g_{(\mathbf{p})}$ in the neighborhood $(2m+1)\times(2n+1)\times(2h+1)$ of point $\mathbf{p}$, given by

$$\sigma^2(g_{\mathbf{p}}) = \frac{\sum_{\mathbf{x}\in\mathcal{C}_m}(g_{(\mathbf{p}+\mathbf{x})} - \bar{g}_{\mathbf{p}})^2}{|\mathbf{C}_m|} \tag{12}$$

where $\bar{g}_{\mathbf{p}}$ is the averaged intensity in the neighborhood of point $\mathbf{p}$ in the MR volumetric image. The correlation score ranges from -1 when the cubic regions are completely different to -1 when they are identical.

From the correlation scores, we obtain a set of many-to-many matches, that is, a point in the initial volumetric image may be paired with more than one point (candidate matches) in the deformed image, and vice versa. Obviously, many candidate matches will be ambiguous, but this problem can be resolved with relaxation techniques [26].

2) Definition of strength of the match: To iteratively disambiguate the matches, we use a function for the strength of the match (SM). Let $\mathbf{p_1}_i$ and $\mathbf{p_2}_j$ represent candidate matches in initial and deformed volumetric image respectively, then, $\mathbf{p_1}_i$ and $\mathbf{p_2}_j$ can be regarded as a pair of potential matched $\mathbf{PM}(\mathbf{p_1}_i, \mathbf{p_2}_j)$ if and only if the $SM(\mathbf{p_1}_i, \mathbf{p_2}_j)$ between $\mathbf{p_1}_i$ and $\mathbf{p_2}_j$ is the largest among the candidate matches of $\mathbf{p_1}_i$ and the largest among the candidate matches of $\mathbf{p_2}_j$.

Suppose that a cubic volumetric image region $\mathcal{N}(\mathbf{p})$ represents the neighborhood of point $\mathbf{p}$, then, we will expect to see many potential matches within their neighborhoods $\mathcal{N}(\mathbf{p_1}_i)$ and $\mathcal{N}(\mathbf{p_2}_j)$ if and only if $(\mathbf{p_1}_i, \mathbf{p_2}_j)$ is a potential match. Incontrast, we will expect to see only a few or even no matches. Let $(\mathbf{n_1}_k, \mathbf{n_2}_l)$ be the potential matches within $\mathcal{N}(\mathbf{p_1}_i)$ and $\mathcal{N}(\mathbf{p_2}_j)$, respectively, where $\mathbf{n_1}_k \in \mathcal{N}(\mathbf{p_1}_i)$ and $\mathbf{n_2}_l \in \mathcal{N}(\mathbf{p_2}_j)$. More strictly, we define a strength function of candidate matches $\mathbf{p_1}_i$ and $\mathbf{p_2}_j$ as:

$$SM(\mathbf{p_1}_i, \mathbf{p_2}_j) = cs(\mathbf{p_1}_i, \mathbf{p_2}_j) + \alpha\sum_{k,l=1}^{s}\frac{cs(\mathbf{n_1}_k, \mathbf{n_2}_l)\cdot\eta(\mathbf{n_1}_k, \mathbf{n_2}_l)}{1 + diff(\mathbf{p_1}_i, \mathbf{p_2}_j; \mathbf{n_1}_k, \mathbf{n_2}_l)} \tag{13}$$

where s represents the total number of the potential matches in the neighborhoods $\mathcal{N}(\mathbf{p_1}_i)$ and $\mathcal{N}(\mathbf{p_2}_j)$ of the candidate match $(\mathbf{p_1}_i, \mathbf{p_2}_j)$, α is a balancing parameter used to balance the weight during iteration, and $diff(\mathbf{p_1}_i, \mathbf{p_2}_j; \mathbf{n_1}_k, \mathbf{n_2}_l)$ is the relative distance difference given by

$$diff(\mathbf{p_1}_i, \mathbf{p_2}_j; \mathbf{n_1}_k, \mathbf{n_2}_l) = \frac{d(\mathbf{p_1}_i, \mathbf{n_1}_k) - d(\mathbf{p_2}_j, \mathbf{n_2}_l)}{dist(\mathbf{p_1}_i, \mathbf{p_2}_j; \mathbf{n_1}_k, \mathbf{n_2}_l)} \tag{14}$$

where $dist(\mathbf{p_1}_i, \mathbf{p_2}_j; \mathbf{n_1}_k, \mathbf{n_2}_l)$ is the average distance between two pairs $(\mathbf{p}_s, \mathbf{n}_s)$. Let us define the Euclidean distance between the pair of points $\mathbf{p}_s$ and $\mathbf{n}_s$ as

$$d(\mathbf{p}_s, \mathbf{n}_s) = \|\mathbf{p}_s - \mathbf{n}_s\|. \tag{15}$$

We then have

$$dist(\mathbf{p_1}_i, \mathbf{p_2}_j; \mathbf{n_1}_k, \mathbf{n_2}_l) = \frac{d(\mathbf{p_1}_i, \mathbf{n_1}_k) + d(\mathbf{p_2}_j, \mathbf{n_2}_l)}{2}. \tag{16}$$

Generally, with better matched pair $(\mathbf{n_1}_k, \mathbf{n_2}_l)$, we expect more contribution to its center pair $(\mathbf{p_1}_i, \mathbf{p_2}_j)$. Moreover, as is well known, we can measure the similarity between two volumetric image regions by minimising the sum of the square of the residual between the two regions. So, the contribution $\eta(\mathbf{n_1}_k, \mathbf{n_2}_l)$ of potentially matched pair $(\mathbf{n_1}_k, \mathbf{n_2}_l)$ in equation (13) can be defined by the residual as follows. Let vector $\mathbf{x}_{\mathbf{n_1}_k} = (x_{\mathbf{n_1}_k}, y_{\mathbf{n_1}_k}, z_{\mathbf{n_1}_k}) \in \mathcal{N}(\mathbf{n_1}_k)$ represent the coordinate of a voxel in $\mathcal{N}(\mathbf{n_1}_k)$, and its corresponding point $\mathbf{n_2}_l$ be regarded as its estimation in the deformed volumetric image, then we can use the sum of the square residual of neighborhoods to substitute for the residual of the point $\mathbf{n_1}_k$. Ideally, the residual $\boldsymbol{\zeta}(\mathbf{n_1}_k, \mathbf{n_2}_l)$ of $\mathbf{n_1}_k$ can be defined as

$$\boldsymbol{\zeta}(\mathbf{n_1}_k, \mathbf{n_2}_l) = \sum_{\mathbf{x}_{\mathbf{n_1}_k} \in \mathcal{N}} \mid g_{\mathbf{n_1}_k}(\mathbf{x}_{\mathbf{n_1}_k}) - g'_{\mathbf{n_2}_l}(\mathbf{x}_{\mathbf{n_1}_k}) \mid^2.$$

Considering the rotation transformation between the initial and final volumetric images, we can rewrite the above equation as

$$\boldsymbol{\zeta}(\mathbf{n_1}_k, \mathbf{n_2}_l) = \sum_{\mathbf{x}_{\mathbf{n_1}_k} \in \mathcal{N}} \mid g_{\mathbf{n_1}_k}(\mathbf{x}_{\mathbf{n_1}_k}) - g'_{\mathbf{n_2}_l}(\mathbf{x}_{\mathbf{n_1}_k}, \boldsymbol{\mathcal{R}}) \mid^2 \tag{17}$$

where $g_{\mathbf{n_1}_k}(\mathbf{x}_{\mathbf{n_1}_k})$ is the intensity values in the image at position $\mathbf{x}_{\mathbf{n_1}_k}$, $g_{\mathbf{n_2}_l}(\mathbf{x}_{\mathbf{n_1}_k}, \boldsymbol{\mathcal{R}})$ is the intensity value of the voxel centered at point $\mathbf{n_2}_l$, and its relative coordinate $\mathbf{x}_{\mathbf{n_2}_l} = (x_{\mathbf{n_2}_l}, y_{\mathbf{n_2}_l}, z_{\mathbf{n_2}_l}) \in \mathcal{N}(\mathbf{n_2}_l)$ satisfies

$$[x_{\mathbf{n_2}_l} \quad y_{\mathbf{n_2}_l} \quad z_{\mathbf{n_2}_l}]^{\mathbf{T}} = \boldsymbol{\mathcal{R}}[x_{\mathbf{n_1}_k} \quad y_{\mathbf{n_1}_k} \quad z_{\mathbf{n_1}_k}]^{\mathbf{T}}$$

Without losing generality, we define the local contributions of the pair $(\mathbf{n_1}_k, \mathbf{n_2}_l)$ via the *Gibbs distribution* in the form

$$\eta(\mathbf{n_1}_k, \mathbf{n_2}_l) = \frac{1}{\mathcal{Z}(\mathbf{n_1}_k, \mathbf{n_2}_l)} \cdot \mathbf{exp}^{-\lambda \cdot \boldsymbol{\zeta}(\mathbf{n_1}_k, \mathbf{n_2}_l)} \tag{18}$$

where the notation $\mathcal{Z}(\mathbf{n_1}_k, \mathbf{n_2}_l)$ represents the partition function (or normalizing constant) of the pair $(\mathbf{n_1}_k, \mathbf{n_2}_l)$. This is given by

$$\mathcal{Z}(\mathbf{n_1}_k, \mathbf{n_2}_l) = \sum_{k,l=1}^{s} \mathbf{exp}^{-\lambda \cdot \boldsymbol{\zeta}(\mathbf{n_1}_k, \mathbf{n_2}_l)} \tag{19}$$

where s has the same meaning as equation (13), the attenuation constant $\lambda = 1/T$ and call T temperature. Here, we expect to select proper λ so that as λ increases (or T decreases), the $\eta(\mathbf{n_1}_k, \mathbf{n_2}_l)$ of those with large residuals quickly decreases, and ultimately the contributions is mainly from those with the smallest residuals. Thus, in our implementation, we define the attenuation constant λ as

$$\lambda = \frac{1}{T} = \{\boldsymbol{\zeta}(\mathbf{n_1}_k, \mathbf{n_2}_l) - \bar{\boldsymbol{\zeta}}\}^2 \tag{20}$$

where $\bar{\boldsymbol{\zeta}}$ represents the average residuals of potential matches within the neighborhood of the candidate pair $(\mathbf{p_1}_i, \mathbf{p_2}_j)$.

3) Relaxation labeling: The relaxation technique was first proposed by Rosenfel et al. [29]. The basic idea is to use iterated local context updates to achieve a globally consistent result [30]. To disambiguate the candidate matches, we define the energy function as the average of the strengths of all candidate matches:

$$\boldsymbol{\varepsilon} = \frac{1}{N} \sum_{i,j=1}^{N} SM(\mathbf{p_1}_i, \mathbf{p_2}_j) \tag{21}$$

where N is the total number of matched pairs in a potential matches set (PMS) at time t.

The matches can be disambiguated by maximizing the energy function $\boldsymbol{\varepsilon}$, using an iterative procedure. Here, we note that since the PMS varies dynamically, the strength function (13) also varies. Therefore, potential matches can be updated constantly, and the iteration will stop when the energy decreases. The relaxation process can be described as follows in pseudo code.

```
set α ← 0
for(i = 0 to total number of points in initial image)
 for(j = 0 to total number of candidates of p1_i
       in final image)
  if(max{cs(p1_i)} → p2_j and max{cs(p2_j)} → p1_i)
    Add pair(p1_i, p2_j) → PMS;
iteration
{
 for(n = 0 to total number of PM pairs)
   Computation the SM(p1_n, p2_n);
 Computation the energy function ε_t;
 if(ε_t ≥ ε_{t-1})
 {
   PMS ← 0;
   for(i = 0 to total number of points in initial image)
     for(j = 0 to total number of candidates of p1_i
           in final image)
       if(max{SM(p1_i)} → p2_j and
          max{SM(p2_j)} → p1_i)
         Add pair(p1_i, p2_j) → PMS;
   α ← α+ △ α
 }
 else
   stop iteration;
}
```

Functions $\boldsymbol{\varepsilon}_t$ and $\boldsymbol{\varepsilon}_{t-1}$ are energies at time t and $t-1$, respectively. If $SM(\mathbf{p_1}_i, \mathbf{p_2}_j)$ is the largest among the candidate matches for $\mathbf{p_1}_i$, then $\mathbf{max}\{SM(\mathbf{p_1}_i)\} \rightarrow \mathbf{p_2}_j$, and $\mathbf{max}\{cs(\mathbf{p_1}_i)\} \rightarrow \mathbf{p_2}_j$ have similar meaning.

Moreover, we should emphasis that the balancing parameter α increases during the first couple of iterations.

It is worth pointing out the similarities and differences between our algorithm and those reported in references

in [26] [28]. First, the above algorithm is a combination of those proposed by Zhang [26] and Chen [28] and, therefore, they are similar in form. Second, by the potential matches as substitutes for high curvature points in the neighborhood of the candidate match $(\mathbf{p_1}_i, \mathbf{p_2}_j)$, the above algorithm can effectively avoid the dissymmetry that may appear in the algorithm proposed in [26]. Third, in addition to differences in distance, our SM function considers the contribution ratio of potential matches of different strength. Normalised *Gibbs distribution* of residual of each pair of potential matches reveals that those pairs that have smaller residual would have larger contribution.

C. Deformation measurement

Well matched pairs of feature points are used to measure local deformation. Let $\mathcal{D}$ be the displacement vector of a given point of high curvature in the initial MR volumetric image relative to its corresponding point in the final image, φ represent the angle between the displacement vector and the xz-plane, and $\mathbf{x}_1 = (x_1 \quad y_1 \quad z_1)^{\mathbf{T}}$ and $\mathbf{x}_2 = (x_2 \quad y_2 \quad z_2)^{\mathbf{T}}$ represent the coordinate of corresponding points in their respective coordinate systems. Then, we have

$$\mathcal{D} = \|\mathbf{x}_1(\boldsymbol{\mathcal{R}}, \boldsymbol{\tau}) - \mathbf{x}_2\| \tag{22}$$

and

$$\varphi = arcsin(\frac{y_2 - y_1^{'}}{\mathcal{D}}) \tag{23}$$

where $y_1^{'}$ satisfies

$$[0 \quad y_1^{'} \quad 0]^{\mathbf{T}} = \boldsymbol{\mathcal{R}}[0 \quad y_1 \quad 0]^{\mathbf{T}} + \boldsymbol{\tau}. \tag{24}$$

III. Experiments and Results

To evaluate the proposed approach, we performed a practical experiment using software that we wrote in Visual C++ and ran on Microsoft Windows XP in a Dell PC with a 2.80 GHz Intel® Pentium® D CPU and 1 GB of RAM.

For the experiment, MR volumetric images (Figure 1) of a volunteer's calf were taken under different status and at different times. In both cases, there were 76 slices, FOV was 20×20 cm, and the slice gap was 2 mm. In this case, we selected 20 neighbouring slices from each of the initial and final MR volume data sets. For both the initial and deformed images, we performed linear interpolation between two neighboring original slices , which gave discrete volumetric images of size $256 \times 256 \times 40$ and sufficient resolution along the z-axis direction.

Figure 3 shows the experiment results. To clarify the extent of deformation, two slices, one from the initial and the other from the deformed series, are superimposed using a uniform coordinate system (Fig.3a). In Figure 3a, the red and blue contours show the edges of the deformed and initial slices, respectively. Figure 3b is their 2D projection of the 3D deformation. Figure 3c shows the 3D mesh model of the final volumetric image, and Figure 3d shows the local deformation field overlaid on the 3D surface model of the final volumetric image. The arrow with the blue tail and white head indicates the direction and magnitude of the local deformation field.

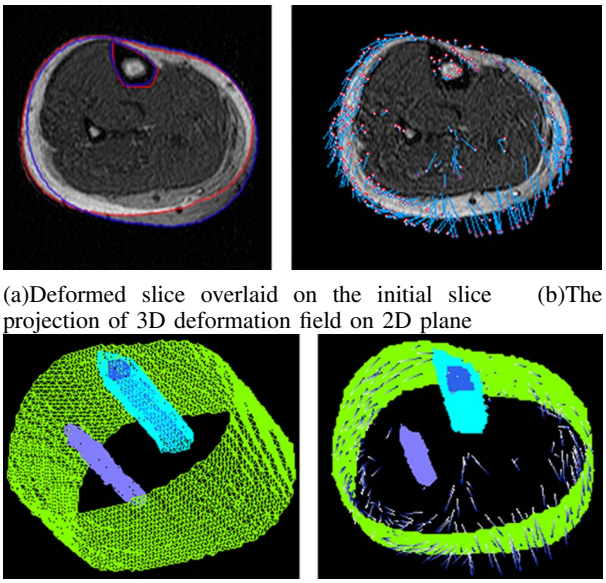

(a)Deformed slice overlaid on the initial slice (b)The projection of 3D deformation field on 2D plane

(c)Mesh model (d)3D local deformation field

Fig. 3. Original MR volumetric image

Figure 3 was obtained with a search cube size of $17 \times 17 \times 7$ voxels and a match cube size of $9 \times 9 \times 5$ voxels. The total number of reference high curvature points in the initial volumetric images is 500. There were 330 pairs of successful matches, of which 297 (90%) were good. The time cost was 10 seconds.

IV. Conclusion

We proposed a method to measure local deformation in soft biological tissues from MR volumetric by matching pairs of feature points. The core idea is to find points in volumetric images taken before deformation that match points well in the image taken after deformation. After matching points we used a relaxation technique to obtain good matches. Our preliminary experimental results reveal that our approach is effective. Compared with similar types of algorithms, our approach has the following advantages:

(1) Independent of the initial contours or boundaries.

(2) Feature points are automatically extracted from volumetric images.

(3) Insensitive to noise.

In the future, we intend to

(1) Improve the algorithm so that it is applicable to large deformations.

(2) Improve the accuracy of feature point matching.

(3) Reduce the number of false matches.

REFERENCES

[1] B.J. Matuszewski, Jian-Kun Shen, Lik-Kwan Shark and Moore C., "Estimation of Internal Body Deformations Using an Elastic Registration Technique," *Proceedings of the International Conference on Medical Information Visualisation-BioMedical Visualisation.* Jul. 2006, pp.15-20.

[2] Jinsoo Cho and Benkeser P.J., "Elastically deformable model-based motion-tracking of left ventricle," *Proceedings of the 26th Annual International Conference of the IEEE EMBS*. Vol. 1, No. 3, Sept. 2004, pp.1925-1928.

[3] X. Papademetris, Sinusas A.J, Dione D.P,Constable R.T and Duncan J.S, "Estimation of 3-D left ventricular deformation from medical images using biomechanical models," *IEEE Transactions on Medical Imaging*. Vol. 21, No. 7, Jul. 2002, pp.786-800.

[4] Chenoune Y, Delechelle E, Petit E, Goissen T, Garot J, Rahmouni A, "Segmentation of cardiac cine-MR images and myocardial deformation assessment using level set methods," *Computerized Medical Imaging and Graphics*. Vol. 29, No. 8, Dec. 2005, pp.607-616.

[5] Kass M., Witkin A. and Terzopoulos D., "Snakes: active contours models," *International Journal of Computer Vision*. Vol. 1, No. 4, Jan. 1987, pp.321-331.

[6] Jochen Lang, Pai D.K. and Woodham R.J., "Robotic acquisition of deformable models," *IEEE International Conference on Robotics and Automation, 2002. Proceedings. ICRA '02*. Vol. 1, 2002, pp.933- 938.

[7] Vicent Caselles, Francine Catte, Tomeu Coll, Francoise Dibos, "A geometric model for active contours in image processing," *Numerische Mathematik*. Vol.66, No.1, Dec. 1993, pp.1-31.

[8] Malladi R., Sethian J.A., Vemuri B.C., "Shape modeling with front propagation: a level set approach," *IEEE Transactions on Pattern Analysis and Machine Intelligence*. Vol.17, No.2, Feb. 1995, pp.158-175.

[9] Caselles Vicent, "Geometric models for active contours," *International Conference on Image Processing, Proceedings*. Vol. 3, Oct. 1995, pp.19-12.

[10] Fuzhen Huang, Jianbo Su, "Face Contour Detection Using Geometric Active Contours," *Proceedings of the 4th World Congress on Intelligent Control and Automation. Shanghai*, Vol.3, 2002, pp.2090- 2093.

[11] E. Zerhouni, D. Parish, W. Rogers, A. Yang, and E. Shapiro, "Human heart: Tagging with MR imaging-A method for noninvasive assessment of myocardial motion," *Radiology*. Vol.169, 1988, pp.59-63.

[12] Amini A.A., Yasheng Chen, Curwen R.W., Mani, V. and Sun J., "Coupled B-snake grids and constrained thin-plate splines foranalysis of 2-D tissue deformations from tagged MRI," *IEEE Transactions on Medical Imaging*. Vol. 17, No. 3, Jun 1998, pp.344-356.

[13] Jiantao Huang, Dana Abendschein, Victor G. Dávila-Román and Amir A. Amini, "Spatio-Temporal Tracking of Myocardial Deformations with a 4-D B-Spline Model from Tagged MRI," *IEEE TRANSACTIONS ON MEDICAL IMAGING*.Vol.18, No.10, Oct. 1999 , pp. 957-971.

[14] Y. P.Wang and A. A. Amini, "Fast computation of tagged MRI motion fields with subspace approximation techniques," *IEEE Workshop on Mathematical Methods in Biomedical Image Analysis, 2000. Proceedings*. June 2000 , pp. 119-126.

[15] Yasheng Chen, Amini A.A., "A MAP framework for tag line detection in SPAMM data using Markov random fields on the B-spline solid," *IEEE Workshop on Mathematical Methods in Biomedical Image Analysis, 2001. MMBIA.2001*. June 2000 , pp.131-138 .

[16] M. Betke, H. Hong, and J. P. Ko, "Automatic 3D Registration of Lung Surfaces in Computed Tomography Scans," *Fourth International Conference on Medical Image Computing and Computer-Assisted Intervention MICCAI 2001*. October 2001, pp. 725-733.

[17] A. Carrillo, J.L. Duerk, J.S.Lewin, D.L. Wilson, "Semiautomatic 3-D image registration as applied to interventional MRI liver cancer treatment," *IEEE Transactions on Medical Imaging*. Vol. 19, No. 3, March 2000 , pp. 175 - 185.

[18] R.S.Lazebnik, T.L.Lancaster, M.S.Breen, J.S.Lewin, D.L.Wilson, "Volume registration using needle paths and point landmarks for evaluation of interventional MRI treatments," *IEEE Transactions on Medical Imaging*. Vol. 22, No. 5, May 2003, pp. 653 - 660.

[19] D.Krechel, D.Pedroso, A.von Wangenheim, "Automatic registration of MRI head volumes using an octree anatomical atlas," *12th IEEE Symposium on Computer-Based Medical Systems, 1999. Proceedings*. June 1999, pp. 60 - 65.

[20] C. Studholme, C. Drapaca, B. Iordanova, V. Cardenas, "Deformation-based mapping of volume change from serial brain MRI in the presence of local tissue contrast change," *IEEE Transactions on Medical Imaging*. Vol. 25, No.5, May 2006, pp. 626 - 639.

[21] L.G. Nyul, J.K. Udupa, P.K. Saha, "Incorporating a measure of local scale in voxel-based 3-D image registration," *IEEE Transactions on Medical Imaging*. Vol.22, No.2, Feb 2003, pp. 228 - 237.

[22] T. Eric, B.Jean-Yves, "Elastic registration of MRI scans using fast DCT," *Engineering in Medicine and Biology Society, 2000. Proceedings of the 22nd Annual International Conference of the IEEE*. Vol.4, July 2000 , pp. 2854 - 2856.

[23] Haili Chui, James Rambo, James Duncan, Robert Schultz, Anand Rangarajan, "Registration of Cortical Anatomical Structures via Robust 3D Point Matching," *Proceedings of the 16th International Conference on Information Processing in Medical Imaging. Visegrad*, Vol.4, July 1999 , pp. 168 - 181.

[24] Berthold K.P Horn, "Closed Form Solution of Absolute Orientation using Unit Quaternions," *Optical Society of America A: Optics, Image Science, and Vision*. Vol.4, No.4, April 1987 , pp. 629-642.

[25] Margrit Betke, Harrison Hong, Jane P. Ko, "Automatic 3D Registration of Lung Surfaces in Computed Tomography Scans," *Proceedings of the 4th International Conference on Medical Image Computing and Computer-Assisted Intervention MICCAI 2001. Utrecht*, October 2001, pp. 725-733.

[26] Zhengyou Zhang, Rachid Deriche, Olivier FAUGERAS, Quang-Tuan LUONG, "A robust technique for matching two uncalibrated images through the recovery of the unknown epipolar geometry," *Special volume on computer vision*. Vol.78, October 1995, pp. 87 - 119.

[27] ZuXun Zhang, JianQin Zhang, "Correlation score measurement," *Digital Photogrammetry*. Jan 1997, pp. 168 - 169.

[28] Chen G.Q., "Robust point feature matching in projective space," *Proceedings of the 2001 IEEE Computer Society Conference on Computer Vision and Pattern Recognition, 2001. CVPR 2001. Hawaii USA*, Vol.1, 2001, pp. 717 - 722.

[29] A. Rosenfeld, R. A. Hummel and S. W. Zucker, "Scene Labeling by Relaxation Operations," *IEEE Transactions on Systems, Man, and Cybemetics*. 1976, pp. 420-433.

[30] Yefeng Zheng, Doermann, D., "Scene Labeling by Relaxation Operations," *IEEE TRANSACTIONS ON PATTERN ANALYSIS AND MACHINE INTELLIGENCE*. Vol. 28, No. 4, April 2006, pp. 643-649.

[31] C. Harris and M.J. Stephens, "A combined corner and edge detector," *Proceedings of The Fourth Alvey Vision Conference.* 1988, pp. 147-151.

第2章　超音波画像による柔軟物の内部変形計測

2.1　緒言

近年，手術シミュレーションにおける臓器のモデリング，デジタルヒューマンに代表される人体の筋骨格モデリング，食品工学における食品素材の力学的モデリング等において，複雑な力学的特性を有する柔軟物のモデリングが必要とされている．柔軟物モデリングに関する研究は，コンピュータグラフィクスの分野で始まり，その成果が手術シミュレーションや人体モデリングに適用された．しかしながら，従来の研究では，表面的な変形特性を表現することが中心的な課題であり，内部の挙動や力学量の分布に関しては，センシングの手法が限られていることもあり，未開拓の部分が多い．著者らは，レオロジー物体のモデリングと同定を柱の一つとして研究を進めてきた [23, 24]．しかしながら，同定を支えるセンシングは，物体の表面形状と表面の分布圧力のセンシングであり，レオロジー物体内部の挙動は未知のまま残されている．結果として，モデル同定の評価が不十分であり，さらには実際のレオロジー物体に表れるであろう変形の非均一性や非線形性，異方性に対応できない可能性が高い．

近年，超音波画像装置や CT，MRI に代表される三次元イメージング技術が発展している [25, 26]．これらの技術を用いることにより，柔軟物の内部挙動を計測し，計測結果をベースにするモデリングが可能になると期待できる．そこで本章では，超音波画像と MRI 画像によりレオロジー物体の内部変形を計測するとともに，レオロジー変形のシミュレーションと比較する．

2.2　超音波画像による内部変形の計測

本節では，超音波画像装置を用いた柔軟物の内部変形のセンシングについて述べる．超音波画像装置は，音波を利用して内部を映像化する装置である．映像化の原理が CT や MRI と比較すると単純なため，リアルタイムでの計測が可能である．超

32

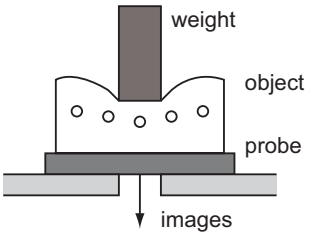

図 2.1: Location of probe and object

図 2.2: Example of ultrasonic image

音波装置の構成は，超音波を対象物内部に送信し，反射波を受信する探触子 (プローブ) と信号処理と画像出力を行う本体装置で構成される．本実験では，リニア探触子を使用する．また，振幅強度を明度に対応付けた B モードで，単純な断面画像を取得する．実験には日立製 EUB–240 を用いた．探触子の共振周波数は 3.5 MHz，フレーム数は 24.6 Hz，解像度は 320×240 画素である．音速は JIS で定められた生体中の平均音速 1530 m/s を用いる．

内部センシングを行うために探触子と対象物が接触していることが必要となる．そのため，Fig. 2.1 に示すように，探触子を対象物の下に設置した．下部から超音波を送受信する．カラギーナンとローカストビーンガムから成るアガーから，ゼリー状の対象物を作成した．カラギーナンは海草から抽出される粉末，ローカストビーンガムはカロブ樹の種子の胚乳部分を精製して得られる粉末である．アガーは寒天より弾力性があり，レオロジー変形が見られる．また濃度が高いほど，弾力性が増し硬さが向上する．内部に水を多く含むため，鮮明な超音波画像を得られる．本実験

33

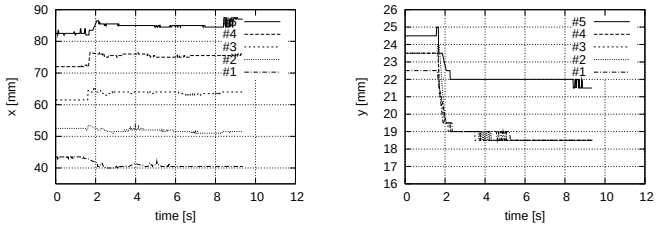

(a-1) coordinate x (a-2) coordinate y

(a) trail 1

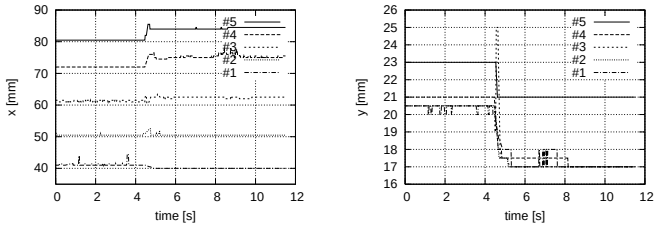

(b-1) coordinate x (b-2) coordinate y

(b) trial 2

図 2.3: Position of markers detected by ultrasonic images

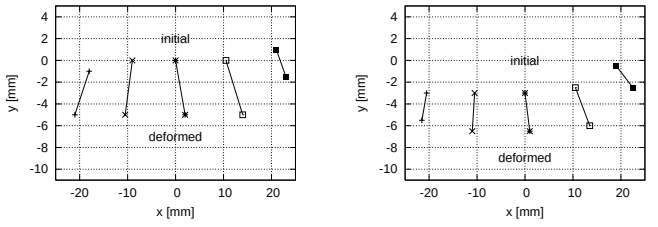

(a) trial 1 (b) trial 2

図 2.4: Position of markers in initial and deformed shapes

表 2.1: Marker coordinates in initial and deformed shapes detected by ultrasonic images (mm)

trial 1		
marker	initial shape	deformed shape
#1	(−18.0, −1.0)	(−21.0, −5.0)
#2	(−9.0, 0.0)	(−10.5, −5.0)
#3	(0.0, 0.0)	(2.0, −5.0)
#4	(10.5, 0.0)	(14.0, −5.0)
#5	(21.0, 1.0)	(23.0, −1.5)
trial 2		
marker	initial shape	deformed shape
#1	(−20.5, −3.0)	(−21.5, −5.5)
#2	(−10.5, −3.0)	(−11.0, −6.5)
#3	(0.0, −3.0)	(1.0, −6.5)
#4	(10.5, −2.5)	(13.5, −6.0)
#5	(19.0, −0.5)	(22.5, −2.5)

では，濃度が 5.0 %のアガーを用いた．対象物は，上面が幅 75 mm の正方形で高さが 30 mm の直方体であり，重量は 200 g である．対象物内部の中央断面にマーカを複数埋め込み，マーカ位置を計測する．マーカは中央に一個，左右に二個ずつおよそ 10 mm 間隔で埋め込んだ．対象物左端のマーカから付けた番号でマーカを識別する．重さ 500g，直径 40mm の円柱状の分銅を対象物体の上部に載せ，物体を変形させる．Fig. 2.2 に撮影画像の一例を示す．画像下部に五個のマーカを確認することができる．マーカの上部に映っているのは，対象物の表面である．さらにその上部には，マーカと表面のゴーストが映っている．撮像画像を処理し，マーカの座標を求める．マーカのゴーストを排除するために，あらかじめ指定した画像内の領域に対して画像処理を行う．変形前の撮影画像よりマーカの初期位置を，変形前と変形後の撮影画像よりマーカの変位を求めることができる．実験環境の湿度は 34 %，気温は 26 ℃で，対象物体の温度は 23 ℃であった．

同じ対象物体を用いて連続で 2 回の計測を行った．Fig. 2.3-(a) は一回目，Fig. 2.3-(b) は二回目の実験結果を表す．中央のマーカの初期位置を原点としている．実際の変位量と比較し，異常と判断できる数値を削除したため，値が一部欠落している．そのため，本稿では初期形状と最終的な変形形状を評価する．初期状態における中央のマーカを原点として位置を計算する．Table 2.1 に，初期位置と負荷後 6 s におけ

35

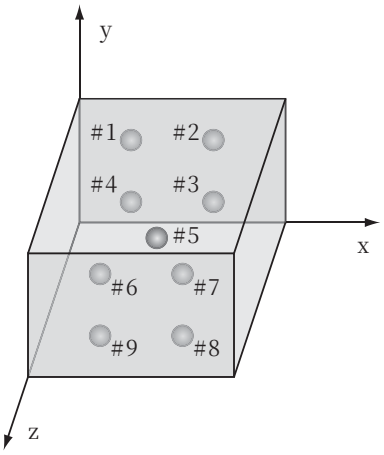

図 2.5: Location of markers in MR imaging

る各マーカの計測結果をまとめる．図示した結果を Fig. 2.4 に示す．

2.3 MRIによる内部変形の計測

MRI では，物体の断面を複数枚撮影し，得られた二次元画像を構成して三次元映像を得る．この断面画像をスライス画像，スライス画像間の間隔をスライス間隔と呼ぶ．MRI の長所は，物体内部を任意の切断面で撮影できること，物体内部の三次元的な変形を得られることである．しかし，撮影時間が長いため，物体の動的変化を得ることは困難である．本実験では，滋賀医科大学に設置されている MRI 装置を使用した．撮影においては，対象物を RF コイル内に設置する．

今回の撮影で使用した RF コイルの内径は 63 mm であり，この中に物体を設置し撮影を行った．RF コイルの内部で物体を垂直に設置するために，幅 55 mm，厚さ 2 mm のアクリル板を挿入した．対象物の材料は，前章で述べたアガーである．大きさ 2 mm のプラスチック製ビーズを，マーカとして物体内部に挿入した．マーカの配置を Fig. 2.5 に示す．また，物体にはガドリニウム系造影剤を入れた．以上のように作成した物体を，縦 55 mm，横 55 mm，高さ 25 mm の大きさに切り，RF コイル内のアクリル板上に設置した．

直径 20 mm の円筒形のアクリル棒を MRI 装置内に通し，一方を固定し他方を人の手で押し下げることにより物体を変形させた．アクリル棒は Fig. 2.5 に示す z 軸に平行である．また，二つの撮影方法を用いた．第一の方法では，スライス間隔 2 mm で物体全体を撮影した．物体に荷重をかけていない状態 (初期状態)，棒を押し下げ物体に荷重をかけ静止させている状態 (変形状態)，棒を持ち上げ荷重を抜いた状態

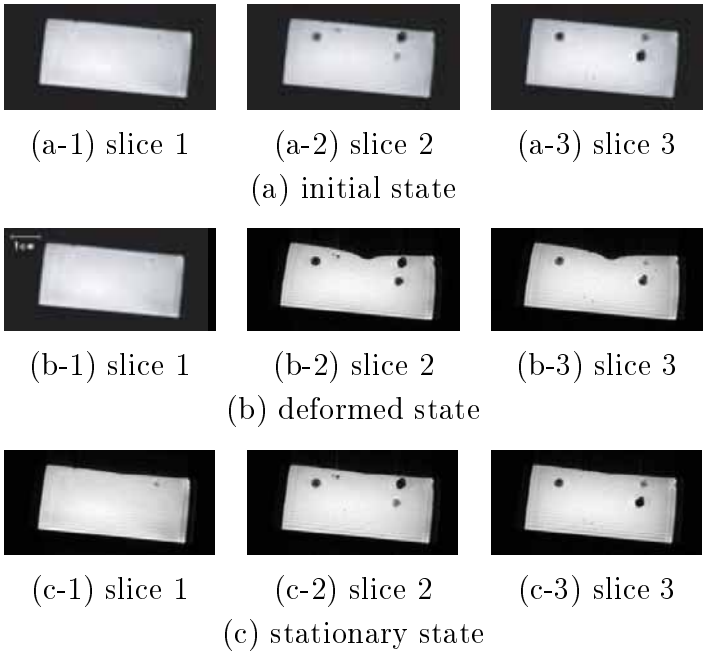

(a-1) slice 1 (a-2) slice 2 (a-3) slice 3

(a) initial state

(b-1) slice 1 (b-2) slice 2 (b-3) slice 3

(b) deformed state

(c-1) slice 1 (c-2) slice 2 (c-3) slice 3

(c) stationary state

図 2.6: MR images at initial, deformed, and stationary states

表 2.2: Marker coordinates at initial, deformed, and stationary states detected by MR images (mm)

marker	initial state	deformed state	stationary state
#1	(12, 21, 11)	(12, 21, 11)	(12, 21, 11)
#2	(45, 25, 10)	(41, 24, 10)	(46, 24, 10)
#3	(45, 17, 12)	(41, 16, 11)	(45, 16, 12)
#4	(17, 24, 18)	(18, 24, 17)	(17, 24, 17)
#5	(25, 20, 28)	(25, 18, 27)	(25, 20, 27)
#6	(12, 21, 42)	(12, 21, 42)	(11, 21, 42)
#7	(44, 27, 43)	(45, 24, 44)	(44, 26, 43)
#8	(45, 17, 43)	(47, 16, 43)	(45, 16, 43)
#9	(11, 7, 44)	(11, 7, 44)	(11, 7, 43)

37

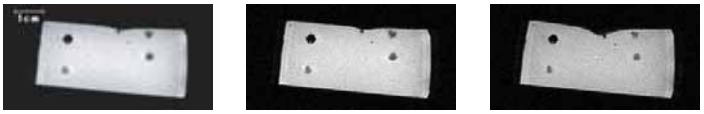

(a) 0.6 s (b) 1.2 s (c) 3.6 s

(d) 7.2 s (e) 9.6 s (f) 12.0 s

図 2.7: Successive images of one cross-section

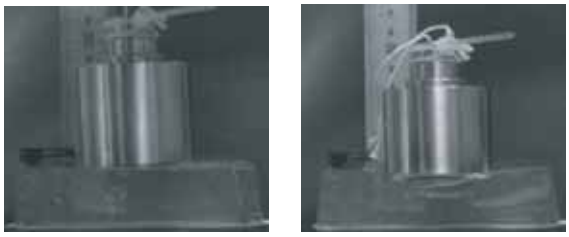

(a) initial shape (b) deformed shape

図 2.8: Deformation of object

(除重状態) を，十分な時間間隔を空けて撮影する．第二の方法では，同じ断面を連続的に撮影する．このとき，棒の押し下げと押し上げを連続的に行う．

第一の方法による撮影結果を示す．スライス間隔 2 mm で 30 枚のスライス画像を撮影した．空間的に連続する 3 枚のスライス画像を Fig. 2.6 に示す．Fig. 2.6-(a) から (c) は初期状態，Fig. 2.6-(d) から (f) は変形状態，Fig. 2.6-(g) から (i) は除重状態である．画像からマーカの位置を確認できる．この画像から物体内部にある 9 つのマーカの位置を求めた結果を Table 2.2 に示す．単位は mm である．

第二の方法による撮影結果を示す．マーカを確認できる一つの断面のみを連続で撮影し，撮影時間をどの程度まで短縮できるのかを調べる．時間間隔 0.6 s で撮影を行った結果を Fig. 2.7 に示す．マーカの位置を確認できることがわかる．なお，画像解像度を下げれば時間間隔を短縮できる．

2.4 評価

外形の比較 CCD カメラにより対象物の変形を撮影し，シミュレーションと比較する．アガーの上中央部に幅 40 mm，重さ 500 g の分銅をのせて変形させた際の様子

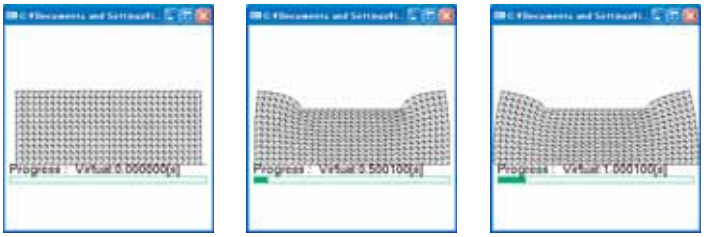

(a) 5 s (b) 10 s (c) 15 s

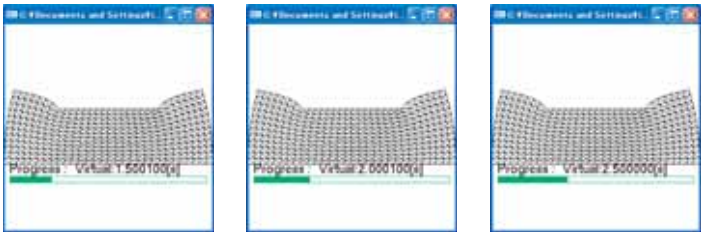

(d) 20 s (e) 25 s (f) 30 s

図 2.9: Simulation of real object deformation

を，シミュレーションと比較する．アガーに分銅をのせた際の物体表面の変位量は 7.5 mm であった．シミュレーション上の物体はレオロジー物体とし，メッシュ間隔を 2.5 mm として縦 12 メッシュ，横 30 メッシュの物体を構築し，物体の中央部分を幅 40 mm で 7.5 mm 強制変位させる．シミュレーション上のレオロジー物体のパラメータは，$E = 0.01 \times 10^6\,\mathrm{N/m^2}$，$C^{\mathrm{ela}} = 0.1 \times 10^6\,\mathrm{Ns/m^2}$，$C^{\mathrm{vis}} = 0.3 \times 10^6\,\mathrm{Ns/m^2}$，$\nu^{\mathrm{ela}} = \nu_1^{\mathrm{vis}} = \nu_2^{\mathrm{vis}} = 0.35$ とし，物体の質量は 200 g とした．Fig. 2.8，Fig. 2.9 に実物体の変形の様子およびシミュレーション上での物体の変形の様子を示す．Fig. 2.8，Fig. 2.9 から，シミュレーションにおいて変形の外観の様子を表現できていることがわかる．

超音波撮像による内部マーカ変位との比較　超音波画像から求めたアガー内部のマーカの変位と，シミュレーションにおける格子点の変位を比較し，モデルを検証する．アガー内のマーカはアガー上部から 10mm の位置に中央から 10 mm 間隔で 5 個配置している．両端のマーカは分銅をのせる位置により変位に影響が出やすいと考えられるため，中央の 3 つのマーカ，すなわちマーカ#2，#3，#4 の変位を比較する．

Fig. 2.10 に，超音波画像によるマーカの変位とシミュレーションにより得られるマーカの変位を比較した結果を示す．Fig. 2.10-(a) から (c) はそれぞれマーカ#2，#3，#4 の変位を示す．実線はシミュレーションにおいて中央部分を強制変位させた結果，破線は中央から 1 メッシュ左にずらして強制変位させた結果を示している．実験結果に関しては，初期位置から定常位置への変位を示した．Fig. 2.10-(b) に示すよう

39

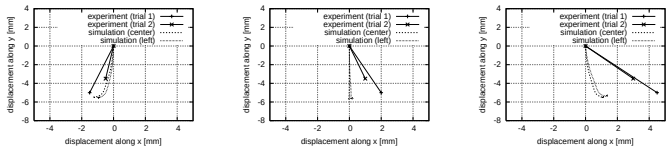

(a) marker #2　(b) marker #3　(c) marker #4

図 2.10: Comparison between simulation and experiment

に，実験における物体中央部のマーカは真下ではなく右斜め下に移動する．これは，物体の中央部に正確に負荷を与えていないことが原因である．すなわち，実物体にのせた分銅は中央部から左側にずれていると考えられる．そこで，中央から 1 メッシュ左にずらして強制変位させるようにシミュレーションを実行した．このシミュレーション結果と第一回目の実験結果を比較する．マーカ#2 では x 軸方向におよそ 1 mm，y 軸方向におよそ 0.5 mm，マーカ#3 では x 軸方向におよそ 1.8 mm，y 軸方向におよそ 0.5 mm，マーカ#4 では x 軸方向におよそ 2.8 mm，y 軸方向におよそ 0.2 mm 程度の誤差が生じている．構築した柔軟物 FE モデルは内部マーカの移動方向と変位量をある程度表すことができるが，x 軸方向の誤差が大きい．第一回目の実験結果との比較においても，同様の評価が得られる．誤差の原因としては，1) パラメータの同定誤差，2) 変形特性の非線型性や異方性，3) 変形特性の非均一性，特にアガーの表面と内部とでパラメータが異なることが挙げられる．

MR 撮像による内部マーカ変位との比較　Table 2.2 に示すように，アクリル棒の真下に位置するマーカ#5 は，y 方向に下向きの変位が確認できる．また除重後 y 方向上向きに戻り変位を生じている．したがって，MRI によりレオレジー変形を計測することが可能であることを確認した．一方，今回の実験では，他のマーカに大きな変位を確認できなかった．これは，中心をアクリル棒で押して変位を与えたため，中心から離れた場所にあるマーカに力が伝わっていない可能性が高い．変位の与え方を再考する必要がある．

2.5　結言

本章で述べたように，FE モデルを用いてアガーの内部変形を定性的に表すことができる．今回のモデルは，線形等方性材料が均一に分布していることを仮定したが，モデルの精度を上げるためには非線形性あるいは異方性や非均一性を導入する必要がある．

40

2006 9th Int. Conf. Control, Automation, Robotics and Vision
Singapore, 5-8th December 2006

Validation of FE Deformation Models using Ultrasonic and MR Images

Junji Muramatsu, Takashi Ikuta, Shinichi Hirai
Dept. Robotics, Ritsumeikan Univ.
Kusatsu, Shiga 525-8577, Japan

Shigehiro Morikawa
Shiga University of Medical Science
Otsu, Shiga 520-2192, Japan

***Abstract*— This paper describes the measurement of inner deformation of a rheological object using ultrasonic and MR images and comparison the measured and simulated deformations. We apply finite element (FE) model to simulate elastic, viscoplastic, and rheological deformation of soft objects. Ultrasonic and MR images are used to reveal the inner deformation of a soft object. Here we report the measurement and its evaluating by comparing measured and simulated deformations.**

***Keywords*—simulation, measurement, FE model, ultrasonic images, MR images**

I. Introduction

Modeling of soft objects such as food dough and biological tissue is a current challenging issue in surgical simulation, human modeling, and food engineering. Physically-based modeling has been proposed in computer graphics to simulate the dynamic behavior of soft objects. This approach has been directly applied to surgical simulation and human modeling. Physical models are built in this approach to compute the deformation of soft objects. The deformed shapes were validated experimentally but the inner deformation has been out of focus because of the lack of sensing method. We have to validate the physical models by comparing the inner deformation of soft objects. In addition, most physical models are based on the assumption that the deformation is isotropic and uniform. Unfortunately, actual soft objects often do not follow this assumption. We should relax this assumption to build more realistic physical models. Here we have to measure the inner deformation of soft objects to build the realistic models.

We have developed the modeling and identification of rheologically deformable objects [1], [2] but the inner deformation has been out of scope. Recent progress in ultrasonography and three dimensional imaging such as CT and MRI is impressive [3], [4]. Using these technologies, we can measure the inner deformation of deformable soft objects for the validation of models as well as the modeling based on the inner deformation measurement. This paper describes the inner measurement of rheological object deformation and the comparison between the measured and simulated deformations.

II. Simulation of Dynamic Deformation using FE Models

a) FE model of elastic object: This section describes FE (Finite Element) model of elastic objects. In FE modeling, an object is described by a set of triangles or tetrahedra. The object deformation is then formulated by the deformation of individual triangles or tetrahedra. In this section, we formulate planar deformation of an object of thickness h. The object is given by a set of triangles. Let T_p be one triangle, of which vertices are P_i, P_j, and P_k. Assume that P_i, P_j, and P_k follow the triangle T_p counterclockwise. Let $[\xi_i, \eta_i]^{\mathrm{T}}$ be the initial position of vertex P_i. Let S_p denotes the area of triangle T_p at its initial shape.

Let two-dimensional vector $\boldsymbol{u}_i$ denotes the displacement of vertex P_i. Deformation of triangle T_p is then described by the displacement of three vertices $\boldsymbol{u}_i$, $\boldsymbol{u}_j$, and $\boldsymbol{u}_k$. Let $\boldsymbol{f}_i^p$ be an elastic force exerted at vertex P_i by the deformation of triangle T_p. Assuming that the elasticity is uniform and isotropic, the elastic deformation is characterized by Lamé's constants λ and μ. Note that Lamé's constants are described by Young's modulus E and Poisson ratio ν as follows:

$$\lambda = \frac{\nu E}{(1+\nu)(1-2\nu)}, \qquad \mu = \frac{E}{2(1+\nu)}. \tag{1}$$

The deformation of triangle T_p yields a set of elastic forces exerted at its vertices:

$$\begin{bmatrix} \boldsymbol{f}_i^p \\ \boldsymbol{f}_j^p \\ \boldsymbol{f}_k^p \end{bmatrix} = K_p \begin{bmatrix} \boldsymbol{u}_i \\ \boldsymbol{u}_j \\ \boldsymbol{u}_k \end{bmatrix}. \tag{2}$$

Partial elastic matrix K_p is given by $\lambda J_p^\lambda + \mu J_p^\mu$, where J_p^λ and J_p^μ are partial connection matrices given as follows:

$$J_p^\lambda = \frac{h}{4S_p} \begin{bmatrix} A_{j,k;j,k} & A_{j,k;k,i} & A_{j,k;i,j} \\ A_{k,i;j,k} & A_{k,i;k,i} & A_{k,i;i,j} \\ A_{i,j;j,k} & A_{i,j;k,i} & A_{i,j;i,j} \end{bmatrix} \tag{3}$$

$$J_p^\mu = \frac{h}{4S_p} \begin{bmatrix} 2B_{j,k;j,k} & 2B_{j,k;k,i} & 2B_{j,k;i,j} \\ 2B_{k,i;j,k} & 2B_{k,i;k,i} & 2B_{k,i;i,j} \\ 2B_{i,j;j,k} & 2B_{i,j;k,i} & 2B_{i,j;i,j} \end{bmatrix} + \frac{h}{4S_p} \begin{bmatrix} C_{j,k;j,k} & C_{j,k;k,i} & C_{j,k;i,j} \\ C_{k,i;j,k} & C_{k,i;k,i} & C_{k,i;i,j} \\ C_{i,j;j,k} & C_{i,j;k,i} & C_{i,j;i,j} \end{bmatrix}. \tag{4}$$

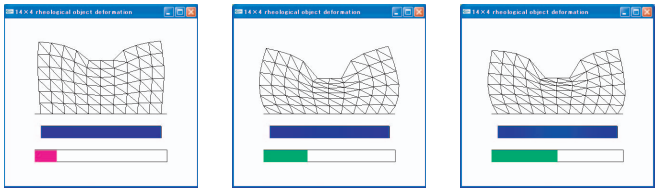

(a) 5 s (b) 10 s (c) 15 s

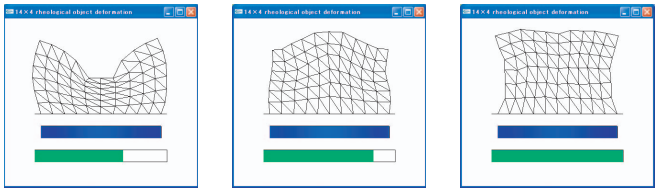

(d) 20 s (e) 25 s (f) 30 s

Fig. 1. Simulation of elastic deformation

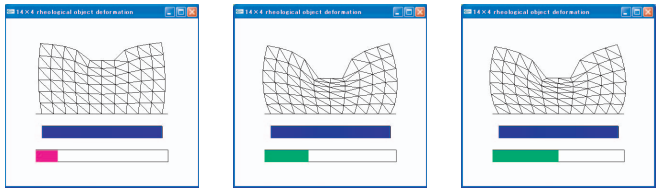

(a) 5 s (b) 10 s (c) 15 s

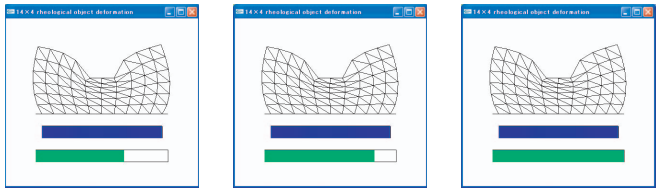

(d) 20 s (e) 25 s (f) 30 s

Fig. 2. Simulation of viscoplastic deformation

where

$$A_{i,j;l,m} = \begin{bmatrix} (\eta_i - \eta_j)(\eta_l - \eta_m) & -(\eta_i - \eta_j)(\xi_l - \xi_m) \\ -(\xi_i - \xi_j)(\eta_l - \eta_m) & (\xi_i - \xi_j)(\xi_l - \xi_m) \end{bmatrix},$$

$$B_{i,j;l,m} = \begin{bmatrix} (\eta_i - \eta_j)(\eta_l - \eta_m) & 0 \\ 0 & (\xi_i - \xi_j)(\xi_l - \xi_m) \end{bmatrix},$$

$$C_{i,j;l,m} = \begin{bmatrix} (\xi_i - \xi_j)(\xi_l - \xi_m) & -(\xi_i - \xi_j)(\eta_l - \eta_m) \\ -(\eta_i - \eta_j)(\xi_l - \xi_m) & (\eta_i - \eta_j)(\eta_l - \eta_m) \end{bmatrix}.$$

Let $\boldsymbol{f}_i$ be a resultant elastic force at nodal point P_i. The resultant force $\boldsymbol{f}_i$ is given by the sum of elastic forces caused by the deformation of triangles involving nodal point P_i:

$$\boldsymbol{f}_i = \sum_{\text{triangle } \mathrm{T}_p \text{ involving vertex } \mathrm{P}_i} \boldsymbol{f}_i^p. \tag{5}$$

Let $\boldsymbol{u}_\mathrm{N}$ be a collective vector consisting of displacement vectors at individual nodal points. A set of elastic forces at individual nodal points is then collectively described as $-K\boldsymbol{u}_\mathrm{N}$. Elastic matrix K can be constructed from partial elastic matrices K_p.

Assuming that mass of a triangle equally concentrates to its three vertices, inertia matrix M_p of triangle T_p is given by a block diagonal matrix as follows:

$$M_p = \frac{\rho h S_p}{3} \begin{bmatrix} I_{2\times 2} & O_{2\times 2} & O_{2\times 2} \\ O_{2\times 2} & I_{2\times 2} & O_{2\times 2} \\ O_{2\times 2} & O_{2\times 2} & I_{2\times 2} \end{bmatrix}. \tag{6}$$

Inertia matrix M of the object can be constructed from partial inertia matrices M_p.

In this section, we assume that an object deforms on the floor, implying that we should incorporate a geometric constraint caused by the floor. We apply Constraint Stabilization Method (CSM) to take the constraint into consideration. Let a geometric constraint be $A^\mathrm{T}\boldsymbol{u}_\mathrm{N} = 0$, where matrix A selects nodal points on which the constraint is imposed. Equation of motion of the constrained nodal points is collectively given by

$$A^\mathrm{T}\ddot{\boldsymbol{u}}_\mathrm{N} + A^\mathrm{T}(2\omega\dot{\boldsymbol{u}}_\mathrm{N} + \omega^2\boldsymbol{u}_\mathrm{N}) = \boldsymbol{0}. \tag{7}$$

Introducing a set of Lagrange's multipliers $\boldsymbol{\lambda}$, which corresponds to a set of constraint forces, a set of equations of motion of individual nodal points on the object is described as follows:

$$-K\boldsymbol{u}_\mathrm{N} + \boldsymbol{f} + A\boldsymbol{\lambda} - M\ddot{\boldsymbol{u}}_\mathrm{N} = 0, \tag{8}$$

where $\boldsymbol{f}$ denotes a set of external forces applied to individual nodal points. Introducing nodal velocity vector $\boldsymbol{v}_\mathrm{N} = \dot{\boldsymbol{u}}_\mathrm{N}$, we have a set of differential equations of the first order:

$$\begin{bmatrix} I & & \\ & M & -A \\ & -A^\mathrm{T} & \end{bmatrix} \begin{bmatrix} \dot{\boldsymbol{u}}_\mathrm{N} \\ \dot{\boldsymbol{v}}_\mathrm{N} \\ \boldsymbol{\lambda} \end{bmatrix} = \begin{bmatrix} \boldsymbol{v}_\mathrm{N} \\ -K\boldsymbol{u}_\mathrm{N} + \boldsymbol{f} \\ A^\mathrm{T}\left(2\omega\boldsymbol{v}_\mathrm{N} + \omega^2\boldsymbol{u}_\mathrm{N}\right) \end{bmatrix}. \tag{9}$$

Giving the values of state variables $\boldsymbol{u}_\mathrm{N}$ and $\boldsymbol{v}_\mathrm{N}$, we can compute the coefficient matrix on the left and the vector on the right. Since the coefficient matrix is regular, we can numerically compute $\dot{\boldsymbol{u}}_\mathrm{N}$ and $\dot{\boldsymbol{v}}_\mathrm{N}$. Thus, applying numerical integration such as Runge-Kutta method, we can numerically compute the displacement and velocity of individual nodal points, resulting that we can compute the deformation of the object.

Fig. 1 shows a simulation result of an elastic object deforming. An elastic object is fixed on the floor. Simulation time is 30 s. The center of the top face is pushed down during the first 0 s, the displacement is kept during the next 10 s, and then the constraint is released. The density of the object is $\rho = 6.4$ and its thickness is $h = 1.0$. The Young's modulus is $E = 10$ and Poisson ratio is $\nu = 0.35$.

b) FE model of viscoplastic object: Viscoplastic deformation can be formulated by Maxwell model, which is a serial connection of an elastic element and a viscous element. Deformation remains after an applied force is released. A set of viscoplastic forces caused by the deformation of a viscoplastic object is given by

$$J^\lambda \boldsymbol{w}^\lambda + J^\mu \boldsymbol{w}^\mu. \tag{10}$$

Connection matrices J^λ and J^μ can be constructed from partial connection matrices J_p^λ and J_p^μ at individual triangles.

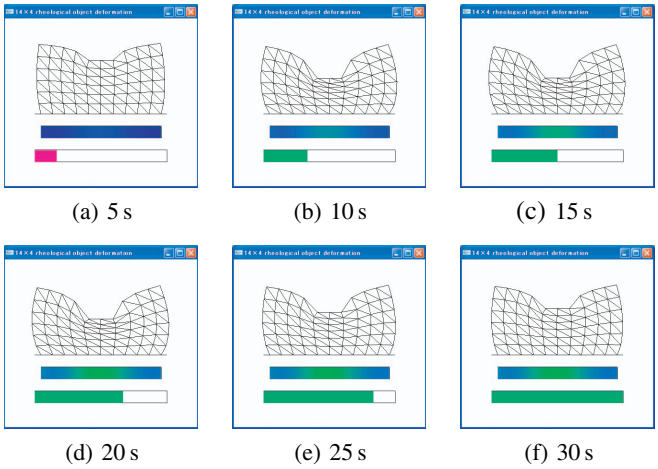

(a) 5 s (b) 10 s (c) 15 s

(d) 20 s (e) 25 s (f) 30 s

Fig. 3. Simulation of rheological deformation

Moreover, vector $\boldsymbol{w}^{\lambda}$ and $\boldsymbol{w}^{\mu}$ satisfy the following differential equations:

$$\dot{\boldsymbol{w}}^{\lambda} = -\frac{\lambda^{\mathrm{ela}}}{\lambda^{\mathrm{vis}}}\boldsymbol{w}^{\lambda} + \lambda^{\mathrm{ela}}\boldsymbol{v}_{\mathrm{N}}, \tag{11}$$

$$\dot{\boldsymbol{w}}^{\mu} = -\frac{\mu^{\mathrm{ela}}}{\mu^{\mathrm{vis}}}\boldsymbol{w}^{\mu} + \mu^{\mathrm{ela}}\boldsymbol{v}_{\mathrm{N}}. \tag{12}$$

Replacing a set of elastic forces $-K\boldsymbol{u}_{\mathrm{N}}$ in the right side of eq.(9) by a set of viscoplastic forces $-\left(J^{\lambda}\boldsymbol{w}^{\lambda} + J^{\mu}\boldsymbol{w}^{\mu}\right)$ and adding differential equations (11) and (12) yield a set of differential equations that describes viscoplastic deformation. Solving the obtained differential equations numerically, we can simulate the deformation of a viscoplastic object. Fig. 2 shows a simulation result of the deformation of a viscoplastic object. Viscoplastic parameters are $E = 90$ and $C = 50$, Poisson's ratios are $\nu^{\mathrm{ela}} = \nu^{\mathrm{vis}} = 0.35$.

c) FE model of rheological object: Rheological deformation can be formulated by three-element model, which is a serial connection of a Voigt model and a viscous element. This element shows both viscoelastic deformation and plastic deformation. A set of rheological forces caused by the deformation of a rheological object is given by

$$(\lambda^{\mathrm{vis}}J^{\lambda} + \mu^{\mathrm{vis}}J^{\mu})\boldsymbol{v}_{\mathrm{N}} + J^{\lambda}\boldsymbol{w}^{\lambda} + J^{\mu}\boldsymbol{w}^{\mu}. \tag{13}$$

Vector $\boldsymbol{w}^{\lambda}$ and $\boldsymbol{w}^{\mu}$ satisfy the following differential equations:

$$\dot{\boldsymbol{w}}^{\lambda} = -\frac{\lambda^{\mathrm{ela}}}{\lambda_1^{\mathrm{vis}} + \lambda_2^{\mathrm{vis}}}\left(\boldsymbol{w}^{\lambda} - \lambda_2^{\mathrm{vis}}\boldsymbol{v}_{\mathrm{N}}\right), \tag{14}$$

$$\dot{\boldsymbol{w}}^{\mu} = -\frac{\mu^{\mathrm{ela}}}{\mu_1^{\mathrm{vis}} + \mu_2^{\mathrm{vis}}}\left(\boldsymbol{w}^{\mu} - \mu_2^{\mathrm{vis}}\boldsymbol{v}_{\mathrm{N}}\right). \tag{15}$$

Parameters λ_1^{vis} and μ_1^{vis} characterize the object viscosity while λ_2^{vis} and μ_2^{vis} determine the object plasticity. Solving the differential equations numerically, we can simulate the deformation of a rheological object. Fig. 3 shows a simulation result of the deformation of a rheological object. Rheological parameters are $E = 30$, $C^{\mathrm{ela}} = 200$, and $C^{\mathrm{vis}} = 500$, Poisson's ratios are $\nu^{\mathrm{ela}} = \nu_1^{\mathrm{vis}} = \nu_2^{\mathrm{vis}} = 0.35$. The three-element model can describe viscoelastic, viscoplastic, and rheological deformations in a coherent manner. Actually, plastic deformation is described by letting $E = 0$. Letting $C^{\mathrm{vis}} = \infty$, the model acn describe viscoelastic deformation.

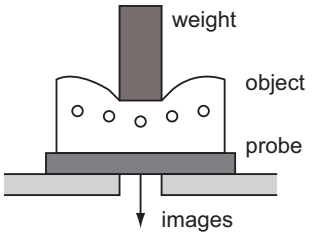

Fig. 4. Location of probe and object

Fig. 5. Example of ultrasonic image

III. Measurement of Inner Deformation via Ultrasonography

This section describes the sensing of inner deformation of a deformable object using ultrasonic imaging device. Ultrasonic waves are transmitted from a probe and the reflected waves are received at the probe. The received wave signals are sent to a computer to construct successive ultrasonic images from the signals. We have used a linear probe and B mode imaging, where the pixel value of an image corresponds to wave amplitude to measure the successive deformation of a cross-sectional plane. We have used Hitachi EUB–240. Resonance frequency of the probe is 3.5 MHz, frame rate is 24.6 Hz, and the resolution of images is 320×240 pixels. We assumed that sound travels at its standard speed in tissue 1530 m/s.

A probe is set below a target object as shown in Fig. 4 so that the probe be in contact with the object to measure its inner deformation. The target object is made of agar consisting of carrageenan and locust bean gum. Carrageenan is a polysaccharide extracted from seaweeds. Locust bean gum is a galactmannan extracted from Carob tree seeds. This agar shows rheological deformation. Since the agar contains mush water, we can obtain distinct ultrasonic images of the target object deformation. We used agar of concentration 5.0 %.

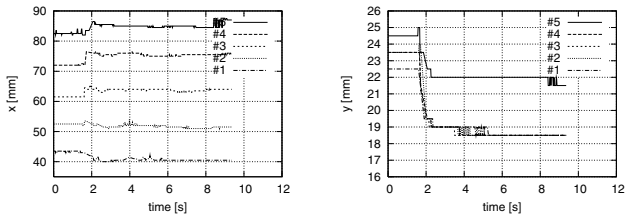

(a-1) coordinate x (a-2) coordinate y

(a) trail 1

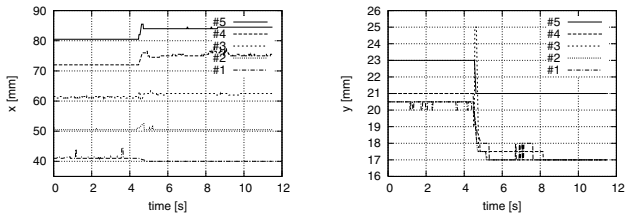

(b-1) coordinate x (b-2) coordinate y

(b) trail 2

Fig. 6. Position of markers detected by ultrasonic images

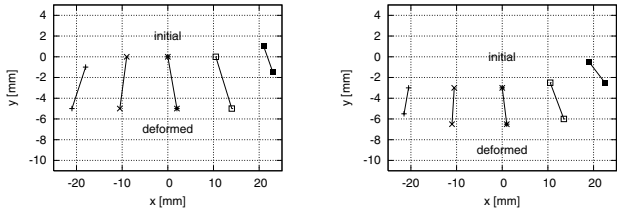

(a) trial 1 (b) trial 2

Fig. 7. Position of markers in initial and deformed shapes

The target object is a rectangular parallelepiped of which top surface is a square of 75 mm length and height is 30 mm. The object weighs 200 g. We inserted five makers along the central cross-sectional plane of the object with the interval of 10 mm. Let us put a cylindrical weight of weight 500 g and diameter 40 mm on the center of the object to surface to deform the object. A measured deformation is shown in Fig. 5. We find five markers at the bottom of the image and the object surface above the markers. Additionally, we find ghosts of markers and the surface above. Positions of markers are computed by processing measured images. We specify a processing region in images to eliminate the ghosts. We can compute the displacements of markers from images before and after deformation. The humidity was 34 % and the temperature was 26 ℃. Temperature of the object surface was 23 ℃.

Fig. 6-(a) and Fig. 6-(b) show the first and the second measurement results. We assumed that the initial position of the middle marker be the origin of the coordinate system. We have eliminated extraordinary measured values comparing the actual deformation, resulting the lack of values. Table I summarizes the measured values at the initial shape and at the deformed shape after 6 s. The values are plotted in Fig. 7.

TABLE I

MARKER COORDINATES IN INITIAL AND DEFORMED SHAPES DETECTED BY ULTRASONIC IMAGES (MM)

trial 1		
marker	initial shape	deformed shape
#1	(−18.0, −1.0)	(−21.0, −5.0)
#2	(−9.0, 0.0)	(−10.5, −5.0)
#3	(0.0, 0.0)	(2.0, −5.0)
#4	(10.5, 0.0)	(14.0, −5.0)
#5	(21.0, 1.0)	(23.0, −1.5)
trial 2		
marker	initial shape	deformed shape
#1	(−20.5, −3.0)	(−21.5, −5.5)
#2	(−10.5, −3.0)	(−11.0, −6.5)
#3	(0.0, −3.0)	(1.0, −6.5)
#4	(10.5, −2.5)	(13.5, −6.0)
#5	(19.0, −0.5)	(22.5, −2.5)

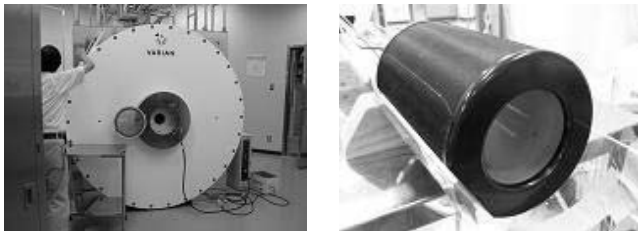

(a) full view (b) RF coil

Fig. 8. MRI device

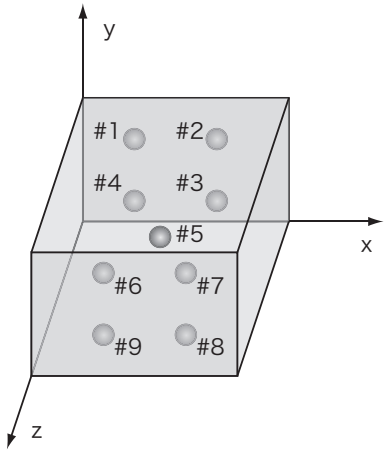

Fig. 9. Location of markers in MR imaging

IV. MEASUREMENT OF INNER DEFORMATION VIA MR IMAGING

An MRI device measures cross-sectional images of a target object and obtain a three-dimensional image by constructing the cross-sectional images. Cross-sectional images are referred to as slice images and the interval between two slice images is referred to as slice interval. MR imaging enables us to detect a cross-sectional image along any plane and to measure three-dimensional deformation inside an object. Unfortunately, it takes much time to obtain a three-dimensional image, making it difficult to capture dynamic deformation of an object. We have used a MRI device shown in Fig. 8-(a), which is installed at Shiga University of Medical Science. A target object is fixed

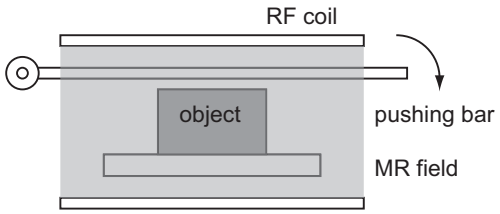

Fig. 10. Setup in MR imaging

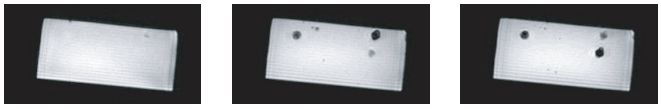

(a-1) slice 1 (a-2) slice 2 (a-3) slice 3
(a) initial state

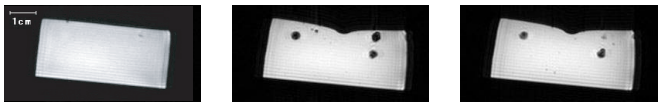

(b-1) slice 1 (b-2) slice 2 (b-3) slice 3
(b) deformed state

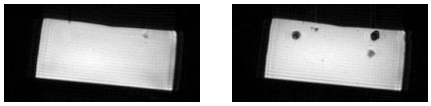

(c-1) slice 1 (c-2) slice 2 (c-3) slice 3
(c) stationary state

Fig. 11. MR images at initial, deformed, and stationary states

inside of an RF coil, shown in Fig. 8-(b), before the coil is inserted into the device for the measurement.

The inner diameter of an RF coil used in our experiment is 63 mm. A target object of width 55 mm, depth 55 mm, and height 25 mm made of agar on an acrylic plate of width 55 mm and thickness 2 mm is inserted into the coil. Plastic beads of diameter 2 mm are inserted in the target object as markers. The location of the markers is illustrated in Fig. 9. Gadolinium medium is mixed with agar to emphasize the image contrast.

TABLE II

MARKER COORDINATES AT INITIAL, DEFORMED, AND STATIONARY STATES DETECTED BY MR IMAGES (MM)

marker	initial state	deformed state	stationary state
#1	(12, 21, 11)	(12, 21, 11)	(12, 21, 11)
#2	(45, 25, 10)	(41, 24, 10)	(46, 24, 10)
#3	(45, 17, 12)	(41, 16, 11)	(45, 16, 12)
#4	(17, 24, 18)	(18, 24, 17)	(17, 24, 17)
#5	(25, 20, 28)	(25, 18, 27)	(25, 20, 27)
#6	(12, 21, 42)	(12, 21, 42)	(11, 21, 42)
#7	(44, 27, 43)	(45, 24, 44)	(44, 26, 43)
#8	(45, 17, 43)	(47, 16, 43)	(45, 16, 43)
#9	(11, 7, 44)	(11, 7, 44)	(11, 7, 43)

An acrylic cylindrical bar of diameter 20 mm is through the coil. One end is fixed and the other end is pushed down manually to deform a target object below the bar, as shown in Fig. 10. The bar is along the z-axis denoted in Fig. 9. We have applied two measurements. The first measurement is three-dimensional and static while the second measurement is two-dimensional and dynamic. In the first measurement, the MRI device obtains the successive three-dimensional images of slice interval 2 mm. The initial shape where no external forces are applied to the object, the deformed shape where the bar is pushed down, and the relaxed shape after the applied forces are released away are measured with enough time intervals. In the second measurement, the MRI device obtains successive images of one cross-sectional plane. The bar is pushed down and is released back dynamically.

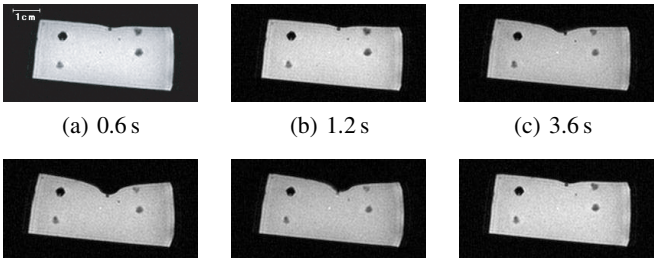

(a) 0.6 s (b) 1.2 s (c) 3.6 s
(d) 7.2 s (e) 9.6 s (f) 12.0 s

Fig. 12. Successive images of one cross-section

The result of the first measurement is shown in Fig. 11. We obtained a set of 30 slice images with slice interval 2 mm. The figure shows successive 3 slices of the 30 images. Fig. 11-(a) through (c) correspond to the initial shape, Fig. 11-(d) through (f) correspond to the deformed shape, and Fig. 11-(g) through (i) correspond to the relaxed shape. The position of markers can be computed from these images. Table II summarizes the computed position of 9 markers inside of a deforming agar object.

The result of the second measurement is shown in Fig. 12. Selecting one slice image where markers can be found and measuring the corresponding cross-sectional plane successively, we examined shorter time interval in the image measurement. We found that time interval of 0.6 s is possible, as shown in the figure. Decreasing the resolution of MR images, we can reduce the time interval more.

V. EVALUATION

d) Comparison between ultrasonic sound images and simulation results: Let us examine FE models by comparing the inner deformation obtained from ultrasonic sound images and simulation results. We have five markers inside of an agar target object. We compare the displacements of the middle three markers, that are, markers #2, #3, and#4. The locations of markers in simulation are described by black circles in Fig. 13. We compute the displacements of markers at the stable deformed shape of the target object. Fig. 14 shows the measured and simulated displacements of the three markers. Fig. 14-(a) through (c) shows respectively the displacements of markers #2, #3, and #4. The solid lines correspond to a simulation result when the center of the top surface of the object is pushed down. The dotted lines correspond to a simulation result when a nodal point deviated from the center to the left side by one mesh is pushed down. Measured

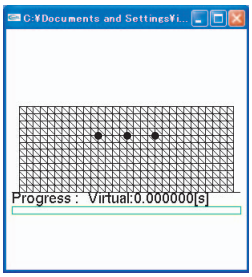

Fig. 13. Location of markers in simulation

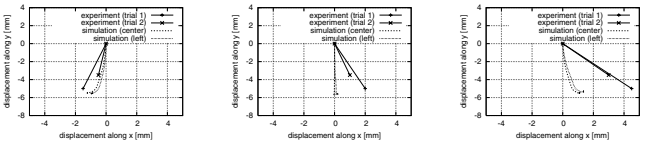

(a) marker #2 (b) marker #3 (c) marker #4

Fig. 14. Comparison between simulation and experiment

displacements from the initial locations to the stable locations are also plotted in the figure. As shown in Fig. 14-(b), the middle marker #3 moves downward but slightly in the right direction. This is caused by the location of the weight is biased to the right direction. Thus, we have computed the dotted lines. Let us compare this simulation with the first measurement. The errors between the measured and simulated results are as follows: 1.0 mm along x-axis and 0.5 mm along y-axis at marker #2, 1.8 mm along x-axis and 0.5 mm along y-axis at marker #3, and 2.8 mm along x-axis and 0.2 mm along y-axis at marker #4. We find that errors along x-axis is relatively large. Comparison with the second measurement also yields this tendency. This discrepancy comes from 1) errors in parameter identification, 2) nonlinearity or non-isotropic nature of deformation, and 3) non-uniform deformation, especially, difference between surface deformation and inner deformation.

e) Comparison between MR images and simulation results: As shown in Table II, marker #5 just under the acrylic pushing bar moves downwards along y-axis. In addition, the marker moves upwards along y-axis after the bar is pulled up. On the other side, displacements of other markers cannot be detected from the MR images. This may be caused by the pushing method we applied. We should reconsider how to deform a target object in the MRI device.

VI. Conclusion

FE models developed in this paper can simulate the inner deformation of an agar object. But, the error along the horizontal axis is relatively large, which may come from nonlinearity or non-isotropic nature of deformation as well as non-uniform deformation, especially, difference between surface deformation and inner deformation. We are going to build FE models considering these properties. We have inserted artificial markers inside a target object to measure the inner deformation of the object. We are going to introduce tracking algorithms in computer vision to measure the inner deformation of actual biological objects.

Acknowledgment

This research was supported by Grant in Aid for Scientific Research (17206024) by the Ministry of Education, Culture, Sports, Science and Technology of Japan.

References

[1] Masafumi Kimura, Yuuta Sugiyama, Seiji Tomokuni, and Shinichi Hirai, *Constructing Rheologically Deformable Virtual Objects*, Proc. IEEE Int. Conf. on Robotics and Automation, pp.3737–3743, Taipei, September, 2003.

[2] Naoki Ueda, Shinichi Hirai, and Hiromi T. Tanaka, *Extracting Rheological Properties of Deformable Objects with Haptic Vision*, Proc. IEEE Int. Conf. on Robotics and Automation, pp.3902–3907, New Orleans, April, 2004.

[3] Frank G. Gress and Ishan Bhattacharya, *Endoscopic Ultrasonography*, Blackwell Publishers, 2001.

[4] Donald W. McRobbie, Elizabeth A. Moore, Martin J. Graves, and Martin R. Prince, *MRI from Picture to Proton*, Cambridge University Press, 2002.

第3章　内部変形計測による非均一弾性特性の同定

3.1　緒言

近年，医療の高度化や多様化が進む中，手術シミュレーションが必要とされている．経験の浅い医師でも，手術シミュレーションで訓練を行うことで，難易度の高い手術を安全に行うことが可能になる．現在，様々な手術シミュレーションシステムが開発されているが，熟練した医師にシステムを使用した意見を聞くと，実際の手術の感触とは違うと答える医師が多い．この原因の一つとして，生体の力学特性の計測が不十分であるため，生体を忠実に再現できていないことが挙げられる．これまでに，生体の力学特性を計測する研究は多く行われている [27, 28, 29, 30, 31, 32]．これらの多くは生体を模擬した試験材料を用いて計測を行っているが，実際の生体とは力学特性が異なる．圧縮試験によって動物体内から取り出した生体組織の力学特性を計測するものもあるが，取り出した後の生体組織は血液が抜けていて弾力がなくなるため力学特性が変ってしまう．そのため，CCD カメラなどにより生体の表面形状を計測する研究も行われている．しかし，生体組織は脂肪などの柔らかい部分や筋肉などの硬い部分が存在するため，力学パラメータの値が場所により異なる．このような生体の非均一性を計測するためには，生体内部の挙動を計測する必要がある．

生体内部の挙動を計測する機器として，コンピュータ断層画像 (Computed Tomography：CT)，超音波装置，磁気共鳴映像（Magnetic Resonance Imaging：MRI）などがある．CT は人体を通過した X 線量を測り，コンピュータを使ってその輪切り断面を画像化する装置である [33]．X 線 CT を用いて乳がんを早期に発見するマンモグラフィーは昔から臨床で用いられている [34]．超音波装置は超音波を対象物に当ててその反響を映像化するものである [35]．超音波装置を用いてしこりの硬さを画像化するエラストグラフィは，ここ数年の間に臨床応用されるようになった [36]．MRI は強力な磁場内に人体を入れ，人体に電波と磁力をパルス状に照射し，人体の水素元素が出す信号を測定，画像化するというものである [37]．術中に患部を撮影しながら手術を進めていく MRI 誘導手術は近年注目を集めている [38]．特に MRI 装置は，被

47

曝がない，神経や血管，靭帯といった微細な組織まで画像化できる，得られた断面画像を再構成することにより三次元での情報が得られるという利点を持つ．このことから，生体の内部の挙動を計測するためには，MRI 装置を使用するのが望ましい．

生体の力学特性を計測するためには，生体に加わる力とそのときに生じる変形が分かればよい．生体の変形は，変形前後の生体内部を MRI 装置で撮影し，得られた画像を解析することにより計測できる．しかし，生体に加わる力は，MRI 空間内にロードセル等の磁性体を持ち込むことができないため計測することが困難である．MRI 空間内でも生体に加わる力を計測することができるように，非磁性体を使用した力センサの研究も行われているが，実用化にはいたっていない [39, 40, 41, 42]．したがって，生体に加わる力を計測しなくても生体の力学特性を計測する手法があれば，MRI 装置を使用して非均一性をもつ生体の力学特性を正確に計測することができる．

本研究は，MRI 装置を用いた柔軟物の内部変形計測結果から非均一 FE モデルの力学パラメータを同定する手法を検証することを目的とする．柔軟物の内部変形計測結果から力学パラメータを同定する手法を提案し，シミュレーションと実験により本手法を検証する．

3.2 FE モデルの変形シミュレーション

本節では，弾性物体の FE モデルと変形シミュレーションの計算式について述べる．まず，二次元の変形シミュレーションについて説明し，それから三次元変形シミュレーションモデルに拡張する．

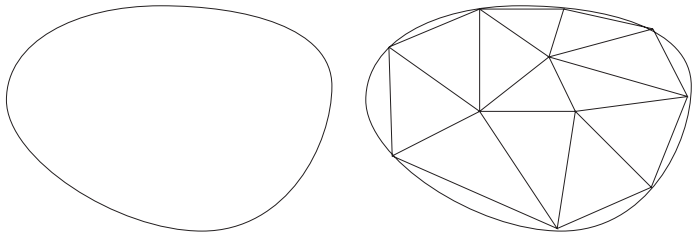

(a) Region (b) Cover by triangles

図 3.1: Cover of two-dimensional region by triangles

3.2.1 二次元変形シミュレーション

本節では，弾性物体の二次元 Finate Element(FE) モデルを述べる．二次元 FE モデルは，Fig. 3.1 に示すように柔軟物体を連続体の三角形要素の集合として表す．これにより，柔軟物の変形は個々の三角形要素の変形の和として表現することが可能になる．そこで，二次元 FE モデルとして厚み h の平面物体の変形を定式化する．物体を三角形の集合で表し，Fig. 3.2 に示すように三角形要素の一つを T^p とする．さらに Tp の頂点を P_i, P_j, P_k とする．ただし，P_i, P_j, P_k は三角形 T^p を反時計回りに辿るとする．頂点 P_i の初期座標を $[\xi_i,\eta_i]^{\mathrm{T}}$ で表す．初期状態における三角形要素 T^p の面積を S^p とする．頂点 P_i の変位を二次元ベクトル $\boldsymbol{u}_i^p$ で表す．三角形 T^p の変形は，三つの頂点の変位 $\boldsymbol{u}_i^p$，$\boldsymbol{u}_j^p$，$\boldsymbol{u}_k^p$ で表される．三角形 T^p の変形により頂点 P_i に生じる弾性力を $\boldsymbol{f}_i^p$ で表す．非均一な弾性特性を表すために，三角形要素ごとにラーメの定数が異なると仮定する．三角形要素の T^p のラーメの定数を λ^p ならびに μ^p で表す．なおラーメの定数は，ヤング率 E^p とポアソン比 ν^p で表すことができる．

$$\lambda^p = \frac{\nu E^p}{(1+\nu^p)(1-2\nu^p)}, \qquad \mu^p = \frac{E^p}{2(1+\nu^p)}. \tag{3.1}$$

三角形 T^p の変形により各頂点に生じる弾性力は，

$$\begin{bmatrix} \boldsymbol{f}_i^p \\ \boldsymbol{f}_j^p \\ \boldsymbol{f}_k^p \end{bmatrix} = \boldsymbol{K}^p \begin{bmatrix} \boldsymbol{u}_i^p \\ \boldsymbol{u}_j^p \\ \boldsymbol{u}_k^p \end{bmatrix} \tag{3.2}$$

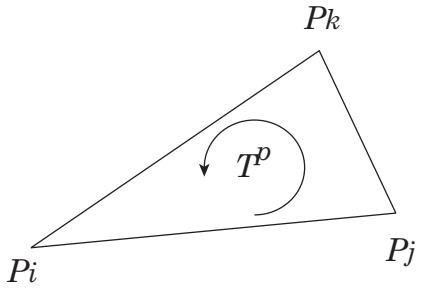

図 3.2: Triangle element

と表される．弾性行列 $\boldsymbol{K}^p$ は $\lambda^p \boldsymbol{J}_\lambda^p + \mu \boldsymbol{J}_\mu^p$ と表すことができる．ここで，$\boldsymbol{J}_\lambda^p$，$\boldsymbol{J}_\mu^p$ は，次式で表される 6×6 の部分接続行列である．

$$\boldsymbol{J}_\lambda^p = \frac{h}{4S^p} \begin{bmatrix} \boldsymbol{A}_{j,k;j,k} & \boldsymbol{A}_{j,k;k,i} & \boldsymbol{A}_{j,k;i,j} \\ \boldsymbol{A}_{k,i;j,k} & \boldsymbol{A}_{k,i;k,i} & \boldsymbol{A}_{k,i;i,j} \\ \boldsymbol{A}_{i,j;j,k} & \boldsymbol{A}_{i,j;k,i} & \boldsymbol{A}_{i,j;i,j} \end{bmatrix}, \tag{3.3}$$

$$\begin{aligned} \boldsymbol{J}_\mu^p &= \frac{h}{4S^p} \begin{bmatrix} 2\boldsymbol{B}_{j,k;j,k} & 2\boldsymbol{B}_{j,k;k,i} & 2\boldsymbol{B}_{j,k;i,j} \\ 2\boldsymbol{B}_{k,i;j,k} & 2\boldsymbol{B}_{k,i;k,i} & 2\boldsymbol{B}_{k,i;i,j} \\ 2\boldsymbol{B}_{i,j;j,k} & 2\boldsymbol{B}_{i,j;k,i} & 2\boldsymbol{B}_{i,j;i,j} \end{bmatrix} \\ &+ \frac{h}{4S^p} \begin{bmatrix} \boldsymbol{C}_{j,k;j,k} & \boldsymbol{C}_{j,k;k,i} & \boldsymbol{C}_{j,k;i,j} \\ \boldsymbol{C}_{k,i;j,k} & \boldsymbol{C}_{k,i;k,i} & \boldsymbol{C}_{k,i;i,j} \\ \boldsymbol{C}_{i,j;j,k} & \boldsymbol{C}_{i,j;k,i} & \boldsymbol{C}_{i,j;i,j} \end{bmatrix} \end{aligned} \tag{3.4}$$

ただし

$$\begin{aligned} \boldsymbol{A}_{i,j;l,m} &= \begin{bmatrix} (\eta_i - \eta_j)(\eta_l - \eta_m) & -(\eta_i - \eta_j)(\xi_l - \xi_m) \\ -(\xi_i - \xi_j)(\eta_l - \eta_m) & (\xi_i - \xi_j)(\xi_l - \xi_m) \end{bmatrix}, \\ \boldsymbol{B}_{i,j;l,m} &= \begin{bmatrix} (\eta_i - \eta_j)(\eta_l - \eta_m) & 0 \\ 0 & (\xi_i - \xi_j)(\xi_l - \xi_m) \end{bmatrix}, \\ \boldsymbol{C}_{i,j;l,m} &= \begin{bmatrix} (\xi_i - \xi_j)(\xi_l - \xi_m) & -(\xi_i - \xi_j)(\eta_l - \eta_m) \\ -(\eta_i - \eta_j)(\xi_l - \xi_m) & (\eta_i - \eta_j)(\eta_l - \eta_m) \end{bmatrix} \end{aligned}$$

である．

Fig. 3.2 において節点 P_i に作用する弾性力を $\boldsymbol{f}_i$ で表す．弾性力 $\boldsymbol{f}_i$ は，節点 P_i を含む三角形要素により発生する力 $\boldsymbol{f}_i^m$ の総和に一致するので

$$\boldsymbol{f}_i = \sum_{m \in L_i} \boldsymbol{f}_i^m \tag{3.5}$$

となる．ここで，L_i は節点 P_i を含む三角形要素の集合である．個々の三角形要素における弾性行列 $\boldsymbol{K}^p$ から，物体全体の弾性行列 $\boldsymbol{K}$ を構成することができる．各頂点における変位ベクトルを並べて得られるベクトルを $\boldsymbol{u}_N$ と表す．各頂点における弾性力はまとめて $-\boldsymbol{K}\boldsymbol{u}_N$ と表すことができる．ρ を物体の密度とする．質量が三角形要素の頂点に集中していると仮定すると，三角形要素 T^p における慣性行列 $\boldsymbol{M}^p$ は次式のように表すことができる．

$$\boldsymbol{M}^p = \frac{\rho h S^p}{3} \boldsymbol{E}_{6\times 6} \tag{3.6}$$

ここで，$\boldsymbol{E}_{6\times 6}$ は単位行列である．個々の三角形要素における慣性行列 $\boldsymbol{M}^p$ から，物体全体の慣性行列 $\boldsymbol{M}$ を構成することができる．物体が床に接した状態を想定して変形シミュレーションを行う場合，物体が床から離れないように拘束する必要がある．ここでは制約安定化法 (Constraint Stabilization Method：CSM) を用いて物体を拘束する．固定のための拘束条件式を $\boldsymbol{A}^T\boldsymbol{u}_N = 0$ とする．行列 $\boldsymbol{A}$ は拘束する節点を表す行列である．これより固定されている節点の運動方程式は次式で表すことができる．

$$\boldsymbol{A}^T\ddot{\boldsymbol{u}}_N + \boldsymbol{A}^T(2\omega\dot{\boldsymbol{u}}_N + \boldsymbol{M}\boldsymbol{u}_N) = \boldsymbol{0}. \tag{3.7}$$

また，拘束力を表すラグランジュの未定乗数 $\boldsymbol{\lambda}$ を導入することで，物体の各節点の運動方程式は次式で表すことができる．

$$-\boldsymbol{K}\boldsymbol{u}_N + \boldsymbol{f} + \boldsymbol{A}\boldsymbol{\lambda} - \boldsymbol{M}\ddot{\boldsymbol{u}}_N = \boldsymbol{0}. \tag{3.8}$$

ここで，$\boldsymbol{f}$ は各節点に加わる外力を示す．節点の速度ベクトル $\boldsymbol{u}_N = \dot{\boldsymbol{u}}_N$ を導入すると，一階の微分方程式系

$$\begin{bmatrix} \boldsymbol{I} & & \\ & \boldsymbol{M} & -\boldsymbol{A} \\ & -\boldsymbol{A}^T & \end{bmatrix} \begin{bmatrix} \dot{\boldsymbol{u}}_N \\ \dot{\boldsymbol{v}}_N \\ \boldsymbol{\lambda} \end{bmatrix} = \begin{bmatrix} \boldsymbol{v}_N \\ -\boldsymbol{K}\boldsymbol{u}_N + \boldsymbol{f} \\ \boldsymbol{A}^T(2\omega\boldsymbol{v}_N + \omega^2\boldsymbol{u}_N) \end{bmatrix} \tag{3.9}$$

を得る．状態変数 $\boldsymbol{u}_N$，$\boldsymbol{v}_N$ の値を与えると，左辺の係数行列と右辺のベクトルの値を求めることができる．左辺の係数行列は正則であるので，上式を数値的に解くことにより $\dot{\boldsymbol{u}}_N$，$\dot{\boldsymbol{v}}_N$ を求めることができる．したがって，Runge-Kutta 法などの数値積分法を用いると，各節点の変位と速度を計算することができ，結果として物体の変形を求めることができる．

3.2.2 三次元変形シミュレーション

三次元 FE モデルでは柔軟物体を連続体の四面体要素の集合として表す．これにより，柔軟物の変形は個々の四面体要素の変形の和として表現することが可能になる．そこで，三次元 FE モデルとして立体物体の変形を定式化する．物体を四面体の集合で表し，Fig. 3.3 に示すように四面体要素の一つを T^p と表す．さらに T^p の頂点を P_i, P_j, P_k, P_l とする．ただし，頂点を P_l とした場合，底面 P_i, P_j, P_k を反時計回りに辿るとする．

$$\begin{bmatrix} \boldsymbol{f}_i^p \\ \boldsymbol{f}_j^p \\ \boldsymbol{f}_k^p \\ \boldsymbol{f}_l^p \end{bmatrix} = \boldsymbol{K}^p \begin{bmatrix} \boldsymbol{u}_i^p \\ \boldsymbol{u}_j^p \\ \boldsymbol{u}_k^p \\ \boldsymbol{u}_l^p \end{bmatrix} \tag{3.10}$$

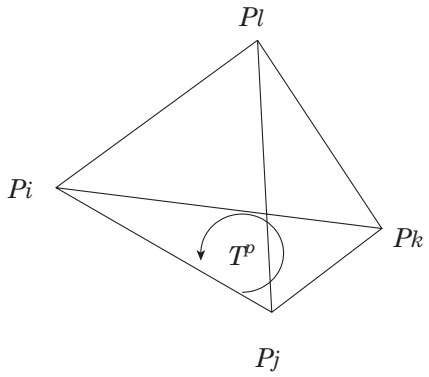

図 3.3: Tetrahedra element

と表される．弾性行列 $\boldsymbol{K}^p$ は $\lambda \boldsymbol{J}^p_\lambda + \mu \boldsymbol{J}^p_\mu$ と表すことができる．ここで，$\boldsymbol{J}^p_\lambda$，$\boldsymbol{J}^p_\mu$ は，次式で表される 12×12 の部分接続行列である．

$$
\boldsymbol{J}^p_\lambda = \frac{1}{36S^p}
\begin{bmatrix}
\boldsymbol{A}_{j,k,l;j,k,l} & -\boldsymbol{A}_{j,k,l;k,l,j} & \boldsymbol{A}_{j,k,l;l,i,j} & -\boldsymbol{A}_{j,k,l;i,j,k} \\
-\boldsymbol{A}_{k,l,i;j,k,l} & \boldsymbol{A}_{k,l,i;k,l,j} & -\boldsymbol{A}_{k,l,i;l,i,j} & \boldsymbol{A}_{k,l,i;i,j,k} \\
\boldsymbol{A}_{l,i,j;j,k,l} & -\boldsymbol{A}_{l,i,j;k,l,j} & \boldsymbol{A}_{l,i,j;l,i,j} & -\boldsymbol{A}_{l,i,j;i,j,k} \\
-\boldsymbol{A}_{i,j,k;j,k,l} & \boldsymbol{A}_{i,j,k;k,l,j} & -\boldsymbol{A}_{i,j,k;l,i,j} & \boldsymbol{A}_{i,j,k;i,j,k}
\end{bmatrix},
$$

$$
\boldsymbol{J}^p_\mu = \frac{1}{36S^p}
\begin{bmatrix}
2\boldsymbol{B}_{j,k,l;j,k,l} & -2\boldsymbol{B}_{j,k,l;k,l,j} & 2\boldsymbol{B}_{j,k,l;l,i,j} & -2\boldsymbol{B}_{j,k,l;i,j,k} \\
-2\boldsymbol{B}_{k,l,i;j,k,l} & 2\boldsymbol{B}_{k,l,i;k,l,j} & -2\boldsymbol{B}_{k,l,i;l,i,j} & 2\boldsymbol{B}_{k,l,i;i,j,k} \\
2\boldsymbol{B}_{l,i,j;j,k,l} & -2\boldsymbol{B}_{l,i,j;k,l,j} & 2\boldsymbol{B}_{l,i,j;l,i,j} & -2\boldsymbol{B}_{l,i,j;i,j,k} \\
-2\boldsymbol{B}_{i,j,k;j,k,l} & 2\boldsymbol{B}_{i,j,k;k,l,j} & -2\boldsymbol{B}_{i,j,k;l,i,j} & 2\boldsymbol{B}_{i,j,k;i,j,k}
\end{bmatrix}
$$

$$
+ \frac{1}{36S^p}
\begin{bmatrix}
\boldsymbol{C}_{j,k,l;j,k,l} & -\boldsymbol{C}_{j,k,l;k,l,i} & \boldsymbol{C}_{j,k,l;l,i,j} & -\boldsymbol{C}_{j,k,l;i,j,k} \\
-\boldsymbol{C}_{k,l,i;j,k,l} & \boldsymbol{C}_{k,l,i;k,l,j} & -\boldsymbol{C}_{k,l,i;l,i,j} & \boldsymbol{C}_{k,l,i;i,j,k} \\
\boldsymbol{C}_{l,i,j;j,k,l} & -\boldsymbol{C}_{l,i,j;k,l,i} & \boldsymbol{C}_{l,i,j;l,i,j} & -\boldsymbol{C}_{l,i,j;i,j,k} \\
-\boldsymbol{C}_{i,j,k;j,k,l} & \boldsymbol{C}_{i,j,k;k,l,i} & -\boldsymbol{C}_{i,j,k;l,i,j} & \boldsymbol{C}_{i,j,k;i,j,k}
\end{bmatrix}
$$

52

ただし

$$
\begin{aligned}
\boldsymbol{A}_{i,j,k;l,m,n} &= \begin{bmatrix} a_{i,j,k}a_{l,m,n} & a_{i,j,k}b_{l,m,n} & a_{i,j,k}c_{l,m,n} \\ b_{i,j,k}a_{l,m,n} & b_{i,j,k}b_{l,m,n} & b_{i,j,k}c_{l,m,n} \\ c_{i,j,k}a_{l,m,n} & c_{i,j,k}b_{l,m,n} & c_{i,j,k}c_{l,m,n} \end{bmatrix}, \\
\boldsymbol{B}_{i,j,k;l,m,n} &= \begin{bmatrix} a_{i,j,k}a_{l,m,n} & 0 & 0 \\ 0 & b_{i,j,k}b_{l,m,n} & 0 \\ 0 & 0 & c_{i,j,k}c_{l,m,n} \end{bmatrix}, \\
\boldsymbol{C}_{i,j,k;l,m,n} &= \begin{bmatrix} \alpha_{i,j,k;l,m,n} & b_{i,j,k}a_{l,m,n} & c_{i,j,k}a_{l,m,n} \\ a_{i,j,k}b_{l,m,n} & \beta_{i,j,k;l,m,n} & c_{i,j,k}b_{l,m,n} \\ a_{i,j,k}c_{l,m,n} & b_{i,j,k}c_{l,m,n} & \gamma_{i,j,k;l,m,n} \end{bmatrix}, \\
\alpha_{i,j,k;l,m,n} &= b_{i,j,k}b_{l,m,n} + c_{i,j,k}c_{l,m,n}, \\
\beta_{i,j,k;l,m,n} &= c_{i,j,k}c_{l,m,n} + a_{i,j,k}a_{l,m,n}, \\
\gamma_{i,j,k;l,m,n} &= a_{i,j,k}a_{l,m,n} + b_{i,j,k}b_{l,m,n}, \\
a_{j,k,l} &= \begin{vmatrix} \eta_j & \eta_k \\ \zeta_j & \zeta_k \end{vmatrix} + \begin{vmatrix} \eta_k & \eta_l \\ \zeta_k & \zeta_l \end{vmatrix} + \begin{vmatrix} \eta_l & \eta_j \\ \zeta_l & \zeta_j \end{vmatrix}, \\
b_{j,k,l} &= \begin{vmatrix} \zeta_j & \zeta_k \\ \xi_j & \xi_k \end{vmatrix} + \begin{vmatrix} \zeta_k & \zeta_l \\ \xi_k & \xi_l \end{vmatrix} + \begin{vmatrix} \zeta_l & \zeta_j \\ \xi_l & \xi_j \end{vmatrix}, \\
c_{j,k,l} &= \begin{vmatrix} \xi_j & \xi_k \\ \eta_j & \eta_k \end{vmatrix} + \begin{vmatrix} \xi_k & \xi_l \\ \eta_k & \eta_l \end{vmatrix} + \begin{vmatrix} \xi_l & \xi_j \\ \eta_l & \eta_j \end{vmatrix}.
\end{aligned}
$$

Fig. 3.3 において，節点 P_i に作用する弾性力を $\boldsymbol{f}_i$ で表す．弾性力 $\boldsymbol{f}_i$ は，節点 P_i を含む四面体要素により発生する力 $\boldsymbol{f}_i^m$ の総和に一致するので

$$
\boldsymbol{f}_i = \sum_{m \in L_i} \boldsymbol{f}_i^p \tag{3.11}
$$

となる．ここで，L_i は節点 P_i を含む四面体要素の集合である．各頂点における変位ベクトルを並べて得られるベクトルを $\boldsymbol{u}_N$ と表す．各頂点における弾性力はまとめて $-\boldsymbol{K}\boldsymbol{u}_N$ と表すことができる．質量が四面体要素の頂点に集中していると仮定すると，四面体要素 T^p における慣性行列 $\boldsymbol{M}^p$ は次式のように表すことができる．

$$
\boldsymbol{M}^p = \frac{\rho S^p}{4} \boldsymbol{E}_{12\times 12} \tag{3.12}
$$

ここで，$\boldsymbol{E}_{12\times 12}$ は単位行列である．個々の四面体要素における慣性行列 $\boldsymbol{M}^p$ から，物体全体の慣性行列 $\boldsymbol{M}$ を構成することができる．以後，式 (3.9) と同様に計算を行う．

53

3.3　力学パラメータ同定方法

本節では，柔軟物の内部変形計測結果から非均一 FE モデルの力学パラメータを同定する手法を述べる．また，二次元モデルを用いて本手法の計算例を示す．

3.3.1　力学パラメータの同定原理

提案する手法の基本的な考え方は，力学パラメータが既知の物体を用いて，力学パラメータが未知の物体を変形させ，双方の内部変形を計測した結果から，未知の力学パラメータを同定するというものである．力学パラメータ同定方法の原理を Fig. 3.4 に示す．力学パラメータが既知である部分のばね係数を k_k，ばねの伸びを u_k, ばねの伸びにより生じる力を f_k とする．また，力学パラメータが未知である部分のばね係数を k_u，ばねの伸びを u_u, ばねの伸びにより生じる力を f_u とする．それぞれの力のつり合い式は次式で表すことができる．

$$f_k = k_k u_k, \tag{3.13}$$

$$f_u = k_u u_u. \tag{3.14}$$

節点 i において力がつり合うため，力学パラメータが未知である部分のばね係数は次式となる．

$$k_u = \frac{k_k u_k}{u_u}. \tag{3.15}$$

本研究で求める力学パラメータは，式 (3.1) におけるヤング率 E^p とポアソン比 ν^p のことであり，以上と同様の考え方を用いる．

本研究の力学パラメータ同定方法を Fig. 3.5 に示す．まず，力学パラメータが既知な物体を用いて力学パラメータが未知な物体を変形させる (Fig. 3.5-**(a)**)．ここで，力学パラメータが既知な物体とは，あらかじめ圧縮試験を行って力学パラメータを求めておいた物体である．また，力学パラメータが未知な物体とは，力学パラメータを同定したい物体のことである．

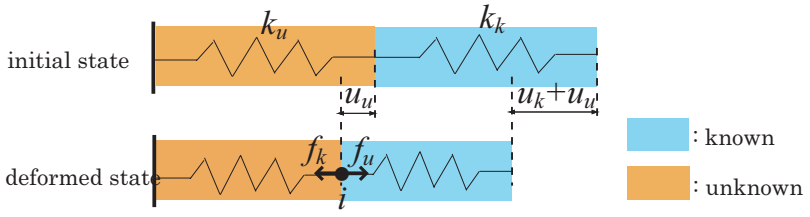

図 3.4: Principle of physical parameters identification

54

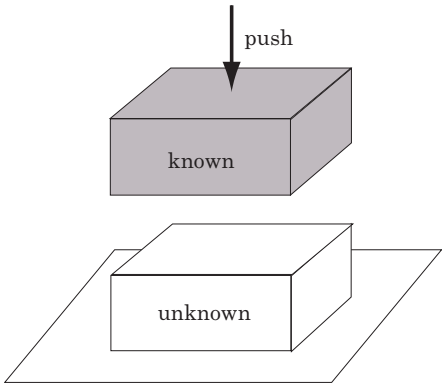

(a) Unknown parameters object is pushed by known parameters object

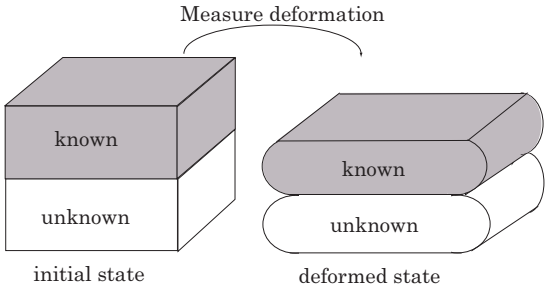

(b) Deformations are measured by MRI

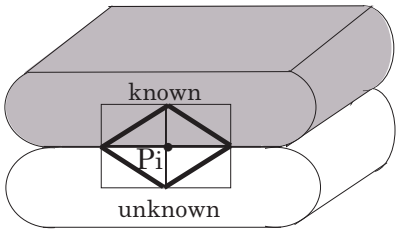

(c) Equilibrium at the i-th nodal point P_i

図 3.5: Method of physical parameters identification

55

変形を加える前の状態（初期状態）と変形を加えた状態（変形状態）を MRI 装置を用いて撮影する (Fig. 3.5-(b))．得られた MRI 画像を解析して双方の物体の内部変形を計測する．MRI 画像からの変形解析方法については第 3.5 章で述べる．内部変形計測結果を式 (3.10) に代入すると，次式のように表すことができる．

$$\begin{bmatrix} \boldsymbol{f}_i^p \\ \boldsymbol{f}_j^p \\ \boldsymbol{f}_k^p \\ \boldsymbol{f}_l^p \end{bmatrix} = \begin{bmatrix} \boldsymbol{A}_\lambda^p & \boldsymbol{A}_\mu^p \\ & \end{bmatrix} \begin{bmatrix} \lambda^p \\ \mu^p \end{bmatrix} \tag{3.16}$$

ここで

$$\begin{aligned} \boldsymbol{A}_\lambda^p &= \boldsymbol{J}_\lambda^p \begin{bmatrix} \boldsymbol{u}_i^p \\ \boldsymbol{u}_j^p \\ \boldsymbol{u}_k^p \\ \boldsymbol{u}_l^p \end{bmatrix} \triangleq \begin{bmatrix} \boldsymbol{A}_{\lambda,i}^p \\ \boldsymbol{A}_{\lambda,j}^p \\ \boldsymbol{A}_{\lambda,k}^p \\ \boldsymbol{A}_{\lambda,l}^p \end{bmatrix}, \\ \boldsymbol{A}_\mu^p &= \boldsymbol{J}_\mu^p \begin{bmatrix} \boldsymbol{u}_i^p \\ \boldsymbol{u}_j^p \\ \boldsymbol{u}_k^p \\ \boldsymbol{u}_l^p \end{bmatrix} \triangleq \begin{bmatrix} \boldsymbol{A}_{\mu,i}^p \\ \boldsymbol{A}_{\mu,j}^p \\ \boldsymbol{A}_{\mu,k}^p \\ \boldsymbol{A}_{\mu,l}^p \end{bmatrix} \end{aligned} \tag{3.17}$$

である．係数行列 $\boldsymbol{A}_\lambda^p$，$\boldsymbol{A}_\mu^p$ は 12×1 の行列となる．

変形状態において力がつりあうため，各節点において力のつり合い式をたてて力学パラメータを同定する (Fig. 3.5-(c))．力学パラメータが既知である部分と未知である部分の境界上にある節点の一つを P_i とする．節点 P_i 回りの四面体要素について考えると，節点 P_i における力のつり合いは次式で表すことができる．

$$\sum_{p \in S_i} \boldsymbol{f}_i^p = 0 \tag{3.18}$$

ここで，S_i は，Fig. 3.5-(c) において太枠で囲った領域で，節点 P_i を含む四面体要素の集合である．四面体要素の集合 S_i は，力学パラメータが既知である四面体要素の集合 K_i と，力学パラメータが未知である四面体要素の集合 U_i から構成される．

$$S_i = K_i + U_i \tag{3.19}$$

したがって，式 (3.18) は，

$$\sum_{p \in U_i} \boldsymbol{f}_i^p = -\sum_{p \in K_i} \boldsymbol{f}_i^p \tag{3.20}$$

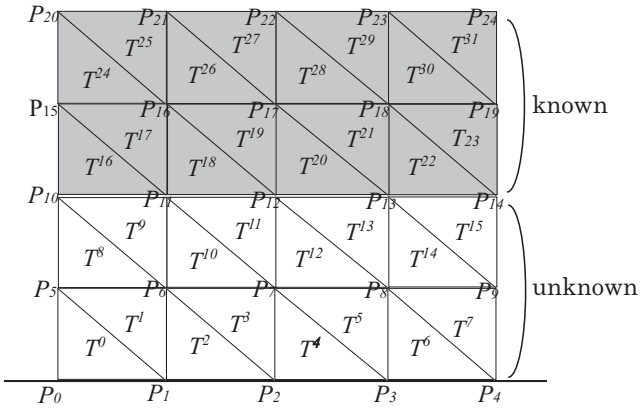

図 3.6: Example of computing physical parameters

表 3.1: Number of parameters and equations

	Parameter λ^p, μ^p $(T^0, T^1, \cdots, T^{15})$	Equation (3.20) $(i = P_5, P_6, \cdots, P_{14})$
Total	$2 \times 16 = 32$	$2 \times 10 = 20$

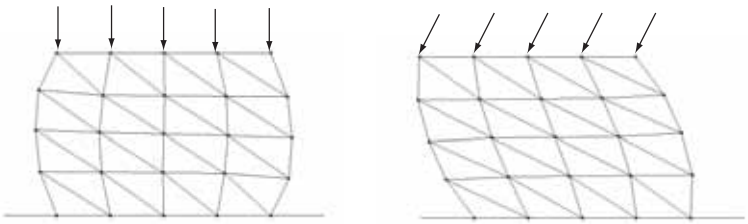

(a) Vertical force (b) Aligned force

図 3.7: Example of pushing operation

となる．ここで，左辺は λ^p，$\mu^p (p \in U_i)$ に関する一次式である．係数行列は，接続行列 $\boldsymbol{J}^p_\lambda$，$\boldsymbol{J}^p_\lambda (p \in U_i)$ と変位ベクトル $\boldsymbol{u}^p_i$，$\boldsymbol{u}^p_j$，$\boldsymbol{u}^p_k$，$\boldsymbol{u}^p_l (p \in U_i)$ により表される．したがって，式 (3.20) を解くことにより，λ^p，μ^p を求めることができる．さらに，式 (3.1) より力学パラメータ E^p，ν^p を同定することができる．

Fig. 3.6 に示す二次元のモデルを用いて，具体的な同定法を述べよう．三次元の力学パラメータ同定方法は二次元の力学パラメータ同定法と同じである．力学パラメータが既知である三角形要素 24 個，未知である三角形要素 24 個から構成されている．形状全体の力学パラメータの未知数の数と節点における力のつり合いによる方程式の本数を Table 3.1 に示す．節点 P_0，P_1，P_2，P_3，P_4 における力のつり合い

57

は，CSM により各節点を床に拘束しており，変形がないため考慮しない．

Table 3.1 より，力学パラメータの未知数が 32 個であるのに対して，節点における力のつり合いによる方程式の本数は 20 本である．この場合，変数の数よりも方程式の本数が少ないため，ノルムを最小にする解を計算する．また，2 通り以上方法で柔軟物体を変形させると方程式の本数を増やすことができる．Fig. 3.7 は変形方法の例である．Fig. 3.7-**(a)** は，物体に対して垂直方向に力を加える方法である．また，Fig. 3.7-**(b)** は，物体に対して斜め方向に力を加える方法である．内部変形計測を 2 通り以上行うことによって，方程式の本数は 20 本から 40 本以上になる．この場合，変数の数よりも方程式の本数が多いため，最小二乗法により解を計算する．

力学パラメータの同定方法には，逐次同定法と一括同定法がある．前者は，力学パラメータが既知な部分と未知な部分が接触している部分から逐次的に力学パラメータを同定する方法である．後者は，全ての節点において力のつり合い式を立てて一括で力学パラメータを同定する方法である．次節では，2 通りの方法で物体を変形をさせた場合，つまり変数の数よりも方程式の本数が多い場合において，逐次同定法と一括同定法を以下に示す．

3.3.2 逐次同定法

逐次同定法の手順を Fig. 3.8 に示す．それぞれの場合において，力のつり合いを考える節点を黒丸で示し，その節点を含む三角形要素を太枠で囲っている．Fig. 3.8-**(a)** において，節点 P_{14} における力のつり合いを考える．節点 P_{14} を含む三角形要素の集合 S_{14} は，

$$S_{14} = \left\{ T^{23},\ T^{22},\ T^{15} \right\} \tag{3.21}$$

となるので，節点 P_{14} における力のつり合いは次式で表すことができる．

$$\boldsymbol{f}_{14}^{23} + \boldsymbol{f}_{14}^{22} + \boldsymbol{f}_{14}^{15} = \boldsymbol{0}. \tag{3.22}$$

力学パラメータが既知である三角形要素の集合 K_{14} と，力学パラメータが未知である三角形要素の集合 U_{14} はそれぞれ，

$$K_{14} = \left\{ T^{23},\ T^{22} \right\}, \quad U_{14} = \left\{ T^{15} \right\} \tag{3.23}$$

であるから，式 (3.22) は，次式のようになる．

$$\boldsymbol{f}_{14}^{15} = -\left(\boldsymbol{f}_{14}^{23} + \boldsymbol{f}_{14}^{22} \right) \tag{3.24}$$

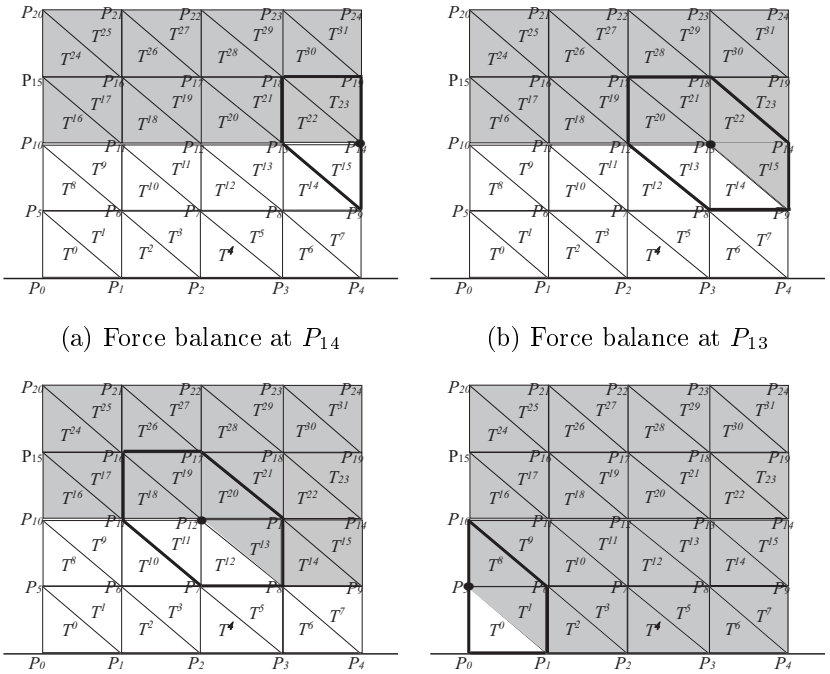

(a) Force balance at P_{14} (b) Force balance at P_{13}

(c) Force balance at P_{12} (d) Force balance at P_5

図 3.8: Overview of incremental physical parameters identification

式 (3.24) に，内部変形計測を 2 通り行った結果を代入すると，

$$\begin{bmatrix} \boldsymbol{A}_{\lambda,14}^{15\ \sharp 1} & \boldsymbol{A}_{\mu,14}^{15\ \sharp 1} \\ \boldsymbol{A}_{\lambda,14}^{15\ \sharp 2} & \boldsymbol{A}_{\mu,14}^{15\ \sharp 2} \end{bmatrix} \begin{bmatrix} \lambda^{15} \\ \mu^{15} \end{bmatrix} = \begin{bmatrix} -\left(\boldsymbol{f}_{14}^{23\ \sharp 1} + \boldsymbol{f}_{14}^{22\ \sharp 1}\right) \\ -\left(\boldsymbol{f}_{14}^{23\ \sharp 2} + \boldsymbol{f}_{14}^{22\ \sharp 2}\right) \end{bmatrix} \tag{3.25}$$

となる．添字の $\sharp 1$，$\sharp 2$ は，それぞれ第 1 試行，第 2 試行により得られた値であることを示す．すなわち，上半分は第 1 試行における値，下半分は第 2 試行における値である．式 (3.25) は，未知数の数より方程式の本数が多いため，最小二乗法を用いて三角形 T^{15} の λ^{15}，μ^{15} を求める．さらに，式 (3.1) より力学パラメータ E^{15}，ν^{15} を同定する．

次に，Fig. 3.8-**(b)** において，節点 P_{13} における力のつり合いを考える．三角形要素 T^{15} の力学パラメータは式 (3.25) より求められているので，この段階で既知である．節点 P_{13} を含む三角形要素の集合 S_{13} は，

$$S_{13} = \left\{T^{22},\ T^{21},\ T^{20},\ T^{13},\ T^{14},\ T^{15}\right\} \tag{3.26}$$

となるので，節点 P_{13} における力のつり合いは次式で表すことができる．

$$\boldsymbol{f}_{13}^{22} + \boldsymbol{f}_{13}^{21} + \boldsymbol{f}_{13}^{20} + \boldsymbol{f}_{13}^{13} + \boldsymbol{f}_{13}^{14} + \boldsymbol{f}_{13}^{15} = \boldsymbol{0}. \tag{3.27}$$

59

力学パラメータが既知である三角形要素の集合 K_{13} と，力学パラメータが未知である三角形要素の集合 U_{13} はそれぞれ，

$$K_{14} = \left\{T^{22},\, T^{21},\, T^{20},\, T^{15}\right\}, \quad U_{14} = \left\{T^{13},\, T^{14}\right\} \tag{3.28}$$

であるから，式 (3.27) は，次式のようになる．

$$\boldsymbol{f}_{13}^{13} + \boldsymbol{f}_{13}^{14} = -\left(\boldsymbol{f}_{13}^{22} + \boldsymbol{f}_{13}^{21} + \boldsymbol{f}_{13}^{20} + \boldsymbol{f}_{13}^{15}\right). \tag{3.29}$$

式 (3.29) に，内部変形計測を 2 通り行った結果を代入すると，

$$\begin{aligned}
&\begin{bmatrix} \boldsymbol{A}_{\lambda,13}^{13\ \sharp 1} & \boldsymbol{A}_{\mu,13}^{13\ \sharp 1} & \boldsymbol{A}_{\lambda,13}^{14\ \sharp 1} & \boldsymbol{A}_{\mu,13}^{14\ \sharp 1} \\ \boldsymbol{A}_{\lambda,13}^{13\ \sharp 2} & \boldsymbol{A}_{\mu,13}^{13\ \sharp 2} & \boldsymbol{A}_{\lambda,13}^{14\ \sharp 2} & \boldsymbol{A}_{\mu,13}^{14\ \sharp 2} \end{bmatrix} \begin{bmatrix} \lambda_{13}^{13} \\ \mu_{13}^{13} \\ \lambda_{13}^{14} \\ \mu_{13}^{14} \end{bmatrix} \\
&= \begin{bmatrix} -\left(\boldsymbol{f}_{13}^{22\ \sharp 1} + \boldsymbol{f}_{13}^{21\ \sharp 1} + \boldsymbol{f}_{13}^{20\ \sharp 1} + \boldsymbol{f}_{13}^{15\ \sharp 1}\right) \\ -\left(\boldsymbol{f}_{13}^{22\ \sharp 2} + \boldsymbol{f}_{13}^{21\ \sharp 2} + \boldsymbol{f}_{13}^{20\ \sharp 2} + \boldsymbol{f}_{13}^{15\ \sharp 2}\right) \end{bmatrix}
\end{aligned} \tag{3.30}$$

となる．添字の $\sharp 1$，$\sharp 2$ は，それぞれ第 1 試行，第 2 試行により得られた値であることを示す．すなわち，ここで，上半分は第 1 試行における値，下半分は第 2 試行における値である．式 (3.30) を解くことによって，三角形 T^{13}，T^{14} の λ^{13}，μ^{13}，λ^{14}，μ^{14} を求める．さらに，式 (3.1) より力学パラメータ E^{13}，ν^{13}，E^{14}，ν^{14} を同定する．

Fig. 3.8-**(c)** では，節点 P_{12} における力のつり合いを考える．三角形要素 T^{13} の力学パラメータは式 (3.30) より求められているので，この段階で既知である．したがって，T^{11}，T^{12} の λ^{11}，μ^{11}，λ^{12}，μ^{12} を求める．さらに，式 (3.1) より力学パラメータ E^{11}，ν^{11}，E^{12}，ν^{12} を同定する．また，Fig. 3.8-**(d)** では，節点 P_5 における力のつり合いを考える．Fig. 3.8-**(a)** の場合と同様に，未知数より方程式の本数が多くなるため，最小二乗法を用いて三角形 T^0 の λ^0，μ^0 を求める．さらに，式 (3.1) より力学パラメータ E^0，ν^0 を同定する．以上のように，力学パラメータを逐次的に同定する．逐次同定法は，ある節点まわりの力のつり合い式から求めた結果を用いて次の節点の力のつり合い式を立てるので，誤差が蓄積していく．次節では，一括で力学パラメータを求める方法を述べる．

3.3.3 一括同定法

全ての節点の力のつり合い式を立てて，一括して力学パラメータを解く．まず，節点 P_5 における力のつり合いを考える．節点 P_5 を含む三角形要素の集合 S_5 は，

$$S_5 = \left\{T^0,\, T^1,\, T^8\right\} \tag{3.31}$$

60

となるので，節点 P_5 における力のつり合いは次式で表すことができる．

$$\boldsymbol{f}_5^0 + \boldsymbol{f}_5^1 + \boldsymbol{f}_5^8 = \boldsymbol{0} \tag{3.32}$$

式 (3.32) に，内部変形計測を 2 通り行った結果を代入すると，

$$\begin{bmatrix} \boldsymbol{A}_5^0 & \boldsymbol{A}_5^1 & \boldsymbol{A}_5^8 \end{bmatrix} \begin{bmatrix} \boldsymbol{X}_5^0 \\ \boldsymbol{X}_5^1 \\ \boldsymbol{X}_5^8 \end{bmatrix} = \begin{bmatrix} 0 \\ 0 \\ 0 \\ 0 \\ 0 \\ 0 \end{bmatrix} \tag{3.33}$$

となる．ここで

$$\begin{aligned}
\boldsymbol{A}_5^0 &= \begin{bmatrix} \boldsymbol{A}_{\lambda,5}^{0\ \sharp 1} & \boldsymbol{A}_{\mu,5}^{0\ \sharp 1} \\ \boldsymbol{A}_{\lambda,5}^{0\ \sharp 2} & \boldsymbol{A}_{\mu,5}^{0\ \sharp 2} \end{bmatrix}, \quad \boldsymbol{X}_5^0 = \begin{bmatrix} \lambda^0 \\ \mu^0 \end{bmatrix}, \\
\boldsymbol{A}_5^1 &= \begin{bmatrix} \boldsymbol{A}_{\mu,5}^{1\ \sharp 1} & \boldsymbol{A}_{\lambda,5}^{1\ \sharp 1} \\ \boldsymbol{A}_{\mu,5}^{1\ \sharp 2} & \boldsymbol{A}_{\lambda,5}^{1\ \sharp 2} \end{bmatrix}, \quad \boldsymbol{X}_5^1 = \begin{bmatrix} \lambda^1 \\ \mu^1 \end{bmatrix}, \\
\boldsymbol{A}_5^8 &= \begin{bmatrix} \boldsymbol{A}_{\mu,5}^{8\ \sharp 1} & \boldsymbol{A}_{\lambda,5}^{8\ \sharp 1} \\ \boldsymbol{A}_{\mu,5}^{8\ \sharp 2} & \boldsymbol{A}_{\lambda,5}^{8\ \sharp 2} \end{bmatrix}, \quad \boldsymbol{X}_5^8 = \begin{bmatrix} \lambda^8 \\ \mu^8 \end{bmatrix}
\end{aligned}$$

である．同様にして，節点 P_6〜P_{14} においてそれぞれ力のつり合い式を立てる．これらを一括にまとめると以下に示す式で表すことができる．

$$\boldsymbol{A}\boldsymbol{X} = \boldsymbol{F} \tag{3.34}$$

61

ここで

$$
\boldsymbol{A} = \begin{bmatrix}
\boldsymbol{A}_5^0 & & & & & & & & & & \\
\boldsymbol{A}_5^1 & \boldsymbol{A}_6^1 & & & & & & & & & \\
 & \boldsymbol{A}_6^2 & & & & & & & & & \\
 & \boldsymbol{A}_6^3 & \boldsymbol{A}_7^3 & & & & & & & & \\
 & & \boldsymbol{A}_7^4 & & & & & & & & \\
 & & \boldsymbol{A}_7^5 & \boldsymbol{A}_8^5 & & & & & & & \\
 & & & \boldsymbol{A}_8^6 & & & & & & & \\
 & & & \boldsymbol{A}_8^7 & \boldsymbol{A}_9^7 & & & & & & \\
\boldsymbol{A}_5^8 & \boldsymbol{A}_6^8 & & & & \boldsymbol{A}_{10}^8 & & & & & \\
 & \boldsymbol{A}_6^9 & & & & \boldsymbol{A}_{10}^9 & \boldsymbol{A}_{11}^9 & & & & \\
 & \boldsymbol{A}_6^{10} & \boldsymbol{A}_7^{10} & & & & \boldsymbol{A}_{11}^{10} & & & & \\
 & & \boldsymbol{A}_7^{11} & & & & \boldsymbol{A}_{11}^{11} & \boldsymbol{A}_{12}^{11} & & & \\
 & & \boldsymbol{A}_7^{12} & \boldsymbol{A}_8^{12} & & & & \boldsymbol{A}_{12}^{12} & & & \\
 & & & \boldsymbol{A}_8^{13} & & & & \boldsymbol{A}_{12}^{13} & \boldsymbol{A}_{13}^{13} & & \\
 & & & \boldsymbol{A}_8^{14} & \boldsymbol{A}_9^{14} & & & & \boldsymbol{A}_{13}^{14} & & \\
 & & & & \boldsymbol{A}_9^{15} & & & & \boldsymbol{A}_{13}^{15} & \boldsymbol{A}_{14}^{15} &
\end{bmatrix}^{\mathrm{T}},
$$

$$
\boldsymbol{X} = \begin{bmatrix} \boldsymbol{X}^0 & \boldsymbol{X}^1 & \boldsymbol{X}^2 & \cdots & \boldsymbol{X}^{13} & \boldsymbol{X}^{14} & \boldsymbol{X}^{15} \end{bmatrix}^{\mathrm{T}},
$$

$$
\boldsymbol{F} = \begin{bmatrix} \boldsymbol{0} & \boldsymbol{0} & \boldsymbol{0} & \boldsymbol{0} & \boldsymbol{0} & \boldsymbol{f}_{10} & \boldsymbol{f}_{11} & \boldsymbol{f}_{12} & \boldsymbol{f}_{13} & \boldsymbol{f}_{14} \end{bmatrix}^{\mathrm{T}}
$$

である．また，$\boldsymbol{f}_{10}$〜$\boldsymbol{f}_{14}$ は，力学パラメータが既知である物体の節点 P_{10}〜P_{14} において生じる力である．係数行列 $\boldsymbol{A}$ は 40×32，変数は 32×1，力学パラメータが既知である物体の節点に生じる力 $\boldsymbol{F}$ は 40×1 のマトリクスである．ここで，1 種類の方法で変形させた場合は，$\boldsymbol{A}$ は 20×32，$\boldsymbol{X}$ は 32×1，$\boldsymbol{F}$ は 20×1 のマトリクスとなる．今回の場合は，変数の数よりも方程式の数が多いため，正規方程式を用いて解を計算する．

3.4　シミュレーションによる検証

前節で述べた力学パラメータ同定方法を用いて，三次元シミュレーションによる力学パラメータの同定を行う．力学パラメータを同定する物体は均一物体と非均一物体である．

62

3.4.1 均一物体の力学パラメータ同定

三次元シミュレーションでは，様々なメッシュの分割方法が考えられる，その代表的なモデルを Fig. 3.9 に示す．Fig. 3.9-**(a)** はメッシュの分割が対称なモデル，Fig. 3.9-**(b)** は非対称なモデルである．有限要素法では，メッシュ要素の分割方法によって安定性や計算時間が変わる．今回は，本手法の有効性のみを検証するため，メッシュ要素の分割による影響が出ない Fig. 3.9-**(a)** の対称なモデルを用いて検証を行う．

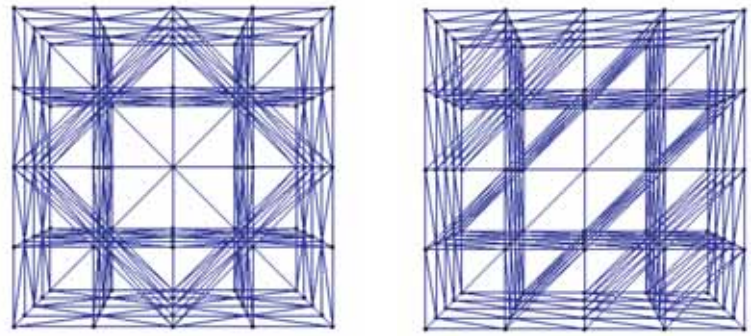

(a) Symmetry model　　(b) Asymmetry model

図 3.9: Example of mesh model

四面体要素のヤング率 E^p とポアソン比 ν^p を Fig. 3.10 に示すように設定する．物体の大きさは 0.04×0.04×0.04m，縦，横，奥行き方向のエッジ数はそれぞれ 4 個，各エッジの幅は 0.01m である．物体の上半分は力学パラメータが既知である均一物体，下半分は力学パラメータが未知である均一物体である．力学パラメータが未知な物体は均一物体であるが，全ての四面体要素において力学パラメータが異なると仮定している．物体を床から離れないように拘束し，物体上面全体を押す．物体上面の節点の変位量は，X 方向に 0.00m，Y 方向に 0.00m，Z 方向に 0.01m である．このときの初期状態から変形状態の変位データを取得する．物体の上半分を力学パラメータが既知である物体，下半分を力学パラメータが未知である物体であると仮定して，未知パラメータを同定する．

力学パラメータを同定した結果を Fig. 3.11 に示す．また，ヤング率の分布を Fig. 3.12-**(a)** に，ポアソン比の分布を Fig. 3.12-**(b)** に示す．Fig. 3.13-**(a)** は，シミュレーションを行ったときの変形状態，Fig. 3.13-**(b)** は同定結果を用いて再度シミュレーションを行ったときの変形状態の様子である．このときの誤差を算出した結果を Table 3.2

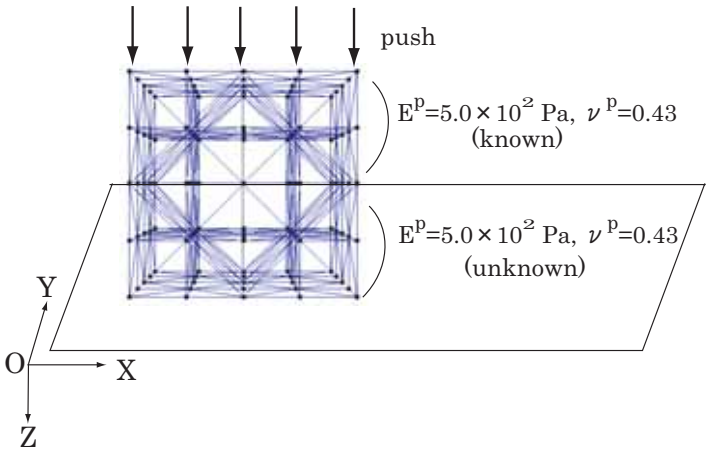

図 3.10: Uniform physical parameters identification

表 3.2: Error of uniform physical parameters identification

True value		Result		Error [%]
E^p [Pa]	ν^p	E^p [Pa]	ν^p	
5.0×10^2	0.43	4.95×10^2	0.43	3.10×10^{-3}

に示す．誤差は以下に示す式を用いて算出し，百分率で表した．

$$Error = \frac{\sum^{nodalnumber}\{(x_i^{sim}-x_i^{re})^2+(y_i^{sim}-y_i^{re})^2+(z_i^{sim}-z_i^{re})^2\}}{width \times height} \tag{3.35}$$

ここで，$(x_i^{sim}, y_i^{sim}, z_i^{sim})$ は，最初にシミュレーションを行ったときの変形状態における節点 i の位置である．$(x_i^{re}, y_i^{re}, z_i^{re})$ は，同定結果を用いて再度シミュレーションを行ったときの変形状態における節点 i の位置である．また，$nodalnumber$ は全節点の数，$height$ と $width$ はそれぞれ物体の縦と横の長さである．

Fig. 3.11 より，同定結果は真値からばらついている．Fig. 3.12-**(a)** より，ヤング率は，430〜440Pa，450〜460Pa となった結果が最も多く，約 240Pa から 670Pa の範囲で比較的均等に分散している．また，Fig. 3.12-**(b)** より，ポアソン比は 0.41〜0.42 となった結果最も多く，0.39 から 0.46 の範囲でばらついている．しかし，Fig. 3.13 より，同定結果を使用して行ったシミュレーションは最初のシミュレーション結果と同じ変形が見られる．Table 3.2 から同定結果の誤差は 1%以下で，非常に小さいことがわかる．

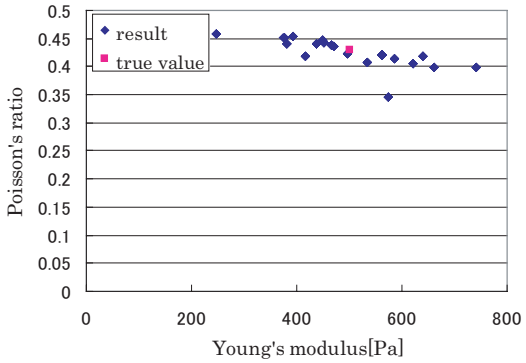

図 3.11: Result of uniform physical parameters identification

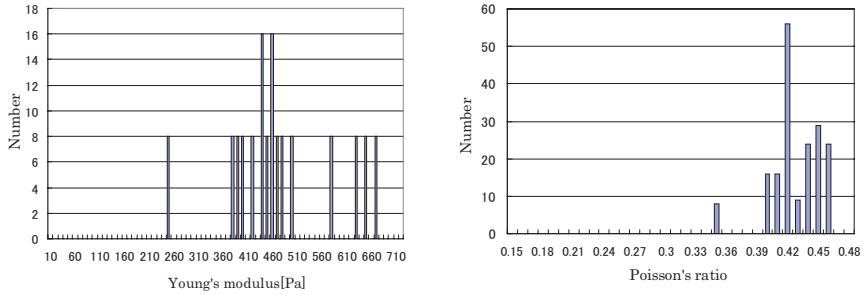

(a) Distribution of Young's modulus (b) Distribution of Poisson's ratio

図 3.12: Distribution of uniform physical parameters identified

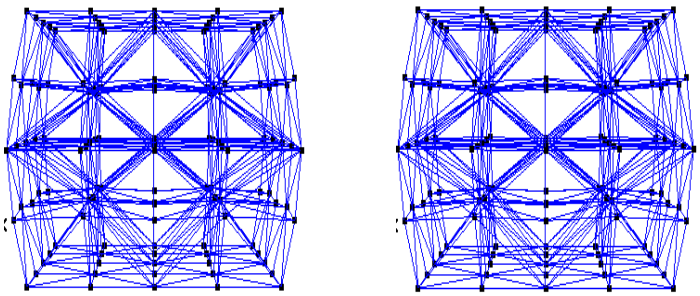

(a) Simulation using true value (b) Simulation using the result

図 3.13: Comparison of simulation using true value and result in uniform parameters identification

65

3.4.2　非均一物体の力学パラメータ同定

四面体要素のヤング率 E^p とポアソン比 ν^p を Fig. 3.14 に示すように設定する．物体の大きさは 0.04×0.04×0.04m，縦，横，奥行き方向のエッジ数はそれぞれ 4 個，各エッジの幅は 0.01m である．物体の上半分は力学パラメータが既知である均一物体，下半分は力学パラメータが未知な物体で，1 層目と 2 層目で力学パラメータの値が異なる非均一物体である．力学パラメータが未知な物体は，それぞれ 1 層目内と 2 層目内で力学パラメータの値は同じだが，全ての四面体要素において力学パラメータが異なると仮定している．物体を床から離れないように拘束し，物体上面全体を押す．物体上面の節点の変位量は，X 方向に 0.00m，Y 方向に 0.00m，Z 方向に 0.01m である．このときの初期状態から変形状態の変位データを取得する．物体の上半分を力学パラメータが既知である均一物体，下半分を力学パラメータが未知である非均一物体と仮定して，未知パラメータを同定する．

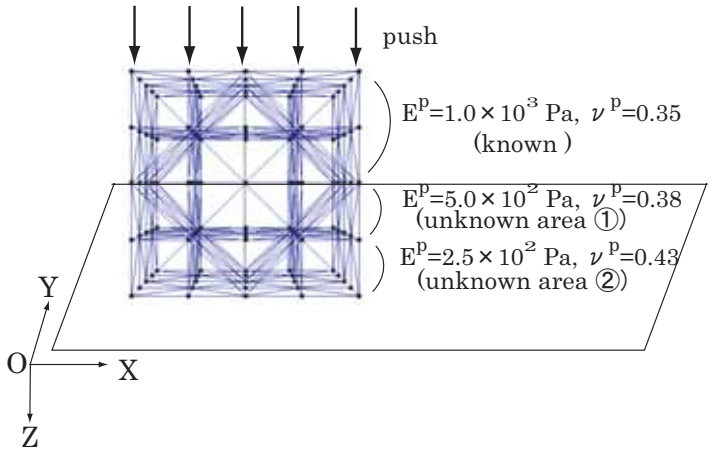

図 3.14: Nonuniform physical parameters identification

1 層目の力学パラメータを同定した結果を Fig. 3.15 に示す．このときのヤング率の分布を Fig. 3.16-**(a)** に，ポアソン比の分布を Fig. 3.16-**(b)** に示す．また，2 層目の力学パラメーを同定した結果を Fig. 3.17 に示す．ことのときのヤング率の分布を Fig. 3.18-**(a)** に，ポアソン比の分布を Fig. 3.18-**(b)** に示す．Fig. 3.19-**(a)** は，シミュレーションを行ったときの変形状態，Fig. 3.19-**(b)** は同定結果を用いて再度シミュレーションを行ったときの変形状態の様子である．このときの誤差を算出した結果を Table 3.3 に示す．誤差は式 (3.35) を用いて算出した．

Fig. 3.15 より，同定結果は真値から大きくばらついている．Fig. 3.16-**(a)** より，ヤング率は約 60Pa から 460Pa の範囲でばらついている．ヤング率の真値は 250Pa だ

66

が，460Pa となった結果の数が最も多い．また，Fig. 3.16-**(b)** より，ポアソン比は 0.35 から 0.47 の範囲でばらついている．ポアソン比の真値は 0.38 だが，0.35 となった結果の数が最も多い．Fig. 3.18-**(a)** より，ヤング率は約 450Pa から 630Pa の狭い範囲で比較的均等に分散している．また，Fig. 3.18-**(b)** より，ポアソン比は 0.35 から 0.46 の範囲でばらついている．しかし，Fig. 3.19 より，同定結果を使用して行ったシミュレーションは最初のシミュレーション結果とほぼ同じ変形を示す．Table 3.3 からも同定結果の誤差が小さいことがわかる．

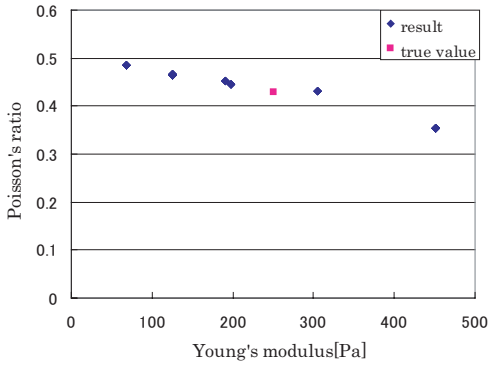

図 3.15: Result of nonuniform parameters identification

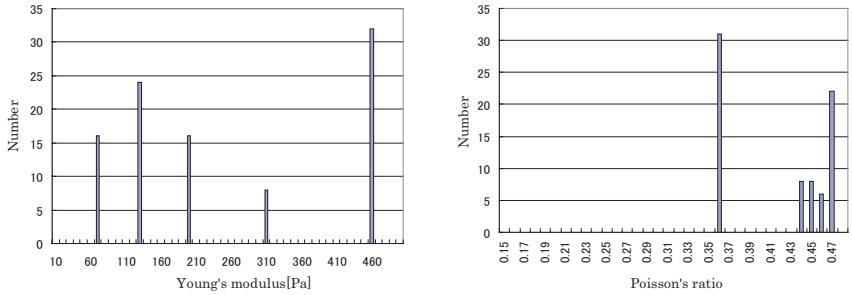

(a) Distribution of Young's modulus　(b) Distribution of Poisson's ratio

図 3.16: Distribution of nonuniform physical parameters identified (area 1)

67

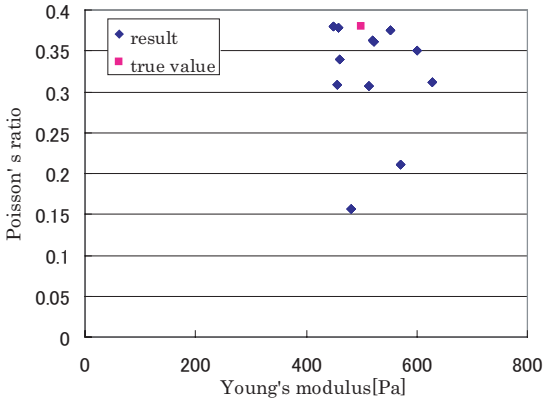

図 3.17: Result of uniform parameters identification

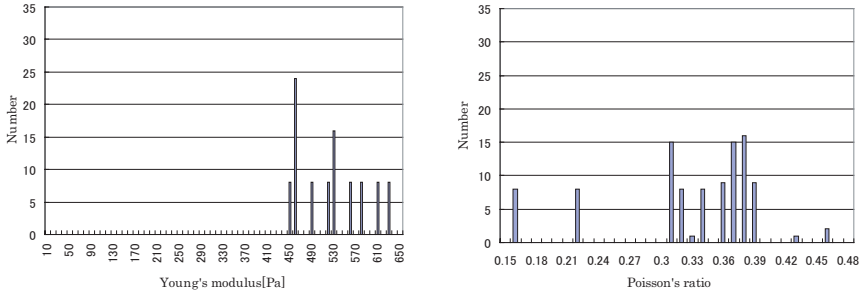

(a) Distribution of Young's modulus (b) Distribution of Poisson's ratio

図 3.18: Distribution of nonuniform physical parameters identified (area 2)

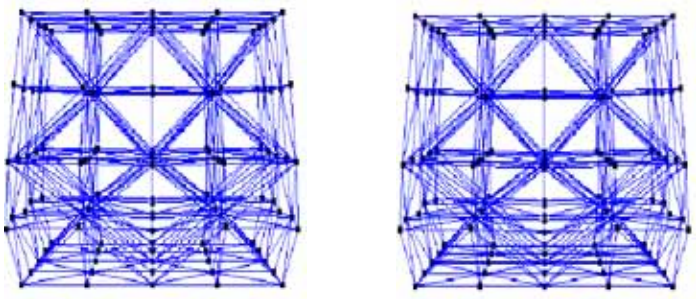

(a) Simulation using true value (b) Simulation using the result

図 3.19: Comparison of simulation using true value and result in nonuniform parameters identification

68

表 3.3: Error of nonuniform physical parameters identification

	True value		Result		Error [%]
	E^p [Pa]	ν^p	E^p [Pa]	ν^p	
Unknown area 1	2.5×10^2	0.43	2.51×10^2	0.43	
Unknown area 2	5.0×10^2	0.38	5.18×10^2	0.32	1.37×10^{-2}

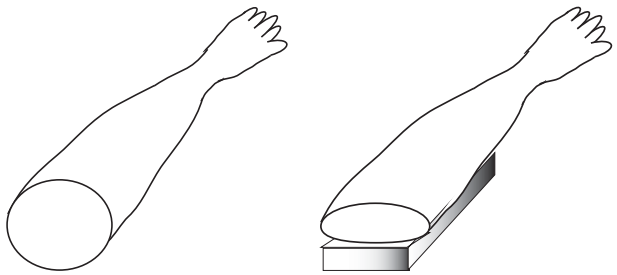

(a) Initial state (b) Deformed state

図 3.20: MRI photographics condition

均一物体，非均一物体の同定結果の分布はどちらもかなりばらついている．しかし，平均をとると真値とほぼ同じ値が得られる．また，最初に行ったシミュレーションと同定結果を用いて行ったシミュレーションとの誤差は非常に小さい．真値と同じ値が得られなくても，最初に行った変形と同じ変形が得られることになる．したがって，全体的な変形は変わらないのであれば，今回の実験程度のばらつきは許容できると考える．

3.5 MRIによる柔軟物の内部変形計測

力学パラメータが既知な物体は人工的に作成した物体を用いるため，変形の計測は容易である．しかし，生体組織内部は似通ったパターンが多く，変形の計測が難しい．そこで，本来ならば力学パラメータが既知な物体と生体組織の両方の内部変形を計測する必要があるが，本章では生体組織の変形計測のみに焦点を当てる．ボランティアの下腿内部を MRI 装置で撮影し，変形計測に最適なアルゴリズムを検証する．

69

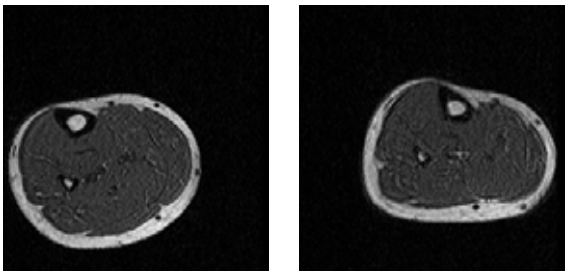

(a) Initial state (b) Deformed state

図 3.21: Calf MR images

3.5.1 レジストレーションとボリュームデータの作成

滋賀医科大学に設置されている MRI 装置を使用して，ボランティアの下腿を撮影した．Fig. 3.20 に示すように，下腿を圧迫していない状態 (初期状態) および下腿の下にプラスチックの箱を置き圧迫した状態 (変形状態) を撮影した．撮影条件は，スライス間隔 2mm，FOV20 × 20cm，積算 2 回とし，それぞれ 76 枚のスライス画像を得た．階調数は 256 のグレースケール画像である．画像サイズは 256 × 256pixels，画素サイズは 0.8mm/pixel である．また，ランドマークとして頸骨が大きく写るように撮影した．初期状態，変形状態において得られたスライス画像の中の一例を Fig. 3.21 に示す．変形状態では，下腿の下にプラスチックの箱をおいたため，下腿下部に変形が見られる．

変形状態では，プラスチックの箱を置くために下腿の位置がずれてしまう．したがって，レジストレーションを行う必要がある．レジストレーションの式を以下に示す．

$$\begin{bmatrix} x_i \\ y_i \end{bmatrix} = \begin{bmatrix} \cos\theta & -\sin\theta \\ \sin\theta & \cos\theta \end{bmatrix} \begin{bmatrix} x_d \\ y_d \end{bmatrix} + \begin{bmatrix} t_x \\ t_y \end{bmatrix} \tag{3.36}$$

ここで，$[x_i, y_i]^T$ と $[x_d, y_d]^T$ はそれぞれ初期状態と変形状態における画像座標，θ は回転角度，$[t_x, t_y]^T$ は並進ベクトルである．

撮影した下腿の MRI 画像に対してレジストレーションを行う．剛体部分である頸骨（下腿の太い方の骨）の周りから同一の点である 3 点をそれぞれ初期状態と変形状態の画像から選択し，変形状態の位置に合わせて初期状態の画像を変換する．レジストレーションを行った結果を Fig. 3.22 に示す．Fig. 3.21 と比較すると，初期状態の画像が変形状態の位置に合わせて変換されていることが分かる．

画像サイズ 0.8mm に対して，スライス間隔が 2mm と大きいため，以下に示す式

70

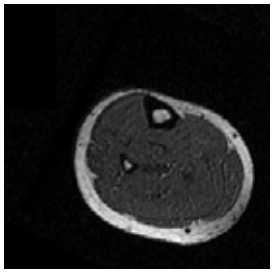

図 3.22: Initial state after registration

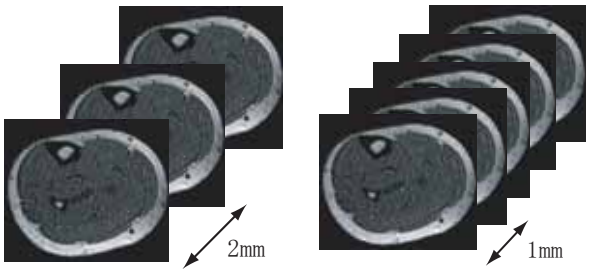

(a) Before interpolation (b) After interpolation

図 3.23: Interpolation between slice images

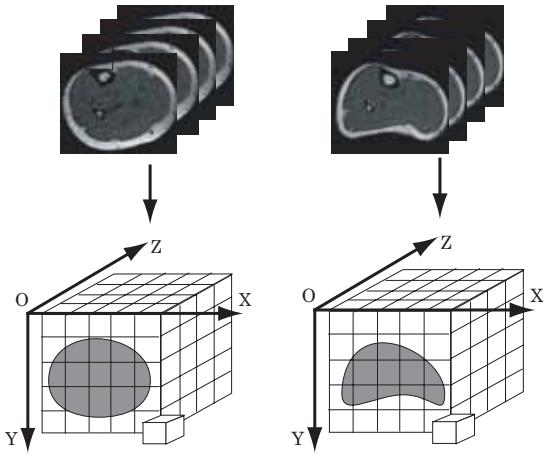

(a) Initial state (b) Deformed state

図 3.24: Construction of volume data by MR images

71

を用いて画像を補間する．

$$I_\alpha(i,j) = (1-\alpha)I_k(i,j) + \alpha I_{k+1}(i,j) \tag{3.37}$$

ここで

$$\alpha = d_k/(d_k + d_{k+1})$$

である．$I_k(i,j)$ と $I_{k+1}(i,j)$ は，それぞれ k 番目と $k+1$ 番目の座標 (i,j) における輝度値である．$I_\alpha(i,j)$ は，k 番目と $k+1$ 番目の画像間を補間した画像の座標 (i,j) における輝度値である．また，d_k は k 番目から $k+1$ 番目の画像への距離と k 番目から補間する画像への距離の比である．d_{k+1} は，それぞれ k 番目と $k+1$ 番目の距離と $k+1$ 番目から補間する画像への距離の比である．Fig. 3.23 に示すように，スライス間隔を 1mm にするために, $d_k = 1/2$，$d_{k+1} = 1/2$ として画像間に画像を一枚補間する．

座標系を Fig. 3.24 に示すように設定し，初期状態と変形状態の断面画像からボリュームデータをそれぞれ生成する．ボリュームデータは，濃度値を格納したボクセルで構成した．ボクセルのサイズは，縦 0.8mm ×横 0.8mm ×奥行き 1mm である．

3.5.2 ブロックマッチング法の評価

下腿の内部変形をオプティカルフローのアルゴリズムを用いて計測する．本節では，アルゴリズムを二次元で簡単に説明する．

ブロックマッチング法は，Fig. 3.25 に示すように連続する 2 枚の画像間でテンプレートをずらしながら最も一致する部分を探索する方法である．ブロックマッチング法は，動きの大きい対象に対しても有効で，輝度値の急激に変化するところでもフローの誤差が少ない．しかし，全探索を行うので処理時間が膨大である，拡大・縮小，回転運動に弱いなどの欠点がある．ブロックマッチングの代表的なものには，Sum of Absolute Difference(SAD) 法, Sum of Squared Difference(SSD) 法, Normalized Correlation Coefficient(NCC) 法などがある [43]．それぞれの特徴を以下に示す．

(a) SAD 法

輝度値をそのまま減算することにより，画像間のマッチングを行う手法であり式 (3.38) によって求められる．差分絶対値和 R_{SAD} が最小となる部分を最も類似した部分として判定する．SAD 法は計算量が少ないため，高速処理が可能である．

$$R_{SAD} = \sum_{i=i_0}^{i_0+S-1} \sum_{j=j_0}^{j_0+T-1} |I_{ini}(i,j) - I_{def}(i+i_1, j+j_1)| \tag{3.38}$$

72

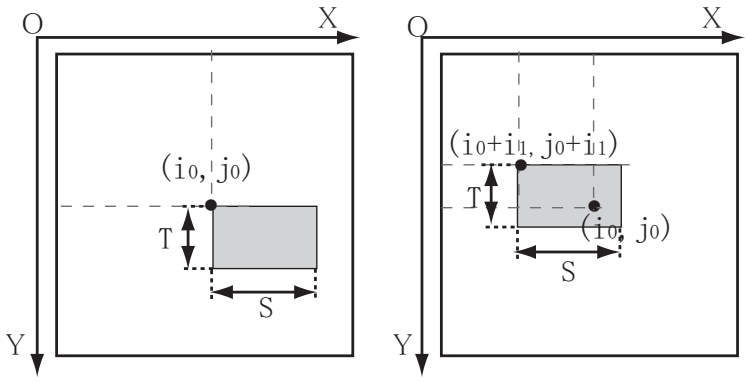

(a) Initial state (b) Deformed state

図 3.25: Method of block matching

ここで，$I_{ini}(i,j)$ は初期状態における画像，$I_{def}(i,j)$ は変形状態の画像である．S，T はそれぞれ縦，横のウィンドウサイズである．また，i_0，j_0 はそれぞれ X，Y 方向のテンプレートの始まる位置である．i_1，j_1 はそれぞれ X，Y 方向の探索領域である．

(b) SSD 法

輝度値をそのまま減算することにより，画像間のマッチングを行う手法であり，式 (3.39) によって求められる．差分二乗和 R_{SSD} が最小となる部分をもっとも類似した部分として判定する．NCC 法と比較して，計算速度は高速であるが，画像間の明るさの変化がある場合は正規化処理を行わないので信頼度は劣る．

$$R_{SSD} = \sum_{i=i_0}^{i_0+S-1} \sum_{j=j_0}^{j_0+T-1} (I_{ini}(i,j) - I_{def}(i+i_1, j+j_1))^2. \tag{3.39}$$

(c) NCC 法

各点の輝度値から局所的な平均値を引き，分散値の類似度でマッチングを取るため，線形な明るさの変化 (画像の輝度値およびコントラストの線形変化とノイズ) に影響されない手法で計算される．しかし，正規化処理のため計算時間が遅くなることが知られている．相関値 R_{NCC} は -1〜1 までを示し，値が大きいほど，画像が類似していることを表す．従って，正規化相互相関法では式 (3.40) の最大値を求める

73

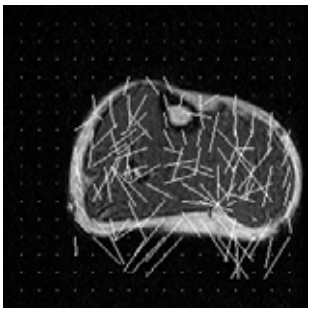

図 3.26: Result of deformation measurement using blockmatching method

処理となる．

$$
\begin{aligned}
R_{NCC} &= \frac{1}{ST}\frac{c_{\mathrm{ini,def}}}{\sqrt{c_{\mathrm{ini,ini}}c_{\mathrm{def,def}}}}, \qquad (3.40)\\
c_{\mathrm{ini,def}} &= \sum_{i=i_0}^{i_0+S-1}\sum_{j=j_0}^{j_0+T-1}(I_{ini}(i,j)-\mu I_{ini})\cdot(I_{def}(i+i_1,j+j_1)-\mu I_{def}),\\
c_{\mathrm{int,ini}} &= \sum_{i=i_0}^{i_0+S-1}\sum_{j=j_0}^{j_0+T-1}(I_{ini}(i,j)-\mu I_{ini})^2,\\
c_{\mathrm{def,def}} &= \sum_{i=i_0}^{i_0+S-1}\sum_{j=j_0}^{j_0+T-1}(I_{def}(i+i_1,j+j_1)-\mu I_{def})^2
\end{aligned}
$$

ここで，μI_{ini}，μI_{def} はそれぞれ初期状態，変形状態のテンプレートにおける局所平均値を示す．

SAD 法は実装が容易で，最も一般的に使用されているため，SAD 法を用いてブロックマッチングを行った．テンプレートサイズを 5×5pixels，X，Y 方向の探索領域を $i_1=\pm 30$pixel，$j_1=\pm 35$pixel としたときの結果を Fig. 3.26 に示す．図中の白い線分は，大きな白い点が初期状態での位置，線分の向きがその点の変形の方向，線分の長さが変形の大きさを表わしている．また，下腿領域外の小さな白い点は，その点の変形ベクトルが 0 であることを表わしている．本実験では，テンプレート中の階調変化がほとんどない計測点については，正確な変形ベクトルを求めることが困難であるとみなし，強制的に変形を 0 としている．Fig. 3.26 より，プラスチックで圧迫した部分は上向きの変形ベクトルをもって変形している．また，変形によって下腿が横にふくらんでいるので，横に広がるベクトルが見られる．生体組織内部は似通った部分が多いので，間違って計測されている部分が多い．

3.5.3 勾配法の評価

勾配法は，連続する 2 枚の画像での対象物の移動量が微小であることを前提にオプティカルフローを求める方法である [44]．勾配法は，各画素の局所的な演算でオプティカルフローが求まるため，処理が簡便で高速である．しかし，微小な移動を前提としているため，移動量が大きい場合には正しくオプティカルフローを求めることができない．また，輝度値が急激に変化するところではフローの誤差が激しく，雑音に弱いという欠点がある．画素値がなめらかに変化していると仮定すると，

$$I(x, y, t) = I(x + \triangle x, y + \triangle y, t + \triangle t) \tag{3.41}$$

となる．右辺をテイラー展開し，2 次の項以降を小さいものとして無視すると次式が得られる．

$$I(x, y, t) \approx I(x, y, t) + \frac{\partial I}{\partial x} \triangle x + \frac{\partial I}{\partial y} \triangle y + \frac{\partial I}{\partial t} \triangle t. \tag{3.42}$$

両辺を $\triangle t$ で割り，整理すると次式となる．

$$\frac{\partial I}{\partial x}\frac{\triangle x}{\triangle t} + \frac{\partial I}{\partial y}\frac{\triangle y}{\triangle t} + \frac{\partial I}{\partial t} = 0. \tag{3.43}$$

微小な時間の微小な移動であることから，次式が成り立つ．

$$\frac{\partial I}{\partial x}\frac{\partial x}{\partial t} + \frac{\partial I}{\partial y}\frac{\partial y}{\partial t} + \frac{\partial I}{\partial t} = 0. \tag{3.44}$$

ここで，$I_x = \partial I/\partial x$，$I_y = \partial I/\partial y$，$I_t = \partial I/\partial t$，$(u, v) = (\partial x/\partial t, \partial y/\partial t)$ とすると時空間拘束式は，

$$I_x u + I_y v + I_t = 0 \tag{3.45}$$

となる．時空間拘束式は各画素に一本のみであるが，未知数は各画素につき u, v と 2 つあり，一般には解くことができない．狭い領域だけではフローが決まらないが，広い領域を見れば決められることがある．この式だけでそれらの値を一意に決定する事はできない．そこで，さらにいくつかの仮定を導入して (u, v) を求める．

(a) Horn-Schunck 法

以下の 2 つの仮定から速度ベクトルを一意に決定する．

- 時空間拘束式 (式 (3.45)) を満たす
- 近傍の画素は似たフローを持ちその変化は滑らかである

75

$$\left(\frac{\partial u}{\partial x}\right)^2+\left(\frac{\partial u}{\partial y}\right)^2+\left(\frac{\partial v}{\partial x}\right)^2+\left(\frac{\partial v}{\partial y}\right)^2=0. \tag{3.46}$$

これらは同時に満たすことができないので，残差の重み付け和

$$E=\int\left[\left(I_x u+I_y v+I_t\right)^2+\lambda\left\{\left(\frac{\partial u}{\partial x}\right)^2+\left(\frac{\partial u}{\partial y}\right)^2+\left(\frac{\partial v}{\partial x}\right)^2+\left(\frac{\partial v}{\partial y}\right)^2\right\}\right]\mathrm{d}x\mathrm{d}y \tag{3.47}$$

を最小化する解を見つける (正則化)．式 (3.47) を微分すると

$$\frac{\partial E}{\partial u_{x,y}} = 2(u_{x,y}-\bar{u}_{x,y})+2\lambda\left(I_x u_{x,y}+I_y v_{x,y}+I_t\right)I_x, \tag{3.48}$$

$$\frac{\partial E}{\partial v_{x,y}} = 2(v_{x,y}-\bar{v}_{x,y})+2\lambda\left(I_x u_{x,y}+I_y v_{x,y}+I_t\right)I_y \tag{3.49}$$

となる．ここで $\bar{u}$，$\bar{v}$ は (x,y) の平均値である．式 (3.47) が最小となるためには，

$$\frac{\partial E}{\partial u_{x,y}} = 0, \tag{3.50}$$

$$\frac{\partial E}{\partial v_{x,y}} = 0 \tag{3.51}$$

となればよいので，

$$\left(1+\lambda\left(I_x\right)^2\right)u_{x,y}+\lambda I_x I_y v_{x,y} = \bar{u}_{x,y}-\lambda I_x I_y, \tag{3.52}$$

$$\left(1+\lambda\left(I_y\right)^2\right)v_{x,y}+\lambda I_x I_y u_{x,y} = \bar{v}_{x,y}-\lambda I_x I_y. \tag{3.53}$$

よって，

$$u_{x,y} = \bar{u}_{x,y}-\frac{I_x\bar{u}_{x,y}+I_y\bar{v}_{x,y}+I_t}{1+\lambda\left(\left(I_x\right)^2+\left(I_y\right)^2\right)}, \tag{3.54}$$

$$v_{x,y} = \bar{v}_{x,y}-\frac{I_x\bar{u}_{x,y}+I_y\bar{v}_{x,y}+I_t}{1+\lambda\left(\left(I_x\right)^2+\left(I_y\right)^2\right)} \tag{3.55}$$

となる．$u_{x,y}$，$v_{x,y}$ は未知の $\bar{u}_{x,y}$，$\bar{v}_{x,y}$ に依存するので，繰り返し漸近法を用いる．$\bar{u}_{x,y}$，$\bar{v}_{x,y}$ の適当な初期値 $\bar{u}^{(0)}_{x,y}$，$\bar{v}^{(0)}_{x,y}$ を設定し，次式で繰り返し計算を行う．

$$u^{(n+1)}_{x,y} = \bar{u}^{(n)}_{x,y}-\frac{I_x\bar{u}^{(n)}_{x,y}+I_y\bar{v}^{(n)}_{x,y}+I_t}{1+\lambda\left(\left(I_x\right)^2+\left(I_y\right)^2\right)}, \tag{3.56}$$

$$v^{(n+1)}_{x,y} = \bar{v}^{(n)}_{x,y}-\frac{I_x\bar{u}^{(n)}_{x,y}+I_y\bar{v}^{(n)}_{x,y}+I_t}{1+\lambda\left(\left(I_x\right)^2+\left(I_y\right)^2\right)}. \tag{3.57}$$

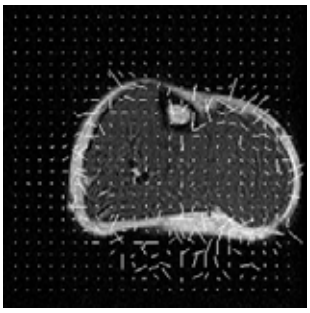

図 3.27: Result of deformation measurement using Horn-Schunck method

Horn-Schunck を用いて下腿の内部変形計測を行った結果を Fig. 3.27 に示す．繰り返し計算回数は 40 回，λ=4 とした．下腿の内部はブロックマッチング法と比較して，精度よく計測されている．しかし，皮膚（内部以外の外側の白い部分）ではフロー誤差が激しくなっている．これは，Horn-Schunck のアルゴリズムが微小な移動を前提としているのに対して，圧迫した部分の移動量のが大きかったためである．

(b) Lucas-Kanade 法

同一物体の濃淡パターン上の局所領域では，オプティカルフローはほぼ一定と考えられる．すなわち「局所領域で得られるオプティカルフローの拘束方程式は同一の解をもつ」という仮定から，オプティカルフローを求める．$m \times m$ の窓サイズにおいて u, v は同じと仮定すると，以下の式に示すように方程式が複数本与えられる．

$$\begin{aligned} I_{x1}u + I_{y1}v &= -I_{t1}, \\ I_{x2}u + I_{y2}v &= -I_{t2}, \\ &\vdots \\ I_{xn}u + I_{yn}v &= -I_{tn}. \end{aligned} \tag{3.58}$$

ここで，$n = m^2$ であるので，変数 2 つに対して方程式は 2 本以上得られることになる．式 (3.58) は，

$$\boldsymbol{CX} = -\boldsymbol{b} \tag{3.59}$$

77

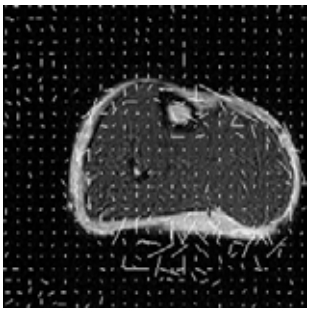

図 3.28: Result of deformation measurement using Lucas-Kanade method

と表すことができる．ここで，

$$\boldsymbol{C} = \begin{bmatrix} I_{x1} & I_{y1} \\ I_{x2} & I_{y2} \\ \vdots & \vdots \\ I_{xn} & I_{yn} \end{bmatrix},$$

$$\boldsymbol{X} = \begin{bmatrix} u \\ v \end{bmatrix},$$

$$\boldsymbol{b} = \begin{bmatrix} -I_{t1} \\ -I_{t2} \\ \vdots \\ -I_{tn} \end{bmatrix}$$

である．(3.59) 式を最小二乗法を用いて解くと，

$$\boldsymbol{C}^T\boldsymbol{C}\boldsymbol{X} = \boldsymbol{C}^T(-\boldsymbol{b}) \tag{3.60}$$

となる．

Lucas-Kanade 法を用いて下腿の内部変形計測を行った結果を Fig. 3.28 に示す．下腿の内部はブロックマッチング法と比較して精度よく計測されているが，Horn-Schunck 法より精度が低い．Horn-Schunck 法と同様に，皮膚の部分ではフローの誤差が激しい．

3.5.4 下腿の内部変形計測

前節で，下腿の皮膚部分はブロックマッチング法，下腿内部は Horn-Schunck 法を用いて計測するのが最も精度よく下腿の変形を計測できることがわかった．そこで，

図 3.29: Revised algorithm

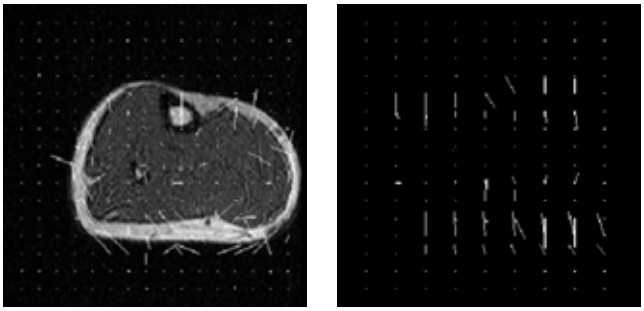

(a) X-Y plane (b) Y-Z plane

図 3.30: Result of deformation measurement using the revised algorithm

79

Fig. 3.29 に示すように，下腿内部以外をブロックマッチング法，下腿内部を Horn-Schunck 法を用いて下腿の変形を計測する．基本はブロックマッチング法を用いて計測し，テンプレートを切り出したときにテンプレート内の階調変化が 30 以下の場合は，Horn-Schunck 法で変形を計測する．このアルゴリズムを三次元に拡張し，下腿の変形を計測した結果を Fig. 3.30 に示す．下腿内部は滑らかに変形ベクトルが計測され，下腿内部以外のプラスチックで圧迫した部分は上向きの変形ベクトルが計測されている．

3.6 CT による実験検証

本手法を実験により検証するために，柔軟物体を作成する．柔軟物体は比較的に均一物体であるため，CT を用いても内部挙動がわかる．本節では，CT を用いた実験により力学パラメータ同定法を検証する．

3.6.1 テストピース

CT を用いて柔軟物の内部変形を計測するために，(株) エクシールコーポレーション製の人肌ゲルを用いて柔軟物を作成する．人肌ゲルはウレタン系オールブレンドを原液とし，イソシアネートの硬化剤を混ぜることによって固めることができる．パラメータが既知な物体は人肌ゲル硬度 5（腕程度のやわらかさ），パラメータが未知な物体は硬度 0（腹部程度のやわらかさ）を使用する．これらをそれぞれ Fig. 3.31 に示す型に流し込む．型内部は，等間隔に十字方向に糸を張り，その交差点にマーカーを配置している．マーカーは M1 の丸座金 (外径 2.8mm，長さ 0.3mm) を用いる．人肌ゲルが硬化した後に型の糸を引き抜くことで，マーカーを物体内部に設定することができる．両物体のサイズは $60 \times 60 \times 30$mm で，マーカーは 10mm 間隔に合計 50 個を配置している．

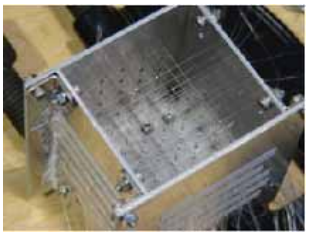

図 3.31: Mold and washer are used in making soft objects

人肌ゲルの力学パラメータを同定した．圧縮同定試験機を用いてヤング率を算出する．人肌ゲルの硬度 5 と硬度 0 から試験片をそれぞれ 3 種類作製し，それぞれヤング率を測定する．3 種類の同定結果の平均を計算し，人肌ゲルの硬度 5 と硬度 0 のヤング率の値とする．作成した試験片のサイズと圧縮同定試験結果，人肌ゲルのヤング率を算出した結果を Table 3.4 に示す．

本実験で用いた圧縮同定試験は縦方向のひずみしか求めることができないため，ポアソン比を求めることができなかった．そこで，初期状態と変形状態の CT 画像から横ひずみと縦ひずみを計測し，ポアソン比を算出した．人肌ゲル横ひずみと縦ひずみ，これらの値からポアソン比を算出した結果を Table 3.5 に示す．

表 3.4: Result of compression test

	Dia.[mm]	Hei.[mm]	Young's mod.[N/m^2]	Ave.[N/m^2]
Hard. 5	30	35	2.78×10^5	2.22×10^5
	40	25	2.01×10^5	
	35	20	1.86×10^5	
Hard. 0	35	30	1.37×10^5	1.25×10^5
	35	25	1.43×10^5	
	35	15	0.95×10^5	

表 3.5: Value of Poisson's ratio

	Longitudinal strain	Transversal strain	Poisson's ratio
Hard. 5	0.32	0.10	0.33
Hard. 0	0.39	0.17	0.44

3.6.2 CT を用いた柔軟物の内部変形計測

和歌山県工業技術センターが所有している産業用 CT スキャナを用いて作成した物体を撮影する．使用した CT スキャナの画像分解能を Table 3.6 に示す．Fig. 3.32 に示すように，硬度 0 の物体の上に硬度 5 の物体を重ねたときを初期状態，アクリル平板を用いて物体全面を高さ 40mm となるまで押したときを変形状態とする．これらの状態を CT で撮影したときの様子を Fig. 3.33 に示す．

物体の内部変形を計測するために，得られた CT の断面画像を 2 値化して，マーカーの移動を計測する．各物体にマーカーは，高さ方向に 2 層，各層で 5×5 個が

81

表 3.6: Resolution of CT scanner

Direction	Resolution [mm]
X	0.29
Y	0.29
Z	0.5

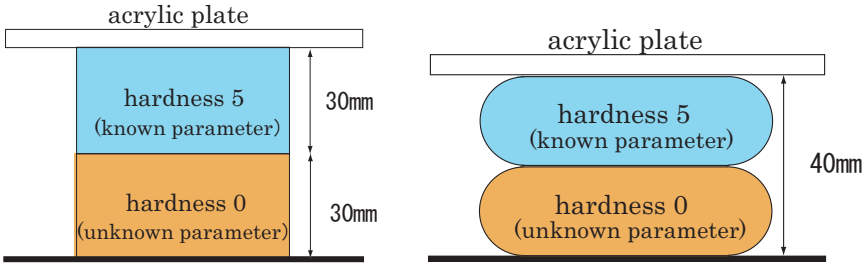

(a) Initial state (b) Deformed state

図 3.32: Deformation of soft objects

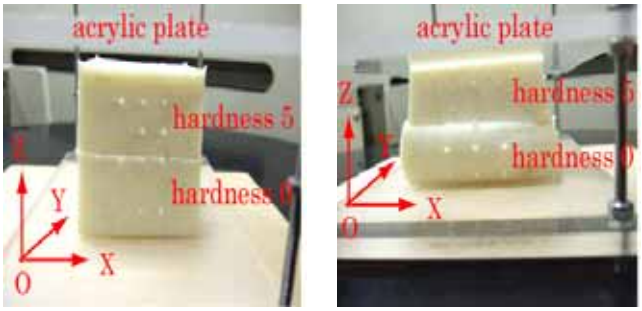

(a) Initial state (b) Deformed state

図 3.33: Soft objects in initial and deformed states

配置されている．硬度 0 の物体の層を 1 層目，2 層目とする．硬度 5 の物体の層を 3 層目，4 層目とする．それぞれの層において得られた CT 画像と 2 値化した画像を示す．1 層目の初期状態と変形状態をそれぞれ Fig. 3.34 と Fig. 3.35 に示す．2 層目の初期状態と変形状態をそれぞれ Fig. 3.36 と Fig. 3.37 に示す．3 層目の初期状態と変形状態をそれぞれ Fig. 3.38 と Fig. 3.39 に示す．4 層目の初期状態と変形状態をそれぞれ Fig. 3.40 と Fig. 3.41 に示す．全ての層において，変形状態では初期状態からマーカーの間隔が広がっている．また，硬度 5 よりも硬度 0 の方がマーカーの間隔の広がり方が大きいことがわかる．

82

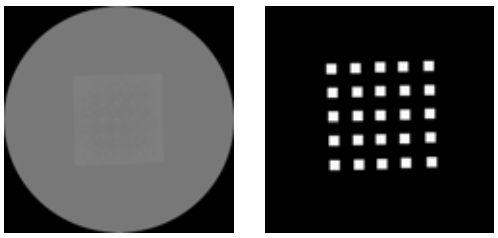

(a) CT image (b) Binarized image

図 3.34: First layer in initial state

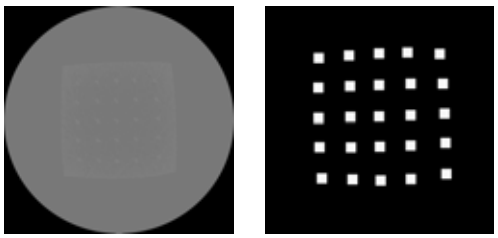

(a) CT image (b) Binarized image

図 3.35: First layer in deformed state

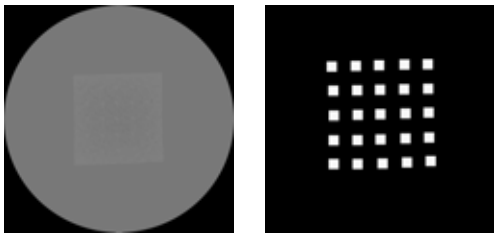

(a) CT image (b) Binarized image

図 3.36: Second layer in initial state

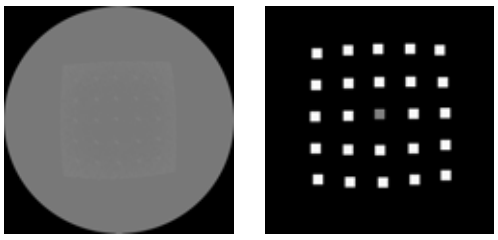

(a) CT image (b) Binarized image

図 3.37: Second layer in deformed state

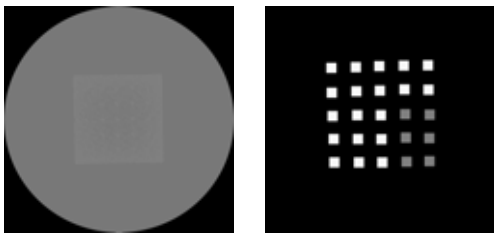

(a) CT image (b) Binarized image

図 3.38: Third layer in initial state

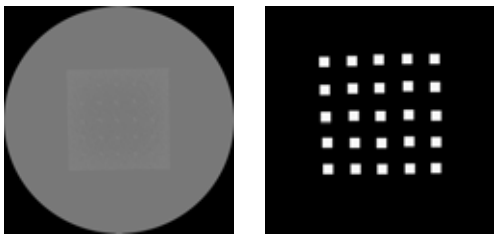

(a) CT image (b) Binarized image

図 3.39: Third layer in deformed state

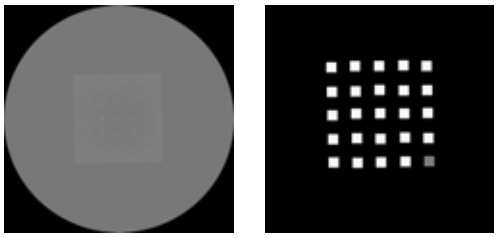

(a) CT image (b) Binarized image

図 3.40: Fourth layer in initial state

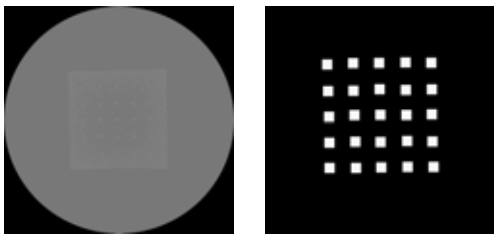

(a) CT image (b) Binarized image

図 3.41: Fourth layer in deformed state

力学パラメータを同定するために，メッシュを生成する．X-Y 平面は，Fig. 3.42-**(a)** に示すようにマーカーの中心を結び物体の輪郭を作る．Y-Z 平面は，2 層目と 3 層目の間にマーカーがないため，節点を補間する．Fig. 3.42-**(b)** に示すように，硬度 0 と硬度 5 の物体の接触面に対して対称な 2 点の中間点を新たな節点として加える．また，マーカーの中心を結び物体の輪郭を作る．これらより，Fig. 3.9-**(a)** に示すメッシュモデルを生成する．物体のサイズは $0.04 \times 0.04 \times 0.04$m で，縦，横，奥行きのエッジ数は 4 つである．

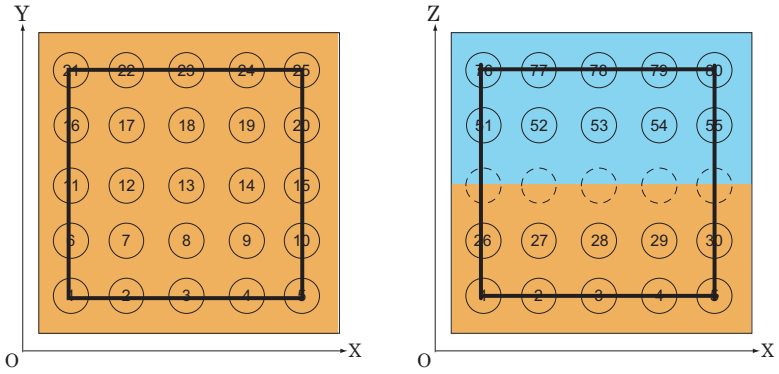

(a) X-Y plane　　(b) X-Z plane

図 3.42: Contour of soft objects

3.6.3　力学パラメータの同定実験

人肌ゲル硬度 5 の物体の力学パラメータが既知，硬度 0 の物体の力学パラメータが未知であると仮定して，硬度 0 の未知パラメータを同定する．力学パラメータが既知である物体のヤング率は Table 3.4，ポアソン比は Table 3.5 における硬度 5 の値である．力学パラメータを同定した結果を Table 3.7 に示す．Table 3.7 において，誤差はシミュレーション条件を実験条件に合わせてシミュレーションを行い，式 (3.35) を用いて計算した．

誤差はシミュレーションより大きいが，1%以下と非常に小さい．今回は均一物体を使用して実験を行っているが，非均一物体を使用して実験を行った場合，あるいは生体組織の力学パラメータ同定を行った場合，同定精度は今回の実験結果より悪くなると考えられる．力学パラメータが既知である物体は未知物体に対してどれくらいのかたさが最適であるのか，メッシュの分割の違いによって同定精度にどれくらい影響するのかも検証する必要がある．

85

表 3.7: Result of physical parameters identification in experiment

	True value		Result		Error [%]
	E^p [Pa]	ν^p	E^p [Pa]	ν^p	
Hardness 5 (known)	2.22×10^5	0.33	-	-	5.51×10^{-2}
Hardness 0 (unknown)	1.25×10^5	0.44	1.55×10^5	0.29	

3.7 結言

本章では，柔軟物の内部変形計測結果から非均一 FE モデルの力学パラメータを同定する手法を提案した．これは被曝がないという利点を持つ MRI 装置を用いて力学パラメータを同定できるように，力の計測なしで生体組織の力学パラメータを同定する手法である．まず，本手法をシミュレーションにより検証した．均一物体と非均一物体と設定した場合についてそれぞれ力学パラメータの同定を行った．同定した結果を用いて再度シミュレーションを行った結果，最初に行ったシミュレーションとほぼ同じ変形が見られ，誤差は 1%以下となった．次に，本手法を用いる際に必要な生体組織の内部変形を計測した．実際に MRI 装置を用いてボランティアの下腿を撮影し，オプティカルフローのアルゴリズムを適用し，それぞれのアルゴリズムの特徴を調べた．そして，ブロックマッチング法と Horn-Schunck 法を融合することで，下腿外部の輝度の変化が激しいところと下腿内部の似通ったパターンが多いところの両方を計測することができた．最後に，本手法を CT を用いた実験により検証した．人肌ゲルにマーカーを埋め込んだ物体を 2 つ作成し，CT を用いて物体の内部変形を計測した．実験条件をシミュレーション条件に合わせ，真値を用いて行ったシミュレーションと同定結果を用いて行ったシミュレーションは，ほぼ同じ変形が見られた．

柔軟物の内部変形計測による非一様 FE モデルの力学パラメータ同定方法の検証

○遠藤 和美，張 鵬林，平井 慎一（立命館大学）
徳本 真一（和歌山県工業技術センター）

Validation of nonuniform physical parameters identification through measurement of inner deformation

○ Kazumi Endo, Zhang Peng-lin and Shinichi Hirai Ritsumeikan Univ.
Shinichi Tokumoto Industrial Technology Center of Wakayama Prefecture

Abstract: This paper describes a method to identify nonuniform physical parameters through measurement of inner deformation. We identify physical parameters by deforming an unknown parameter object using a known parameter object. We evaluate our method in simulation and experimentally.

1 はじめに

近年，手術シミュレーション分野において，柔軟物のモデリングが必要とされている．生体組織は変形特性が非一様で，力学パラメータの値が場所により異なる．このような，非一様な変形特性を持つ物体の力学パラメータを同定する方法は確立されていない．筆者らは，超音波装置や MRI，CT による柔軟物の内部変形の計測結果から力学パラメータを同定する手法を提案した [1]．本論文では，この手法を用いてシミュレーションと実験において力学パラメータ同定を行うことによって提案した手法の有効性を検証する．

2 力学パラメータ同定方法

超音波装置や CT，MRI による内部変形の計測結果から FE モデルの力学パラメータを同定する方法を述べる．あらかじめ圧縮同定試験によって力学パラメータを求めておいた物体を用いて，力学パラメータが未知の物体を変形させる．ここで，力学パラメータとはヤング率とポアソン比である．Fig.1 は，力学パラメータが既知である部分（色を塗った部分）と，未知である部分（色を塗っていない部分）が接触している様子を示している．FE モデルでは物体を四面体要素の集合として表現している．節点 i 回りの四面体要素（Fig.1 の太枠で囲った領域）について考えると，節点 i における力のつりあいは，

$$\sum_{T\in U_i} \boldsymbol{f}_i^T = -\sum_{T\in K_i} \boldsymbol{f}_i^T \qquad (1)$$

となる．ここで，K_i は力学パラメータが既知である四面体要素の集合，U_i は力学パラメータが未知である四面体要素の集合である．また，$\boldsymbol{f}_i^T$ は四面体要素 T の変形により節点 i に生じる弾性力である．式 (1) に内部変形計測結果を代入し，整理することにより力学パラメータが未知である物体の各四面体要素のヤング率とポアソン比に関する一次式となる．

3 シミュレーションによる検証

前章で述べた力学パラメータ同定方法を用いて，シミュレーションによる力学パラメータの同定を行う．シミュレーションでは，物体を Fig.2 に示すようにメッシュを分割し，四面体要素のヤング率 E とポアソン比 ν を設定する．物体の大きさは 0.04×0.04×0.04m，縦，横，奥行き方向のエッジ数はそれぞれ 4 個，各エッジの幅は 0.01m である．物体を床から離れないように拘束し，物体上面全体を押す．物体上面の節点の変位量は，X 方向に 0.00m，Y 方向に 0.00m，Z 方向に 0.01m である．初期状態から変形状態の変位データを取得する．物体の上半分を力学パラメータが既知である一様物体，下半分を力学パラメータが未知である非一様物体と仮定して，未知パラメータを同定する．力学パラメータが同じ四面体要素の領域ごとに平均値を算出した結果を Table 1 に示す．誤差は非常に小さく，本手法の計算アルゴリズムが有効であることが確認できる．

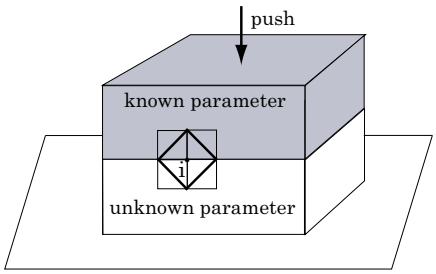

Fig.1 The method of physical parameters identification

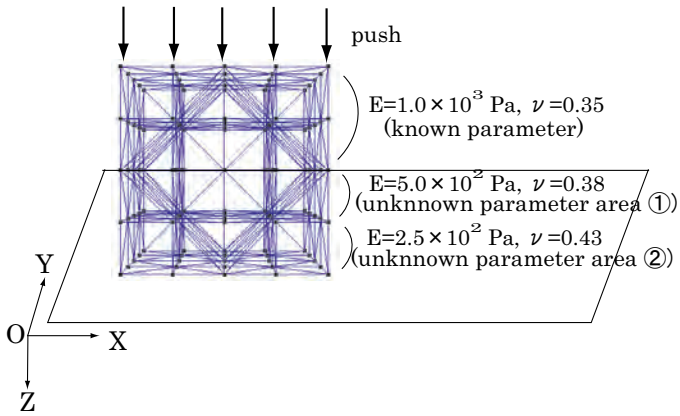

Fig.2 The size of the object in simulation

Table 1　The result of physical parameters identification in simulation

	true value		result		error [%]
	E [Pa]	ν	E [Pa]	ν	
area	2.5×10^2	0.43	2.51×10^2	0.43	
area	5.0×10^2	0.38	5.18×10^2	0.32	1.37×10^{-2}

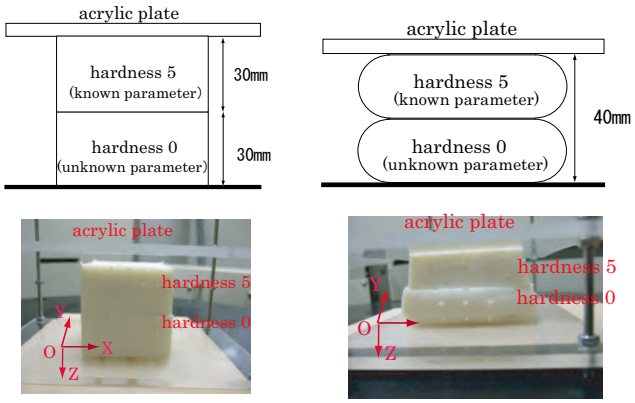

(a) initial state　　(b) deformed state

Fig.3　Soft objects in initial and deformed states

4　CT による実験検証

今回は，力学パラメータが一様な物体を使用して実験を行う．CT を用いて柔軟物の内部変形を計測するために，柔軟物を作成する．パラメータが既知な物体は（株）エクシールコーポレーション製の人肌ゲル硬度 5（腕程度のやわらかさ），パラメータが未知な物体は硬度 0（腹部程度のやわらかさ）を用いて作成した．人肌ゲルはウレタン系オールブレンドを原液とし，イソシアネートの硬化剤を混ぜることによって固めることができる．物体の内部変形を計測するために，人肌ゲルを流し込む型の内部に等間隔に十字方向に糸を張り，その交差点にマーカーを配置している．マーカーは M1 の丸座金 (外径 2.8mm，長さ 0.3mm）で，人肌ゲルが硬化した後に糸を引き抜くことで，マーカーを物体内部に設定することができる．両物体のサイズは $60\times60\times30$mm で，マーカーは 10mm 間隔に合計 50 個を配置している．本実験では内部変形を計測するためにマーカーを使用したが，生体を対象とした場合は血管や組織などの特徴点をもとに生体内部の変形を計測する．Fig.3 に示すように 2 つの物体を重ねアクリル平板を用いて物体全面を高さ 40mm となるまで押す．初期状態と変形状態の様子を CT で撮影する．CT の画像分解能は，X，Y 方向が 0.29mm，Z 方向が 0.5mm である．得られた断面画像を 2 値化し，両物体の内部変形を計測する．

本実験に用いる柔軟物の力学パラメータを計測する．人肌ゲルの硬度 5 と硬度 0 から試験片を製作し，圧縮同定試験機を用いてヤング率を算出する．今回用いた圧縮試験機は，横歪が計測することができないためポアソン比を同定することができない．そこで，初期状態と変形状態の CT 画像から計測した横歪と縦歪の値からポアソン比を算出する．本実験に用いる柔軟物の力学パラメータを Table 2 に示す．

Table 2　Physical parameters of soft objects

	E [Pa]	ν
hardness 5	2.22×10^5	0.44
hardness 0	1.25×10^5	0.33

Table 3　The result of physical parameters identification in experiment

	E [Pa]	ν
physical parameters (hardness 0)	1.25×10^5	0.33
result	1.39×10^5	0.28

Table 2 に示す力学パラメータの値から力学パラメータの同定を行う．人肌ゲル硬度 5 の物体の力学パラメータが既知，硬度 0 の物体の力学パラメータが未知であると仮定して，硬度 0 の未知パラメータを同定した結果を Table 3 に示す．ヤング率は精度よく同定できているが，ポアソン比は 0.05 の違いがある．シミュレーションで同程度の違いがあるが誤差は非常に小さいため，これは許容できると考える．

今回は力学パラメータが一様な物体を使用して実験を行っているが，非一様物体を使用して実験を行った場合，あるいは生体組織の力学パラメータ同定を行った場合，同定精度は今回の実験結果より悪くなると考えられる．力学パラメータが既知である物体は未知物体に対してどれくらいのかたさが最適であるのか，メッシュの分割の違いによって同定精度にどれくらい影響するのかも検証する必要がある．

5　おわりに

本論文では，非一様 FE モデルの力学パラメータ同定法をシミュレーションと実験により検証した．シミュレーションでは，非一様物体の力学パラメータを同定することができ，本手法の計算アルゴリズムが有効であることを示した．実験では，CT を用いた柔軟物の内部変形計測結果から力学パラメータを同定することが可能であることを確認した．今後は，人肌ゲルで非一様物体を製作し，実験検証する．また，生体組織を用いて本手法を検証する予定である．

参考文献

[1] 遠藤 和美, 村松 潤治, 平井 慎一, ”柔軟物の内部変形計測による FE モデルの力学パラメータ同定”, ロボティクス・メカトロニクス’07 講演会, 2007.

[2] 徳本 真一, 平井 慎一, ”CT スキャナを用いたパラメータ同定のための柔軟物の内部変形計測” ロボティクス・メカトロニクス’07 講演会, 2007.

柔軟物の内部変形計測による FE モデルの力学パラメータ同定

Physical parameters identification of FE model through measurement of inner deformation

○ 遠藤 和美（立命館大学），村松 潤治（立命館大学），平井 慎一（立命館大学）

Kazumi ENDO, Ritsumeikan Univ.
Junji MURAMATSU, Ritsumeikan Univ.
Shinichi HIRAI, Ritsumeikan Univ.

Abstract: This paper describes the method to identify the parameters of 2D FE (Finite Element) deformation model from the measured inner deformation of soft objects. First, we formulate 2D elastic deformation and apply FE method to compute the deformation numerically. Next, we describe the method to measure the deformation of soft objects. We propose to deform an object to be identified by another object of which physical parameters are known. During this process, inner deformation of the two objects are measured by CT or MRI technique. Soft objects are pushed by the objects which of the parameters identification is tested in advance. Finally, we formulate a method to identify the model parameters from the measured deformations.

Key words: physical parameters, identification, FE model, deformation

1 緒言

近年，手術シミュレーションにおいて，柔軟物のモデリングが必要とされている．従来の研究では，表面形状の計測が主であり，内部挙動に関しては未知である部分が多かった．そこで，超音波装置および MRI を用いた柔軟物内部の変形計測が行われている [1]．これらの力学パラメータ同定は，内部変形計測結果と変形シミュレーションを比較することにより行われている．この方法は，一様な性質を持つ物体であれば問題ない．しかし，生体組織は変形特性が非一様で，力学パラメータの値が場所により異なる．このような，非一様な変形特性の同定方法は確立されていない．

本論文では，弾性物体の FE モデルについて述べ，柔軟物の内部変形の計測結果から力学パラメータを同定する手法を提案する．また，その手法を用いてシミュレーションによる力学パラメータ同定を行う．

2 弾性体の FE モデル

FE モデルでは，Fig.1 に示すように，柔軟物体を三角形要素あるいは四面体要素の集合として表す．これにより，柔軟物の変形は個々の三角形要素や四面体要素の変形の和として表現することが可能になる．物体を三角形要素の集合で表し，三角形要素の一つを T^p とする．Fig.2 に示すように，P_i，P_j，P_k は三角形 T^p を反時計回りに辿るとする．

三角形要素 T^p の節点 P_i の変位を二次元ベクトル $\boldsymbol{u}_i^p$ で表す．三角形 T^p の変形は三つの節点の変位 $\boldsymbol{u}_i^p$，$\boldsymbol{u}_j^p$，$\boldsymbol{u}_k^p$ で表される．三角形 T^p の変形により節点 P_i に生じる弾性力を $\boldsymbol{f}_i^p$ で表す．非一様な弾性特性を表すために，三角形要素あるいは四面体要素ごとにラーメの定数が異なると仮定する．三角形要素 T_p のラーメの定数を λ^p ならびに μ^p で表す．なおラーメの定数は，ヤング率 E^p とポアソン比 ν^p で表すことができる．

$$\lambda^p = \frac{\nu^p E^p}{(1+\nu^p)(1-2\nu^p)}, \qquad \mu^p = \frac{E^p}{2(1+\nu^p)} \tag{1}$$

三角形 T^p の変形により各節点に生じる弾性力は

$$\begin{bmatrix} \boldsymbol{f}_i^p \\ \boldsymbol{f}_j^p \\ \boldsymbol{f}_k^p \end{bmatrix} = \boldsymbol{K}_p \begin{bmatrix} \boldsymbol{u}_i^p \\ \boldsymbol{u}_j^p \\ \boldsymbol{u}_k^p \end{bmatrix} \tag{2}$$

と表される．弾性行列 $\boldsymbol{K}_p$ は $\lambda^p \boldsymbol{J}_\lambda^p + \mu^p \boldsymbol{J}_\mu^p$ と表すことができる．ここで，$\boldsymbol{J}_\lambda^p$，$\boldsymbol{J}_\mu^p$ は，初期状態の節点の位置で構成される 6×6 の部分接続行列である．

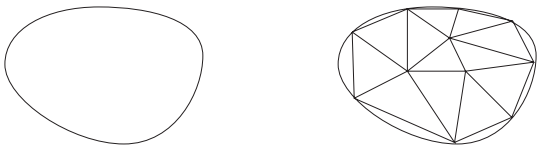

(a) region (b) cover by triangles

Fig.1 Cover of two-dimensional region by triangles

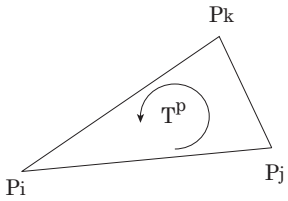

Fig.2 triangle element

3 内部変形の計測

Fig.3 に示すように，あらかじめ同定試験によって力学パラメータを求めておいた物体を用いて，柔軟物体に変形を加える．このときの内部変形の様子を超音波装置や CT，MRI を用いて撮影する．得られた画像に，オプティカルフローのアルゴリズムを用いて，内部変形の計測を行う [2]．計測結果を (2) 式に代入すると，次式のように表すことができる．

$$\begin{bmatrix} \boldsymbol{f}_i^p \\ \boldsymbol{f}_j^p \\ \boldsymbol{f}_k^p \end{bmatrix} = \begin{bmatrix} \boldsymbol{A}_\lambda^p & \boldsymbol{A}_\mu^p \end{bmatrix} \begin{bmatrix} \lambda^p \\ \mu^p \end{bmatrix} \tag{3}$$

ここで，

$$\boldsymbol{A}_\lambda^p = \boldsymbol{J}_\lambda^p \begin{bmatrix} \boldsymbol{u}_i^p \\ \boldsymbol{u}_j^p \\ \boldsymbol{u}_k^p \end{bmatrix} \triangleq \begin{bmatrix} \boldsymbol{A}_{\lambda,i}^p \\ \boldsymbol{A}_{\lambda,j}^p \\ \boldsymbol{A}_{\lambda,k}^p \end{bmatrix}$$

$$\boldsymbol{A}_\mu^p = \boldsymbol{J}_\mu^p \begin{bmatrix} \boldsymbol{u}_i^p \\ \boldsymbol{u}_j^p \\ \boldsymbol{u}_k^p \end{bmatrix} \triangleq \begin{bmatrix} \boldsymbol{A}_{\mu,i}^p \\ \boldsymbol{A}_{\mu,j}^p \\ \boldsymbol{A}_{\mu,k}^p \end{bmatrix} \tag{4}$$

である．係数行列 $\boldsymbol{A}_\lambda^p$，$\boldsymbol{A}_\mu^p$ は 6×1 の行列となる．

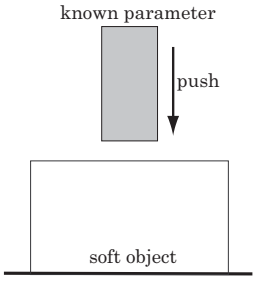

Fig.3　Pushing operation

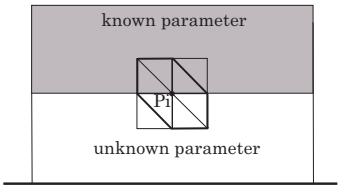

Fig.4　The method of parameters identification

4　力学パラメータの同定方法

超音波装置や CT，MRI による内部変形の計測結果から FE モデルの力学パラメータを同定する方法を述べる．ここで，力学パラメータとは，(1) 式で示したラーメの定数 λ^p，μ^p のことである．従来から，ラーメの定数を求めるために，引っ張り試験を行い，その結果からヤング率とポアソン比を求める方法が用いられている．このとき，試験片の変形とともに，試験片に印加する力を計測する必要がある．一方，生体組織に対してラーメの定数を求めるときには，力を計測することが困難である場合が多い．特に，MR 空間内に磁性体材料を持ち込むことができないため，ロードセル等の力を計測する装置を用いることができない．そこで，本章では，力を計測することなく，ラーメの定数を求める手法を提案する．

基本的な考え方は，力学パラメータが既知の物体を用いて，力学パラメータが未知の物体を変形させ，双方の内部変形を計測した結果から，未知の力学パラメータを同定するというものである．Fig.4 に示すように，力学パラメータが既知である部分（色を塗った部分）と，未知である部分（色を塗っていない部分）が接触しているとする．力学パラメータが既知である部分と未知である部分の境界上にある節点の一つを P_i で表す．節点 P_i 回りの三角形要素について考えると，節点 P_i における力のつりあいは次式で表すことができる．

$$\sum_{p\in S_i} \boldsymbol{f}_i^p = 0 \tag{5}$$

ここで，S_i は，Fig.4 において太枠で囲った領域で，節点 P_i を含む三角要素の集合である．三角要素の集合 S_i は，力学パラメータが既知である三角形要素の集合 K_i と，力学パラメータが未知である三角形要素の集合 U_i から構成される．

$$S_i = K_i + U_i \tag{6}$$

したがって，(5) 式は，

$$\sum_{p\in U_i} \boldsymbol{f}_i^p = -\sum_{p\in K_i} \boldsymbol{f}_i^p \tag{7}$$

となる．ここで，左辺は未知パラメータ λ^p，$\mu^p (p \in U_i)$ に関する一次式である．係数行列は，接続行列 $\boldsymbol{J}_\lambda^p$，$\boldsymbol{J}_\lambda^p (p \in U_i)$ と変位ベクトル $\boldsymbol{u}_i^p$，$\boldsymbol{u}_j^p$，$\boldsymbol{u}_k^p (p \in U_i)$ により表される．したがって，(7) 式を解くことにより，未知パラメータ λ^p，μ^p を求めることができる．

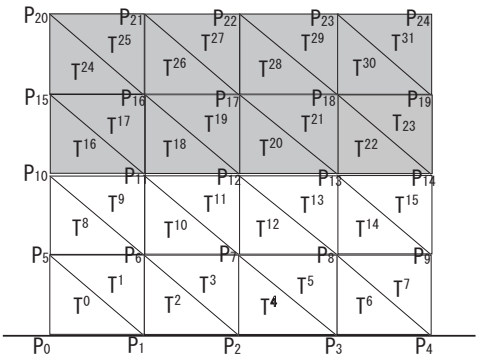

Fig.5　Example of computing physical parameters

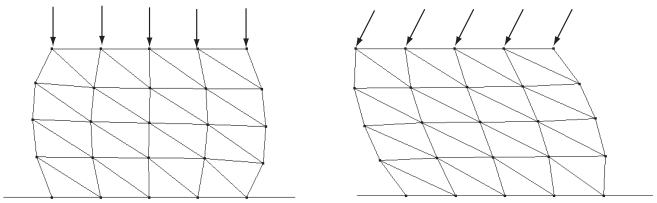

(a) vertical force　　(b) aligned force

Fig.6　Example of pushing operation

Table 1　The number of parameters and equations

	parameter λ^p, μ^p (T^0, T^1, $\cdots$, T^{15})	equation (7) ($i = P_5$, P_6, $\cdots$, P_{14})
total	$2 \times 16 = 32$	$2 \times 10 = 20$

力学パラメータの計算例を Fig.5 に示す形状を用いて示す．Fig.5 は，力学パラメータが既知である三角形要素 24 個，未知である三角形要素 24 個から構成されている．形状全体の力学パラメータの未知数の数と節点における力のつりあいによる方程式の本数を Table 1 に示す．節点 P_0，P_1，P_2，P_3，P_4 における力のつりあいは，各節点が床と接触しており，床から抗力を受けるため考慮しない．Table 1 より，力学パラメータの未知数が 32 個であるのに対して，節点における力のつりあいによる方程式の本数は 20 本である．未知数の数より，方程式の本数が少ないので，パラメータを求めることができない．そこで，方程式の本数を増やすために，2 通りの方法で柔軟物体を変形させる．Fig.6 は変形方法の例である．Fig.6(a) は，物体に対して垂直方向に力を加える方法である．また，Fig.6(b) は，物体に対して斜め方向に力を加える方法である．内部変形計測を 2 通り行うことによって，方程式の本数は 20 本から 40 本に増加するため，力学パラメータを同定することができる．

次に，力学パラメータ同定の手順を Fig.7 に示す．それぞれの場合において，力のつりあいを考える節点を黒丸で示し，その節点を含む三角形要素を太枠で囲った． Fig.7(a) で，節点 P_{14} における力のつりあいを考える．節点 P_{14} を含む三角形要素の集合 S_{14} は，

$$S_{14} = \left\{T^{23},\ T^{22},\ T^{15}\right\} \tag{8}$$

となるので，節点 P_{14} における力のつりあいは次式で表すことができる．

$$\boldsymbol{f}_{14}^{23} + \boldsymbol{f}_{14}^{22} + \boldsymbol{f}_{14}^{15} = 0 \tag{9}$$

力学パラメータが既知である三角形要素の集合 K_{14} と，力学パラメータが未知である三角形要素の集合 U_{14} はそれぞれ，

$$K_{14} = \left\{T^{23},\ T^{22}\right\}, \quad U_{14} = \left\{T^{15}\right\} \tag{10}$$

であるから，(9) 式は，次式のようになる．

$$\boldsymbol{f}_{14}^{15} = -\left(\boldsymbol{f}_{14}^{23} + \boldsymbol{f}_{14}^{22}\right) \tag{11}$$

(11) 式に，内部変形計測を 2 通り行った結果を代入すると，

$$\begin{bmatrix} \boldsymbol{A}_{\lambda,14}^{15\ \sharp 1} & \boldsymbol{A}_{\mu,14}^{15\ \sharp 1} \\ \boldsymbol{A}_{\lambda,14}^{15\ \sharp 2} & \boldsymbol{A}_{\mu,14}^{15\ \sharp 2} \end{bmatrix} \begin{bmatrix} \lambda^{15} \\ \mu^{15} \end{bmatrix} = \begin{bmatrix} -\left(\boldsymbol{f}_{14}^{23\ \sharp 1} + \boldsymbol{f}_{14}^{22\ \sharp 1}\right) \\ -\left(\boldsymbol{f}_{14}^{23\ \sharp 2} + \boldsymbol{f}_{14}^{22\ \sharp 2}\right) \end{bmatrix} \tag{12}$$

となる．添字の ♯1，♯2 は，それぞれ第 1 試行，第 2 試行により得られた値であることを示す．すなわち，上半分は第 1 試行における値，下半分は第 2 試行における値である．(12) 式は，未知数の数より方程式の本数が多いため，最小二乗法を用いて三角形 T^{15} の力学パラメータ λ^{15}，μ^{15} を求める．

次に，Fig.7 の (b) において，節点 P_{13} における力のつりあいを考える．三角形要素 T^{15} の力学パラメータは (12) 式より求められているので，この段階で既知である．節点 P_{13} を含む三角形要素の集合 S_{13} は，

$$S_{13} = \left\{T^{22},\ T^{21},\ T^{20},\ T^{13},\ T^{14},\ T^{15}\right\} \tag{13}$$

となるので，節点 P_{13} における力のつりあいは次式で表すことができる．

$$\boldsymbol{f}_{13}^{22} + \boldsymbol{f}_{13}^{21} + \boldsymbol{f}_{13}^{20} + \boldsymbol{f}_{13}^{13} + \boldsymbol{f}_{13}^{14} + \boldsymbol{f}_{13}^{15} = 0 \tag{14}$$

力学パラメータが既知である三角形要素の集合 K_{13} と，力学パラメータが未知である三角形要素の集合 U_{13} はそれぞれ，

$$K_{14} = \left\{T^{22},\ T^{21},\ T^{20},\ T^{15}\right\}, \quad U_{14} = \left\{T^{13},\ T^{14}\right\} \tag{15}$$

であるから，(14) 式は，次式のようになる．

$$\boldsymbol{f}_{13}^{13} + \boldsymbol{f}_{13}^{14} = -\left(\boldsymbol{f}_{13}^{22} + \boldsymbol{f}_{13}^{21} + \boldsymbol{f}_{13}^{20} + \boldsymbol{f}_{13}^{15}\right) \tag{16}$$

(16) 式に，内部変形計測を 2 通り行った結果を代入すると，

$$\begin{bmatrix} \boldsymbol{A}_{\lambda,13}^{13\ \sharp 1} & \boldsymbol{A}_{\mu,13}^{13\ \sharp 1} & \boldsymbol{A}_{\lambda,13}^{14\ \sharp 1} & \boldsymbol{A}_{\mu,13}^{14\ \sharp 1} \\ \boldsymbol{A}_{\lambda,13}^{13\ \sharp 2} & \boldsymbol{A}_{\mu,13}^{13\ \sharp 2} & \boldsymbol{A}_{\lambda,13}^{14\ \sharp 2} & \boldsymbol{A}_{\mu,13}^{14\ \sharp 2} \end{bmatrix} \begin{bmatrix} \lambda_{13}^{13} \\ \mu_{13}^{13} \\ \lambda_{13}^{14} \\ \mu_{13}^{14} \end{bmatrix} = \begin{bmatrix} -\left(\boldsymbol{f}_{13}^{22\ \sharp 1} + \boldsymbol{f}_{13}^{21\ \sharp 1} + \boldsymbol{f}_{13}^{20\ \sharp 1} + \boldsymbol{f}_{13}^{15\ \sharp 1}\right) \\ -\left(\boldsymbol{f}_{13}^{22\ \sharp 2} + \boldsymbol{f}_{13}^{21\ \sharp 2} + \boldsymbol{f}_{13}^{20\ \sharp 2} + \boldsymbol{f}_{13}^{15\ \sharp 2}\right) \end{bmatrix} \tag{17}$$

となる．添字の ♯1，♯2 は，それぞれ第 1 試行，第 2 試行により得られた値であることを示す．すなわち，ここで，上半分は第 1 試行における値，下半分は第 2 試行における値である．(17) 式を解くことによって，三角形 T^{13}，T^{14} の力学パラメータ λ^{13}，μ^{13}，λ^{14}，μ^{14} を同定することができる．

Fig.7(c) では，節点 P_{12} における力のつりあいを考える．三角形要素 T^{13} の力学パラメータは (17) 式より求められているので，この段階で既知である．したがって，T^{11}，T^{12} の力学パラメータ λ^{11}，μ^{11}，λ^{12}，μ^{12} を同定する．また，Fig.7(d) では，節点 P_5 における力のつりあいを考える．Fig.7(a) の場合と同様に，未知数より方程式の本数が多くなるため，最小二乗法を用いて三角形 T^0 力学パラメータ λ^0，μ^0 を同定する．以上の計算を行うことにより，パラメータを逐次的に同定する．

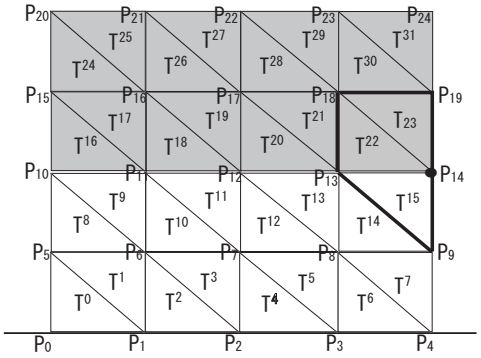

(a) Force balance at P_{14}

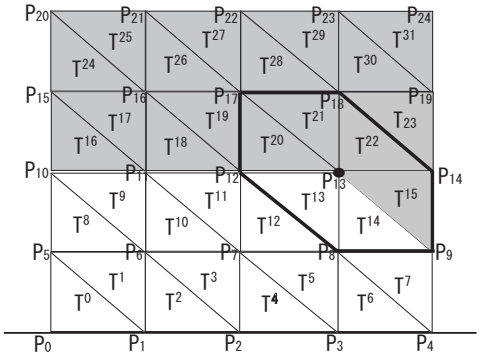

(b) Force balance at P_{15}

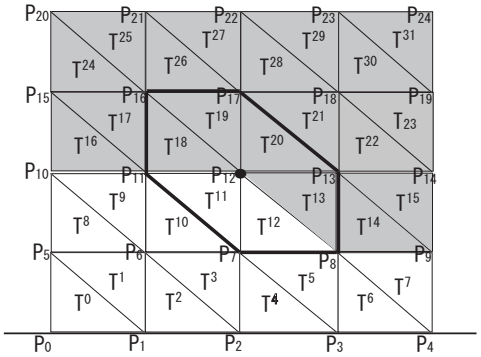

(c) Force balance at P_{12}

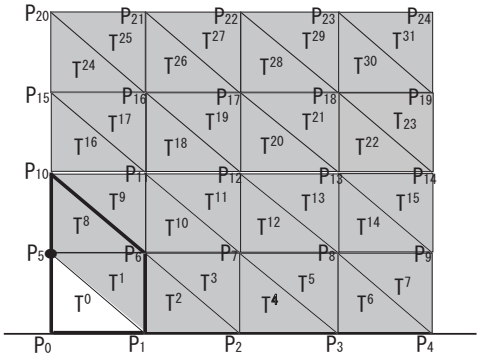

(d) Force balance at P_5

Fig.7 Overview of parameters identification

Table 2 The result of parameters identidfication

First trial		Second trial		T^{13}		T^{14}	
X direction[m]	Y direction [m]	X direction [m]	Y direction [m]	λ^{13}	μ^{13}	λ^{14}	μ^{14}
0.00	0.025	0.025	0.025	1.12×10^4	1.89×10^3	0.93×10^4	1.70×10^3
0.00	0.03	0.03	0.03	1.10×10^4	1.87×10^3	1.10×10^4	1.73×10^3
0.00	0.05	0.05	0.05	2.07×10^4	0.76×10^3	1.11×10^4	1.01×10^3
0.00	0.05	0.1	0.1	2.09×10^4	0.77×10^3	1.10×10^4	1.01×10^3

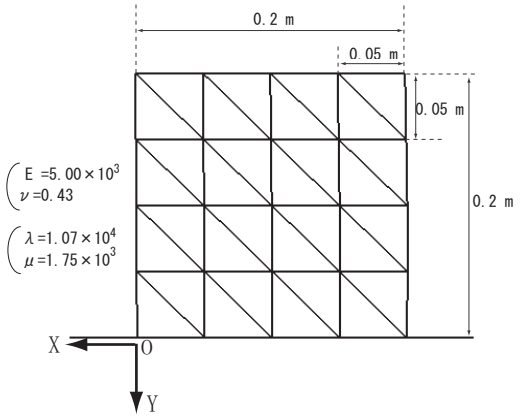

Fig.8 The size of the object in simulation

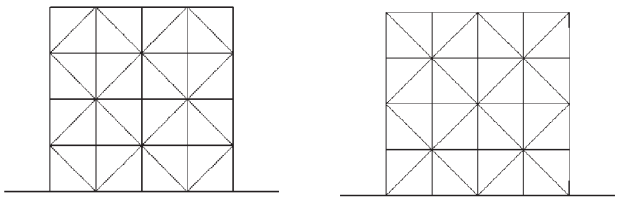

(a) type 1 (b) type 2

Fig.9 Example of mesh model

5 力学パラメータ同定の数値計算例

本章では，前章で述べた力学パラメータ同定方法を用いて，シミュレーションによる力学パラメータの同定を行う．Fig.8(b) に示すように，物体の大きさは，0.2m×0.2m である．横エッジ数と横エッジ数は 4 個で，各エッジの幅は 0.05m である．全ての三角形要素のヤング率とポアソン比を，それぞれ $E^p = 5.0 \times 10^3$，$\nu^p = 0.43$ と設定する．したがって，(2) 式より，ラーメの定数は，$\lambda^p = 1.07 \times 10^4$，$\mu^p = 1.75 \times 10^3$ となる．変形方法は，物体上面の節点の変位量を決定して変形をさせる強制変位法である．2 通りの方法で物体を変形させ，Fig.7(b) の場合において，力学パラメータの同定を行った．つまり，三角形要素 T^{22}，T^{21}，T^{20}，T^{15} の力学パラメータが既知であるとして，P_{13} における力のつりあいを考えることにより，T^{13}，T^{14} の力学パラメータ λ^{13}，μ^{13}，λ^{14}，μ^{14} を同定した．物体上面の節点 P_{20}，P_{21}，P_{22}，P_{23}，P_{24} に与えた強制変位量と，そのときの同定結果を Table 2 に示す．なお，強制変位量は，X 方向は左向きを正，Y 方向は下向きを正としている．Table 2 より，強制変位量が小さい場合，比較的精度よく同定できていることがわかる．しかし，強制変位量を大きくすると，同定精度が落ちる．これは，メッシュの生成法に原因があると考える．今回使用したモデル以外に，メッシュの生成法は，Fig.9 に示すようなモデルが考えられる．今後，これらのモデルを使用して，力学パラメータを同定することを検討する．

6 結言

本論文では，柔軟物の内部変形計測結果から，FE モデルの力学パラメータを同定する手法を提案した．また，その手法を用いて，シミュレーションによる力学パラメータの同定を行った．強制変位量によって，同定精度にばらつきが見られる．今後は，メッシュの生成法を変更して，力学パラメータ同定を行う予定である．また，実際に超音波装置や CT，MRI を用いて柔軟物の内部変形計測を行い，力学パラメータ同定手法の検証を行う．

参考文献

[1] 活田 崇至, 村松 潤治, 早見 信一郎, 森川 茂廣, 平井 慎一, ”超音波画像と MRI を用いた内部計測による柔軟物の FE モデルの検証”, ロボティクスシンポジア予稿集, 2006.

[2] 遠藤 和美, 張 鵬林, 村松 潤治, 平井 慎一, 森川 茂廣, ”MRI ボリュームデータにおける 3 次元ブロックマッチングを用いた FE モデルパラメータの同定”, 計測自動制御学会システムインテグレーション部門学術講演会, pp.1036-1037, 2006.

MRI ボリュームデータにおける 3 次元ブロックマッチングを用いた FE モデルパラメータの同定

○遠藤 和美，張 鵬林，村松 潤治，平井 慎一（立命館大学）
森川 茂廣（滋賀医科大学）

Identification of FE model parameters from MRI volume data using 3D block matching

○Kazumi ENDO, Zhang Peng-lin, Junji MURAMATSU and Shinichi HIRAI Ritsumeikan Univ.
Shigehiro MORIKAWA Shiga Univ. of Medical Science

Abstract: MRI provides 3D information of internal organs and tissues by reconstructing slices. Therefore, we can construct an accurate 3D FE deformation model of soft objects. This paper describes the measurement of inner deformation of the calf using MR images to identify of FE model parameters of the calf. First, we apply 3D block matching to initial and deformed volume data sets of MR images. Next, we propose the method to identify the parameters of the FE model.

1 はじめに

近年，手術シミュレーションにおいて，柔軟物のモデリングが必要とされている．従来の研究では，表面形状の計測が主であり，内部挙動の計測は行われていなかったため，正確にモデルパラメータを同定することは困難であった．この問題を解決するために，超音波装置および MRI を用いた柔軟物内部の変形計測が行われている [1]．しかしながら，これらのモデルは 2 次元であり，手術シミュレーションに適用するためには，3 次元のモデリングが必要となる．本論文では，MRI によって撮影した下腿の断面画像からボリュームデータを生成し，3 次元ブロックマッチングを用いて変形を計測する．また，計測結果を用いて，FE モデルのパラメータ同定手法を提案する．

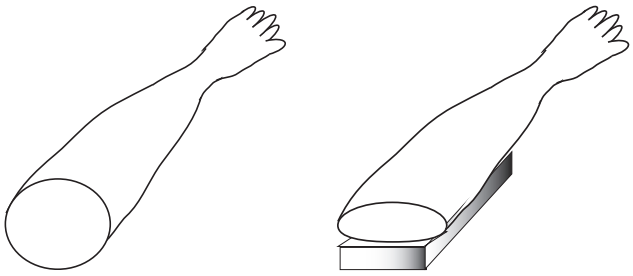

(a) Initial state (b) Deformed state

Fig. 1: MRI photographics condition

2 ボリュームデータの生成

本実験では，MRI 装置によって下腿を撮影した．Fig.1 に示すように，下腿を圧迫していない状態 (初期状態) および下腿の下にプラスチックの箱を置き圧迫した状態 (変形状態) を撮影した．撮影条件は，スライス間隔 2mm，FOV20 × 20cm，積算 2 回とし，それぞれ 76 枚のスライス画像を得た．画像サイズは 256 × 256pixels，画素サイズは 0.8mm/pixel である．変形状態では，プラスチックの箱を置くために下腿の位置をずらしたため，レジストレーションを行う必要がある．剛体部分である頸骨（下腿の太い方の骨）の周りから同一の点である 3 点を，それぞれ初期状態と変形状態の画像から選択してレジストレーションを行った．Fig.2 に示すように，座標系を設定し，初期状態と変形状態の断面画像からボリュームデータをそれぞれ生成する．ボリュームデータは，濃度値を格納したボクセルで構成した．ボクセルのサイズは，縦 0.8mm ×横 0.8mm ×奥行き 2mm である．

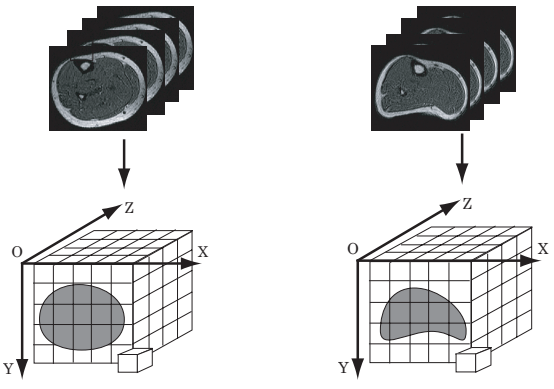

(a) Initial state (b) Deformed state

Fig. 2: Construction of volume data by MR images

3　ブロックマッチングによる変形計測

生成したボリュームデータに対し，3 次元ブロックマッチングを行う．マッチングの方法は SAD(Sum of Absolute Difference) を用いる．SAD は，

$$R_{SAD} = \sum_{i=i_0}^{i_0+S-1} \sum_{j=j_0}^{j_0+T-1} \sum_{k=k_0}^{k_0+U-1} |M_{ini}(i,j,k) - M_{def}(i+i_1, j+j_1, k+k_1)|$$

で表わされ，差分絶対値和 R_{SAD} が最小となる部分を最も類似した部分として判定する．ここで，$M_{ini}(i,j,k)$ は初期状態における三次元 MR 画像でテンプレートとし，$M_{def}(i,j,k)$ は変形状態の三次元 MR 画像である．S，T，U はそれぞれ縦，横，奥行きのウィンドウサイズで，3 × 3 × 3pixels とした．また，i_0，j_0，k_0 はそれぞれ x，y，z 方向のテンプレートの始まる位置である．x，y，z 方向の探索領域は，$i_1 = [-15 \sim +15]$，$j_1 = [-15 \sim +15]$，$k_1 = [-1 \sim +1]$ とした．Fig.3(a) に X-Y 平面の変形前の様子を，Fig.3(b) に変形計測結果を示す．また，Y-Z 平面の変形計測結果を Fig.4 に示す．Fig.3 および Fig.4 において，Y 負方向に下腿を変形させている．白い線分は，大きな白い点が初期状態での位置，線分の向きがその点の変形の方向，線分の長さが変形の大きさを表わしている．また，下腿領域外の小さな白い点は，その点の変形ベクトルが 0 であることを表わしている．また，本実験では，テンプレート中の階調変化がほとんどない計測点については，正確な変形ベクトルを求めることが困難であるとみなし，強制的に変形を 0 としている．Fig.3 の X-Y 平面の実験結果より，一部雑音が含まれているが，圧迫した部分は上向きの変形ベクトルをもって変形していることがわかる．頸骨の周りについては様々な方向の変形が見られる．これは，レジストレーションを行った際に，初期状態と変形状態との位置合わせを正確に行うことができなかったためと考えられる．今後，レジストレーションの方法を再考する必要がある．また，Fig.4 では，X-Y 平面の実験結果と同様，圧迫した部分のベクトルは上向きとなっている．今回の実験では，下腿は Y 方向には変形しているが，Z 方向にはほとんど変形していない．これは実験結果から確認できる．しかし，3 次元ブロックマッチングの効果を確認するためには，X，Y，Z 方向のすべての方向に変形させて計測を行う必要がある．

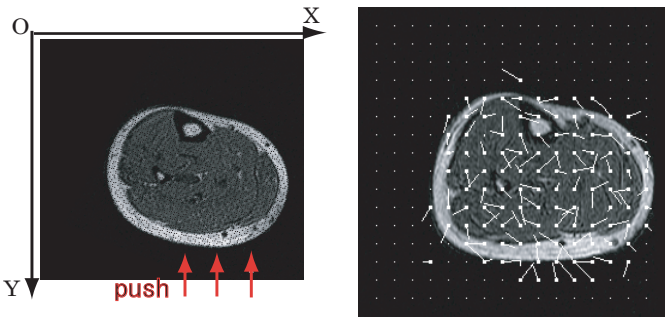

(a) Initial state　　(b) Deformed state

Fig. 3: The result of block matching (X-Y plane)

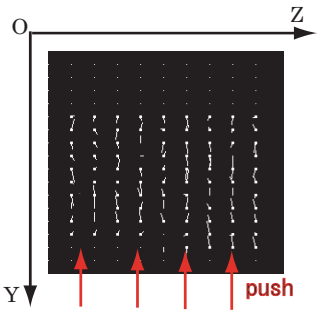

Fig. 4: The result of block matching (Y-Z plane)

4　FE モデルのパラメータ同定

文献 [1] を参考に，FE モデルのパラメータ同定を行う．三次元の FE モデルでは，Fig.5 に示すように下腿を四面体要素の集合として表わす．これにより，下腿の変形は四面体要素の変形の和として表現することが可能となる．MRI で撮影した実験条件とシミュレーションの条件を合わせ，変形シミュレーションを行う．MRI の計測結果とシミュレーション結果を比較することにより，パラメータを同定する．

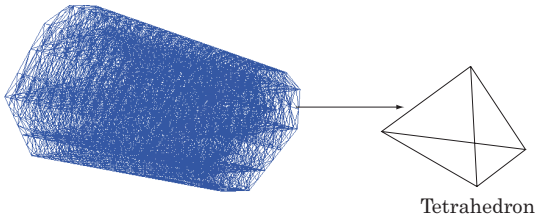

Fig. 5: FE model

5　おわりに

本論文では，下腿の MRI 断面画像からボリュームデータを生成し，3 次元ブロックマッチングを用いて変形の計測を行った．また，計測結果から FE モデルパラメータを同定する手法を提案した．今後は，実際に FE モデルの変形シミュレーションからパラメータ同定を行い，さらに，非線形性，異方性，および非均一性を導入する．

参考文献

[1] 活田 崇至，村松 潤治，早見 信一郎，森川 茂廣，平井 慎一，田中 弘美，”超音波画像と MRI を用いた内部計測による柔軟物の FE モデルの検証”，ロボティクスシンポジア予稿集，2006.

[2] 上野 育子，亀田 昌志，井上 敬，小川 彰，”3.0Tesla 高解像度 MR 画像からの脳領域抽出”，電子情報通信学会論文誌 D，Vol.J89-D，No.1，pp107-120，2006.

[3] 鳥脇 純一郎，3 次元ディジタル画像処理，昭晃堂，2002.

CT スキャナを用いたパラメータ同定のための柔軟物の内部変形計測

和歌山県工業技術センター ○徳本 真一，　立命館大学　理工学部　平井 慎一

Internal Deformation Measurements of Flexible Object for Identification of Parameters by CT Scanner

○Shinichi TOKUMOTO System Division, Industrial Technology Center of Wakayama Prefecture and Shinichi Hirai College of Science and Engineering, Ritsumeikan University

Abstract: In industry field, in order to manipulate flexible object as food and medicine and rubber product automatically, it is necessary to model deformations of these objects. In this paper, we will measure internal deformation of flexible object by industrial CT scanner for identification of model parameters. We will make the object of a cubic, half oval shape that metallic elements ware arranged in the object at equal intervals as a marker. And, we will measure internal deformation by CT scanner when the object is deformed by compulsion displacement in various deformable conditions.

1. 緒言

近年の産業分野においては，生産工程が高度に自動化されており，食品や医薬品，ゴム製品などを扱う作業の工程においても，自動化の要求が高まっている．これら柔軟物の変形を扱う操作を自動化するためには，物体のモデル化が必要である[1)]が，モデル化するためには実際の物体の変形を計測し，モデルのパラメータを同定する必要がある．

本研究では，柔軟物体をモデリングする際のモデルパラメータを同定するために，物体が変形する時の内部変形情報を，産業用 CT スキャナを用いて計測する．まず，物体内部にマーカーとして等間隔に金属部品を配置した，立方体や半楕円形状の柔軟物体を作成する．それら柔軟物体に対していくつかの強制変位を加え、内部の変形状態を産業用 CT スキャナで撮影する．その断層データを積層化することでボクセルモデルを取得し，物体内部のマーカー位置を計測する．

2. 産業用 CT スキャナ

本研究において，産業用ＣＴスキャナとして東芝 IT コントロールシステム製 CT スキャナ「TOSCANER-24200AV」を使用する．Table 1 に産業用 CT スキャナの仕様を示す．本 CT スキャナは第 2 世代のトラバース・ローテーション方式である．X 線源および検出器は固定されており，テーブルがトラバース・ローテーション運動する．

Table. 1 Specifications of CT Scanner

スキャン方式	トラバースローテーション方式
X 線出力	200KV or 400KV
透過能力	**鉄** 100mm，**アルミ** 300mm
スライスエリア	φ150mm，φ300mm， φ600mm　**可変**
スライス厚	1.0mm，2.0mm，4.0mm　**可変**
再構成画素	512×512 or 1024×1024 or 2048×2048

2. 変形計測方法

2.1 柔軟物体の作成

本研究に用いる柔軟物として（株）エクシールコーポレーション製の「人肌のゲル」を用いる．「人肌のゲル」はウレタン系のポリオールブレンドを原液とし，イソシアネートの硬化剤を用いて硬化させることのできる物体である．また，物体の内部変形を計測するためのマーカーとして，できるだけ変形の障害とならないように，M1 の丸座金（外経 2.8 [mm]　長さ 0.3[mm]）を使用した．

型を作成し，柔軟物体をその中で固める必要があるが，CT で取ったデータを解析するためには，ある程度等間隔にマーカーを配置しておく必要がある．そのため型内部に等間隔に十字方向に糸を張り，その交差点に座金を配置するようにした．そして原液を流し，物

体が硬化した後に糸を引き抜く．これによって，型に原液を流し込んでもマーカーの位置が移動することはなく，初期に設定したマーカーの位置を保持できる．本研究では，柔軟物体として 60×60×60[mm]の立方体形状と，130×110×50[mm]の半楕円形状を用意した．マーカーである座金は 10[mm]間隔に配置している．

2.1 柔軟物の変形条件の設定

本研究では，製作した立方体形状と半楕円形状の柔軟物体に強制変位を加える．まずは立方体形状の強制変位の条件は Fig.1-(a)，(b)に示す 2 種類である．(a)は幅 13[mm]の長方形物体を柔軟物体の上部中央に押し当て，押し下げる場合である．白がフリーの状態，赤が高さ 45[mm]まで押し下げた状態, 青が高さ 35[mm]まで押し下げた状態である．(b)は柔軟物体上部全体を押し下げる場合である. 白はフリーの状態, 赤は高さ 45[mm]まで押し下げた状態，青は高さ 35[mm]まで押し下げた状態である．次に半楕円形状の強制変位の条件は Fig.1-(c)に示す．半楕円形状の長軸方向に対して，両側から側面全体を押す. 白はフリー状態, 赤は幅 100[mm], 青は幅 80[mm]まで強制変位を与える．

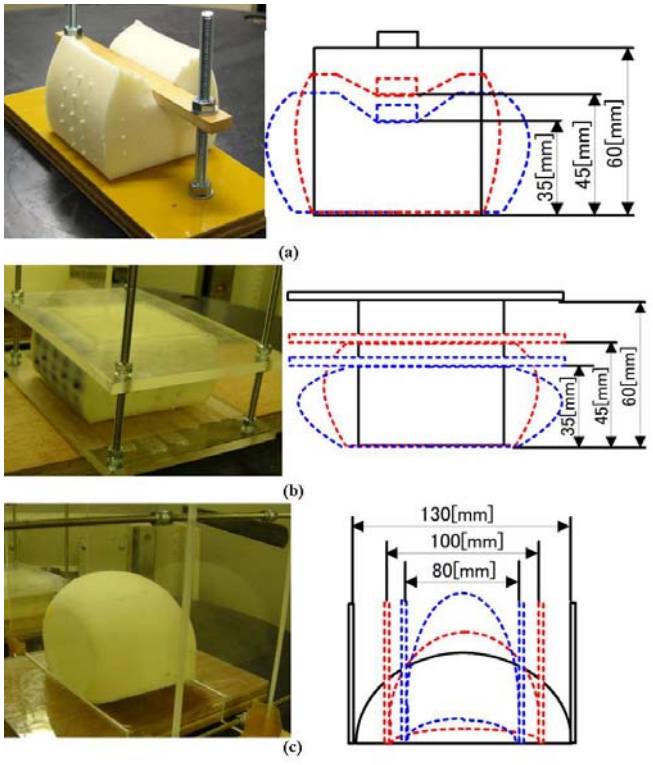

Fig.1 Deformable Conditions

3. 変形計測方法

Fig.2 にそれぞれの計測結果を示す．撮影時のＣＴスキャナの画像分解能は x，y 方向は 0.29[mm]，z 方向は 0.5[mm]である．Fig.2 の(a)，(b)，(c)はそれぞれ Fig.1 の(a)，(b)，(c)の計測結果である．

詳細な紙面では省くが，(a)の場合，押付量が大きければ大きいほど，変形は中央から前後左右に広がっている．また押付板の下側は，上から変形が加えられているが，周囲の拘束により前後左右に変形しにくいため，下に変形する量が相対的に他の方向よりも大きいことがわかった．(b)については(a)と同様に押付量が大きければ大きいほど，変形は中央から前後左右に広がっているが，上面全体が押されているため変形は等間隔に近い．

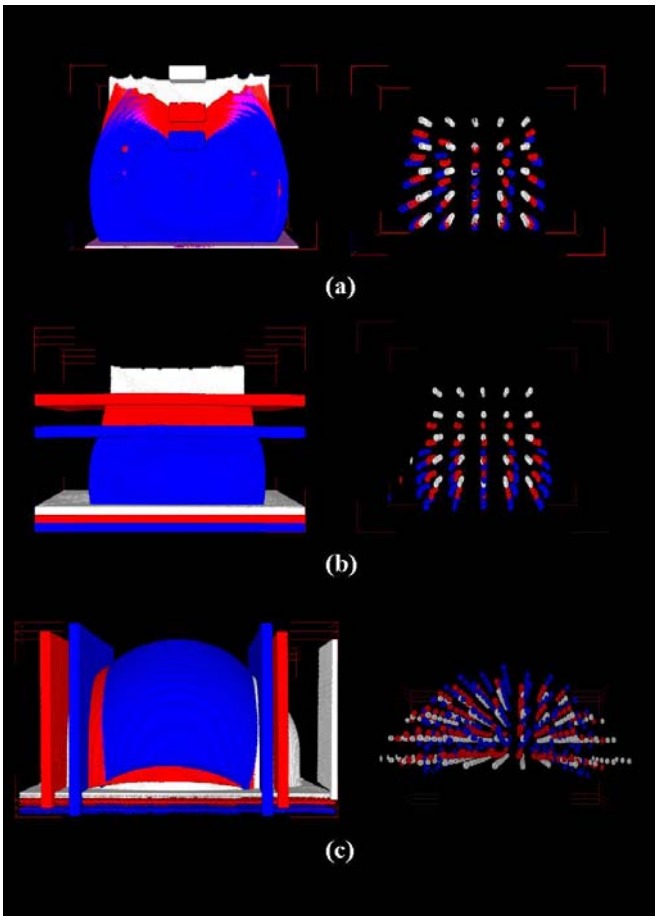

Fig.2 Measurement Results by CT Scanner

4. 結言

本研究では，柔軟物体をモデリングする際のモデルパラメータを同定するために，物体が変形する時の内部変形情報を，産業用 CT スキャナを用いて計測した．今後はこのデータをもとに，柔軟物体のモデルパラメータを同定し，モデリング方法についての検証を行う予定である．

参考文献

1) 友國，杉山，平井 : 実時間計算可能な仮想レオロジー物体の構築, 日本バーチャルリアリティ学会誌, Vol.8, No.3 ， pp-247-254，2003

完了報告書

本報告書は、平成 17 年度科学研究費補助金基盤研究 A「内部センシングに基づく柔軟物のリアリティーベースモデリングに関する研究」に係る委託試験の成果を示す。試験題目、試験目的、試験内容は以下のとおりである。

（1） 試験題目　X 線計測装置を用いた内部変形計測試験

（2） 試験目的　本受託試験では、和歌山県工業技術センターが所有している産業用 CT スキャナを用いて、外部から変形が与えられた粘弾性物体内部の変形の推移を計測することを目的とする。

（3） 試験内容　本試験では内部にマーカーとして金属ワッシャーを等間隔に配置した立方体形状のウレタン系粘弾性物体を製作する。その物体に外部から圧力を印加した場合の内部の変形状態を、和歌山県工業技術センターが所有している産業用 CT スキャナを用いて内部変形の 3 次元位置計測をおこなう。

（4） 試験担当者　和歌山県工業技術センター　システム技術部　副主査研究員　徳本真一

試験結果

1．試験装置

本試験において、粘弾性物体の内部変形を計測する産業用 CT スキャナを Fig.1 に示す。本 CT スキャナの場合、スライスエリアを最小の φ150mm とし画素サイズを 512×512[Pixel]とした場合、X、Y 方向の空間分解能は 150÷512＝0.29[mm]となる。Z 方向に関しては、スライス厚が最小で 1[mm]のため分解能が 1[mm]であるが、スライスピッチの最小が 0.5[mm]であるため再構成では仮想的に 0.5[mm]の分解能で計算できる。

産業用ＣＴスキャナ

TOSCANER-24200AV

スキャン　トラバースローテーション方式

Ｘ線出力　400kV、透過能力　鉄100mm、アルミ300mm

ｽﾗｲｽｴﾘｱ　　φ150mm、φ300mm、φ600mm　可変

ｽﾗｲｽ厚　　1.0mm、2.0mm、4.0mm　可変

再構成画素　512×512　or　1024×1024　or　2048×2048

ｽｷｬﾝﾓｰﾄﾞ　　nomal(fast)　or　fine(slow)

　　ful(360)　　or　half(180)

ﾏﾙﾁｽｷｬﾝﾋﾟｯﾁ　min.0.5mm

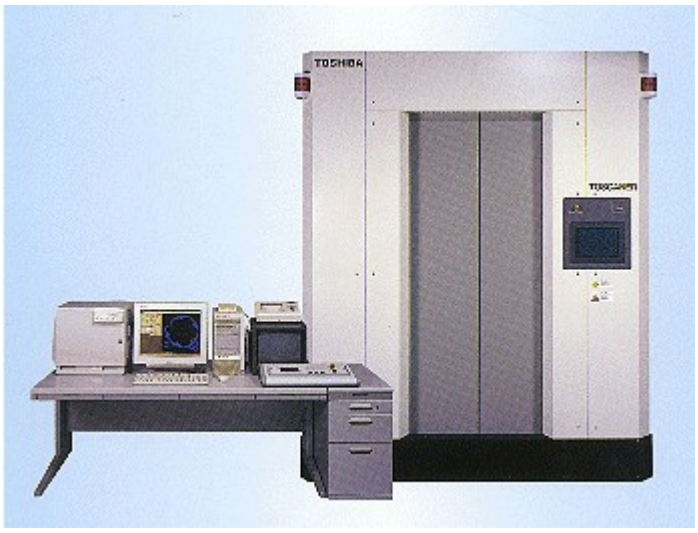

Fig 1　産業用 CT スキャナ仕様

２．粘弾性物体の作成

本試験において、粘弾性物体には昨年度に続き「人肌ゲル」を用いる。人肌ゲルはウレタン系のポリオールブレンドを原液とし、イソシアネートの硬化剤を用いて硬化させることのできる物体である。(Fig.2 参照)

Fig 2　人肌ゲル原液

つぎに変形の内部形状のマーカーとして、M1 の丸座金（外経 2.5［mm］　厚さ 0.3[mm]）を用いた。物体内部に丸座金のマーカーを設置する方法として、Fig.3 に示すように丸座金を十字に張った糸を通して固定し、人肌ゲルを型に流し固まってから糸を引き抜くという方法をとった。本試験では 2 種類硬度を持つ人肌ゲルを組み合わせて変形計測試験を行った。使用した硬度は「硬度０」と「硬度５」である。粘弾性物体を製作した型は Fig.4 に示す。以上の型を用いて製作した内部にマーカーとして丸座金を配置した粘弾性物体を製作した。粘弾性物体の縦・横サイズは 60[mm]×60[mm]で統一し、その方向に 1[cm]間隔に 5×5 個配置している。

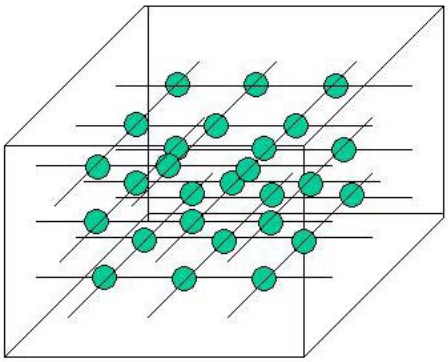

Fig 3　マーカー埋め込み方法

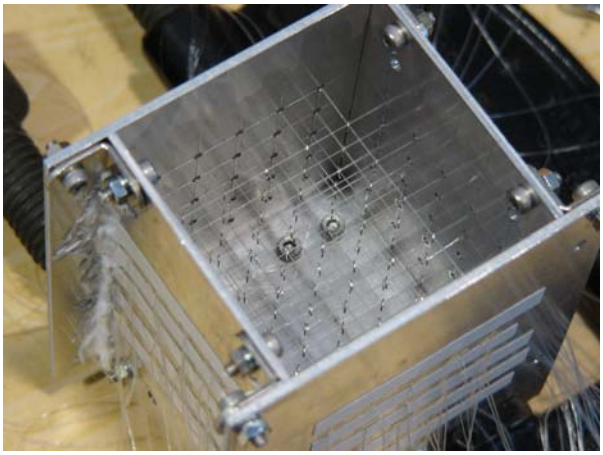

Fig 4　立方体形状用型

３．変形条件

粘弾性物体の変形条件については、以下に示す。

３－１．立方体形状の変形条件１

「硬度０」と「硬度５」の人肌ゲルを組み合わせて、Fig.5 の初期形状に示す様な立方体形状の粘弾性物体を製作した。初期形状の写真は Fig.6 に示す。粘弾性物体の全体のサイズは 60[mm]×60[mm]×60[mm]で、「硬度５」の部分はその上部 30[mm]である。下部 30[mm]は「硬度０」になっている。

この粘弾性物体を Fig.5 の変形形状に示す様に、幅 13[mm]のアクリル板を上から高さ 40[mm]まで押し付けることによって変形させる。変形後の形状は Fig.7 に示す。マーカーである丸座金の配置は Fig.8 に示す。「硬度５」「硬度０」それぞれ高さ方向に２列分配置している。マーカーNo.1～50 は「硬度５」内に、マーカーNo.50～100 は「硬度０」内に配置される。

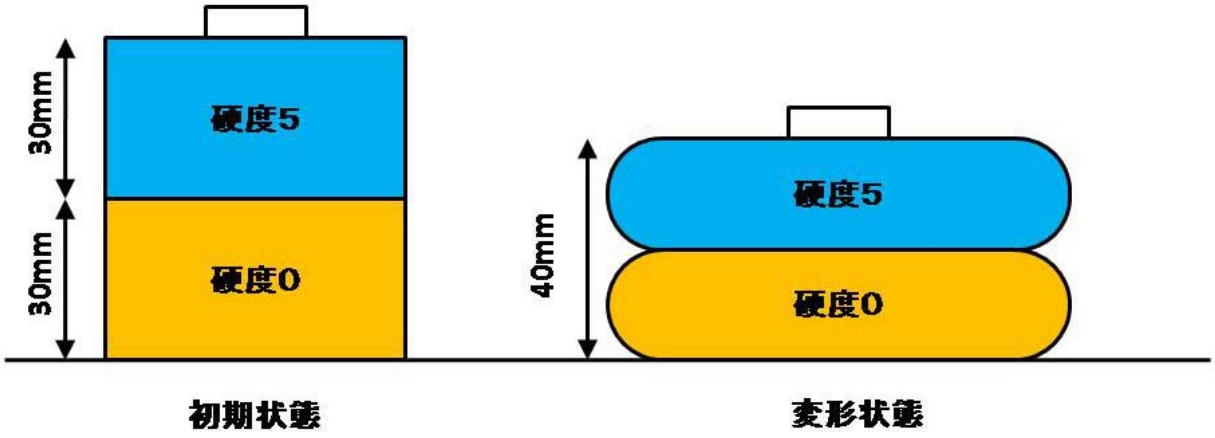

Fig 5　変形条件１

Fig 6　初期形状

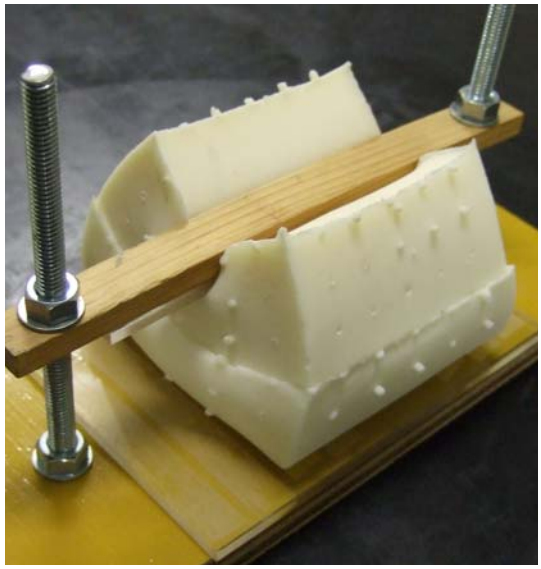

Fig 7　変形形状

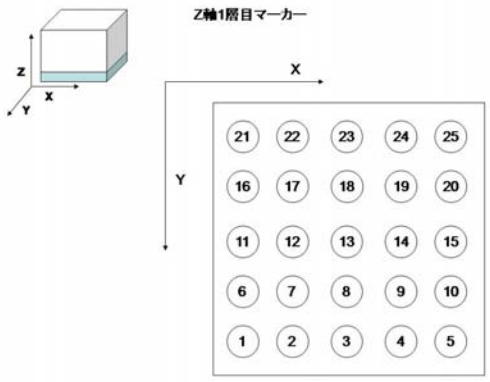

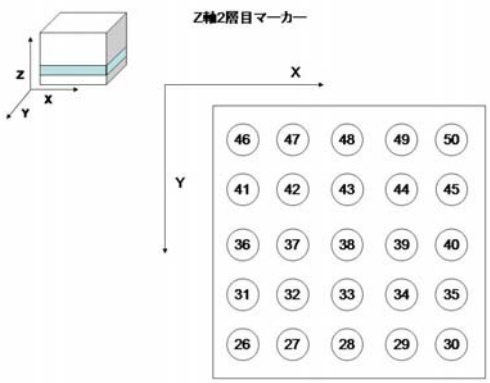

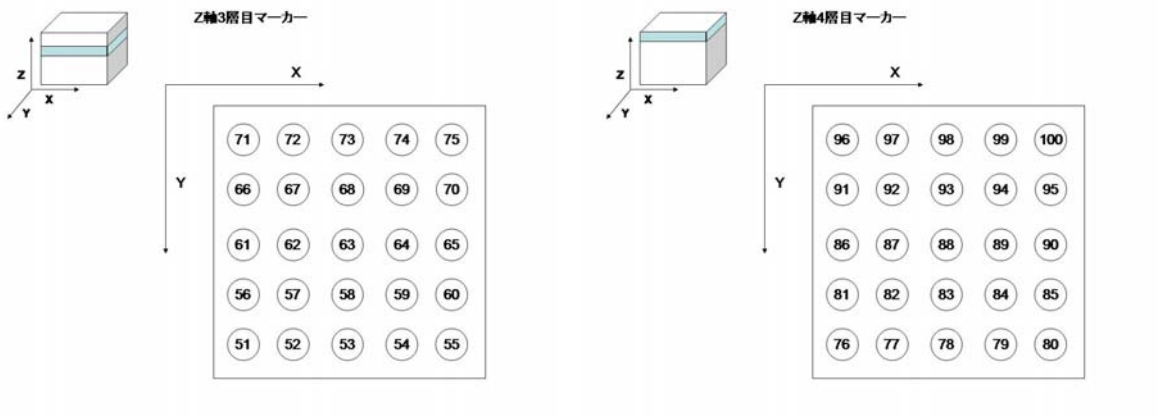

Fig 8　マーカー位置

３－２．立方体形状の変形条件２

「硬度０」と「硬度５」の配置は３－１と同じであるが、変形条件が異なる。Fig.9 に示す様に上部から高さ 40[mm]まで、粘弾性物体全体を押しつぶすように変形させる。初期形状、変形形状は Fig.10、Fig.11 に示す。マーカー配置は３－１と同じである。

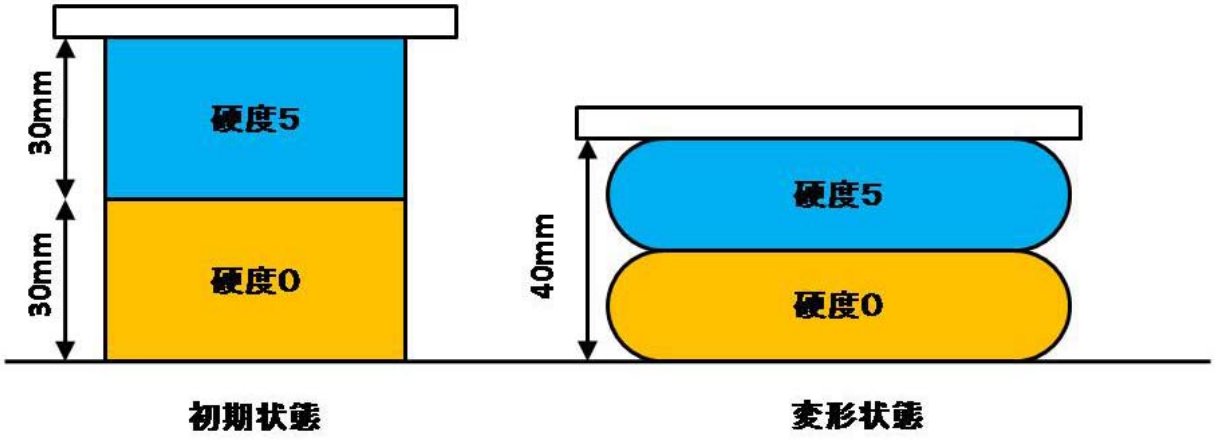

Fig 9　変形条件２

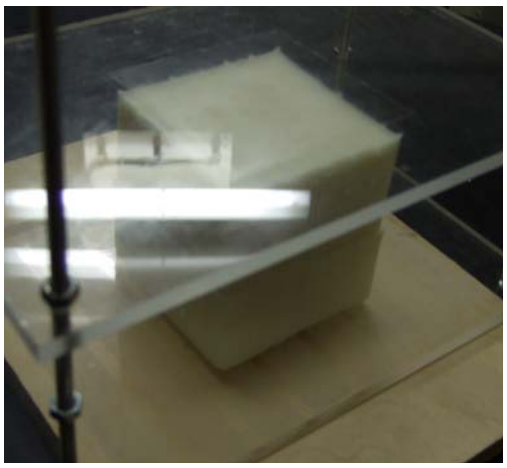

Fig 10　初期形状

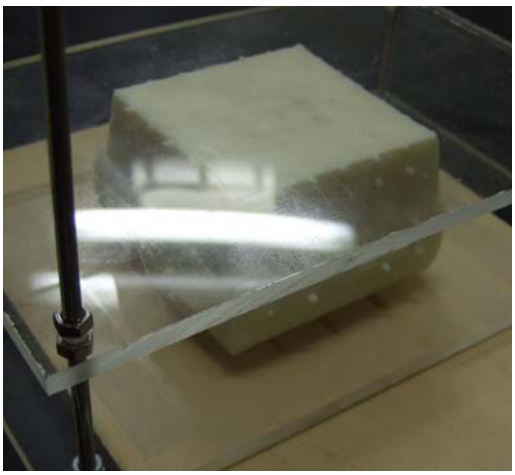

Fig 11　変形形状

３－３．立方体形状の変形条件３

「硬度０」と「硬度５」の配置はFig.12に示す配置にする。上方30[mm]は「硬度５」、中15[mm]は「硬度０」、下方 15[mm]は「硬度５」に設定する。マーカーの配置は３－１、３－２と同じであるため、マーカーNo.1～25は「硬度５」内に、マーカーNo.26～50は「硬度０」内に、マーカーNo.51～100は「硬度５」内に配置される。初期形状、変形形状はFig.13、Fig.14に示す。

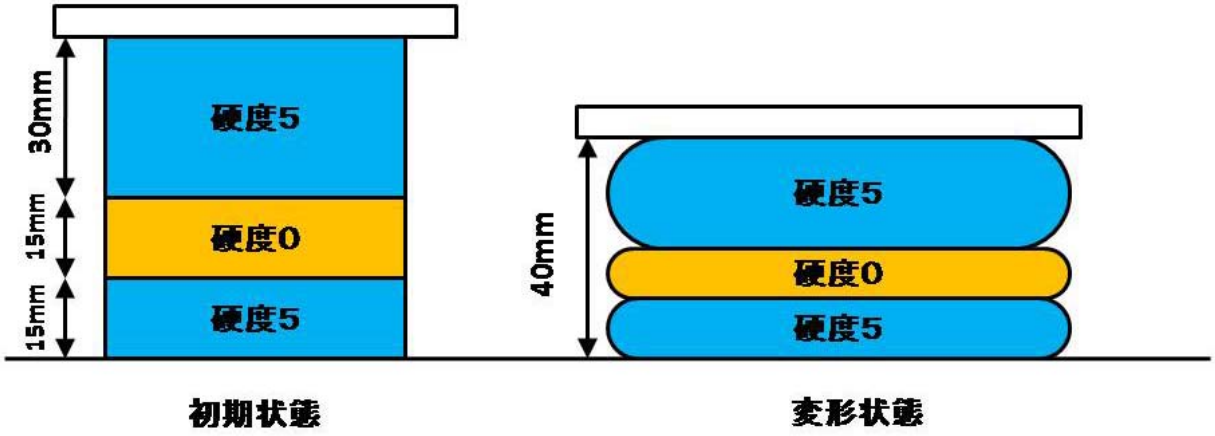

Fig 12　変形条件３

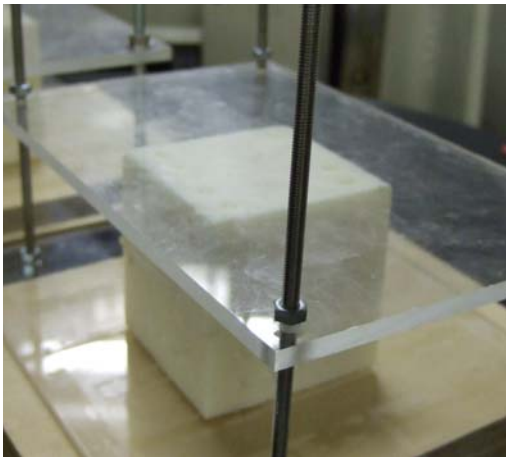

Fig 13　初期形状

Fig 14　変形形状

３－４．立方体形状の変形条件４

「硬度０」と「硬度５」の配置は Fig.15 に示す配置にする。３－３の「硬度０」と「硬度５」が入れ替わり、上方 30[mm]は「硬度０」、中 15[mm]は「硬度５」、下方 15[mm]は「硬度０」に設定する。マーカーNo.1～25 は「硬度０」内に、マーカーNo.26～50 は「硬度５」内に、マーカーNo.51～100 は「硬度０」内に配置される。初期形状、変形形状は Fig.16、Fig.17 に示す。

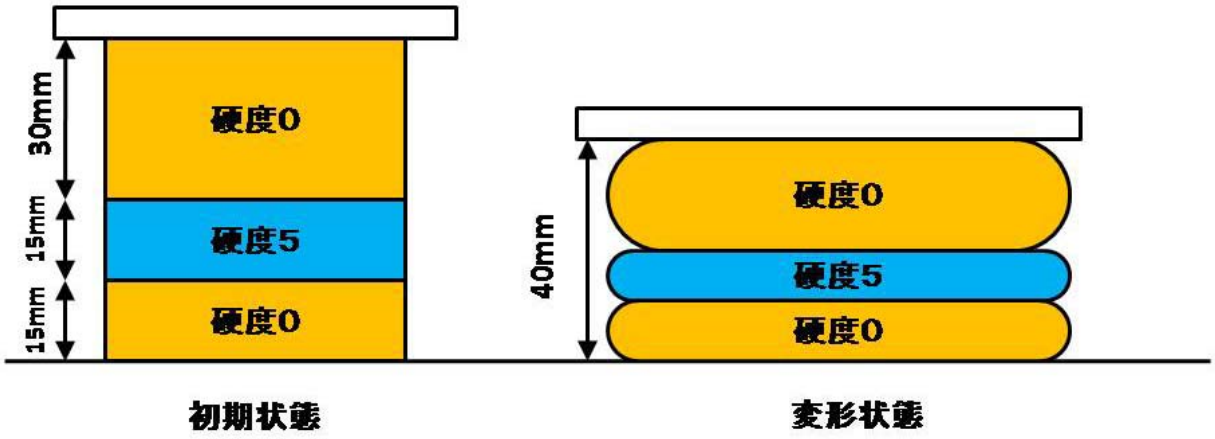

Fig 15　変形条件４

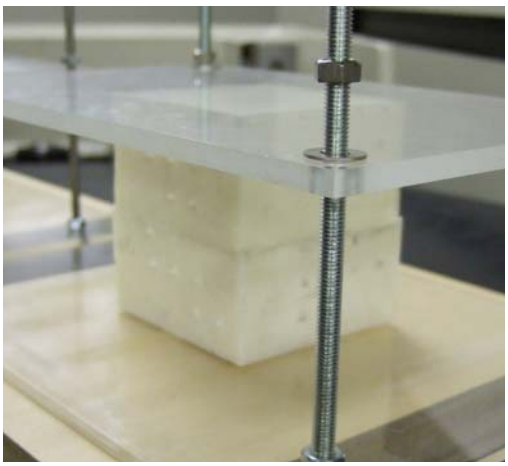

Fig 16　初期形状

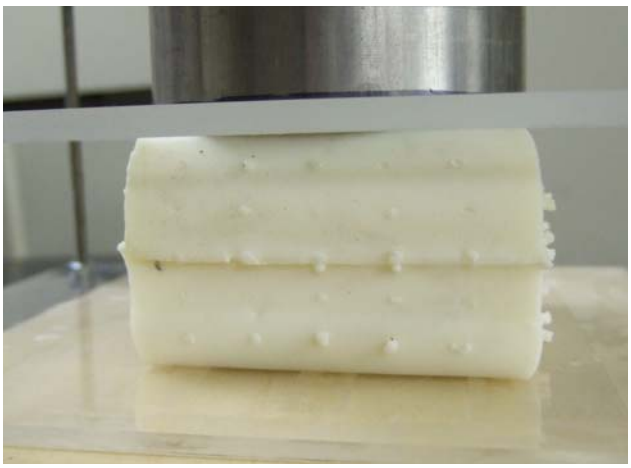

Fig 17　変形形状

なお撮影時のＣＴスキャナの画像分解能は

３－１、３－２：ｘ、ｙ方向は 0.07[mm]、ｚ方向は 0.5[mm]

３－３、３－４：ｘ、ｙ方向は 0.29[mm]、ｚ方向は 0.5[mm]

４．立方体形状の変形計測結果

４－１．変形状態１の計測結果

Fig.18 に粘弾性物体の表面形状の変形を示す。青が初期形状、赤が変形形状の表面形状を示す。上から押さえられることによって高さ方向に対して垂直な断面では周囲に広がっているのがわかる。高さ方向の中央部で粘弾性物体の物理特性が変わっているため、上段部分と下段部分で変形量が異なっているのがわかる。Fig.19 にマーカー位置を示す。青が初期形状、赤が変形形状のマーカーの位置を示す。図から分かる物体上部を押されることで、マーカーが中央から周辺へ、より下へ移動しているのが分かる。

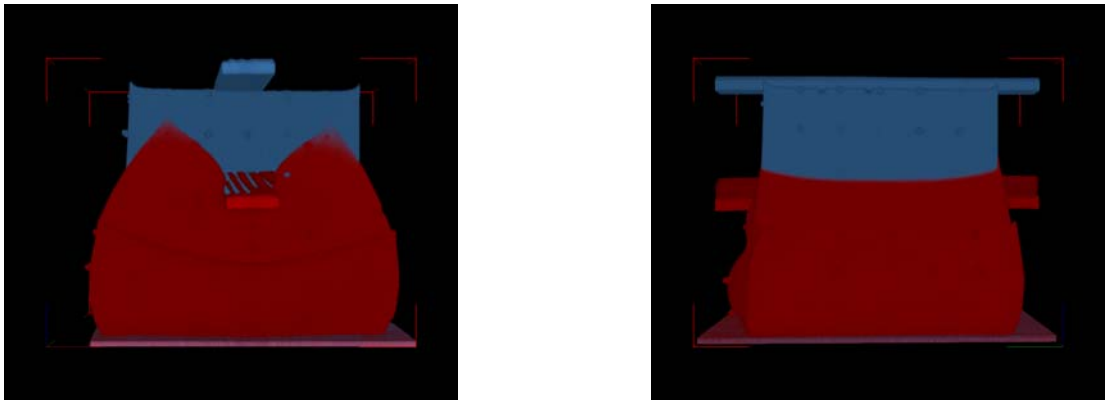

(a)FRONT SHAPE　　(b)LEFT SHAPE

Fig 18　表面形状（青:初期形状、赤:変形形状）

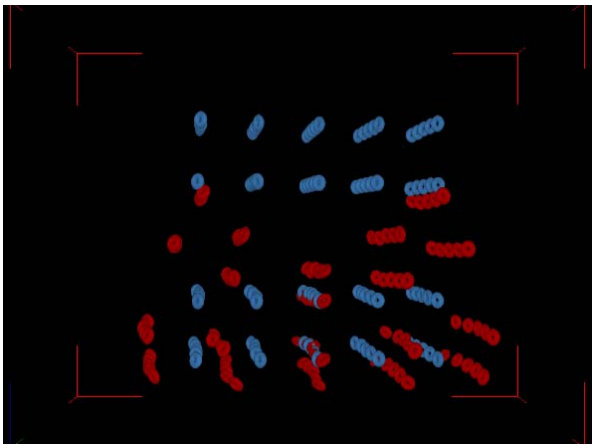

(a) FRONT

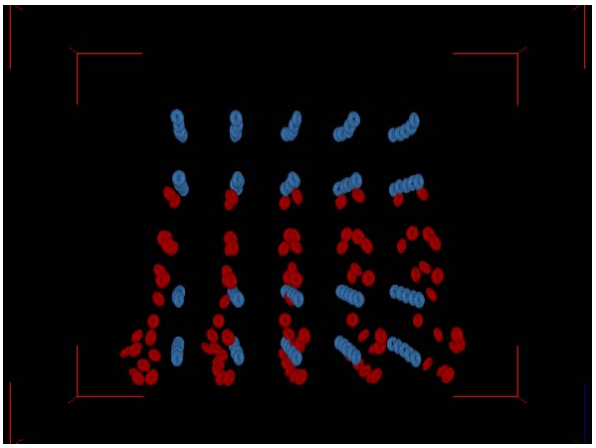

(b) LEFT

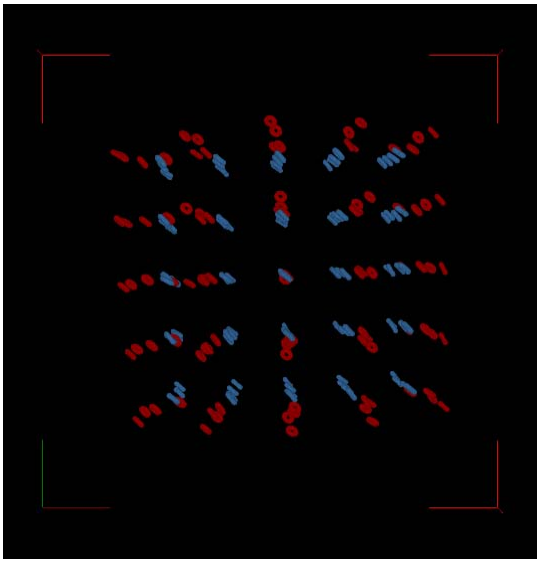

(C) TOP

Fig 19　マーカー位置 CT データ（青:初期形状、赤:変形形状）

Table.1 に各マーカーの三次元座標を示す。

Table 1　変形状態 1 のマーカー座標（単位[mm]）

初期形状

No.	x	y	z
1	28.49	69.87	12.50
2	38.60	69.43	12.50
3	48.12	68.92	12.50
4	58.08	68.26	12.50
5	68.85	67.60	12.50
6	27.76	59.62	12.50
7	37.72	59.11	12.50
8	47.24	58.59	12.50
9	57.13	58.08	12.50
10	67.97	57.35	12.50
11	27.17	49.80	12.50
12	37.28	49.29	12.50
13	46.73	48.85	12.50
14	56.91	48.34	12.50
15	67.24	47.75	12.50
16	26.66	39.70	12.50
17	36.84	39.18	12.50
18	46.44	38.67	12.50
19	56.47	38.23	12.50
20	66.80	37.79	12.50
21	26.00	29.66	12.00
22	35.89	29.15	12.50
23	46.07	28.56	12.50
24	55.59	28.27	12.00
25	66.28	27.83	12.00
26	27.98	69.65	22.00
27	37.94	69.43	22.00
28	48.34	68.85	22.00
29	58.45	68.19	22.00
30	68.26	67.38	22.00
31	27.69	59.69	22.00
32	37.57	59.33	22.00
33	47.24	58.81	22.00
34	57.64	58.08	22.00
35	67.38	57.50	22.00
36	27.47	49.66	22.00
37	37.43	49.15	22.00
38	46.73	48.63	22.00
39	57.20	48.05	22.00
40	66.80	47.46	22.00
41	26.95	39.26	22.00
42	36.77	38.96	22.00
43	46.36	38.45	22.00
44	56.32	37.94	22.00
45	66.28	37.43	22.00
46	26.07	29.30	22.00
47	36.04	28.64	22.00
48	45.78	28.20	22.00
49	56.25	27.61	22.00
50	65.92	27.17	22.00

No.	x	y	z
51	28.27	68.99	41.00
52	38.38	68.63	41.50
53	48.19	68.41	41.50
54	58.23	67.90	42.00
55	67.75	67.38	42.00
56	27.69	59.03	41.00
57	37.79	58.81	41.50
58	47.53	58.67	41.50
59	57.71	57.71	42.00
60	67.46	57.64	42.00
61	27.03	49.88	41.00
62	37.28	49.15	41.50
63	47.02	48.93	41.50
64	57.13	48.19	42.00
65	67.16	48.27	42.00
66	26.44	39.92	41.00
67	36.62	39.11	41.50
68	46.36	38.60	41.50
69	56.62	37.79	41.50
70	66.50	37.72	42.00
71	25.93	29.44	41.00
72	36.18	28.93	41.50
73	45.85	28.20	41.50
74	56.03	27.76	41.50
75	65.99	27.32	41.50
76	27.98	69.14	51.00
77	38.01	68.99	51.00
78	47.68	68.48	51.00
79	57.86	68.04	51.50
80	67.60	67.68	52.50
81	27.54	59.40	51.00
82	37.43	58.74	51.00
83	47.17	58.67	51.00
84	57.35	57.93	51.50
85	67.09	57.86	52.00
86	27.03	49.80	51.50
87	36.84	48.85	51.00
88	46.80	48.41	51.00
89	56.84	48.19	51.50
90	66.50	47.68	52.00
91	26.51	39.84	51.50
92	36.33	39.48	51.00
93	46.29	38.53	51.00
94	56.32	38.53	51.50
95	66.06	38.16	52.00
96	26.07	29.59	51.00
97	35.89	28.78	51.00
98	45.85	28.42	51.00
99	55.88	27.98	51.00
100	65.48	27.98	52.00

变形形状

No.	x	y	z
1	21.46	74.93	9.50
2	34.57	75.88	9.00
3	48.34	76.25	8.00
4	63.06	74.56	8.50
5	77.20	71.26	10.00
6	20.07	62.11	9.50
7	32.96	62.18	9.00
8	47.31	61.82	8.50
9	62.55	60.50	8.50
10	76.46	58.67	10.00
11	19.19	50.17	9.50
12	32.45	49.51	9.00
13	46.66	48.85	9.00
14	61.96	47.97	9.00
15	75.51	47.02	10.00
16	18.90	37.72	9.50
17	31.93	36.47	9.00
18	46.29	35.60	8.50
19	61.38	34.86	9.00
20	74.49	34.79	10.00
21	18.82	25.49	9.50
22	31.42	23.44	9.00
23	46.00	21.75	8.50
24	59.40	21.83	8.50
25	72.95	22.92	10.00
26	19.12	75.29	16.00
27	32.45	77.34	14.00
28	49.22	77.86	12.00
29	65.26	74.85	13.50
30	77.78	71.34	16.50
31	17.94	62.77	16.00
32	30.83	63.50	14.00
33	47.39	63.43	12.50
34	65.04	61.23	13.50
35	77.27	58.89	16.50
36	17.36	50.02	16.00
37	30.47	49.15	14.00
38	46.66	48.12	13.00
39	64.38	47.24	14.50
40	76.54	46.51	16.50
41	17.36	36.99	16.00
42	30.47	35.38	14.00
43	46.36	34.06	12.50
44	62.33	33.69	14.00
45	75.22	33.98	16.50
46	17.29	24.32	16.00
47	30.25	21.31	14.00
48	45.41	19.48	13.00
49	61.45	20.00	14.50
50	73.75	21.46	16.50

No.	x	y	z
51	24.02	71.26	30.00
52	34.50	72.07	24.50
53	48.56	72.22	21.50
54	62.70	70.68	25.00
55	72.07	68.85	31.00
56	23.36	60.42	30.00
57	33.69	60.64	24.50
58	47.68	60.50	21.00
59	61.96	58.96	25.00
60	71.56	58.30	31.00
61	22.49	50.24	30.00
62	32.89	49.37	24.50
63	46.73	48.93	21.50
64	61.30	47.83	25.00
65	71.19	47.90	31.00
66	21.75	39.04	30.00
67	32.01	37.50	25.00
68	45.85	36.55	21.50
69	60.57	35.52	25.50
70	70.39	36.18	31.00
71	21.09	27.69	30.50
72	31.35	25.63	25.00
73	45.12	23.58	22.00
74	59.77	23.73	26.00
75	69.73	24.83	31.50
76	27.76	70.61	39.00
77	35.38	71.85	32.00
78	47.68	72.00	26.50
79	60.72	70.46	32.00
80	67.46	68.92	39.50
81	27.03	60.35	38.50
82	34.42	60.21	32.00
83	46.95	60.13	26.00
84	60.21	58.96	32.00
85	67.02	58.59	39.00
86	26.37	50.02	38.50
87	33.62	49.15	32.50
88	46.36	48.49	26.50
89	59.77	48.12	32.50
90	66.43	47.68	39.00
91	25.71	39.33	39.00
92	32.89	38.53	32.50
93	45.56	37.13	26.50
94	59.03	37.13	32.50
95	65.84	37.35	39.50
96	25.20	28.49	39.00
97	32.45	26.37	33.00
98	44.97	24.83	27.00
99	58.23	25.05	32.50
100	65.04	26.59	39.50

４－２．変形状態２の計測結果

Fig.20、Fig.21 に粘弾性物体の表面形状の変形を示す。青が初期形状、赤が変形形状の表面形状を示す。４－１と同じく、上から押さえられることによって高さ方向に対して垂直な断面では周囲に広がっているのがわかる。ただ上部全体が押されているため、４－１より変形が大きいことがわかる。高さ方向の中央部で粘弾性物体の物理特性が変わっているため、上段部分と下段部分で変形量が異なっているのがわかる。Fig.22 にマーカー位置を示す。青が初期形状、赤が変形形状のマーカーの位置を示す。図から分かる物体上部を押されることで、マーカーが中央から周辺へ、より下へ移動しているのが分かる。

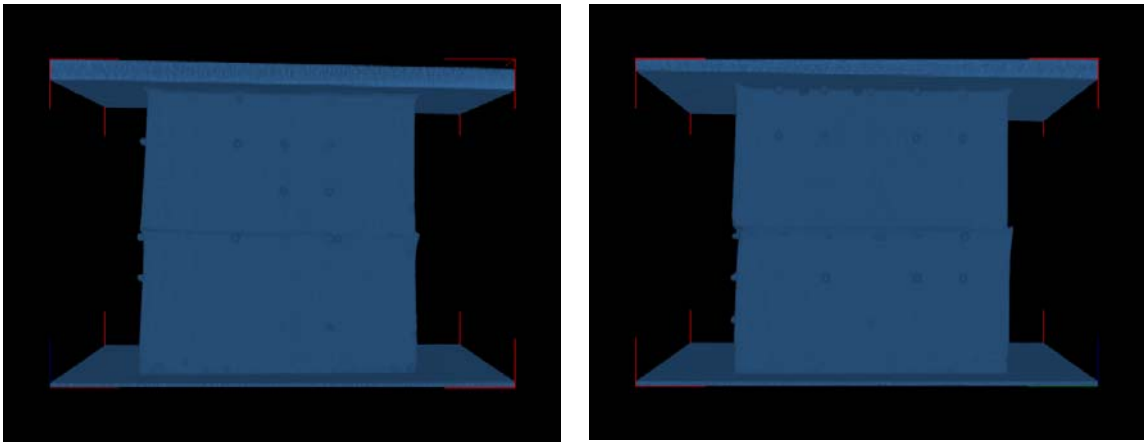

(a)FRONT SHAPE　　(b)LEFT SHAPE

Fig 20　初期形状の表面形状

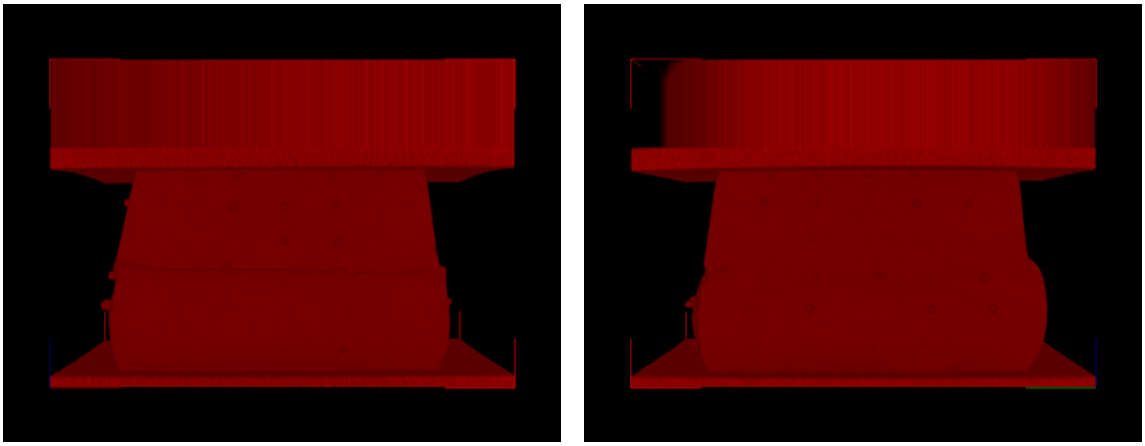

(a)FRONT SHAPE　　(b)LEFT SHAPE

Fig 21　変形形状の表面形状

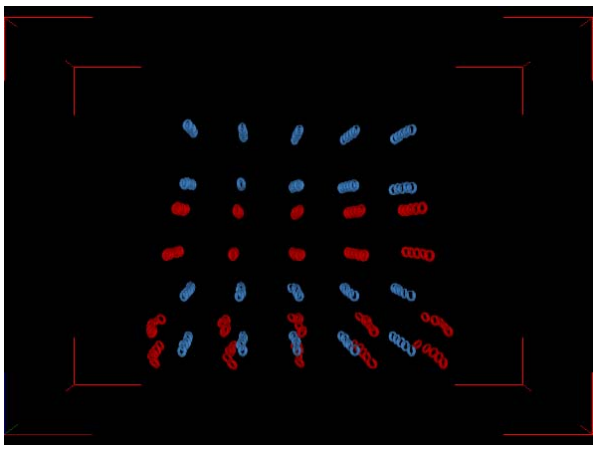

(a) FRONT

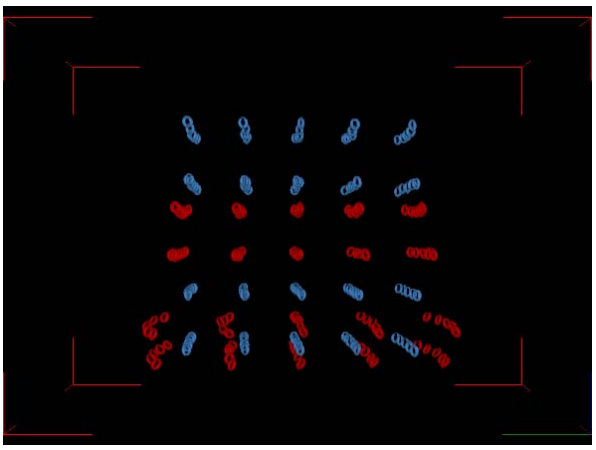

(b) LEFT

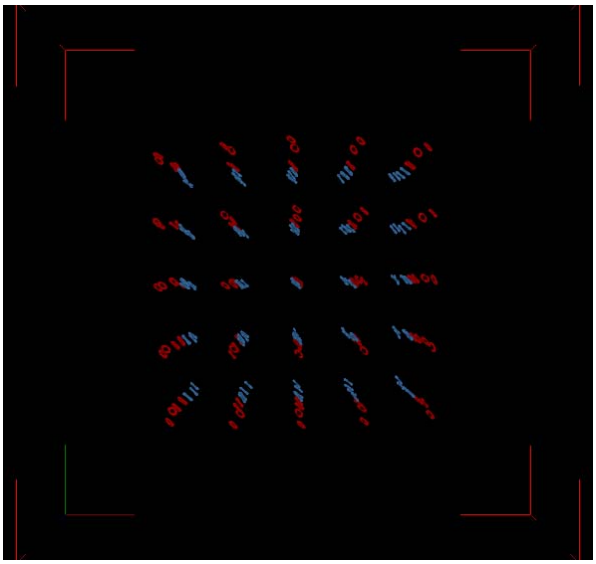

(C) TOP

Fig 22　マーカー位置 CT データ（青:初期形状、赤:変形形状）

Table.2 に各マーカーの三次元座標を示す。

Table 2　変形状態２のマーカー座標（単位[mm]）

初期形状

No.	x	y	z
1	28.93	66.65	12.00
2	39.11	66.43	12.50
3	48.63	66.14	12.50
4	58.59	65.70	12.50
5	69.36	65.33	12.50
6	28.71	56.32	12.00
7	38.67	56.03	12.50
8	48.19	55.74	12.50
9	58.08	55.44	12.50
10	68.85	55.00	12.50
11	28.42	46.51	12.50
12	38.60	46.22	12.00
13	48.05	46.00	12.50
14	58.15	45.63	12.50
15	68.55	45.26	12.00
16	28.13	36.33	12.00
17	38.38	36.04	12.50
18	47.97	35.74	12.50
19	58.15	35.45	12.50
20	68.41	35.23	12.50
21	27.61	26.37	12.00
22	37.65	26.00	12.00
23	47.90	25.56	12.00
24	57.42	25.42	12.00
25	68.12	25.20	12.00
26	28.49	66.28	21.50
27	38.53	66.36	21.50
28	48.93	66.06	21.50
29	59.03	65.63	22.00
30	68.92	65.04	22.00
31	28.56	56.32	22.00
32	38.45	56.25	22.00
33	48.12	55.96	22.00
34	58.52	55.44	22.00
35	68.33	55.08	22.00
36	28.56	46.29	22.00
37	38.60	46.07	22.00
38	47.97	45.70	22.00
39	58.45	45.34	22.00
40	68.04	45.04	22.00
41	28.42	35.89	22.00
42	38.23	35.74	22.00
43	47.83	35.45	21.50
44	57.86	35.23	22.00
45	67.90	34.94	22.00
46	27.69	25.78	21.50
47	37.72	25.42	21.50
48	47.53	25.20	21.50
49	58.01	24.83	21.50
50	67.75	24.61	21.50

No.	x	y	z
51	28.86	65.48	41.00
52	39.04	65.48	41.50
53	48.78	65.48	41.50
54	58.89	65.19	42.00
55	68.41	64.89	42.00
56	28.56	55.52	41.00
57	38.67	55.59	41.50
58	48.41	55.66	41.50
59	58.59	55.00	41.50
60	68.41	55.15	42.00
61	28.13	46.36	41.00
62	38.38	45.92	41.50
63	48.12	45.92	41.50
64	58.30	45.48	42.00
65	68.33	45.85	42.00
66	27.76	36.40	41.00
67	38.01	35.82	41.00
68	47.75	35.60	41.50
69	58.01	35.01	41.50
70	67.97	35.23	41.50
71	27.54	25.93	40.50
72	37.79	25.63	41.00
73	47.53	25.20	41.00
74	57.71	24.98	41.50
75	67.75	24.83	41.50
76	28.56	65.63	51.00
77	38.60	65.70	51.00
78	48.34	65.48	51.00
79	58.45	65.26	51.50
80	68.26	65.19	52.00
81	28.34	55.88	51.00
82	38.23	55.44	51.00
83	48.05	55.59	51.00
84	58.23	55.15	51.50
85	67.97	55.37	52.00
86	28.13	46.22	51.00
87	37.94	45.56	51.00
88	47.90	45.34	50.50
89	57.93	45.41	51.00
90	67.68	45.19	52.00
91	27.83	36.25	51.00
92	37.65	36.11	50.50
93	47.68	35.45	51.00
94	57.71	35.74	51.00
95	67.46	35.60	52.00
96	27.61	26.00	51.00
97	37.50	25.42	50.50
98	47.46	25.34	50.50
99	57.57	25.20	51.00
100	67.16	25.42	51.50

变形形状

No.	x	y	z
1	23.73	71.78	10.50
2	36.55	72.29	10.00
3	48.34	72.58	10.00
4	60.86	72.07	10.00
5	75.29	70.17	10.00
6	22.78	58.74	10.50
7	35.74	58.81	10.50
8	47.75	58.67	10.50
9	60.50	58.08	10.00
10	75.00	57.13	10.00
11	22.27	46.66	10.50
12	35.60	46.29	10.50
13	47.53	46.14	11.00
14	60.57	45.70	10.50
15	74.63	45.19	10.00
16	22.27	34.06	10.50
17	35.30	33.47	10.50
18	47.46	33.11	10.50
19	60.42	32.59	10.00
20	73.90	32.45	10.50
21	22.34	21.68	10.00
22	34.86	20.73	10.00
23	47.39	19.70	10.50
24	59.11	19.56	10.00
25	72.58	20.07	10.50
26	22.05	72.44	15.50
27	35.30	73.61	15.50
28	48.93	73.90	15.50
29	62.11	72.66	15.00
30	75.15	70.75	15.50
31	21.09	59.40	15.50
32	34.57	59.84	15.50
33	47.83	60.13	16.00
34	62.04	58.96	15.50
35	75.37	57.64	15.50
36	20.87	46.36	16.00
37	34.64	46.00	16.00
38	47.53	45.48	16.50
39	61.89	45.19	16.00
40	75.07	44.75	15.50
41	21.17	33.11	16.00
42	34.64	32.45	16.00
43	47.46	31.86	16.00
44	60.57	31.57	15.50
45	74.19	31.64	15.50
46	21.61	19.78	15.50
47	34.57	18.46	16.00
48	47.02	17.80	16.00
49	60.35	17.72	16.00
50	72.80	18.24	15.50

No.	x	y	z
51	26.22	68.12	29.00
52	37.65	68.04	28.50
53	48.78	68.12	28.50
54	60.28	67.82	28.50
55	71.12	67.68	29.00
56	25.85	56.91	29.00
57	37.35	56.98	28.50
58	48.41	57.13	28.50
59	59.99	56.40	28.50
60	71.12	56.62	29.00
61	25.34	46.51	29.00
62	36.91	46.00	28.50
63	48.05	46.07	28.50
64	59.77	45.56	29.00
65	71.19	45.92	29.00
66	24.90	35.16	29.00
67	36.47	34.50	28.50
68	47.61	34.28	29.00
69	59.47	33.54	29.00
70	70.83	33.84	29.00
71	24.61	23.29	28.50
72	36.18	22.92	29.00
73	47.31	22.27	29.00
74	59.11	22.05	29.00
75	70.61	22.05	29.00
76	26.95	67.46	37.00
77	37.87	67.53	36.50
78	48.34	67.31	36.00
79	59.33	67.09	36.50
80	69.95	67.16	37.00
81	26.81	56.84	37.00
82	37.50	56.40	36.50
83	48.12	56.62	36.00
84	59.11	56.18	36.50
85	69.65	56.40	37.00
86	26.59	46.36	37.00
87	37.21	45.70	36.50
88	47.97	45.56	36.50
89	58.81	45.63	36.50
90	69.36	45.34	37.00
91	26.22	35.60	37.00
92	36.77	35.45	36.50
93	47.68	34.79	36.50
94	58.59	35.08	36.50
95	69.21	34.94	37.00
96	25.85	24.39	37.00
97	36.62	23.80	36.50
98	47.46	23.73	36.50
99	58.45	23.51	36.50
100	68.99	23.80	37.00

４－３．変形状態３の計測結果

Fig.23 に粘弾性物体の表面形状の変形を示す．青が初期形状，赤が変形形状の表面形状を示す．「硬度０」の層が「硬度５」の層に比べてＸ－Ｙ方向に大きく変形しているのがわかる．Fig.24 にマーカー位置を示す．青が初期形状，赤が変形形状のマーカーの位置を示す．図からも下から２段目の層のマーカー（「硬度０」領域）がほかの層に比べてＸ－Ｙ方向に広がっているのがわかる．

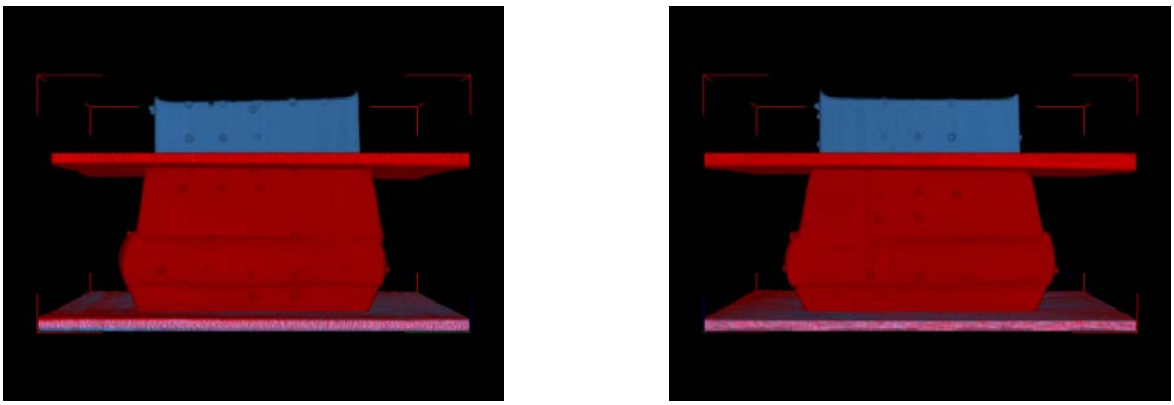

(a)FRONT SHAPE　　(b)LEFT SHAPE

Fig 23　表面形状（青:初期形状，赤:変形形状）

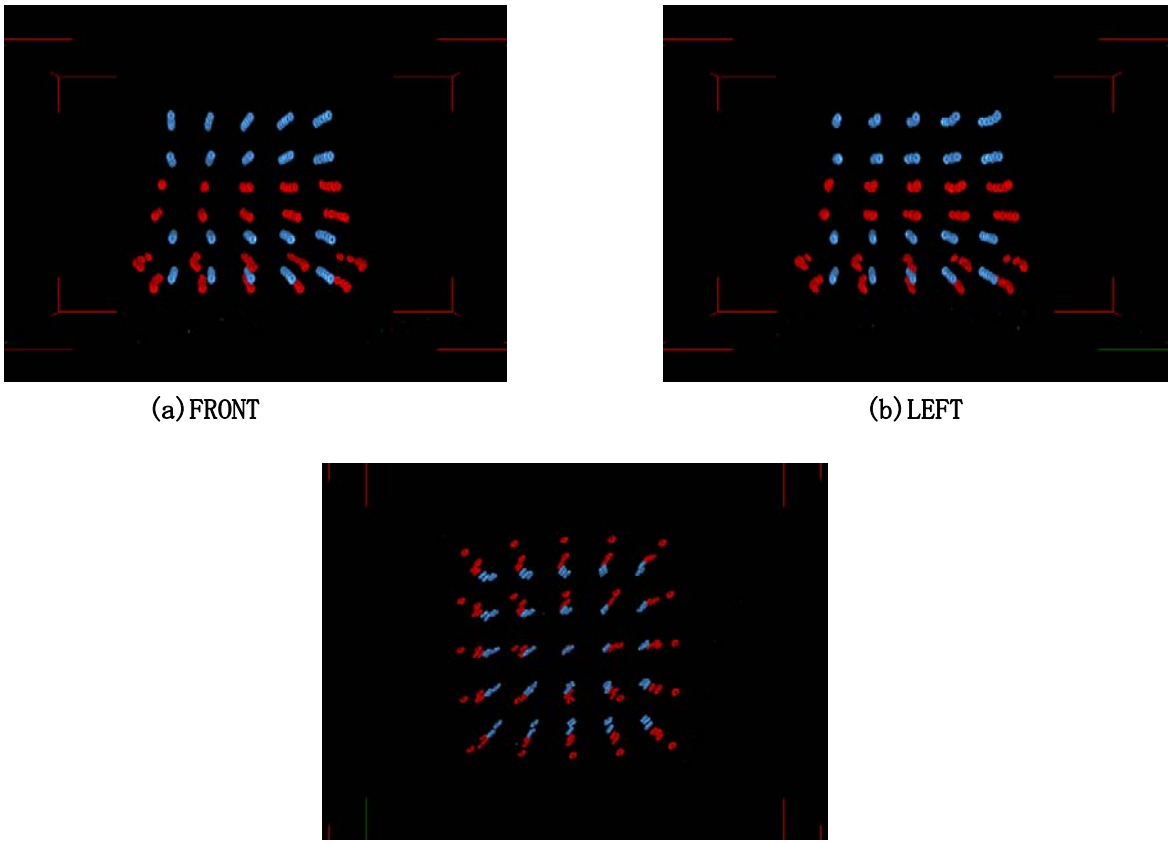

(a)FRONT　　(b)LEFT

(C)TOP

Fig 24　マーカー位置 CT データ（青:初期形状，赤:変形形状）

Table.3 に各マーカーの三次元座標を示す．

Table 3　変形状態３のマーカー座標（単位[mm]）

初期形状

No	x	y	z
1	500.47	936.17	10.50
2	510.43	936.76	10.50
3	520.68	936.76	10.50
4	530.64	937.34	10.50
5	540.31	937.34	10.50
6	500.76	926.21	10.50
7	510.72	926.50	10.50
8	520.98	926.80	10.50
9	530.94	927.38	10.50
10	540.61	927.38	10.50
11	501.35	916.25	10.50
12	511.02	916.54	10.50
13	521.27	916.54	10.50
14	531.23	917.13	10.50
15	540.90	917.42	10.50
16	501.35	906.29	10.50
17	511.60	906.88	10.50
18	521.27	906.88	10.50
19	531.52	907.17	10.50
20	541.19	907.46	10.50
21	501.64	896.33	10.50
22	511.60	896.33	10.50
23	521.56	896.91	10.50
24	531.82	897.21	10.50
25	541.48	897.50	10.50
26	500.47	935.88	20.50
27	510.14	936.46	20.50
28	520.39	936.76	20.50
29	530.35	937.05	20.50
30	540.31	937.34	20.50
31	500.76	926.21	20.50
32	510.72	926.50	20.50
33	520.98	926.80	20.50
34	530.64	927.09	20.50
35	540.61	927.38	20.50
36	501.05	916.25	20.50
37	511.02	916.54	20.50
38	521.56	916.84	20.50
39	531.23	917.13	20.50
40	540.90	917.42	20.50
41	501.64	906.00	20.50
42	511.60	906.29	20.50
43	521.56	906.58	20.50
44	531.52	906.88	20.50
45	541.48	907.75	20.50
46	501.93	896.04	20.50
47	511.89	896.33	20.50
48	522.15	896.62	20.00
49	531.52	896.91	20.00
50	541.78	897.21	20.00

No	x	y	z
51	499.88	934.71	40.00
52	510.14	935.29	40.50
53	519.80	936.17	40.50
54	530.06	936.46	41.00
55	539.43	936.76	41.00
56	500.47	924.45	40.50
57	510.43	925.33	40.50
58	520.10	926.21	40.50
59	530.35	926.21	41.00
60	540.02	927.09	41.00
61	500.76	915.37	40.50
62	510.72	915.66	41.00
63	520.39	916.54	41.00
64	530.64	916.84	41.00
65	540.61	917.71	41.00
66	501.05	905.41	40.50
67	511.31	905.70	41.00
68	520.98	906.29	41.00
69	531.23	906.29	41.00
70	540.90	907.17	41.00
71	501.64	894.86	41.00
72	511.60	895.45	41.00
73	521.27	895.74	41.00
74	531.52	896.33	41.00
75	541.48	896.91	41.00
76	499.59	935.00	50.00
77	509.84	935.59	50.00
78	519.51	936.17	50.00
79	529.47	936.76	50.50
80	539.43	937.34	51.00
81	500.18	925.04	50.50
82	510.14	925.33	50.00
83	519.80	926.21	50.00
84	530.06	926.50	50.50
85	539.73	927.38	51.00
86	500.76	915.66	50.50
87	510.43	915.66	50.50
88	520.39	915.96	50.50
89	530.64	916.84	50.50
90	540.02	917.42	51.00
91	501.05	905.70	51.00
92	510.72	906.29	50.50
93	520.98	906.29	50.50
94	530.94	907.17	50.50
95	540.61	907.75	51.00
96	501.64	895.45	51.00
97	511.60	895.45	51.00
98	521.56	896.04	50.50
99	531.52	896.62	51.00
100	540.90	897.50	51.00

変形形状

No.	x	y	z
1	1230.76	855.59	10.50
2	1241.02	856.46	11.00
3	1250.98	857.05	11.00
4	1260.94	857.34	10.50
5	1270.90	857.93	10.50
6	1231.05	845.63	10.50
7	1241.02	846.21	10.50
8	1251.27	846.50	10.50
9	1261.23	847.09	10.50
10	1271.19	847.68	10.50
11	1231.35	835.96	10.50
12	1241.89	836.25	10.50
13	1251.56	836.54	10.50
14	1261.82	837.13	10.50
15	1271.78	837.71	10.50
16	1231.93	825.70	10.50
17	1242.19	826.00	10.50
18	1252.15	826.58	10.50
19	1262.11	827.17	10.50
20	1272.07	827.75	10.50
21	1232.23	815.74	10.00
22	1242.77	816.33	10.50
23	1252.73	816.62	10.50
24	1262.40	817.21	10.50
25	1272.66	817.79	10.50
26	1230.76	855.59	20.50
27	1240.72	855.88	20.50
28	1250.98	856.46	20.50
29	1260.94	856.76	20.50
30	1270.90	857.34	20.50
31	1231.05	845.63	20.50
32	1241.31	846.21	20.50
33	1251.27	846.80	20.50
34	1261.23	847.09	20.50
35	1271.19	847.68	20.50
36	1231.35	835.66	20.50
37	1241.60	836.25	20.50
38	1251.86	836.84	20.50
39	1261.52	837.13	20.50
40	1271.78	837.71	20.50
41	1231.93	825.70	20.50
42	1241.60	826.00	20.50
43	1251.86	826.88	20.50
44	1261.82	827.17	20.50
45	1271.78	827.75	20.50
46	1231.93	815.74	20.00
47	1242.48	816.33	20.50
48	1252.44	816.62	20.50
49	1262.11	817.21	20.50
50	1272.36	817.79	20.50

No.	x	y	z
51	1230.76	856.46	39.50
52	1240.72	856.76	39.50
53	1250.39	857.05	39.50
54	1260.94	857.34	39.50
55	1270.61	857.64	39.50
56	1231.35	846.50	39.50
57	1241.02	846.50	39.50
58	1250.68	846.80	39.50
59	1260.94	847.09	39.50
60	1270.90	847.38	40.00
61	1231.64	836.25	39.50
62	1241.60	836.54	39.50
63	1251.27	836.84	39.50
64	1261.82	837.13	39.50
65	1271.19	837.42	40.00
66	1232.23	826.29	39.50
67	1241.89	826.29	39.50
68	1251.56	826.58	40.00
69	1262.11	827.17	40.00
70	1271.78	827.46	40.00
71	1232.52	816.33	40.00
72	1242.19	816.33	40.00
73	1252.73	816.62	40.00
74	1262.70	816.91	40.00
75	1272.36	817.50	40.50
76	1230.76	855.88	49.50
77	1240.43	856.17	49.00
78	1250.68	856.76	49.00
79	1260.06	857.05	49.50
80	1270.61	857.34	49.50
81	1231.35	846.21	49.00
82	1241.31	846.50	49.00
83	1250.98	846.80	49.00
84	1260.94	847.09	49.50
85	1271.19	847.38	49.50
86	1231.64	835.96	49.00
87	1241.60	836.25	49.00
88	1251.27	836.54	49.00
89	1261.23	836.84	49.50
90	1271.48	837.42	49.50
91	1231.93	826.29	49.00
92	1241.89	826.58	49.50
93	1251.56	826.88	49.50
94	1261.23	827.17	49.50
95	1272.07	827.75	49.50
96	1232.52	816.33	49.50
97	1242.48	816.62	49.50
98	1252.15	816.62	50.00
99	1262.11	817.21	50.00
100	1272.66	817.50	50.00

４－４．変形状態４の計測結果

Fig.25 に粘弾性物体の表面形状の変形を示す．青が初期形状，赤が変形形状の表面形状を示す．４－３とは異なり，「硬度０」の層に挟まれている「硬度５」の層はＸ－Ｙ方向にはあまり変形していない．それによって「硬度０」の部分もＸ－Ｙ方向の変形が抑制されているのがわかる．Fig.26 にマーカー位置を示す．青が初期形状，赤が変形形状のマーカーの位置を示す．マーカーの位置からも４－３に比べて変形量は小さいことがわかる．

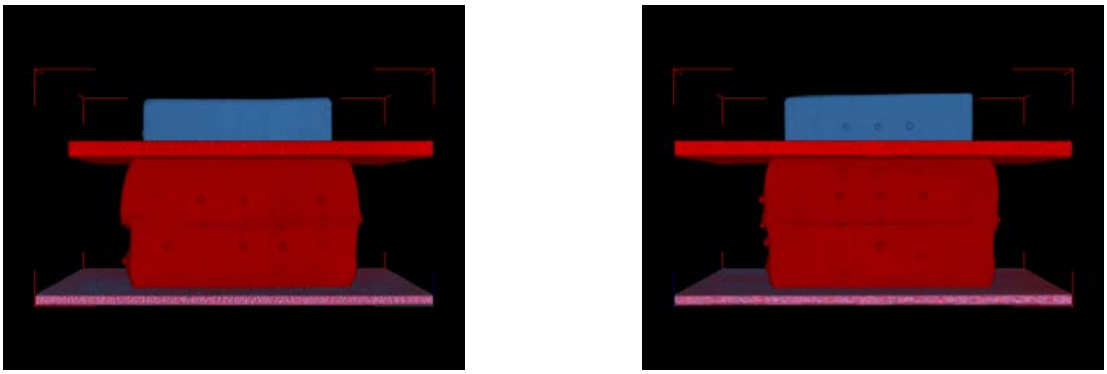

(a)FRONT SHAPE　　(b)LEFT SHAPE

Fig 25　表面形状（青:初期形状，赤:変形形状）

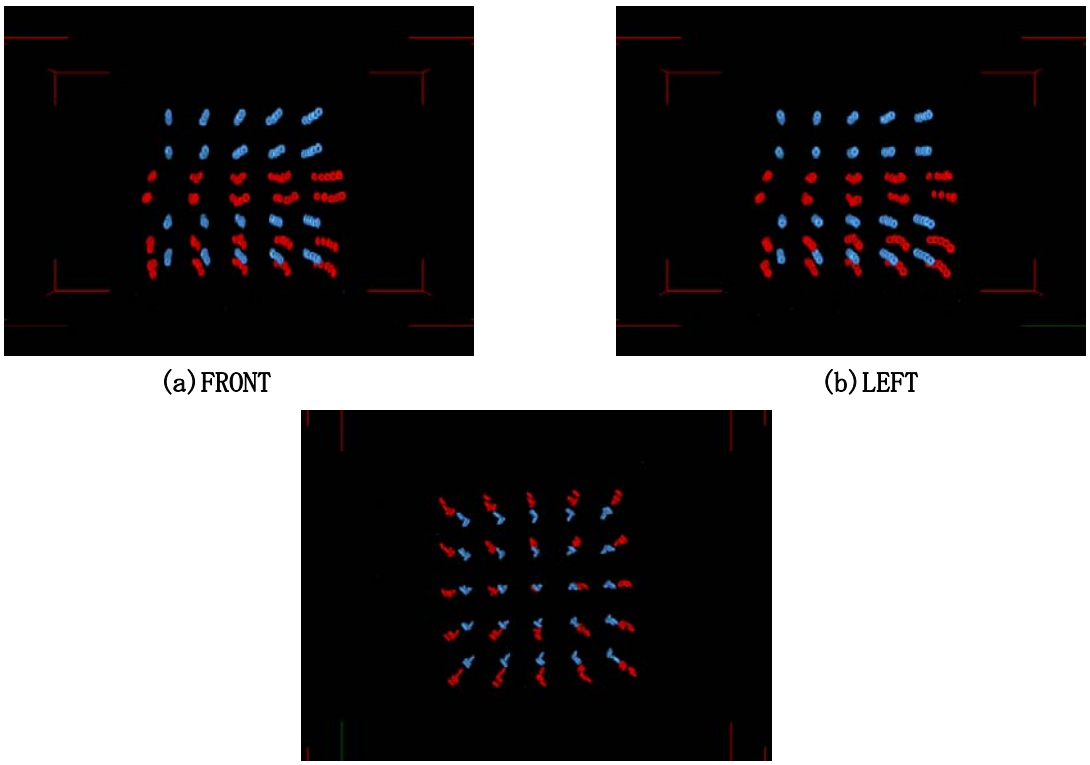

(a)FRONT　　(b)LEFT

(C)TOP

Fig 26　マーカー位置 CT データ（青:初期形状，赤:変形形状）

Table.4 に各マーカーの三次元座標を示す．

Table 4　変形状態４のマーカー座標（単位[mm]）

初期形状

No.	x	y	z
1	496.07	940.27	8.50
2	508.09	941.15	8.00
3	520.10	942.03	8.50
4	532.11	942.03	8.50
5	544.12	941.74	8.50
6	496.07	928.26	8.50
7	508.38	929.14	8.00
8	520.68	929.43	8.00
9	532.70	930.02	8.00
10	545.00	930.02	8.50
11	496.07	916.54	8.50
12	508.67	916.84	8.50
13	520.98	916.54	8.50
14	533.57	917.13	8.50
15	545.59	917.71	8.50
16	496.66	904.53	8.00
17	509.26	904.53	8.00
18	521.27	904.82	8.00
19	533.57	905.12	8.00
20	545.88	905.70	8.00
21	497.54	892.23	8.00
22	509.55	891.93	8.00
23	521.56	891.93	8.00
24	533.87	892.81	8.00
25	545.59	893.69	8.50
26	492.85	942.62	14.00
27	506.33	944.96	14.00
28	519.80	946.13	14.00
29	532.70	946.13	14.00
30	546.46	945.25	14.00
31	491.97	929.43	14.00
32	506.04	930.61	14.00
33	520.39	931.48	14.00
34	533.87	931.78	14.00
35	548.52	931.48	14.00
36	491.68	916.25	14.00
37	506.33	916.84	13.50
38	520.98	917.13	14.00
39	535.04	917.42	14.00
40	549.98	918.30	14.00
41	492.56	902.77	13.50
42	507.21	902.48	14.00
43	521.56	902.77	13.50
44	535.04	903.36	13.50
45	549.98	904.82	14.00
46	494.61	889.30	13.50
47	508.38	888.13	13.50
48	522.15	887.83	13.50
49	535.04	888.42	13.50
50	549.10	890.47	13.50

No.	x	y	z
51	496.07	937.64	26.50
52	507.79	938.52	26.50
53	519.22	939.69	26.50
54	531.23	939.98	26.00
55	542.36	940.57	26.50
56	496.37	925.92	26.50
57	508.09	927.09	26.00
58	519.80	927.97	26.00
59	531.82	928.26	26.00
60	543.24	929.14	26.00
61	496.66	915.08	26.00
62	508.67	915.66	26.00
63	520.10	916.54	26.00
64	532.40	916.84	26.00
65	544.12	918.01	26.00
66	497.25	903.36	26.00
67	509.26	903.36	26.00
68	520.68	904.24	26.00
69	532.70	904.24	26.00
70	544.41	905.41	26.00
71	497.83	891.05	26.00
72	509.84	891.64	26.00
73	521.27	891.64	26.00
74	533.28	892.52	26.00
75	545.00	893.40	26.00
76	497.25	936.76	34.00
77	508.38	937.64	34.00
78	519.22	938.22	33.50
79	530.35	938.81	33.50
80	541.19	939.39	34.00
81	497.83	925.92	34.00
82	508.67	926.21	33.50
83	519.51	927.38	33.00
84	530.94	927.38	33.50
85	541.78	928.55	33.50
86	498.42	915.08	34.00
87	509.26	915.37	33.50
88	520.10	915.96	33.50
89	531.23	916.84	33.00
90	542.07	917.13	33.50
91	499.00	904.24	34.00
92	509.84	904.82	33.50
93	520.68	904.82	33.00
94	531.82	906.00	33.00
95	542.66	906.58	33.50
96	499.59	892.81	34.00
97	510.43	892.81	33.50
98	521.56	893.69	33.00
99	532.70	894.28	33.00
100	543.24	895.16	33.50

変形形状

No.	x	y	z
1	1226.37	859.10	7.50
2	1238.67	860.27	7.50
3	1250.10	861.45	8.00
4	1262.40	862.03	7.50
5	1274.12	862.32	7.00
6	1226.07	846.80	8.00
7	1238.67	847.97	8.50
8	1250.98	848.55	8.50
9	1262.70	849.43	8.50
10	1275.00	850.02	7.50
11	1226.66	835.37	8.00
12	1239.84	835.96	8.50
13	1251.56	836.54	9.00
14	1263.28	837.13	8.50
15	1276.17	838.01	8.00
16	1227.54	823.36	7.50
17	1240.43	823.95	8.50
18	1252.15	824.53	9.00
19	1263.87	825.12	8.50
20	1276.46	826.00	7.50
21	1228.71	811.64	7.00
22	1241.31	811.93	7.50
23	1252.73	812.23	8.00
24	1264.16	813.11	7.50
25	1276.46	813.98	7.50
26	1225.49	858.81	14.00
27	1237.79	859.98	14.50
28	1250.10	861.15	14.50
29	1262.40	861.74	14.00
30	1274.71	862.03	14.00
31	1226.07	847.38	14.50
32	1238.09	848.26	14.50
33	1250.68	849.14	15.00
34	1263.28	849.73	14.50
35	1275.59	850.61	14.50
36	1226.07	835.08	14.50
37	1238.67	835.66	15.00
38	1251.86	836.25	15.50
39	1263.87	837.13	15.00
40	1276.46	838.01	14.50
41	1227.54	822.48	14.50
42	1239.26	823.07	15.00
43	1251.86	823.65	15.00
44	1264.45	824.53	15.00
45	1276.76	825.70	14.00
46	1227.83	810.76	14.00
47	1240.43	811.05	14.50
48	1252.73	811.93	15.00
49	1264.75	812.52	14.50
50	1276.76	813.69	14.00

No.	x	y	z
51	1224.61	861.15	27.00
52	1237.21	862.32	27.00
53	1249.51	862.91	26.50
54	1262.40	863.50	26.50
55	1274.41	863.50	27.00
56	1224.90	848.26	26.50
57	1237.79	849.14	26.50
58	1250.10	850.02	26.50
59	1262.99	850.31	26.50
60	1275.88	850.61	27.00
61	1225.20	835.37	26.50
62	1238.38	836.25	26.00
63	1250.68	836.84	26.00
64	1264.75	837.13	26.50
65	1277.34	837.71	27.00
66	1226.07	822.77	27.00
67	1251.86	822.77	26.50
68	1238.96	822.77	26.50
69	1265.33	823.95	27.00
70	1277.93	825.12	27.00
71	1253.03	809.59	27.50
72	1239.84	809.59	27.00
73	1227.25	809.88	27.50
74	1265.92	810.76	27.50
75	1278.52	812.52	28.00
76	1225.78	858.81	33.00
77	1237.79	859.69	33.00
78	1249.51	860.86	32.50
79	1260.94	861.45	33.00
80	1273.54	861.74	33.00
81	1226.37	847.09	33.00
82	1238.67	847.68	32.50
83	1250.10	848.26	32.00
84	1262.40	849.14	32.50
85	1275.00	849.73	32.50
86	1226.66	835.08	32.50
87	1239.55	835.66	32.50
88	1250.68	836.25	32.00
89	1262.99	836.84	32.50
90	1276.17	837.71	33.00
91	1227.54	823.65	32.50
92	1239.84	823.95	32.50
93	1251.27	824.53	32.00
94	1263.28	825.41	32.50
95	1277.05	826.29	33.00
96	1228.71	811.05	33.00
97	1241.02	811.35	33.00
98	1252.15	811.35	33.00
99	1264.16	812.23	33.00
100	1277.93	813.98	33.00

５．終わりに

本受託試験では，内部にマーカーとして金属ワッシャーを等間隔に配置した立方体形状のウレタン系粘弾性物体を製作した。その物体に外部から圧力を印加した場合の内部の変形状態を、和歌山県工業技術センターが所有している産業用 CT スキャナを用いて内部変形の 3 次元位置計測を行った.

完了報告書

本報告書は，平成 17 年度科学研究費補助金基盤研究 A「内部センシングに基づく柔軟物のリアリティーベースモデリングに関する研究」に係る委託試験の成果を示す．試験題目，試験目的，試験内容は以下のとおりである．

（1） 試験題目　X 線計測装置を用いた粘弾性物体の内部変形計測試験

（2） 試験目的　本受託試験では、和歌山県工業技術センターが所有している産業用 CT スキャナ、を用いて、外部から変形が与えられた粘弾性物体内部の変形の推移を計測することを目的とする。

（3） 試験内容　内部にマーカーとして金属の粒状物体もしくはワッシャーを等間隔に配置したウレタン系粘弾性物体を製作する。その物体に外部から圧力をかけた状態で、和歌山県工業技術センターが所有している産業用 CT スキャナを用いて内部変形の 3 次元位置計測をおこなう。

（4） 試験担当者　和歌山県工業技術センター　システム技術部　副主査研究員　徳本真一

試験結果

1．試験装置

本試験において、粘弾性物体の内部変形を計測する産業用 CT スキャナを Fig.1 に示す．本 CT スキャナの場合，スライスエリアを最小の φ150mm とし画素サイズを 512×512[Pixel]とした場合，X，Y 方向の空間分解能は 150÷512＝0.29[mm]となる．Z 方向に関しては，スライス厚が最小で 1[mm]のため分解能が 1[mm]であるが，スライスピッチの最小が 0.5[mm]であるため再構成では仮想的に 0.5[mm]の分解能で計算できる．

産業用ＣＴスキャナ

TOSCANER-24200AV

スキャン　トラバースローテーション方式

Ｘ線出力　400kV，透過能力　鉄100mm，アルミ300mm

ｽﾗｲｽｴﾘｱ　　φ150mm，φ300mm，φ600mm　可変

ｽﾗｲｽ厚　　1.0mm，2.0mm，4.0mm　可変

再構成画素　512×512　or　1024×1024　or　2048×2048

ｽｷｬﾝﾓｰﾄﾞ　　nomal(fast)　or　fine(slow)

　　ful(360)　　or　half(180)

ﾏﾙﾁｽｷｬﾝﾋﾟｯﾁ　min.0.5mm

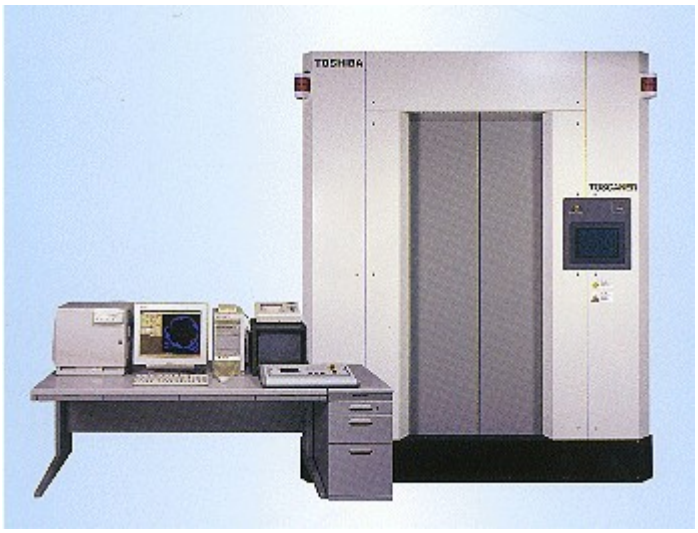

Fig 1　産業用 CT スキャナ仕様

２．粘弾性物体の作成

本試験において，粘弾性物体には昨年度に続き「人肌ゲル」を用いる．人肌ゲルはウレタン系のポリオールブレンドを原液とし、イソシアネートの硬化剤を用いて硬化させることのできる物体である．(Fig.2 参照)

Fig 2　人肌ゲル原液

つぎに変形の内部形状のマーカーとして，M1 の丸座金（外経 2.8 [mm]　長さ 0.3[mm]）を用いた．物体内部に丸座金のマーカーを設置する方法として，Fig.3 に示すように丸座金を十字に張った糸を通して固定し，人肌ゲルを型に流し固まってから糸を引き抜くという方法をとった．本試験では 2 種類の形状の粘弾性物体を製作する．一つは立方体形状，もう一つは半楕円形状である．立方体形状の粘弾性物体を製作した型は Fig.4 に示す．半楕円形状の粘弾性物体を製作するために用いた型は Fig.5 に示す．以上の型を用いて製作した粘弾性物体を Fig.6，Fig.7 に示す．Fig.3 は立方体形状，Fig.4 は半楕円形状の粘弾性物体である．

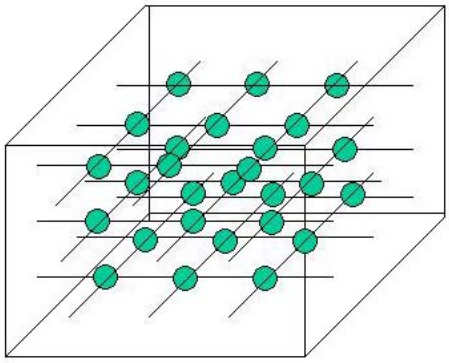

Fig 3　マーカー埋め込み方法

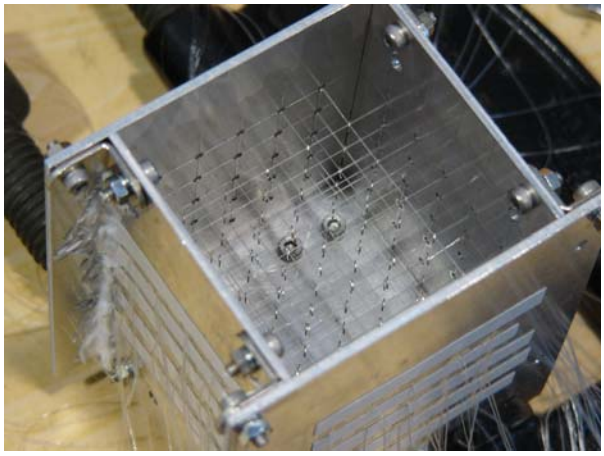

Fig 4　立方体形状用型

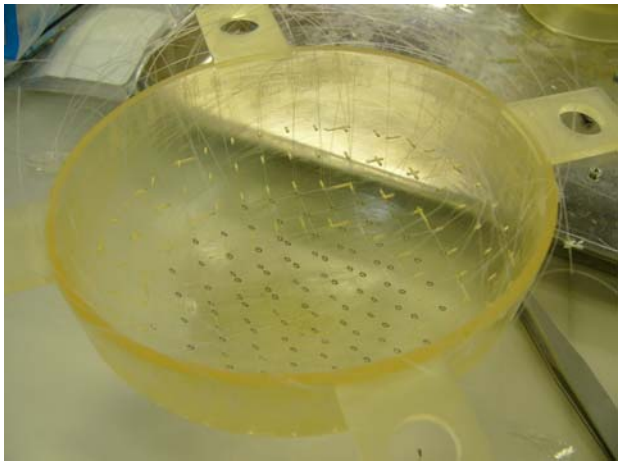

Fig 5　半楕円形状用型

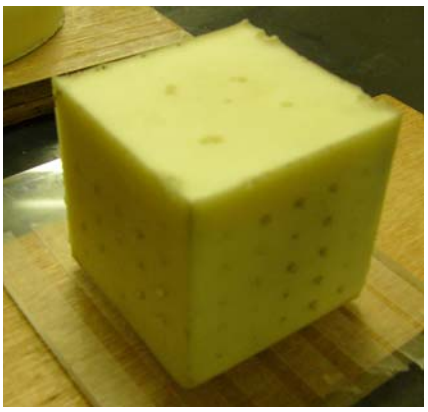

Fig 6　粘弾性物体（立方体形状）

Fig 7　粘弾性物体（半楕円形状）

本研究で作成した粘弾性物体の形状は立方体形状の場合，60×60×60[mm]である．マーカーとして配置した丸座金は，1[cm]間隔に 5×5×5 個配置した．半楕円形状の場合，形状は 130×110×70[mm]，内部に配置した丸座金は 1[cm]間隔に 286 個配置した．

３．変形条件

立方体形状，半楕円形状の粘弾性物体の変形条件については，以下に示す．

３－１．立方体形状の変形条件

立方体形状は，アクリル板を上から押し付けることによって変形させる．押し付け高さは Fig.8 に示すように 2 段階設定する．第 1 段階は赤で示すように，高さ 45[mm]まで変形させる．第 2 段階は青で示すように，高さ 35[mm]まで変形させる．実際の変形の写真を Fig.9，Fig.10 に示す．Fig.9 は高さ 45[mm]の変形，Fig.10 は高さ 35[mm]の変形を示す．

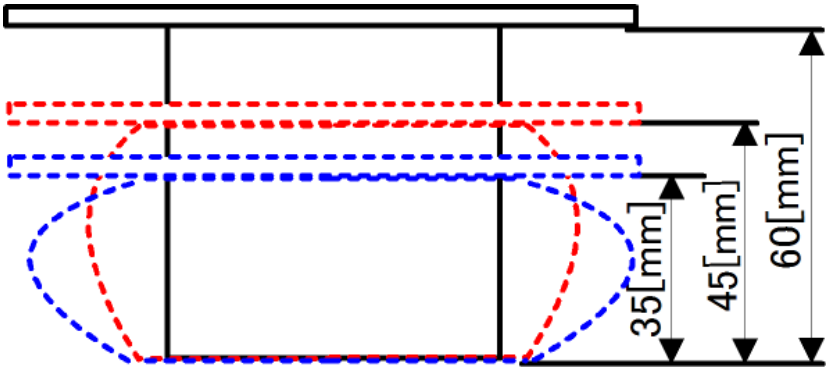

Fig 8　変形条件（立方体型）

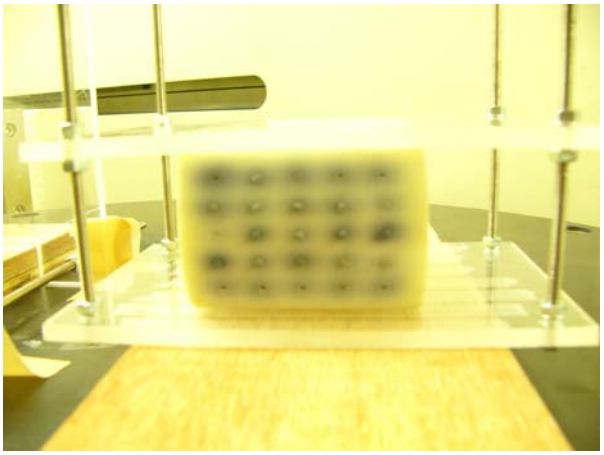

Fig 9　変形（高さ 45[mm]）

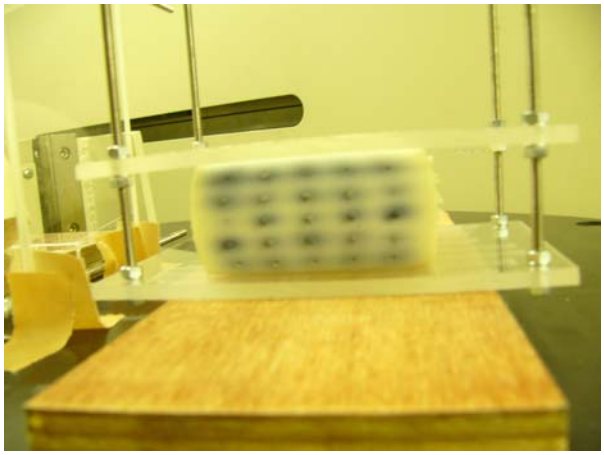

Fig 10　変形（高さ 35[mm]）

３－２．半楕円形状の変形条件

半楕円形状は，アクリル板を長手方向の左右両側から上から押し付けることによって変形させる．左右からの押し付け量はFig. 11 に示すように２段階設定する．第１段階は赤で示すように，幅 100[mm]まで変形させる．第２段階は青で示すように，幅 80[mm]まで変形させる．実際の変形の写真をFig. 12, Fig. 13 に示す．Fig. 12 は幅 100[mm]の変形，Fig. 13 は幅 80[mm]の変形を示す．

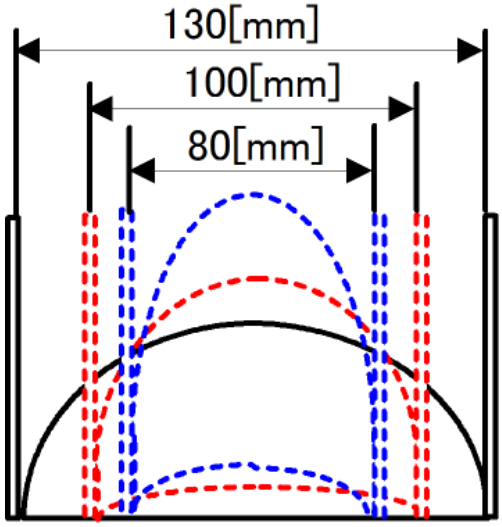

Fig 11　変形条件（半楕円形状）

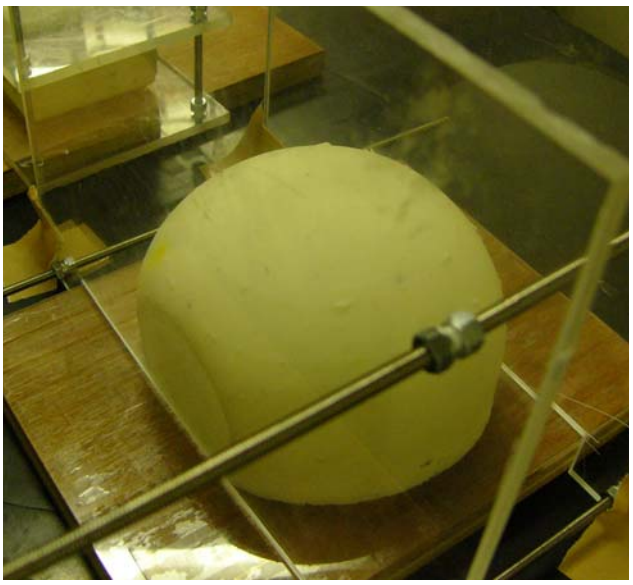

Fig 12　変形（幅 100[mm]）

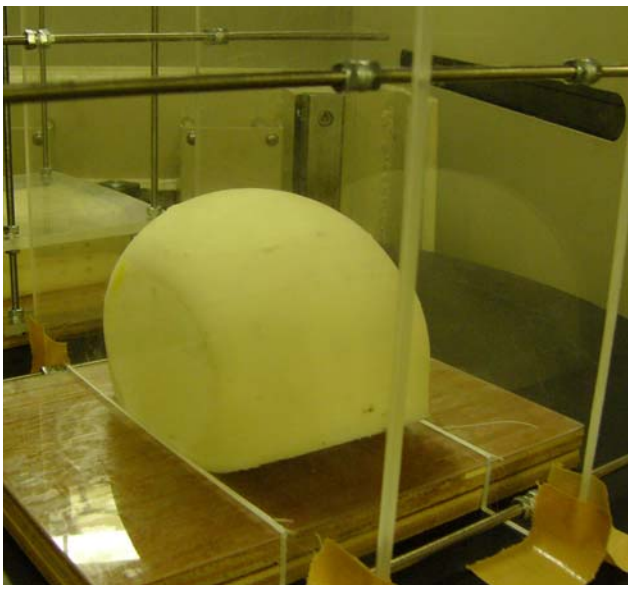

Fig 13　変形（幅 80[mm]）

なお撮影時のＣＴスキャナの画像分解能はｘ，ｙ方向は 0.29[mm]，ｚ方向は 0.5[mm]である．

４．変形計測結果

４－１．立方体形状の変形計測結果

Fig.14 に粘弾性物体の表面形状の変形を示す．白が初期形状，赤が中央上部を高さ 45[mm]まで強制的に変形させた時，青色が高さ 35[mm]まで変形させた場合の表面形状を示す．上から押さえられることによって高さ方向に対して垂直な断面では周囲に広がっているのがわかる．Fig.15 にマーカー位置を示す．白が初期形状，赤が中央上部を高さ 45[mm]まで強制的に変形させた時，青色が高さ 35[mm]まで変形させた場合のマーカーの位置を示す．図から分かる物体上部を押されることで，マーカーが中央から周辺へ，より下へ移動しているのが分かる．

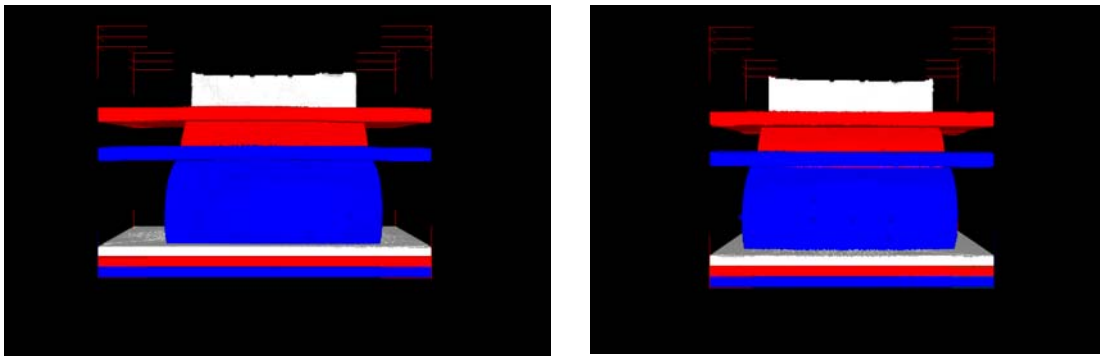

(a)FRONT SHAPE　　(b)LEFT SHAPE

Fig 14　表面形状（白:初期形状，赤:高さ 45[mm]変形，青:高さ 35[mm]変形）

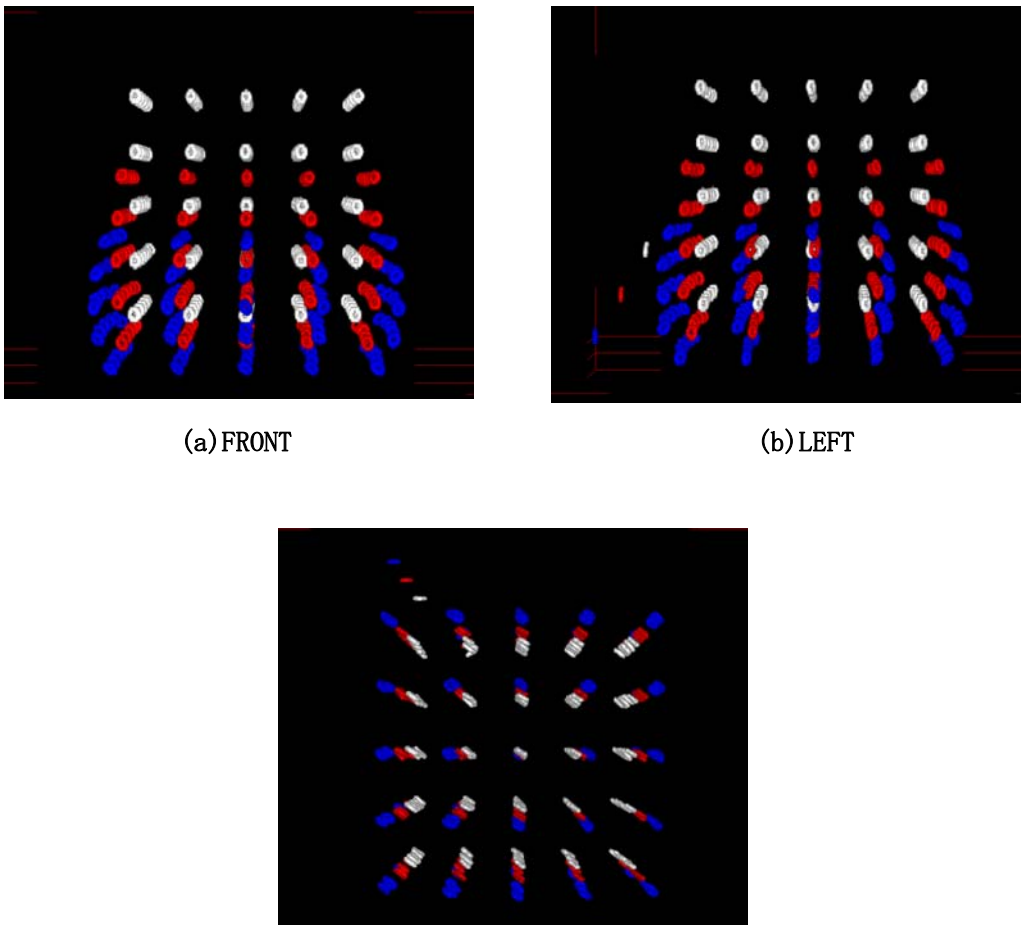

Fig 15　マーカー位置 CT データ（白:初期形状，赤:高さ 45[mm]変形，青:高さ 35[mm]変形）

マーカーの数は 5×5×5＝125 個あるため,Fig.16 に示すようにマーカーにナンバーを割り当てる.以降に示す No は，マーカーのナンバーである．Table.1 に各マーカーの三次元座標を示す.

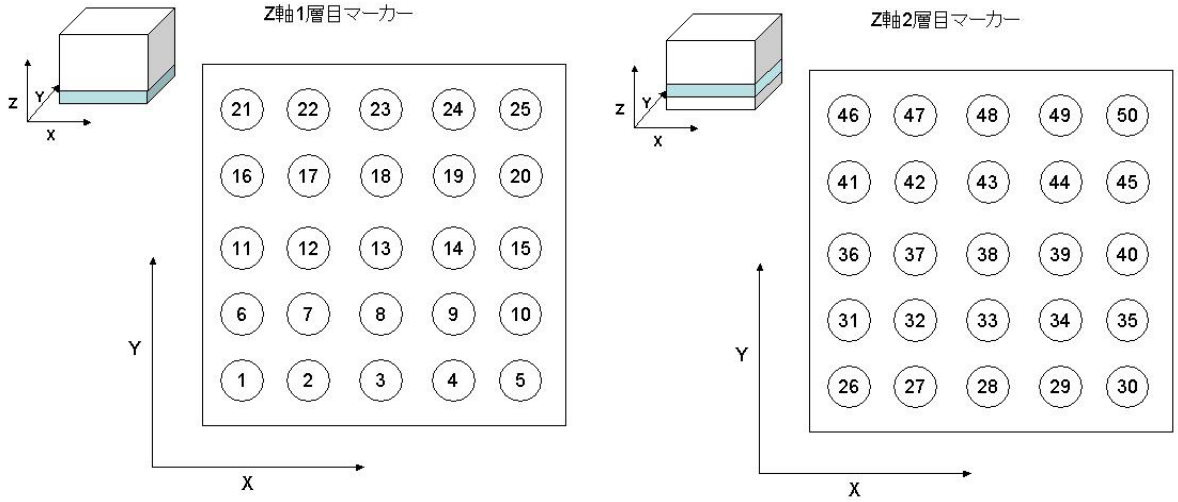

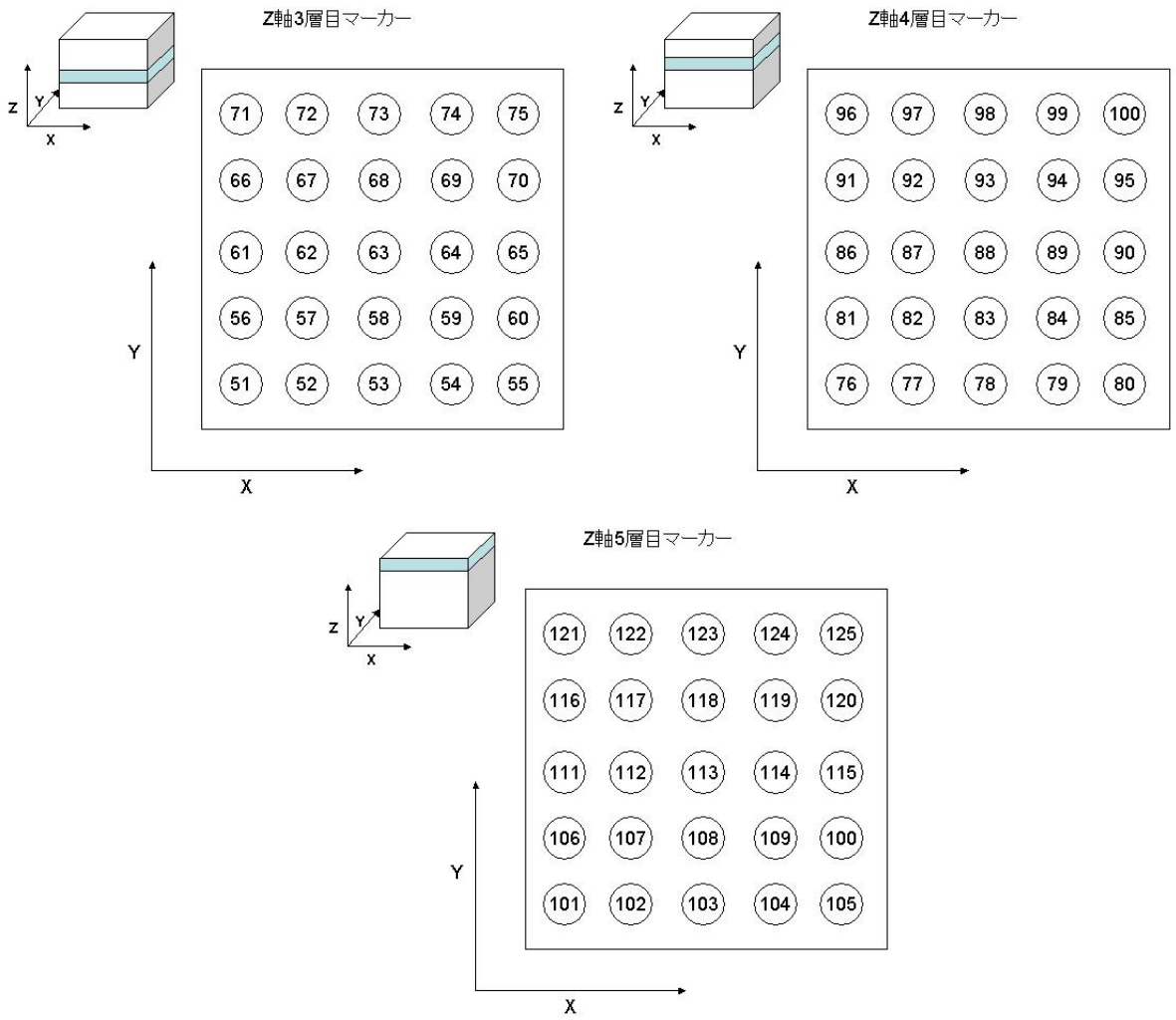

Fig 16　マーカーナンバー

Table 1　マーカー座標（単位[mm]）

初期形状

No.	X	Y	Z	No.	X	Y	Z	No.	X	Y	Z	No.	X	Y	Z
1	26.97	64.67	12.0	33	46.69	54.81	22.0	65	66.70	44.66	31.5	97	37.41	24.94	41.5
2	36.83	64.67	12.0	34	56.55	54.81	21.5	66	27.26	34.80	31.5	98	47.27	24.65	41.5
3	46.69	64.96	12.0	35	66.41	55.10	21.5	67	37.12	34.51	31.5	99	57.13	24.94	41.5
4	56.55	64.67	12.0	36	27.26	44.66	22.0	68	46.98	34.80	31.5	100	66.99	25.23	41.5
5	66.41	64.38	12.0	37	37.12	44.95	22.0	69	57.13	34.80	31.5	101	26.68	64.67	51.5
6	26.97	54.81	12.0	38	46.98	44.95	22.0	70	66.99	35.09	31.5	102	36.54	64.67	51.5
7	36.83	54.81	12.0	39	56.84	44.95	22.0	71	27.55	24.36	31.5	103	46.69	64.96	51.5
8	46.69	55.10	12.0	40	66.70	44.95	21.5	72	37.12	24.65	31.5	104	56.55	64.96	51.5
9	56.55	54.81	12.0	41	27.26	34.80	21.5	73	47.27	24.65	31.5	105	66.41	64.96	51.5
10	66.70	54.81	12.0	42	37.12	34.80	22.0	74	57.42	24.94	31.5	106	26.97	54.52	51.5
11	27.26	44.95	12.0	43	46.98	35.09	21.5	75	66.99	24.65	31.5	107	36.83	54.81	51.5
12	36.83	44.66	12.0	44	57.13	34.80	21.5	76	26.68	64.67	41.5	108	46.69	54.81	51.5
13	46.69	44.95	12.0	45	66.70	34.80	21.5	77	36.83	64.67	41.5	109	56.55	54.81	51.5
14	56.55	44.66	12.0	46	27.55	24.65	21.5	78	46.69	64.67	41.5	110	66.41	55.10	51.5
15	66.70	44.66	12.0	47	37.41	24.94	22.0	79	55.97	64.67	41.5	111	27.26	44.66	51.5
16	27.55	34.80	12.0	48	47.27	24.94	21.5	80	66.41	64.96	41.5	112	37.12	44.66	51.5
17	37.12	34.80	12.0	49	57.42	25.23	21.5	81	26.97	54.52	41.5	113	46.98	44.95	51.5
18	46.98	35.09	12.0	50	66.99	25.23	21.5	82	37.12	54.52	41.5	114	56.84	44.95	51.5
19	57.13	35.38	12.0	51	26.97	64.38	31.5	83	46.69	54.52	41.5	115	66.70	44.95	51.5
20	66.99	35.09	12.0	52	36.83	64.67	31.5	84	56.26	54.81	41.5	116	27.26	34.80	51.5
21	27.84	24.65	12.0	53	46.69	64.67	31.5	85	66.70	54.81	41.5	117	37.12	34.80	51.5
22	37.70	24.65	12.0	54	56.84	64.67	31.5	86	27.26	44.37	41.5	118	46.98	34.80	51.5
23	47.27	24.94	12.0	55	66.41	64.38	31.5	87	37.41	44.66	41.5	119	56.84	35.09	51.5
24	57.42	24.94	12.0	56	26.97	54.52	31.5	88	46.98	44.66	41.5	120	66.70	34.80	51.5
25	67.28	24.94	12.0	57	36.83	54.52	31.5	89	56.55	44.95	41.5	121	27.26	24.65	51.5
26	26.68	64.67	22.0	58	46.69	54.52	31.5	90	66.70	44.66	41.5	122	37.41	24.65	51.5
27	36.83	64.96	22.0	59	56.84	54.52	31.5	91	27.55	34.51	41.5	123	47.27	24.65	51.5
28	46.69	64.96	22.0	60	66.41	54.52	31.5	92	37.41	34.80	41.5	124	57.13	24.65	51.5
29	56.55	64.96	22.0	61	27.26	44.66	31.5	93	47.27	34.51	41.5	125	66.99	24.94	51.5
30	66.41	64.96	22.0	62	37.12	44.66	31.5	94	56.84	35.09	41.5				
31	26.97	54.52	22.0	63	46.98	44.66	31.5	95	66.99	34.80	41.5				
32	36.83	54.81	22.0	64	57.13	44.66	31.5	96	27.55	24.94	41.5				

変形形状（高さ 45[mm]変形）

No.	X	Y	Z	No.	X	Y	Z	No.	X	Y	Z	No.	X	Y	Z
1	24.94	66.70	10.5	33	46.69	56.26	18.5	65	70.18	44.37	25.5	97	35.96	21.17	33.0
2	35.67	66.70	11.0	34	58.29	56.26	18.5	66	23.78	32.77	25.5	98	47.27	20.88	33.0
3	46.69	66.99	11.0	35	69.89	56.26	18.0	67	35.38	32.48	25.5	99	58.29	21.17	33.0
4	57.42	66.99	11.0	36	23.78	44.37	18.0	68	46.98	32.77	25.5	100	69.89	21.75	33.0
5	68.44	66.41	10.5	37	35.38	44.66	18.5	69	58.87	32.77	25.5	101	23.78	67.28	40.0
6	24.65	55.68	10.5	38	46.69	44.66	18.5	70	70.18	33.06	25.5	102	35.38	67.57	40.0
7	35.67	55.68	11.0	39	58.58	44.66	18.5	71	24.07	20.88	25.5	103	46.40	67.57	40.0
8	46.69	55.97	11.0	40	69.89	44.66	18.0	72	35.38	20.88	25.5	104	57.71	67.57	40.0
9	57.71	55.68	11.0	41	24.07	33.06	18.0	73	47.27	20.88	25.5	105	69.02	67.57	40.5
10	68.73	55.68	11.0	42	35.67	33.06	18.5	74	59.16	21.17	25.5	106	24.07	55.68	40.0
11	24.94	44.66	11.0	43	46.98	33.06	18.5	75	70.18	21.17	25.5	107	35.38	55.97	40.0
12	35.67	44.66	11.0	44	58.58	33.06	18.5	76	23.49	67.57	32.5	108	46.69	55.97	40.0
13	46.69	44.66	11.0	45	70.18	33.06	18.0	77	35.09	67.86	32.5	109	58.00	55.97	40.0
14	57.71	44.66	11.0	46	24.36	21.46	18.0	78	46.40	67.86	32.5	110	69.31	55.97	40.5
15	69.02	44.66	11.0	47	35.96	21.46	18.0	79	57.71	67.86	33.0	111	24.07	44.66	40.0
16	25.23	33.64	10.5	48	47.27	21.46	18.0	80	69.60	67.86	33.0	112	35.67	44.66	40.0
17	35.96	33.64	11.0	49	58.87	21.75	18.0	81	23.49	55.97	32.5	113	46.98	44.66	40.0
18	46.98	33.93	11.0	50	69.89	22.04	18.0	82	35.09	55.97	32.5	114	58.00	44.66	40.0
19	58.00	34.22	11.0	51	23.49	67.57	25.0	83	46.69	56.26	32.5	115	69.60	44.95	40.5
20	69.02	34.22	10.5	52	35.09	68.15	25.5	84	58.00	56.26	32.5	116	24.36	33.35	40.0
21	25.81	22.33	10.5	53	46.69	68.15	25.5	85	69.89	55.97	33.0	117	35.96	33.06	40.0
22	36.54	22.33	10.5	54	58.58	68.15	25.5	86	23.78	44.08	32.5	118	46.98	33.06	40.0
23	47.27	22.62	11.0	55	69.89	67.57	25.5	87	35.38	44.37	32.5	119	58.00	33.35	40.5
24	58.58	22.62	10.5	56	23.49	55.97	25.5	88	46.98	44.37	33.0	120	69.31	33.35	40.5
25	69.31	22.91	10.5	57	35.09	55.97	25.5	89	58.00	44.66	32.5	121	24.65	21.75	40.5
26	23.49	67.57	18.0	58	46.69	56.26	25.5	90	70.18	44.37	33.0	122	36.25	21.46	40.5
27	35.09	68.15	18.0	59	58.58	55.97	25.5	91	24.07	32.77	32.5	123	47.27	21.75	40.5
28	46.69	68.15	18.5	60	69.89	55.97	25.5	92	35.67	32.77	32.5	124	58.00	21.75	40.5
29	58.00	68.15	18.5	61	23.49	44.37	25.5	93	47.27	32.48	32.5	125	69.31	22.33	40.5
30	69.60	67.86	18.0	62	35.09	44.37	25.5	94	58.29	33.06	32.5				
31	23.49	55.97	18.0	63	46.98	44.37	25.5	95	70.18	33.06	33.0				
32	35.38	56.26	18.5	64	58.87	44.37	25.5	96	24.36	21.17	33.0				

変形形状（高さ 35[mm]変形）

No.	X	Y	Z
1	22.91	68.73	10.00
2	34.80	69.02	10.00
3	46.69	69.31	10.00
4	58.29	69.02	10.00
5	70.47	68.44	10.00
6	22.62	56.55	10.00
7	34.51	56.55	10.00
8	46.69	57.13	10.50
9	58.87	56.84	10.00
10	71.05	56.55	10.00
11	22.62	44.95	10.50
12	34.80	44.66	10.50
13	46.69	44.66	10.50
14	58.87	44.66	10.50
15	71.05	44.66	10.00
16	23.49	32.77	10.00
17	35.09	32.77	10.00
18	46.98	32.77	10.50
19	59.16	33.35	10.00
20	71.34	33.35	10.00
21	24.07	20.30	10.00
22	35.67	20.01	10.00
23	47.56	20.30	10.00
24	59.45	20.30	10.00
25	71.34	20.88	10.00
26	20.30	71.05	15.50
27	33.64	71.92	16.00
28	46.40	71.92	16.00
29	59.45	71.92	16.00
30	72.79	71.05	15.50
31	19.72	57.42	15.50
32	33.35	58.00	16.00

No.	X	Y	Z
33	46.69	58.29	16.00
34	60.03	58.00	16.00
35	73.37	58.00	16.00
36	20.01	44.37	15.50
37	33.64	44.66	16.50
38	46.98	44.95	16.50
39	60.32	44.66	16.00
40	73.66	44.95	16.00
41	20.59	31.32	15.50
42	33.93	31.32	16.00
43	47.27	31.32	16.00
44	60.61	31.32	16.00
45	73.66	31.61	16.00
46	21.46	18.27	15.00
47	34.51	17.98	15.50
48	47.56	17.69	15.50
49	60.61	18.27	15.50
50	73.37	18.85	15.50
51	20.01	71.34	21.00
52	33.06	72.21	21.00
53	46.69	72.50	21.00
54	60.32	72.21	21.00
55	73.37	71.05	21.00
56	19.43	57.71	21.00
57	33.06	58.00	21.00
58	46.69	58.29	21.50
59	60.90	58.00	21.50
60	73.95	57.71	21.50
61	19.43	44.37	21.00
62	33.06	44.37	21.50
63	46.98	44.37	21.50
64	61.19	44.37	21.50

No.	X	Y	Z
65	74.24	44.66	21.50
66	19.72	30.74	21.00
67	33.35	30.16	21.50
68	46.98	30.45	21.50
69	61.19	30.74	21.50
70	74.53	31.32	21.50
71	20.59	17.11	21.00
72	33.93	16.53	21.00
73	47.27	16.53	21.00
74	61.19	17.11	21.00
75	73.95	17.69	21.00
76	19.72	71.34	26.50
77	33.35	71.92	26.50
78	46.40	71.92	26.50
79	59.16	71.92	26.50
80	73.08	71.34	27.00
81	19.72	58.00	26.50
82	33.06	58.00	26.50
83	46.69	58.29	26.50
84	59.74	58.29	26.50
85	73.95	57.71	27.00
86	19.72	44.08	26.50
87	33.35	44.37	26.50
88	46.98	44.37	26.50
89	60.03	44.66	26.50
90	74.24	44.37	26.50
91	20.30	30.74	26.50
92	33.64	30.74	26.50
93	47.27	30.45	26.50
94	60.32	31.03	26.50
95	73.95	31.32	27.00
96	21.17	17.69	26.50

No.	X	Y	Z
97	34.22	17.11	26.50
98	47.56	16.82	26.50
99	60.32	17.40	26.50
100	73.66	18.27	27.00
101	20.88	70.18	32.00
102	33.93	70.47	32.00
103	46.40	70.76	32.00
104	58.87	70.76	32.50
105	71.92	70.47	32.50
106	20.88	57.13	32.00
107	33.93	57.42	32.00
108	46.69	57.71	32.00
109	59.16	57.71	32.00
110	72.21	57.42	32.50
111	20.88	44.37	32.00
112	33.93	44.66	32.00
113	46.98	44.66	32.00
114	59.45	44.95	32.00
115	72.50	44.95	32.50
116	21.46	31.90	32.00
117	34.51	31.61	32.00
118	46.98	31.61	32.00
119	59.45	31.90	32.00
120	72.50	32.19	32.50
121	22.04	18.56	32.50
122	34.80	18.27	32.50
123	47.27	18.27	32.50
124	59.45	18.56	32.50
125	71.92	19.43	32.50

ここで，Fig.17 に X-Y 平面上 Z 層 1 層目のマーカー位置の変移を示す．また，Fig.18 に X-Y 平面上 Z 層 3 層目のマーカー位置の変移を示す．Z 層 3 層目つまり Z 方向中央の方が，Z 層 1 層目つまり Z 方向下部よりも変位量は大きい．またその変位量は中心から放射状に，周囲にいくに従って変位量が大きいことがわかる．

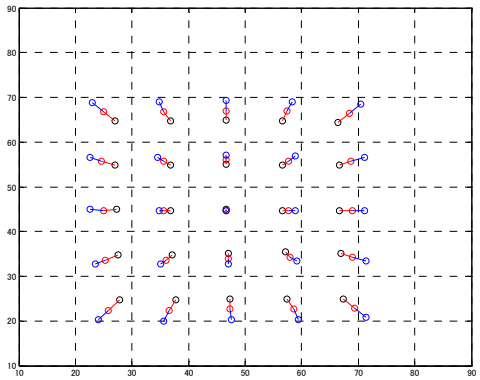

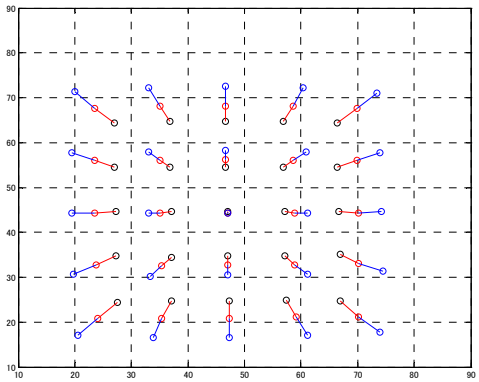

Fig 17　X-Y 平面　Z 層 1 層目マーカー変位　　**Fig 18　X-Y 平面　Z 層 3 層目マーカー変位**

つぎに Fig.19 に X-Z 平面上 Y 層 1 層目のマーカー位置の変移を示す．また，Fig.20 に X-Z 平面上 Y 層 3 層目のマーカー位置の変移を示す．図からわかるが外側（Y 層 1 層目）であっても中央部（Y 層 3 層目）であっても変位量はそれほど変わらない．Z 方向真中のマーカーの方が，上部や下部のマ

ーカーよりもX方向両側への広がりが大きいことがわかる．

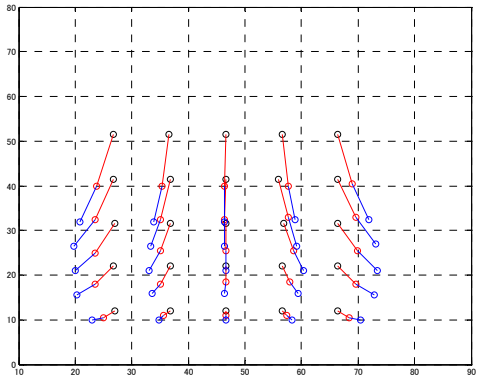

Fig 19　X-Z 平面　Y 層 1 層目マーカー変位

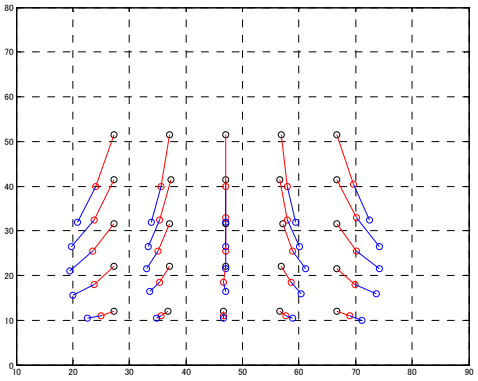

Fig 20　X-Z 平面　Y 層 3 層目マーカー変位

４－２．半楕円形状の変形計測結果

Fig.21 に半楕円型粘弾性物体の表面形状の変形を示す．白が初期形状，赤が長手方向左右から100[mm]まで強制的に押しつぶして変形させた時，青色が80[mm]まで押しつぶして変形させた場合の表面形状を示す．左右から押しつぶされることによって，中央部が上に変形し，せり上がっているのがわかる．Fig.22 にマーカー位置を示す．白が初期形状，赤が長手方向左右から 100[mm]まで強制的に押しつぶして変形させた時，青色が 80[mm]まで押しつぶして変形させた場合のマーカーの位置を示す．表面形状と同じく，左右から押しつぶされることで，中央部のマーカーは上に移動しているのがわかる．

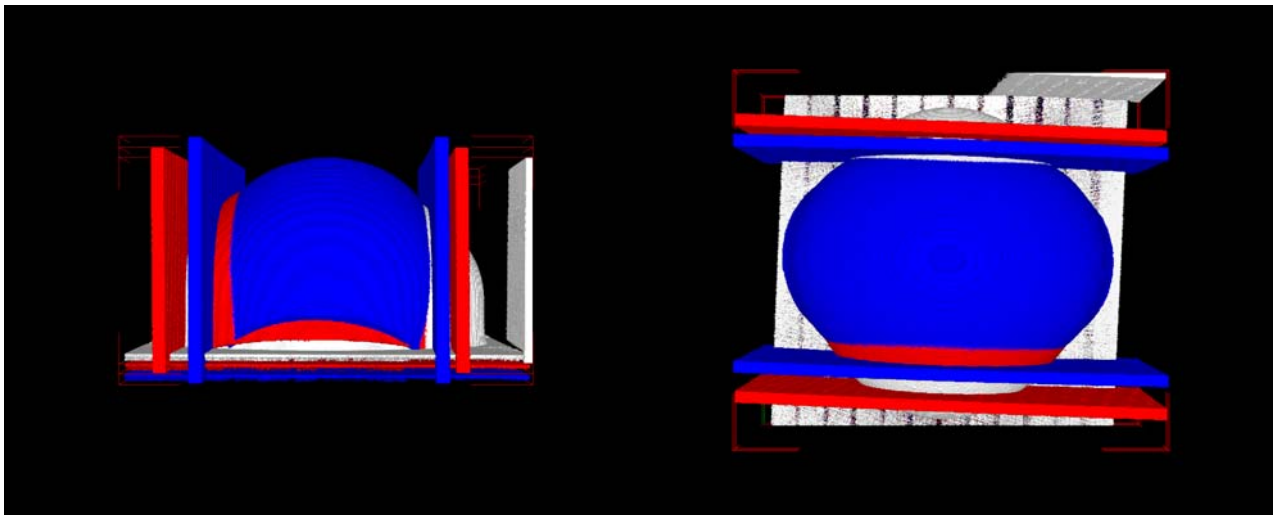

(a)SIDE SHAPE　　(b)TOP SHAPE

Fig 21 表面形状（白:初期形状，赤:幅 100[mm]，青:幅 80[mm]）

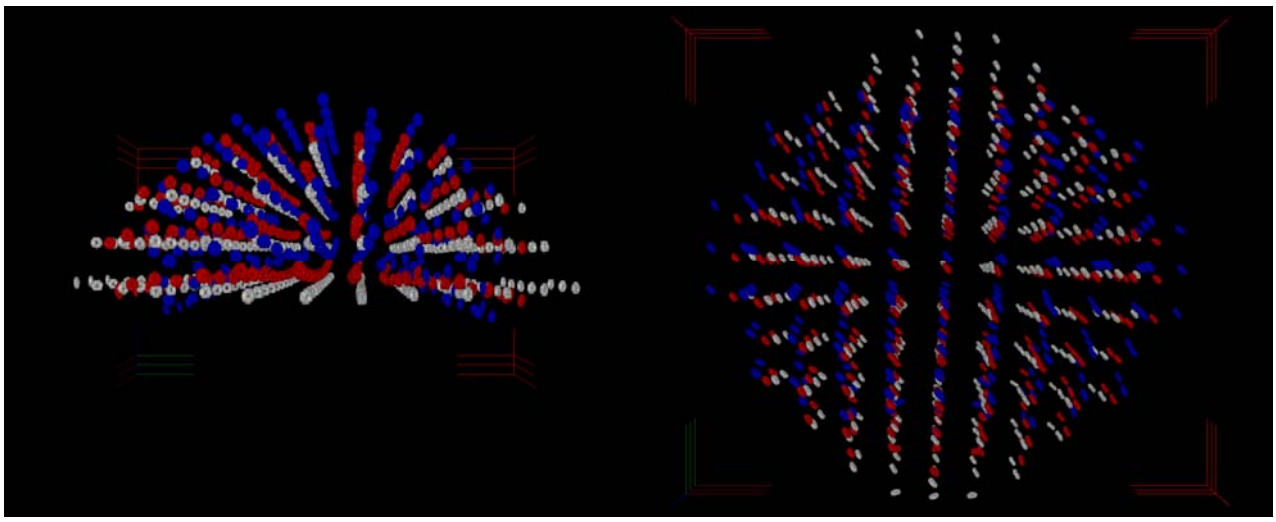

(a)SIDE SHAPE　　(b)TOP SHAPE

Fig 22 マーカー位置 CT データ（白:初期形状，赤:幅 100[mm]，青:80[mm]）

マーカーの数は 286 個あるが，Fig.23 に示すようにマーカーにナンバーを割り当てる．以降に示す No は，マーカーのナンバーである．Table.2 に各マーカーの三次元座標を示す．

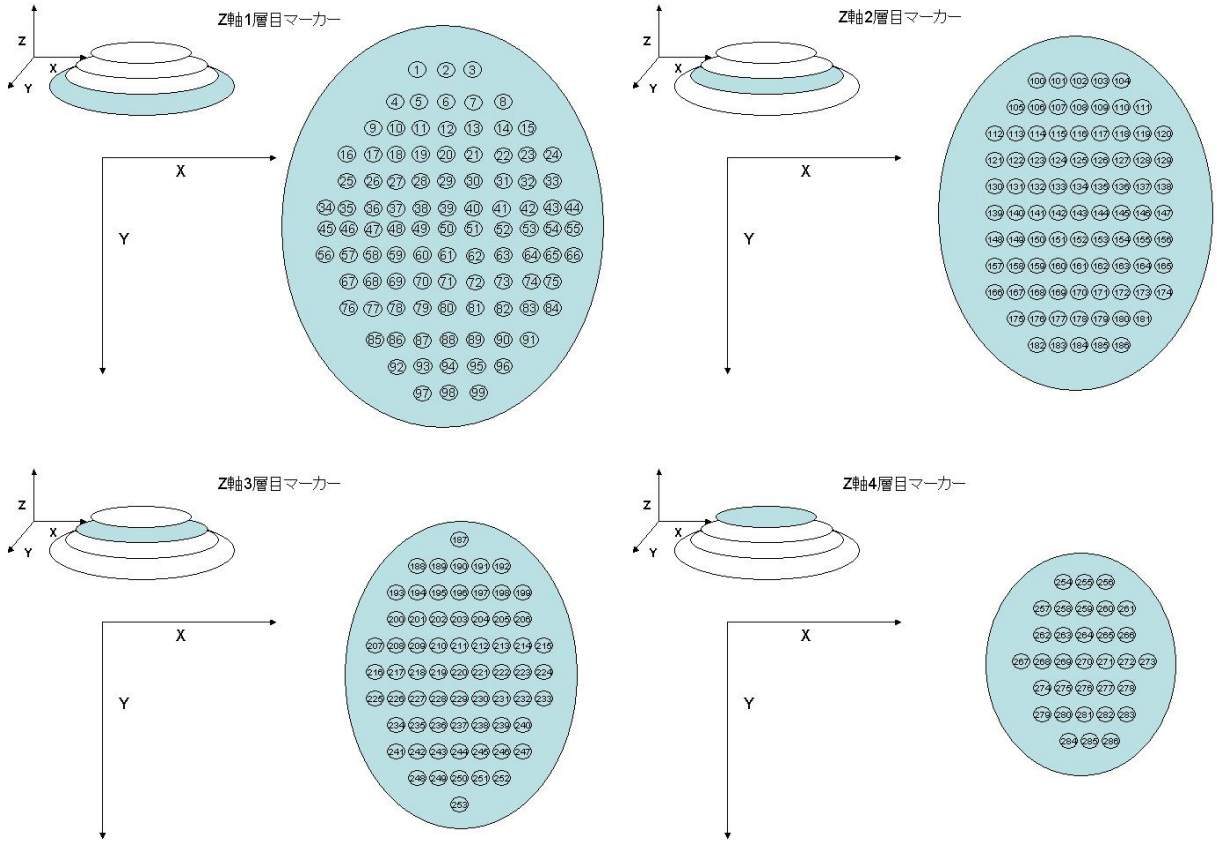

Fig 23　マーカーナンバー

初期形状

Table 2　マーカー座標（単位[mm]）

No.	X	Y	Z
1	68.44	10.44	31.0
2	78.30	10.44	31.0
3	88.45	11.31	31.0
4	58.00	19.14	30.5
5	68.15	19.72	30.5
6	77.72	20.01	31.0
7	87.87	20.59	31.0
8	98.02	21.17	31.0
9	47.85	28.42	30.5
10	57.42	29.29	30.5
11	67.57	29.29	30.5
12	77.43	29.87	30.5
13	87.58	30.45	31.0
14	97.73	31.03	31.0
15	107.59	31.61	31.5
16	37.41	37.99	30.5
17	47.56	38.57	30.5
18	57.42	39.15	30.5
19	67.28	39.44	30.5
20	77.14	40.02	30.5
21	87.29	40.31	30.5
22	97.15	40.89	31.0
23	107.30	41.18	31.0
24	117.16	41.76	31.5
25	36.54	47.85	30.5
26	46.98	48.14	30.5
27	56.55	49.01	30.0
28	66.41	49.30	30.5
29	76.56	49.88	30.5
30	86.71	50.17	30.5
31	96.86	51.04	30.5
32	106.43	51.33	31.0
33	116.58	51.91	31.0
34	26.10	57.42	30.0
35	35.96	57.71	30.0
36	46.11	58.29	30.0
37	56.26	58.87	30.0
38	65.83	59.16	30.5
39	75.98	59.74	30.5
40	86.13	60.32	30.5
41	96.28	60.90	30.5
42	106.14	61.48	31.0
43	116.00	61.77	31.0
44	125.86	62.35	31.5
45	25.52	67.57	30.0
46	35.38	67.86	30.0
47	45.53	68.44	30.0
48	55.68	69.02	30.0
49	65.54	69.31	30.0
50	75.11	69.89	30.0
51	85.55	70.47	30.5
52	95.70	71.05	30.5
53	105.27	71.63	30.5
54	115.42	72.21	31.0
55	125.28	72.50	31.0
56	25.52	77.43	30.0
57	35.38	77.72	30.0
58	45.53	78.30	30.0
59	55.39	79.17	30.0
60	65.25	79.46	30.0
61	75.11	79.75	30.0
62	85.26	80.62	30.0
63	95.41	81.20	30.5
64	104.98	81.49	30.5
65	114.84	82.36	31.0
66	124.70	82.65	31.0
67	35.09	87.87	30.0
68	44.95	88.16	30.0
69	54.81	89.03	30.0
70	64.96	89.32	30.0
71	74.82	89.90	30.0
72	84.97	90.48	30.0
73	94.83	91.06	30.5
74	104.69	91.35	30.5
75	114.55	91.93	30.5
76	34.22	98.02	30.0
77	44.08	98.31	30.0
78	54.23	98.89	30.0
79	63.80	99.47	30.0
80	73.95	100.05	30.0
81	83.81	100.63	30.0
82	93.67	101.21	30.0
83	103.82	101.50	30.5
84	113.68	102.08	31.0
85	43.79	108.17	30.0
86	53.65	108.75	29.5
87	63.51	109.04	30.0
88	73.66	109.62	30.0
89	83.52	110.20	30.0
90	93.67	110.78	30.0
91	103.53	111.36	30.5
92	53.07	118.61	30.0
93	62.93	119.19	30.0
94	73.08	119.77	30.0
95	82.94	120.35	30.0
96	93.09	120.93	30.5
97	62.35	129.34	30.0
98	72.21	129.92	30.0
99	82.07	130.21	30.0
100	58.00	19.14	40.5
101	67.86	19.43	41.0
102	77.72	20.01	41.0
103	87.87	20.59	41.0
104	97.73	21.17	41.0
105	47.56	28.42	40.5
106	57.42	29.00	40.5
107	67.57	29.29	40.5
108	77.43	29.87	40.5
109	87.87	30.45	41.0
110	97.44	31.03	41.0
111	107.30	31.61	41.0
112	36.83	37.99	40.5
113	46.98	38.57	40.5
114	56.84	39.15	40.5
115	66.70	39.44	40.5
116	77.14	40.02	40.5
117	87.00	40.60	40.5
118	97.15	41.18	41.0
119	106.72	41.47	41.0
120	116.58	42.05	41.5
121	36.25	47.85	40.0
122	46.40	48.43	40.0
123	56.55	49.01	40.5
124	66.70	49.30	40.0
125	76.56	49.88	40.5
126	86.42	50.46	40.5
127	96.28	51.04	40.5
128	106.43	51.62	41.0
129	116.29	51.91	41.0
130	35.96	58.00	40.0
131	45.82	58.29	40.0
132	55.97	58.87	40.0
133	65.83	59.45	40.0
134	76.27	59.74	40.0
135	85.84	60.61	40.5
136	95.70	60.90	40.5
137	105.85	61.48	40.5
138	115.71	62.06	41.0
139	35.38	67.86	40.0
140	45.53	68.44	40.0
141	55.39	69.02	40.0
142	65.25	69.31	40.0
143	75.40	69.89	40.0
144	85.55	70.47	40.5
145	95.70	71.05	40.5
146	105.27	71.34	40.5
147	115.13	71.92	41.0
148	35.09	78.01	40.0
149	45.24	78.59	40.0
150	55.10	78.88	40.0
151	64.96	79.46	40.0
152	74.82	80.04	40.0
153	84.97	80.62	40.0
154	95.12	81.20	40.5
155	104.69	81.78	40.5
156	114.55	82.36	41.0
157	34.51	87.87	40.0
158	44.66	88.45	40.0
159	54.81	88.74	40.0
160	64.67	89.32	40.0
161	74.53	89.90	40.0
162	84.68	90.48	40.0
163	94.54	91.06	40.0
164	104.40	91.64	40.5
165	114.26	91.93	40.5
166	33.64	97.73	40.0
167	43.79	98.31	40.0
168	53.65	98.89	40.0
169	63.51	99.18	40.0
170	73.95	99.76	40.0
171	84.10	100.34	40.0
172	93.96	100.92	40.0
173	103.82	101.50	40.5
174	113.68	102.08	40.5
175	43.50	108.46	40.0
176	53.36	108.75	40.0
177	63.22	109.33	40.0
178	73.37	109.62	40.0
179	83.52	110.49	40.0
180	93.38	110.78	40.0
181	103.24	111.65	40.5
182	52.78	118.90	39.5
183	62.64	119.19	40.0
184	72.79	119.77	40.0
185	82.65	120.35	40.0
186	92.80	120.93	40.0
187	78.01	20.59	50.5
188	57.42	29.29	50.5
189	67.28	29.58	50.5
190	77.72	30.16	50.5
191	87.58	30.74	51.0
192	97.44	31.32	51.0
193	46.98	38.57	50.5
194	56.84	39.15	50.5
195	66.70	39.73	50.5
196	77.14	40.02	50.5
197	87.00	40.60	50.5
198	97.15	41.18	51.0
199	106.72	41.47	51.0
200	46.40	48.72	50.0
201	56.26	49.30	50.0
202	66.41	49.59	50.5
203	76.85	50.17	50.5
204	86.42	50.75	50.5
205	96.57	51.33	50.5
206	106.14	51.62	51.0
207	35.96	58.00	50.0
208	46.11	58.58	50.0
209	55.97	58.87	50.0
210	66.12	59.45	50.0
211	75.98	60.03	50.0
212	86.13	60.61	50.5
213	95.99	61.19	50.5
214	105.85	61.77	50.5
215	115.71	62.06	51.0
216	35.38	68.15	50.0
217	45.53	68.73	50.0
218	55.10	69.02	50.0
219	64.96	69.60	50.0
220	75.40	70.18	50.0
221	85.55	70.76	50.0
222	95.41	71.05	50.5
223	105.27	71.63	50.5
224	115.13	72.21	51.0
225	34.80	78.01	50.0
226	44.95	78.59	50.0
227	54.81	79.17	50.0
228	64.67	79.75	50.0
229	75.11	80.04	50.0
230	84.97	80.62	50.0
231	95.12	81.20	50.5
232	104.69	81.78	50.5
233	114.55	82.36	51.0
234	44.37	88.45	50.0
235	54.23	89.03	50.0
236	64.09	89.61	50.0
237	74.53	89.90	50.0
238	84.68	90.48	50.0
239	94.25	91.06	50.0
240	104.11	91.64	50.5
241	43.79	98.60	50.0
242	53.65	99.18	50.0
243	63.80	99.47	50.0
244	73.95	100.05	50.0
245	83.81	100.63	50.0
246	93.96	101.21	50.5
247	103.82	101.79	50.5
248	53.07	109.04	50.0
249	63.22	109.33	50.0
250	73.37	109.91	50.0
251	83.52	110.49	50.0
252	93.38	111.07	50.5
253	72.50	119.77	50.0
254	66.70	39.73	60.5
255	76.85	40.31	60.5
256	86.71	40.89	60.5
257	55.97	49.30	60.5
258	66.12	49.88	60.5
259	76.27	50.17	60.5
260	86.42	51.04	60.5
261	95.99	51.62	60.5
262	55.39	59.16	60.0
263	65.54	59.74	60.0
264	75.69	60.03	60.0
265	85.84	60.61	60.5
266	95.70	61.19	60.5
267	45.24	68.73	60.0
268	54.81	69.31	60.0
269	64.96	69.60	60.0
270	75.40	70.18	60.0
271	85.26	70.76	60.0
272	95.41	71.34	60.5
273	104.98	71.92	60.5
274	54.52	79.46	60.0
275	64.38	79.75	60.0
276	74.82	80.33	60.0
277	84.97	80.62	60.0
278	94.83	81.20	60.5
279	53.94	89.32	60.0
280	63.80	89.61	60.0
281	74.24	90.19	60.0
282	84.39	90.77	60.0
283	94.25	91.35	60.5
284	63.22	99.76	60.0
285	73.66	100.34	60.0
286	83.81	100.63	60.0

変形形状（幅 100[mm]）

No.	X	Y	Z
1	67.57	21.17	32.0
2	77.72	22.04	32.0
3	88.16	21.75	32.5
4	55.97	25.23	33.5
5	66.70	28.13	33.5
6	77.14	29.58	33.5
7	88.45	29.00	34.0
8	99.18	27.26	34.0
9	45.53	31.03	35.0
10	55.10	33.64	34.5
11	66.12	35.67	34.5
12	76.85	36.83	35.0
13	88.45	36.83	35.0
14	99.18	35.67	35.5
15	109.33	34.22	36.0
16	34.51	38.57	36.5
17	44.66	40.31	35.5
18	55.10	42.34	35.5
19	65.54	43.79	35.5
20	76.56	44.95	35.5
21	87.87	44.66	35.5
22	98.89	44.37	36.0
23	109.33	43.21	36.5
24	119.19	42.63	37.5
25	33.35	47.85	37.0
26	43.79	49.30	36.5
27	54.23	50.75	36.0
28	64.96	52.20	36.0
29	75.98	53.07	36.0
30	87.29	53.07	36.5
31	98.31	53.07	36.5
32	108.75	52.78	37.5
33	118.90	52.49	38.0
34	22.62	56.55	38.0
35	32.48	57.42	37.5
36	42.92	58.29	37.0
37	53.36	59.45	36.5
38	64.38	60.32	36.5
39	75.40	61.19	36.5
40	87.00	61.48	36.5
41	98.02	61.77	37.0
42	108.46	61.77	37.5
43	118.61	62.06	38.5
44	128.76	62.06	39.5
45	21.75	66.70	38.0
46	31.61	66.99	37.5
47	42.34	67.57	37.0
48	53.07	68.44	36.5
49	63.80	69.02	36.5
50	74.82	69.60	36.5
51	86.42	70.18	36.5
52	97.73	70.76	37.0
53	107.88	71.05	37.5
54	118.32	71.63	38.5
55	128.18	71.92	39.5
56	21.75	76.27	38.0
57	31.61	76.56	37.0
58	41.76	76.56	36.5
59	52.49	77.14	36.0
60	63.51	77.14	36.0
61	74.82	77.43	36.0
62	86.13	78.30	36.5
63	97.44	79.46	37.0
64	107.59	80.33	37.5
65	117.74	81.20	38.5
66	127.60	82.07	39.5
67	31.32	85.84	36.5
68	41.76	85.55	36.0
69	52.20	85.55	35.5
70	63.22	84.97	35.5
71	74.24	85.26	35.5
72	85.84	86.42	36.0
73	96.86	87.87	36.5
74	107.30	89.03	37.0
75	117.16	90.48	38.0
76	31.03	95.70	36.0
77	40.89	95.12	35.5
78	51.62	94.25	35.0
79	62.35	93.38	35.0
80	73.66	93.38	35.0
81	85.26	94.54	35.0
82	95.70	96.28	35.5
83	106.14	98.31	36.0
84	116.00	100.05	37.0
85	41.47	103.82	34.0
86	51.33	102.37	34.0
87	62.06	100.92	34.0
88	73.66	100.63	34.0
89	84.68	102.08	34.0
90	95.70	104.69	34.5
91	105.56	107.30	35.0
92	51.33	110.78	32.5
93	61.77	108.46	32.5
94	73.08	107.88	32.5
95	84.39	109.62	33.0
96	94.83	112.81	33.0
97	62.35	116.58	30.5
98	72.50	116.00	30.5
99	82.94	117.45	31.0
100	56.84	22.62	44.0
101	66.70	24.65	44.5
102	77.14	26.10	44.5
103	88.16	25.81	44.5
104	98.31	24.65	45.0
105	45.82	29.87	45.5
106	55.68	31.90	45.5
107	66.41	33.64	45.5
108	77.14	34.51	45.5
109	88.16	34.51	45.5
110	98.31	33.93	46.0
111	108.46	33.06	46.5
112	34.80	37.99	46.5
113	44.95	39.44	46.0
114	55.10	40.89	46.0
115	65.54	42.34	46.0
116	76.56	43.21	46.0
117	87.29	43.50	46.5
118	98.02	43.21	46.5
119	107.88	42.92	47.0
120	118.03	42.34	48.0
121	33.93	47.56	47.0
122	44.08	48.72	46.5
123	54.52	50.17	46.5
124	65.54	51.04	46.5
125	75.98	51.91	46.5
126	86.71	52.20	47.0
127	97.44	52.20	47.0
128	108.17	52.20	47.5
129	118.03	52.20	48.5
130	33.06	57.13	47.5
131	43.50	58.00	47.0
132	53.94	59.16	47.0
133	64.38	60.03	46.5
134	75.69	60.61	46.5
135	86.42	61.19	47.0
136	96.86	61.48	47.5
137	107.30	61.48	48.0
138	117.74	61.77	48.5
139	32.48	66.99	47.5
140	42.92	67.57	47.0
141	53.07	68.15	47.0
142	63.80	68.73	47.0
143	74.82	69.31	47.0
144	85.84	69.89	47.0
145	96.86	70.47	47.5
146	107.01	71.05	48.0
147	117.16	71.34	48.5
148	32.19	76.85	47.5
149	42.63	77.14	47.0
150	53.07	77.43	46.5
151	63.51	77.72	46.5
152	74.24	78.30	46.5
153	85.55	78.88	47.0
154	96.28	79.75	47.5
155	106.43	80.62	48.0
156	116.58	81.49	48.5
157	31.61	86.42	47.0
158	42.05	86.42	46.5
159	52.49	86.13	46.0
160	63.22	86.42	46.0
161	74.24	86.71	46.5
162	85.55	87.58	46.5
163	95.99	88.45	47.0
164	106.14	89.90	47.5
165	116.29	91.06	48.0
166	31.32	96.28	46.0
167	41.47	95.70	45.5
168	51.62	95.41	45.5
169	62.06	94.83	45.5
170	73.37	95.12	46.0
171	84.68	95.99	46.0
172	95.41	97.73	46.0
173	105.27	99.18	46.5
174	115.13	100.63	47.0
175	41.47	105.56	44.5
176	51.62	104.40	44.5
177	62.06	103.53	44.5
178	73.08	103.24	45.0
179	84.10	104.69	45.0
180	94.54	106.43	45.0
181	104.40	108.75	45.5
182	51.91	113.68	43.0
183	61.77	111.94	43.5
184	72.79	111.36	43.5
185	83.52	112.81	43.5
186	93.38	115.42	43.5
187	77.72	22.91	54.0
188	56.26	30.45	55.5
189	66.41	31.61	55.5
190	77.14	32.48	55.5
191	87.58	32.48	56.0
192	97.73	32.48	56.0
193	45.53	38.86	56.5
194	55.39	40.02	56.0
195	65.83	40.89	56.5
196	76.85	41.76	56.5
197	87.00	42.05	56.5
198	97.44	42.05	57.0
199	107.59	42.05	57.5
200	44.66	48.43	57.0
201	54.81	49.59	56.5
202	65.25	50.46	57.0
203	76.27	51.04	57.0
204	86.71	51.62	57.0
205	97.15	51.62	57.5
206	107.01	51.91	58.0
207	34.22	57.13	57.5
208	44.37	58.00	57.0
209	54.23	58.87	57.0
210	64.96	59.45	57.0
211	75.69	60.03	57.0
212	86.42	60.61	57.0
213	96.57	61.19	57.5
214	106.72	61.48	58.0
215	116.58	61.77	58.5
216	33.35	67.28	57.5
217	43.50	67.86	57.0
218	53.36	68.44	57.0
219	63.80	69.02	57.0
220	74.82	69.60	57.0
221	85.84	69.89	57.5
222	95.99	70.47	57.5
223	106.14	71.05	58.0
224	116.29	71.63	58.5
225	32.77	77.14	57.5
226	42.92	77.43	57.0
227	53.07	78.01	57.0
228	63.51	78.30	57.0
229	74.82	78.59	57.0
230	85.26	79.46	57.5
231	95.99	80.33	57.5
232	105.85	80.91	58.0
233	115.71	81.78	58.5
234	42.63	87.00	56.5
235	52.49	87.29	56.5
236	62.93	87.58	56.5
237	73.95	87.87	56.5
238	84.97	88.45	57.0
239	94.83	89.61	57.0
240	105.27	90.48	57.5
241	42.05	97.15	56.0
242	51.91	96.86	56.0
243	62.64	96.86	56.0
244	73.66	96.86	56.0
245	84.10	98.02	56.5
246	94.54	99.18	56.5
247	104.40	100.34	57.0
248	51.91	106.43	55.0
249	62.35	106.14	55.0
250	73.08	106.14	55.0
251	83.52	107.30	55.0
252	93.67	108.75	55.5
253	72.21	115.42	53.0
254	65.83	40.02	66.5
255	76.27	40.60	66.5
256	86.71	41.18	66.5
257	55.10	49.01	67.0
258	65.25	49.59	67.0
259	75.69	50.46	67.0
260	86.13	51.04	67.0
261	96.28	51.33	67.5
262	54.23	58.87	67.0
263	64.67	59.45	67.0
264	75.11	60.03	67.0
265	85.55	60.32	67.5
266	95.99	60.90	68.0
267	43.79	67.86	67.0
268	53.65	68.44	67.0
269	64.09	69.02	67.0
270	74.82	69.60	67.0
271	85.26	70.18	67.5
272	95.70	70.76	67.5
273	105.56	71.34	68.0
274	53.07	78.30	67.0
275	63.51	78.88	67.0
276	74.24	79.17	67.0
277	84.68	79.75	67.5
278	95.12	80.62	67.5
279	52.78	88.16	66.5
280	62.93	88.45	66.5
281	73.66	89.03	66.5
282	84.39	89.61	67.0
283	94.25	90.19	67.5
284	62.35	98.02	66.0
285	73.08	98.60	66.0
286	83.52	99.18	66.0

変形形状２（幅 80[mm]）

No.	X	Y	Z
1	66.99	32.77	32.0
2	77.14	33.35	32.0
3	87.58	33.35	32.0
4	54.81	36.25	35.0
5	65.83	39.44	34.5
6	76.85	40.60	35.0
7	88.45	40.02	35.0
8	99.47	37.70	36.0
9	43.21	37.70	39.5
10	53.07	42.34	38.5
11	64.96	45.24	38.0
12	76.27	46.40	38.0
13	88.74	46.11	38.5
14	100.63	43.79	39.5
15	111.07	40.60	40.5
16	31.90	42.05	43.5
17	41.76	45.53	42.5
18	52.49	49.01	41.5
19	64.09	51.33	41.0
20	76.27	52.49	41.0
21	88.74	52.20	41.5
22	100.63	50.75	42.5
23	111.65	48.14	43.5
24	121.51	45.82	45.0
25	30.16	50.75	46.0
26	40.60	53.07	44.5
27	51.33	55.68	44.0
28	63.22	57.71	43.5
29	75.69	58.87	43.5
30	88.45	58.58	44.0
31	100.63	57.71	44.5
32	111.65	56.55	45.5
33	121.80	55.10	47.0
34	19.14	58.58	49.0
35	28.71	59.74	47.5
36	39.44	61.48	46.0
37	50.46	62.93	45.0
38	62.35	64.38	45.0
39	75.11	65.25	45.0
40	88.45	65.54	45.0
41	100.63	65.25	46.0
42	111.65	64.96	47.0
43	122.09	64.38	48.5
44	131.95	64.09	50.5
45	17.98	69.02	49.5
46	27.55	69.31	47.5
47	38.28	69.89	46.5
48	49.88	70.76	45.5
49	62.06	71.34	45.5
50	74.53	71.92	45.5
51	88.16	72.79	45.5
52	100.63	73.08	46.0
53	111.36	73.37	47.0
54	121.80	73.95	48.5
55	131.66	74.53	50.5
56	18.27	78.88	48.5
57	27.84	78.59	47.0
58	37.99	78.30	45.5
59	49.59	78.30	44.5
60	61.48	78.01	44.5
61	74.82	78.59	44.5
62	87.87	79.46	45.0
63	100.34	80.91	45.5
64	111.36	82.07	46.5
65	121.22	83.52	48.0
66	130.79	84.68	50.0
67	27.84	87.87	45.5
68	37.99	86.42	44.0
69	49.01	85.55	43.0
70	61.48	84.39	42.5
71	74.24	84.39	42.5
72	87.58	85.55	43.0
73	99.76	87.87	44.0
74	110.49	89.90	45.0
75	120.64	92.51	46.5
76	28.42	97.15	43.0
77	37.99	94.83	41.5
78	49.01	92.22	40.5
79	60.61	90.48	40.0
80	73.37	90.19	40.0
81	86.71	91.64	40.5
82	98.31	94.25	41.0
83	109.04	97.73	42.0
84	118.61	101.50	43.5
85	39.15	102.08	38.0
86	49.88	98.31	37.5
87	61.19	95.99	37.0
88	73.66	95.41	37.0
89	85.84	96.86	37.0
90	97.44	100.34	38.0
91	107.88	104.98	39.0
92	51.04	104.69	33.5
93	61.77	102.37	33.5
94	73.37	101.50	33.5
95	84.68	102.95	33.5
96	95.70	106.43	34.0
97	62.64	109.62	30.5
98	72.79	109.04	30.5
99	83.23	110.49	30.5
100	55.97	32.77	46.0
101	66.12	35.67	46.0
102	76.85	36.83	46.5
103	87.87	36.54	46.5
104	98.31	34.22	47.0
105	44.37	34.80	50.5
106	54.23	38.86	50.5
107	65.25	41.76	50.0
108	76.56	43.21	50.5
109	88.45	42.63	50.5
110	99.18	40.60	51.0
111	109.33	37.70	51.5
112	33.35	40.60	54.0
113	42.92	43.50	53.5
114	53.07	46.40	53.0
115	64.38	48.72	53.0
116	76.27	49.59	53.0
117	87.87	49.59	53.5
118	99.47	48.43	53.5
119	109.62	46.69	54.5
120	119.48	44.95	55.5
121	31.90	50.17	56.0
122	41.76	52.20	55.5
123	52.49	54.23	55.0
124	64.09	55.97	54.5
125	75.69	56.84	54.5
126	87.58	56.84	55.0
127	98.89	56.55	55.5
128	109.91	55.39	56.5
129	120.06	54.52	57.5
130	30.45	59.74	57.5
131	40.89	60.90	56.5
132	51.62	62.35	56.0
133	63.22	63.51	56.0
134	75.69	64.09	55.5
135	87.29	64.67	56.0
136	98.60	64.67	56.5
137	109.62	64.38	57.5
138	120.06	64.09	58.5
139	29.58	69.60	58.0
140	40.31	70.18	57.0
141	50.75	70.76	56.5
142	62.64	71.34	56.0
143	74.53	71.92	56.5
144	87.00	72.50	56.5
145	98.89	73.08	57.0
146	109.33	73.37	57.5
147	119.48	73.95	59.0
148	29.29	79.46	57.0
149	39.73	79.17	56.0
150	50.75	79.17	56.0
151	62.06	79.17	55.5
152	74.24	79.75	55.5
153	86.71	80.33	56.0
154	98.31	81.49	56.5
155	109.04	82.65	57.0
156	118.90	83.81	58.0
157	29.29	89.03	55.5
158	39.44	87.87	55.0
159	50.46	87.00	54.5
160	62.06	86.42	54.0
161	73.95	86.42	54.5
162	86.71	87.58	54.5
163	98.02	89.32	55.0
164	108.46	91.35	55.5
165	118.32	93.38	56.5
166	29.87	98.60	53.5
167	39.44	96.86	52.5
168	49.88	94.83	52.0
169	60.90	93.38	52.0
170	73.66	93.09	52.0
171	85.84	94.25	52.5
172	97.15	96.86	52.5
173	107.30	99.76	53.5
174	116.87	102.66	54.0
175	40.31	105.27	49.0
176	50.46	101.79	49.0
177	61.48	99.76	49.0
178	73.37	98.89	49.0
179	84.97	100.63	49.0
180	95.99	103.53	49.5
181	105.85	107.88	50.0
182	51.62	108.17	44.5
183	62.06	105.85	44.5
184	73.08	104.98	44.5
185	83.81	106.43	44.5
186	93.96	109.62	45.0
187	77.43	31.61	56.0
188	55.68	34.80	60.5
189	65.83	37.12	60.5
190	76.85	38.28	61.0
191	87.58	37.99	61.0
192	97.73	36.83	61.5
193	44.66	41.76	63.5
194	54.52	43.79	63.5
195	64.96	45.53	63.5
196	76.56	46.40	63.5
197	87.58	46.40	64.0
198	98.31	45.53	64.0
199	108.17	44.66	64.5
200	43.21	51.04	65.5
201	53.36	52.78	65.0
202	64.38	53.94	65.0
203	75.98	54.81	65.0
204	87.00	55.10	65.5
205	98.02	54.81	66.0
206	108.17	54.23	66.5
207	32.48	59.45	67.5
208	42.63	60.61	66.5
209	52.78	61.77	66.0
210	64.09	62.64	66.0
211	75.69	63.22	66.0
212	87.00	63.80	66.5
213	97.73	63.80	67.0
214	108.17	64.09	67.5
215	31.03	80.04	67.0
216	118.03	64.09	68.5
217	31.61	69.89	67.5
218	41.76	70.47	67.0
219	51.91	71.05	66.5
220	62.93	71.63	66.5
221	74.82	71.92	66.5
222	86.42	72.50	67.0
223	97.44	73.08	67.0
224	107.88	73.66	67.5
225	117.74	73.95	68.5
226	41.18	79.75	66.5
227	51.62	80.04	66.0
228	62.64	80.33	66.0
229	74.53	80.62	66.0
230	85.84	81.49	66.5
231	97.15	82.36	66.5
232	107.30	83.52	67.5
233	117.16	84.39	68.0
234	40.89	89.61	65.0
235	51.04	89.03	65.0
236	62.06	88.74	65.0
237	73.95	89.03	65.0
238	85.55	89.90	65.0
239	96.28	91.35	65.5
240	106.43	92.80	66.0
241	40.89	99.18	63.0
242	51.04	98.02	62.5
243	62.06	97.15	62.5
244	73.66	96.86	63.0
245	84.68	98.31	63.0
246	95.70	100.05	63.0
247	105.56	102.37	63.5
248	51.62	106.43	59.5
249	62.06	104.98	59.5
250	73.37	104.40	59.5
251	84.10	105.85	59.5
252	94.25	108.46	60.0
253	72.50	110.78	54.5
254	65.54	42.92	73.0
255	76.27	43.79	73.0
256	86.71	43.79	73.5
257	54.23	51.33	75.0
258	64.96	52.49	75.0
259	75.69	53.07	75.0
260	86.42	53.65	75.5
261	96.57	53.65	75.5
262	53.65	61.19	76.0
263	64.09	62.06	76.0
264	75.11	62.64	76.0
265	85.84	62.93	76.5
266	96.57	63.22	77.0
267	42.63	70.47	76.5
268	52.78	71.05	76.5
269	63.51	71.63	76.5
270	74.82	72.21	76.5
271	85.55	72.79	76.5
272	96.28	73.37	77.0
273	106.43	73.95	77.5
274	52.20	80.91	76.0
275	62.93	81.20	76.0
276	74.24	81.78	76.0
277	85.26	82.36	76.0
278	95.70	83.23	76.5
279	51.91	91.06	74.5
280	62.35	90.77	74.5
281	73.66	91.06	74.5
282	84.68	91.93	75.0
283	94.83	93.09	75.0
284	62.06	100.34	72.0
285	73.08	100.63	72.5
286	83.81	101.21	72.5

ここで，Fig.24 に X-Y 平面上 Z 層 1 層目のマーカー位置の変移を示す．また，Fig.25 に X-Y 平面上 Z 層 4 層目のマーカー位置の変移を示す．Fig.24 から，Z 層 1 層目つまり Z 方向最下部では，Y 方向両側から押しつぶされているため，Y 方向の両側は中央部に押されていることがわかる．それに対して Y 方向中央部は両端から押されているため，若干 X 方向に広がっているが X-Y 方向の変位量は小さい．Fig.25 から，Z 方向最下部では，Y 方向の中央部にあるため X-Y 方向の変位量は小さい．

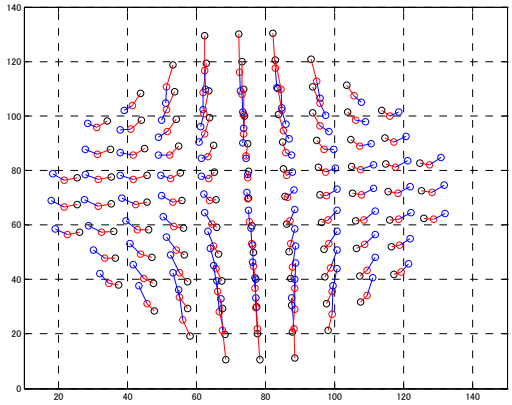

Fig 24　X-Y 平面　Z 層 1 層目マーカー変位

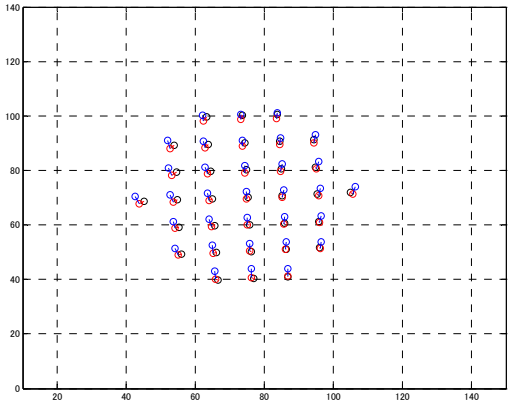

Fig 25　X-Y 平面　Z 層 4 層目マーカー変位

Fig.26 に X-Z 平面上 Y 層中央層のマーカー位置の変移を示す．また，Fig.27 に X-Z 平面上 Y 層中央層から Y＋方向に 5 層目のマーカー位置の変移を示す．Fig.24，Fig.25 から Y 方向中央部は X-Y 方向には変位量が少ないことがわかったが，Fig.26 を見ると Z＋方向に大きく変位していることがわかった．Fig.27 から，Y 方向両端部は Z 方向の変位はそれほど大きくないことがわかった．

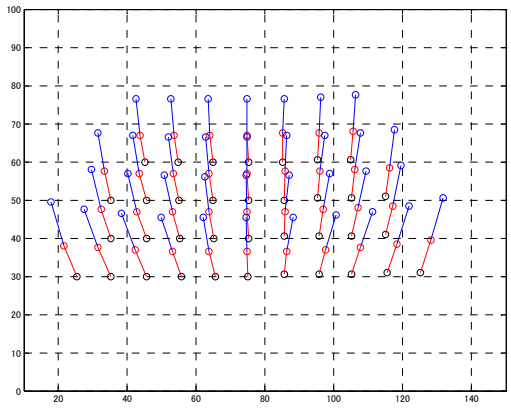

Fig 26　X-Z 平面　Y 層中央層マーカー変位

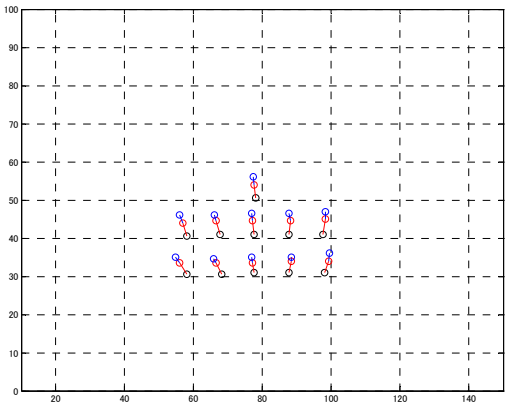

Fig 27　X-Z 平面　Y 層中央から＋5 層目マーカー変位

つぎに Fig.28 に Y-Z 平面上 X 層中央層のマーカー位置の変位を示す．また，Fig.29 に Y-Z 平面上 X 層中央層から X＋方向に 4 層目のマーカー位置の変位を示す．Fig.28 から Y 軸両端のマーカーは，Y 軸中央方向へ大きく変位していることがわかる．それに対して Y 軸中央部のマーカーは Z＋方向へ

大きく変位していることがわかる．Fig.29 は Y 軸方向の中央部であるので Z＋方向に大きく変位していることがわかる．

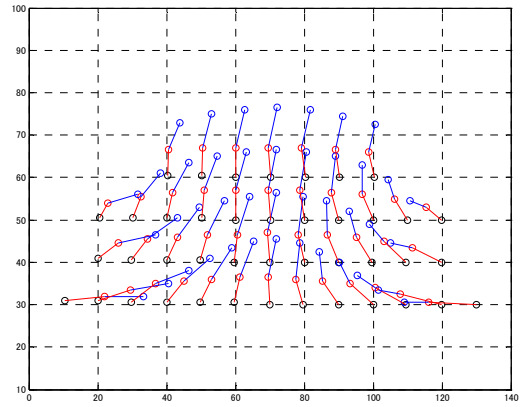

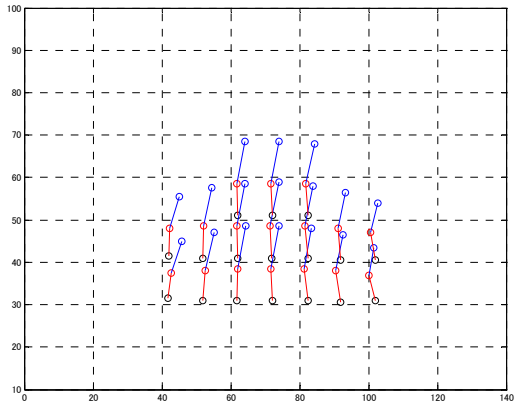

Fig 28　Y-Z 平面　X 層中央層目マーカー変位　　Fig 29　Y-Z 平面　X 層中央から+4 層目マーカー変位

５．終わりに

本受託試験では，和歌山県工業技術センターが所有している産業用 CT スキャナを用い，外部から粘弾性物体に応力を加えた時の内部変形を計測した．

人肌ゲルによって作成した粘弾性物体を作成し，物体の内部に金属のマーカーを等間隔に配置した．その物体に外部から強制変位をかけた状態で，産業用 CT スキャナを用いて内部変形を 3 次元的に計測した．

試験成果報告書

本報告書は，平成 17 年度科学研究費補助金基盤研究 A「内部センシングに基づく柔軟物のリアリティーベースモデリングに関する研究」に係る委託試験の成果を示す．試験題目，試験目的，試験内容は以下のとおりである．

（1） 試験題目　産業用 CT スキャナを用いた粘弾性物体の内部変形測定試験

（2） 試験目的　本受託試験では、和歌山県工業技術センターが所有している産業用 CT スキャナを用い、外部から粘弾性物体に応力を加えた時の内部変形を計測することを目的とする．

（3） 試験内容　物体の中にプラスティックまたは金属の粒状物体が等間隔に配置された食品生地、シリコンゴム等の粘弾性物体を製作する．その物体に外部から応力をかけた状態で，和歌山県工業技術センターが所有している産業用 CT スキャナを用いて，内部変形を 3 次元的に計測する．

試験結果

1．試験装置

本試験において、粘弾性物体の内部変形を計測する産業用 CT スキャナを Fig.1 に示す．本 CT スキャナの場合，スライスエリアを最小の φ150mm とし画素サイズを 512×512[Pixel]とした場合，X，Y 方向の空間分解能は 150÷512＝0.29[mm]となる．Z 方向に関しては，スライス厚が最小で 1[mm]のため分解能が 1[mm]であるが，スライスピッチの最小が 0.5[mm]であるため再構成では仮想的に 0.5[mm]の分解能で計算できる．

産業用ＣＴスキャナ

TOSCANER-24200AV

スキャン　トラバースローテーション方式

Ｘ線出力　400kV，透過能力　鉄100mm，アルミ300mm

ｽﾗｲｽｴﾘｱ　　φ150mm，φ300mm，φ600mm　可変

ｽﾗｲｽ厚　　1.0mm，2.0mm，4.0mm　可変

再構成画素　512×512　or　1024×1024

ｽｷｬﾝﾓｰﾄﾞ　　nomal(fast)　or　fine(slow)

　　ful(360)　　or　half(180)

ﾏﾙﾁｽｷｬﾝﾋﾟｯﾁ　min.0.5mm

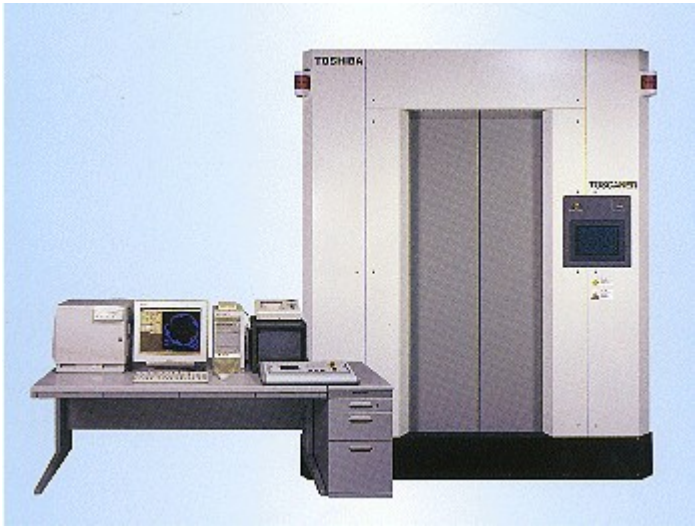

Fig 1　産業用 CT スキャナ仕様

２．粘弾性物体作成方法の検討

本試験においては，以下の項目について検討する．

(a) 対象とする柔軟物

(b) 物体変形の条件

(c) 目印（マーキング）の埋め込み方法

まず（a）について検討した．対象となる粘弾性物体を食品特に従来と同じく生地に絞る場合，小麦粉を練ったものが有効である．しかしながら測定中に水分が蒸発してしまい，特性が変化するため再現性のある測定が難しい．水の代わりに蒸発の少ない油脂を使ってこねる方法も検討を行った．通常小麦粉に適量の水を加えてこねた場合，グルテンという蛋白質が生成され，それが生地に粘弾性を持

たせているが，油を加えた場合グルテンは分解されるため，生地に粘弾性的性質はなくなってしまい，当初の目的から外れてしまう事がわかった．

そこで，本研究に用いる粘弾性物体は人肌ゲルを利用することとした．人肌ゲルはウレタン系のポリオールブレンドを原液とし、イソシアネートの硬化剤を用いて硬化させることのできる物体である．（Fig.2 参照）

Fig 2　人肌ゲル原液

つぎに（b）について，検討した．変形計測において，本当は変形中の内部形状も計測できるのが理想的ではあるが，センター所有の CT では計測に時間がかかることもあり，初期形状及び変形後の定常状態の形状しか計測できないと考えられる．そこで本試験では，一定の外部変位を加えられるような，押付け装置を製作した（Fig.3 参照）．これを用いて人肌ゲルで製作した粘弾性物体に，強制的な外部位置拘束を加えた状態で CT 撮影を行い物体の内部変位を計測する．CT の撮影において，比重の大きな物体を撮影エリア内においている場合，本来計測したい物体を測定する上において大きな撮影ノイズである．そのため押付け装置はできるだけ金属類を使わず，可能な限り木材を使用した．大体が難しい部分のみ金属を利用した．

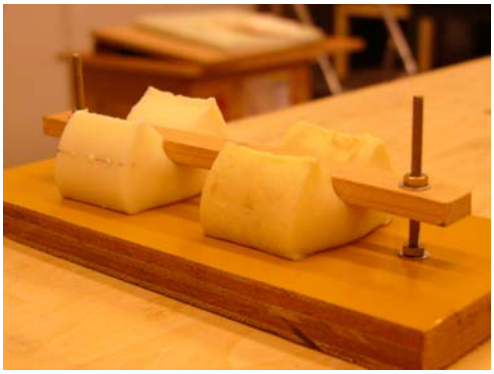

Fig 3　押付け装置（押し付け状態）

最後に（c）について検討した．粘弾性物体に埋め込むマーキングは金属類の粒を利用するのがベストであると考えられる．試験片の初期形状は型に物体を流し込むという形になるが，Fig.4 に示すように型内部に針金のような細い棒状にアルミ球を取り付け，ねじりを加えると球から外れるように細工しておく方法を提案した．しかしながら上記の方法を試したが，棒をスムーズに抜き取ることは

困難で，棒を抜き取る際に中のマーカーも引っ張ってしまいマーカーの初期位置が変わってしまった．棒に離型剤を塗っても結果はあまり変わらなかった．

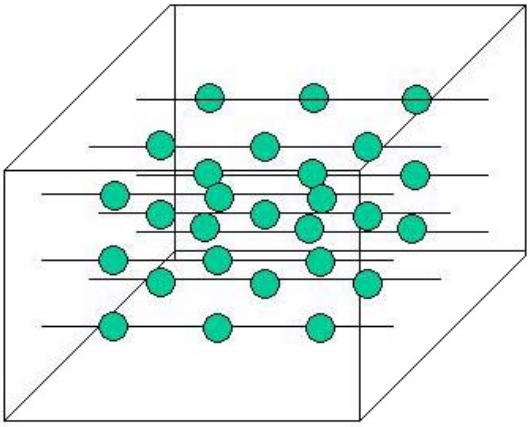

Fig 4　マーキング埋め込み方法

そこで金属の棒ではなく接着糸（繊維）を用いてマーカーを固定することを検討した．棒ではどうしても人肌ゲルトの接着面積が大きく抜きにくくなってしまう．そのためより接着面積の小さい糸を使うことを選択した．糸を引き抜くと，多少糸くずは残るが比較的容易に引き抜くことができる．さらに今回用いる接着糸は，熱をかけると溶解する糸であり（Fig.5），ある程度熱がかかっている状態であると，よりスムーズに引き抜くことができる．

Fig 5　接着糸

この糸を用いて Fig.6 に示すように，型の中に糸を張った状態でセットし等間隔にマーカーをセットする．マーカーには M3 のスプリングワッシャを用いた。低温（40～60℃）で人肌ゲルを固めて，その状態のまま糸を引き抜いて作った（Fig.7）．このテストピースは２本の糸を張り，それぞれ 3 つのマーカーを埋めている．

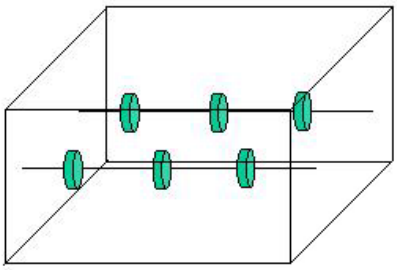

Fig 6　内部にワッシャー(M3)を埋め込む

Fig 7　テストピース

３．CT 測定結果

Fig.8 に人肌ゲルの初期形状をＣＴスキャナで計測した画像を示す.人肌ゲルの初期形状はｘ，ｙ，ｚ方向に 30×40×28[mm]の大きさを持つ．撮影時のＣＴスキャナの画像分解能はｘ，ｙ方向は 0.15[mm]，ｚ方向は 1[mm]である.

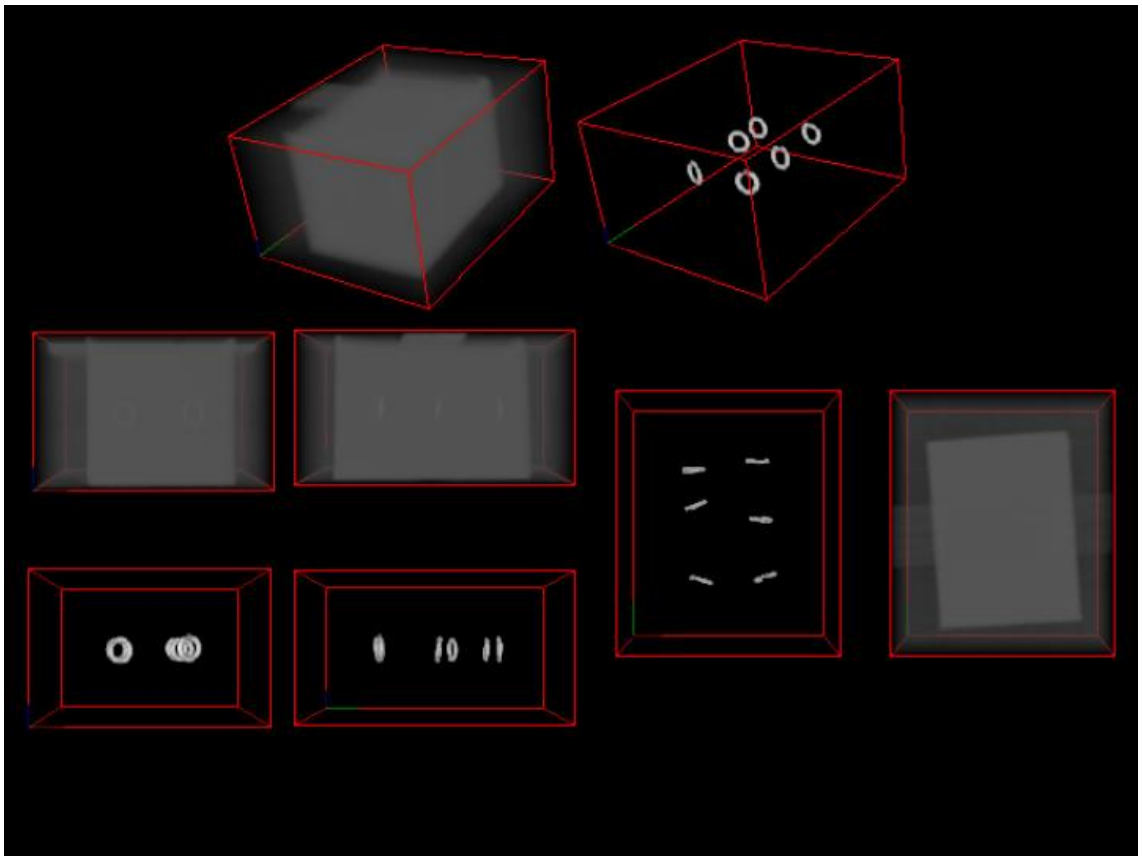

Fig 8　CT スキャン結果（初期形状）

図から分かるが，人肌ゲルを固める際に，等間隔に配置していたマーカーが移動してしまった.Fig.10 に強制変位を加えた場合の人肌ゲル変形後の CT データを示す.強制変位は外部から長方形(幅 13[mm]）を下から 14[mm]のところまで下げた．（Fig.9 参照）

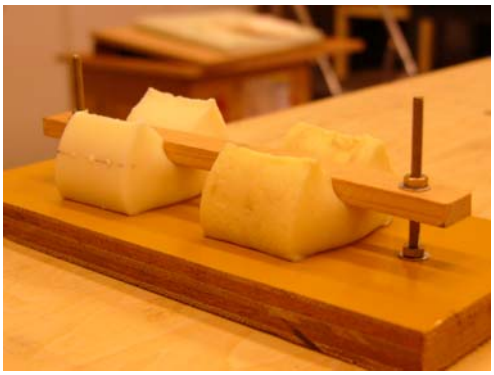

Fig 9　強制変位印加時

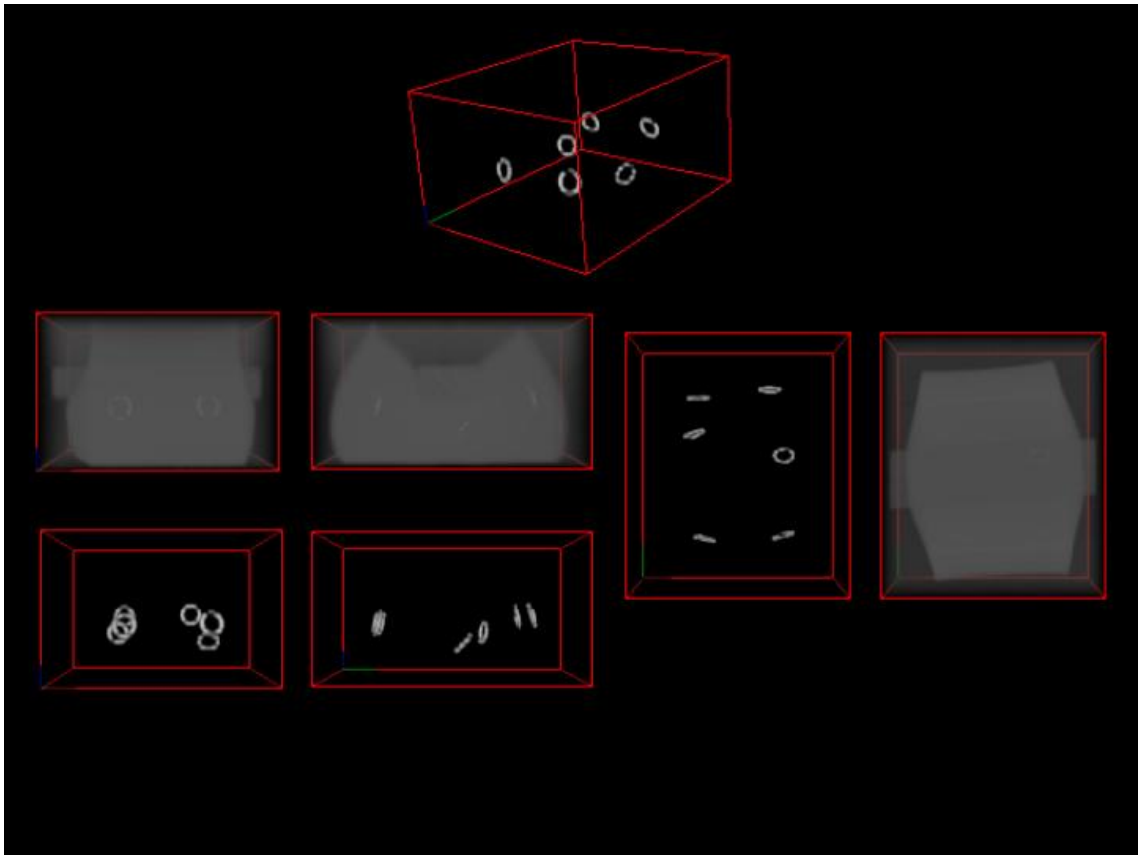

Fig 10　CT スキャン結果（変形形状）

解析データからマーカーの中心位置の 3 次元データを Table.1 に示す. 表中の番号とマーカーの位置の対応は Fig.11 に示す.

Table 1　マーカー中心位置の 3 次元座標

		X[mm]	Y[mm]	Z[mm]
Initial	1	16.95	14.70	14
	2	31.50	15.60	15
	3	15.75	31.65	14
	4	30.45	28.50	14
	5	15.15	39.75	14
	6	29.55	41.85	15

		X[mm]	Y[mm]	Z[mm]
Deformed	1	15.45	10.80	11
	2	33.90	11.55	12
	3	12.75	35.10	9
	4	34.05	29.85	7
	5	13.80	43.35	13
	6	30.45	45.15	13

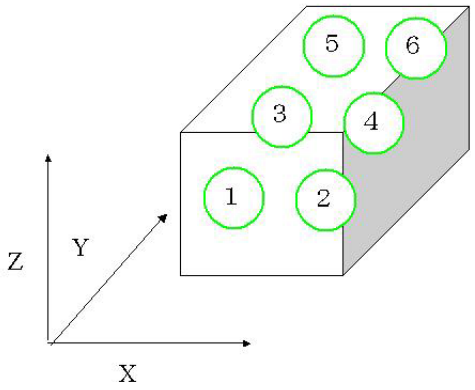

Fig 11　マーカーナンバー

Fig. 12 に初期形状と変形形状のマーカー位置を重ねて比較できるようにした。赤が初期形状，灰色が変形後のマーカーの位置を示す．図から分かる物体中央部を押されることで，マーカーが中央から周辺へ，またより下へ移動しているのが分かる．

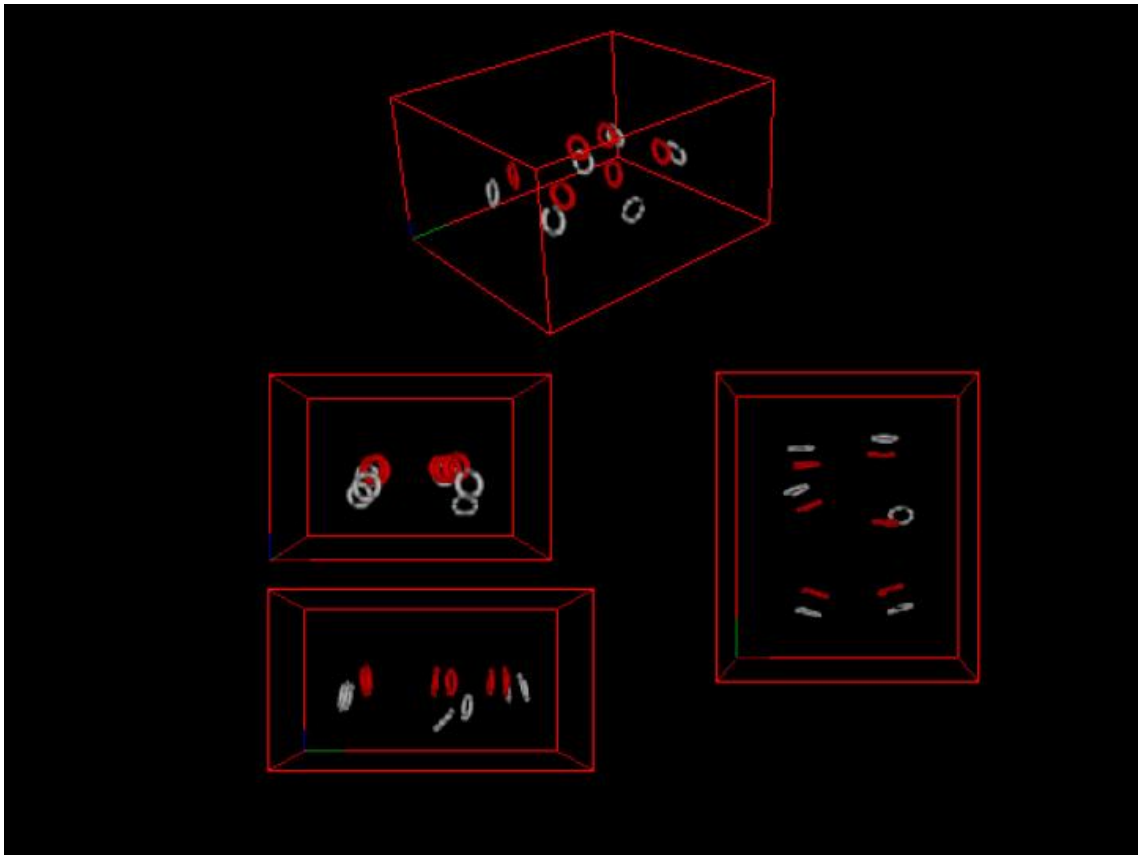

Fig 12　CT データ比較（初期形状，変形形状）

この図から分かるが，人肌ゲルを固める際に，等間隔に配置していたマーカーが移動してしまった．この原因には以下が挙げられる．

① 金属の棒の場合と同じく糸を抜く時にマーカーも引っ張ってしまい移動した

② 一本の糸でマーカーを設置しているため，人肌ゲルの液体の充填中に移動した

③ 低温で人肌ゲルを固めている際，液体温度によってマーカーを支えている糸が切れてしまいマーカーが移動した．

④ 人肌ゲル凝固の際の発熱によって，マーカーが移動した．

⑤ 人肌ゲル凝固の際の発熱によって，マーカーを支えている糸が切れ，マーカーが移動した．

図を見る限り，人肌ゲルの凝固の際に糸が切れたとは考えにくいため，③と⑤は除外される．①の場合，まず糸を引き抜く前の状態を CT で計測しておく必要があった．②と④についても糸を引き抜く前の状態を CT で計測する必要がある．②の場合の解決方法としては，Fig.13 に示すように十字に糸を張り，マーカーの位置を固定するという方法で解決できる．

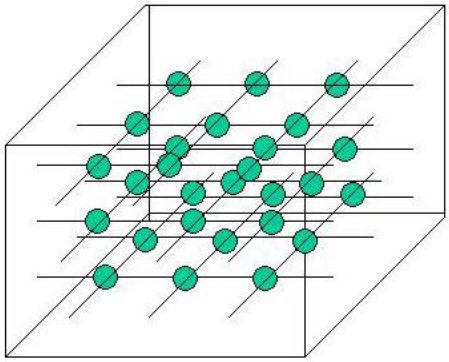

Fig 13　マーカー埋め込み方法

ここでFig.13に示した方法で粘弾性物体を作成するために，Fig.14に示す型を作成し，十字方向に糸を張りその交差点にマーカーとしてM1の丸座金（外経2.8［mm］　長さ0.3[mm]）を配置した．粘弾性物体の形状は60×60×60[mm]丸座金は1[cm]間隔に5×5×5個配置した．Fig.15-(a)に，計測のためCT装置内に設置した粘弾性物体の初期形状を，Fig.15-(b)に変形形状を示す．

Fig 14　型

変形条件については,強制変位を物体上部から与えた.押付け物体は幅13[mm]の長方形物体である.また強制変位は高さ45[mm]までと35[mm]の２種類の強制変位を加えた場合の物体の変形を計測する.撮影時のＣＴスキャナの画像分解能はｘ，ｙ方向は0.29[mm]，ｚ方向は0.5[mm]である.

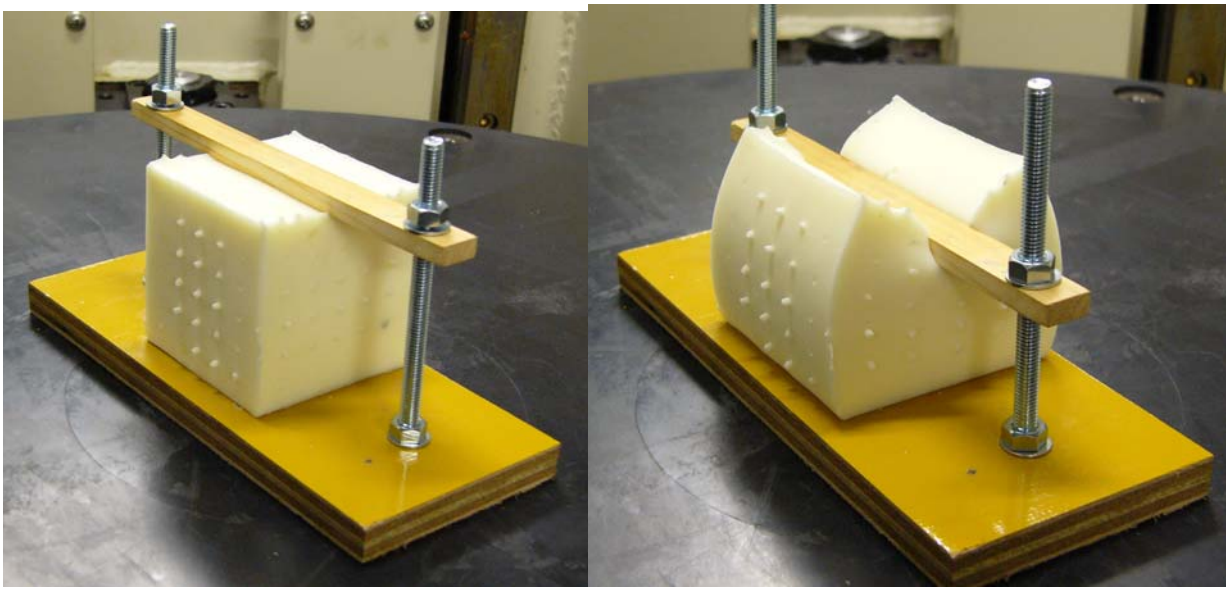

(a)初期形状　　(b)変形形状

Fig 15　レオロジー物体

Fig.16 に初期形状と変形形状のマーカー位置を重ねて比較できるようにした。白が初期形状，赤が中央上部を高さ 45[mm]まで強制的に変形させた時，青色が高さ 35[mm]まで変形させた場合のマーカーの位置を示す．図から分かる物体中央部を押されることで，マーカーが中央から周辺へ，より下へ移動しているのが分かる．Fig.18 に人肌ゲルの外部形状を示す．Fig.17 と同じく，白が初期形状，赤が中央上部を高さ 45[mm]まで強制的に変形させた時，青色が高さ 35[mm]まで変形させた形状を示す．

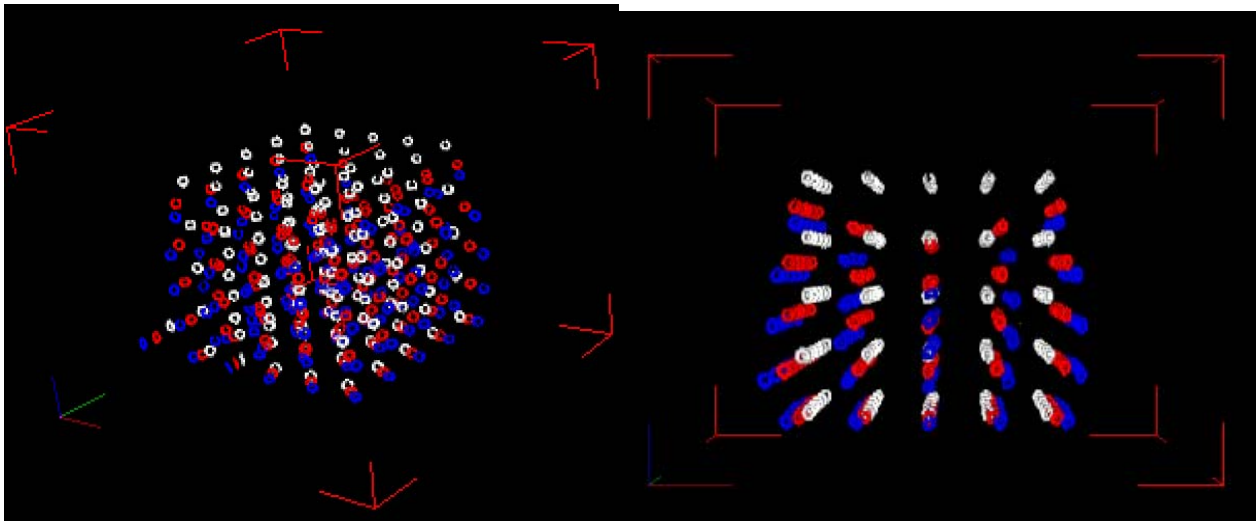

(a) 3D　　(b)FRONT

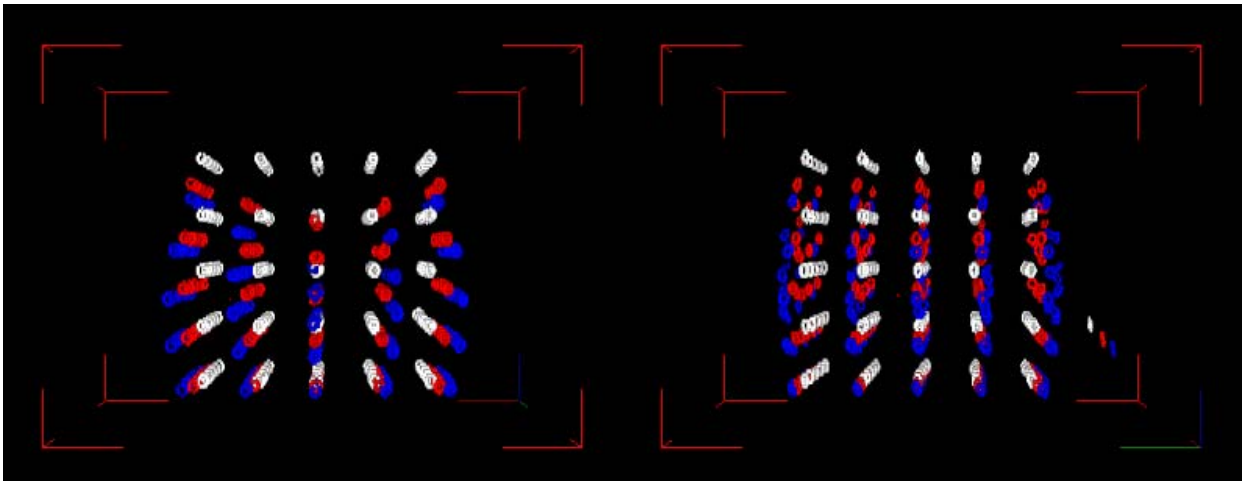

(c)BACK　　(d)LEFT

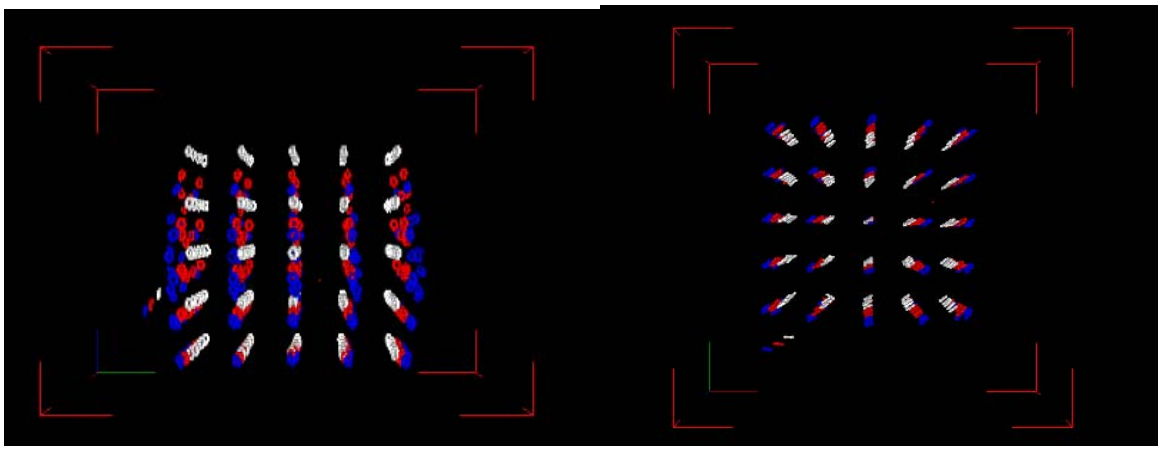

(e) RIGHT　　(f)TOP

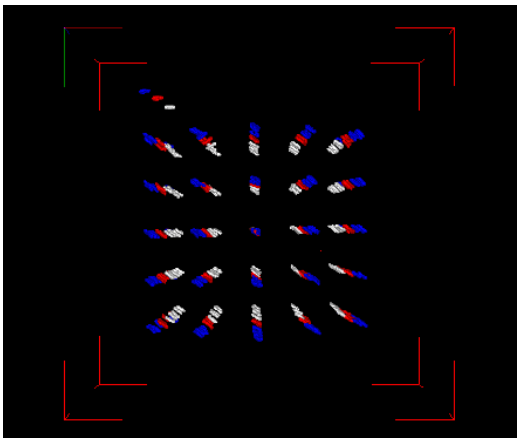

(g)BOTTOM

Fig 16　CT データ（マーカー比較，白:初期形状，赤:高さ 45[mm]変形，青:高さ 35[mm]変形）

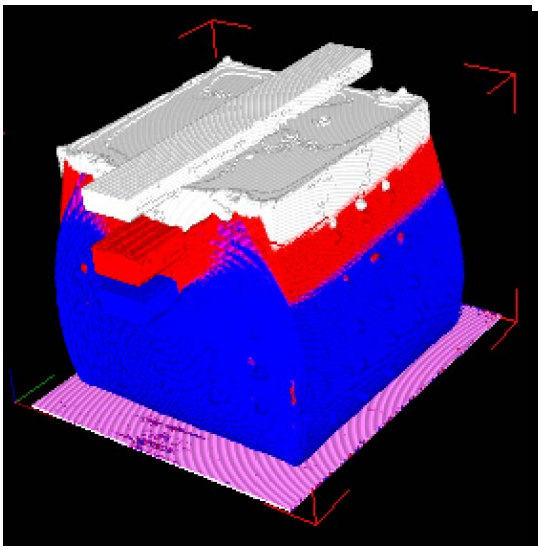

(a) 3D

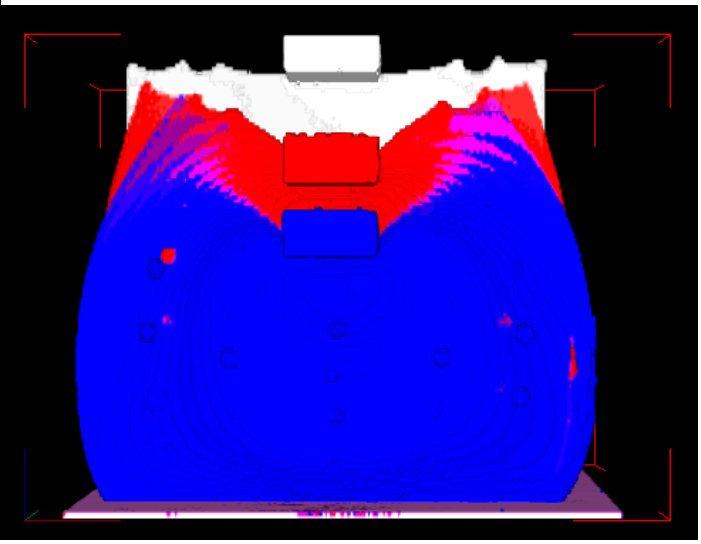

(b) FRONT

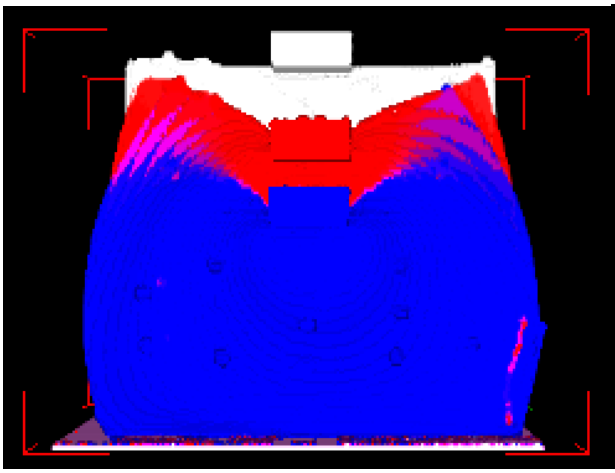

(c) BACK

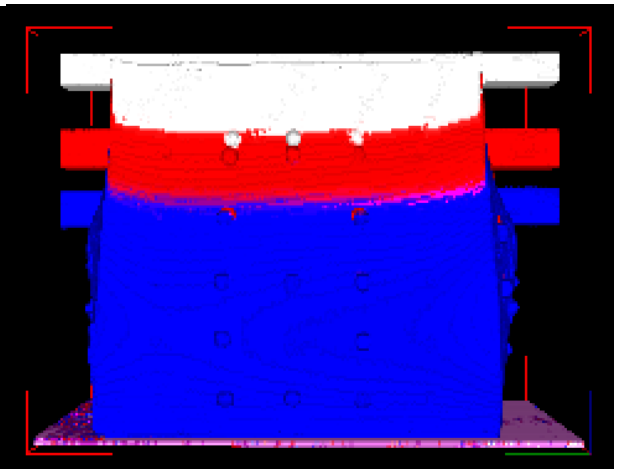

(d) LEFT

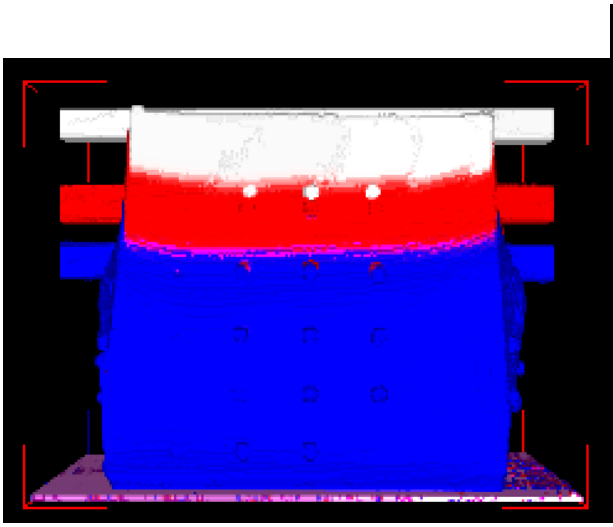

(e) RIGHT

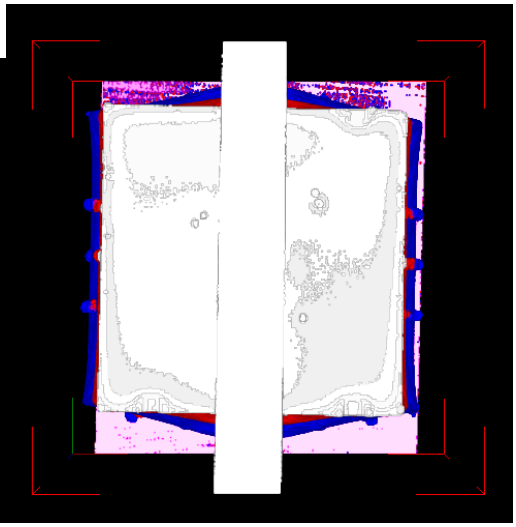

(f) TOP

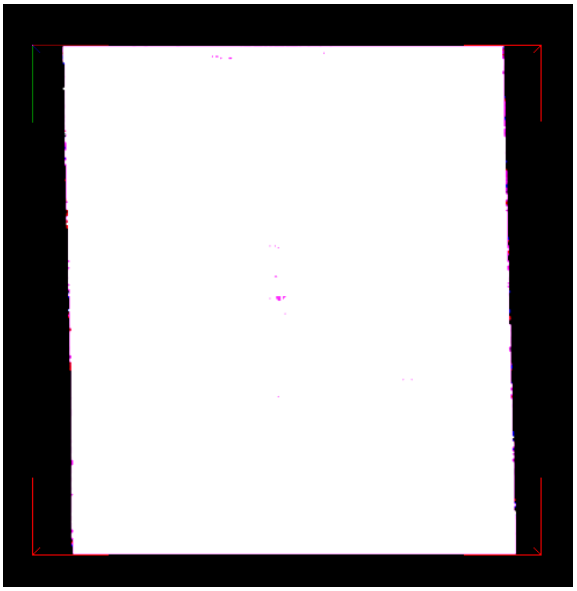

(g)BOTTOM

Fig 17　外部形状 CT データ（白:初期形状，赤:高さ 45[㎜]変形，青:高さ 35[㎜]変形）

マーカーの数は 5×5×5＝125 個あるため,Fig.18 に示すようにマーカーにナンバーを割り当てる．以降に示す No は，マーカーのナンバーである．Table.2 に各マーカーの三次元座標を示す．なお初期形状における粘弾性物体の位置・姿勢は Fig.19 に示す．

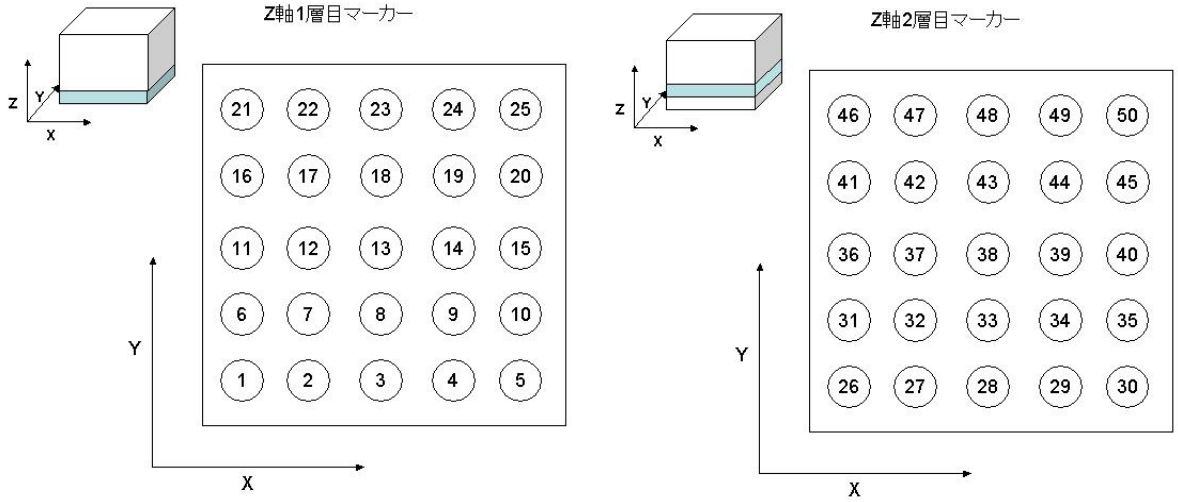

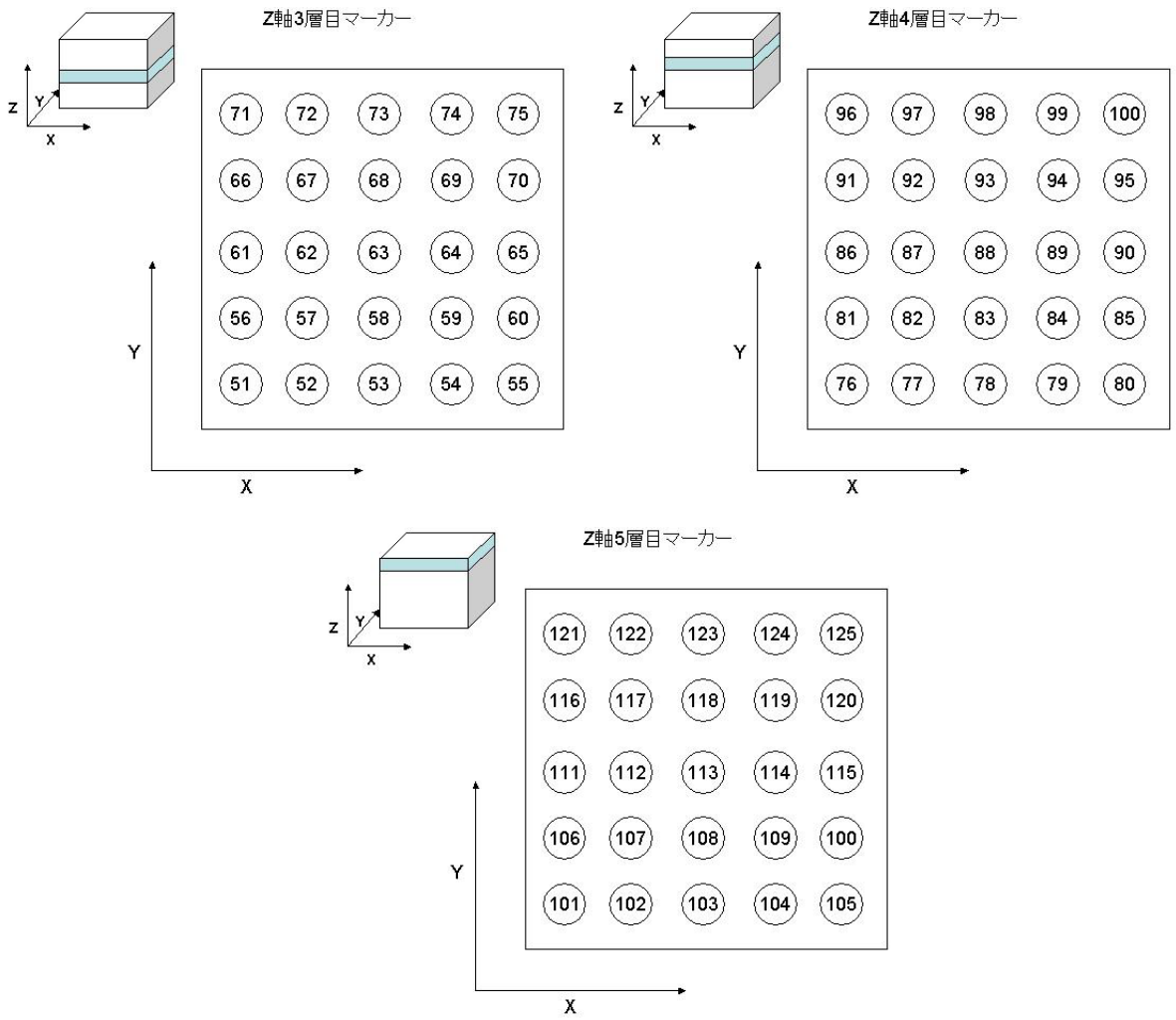

Fig 18　マーカーナンバー

Table 2　マーカー座標（単位[mm]）

初期形状

No.	X	Y	Z	No.	X	Y	Z	No.	X	Y	Z	No.	X	Y	Z
1	22.62	25.81	9.00	33	42.34	35.38	18.5	65	62.06	44.66	28.5	97	33.06	65.25	38.0
2	32.19	25.52	9.00	34	52.20	35.09	18.5	66	22.62	55.68	28.5	98	42.63	65.25	38.0
3	42.05	25.23	9.00	35	62.06	34.80	18.5	67	32.48	55.39	28.5	99	52.78	64.67	38.0
4	51.91	25.23	9.00	36	22.62	45.53	18.5	68	42.63	55.10	28.5	100	62.64	64.38	38.0
5	61.77	24.94	9.00	37	32.48	45.53	18.5	69	52.49	55.10	28.5	101	22.33	25.52	48.0
6	22.62	35.67	9.00	38	42.63	44.95	18.5	70	62.35	54.52	28.5	102	32.48	25.23	48.0
7	32.48	35.38	9.00	39	52.20	44.66	18.5	71	22.91	65.54	28.5	103	42.92	25.23	48.0
8	42.34	35.09	9.00	40	62.35	44.66	18.5	72	32.48	65.25	28.5	104	52.20	24.94	48.0
9	52.20	35.09	9.00	41	22.91	55.68	18.5	73	42.92	65.25	28.5	105	62.06	24.65	48.0
10	62.06	34.80	9.00	42	32.77	55.39	18.5	74	52.78	64.96	28.5	106	22.62	35.67	48.0
11	22.62	45.82	9.00	43	42.63	55.10	18.5	75	62.64	64.67	28.5	107	32.48	35.38	48.0
12	32.48	45.53	9.00	44	52.49	54.81	18.5	76	22.33	25.81	38.0	108	42.34	35.09	48.0
13	42.34	45.24	9.00	45	62.35	54.52	18.5	77	32.77	25.52	38.0	109	52.20	35.09	48.0
14	52.49	44.95	9.00	46	22.91	65.54	18.5	78	42.34	25.52	38.0	110	62.35	34.80	48.0
15	62.06	44.37	9.00	47	32.77	64.96	18.5	79	51.91	25.23	38.0	111	22.62	45.53	48.0
16	22.62	55.39	9.00	48	42.92	64.67	18.5	80	62.06	24.94	38.0	112	32.77	45.24	48.0
17	32.48	55.10	9.00	49	52.78	64.38	18.5	81	22.33	35.96	38.0	113	42.34	44.95	48.0
18	42.63	54.81	9.00	50	62.64	64.38	18.5	82	32.77	35.67	38.0	114	52.49	44.95	48.0
19	52.49	54.52	9.00	51	22.33	26.10	28.5	83	42.34	35.38	38.0	115	62.35	44.66	48.0
20	62.06	54.23	9.00	52	31.90	25.81	28.5	84	52.20	35.09	38.0	116	22.91	55.68	48.0
21	22.62	65.54	9.00	53	42.05	25.52	28.5	85	62.06	34.80	38.0	117	32.77	55.39	48.0
22	32.77	65.54	9.00	54	51.91	25.23	28.5	86	22.62	45.82	38.0	118	42.63	55.10	48.0
23	42.63	64.96	9.00	55	61.77	24.94	28.5	87	32.77	45.53	38.0	119	52.49	54.81	48.0
24	52.78	64.67	9.00	56	22.62	35.96	28.5	88	42.34	45.24	38.0	120	62.64	54.52	48.0
25	62.64	64.38	9.00	57	32.19	35.67	28.5	89	52.20	44.95	38.0	121	22.91	65.54	48.0
26	22.62	25.81	18.50	58	42.34	35.38	28.5	90	62.06	44.95	38.0	122	33.06	65.54	48.0
27	32.19	25.52	18.50	59	52.20	35.38	28.5	91	22.91	55.68	38.0	123	42.63	65.25	48.0
28	42.05	25.23	18.50	60	62.06	35.09	28.5	92	32.77	55.10	38.0	124	52.49	64.96	48.0
29	51.91	24.94	18.50	61	22.62	45.82	28.5	93	42.63	55.10	38.0	125	62.64	64.67	48.0
30	62.06	24.94	18.50	62	32.19	45.53	28.5	94	52.49	54.81	38.0				
31	22.62	35.67	18.50	63	42.34	45.24	28.5	95	62.35	54.52	38.0				
32	32.48	35.38	18.50	64	52.49	44.95	28.5	96	22.91	65.25	38.0				

変形形状（高さ 45[mm]変形）

No.	X	Y	Z	No.	X	Y	Z	No.	X	Y	Z	No.	X	Y	Z
1	20.88	24.94	8.0	33	42.34	34.51	16.0	65	65.25	44.66	25.50	97	31.03	67.57	32.0
2	31.32	24.36	8.5	34	53.65	34.22	16.5	66	19.72	56.55	25.50	98	42.92	67.86	30.5
3	42.34	24.07	8.0	35	64.96	34.22	17.0	67	30.45	56.55	24.00	99	54.81	66.99	32.0
4	52.78	24.36	8.0	36	20.01	45.82	17.0	68	42.92	56.26	23.50	100	65.54	65.83	34.5
5	63.51	24.07	8.0	37	31.03	45.53	16.5	69	54.81	55.97	24.50	101	20.30	24.65	43.5
6	20.88	35.38	8.5	38	42.34	45.24	16.5	70	65.54	55.39	25.50	102	29.87	23.20	40.0
7	31.61	35.09	8.5	39	53.94	44.66	16.5	71	20.01	67.28	25.50	103	42.34	22.33	37.0
8	42.34	3.48	8.5	40	64.96	44.66	17.0	72	30.74	67.57	24.00	104	54.52	22.62	40.0
9	53.07	34.80	8.5	41	20.30	56.55	17.0	73	43.21	67.28	23.50	105	63.80	23.49	43.5
10	63.80	34.51	8.5	42	31.32	56.55	16.5	74	54.81	66.99	24.50	106	20.59	35.09	43.0
11	20.88	45.82	8.5	43	42.63	55.97	16.5	75	65.54	66.12	25.50	107	29.87	34.51	40.0
12	31.61	45.82	8.5	44	54.23	55.68	16.5	76	19.14	24.36	34.00	108	42.34	34.22	37.0
13	42.63	45.24	8.5	45	64.96	55.10	17.0	77	30.74	23.20	32.00	109	54.81	33.93	40.5
14	53.36	44.95	8.5	46	20.59	66.99	16.5	78	42.34	22.91	30.50	110	64.09	33.93	43.5
15	63.80	44.37	8.5	47	31.32	66.99	16.5	79	54.23	22.91	32.00	111	20.59	45.53	43.5
16	21.17	55.97	8.5	48	42.92	66.99	16.0	80	64.96	23.49	34.00	112	30.16	45.53	40.0
17	31.61	55.68	8.5	49	54.23	66.99	16.5	81	19.43	35.38	34.00	113	42.63	45.24	37.0
18	42.63	55.39	8.5	50	65.25	66.12	16.5	82	30.45	34.51	31.50	114	54.81	44.66	40.0
19	53.36	55.10	8.5	51	19.14	24.94	25.5	83	42.34	34.22	30.50	115	64.38	44.37	43.5
20	64.09	54.81	8.5	52	30.16	23.78	24.0	84	54.52	33.93	32.00	116	20.88	56.26	43.5
21	21.46	66.70	8.0	53	42.05	23.20	23.5	85	65.25	33.93	34.00	117	30.45	56.55	40.0
22	31.90	66.70	8.5	54	53.94	22.91	24.0	86	19.72	46.11	34.00	118	42.63	56.26	37.0
23	42.92	66.12	8.0	55	64.96	23.49	25.5	87	30.45	45.53	31.50	119	54.81	55.68	40.5
24	53.65	65.83	8.5	56	19.43	35.38	25.5	88	42.34	45.24	30.50	120	64.38	55.10	43.5
25	64.09	65.25	8.0	57	30.16	35.09	24.0	89	54.81	44.95	32.00	121	21.17	66.70	43.5
26	20.01	24.36	16.5	58	42.34	34.22	23.5	90	65.25	44.66	34.00	122	30.74	67.86	40.0
27	30.74	23.49	16.5	59	54.23	34.22	24.5	91	19.72	56.55	34.00	123	42.92	68.15	37.5
28	42.05	23.20	16.5	60	64.96	34.22	25.5	92	30.74	56.55	32.00	124	54.81	66.99	40.5
29	53.65	23.20	16.5	61	19.43	45.82	25.5	93	42.63	56.55	30.50	125	64.67	65.83	44.0
30	64.67	23.20	16.5	62	30.16	45.53	24.0	94	54.81	55.97	32.00				
31	20.01	34.80	16.5	63	42.63	45.53	23.5	95	65.25	55.39	34.00				
32	30.74	34.51	16.5	64	54.52	44.95	24.5	96	20.01	66.99	34.00				

変形形状（高さ 35[mm]変形）

No.	X	Y	Z
1	19.72	24.07	7.50
2	30.45	23.49	7.50
3	42.34	22.91	7.50
4	54.23	23.20	7.50
5	65.25	23.20	7.50
6	18.85	35.09	7.50
7	30.16	34.51	7.50
8	42.34	33.93	7.50
9	54.23	34.22	7.50
10	65.54	33.93	7.50
11	18.85	45.82	8.00
12	30.16	45.82	8.00
13	42.63	45.24	7.50
14	54.52	44.95	7.50
15	65.83	44.37	8.00
16	19.14	56.26	8.00
17	30.45	56.26	7.50
18	42.63	56.26	7.50
19	54.81	55.68	7.50
20	65.83	55.10	7.50
21	19.72	67.57	7.50
22	30.74	68.15	7.50
23	42.92	67.57	7.50
24	54.81	66.99	7.50
25	65.83	66.12	7.50
26	17.11	23.20	15.50
27	29.00	21.75	14.50
28	42.05	20.88	13.50
29	55.39	21.17	14.50
30	67.28	22.62	15.50
31	17.11	34.22	15.50
32	28.71	33.64	14.50

No.	X	Y	Z
33	42.34	33.06	14.0
34	55.68	33.06	14.5
35	67.57	33.35	15.5
36	17.40	45.82	15.5
37	29.00	45.53	14.5
38	42.63	44.95	14.0
39	55.68	44.66	14.5
40	67.86	44.66	15.5
41	17.40	57.42	15.5
42	29.29	57.42	14.5
43	42.63	57.13	14.0
44	55.97	56.55	14.5
45	67.86	55.68	15.5
46	17.40	68.15	15.5
47	29.29	68.73	14.5
48	42.63	69.02	13.5
49	55.97	68.15	14.5
50	67.86	66.70	15.5
51	16.53	23.49	23.5
52	28.13	21.75	21.0
53	42.34	20.30	19.0
54	55.97	20.88	21.0
55	67.57	22.04	23.5
56	16.82	34.80	23.5
57	27.84	33.93	21.0
58	42.34	33.06	19.0
59	56.26	33.06	21.0
60	67.57	33.35	23.5
61	16.82	45.82	23.5
62	27.84	45.82	21.0
63	42.92	45.24	19.5
64	56.84	44.95	21.0

No.	X	Y	Z
65	68.15	44.66	23.5
66	17.40	57.42	23.5
67	28.13	57.71	21.0
68	43.21	57.71	19.0
69	56.84	57.13	21.0
70	67.86	55.97	23.5
71	17.69	68.73	23.5
72	28.71	69.89	21.0
73	43.21	70.47	19.5
74	57.13	69.02	21.0
75	68.44	67.28	23.5
76	17.40	23.20	32.0
77	28.71	21.17	27.0
78	42.34	20.01	24.5
79	56.26	20.59	28.0
80	66.70	22.04	32.0
81	17.40	34.80	31.5
82	28.42	33.35	27.0
83	42.34	33.06	24.0
84	56.55	32.77	27.5
85	66.99	33.35	32.0
86	17.69	46.11	32.0
87	28.13	45.53	27.0
88	42.63	45.24	24.0
89	57.13	44.66	27.5
90	66.99	44.66	32.0
91	18.27	57.42	32.0
92	28.71	57.71	27.0
93	42.92	58.00	24.0
94	57.13	56.84	27.5
95	67.28	55.97	32.0
96	18.56	68.15	32.0

No.	X	Y	Z
97	29.00	70.18	27.5
98	42.92	70.76	24.5
99	57.13	69.02	27.5
100	67.28	66.70	32.0
101	20.59	23.49	40.5
102	28.42	21.46	34.5
103	42.63	19.14	29.0
104	55.68	20.88	35.0
105	63.80	22.33	41.0
106	20.59	34.51	40.5
107	28.71	33.64	34.5
108	42.63	32.77	28.5
109	55.97	33.06	35.0
110	64.09	33.35	40.5
111	20.88	45.53	40.5
112	28.71	45.53	34.5
113	42.63	44.95	28.5
114	56.55	44.66	35.5
115	64.09	44.37	40.5
116	21.46	56.84	40.5
117	29.00	57.13	34.5
118	42.92	57.13	28.5
119	56.55	56.55	35.0
120	64.38	55.39	40.5
121	21.75	67.57	41.0
122	29.58	69.60	35.0
123	43.21	70.47	29.0
124	56.26	68.73	35.5
125	64.38	66.41	41.0

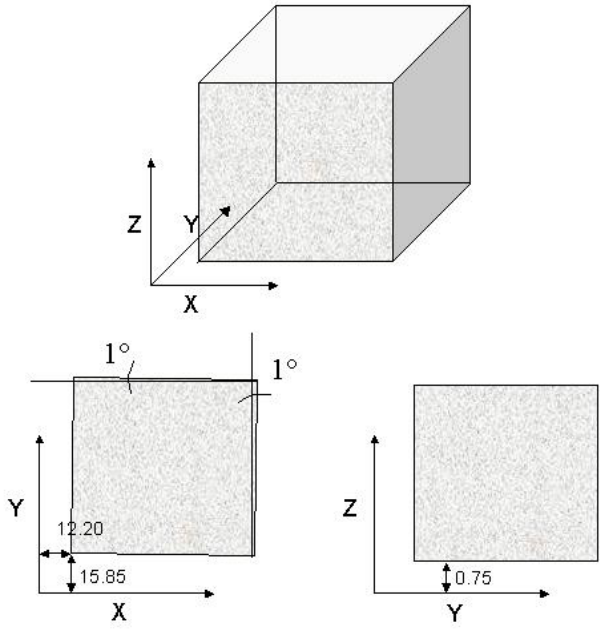

Fig 19　粘弾性物体初期位置

4．終わりに

本受託試験では，和歌山県工業技術センターが所有している産業用 CT スキャナを用い，外部から粘弾性物体に応力を加えた時の内部変形を計測した．

人肌ゲルによって作成した粘弾性物体を作成し，物体の内部に金属のマーカーを等間隔に配置した．

その物体に外部から強制変位をかけた状態で，産業用 CT スキャナを用いて内部変形を 3 次元的に計測した.

第4章　柔軟物の適応的モデリング

4.1　緒言

本章では柔軟物の適応的なモデリング手法について述べる．柔軟物の変形モデルにおいて，メッシュを細かくするとモデルの表現力と精度は向上するが，計算時間を多く要する．メッシュが粗いと計算時間は短縮できるが，モデルの表現力と精度が低下する．モデルの精度と計算時間を両立させるためには，一様なメッシュではなく，必要に応じてメッシュの粗密を変化させる適応的なモデリング手法が望まれる．

アダプティブメッシュは，モデルの粗密を制御するために操作中の力学量を評価し，メッシュの粗密を適応的に変化させる手法である．アダプティブメッシュでは，力学量の変化が大きい部分ではメッシュを細かく，変化が小さい部分ではメッシュを粗くする．本章ではアダプティブメッシュの構成法とその評価について述べる．また，階層的なメッシュにより，モデルの表現力と計算時間を両立させることができる．階層的なメッシュ表現では，表面と内部で粗密が異なるメッシュを採用し，モデルの表現力と計算時間を両立させる．階層的なメッシュ表現の構成法とその評価，特に力の再現性について述べる．柔軟物の変形には，位相が保たれる形状変化と切断や合併のような位相変化がある．アダプティブメッシュは，柔軟物の位相変化を表現することができる．この手法では，切断に伴い各ノードに作用する力を評価し，その評価を基にメッシュ構造の位相を変化させる．切断モデルの構成法とその評価について述べる．

4.2　アダプティブメッシュモデル

Bisection Refinement-Based Real-Time Adaptive Mesh Model For Deformation and Cutting of Soft Objects

(Invited Paper)

Hiromi T.Tanaka*, Yoshinori Tsujino*, Takahiro Kamada* Huynh Quang Huy Viet*
*Deparment of Human and Computer Intelligence, Ritsumeikan University
4F Creation Core Building, 1-1-1 Noji-higashi, Kusatsu, Shiga 525-8577, Japan
Email: hiromi@ci.ritsumei.ac.jp, huyviet@acm.org

***Abstract*— The subjects described in this paper are a real-time adaptive modeling method for deformable objects and an adaptive cutting method for 3D surface meshes.**

In the literature so far, adaptive models with high resolution representations at regions of high deformation have not been investigated. In this paper we propose a new method for real-time modeling of soft objects, of which high resolutions dynamically adapt to the regions of high deformation. In order to reduce the computational cost in comparison with the previous methods we use the bisection refinement algorithm. The experimental results show the effectiveness of the proposed method.

The cutting operation of 3D surface meshes plays an important role in surgery simulators. One of the important requirements for surgical simulators is the visual reality. We propose a new strategy for cutting on surface mesh: refinement and separate strategy consisting of the refinement followed by the separation of the refined mesh element. Since the advantage of the low computational cost, the bisection refinement method is utilized for the refinement process. The proposed strategy gives the faithful representation of the interaction path.

Keywords: **Deformable Objects, Adaptive Bisection Refinement, Mass-Spring Model, Surgical Simulation, Cutting Simulation**

I. INTRODUCTION

The real-time interactive models and simulations of behaviors of deformable objects play important roles in several fields such as robotics, computer graphics, CAD, computer aided surgery. In mesh-based representation of a given object, the preciseness in representing is related to the number of its cells which is called the resolution of the mesh. To control the computational time for modeling, the concept of multi-resolution model have been introduced [1], [2], [3], [4], [5], [6]. Multi-resolution models are the models that represent objects and their behaviors at different levels of resolution. The main advantage of a multi-resolution model is in reducing the computational cost by way of reducing the data for modeling in any place that low resolution representation is appropriate.

Throughout a simulation, to obtain a realistic behavior, different regions of interest in the model of an object might require to be represented by a high resolution and hence need to be refined. The regions of interest have been classified as: regions of contact, regions of high deformation and regions of high curvature.

There are two approaches that have been used for refinement a mesh: the approach based on the known Delaunay algorithm [7] and the approach based on the longest-side bisection algorithms [8], [9], [10], [11], [12]. The second approach guarantees the generation of good-quality of surface triangulation and volume tetrahedralization with linear time complexity, comparing to the computational cost of O(NlogN) of that of the first approach.

In [6], [3] the models for real time deformation of soft objects with high resolution at regions of contact have been proposed, the Delaunay algorithms have been used for mesh refinement. However in the literature so far, adaptive models with high resolution representation at regions of high deformation have not been investigated.

In this paper we propose a new method for real-time adaptive modeling of soft object with high resolutions for regions of high deformation. In order to reduce the computational cost in comparison with the previous methods we use the bisection refinement algorithm proposed in the preceding researches [8], [9], [10].The experimental results show the effectiveness of the proposed method.

Surgical simulators have been developed to create environments to help train physicians in learning skills of surgical operations at many research centers. The virtual cutting operation plays an important role in surgery simulators. The virtual cutting methods can be divided into two categories: (i) volume cutting method that consists of cutting methods on a tetrahedral mesh and (ii) surface cutting method that consists of cutting methods on a 3D surface mesh. One of the important requirements for cutting methods is the issue of accuracy representation of the interaction path of a surgical tool.

In addition the cutting techniques may also be classified into two major categories based on the implementation of a cutting operation; those that remove intersected meshes [13] and those that re-mesh intersected meshes [14], [15], [16], [17], [18], [19], [20]. The methods of the first category simply dismiss mesh elements that intersect the cutting tool; the

1–4244–0342–1/06/$20.00

methods of the second category recreate the path passed over by the tool through the intersected mesh elements by way of re-meshing them. The methods of the second category have the disadvantage of the supplemental cost for computing the intersection path but provide a good visual representation of the path passed over by the cutting tool. In order to have the accuracy representation of the intersection path without considerably scarifying the cost of computation of deformation, there is a strategy proposed and implemented on tetrahedral meshes: refinement and remove strategy [21]. This strategy composes of the refinement followed by the elimination of the mesh elements (tetrahedral) on the surface cut. Despite the fact that the sizes of removed mesh elements are small due to the previous mesh refinement process, the approach still has the drawback of creating non-smooth cuts, and hence are still not appropriate for a realistic simulator. Moreover, there are not the implementations of this strategy on surface meshes.

We propose a new strategy for cutting on surface mesh: refinement and separate strategy consisting of the refinement followed by the separation of the refined mesh element. Since the advantage of the low computational cost (linear time complexity comparing to $O(NlogN)$ time complexity of Delaunay refinement methods), the longest-edge refinement method [11] is utilized for the refinement process. The proposed strategy gives the faithful representation of the interaction path in comparing with the conventional methods. In addition the proposed strategy also allows the feasibility of haptic rendering in levels of detail and maintaining the high haptic update rates.

The remainder of the article is organized as follows: next section reviews the bisection refinement algorithm. Section 3 presents the method for adaptive modeling the deformation of a soft object with high resolution for regions of high deformation. Section 4 details the data structure and the adaptive cutting algorithm for 3D surface meshes. Section 5 describes experimental results and discussions. Finally section 6 is devoted for conclusions and future works.

II. Tetrahedral Mesh Bisection Refinement

We have developed a parallel algorithm of adaptive mesh generation that recursively bisects tetrahedral elements by increasing the number of mesh nodes according to local volume properties, such as orientation and curvatures of isosurfaces, until the entire volume has been approximated within a specified level of view-invariant accuracy. We summarize the algorithm in this section. The details of the algorithm are described in [8], [9], [10]. We apply this algorithm for simulation of soft object in adaptive resolution model, as will be presented in next section.

A. Recursive Binary Subdivision

The algorithm for constructing the hierarchical representation is based on a stepwise refinement of an initially given mesh. Given accuracy criteria, binary subdivision of the parent tetrahedron T_p occurs when the accuracy criteria, Acc_Thresh, is violated for any six edges of T_p. The subdivision of T_p into two left and right tetrahedron, T_l and T_r, occurs by the creation of a new node, M, the middle point of the base edge $E(=\overrightarrow{P_1P_2})$ of maximum length, followed by initialization of M with the local properties, i.e., the field value, orientation, curvatures of an isosurface containing M. Then, the violation of Acc_Thresh is recursively evaluated for each T_l and T_r independently.

B. Tetrahedral Primitives

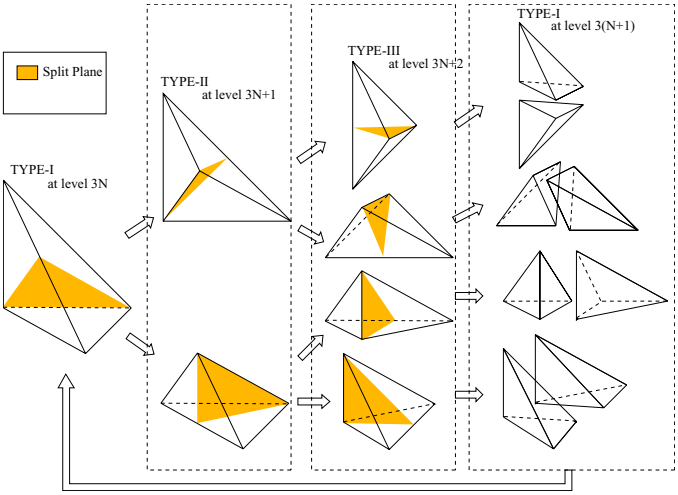

Fig. 1. Cyclic subdivision of a tetrahedron into TYPE-I, TYPE-II and TYPE-III primitives

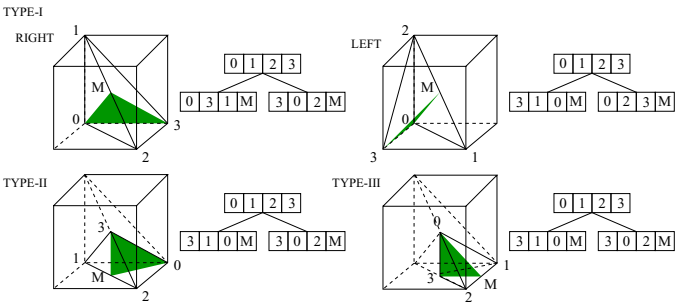

Fig. 2. Recursive definition of T_l and T_r for three primitives

In recursive binary-subdivision, only three tetrahedral primitives including mirror-symmetry, TYPE-I, TYPE-II, TYPE-III, are generated at level 3N,3N+1,3N+2,respectively, as shown in Fig. 1. Fig. 2 shows recursive definitions of T_l and T_r using the parent node (P_0,P_1,P_2,P_3) and M for TYPE-I, TYPE-II, TYPE-III. As Fig. 1 shows three successive subdivision of a parent tetrahedron T_p of TYPE-I at level 3N, generate the same type of great-ground children of TYPE-I cyclically at level 3(N+1) with each edge length and its volume decreased by 2 and by 8 respectively.

Face shapes of TYPE-I, TYPE-II, TYPE-III are either an isosceles triangle or a right triangle. With ratio of maxim to minimum edge length $\sqrt{3}$ at TYPE-I, $2\sqrt{2}/\sqrt{3}$ at TYPE-II, 2 at TYPE-III, respectively. This binary tetrahedrization using the middle points thus satisfies the equi-angular requirement.

Another advantage of the binary tetrahedrization is that it provides a more continuous level of volume approximation, because a tree with fewer descendants has more levels of approximation for a given range of volume variation.

C. Binary Subdivision Algorithm

Above steps for recursive binary subdivision of tetrahedron are summarized in the following pseudo code.

Procedure Divide_Tetrahedron(T_p,Acc_Thresh)
begin
*Step 1: (*Collect subdivision requests from neighbors for crack handling discontinuities *)*
If Neighbor_Require_for_Subdivision(T_p,Acc_Thresh) then require for subdivision of T_p;
Step 2: (Neighbors require for subdivision of Tp*)*
Divide a parent tetrahedron T_p into T_l and T_r and process them independently
*Step 2.1: (*Initialize T_l and T_r using the parent nodes (P_0, P_1, P_2, P_3) of T_p and M *)*
Step 2.2: (Recursive Subdivision of T_l and T_r *)*
Divide_Tetrahedron(T_l,Acc_Thresh);
Divide_Tetrahedron(T_r,Acc_Thresh);
end

At each recursion, the volume of every tetrahedron decreases by 2, therefore the upper bound of recursion n_{max} is given as,

$$n_{max} \leq \log_2(InitCubeSize^3) \tag{1}$$

where $InitCubeSize$ is the edge length of an initial mesh element,i.e InitCubicCell.

III. Adaptive Volumetric Mass-Spring Model

The mass-spring models comprising mass node, springs and dampers for representing deformation are widely applied because of the effectiveness in computation and the simplicity in implementation. However, in the large mass-spring models computation for deformation which covers the entire nodes of the object makes the real-time simulation difficult. Therefore combining locally refinement methods with mass-spring models have been utilized to reduce the cost of computation. This section presents the model that allows the automatic adaptation of the resolution at regions of high deformation.

A. Regions of High Deformation

In order to have realistic behaviour, the regions of interest should be refined during a simulation. In this research we focus on the regions of high deformation due to bending in a deformation process. In a deformation process of an object modeled by a tetrahedral mesh, the regions of high deformation can be characterized by a high local rate of change of the edge's length with its initial length in a tetrahedron:

$$\frac{L}{L_{init}} > T_c \tag{2}$$

In other words the regions of high deformation are tetrahedrons of which the rate of change of the edge's length exceed a criterion T_c. We use the bisection algorithm mentioned in the previous section for refinement in the regions of high deformation.

B. The Parameters of Mass-Spring System

While refining a mass-spring mesh it is necessary to supplement extra masses, springs and dampers. In order to guarantee the consistency of the behavior at different resolutions, a methodology for assigning mass values, spring and damper parameters have been proposed in [22], [6]. Given a material density D the mass value m_i of each vertex i according to the volume V_j of its adjacent tetrahedron T_j is as follows:

$$m = \frac{D\Sigma_j V_j}{4}, \tag{3}$$

Let E be the material elastic modulus, if L_{init} is a resting length of the spring/edge of a tetrahedral, the stiffness value of edge e is obtained by summing all of the contributions of the tetrahedron V_j incident on e:

$$k = \frac{E\Sigma_j V_j}{L_{init}^2} \tag{4}$$

The damper value of an edge e linking a mass m_i with mass m_j is given as follows [6]:

$$c = \frac{2\sqrt{k(m_i + m_j)}}{L_{init}} \tag{5}$$

where k is the stiffness value of the edge e.

IV. Adaptive Cutting Method for 3D Surface Meshes

A. Backward Longest-Edge Refinement Algorithm

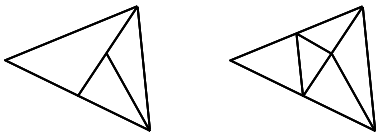

Fig. 3. Non-conforming mesh and conforming mesh

As a preliminary for presenting the proposed method, in this section we introduce the backward longest-edge refinement algorithm of Rivara [11] for triangular mesh refinement. The requirement of a refinement of a mesh is to satisfy the main properties: conforming, well shaped and smooth. A conforming mesh is a mesh without any "T-junctions". T junction is a non-conforming point which is defined as an interior point of an edge of one triangle and common vertex of two other adjoin triangles. Rivara proposed the backward longest-edge bisection refinement algorithm. The method only bisects along the longest-edge of a triangle; this guarantees the construction of non-degenerate and smooth irregular triangulations whose

geometrical properties only depend on the initial mesh. In order to maintain a conforming mesh, the local refinement of a given triangle involves refinement of the triangle itself and refinement of its longest edge neighbors.

Longest-side propagation path is a concept utilized in the backward longest-edge refinement algorithm. It is defined as follows: For any triangle t_0 of any conforming triangulation T, the longest-edge propagation path of t_0 will be the ordered list of all the triangles $t_0, t_1, t_2, ...t_{n-1}, t_n$, such that t_i is the neighbor triangle of t_{i-1}, by the longest-edge of t_{i-1}, for $i = 1, 2, ..n$. The longest-edge propagation path pf triangle t_0 is denoted as $LSPP(t_0)$.

Figure 4 explains the backward longest-edge refinement algorithm: Fig. 4a gives the initial triangulation; Fig. 4b gives the first step of the process; Fig. 4c gives the second step in the process and Fig. 4d gives the final triangulation.

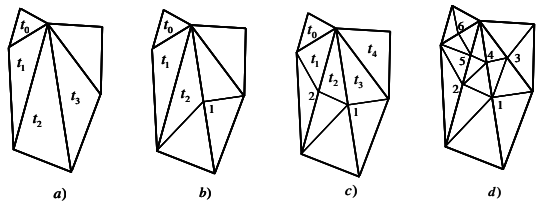

Fig. 4. Backward longest-edge bisection of triangle t_0

Figure 5 shows the backward longest-edge refinement algorithm. We utilize this algorithm to develop an algorithm for cutting on 3D surface mesh.

- **Backward-longest-edge-refinement** (T)
  - Sign all triangles which have unacceptable size and add them to T_0
  - i=0
  - **White** T_i is not empty **Do**
    - Run BackwardLongestEdgeBisection(t) for all triangles t in T_i
    - i=i+1
    - Sign all triangles which have unacceptable size and add them to T_i
- **Backward-longest-size-bisection** (t)
  - **While** t remains without being bisected **Do**
    - Find the LSPP(t)
    - **If** t*, the last triangle of the **LSPP**(t) , is a terminal boundary triangle **Then** bisect t*
    - **Else** bisect the (last) pair of terminal triangles of the LSPP(t)
- **LEPP**(t)
  - L=**null**
  - i=1
  - L[i]=t
  - **If** t has a neighbor t_{nb} on its longest edge **Then**
    - L[i]= t_{nb}
    - WHILE L[i] has a longest edge neighbor different from L[i-1] Do
      - Let t_{nb} be the longest edge neighbor of L[i-1]
      - i=i+1
      - L[i]= t_{nb}
  - **Return** L

Fig. 5. Backward longest-edge refinement algorithm

B. Data structure of 3D surface mass-spring mesh

The objects of the surgical simulation are represented by 3D surface meshes. The surface mesh of the object can be taken from laser scanner. The VRML output file of a laser scanner is used in a data structure based on winged-edge data structure, which includes the physical parameters of a damped mass-spring model. Figure 2 shows a diagram of the data structure. The points in diagram is the vertices, the bars are winged edges which have the functionality of a damped spring. The data which is stored at each vertices are their 3D coordinates, the value of mass and the information of an edge adjacent to vertex, the data which is stored at each edge are the start of node, the end of node of vertex, the parameters of a damper and a spring, the previous edge for left face, the next edge for left face. This data structure allows quick computation of finding the adjacent triangles for cutting algorithm, and performing of deformation.

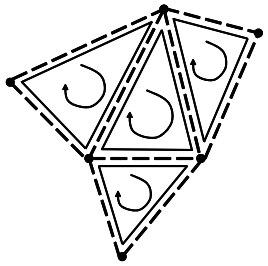

Fig. 6. The Winged Edge Data Structure for Mass-Spring Mesh

C. Cutting Algorithm

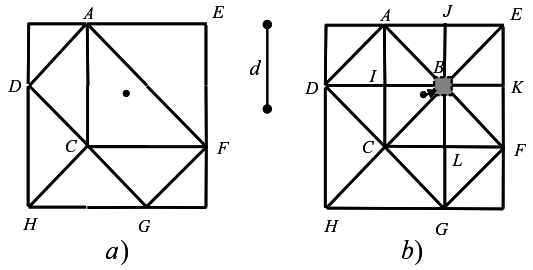

Fig. 7. Initial interacting point.

There are different approaches for changing the topology of an object such as destroying the mesh elements or dividing them. In our proposed method, to yield accuracy representation of cutting paths, instead of simple dividing the triangles (the mesh elements), we refine them by subdividing into smaller triangles using the longest-edge refinement algorithm mentioned in the previous section. The virtual cut is performed by way of separating the subdivided smaller triangles.

At first the triangle that is collided by the surgical tool is refined by using the backward longest-edge refinement algorithm mentioned in previous section, as showed in the Fig. 7b. The vertex that is nearest the colliding point is considered as the initial vertex for performing cutting.

Suppose that a virtual cut is being carried out at a vertex, we call this vertex as the reference vertex, the cut is performed by repetition of the following steps:

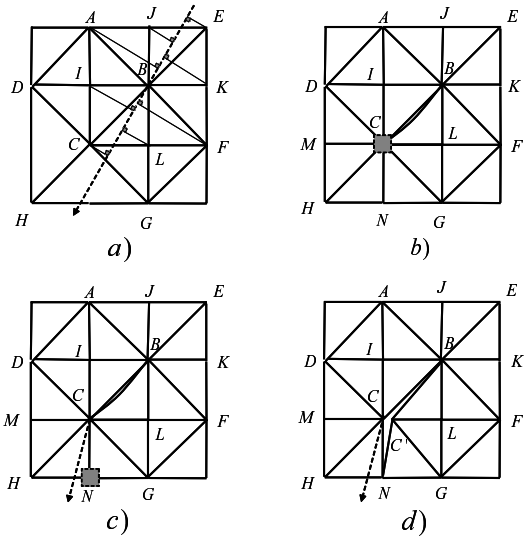

Fig. 8. Remeshing and making new point in a cutting process.

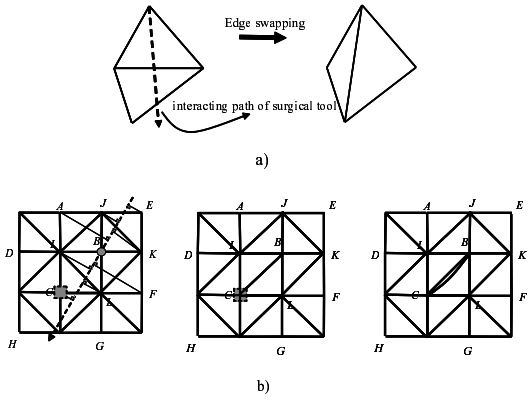

Fig. 9. Swapping an edge in a cutting process.

1. Finding the next vertex in cutting path: The next vertex is the vertex which is adjacent to the reference vertex and has the closest distance toward the direction of the motion of a surgical tool. The edge linking the reference vertex to the next vertex is called reference edge. Figure 8a shows how to choose the next vertex.

2. Changing the topology: The triangles sharing the next vertex from the reference vertex in cutting path are refined by the longest-edge refinement algorithm until the longest-edge l of the subdivided smaller triangles is satisfied the requirement of $d/2 < l < d$, where d is a predefined distance. Notice that the requirement of $l > d/2$ is to assure the termination for a refinement process. Figure 8b. gives an illustration a process of refinement of the triangles sharing the next vertex.

3. Changing the adjacent information of two triangles along the cutting path: The reference vertex is duplicated and the adjacent information of two triangles sharing the reference vertex is updated as not adjacent. Figure 8c and d clarifies this step when considering the vertex C as a reference vertex.

In the case that the next vertex is not belong the same triangle of the reference vertex and the edge which is shared by the two triangles is the longest edge as shown Fig. 9a, this edge is swapped so as the next vertex is connected with the reference vertex by an edge, and the cutting process is continued as described in Step 2 and Step 3 (see Fig. 9b).

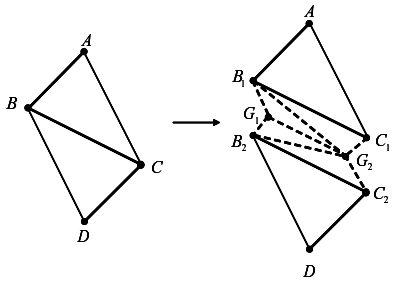

Fig. 10. Groove Generation

We described the algorithm for cutting on a 3D triangle mesh, we also need another algorithm to generate the groove for a cutting path. As shown in Fig. 10, when the triangles ABC and BCD are divided and the vertices V_1, V_2, V_3, V_4 are created, the bottom of the groove is generated at the tip positions of the cutting tool G_1 and G_2.

V. Experimental Results

A. Experimental Results on the Adaptive Deformable Model

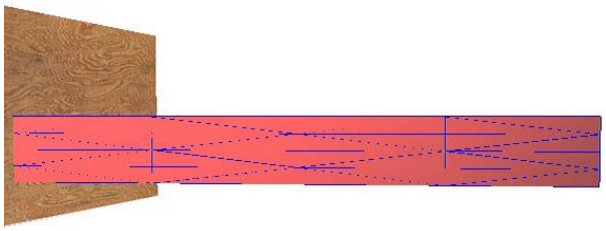

(a)Low resolution model

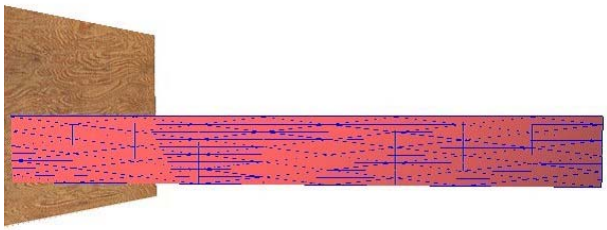

(b)High resolution model

Fig. 11. The initial shape of a cuboid object.

Figure 11 shows a cuboid object modeled by tetrahedral meshes. One end of the object is fixed and the other end is free. Figure11(a) shows a low resolution model and Fig.11(b) shows a high resolution model. We examine the deformation of the object in an adaptive resolution model in comparison with the low and high resolution models. The object is deformed by

a constant force perpendicular to the axis direction of the object at the right end. In the experiment the elastic modulus E is set to $5.0 \times 10^4[Pa]$ and the density is set to $1.0 \times 10^2[kg/m^3]$.

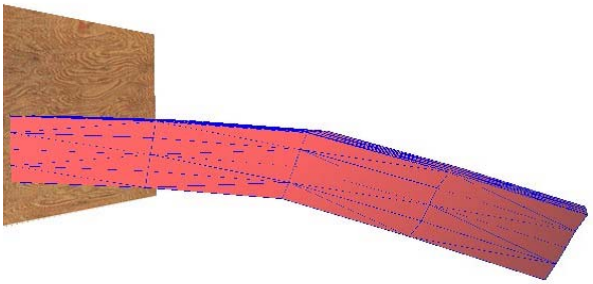

(a)Low resolution model

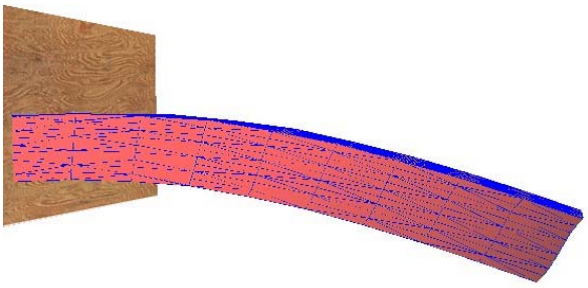

(b)High resolution model

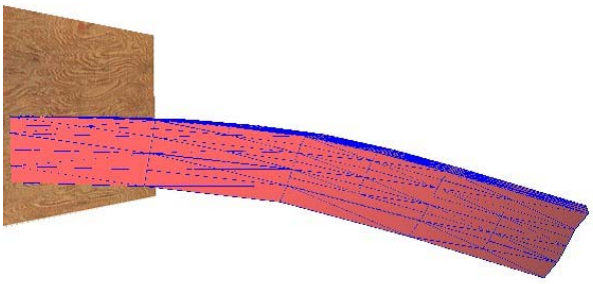

(c)Adaptive resolution model

Fig. 12. The deformation states in low, high and adaptive resolution model.

Figure 12(a) and (b) show the deformed shape of the object in low and high resolution models. As predicted, the deformed shape of the object in high resolution model is smooth and on the other side in low resolution model, that of the object is rough.

We apply the proposed adaptive resolution model as mentioned in Sect.III for the object which is initially modeled in the low resolution identical to the resolution of the model showed in the Fig. 12(a). During the deformation process, the regions of high deformation in the model are gradually refined by the bisection refinement algorithm presented in Sect.II. In this experiment, the regions of high deformation is defined by the criterion $T_c = 1.05$. A tetrahedron in the regions of high deformation is refined to 1/8 of its initial volume. Figure 12(c) shows the deformed shape of the object in the adaptive resolution model. Visually it is quite similar to the deformed shape in the high resolution model. We almost cannot recognize the difference in the shapes.

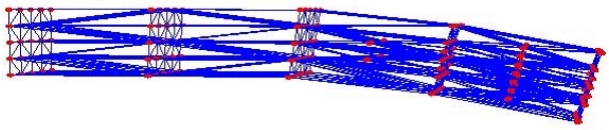

(c-1)

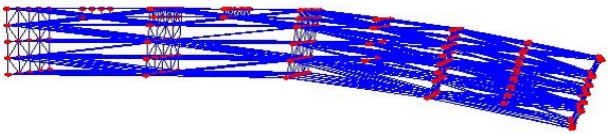

(c-2)

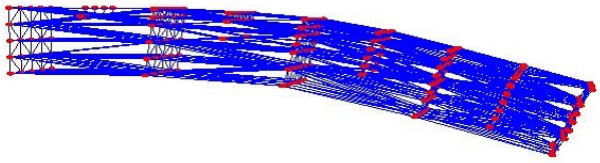

(c-3)

Fig. 13. The intermediate deformation states in the adaptive resolution model.

Figure 13 show the intermediate states in the deformation process of the above adaptive resolution model. The mesh is gradually refined at the regions of high deformation.

TABLE I

THE NUMBER OF MESH ELEMENTS

Resolution Model	Node Number	Tetrahedron Number
Low	125	384
High	1000	4374
Adaptive	299	1048

TableI shows the number of nodes and tetrahedron in the adaptive resolution model in comparison with the low and high resolution models.

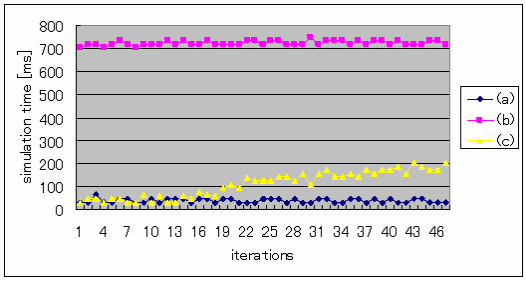

Fig. 14. The comparison of computational time in low, high and adaptive models.

Figure14 shows diagram of the computational time per iteration for low, high and adaptive resolution model. It shows that the computational time varies among the resolution model.

It stays high for the high resolution model, low for the low resolution model and is gradually increasing for the adaptive resolution model in corresponding to high deformation states. Despite the time consumption in the refinement process, the computational time of the adaptive resolution model stay quite low in comparison with that of high resolution model throughout the deformation process.

B. Experimental Results of the Adaptive Cutting Method

Regarding with the issue of accuracy representation of the interaction path of a surgical tool, it is difficult to compare the proposed method which is based on the refinement and separate strategy with that of the refinement and removal strategy. However, in any situations, the fact that separating process of the refinement and separate strategy do not dismiss mesh elements definitely increases the accuracy much more than that of refinement and removal strategy. Here we show the results of the proposed method. We build the system as showed in Fig. 15 to implement the proposed method. The handling of the virtual object in 3D virtual space is performed by using the haptic interface device Phantom. The visual result is represented realistically in the X3D display screen.

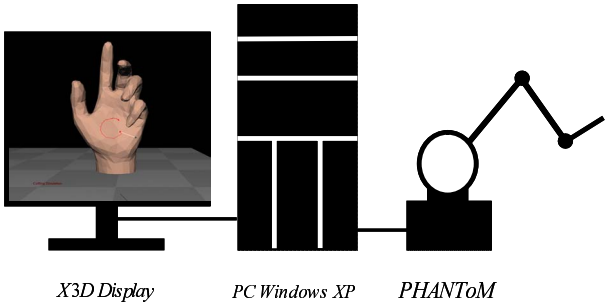

Fig. 15. System diagram.

Figure 16 shows the wire frame representation of a virtual cutting of a hand which is model by the 3D surface triangle mesh: Fig.16a gives the original representation of the hand and Fig.16b gives the result of the virtual cutting.

Fig.17a show the enlargement of the result, the cutting path appears delicately; the very small shakes of the hand handling the Phantom arm are captured and expressed faithfully in zigzags. This show the effectiveness of the proposed method in accurate representation of the motion of the surgical tool. In fact if the friction force in hand surface is considered, the real motion of hand, which handles the Phantom arm, will become smooth. However, this does not affect the effectiveness of the proposed algorithm.

Fig.17b shows the result without using mesh refinement algorithm for the same motion of cutting tool of the previous experiment, the cutting path is far different from the motion of cutting tool (white line). In Fig.18, we show a result of cutting with groove generation.

VI. Conclusions

We propose a new method for realtime modeling of soft objects, of which high resolutions dynamically adapt to the regions of high deformation. In order to reduce the computational cost in comparison with the previous methods we use the bisection refinement algorithm. We also introduces a new virtual cutting method for accuracy representation of the motion of a surgical tool. The main contribution of the work is a real-time 3D surface cutting algorithm that cooperates with the longest-edge based local refinement algorithm for unstructured triangular meshes. The experiment results show the performance of the approach.

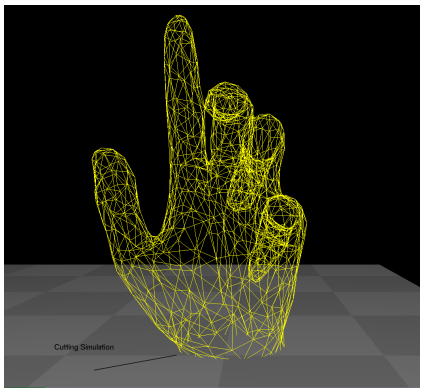

(a) Original 3D hand

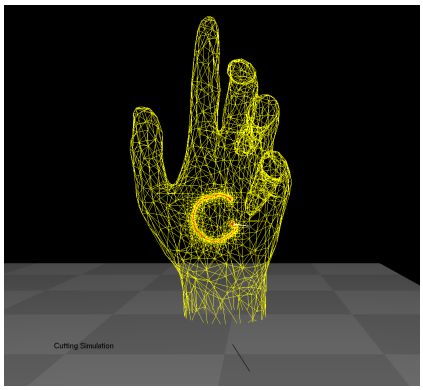

(b) A virtual cutting

Fig. 16. Wire frame representation.

References

[1] D. Hutchinson, M. Preston, and T. Hewitt, "Adaptive refinement for mass/spring simulations," in *Proceedings of the European workshop on Computer Animation and Simulation*, 1996, pp. 31–45.

[2] F. Ganovelli, P. Cignoni, and R. Scopigno, "Introducing multiresolution representation in deformable modeling," in *SCCG '99 Conference Proceedings*, Budmerice (Slovakia), April 1999, pp. 149–158.

[3] F. Ganovelli, P. Cignoni, C. Montani, and R. Scopigno, "A multiresolution model for soft objects supporting interactive cuts and lacerations." *Computer Graphics Forum*, vol. 19, no. 3, pp. 271–282, 2000.

[4] G. Debunne, M. Desbrun, M.-P. Cani, and A. Barr, "Adaptive simulation of soft bodies in real-time," in *Computer Animation*, May 2000, pp. 133–144.

[5] X. Wu, M. S. Downes, T. Goktekin, and F. Tendick, "Adaptive nonlinear finite elements for deformable body simulation using dynamic progressive meshes," in *Eurographics*, 2001, pp. 439–448.

[6] C. Paloc, F. Bello, R. Kitney, and A. Darzi, "Online multiresolution volumetric mass spring model for real time soft tissue deformation," in *Proceedings of the 5th International Conference on Medical Image Computing and Computer-Assisted Intervention*, 2002, pp. 219–226.

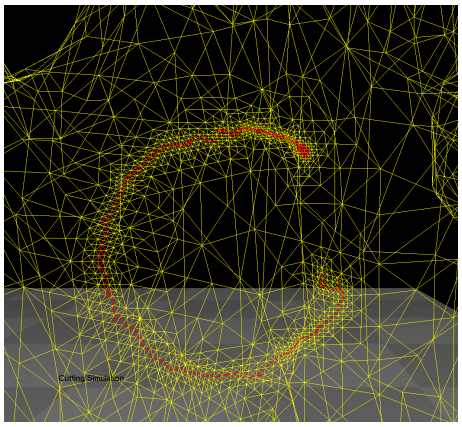

(a) Cutting with mesh refinement

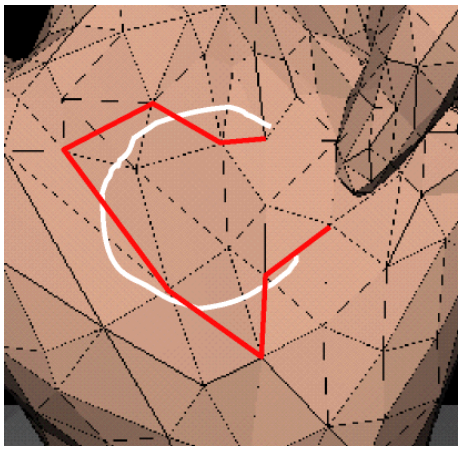

(b) Cutting without mesh refinement

Fig. 17. Comparison of the algorithm with and without mesh refinement.

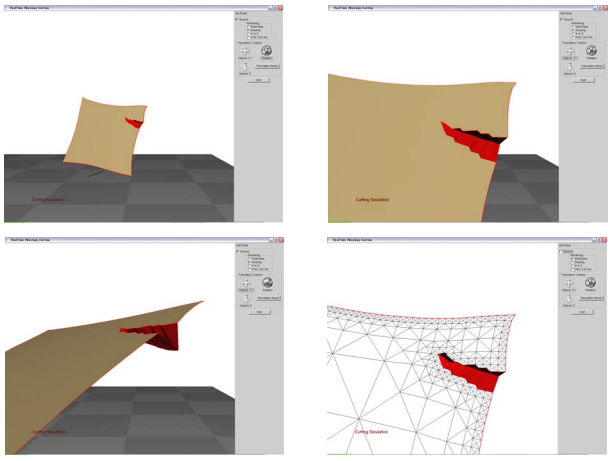

Fig. 18. Cut a groove on a surface

[7] J. Shewchuk, "Tetrahedral mesh generation by delaunay refinement," in *Proceedings of the Fourteenth Annual Symposium on Computational Geometry*, Minneapolis, Minnesota, 1998, pp. 86–95.

[8] H. T.Tanaka and F. Kishino, "Adaptive mesh generation for surface reconstruction: Parallel hierarchical triangulation without discontinuities," in *Proc. IEEE Conf. Computer Vision Pattern Recognition (CVPR93)*, New York City, 1993, pp. 88–94.

[9] H. T.Tanaka, "Accuracy-based sampling and reconstruction with adaptive meshes for parallel hierarchical triangulation," *Computer Vision and Image Understanding*, vol. 61, no. 3, pp. 335–350, 1995.

[10] H. T.Tanaka, Y. Takama, and H. Wakabayashi, "Accuracy-based sampling and reconstruction with adaptive grid for parallel hierarchical tetrahedrization," in *Proc. the 2003 Eurographics/IEEE TVCG Workshop on Volume graphics*, Tokyo, Japan, 2003, pp. 79–86.

[11] M.-C. Rivara, "New mathematical tools and techniques for the refinementand/or improvement of unstructured triangulations," in *5th International Meshing Roundtable*, 1996, pp. 77–86.

[12] J. M. Maubach, "Local bisection refinement for n - simplicial grids generated by reflection," *SIAM J. Scientific Computing*, vol. 16, 1995.

[13] S. Cotin, H. Delingette, and N. Ayache, "A hybrid elastic model for real-time cutting, deformations, and force feedback for surgery training and simulation." *The Visual Computer*, vol. 16, no. 7, pp. 437–452, 2000.

[14] C. D. Bruyns and S. Senger, "Interactive cutting of 3d surface meshes," *Computers & Graphics*, vol. 25, pp. 635–642, 2001.

[15] H.-W. Nienhuys and A. F. van der Stappen, "A surgery simulation supporting cuts and finite element deformation," in *Medical Image Computing and Computer-Assisted Intervention*, Utrecht, The Netherlands, 2001, pp. 153–160.

[16] C. Basdogan, "Simulation of instrument-tissue interactions and system integration," in *Medicine Meets Virtual Reality 2001*, 2001.

[17] D. Bielser, P. Glardon, M. Teschner, and M. Gross, "A state machine for real-time cutting of tetrahedral meshes," *Journal of Graphical Models*, vol. 66, no. 6, pp. 398–417, 2004.

[18] M. Harders, D. Steinemann, M. Gross, and G. Szekely, "A hybrid cutting approach for hysteroscopy simulation," in *Conference on Medical Image Computing and Computer-Assisted Intervention*, Palm Springs, USA, 2005.

[19] F. Ganovelli, P. Cignoni, C. Montani, and R. Scopigno, "Enabling cuts on multiresolution representation," *The Visual Computer*, vol. 17, no. 5, pp. 274–286, 2001.

[20] C. Mendoza and C. Laugier, "Simulating soft tissue cutting using finite element models," in *Proc. of the IEEE Int. Conf. on Robotics and Automation*, Taipei, Taiwan, 2003, pp. 1109–1114.

[21] C. Forest., H. Delingette, and N. Ayache, "Removing tetrahedra from manifold tetrahedralisation : application to real-time surgical simulation," *Medical Image Analysis*, vol. 9, no. 2, pp. 113–122, 2005.

[22] A. V. Gelder, "Approximate simulation of elastic membranes by triangulated spring meshes," *Journal of Graphics Tools*, vol. 3, no. 2, pp. 21–42, 1998.

[23] T. McInerney and D. Terzopoulos, "Deformable models in medical images analysis: a survey," 1996.

[24] J. Montagnat, H. Delingette, and N. Ayache, "A review of deformable surfaces: topology, geometry and deformation," *Image and Vision Computing*, vol. 19, no. 14, pp. 1023–1040, 2001.

[25] H. Nienhuys and A. Stappen, "A surgery simulation supporting cuts and finite element deformation," in *Proc. Fourth Int. Conf. on Med. Image Comput. and Computer-Assisted Intervention (MICCAI 2001)*, Utrecht, The Netherlands, 2001, pp. 145–152.

[26] ——, "Supporting cuts and finite element deformation in interactive surgery simulation," Utrecht University, Institute of Information and Computing Sciences, PO Box 80.089, 3508 TB, The Netherlands, Tech. Rep. UU-CS-2001-16, 2001.

[27] A. Tanaka, K. Hirota, and T. Kaneko, "Deforming and cutting operation with force sensation," *Journal of Robotics and Mechatronics*, vol. 12, no. 3, pp. 292–303, 2000.

[28] J. Shewchuk, *PhD thesis, Delaunay Refinement Mesh Generation*. Pittsburgh, Pennsylvania: School of Computer Science, Carnegie Mellon University, 1997.

[29] J. Ruppert, "A delaunay refinement algorithm for quality 2-dimensional mesh generation," *Journal of Algorithms*, vol. 18, no. 3, pp. 548–585, 1995.

[30] M. Desbrun, P. Schroder, and A. Barr, "Interactive animation of structured deformable objects," in *Graphics Interface*.

[31] H. D. Stephane Cotin and N. Ayache, "Real-time elastic deformations of soft tissues for surgery simulation," *IEEE Transactions on Visualization and Computer Graphics*, vol. 5, no. 1, pp. 62–73, 1999.

[32] M. Garland, "Multiresolution modeling: Survey and future opportunities," in *EUROGRAPHICS '99, State of the Art Report*.

[33] C. Paloc, F. Bello, R. Kitney, and A. Darzi, "Virtual reality surgical training and assessment system," in *Computer Assisted Radiology and Surgery*, 2001, pp. 207–212.

A Real-Time Dynamic Adaptive Deformable Mesh Model for soft objects based on bisection refinement and binary simplification algorithms

Yoshinori Tsujino, Huynh Quang Huy Viet, Hiromi T.Tanaka
Deparment of Human and Computer Intelligence, Ritsumeikan University, Japan

Abstract— **In the literature so far, adaptive models with high resolution representations at regions of high deformation have not been investigated. In this paper we propose a new method for real-time modeling of soft objects, of which high resolutions dynamically adapt to the regions of high deformation. In order to reduce the computational cost in comparison with the previous methods we use the bisection refinement algorithm. The experimental results show the effectiveness of the proposed method.**

Keywords: **Tetrahedral Meshes, Cracks, Adaptive Refinement, Binary Subdivision, Binary Simplification, Mass-Spring Model, Deformable Objects**

I. Introduction

The real-time interactive models and simulations of behaviors of deformable objects play important roles in several fields such as robotics, computer graphics, CAD, computer aided surgery. In mesh-based representation of a given object, the preciseness in representing is related to the number of its cells which is called the resolution of the mesh. To control the computational time for modeling, the concept of multi-resolution model have been introduced [1], [2], [3], [4], [5], [6]. Multi-resolution models are the models that represent objects and their behaviors at different levels of resolution. The main advantage of a multi-resolution model is in reducing the computational cost by way of reducing the data for modeling in any place that low resolution representation is appropriate.

Throughout a simulation, to obtain a realistic behavior, different regions of interest in the model of an object might require to be represented by a high resolution and hence need to be refined. The regions of interest have been classified as: regions of contact, regions of high deformation and regions of high curvature.

There are two approaches that have been used for refinement a mesh: the approach based on the known Delaunay algorithm [7] and the approach based on the longest-side bisection algorithms [8], [9], [10], [11], [12]. The second approach guarantees the generation of good-quality of surface triangulation and volume tetrahedralization with *linear time* complexity, comparing to the computational cost of O(NlogN) of that of the first approach.

In [6], [3] the models for real time deformation of soft objects with high resolution at regions of contact have been proposed, the Delaunay algorithms have been used for mesh refinement. However in the literature so far, adaptive models with high resolution representation at regions of high deformation have not been investigated.

In this paper we propose a new method for real-time adaptive modeling of soft object with high resolutions for regions of high deformation. In order to reduce the computational cost in comparison with the previous methods we use the bisection refinement algorithm proposed in the preceding researches [8], [9], [10]. The experimental results show the effectiveness of the proposed method.

The remainder of the article is organized as follows: next section reviews the bisection refinement algorithm. Section 3 presents the method for adaptive modeling the deformation of a soft object with high resolution for regions of high deformation. Section 4 describes experimental results and discussions. Finally section 5 is devoted for conclusions and future works.

II. Bisection Refinement-based Tetrahedral Adaptive Mesh

We first give an over view of the tetrahedral adaptive mesh, which had been developed for multi-resolution volume modeling [10], as shown in Figure 1. The mesh generation algorithm recursively bisects tetrahedra elements by increasing the number of mesh nodes according to local volume properties, such as the field value and its gradient, i.e., the orientation and curvatures of isosurfaces, until the entire volume has been approximated within a specified level of view-invariant accuracy.

A. Recursive Binary Subdivision

The algorithm for constructing the hierarchical representation is based on a stepwise refinement of an initially given grid. Given accuracy criteria, binary subdivision of the parent tetrahedron T_p occurs when the accuracy criteria, Acc_Thresh, is violated for any six edges of T_p. The subdivision of T_p into two left and right tetrahedron, T_l and T_r, occurs by the creation of a new node, M, the middle point of the base edge $E(= \overrightarrow{P_1P_2})$ of maximum length, followed by initialization of M with the local properties, such as the field value and its gradient, i.e., the orientation, curvatures of an isosurface containing M. Then, the violation of Acc_Thresh is recursively evaluated for each T_l and T_r independently.

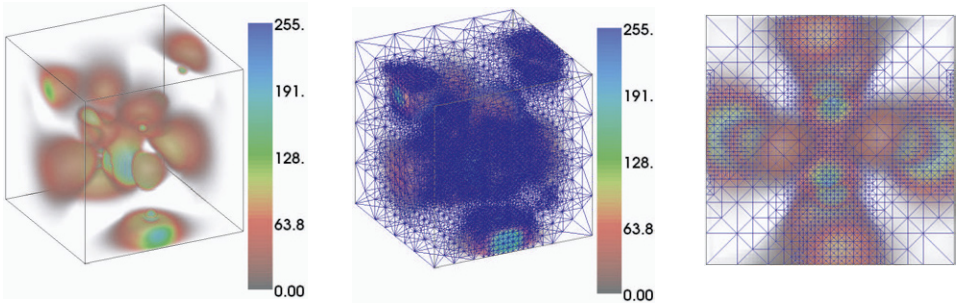

(a)input volume data (b)adaptive mesh (c)Projected (b) to YZ plane

Fig. 1. Tetrahedral adaptive mesh of volume data

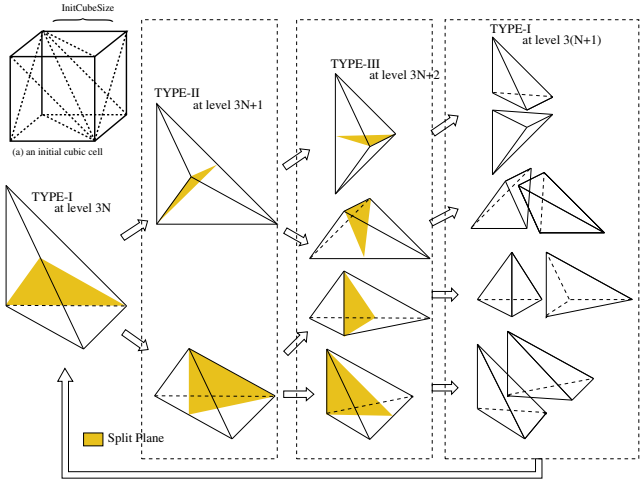

Fig. 2. Cyclic subdivision of a tetrahedron into TYPE-I, TYPE-II and TYPE-III primitives

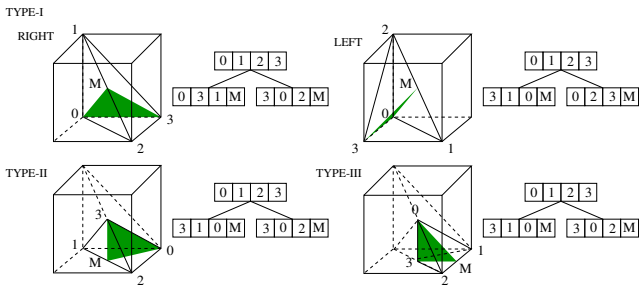

Fig. 3. Recursive definition of T_l and T_r for three primitives

B. Tetrahedral Primitives

In recursive binary-subdivision, only three tetrahedral primitives including mirror-symmetry, TYPE-I, TYPE-II, TYPE-III, are generated at level 3N,3N+1,3N+2,respectively, as shown in Fig. 2. Fig. 3 shows recursive definitions of T_l and T_r using the parent node (P_0,P_1,P_2,P_3) and M for TYPE-I, TYPE-II, TYPE-III. As Fig. 2 shows three successive subdivision of a parent tetrahedron T_p of TYPE-I at level 3N, generate the same type of great-ground children of TYPE-I cyclically at level 3(N+1) with each edge length and its volume decreased by 2 and by 8 respectively.

Face shapes of TYPE-I, TYPE-II, TYPE-III are either an isosceles triangle or a right triangle. With ratio of maxim to minimum edge length $\sqrt{3}$ at TYPE-I, $2\sqrt{2}/\sqrt{3}$ at TYPE-II, 2 at TYPE-III, respectively. This binary tetrahedrization using the middle points thus satisfies the equi-angular requirement. Another advantage of the binary tetrahedrization is that it provides a more continuous level of volume approximation, because a tree with fewer descendants has more levels of approximation for a given range of volume variation.

C. Crack Handling for Discontinuities

The major problem with adaptive subdivision techniques is that *cracks*,i.e., discontinuities, may arise if each tetrahedron is subdivided independently.

When there is a large field variation near the initial grid element, a crack may be formed along the boundary between the grid elements. This crack is caused by the unilateral subdivision of a grid element on one side of the large field variation. In order to avoid cracks between adjacent tetrahedron, we had developed a parallel algorithm that detects and preserves both C^0 and C^1 discontinuities of field values, without the formation of cracks. This crack handling algorithm collects field discontinuity information by recursively expanding the neighborhood of adjacent tetrahedra until the discontinuities are observed. The boundary reached by this recursive expansion defines the 3D region of reference for a grid element. This local definition of a *bounded* region of reference allows each grid element to be subdivided independently. Thus, the parallel computation of hierarchical tetrahedrization with no cracks is performed in bounded time and space.

III. Adaptive Volumetric Mass-Spring Model

The mass-spring models comprising mass node, springs and dampers for representing deformation are widely applied because of the effectiveness in computation and the simplicity in implementation. However, in the large mass-spring models computation for deformation which covers the entire nodes of the object makes the real-time simulation difficult. Therefore combining locally refinement methods with mass-spring models have been utilized to reduce the cost of computation. This section presents the model that

allows the automatic adaptation of the resolution at regions of high deformation.

A. Regions of High Deformation

Throughout a simulation process, it is necessary to refine different regions in order to have high precision for representing realistic behaviours, and to simplify the refined regions for fast computation of the simulation when the high precision is not required any more. The regions of interest has been classified as: Regions of contact, regions of high deformation and regions of high curvature. In this research we focus on the regions of high deformation due to bending in a deformation process. In a deformation process of an object modeled by a tetrahedral mesh, the regions of high deformation can be characterized by a high local change rate of the edge length with the initial edge length of a tetrahedron:

$$T = \frac{L}{L_{init}} \tag{1}$$

here, L is the length in the present status, L_{init} is the initial length.

In other words the regions of high deformation are tetrahedrons of which the change rate of the edge length T exceed a given criterion T_r. Since the tetrahedrons at the surface of a model directly effect the deformation, for reducing the computation cost, it is possible to define regions of high deformation as tetrahedrons at the surface or the boundary of a model that the change rate of the length of an edge exceed a given criterion.

B. Bisection Refinement

We use the bisection algorithm mentioned in the previous section for refining the regions of high deformation. In the bisection algorithm a tetrahedron is subdivided into two smaller tetrahedrons at the point of the base edge. The algorithm is easy to implement and moreover its computation complexity is linear time. The main problem with the bisection refinement is discontinuities or cracks. The crack handling algorithm is presented in detail in [9], [13], [10].

C. The Parameters of Mass-Spring System

While refining a mass-spring mesh it is necessary to supplement extra masses, springs and dampers. In order to guarantee the consistency of the behavior at different resolutions, a methodology for assigning mass values, spring and damper parameters have been proposed in [14], [6]. Given a material density D the mass value m_i of each vertex i according to the volume V_j of its adjacent tetrahedron T_j is as follows:

$$m = \frac{D\Sigma_j V_j}{4}, \tag{2}$$

Let E be the material elastic modulus, if L_{init} is a resting length of the spring/edge of a tetrahedral, the stiffness value of edge e is obtained by summing all of the contributions of the tetrahedron V_j incident on e:

$$k = \frac{E\Sigma_j V_j}{L_{init}^2} \tag{3}$$

The damper value of an edge e linking a mass m_i with mass m_j is given as follows [6]:

$$c = \frac{2\sqrt{k(m_i + m_j)}}{L_{init}} \tag{4}$$

where k is the stiffness value of the edge e.

In the binary subdivision, every tetrahedron is subdivided at the middle point of its base edge, i.e., the longest edge, we can associate a base edge L(n) after the nth subdivision with the bounding volume V(n) of a group of tetrahedra sharing L(n), which we call a diamond, as shown in Fig.4(a). If $L(n)$ is a diagonal edge inside a cubic cell at level n(=3N) then *V(n)* is the cubic cell itself consisting of six tetrahedra sharing $L(n)$. If $L(n)$ is a diagonal edge on a bounding face shared by adjacent cubic cell, then *V(n)* consists of 4 tetrahedron, two from its own cubic cell and other two from the adjacent cell. If, $L(n)$ is parallel to one of the X, Y, Z coordinate axes, then *V(n)* consists of eight tetrahedron from four adjacent cells sharing $L(n)$.

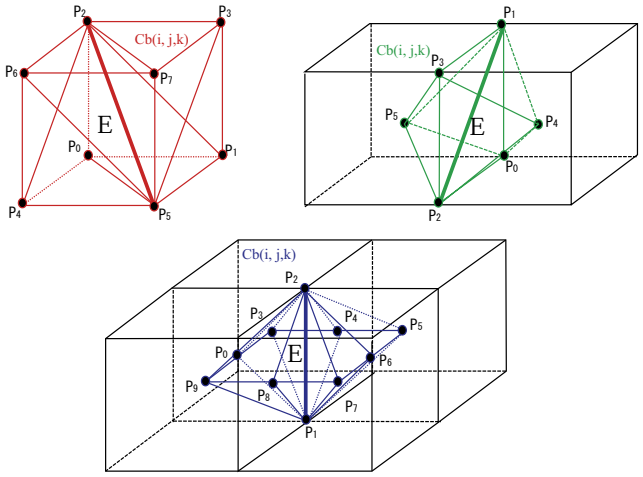

Fig. 4. The bounding volume of E at level n(=3N), n+1(=3N+1), and n+2(=3N+2)

Therefore at a division level n, the stiffness parameter $k(n)$ and damper parameter $c(n)$ of an edge e linking a mass m_i with mass m_j can be expressed as,

$$k(n) = \frac{EV(n)}{L(n)^2} \tag{5}$$

$$c(n) = \frac{2\sqrt{k(n)(m_i + m_j)}}{L(n)} \tag{6}$$

$$CubeSize(n) = 2^{-\lfloor \frac{n}{3} \rfloor} \times intCubeSize. \tag{7}$$

$$L(n) = A \times CubeSize(n). \tag{8}$$

$$V(n) = B \times CubeSize(n)^3. \tag{9}$$

where

$$A = \begin{cases} \sqrt{3} & if(n \ mod \ 3) == 0 \\ \sqrt{2} & if(n \ mod \ 3) == 1 \\ 1 & otherwise \end{cases} \quad (10)$$

$$B = \begin{cases} 1 & if(n \ mod \ 3) == 0 \\ \frac{1}{3} & otherwise \end{cases} \quad (11)$$

D. Binary Simplification

During a simulation, a region of high deformation can become a region of low deformation and hence it should be restored to its original resolution in order to reduce the computation cost. When an edge of a subdivided tetrahedron becomes shorter to a given criterion T_s, we perform a combination procedure to simplify the refined mesh. The refined tetrahedrons are gradually combined to original tetrahedrons as showed in the figure 5. To guarantee the consistency of the behavior at different resolutions, the mass, spring and damper parameters are calculated by the formulas mentioned in the previous section.

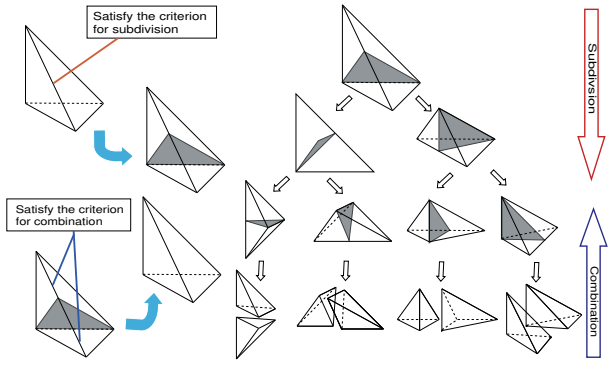

Fig. 5. Refinement and simplification processes

E. Time step control

In simulations the Runge-Kutta is used for solving the differential equations of mass-spring system. The choice of the time step depends on values of mass, spring, damper parameter and the density of the mesh. The maximum time step and minimum time step are parameters to ensure that the behaviour of the model is appropriate and real-time. These parameters are dependent upon the smallest edge length of the mesh [6]. In our work, the size control over the mesh elements to ensure the appropriate and real-time behaviour of the model is carried out by way of restraining the subdivision level in the bisection refinement algorithm.

IV. Experimental Results

A. On-the-go refinement and simplification in regions of interest

Figure 6 shows a cuboid object modeled by tetrahedral meshes. One end of the object is fixed and the other end is free. Figure 6(a) shows a low resolution model and Fig. 6(b) shows a high resolution model. We examine the deformation of the object in an adaptive resolution model in comparison with the low and high resolution models. The object is deformed by a constant force perpendicular to the axis direction of the object at the right end, and is released to return the original shape after a given time. In the experiment the elastic modulus E is set to $5.0 \times 10^4[Pa]$ and the density is set to $1.0 \times 10^2[kg/m^3]$.

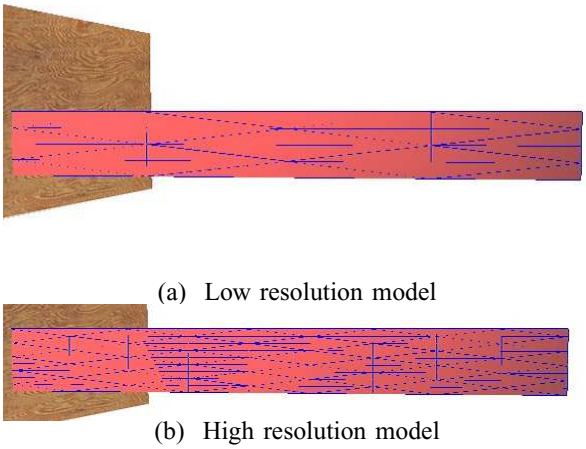

(a) Low resolution model

(b) High resolution model

Fig. 6. The initial shape of a cuboid object.

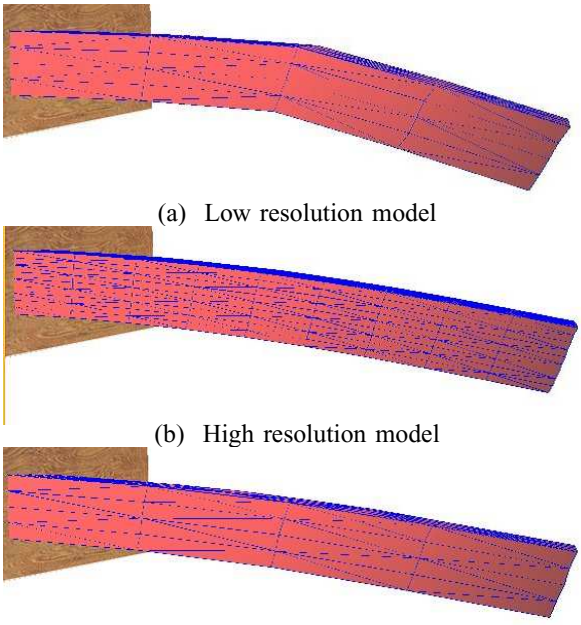

(a) Low resolution model

(b) High resolution model

(c) Adaptive resolution model

Fig. 7. The deformation states in low, high and adaptive resolution model.

Figure 7(a) and (b) show the deformed shape of the object in low and high resolution models. As predicted, in high resolution model the deformed shape of the object is realistic, and on the other side in low resolution model the deformed shape is rough.

We apply the proposed adaptive resolution model as mentioned in Sect.III for the object which is initially modeled

at the low resolution. During the deformation process, the regions of high deformation in the model are gradually refined by the bisection refinement algorithm presented in Sect.II. In this experiment, the regions of high deformation is defined by the criterion $T_c = 1.05$. A tetrahedron in the regions of high deformation is refined to 1/8 of its initial volume. Figure 7(c) shows the deformed shape of the object in the adaptive resolution model. Visually it is quite similar to the deformed shape in the high resolution model. We almost cannot recognize the difference in the shapes.

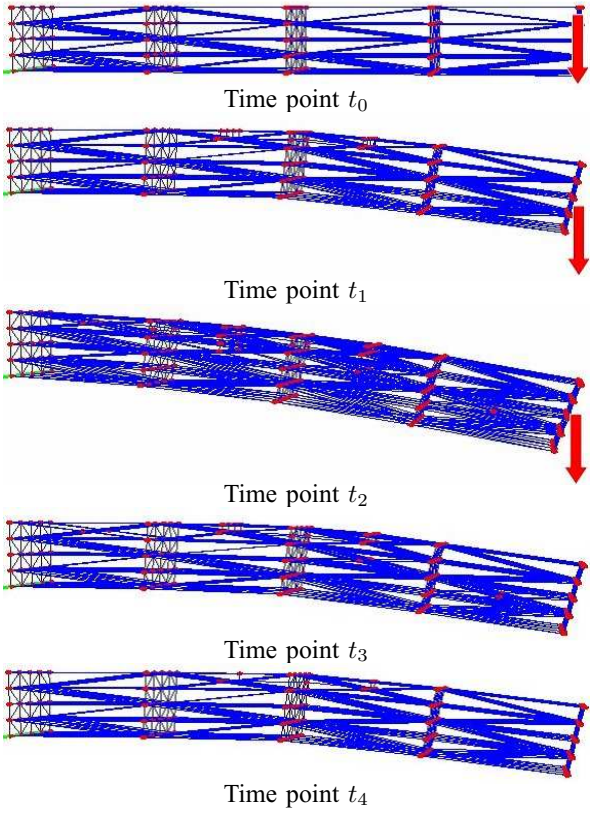

Fig. 8. The intermediate deformation states of the object in the adaptive resolution model.

Figure 8 show the intermediate states of the deformation process in the above adaptive resolution model. The time point t_2 is the time point that the object is released to return to the original shape. The mesh is gradually refined and then simplified at the regions of high deformation.

TABLE I
THE NUMBER OF MESH ELEMENTS

Resolution Model	Node Number	Tetrahedron Number
Low	125	384
High	1000	4374
Adaptive	299	1048

TableI shows the number of nodes and tetrahedrons at the time point t_2 (see Fig. 8) in the adaptive resolution model in comparison with the low and high resolution models.

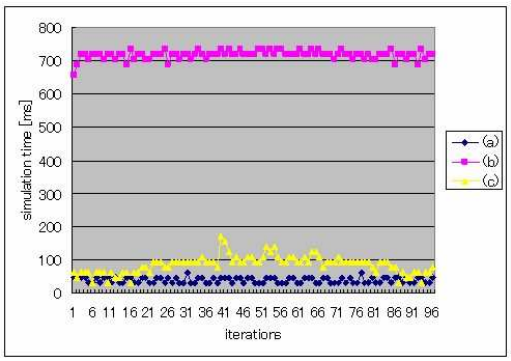

Fig. 9. The comparison of computational time in low, high and adaptive models. (a) Low-resolution. (b) High-resolution. (c) Adaptive-resolution

Figure 9 shows diagram of the computational time per iteration for low, high and adaptive resolution model. It shows that the computational time varies among the resolution models. It stays high for the high resolution model, low for the low resolution model and is gradually increasing for the adaptive resolution model in corresponding to high deformation states. Despite the time consumption in the refinement process, the computational time of the adaptive resolution model stay quite low in comparison with that of high resolution model throughout the deformation process.

The figure 10 shows a cross section of the object in refinement and simplification processes at a region of contact. In the time of contacting with the point, the object is deformed and the mesh is refined. After being released, the object gradually returns to the original shape in corresponding to the simplification process.

B. The stability of the dynamic change of the resolution

In this experiment we investigate the effect of the dynamic change of the resolution during a deformation process.

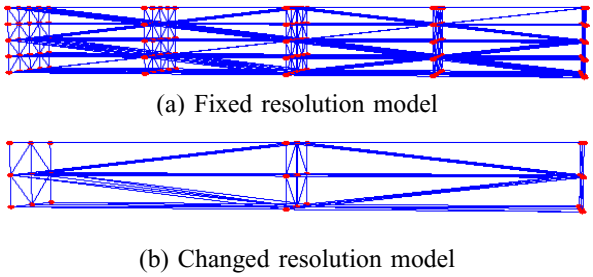

(a) Fixed resolution model

(b) Changed resolution model

Fig. 11. The object in the fixed and changed resolution models.

Figure 11(a) shows the object in an unchanged high resolution model. Figure 11(b) shows the object in a low resolution model which is gradually changed during the simulation. We investigate the oscillations status of a point in the object which is fixed at two ends and released from its initial position under the effect of the gravitational force.

Figure 12 shows the oscillations status of the point in the middle at the bottom of the object in fixed and changed

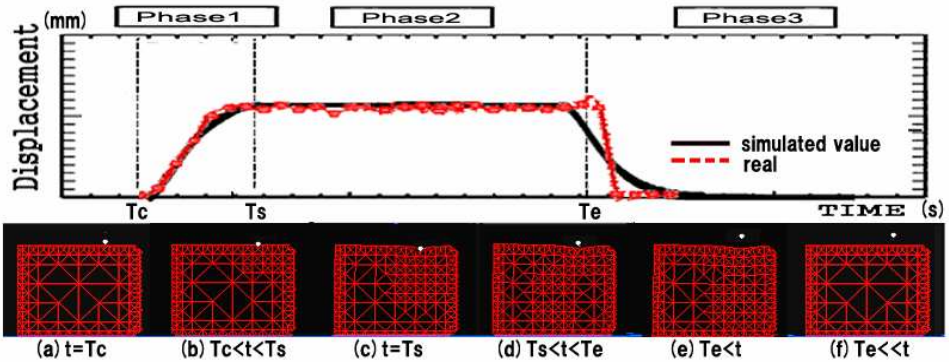

Fig. 10. Adaptive refinement in a region of collision

resolution models. The resolution is changed gradually until obtaining the same resolution of the high resolution model. The graph in the figure shows that the positions of the point in two models are different when changing the resolution and become identical in the stationary state.

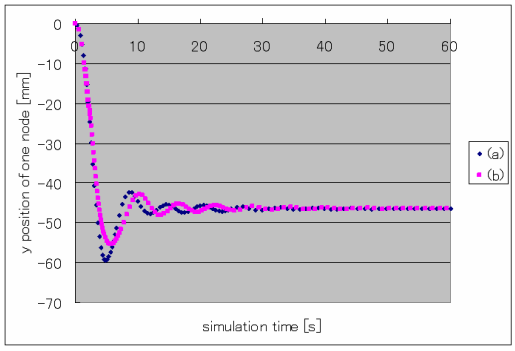

Fig. 12. Comparison of the node position at several model. (a) Fixed resolution model. (b) Changed resolution model.

V. Conclusions

We propose a new method for real-time modeling of soft objects, of which high resolutions dynamically adapt to the regions of high deformation. In order to reduce the computational cost in comparison with the previous methods we use the bisection refinement algorithm of which computational complexity is linear time. The experiment results show the performance of the proposed method.

References

[1] D. Hutchinson, M. Preston, and T. Hewitt, "Adaptive refinement for mass/spring simulations," in *Proceedings of the European workshop on Computer Animation and Simulation*, 1996, pp. 31–45.

[2] F. Ganovelli, P. Cignoni, and R. Scopigno, "Introducing multiresolution representation in deformable modeling," in *SCCG '99 Conference Proceedings*, Budmerice (Slovakia), April 1999, pp. 149–158.

[3] F. Ganovelli, P. Cignoni, C. Montani, and R. Scopigno, "A multiresolution model for soft objects supporting interactive cuts and lacerations." *Computer Graphics Forum*, vol. 19, no. 3, pp. 271–282, 2000.

[4] G. Debunne, M. Desbrun, M.-P. Cani, and A. Barr, "Adaptive simulation of soft bodies in real-time," in *Computer Animation*, May 2000, pp. 133–144.

[5] X. Wu, M. S. Downes, T. Goktekin, and F. Tendick, "Adaptive nonlinear finite elements for deformable body simulation using dynamic progressive meshes," in *Eurographics*, 2001, pp. 439–448.

[6] C. Paloc, F. Bello, R. Kitney, and A. Darzi, "Online multiresolution volumetric mass spring model for real time soft tissue deformation," in *Proceedings of the 5th International Conference on Medical Image Computing and Computer-Assisted Intervention*, 2002, pp. 219–226.

[7] J. Shewchuk, "Tetrahedral mesh generation by delaunay refinement," in *Proceedings of the Fourteenth Annual Symposium on Computational Geometry*, Minneapolis, Minnesota, 1998, pp. 86–95.

[8] H. T.Tanaka and F. Kishino, "Adaptive mesh generation for surface reconstruction: Parallel hierarchical triangulation without discontinuities," in *Proc. IEEE Conf. Computer Vision Pattern Recognition (CVPR93)*, New York City, 1993, pp. 88–94.

[9] H. T.Tanaka, "Accuracy-based sampling and reconstruction with adaptive meshes for parallel hierarchical triangulation," *Computer Vision and Image Understanding*, vol. 61, no. 3, pp. 335–350, 1995.

[10] H. T.Tanaka, Y. Takama, and H. Wakabayashi, "Accuracy-based sampling and reconstruction with adaptive grid for parallel hierarchical tetrahedrization," in *Proc. the 2003 Eurographics/IEEE TVCG Workshop on Volume graphics*, Tokyo, Japan, 2003, pp. 79–86.

[11] M.-C. Rivara, "New mathematical tools and techniques for the refinementand/or improvement of unstructured triangulations," in *5th International Meshing Roundtable*, 1996, pp. 77–86.

[12] J. M. Maubach, "Local bisection refinement for n - simplicial grids generated by reflection," *SIAM J. Scientific Computing*, vol. 16, 1995.

[13] A. Tanaka, K. Hirota, and T. Kaneko, "Deforming and cutting operation with force sensation," *Journal of Robotics and Mechatronics*, vol. 12, no. 3, pp. 292–303, 2000.

[14] A. V. Gelder, "Approximate simulation of elastic membranes by triangulated spring meshes," *Journal of Graphics Tools*, vol. 3, no. 2, pp. 21–42, 1998.

[15] J. Shewchuk, *PhD thesis, Delaunay Refinement Mesh Generation*. Pittsburgh, Pennsylvania: School of Computer Science, Carnegie Mellon University, 1997.

[16] J. Ruppert, "A delaunay refinement algorithm for quality 2-dimensional mesh generation," *Journal of Algorithms*, vol. 18, no. 3, pp. 548–585, 1995.

[17] M. Desbrun, P. Schroder, and A. Barr, "Interactive animation of structured deformable objects," in *Graphics Interface*.

[18] H. D. Stephane Cotin and N. Ayache, "Real-time elastic deformations of soft tissues for surgery simulation," *IEEE Transactions on Visualization and Computer Graphics*, vol. 5, no. 1, pp. 62–73, 1999.

[19] M. Garland, "Multiresolution modeling: Survey and future opportunities," in *EUROGRAPHICS '99, State of the Art Report*.

[20] C. Paloc, F. Bello, R. Kitney, and A. Darzi, "Virtual reality surgical training and assessment system," in *Computer Assisted Radiology and Surgery*, 2001, pp. 207–212.

4.3　階層的メッシュモデル

167

Proceedings of the 2007 IEEE/RSJ International
Conference on Intelligent Robots and Systems
San Diego, CA, USA, Oct 29 - Nov 2, 2007

On the Precision and Efficiency of Hierarchical Rheology MSD Model

Takeshi Ikawa
Division of Information and Computer Science, Graduate School of Engineering, Osaka Electro-Communication University

Hiroshi Noborio
Department of Computer Science, Osaka Electro-Communication University

Abstract— **In this paper, we model a rheology object whose main characteristic is the existence of residual displacement. In order to speed up calculation, to keep the stability, and also to control the residual replacement, we adopt MSD (Mass-Spring-Damper) voxel-lattice model and calibrate their physical parameters by using differences against experimentally captured shapes. In general, a human operator manipulates the MSD model by the most popular graphics software OpenGL and force feedback device PHANTOM in a 3-D CG environment. In order to get wonderful visual and tactile realities, we need force and shape calculations less than a couple of 10 milli-seconds. For saving computational cost, we propose the octree-based MSD model. Based on several experimental and comparative results, we check whether twin goals such as efficiency of calculation time and precision of shape deformation are compatible or not in the octree-based MSD model.**

I. Introduction

In order to feel artificial visual and tactile realities by the most popular graphics software OpenGL and force feedback device PHANTOM in a 3-D CG environment, we initially construct many kinds of smart physical models such as collision model, deformation model, friction model and so on. In the last decade, the haptics community has been aggressively studying several types of virtual elastic and visco-elastic models for haptic rendering [1],[2],[3],[4],[5]. Unfortunately in such a CG community, few researchers have tried to model a rheology object and also to control its residual displacement. In general, modeling a rheology object is more difficult than doing an elastic or visco-elastic object because we cannot understand how to control the residual displacement. For example, Finite Element Method (FEM) as the most typical model is perhaps useless because it does not include any physical parameter to control the residual displacement. Therefore during a few years, we have improved MSD (Mass-Spring-Damper) model and also have calibrated their physical unknown parameters by minimizing differences against many kinds of experimentally captured data [6],[7],[8].

In this paper, we acquire twin goals, that is, computation efficiency and shape precision of proposed MSD rheology model. For the cost cut, we adopt the octree structure as the MSD hierarchical model [9],[10],[11]. The octree has been widely used as 3-D hierarchical data structure in positioning. As shown in [12],[13], many researchers have already used the octree representation for modeling some elastic object. However, there is not any description concerning to the trade-off between computational efficiency and shape precision between a real rheology object and its virtual one. The purpose of this research is to save computation cost and simultaneously to maintain shape precision by usage of the octree. Therefore, we carefully check whether the twin goals are compatible or not under many kinds of comparative (calculation virtual and experimental real) results. In our comparison, we see calculation time of octree-based MSD model is almost two times faster than that of classic MSD model even though the octree has low resolution. In addition to this, computation cost of the classic model experimentally and theoretically increases 8 times larger as long as the resolution level increments, on the other hand, computation cost of our octree-based hierarchical model experimentally and theoretically increases 5 times larger as long as the resolution level increments. Therefore, the difference increases exponentially as long as resolution of the octree increments monotonously. Needless to say, this cost cut comes from decreasing memory storage of the octree. For this reason, the difference between memory capacities of classic and octree-based MSD models also increases exponentially as long as the resolution of octree increments monotonously. Nevertheless, deformation shape of octree-based MSD model is equivalent to that of classic MSD model. As a result, we determine the octree-based MSD rheology model is quite suitable for feeling artificial visual and tactile realities by OpenGL and PHANTOM.

The section 2 describes classic voxel/lattice structure and new octree-based structure with many basic MSD elements which consist of Voigt and damper parts. In addition, we explain how to calculate force propagation and shape deformation in these structures. Each element is calculated by solving dynamic (quadratic differential) equation. The ordinary differential equation is approximately integrated by the Euler method. Section 3 firstly explains how to gather many real capturing data and also how to calibrate all the physical parameters in four kinds of voxel/lattice structures. Then, in order to check whether the above twin goals are compatible or not in our new octree-based MSD model, we prepare many experimental and competitive results concerning to shape precision and computation cost for the classic and three types of octree-based voxel/lattice MSD structures. Finally in section 4, we give a few conclusions.

II. Virtual Rheology Object

In general, a rheology object has elastic and viscous properties. In addition, if we push the object, there is a residual displacement. In our living life, there are a lot of theology objects such as human organs, foods, cloths, and

1-4244-0912-8/07/$25.00 ©2007 IEEE.

so on (Fig.1). In this section, we explain how to model the rheology object. For this purpose, we use the MSD model which consists of many basic MSD elements with two neighbor masses, two dampers and one spring. Secondly, we indicate how to give external forces at some surface masses and then show how to propagate internal forces between neighbor masses. In succession, we explain our basic voxel/lattice MSD model which all the basic elements are allocated. Finally, we construct its octree-based model by combining many small voxels into one large voxel. Also, we indicate how to locate basic MSD elements in the octree-based MSD model.

Fig. 1. Practical rheology object.

A. Basic MSD Element

As illustrated in Fig.2, we introduce our MSD element which consists of Voigt part and damper part serially [8]. We briefly introduce properties generated from three coefficients. The larger the coefficient K is, the stronger the elasticity is. K controls displacement of deformation behavior. Moreover, the larger the coefficient C_1 is, the stronger the viscosity is. C_1 controls speed of the behavior. Furthermore, the larger the coefficient C_2 is, the larger the residual displacement is. If C_2 is small enough, the object appears elastic or visco-elastic property. On the other hand, if C_2 is large enough, the object appears plastic property. In addition, length ratio of Voigt and the other parts is denoted as a: $1-a$ (Fig.2). By changing the ratio, all the above properties are differently condensed.

In this research, we use the *Euler* method and the time step 2 [ms] to integrate quadratic dynamic equations. In this situation, we should keep K, C_1, C_2 within intervals $500 \leq K \leq 30000$, $100 \leq C_1 \leq 20000$ and $500 \leq C_2 \leq 30000$, $0.5 \leq a \leq 0.9$. If it is so, deformation of virtual rheology object is almost stable. Otherwise, each element becomes unstable and shape of rheology model is crushed. In this research, the weight is fixed as $M = M_{object}/n \times n \times n$ if all models consist of $(n-1) \times (n-1) \times (n-1)$ voxels.

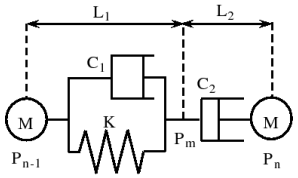

Fig. 2. Mass-spring-damper basic element.

In this paragraph, we explain how to propagate internal forces in the model 1. In our basic element shown in Fig.2, let O be the origin of coordinate system. Also, let P_{n-1} and P_n be coordinates of element endpoints. An initial length of Voigt part is given by L_1 and the other damper part is given by L_2. Therefore, we set $a = L_1/(L_1+L_2)$. Let M be mass at each endpoint. Let P_m be position of connecting point between Voigt and damper parts. Furthermore, d_n = P_n - P_{n-1} is defined. Since these positions P_{n-1}, P_m and P_n exist on the straight line, P_m can be defined under a parameter k as follows: $P_m = kd_n + P_{n-1}$. Here, time varying direction vector is defined as $e_n = d_n/\mid d_n \mid$, and also time varying length coefficient is defined as $Z_n = k \mid d_n \mid$.

Let F_{int} be an internal force applied to a mass point P_n. The force F_{int} equals to a force acting in the Voigt part. Thus, we have the following equation.

$$F_{int} = -C_1 \dot{Z}_n e_n - k(Z_n - L_1)e_n \tag{1}$$

Also, the force F_{int} coincides the force acting to a damper part. In consequence, we obtain the following equation.

$$F_{int} = -C_2(\frac{d}{dt}(|d_n| - Z_n))e_n \tag{2}$$

Here, an external force applied to a mass point P_n is defined as F_{ext}. Consequently, the dynamic equation of the mass point P_n is denoted as

$$M\ddot{P}_n = F_{int} + F_{ext} \tag{3}$$

From three equations (1), (2) and (3), we calculate the dynamic equation of three element model. First of all, by eliminating F_{int} in the equations (1) and (2), we directly obtain the parameter k. By substituting k into each of equations (1) and (2), we obtain the internal force F_{int} and consequently generate a motion of mass point P_n.

B. Classic Voxel/Lattice Structure

A real rheology object is located in a 3-D environment. In this research, we firstly represent the real object by the set of voxels with same size. This is the virtual voxel model of real rheology object. Secondly, we allocate mass points at all the corners of voxels. Finally, we connect each mass to all the neighbor masses by the basic MSD elements. In general, each mass has at most 26 neighbor masses, and therefore we connect them by 26 basic elements with three kinds of distances along X, Y, Z, XY, XZ, YZ, XYZ directions. This is the virtual voxel/lattice model of real rheology object. This model can express several kinds of force propagation and shape deformation flexibly by changing physical parameters of basic MSD elements.

The elements are inserted between neighboring mass points as illustrated in Fig.3(b). The virtual rheology object is deformed by expanding and contracting the elements. Let $P_{i,j,k}$ be position vector corresponding to mass point (i,j,k) (i,j,k are integers, $1 \leq i \leq N_x$, $1 \leq j \leq N_y$ and $1 \leq k \leq N_z$, N_x, N_y, N_z: numbers of masses along X, Y, Z axes, respectively). Let us derive quadratic differential equation of each mass

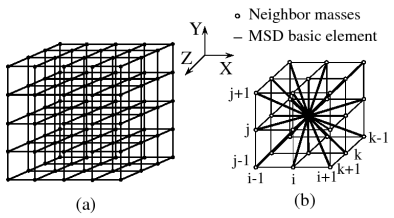

Fig. 3. (a) Voxel structure approximating whole object. (b) Lattice structure connecting neighbor masses.

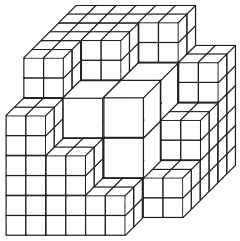

Fig. 4. Inside and outside of hierarchical structure.

at $P_{i,j,k}$. Each internal force acting on $P_{i,j,k}$ by the element between $P_{i,j,k}$ and its neighbor $P_{i+\alpha,j+\beta,k+\gamma}$ is denoted by $F_{i,j,k}^{\alpha,\beta,\gamma}$. For each mass, 6 shorter elements whose distance is denoted as l, 12 normal elements whose distance is denoted as $\sqrt{2}l$, and 8 longer elements whose distance is denoted as $\sqrt{3}l$ are located.

Therefore, total internal force $F_{i,j,k}^{int}$ acting on $P_{i,j,k}$ is given by the sum of 26(= 6 + 12 + 8) internal forces $F_{i,j,k}^{\alpha,\beta,\gamma}$. Moreover, if the sum of active external forces at $P_{i,j,k}$ is denoted by $F_{i,j,k}^{ext}$, we obtain the following quadratic differential equation. This summation requires small calculation time.

$$M\ddot{P}_{i,j,k} = F_{i,j,k}^{int} + F_{i,j,k}^{ext} \tag{4}$$

In order to calculate next position $P_{i,j,k}$ ($1 \leq i \leq N_x$, $1 \leq j \leq N_y$ and $1 \leq k \leq N_z$) at each mass, we should solve the above differential equation. In this research, we select the *Euler* method as an efficient method while keeping shape stability.

$$F_{i,j,k}^{int} = \sum_{\substack{\alpha,\beta,\gamma\in\{-1,0,1\} \\ (\alpha,\beta,\gamma)\neq(0,0,0)}} F_{i,j,k}^{\alpha,\beta,\gamma} \tag{5}$$

C. New Octree Structure

To save calculation time of force propagation and simultaneously shape deformation in the classic voxel/lattice structure, we should decrease the number of voxels and also that of basic elements. For this purpose, we use the octree representation. In the octree, we can merge eight smaller voxels into one larger voxel inside the virtual rheology object. Especially using the octree, we maintain the number of voxels outside the virtual rheology object as shown in Fig.4. This is the merit of rheology MSD model because the surface smaller voxels is received by external forces of complex human operation. That is, the voxel resolution outside the MSD model is kept, on the other hand, the voxel resolution inside the MSD model becomes larger as illustrated in Fig.4. As a result, saving calculations of force propagation and synchronously shape deformation inside the virtual rheology object is achieved by enlarging core larger voxels. The problem is to keep similar precisions of forces and positions. For this purpose, we classify and calibrate physical parameters such as masses and coefficients for each voxel whose size differs from each other.

If we represent an arbitrary real rheology object, we enclose the object by an initial cube. Then, we divide the cube into eight sub-cubes recursively until an expected cube resolution. Initially in the depth 0 of octree structure, we have one voxel and $2\times2\times2$ masses. In succession, we have $2\times2\times2$ voxels and $3\times3\times3$ masses in the depth 1, and also we have $4\times4\times4$ voxels and $5\times5\times5$ masses in the depth 2. The relation between the octree level and the cube resolution is illustrated in Fig.5.

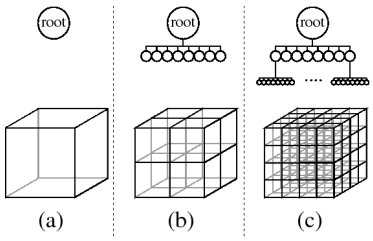

Fig. 5. A relation between node level and voxel resolution. (a) depth 0 ($2\times2\times2$ masses), (b) depth 1 ($3\times3\times3$ masses), and (c) depth 2 ($5\times5\times5$ masses).

In the octree, we firstly find two voxels with different scales in the depth 3 of voxel resolution $8\times8\times8$. Therefore, we check several kinds of octrees whose depths are larger than the depth 3. In Fig.6, three 2-D sliced octree for voxel resolution $2\times2\times2$, $4\times4\times4$ and $8\times8\times8$ are indicated. The gray surrounding voxels are successively divided into smaller ones.

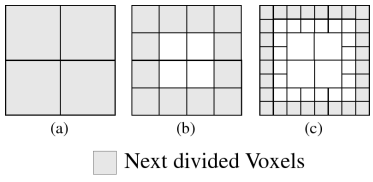

Fig. 6. Three sliced octree representations. (a) depth 1 ($3\times3\times3$ masses), (b) depth 2 ($5\times5\times5$ masses), and (c) depth 3 ($9\times9\times9$ masses).

In the octree, a parent node (cube) is divided into eight child (cubes). Each node (cube) has maximum X,Y,Z positions (X_{max},Y_{max},Z_{max}), and also minimum X,Y,Z positions (X_{min},Y_{min},Z_{min}). By averaging those X,Y,Z positions, we can get half X,Y,Z positions ($X_{half},Y_{half},Z_{half}$) in order to construct eight child nodes (cubes) as described in Fig.7 [9], [10], [11]. The correspondence between voxel and node is determined in Fig.8. As mentioned previously, our purpose using the octree controls all the mass points of virtual rheology object efficiently. Therefore, each node (voxel)

represent eight vertices as mass positions by combining one of X_{min}, Y_{min}, Z_{min}, and the other of X_{max}, Y_{max}, Z_{max}. Finally, the initial cube (whole space) is represented as the minimum cube enclosing virtual rheology object which equals to the real one.

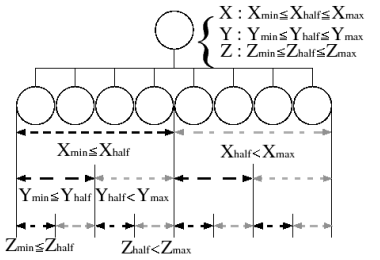

Fig. 7. Our parent node and its eight child nodes.

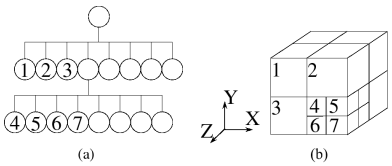

Fig. 8. The correspondence between node and voxel.

D. Element Location in the Octree

In the classic voxel/lattics structure, each mass always has 26 neighbor masses inside the virtual rheology model. Therefore, we connect each mass to 26 neighbor masses by the basic elements. For the mass, 6 shorter elements whose distance is denoted as l, 12 normal elements whose distance is denoted as $\sqrt{2}l$, and 8 longer elements whose distance is denoted as $\sqrt{3}l$ are located. As contrasted with this, in the hierarchical voxel/lattice structure, each mass do not always have 26 neighbor masses even inside the virtual rheology model. Therefore, we cannot sometimes connect the mass to neighbor masses along some directions by the basic elements. Also, we sometimes obliged to connect the mass to neighbor masses along some directions by the basic elements whose lengths are longer than $\sqrt{3}l$.

In this research, we firstly gather all the voxels connecting the mass (Fig.9). If all sizes of voxels equal to each other, the mass has 26 neighbor masses and we connect them each other by the basic elements whose lengths are l, $\sqrt{2}l$, and $\sqrt{3}l$ (Fig.9(a)). Otherwise, that is, if sizes of neighbor voxels differ from each other, we connect the mass to the closest neighbor mass for each direction by l, $\sqrt{2}l$, $\sqrt{3}l$, or longer length (Fig.9(b)). Here, there are sometimes directions not to find any closest neighbor mass (Fig.9(c)). No basic element means force propagation is broken for the direction. In order to moderate this side effect, we individually calibrate four physical parameters of basic MSD elements per each size of voxel as shown in Fig.10.

E. Three Kinds of Octree-Based MSD Models

In this research, we prepare three kinds of octrees as follows: All are directly located on the floor.

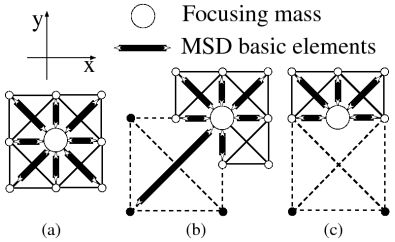

Fig. 9. Many types of mass connections by the basic elements.

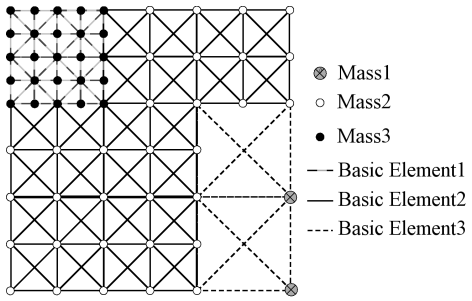

Fig. 10. Hierarchical structure with three kinds of masses and elements.

type 0 An octree model whose high resolution voxels are located around the virtual rheology object.

type 1 Another octree model whose high resolution voxels are visible outside the virtual rheology object.

type 2 The other octree model whose high resolution voxels are visible outside the virtual rheology object and also are not located at the corners.

The type 0 is the original hierarchical model as shown in Fig.11(a). Type 1 is an improved model by neglecting high digitalization in areas where we cannot watch (Fig.11(b)). In addition, the type 2 is another improved model by neglecting high digitalization in corners where deformation of real rheology object can be negligible (Fig.11(c)).

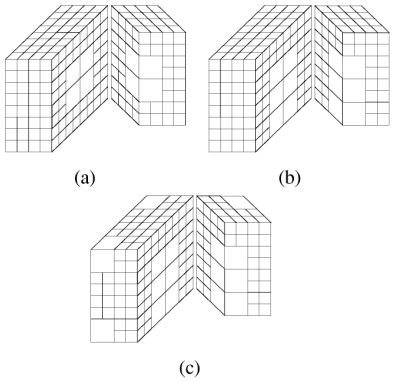

Fig. 11. Three kinds of octree-based MSD models, (a) type 0, (b) type 1, (c) type 2.

As compared with the classic voxel/lattice structure, we theoretically evaluate decreasing percentages of mass numbers and element numbers in the types 0, 1, and 2 for the digitalization $9 \times 9 \times 9$, $17 \times 17 \times 17$, and, $33 \times 33 \times 33$, respectively, as shown in Table I and Table II. Note that **saving**

ratio is calculated by ((calculation time of the classic model)-(calculation time of each octree-based model)/(calculation time of the classic model) $\times$ 100). These mean theoretical saving percentage of calculation time of deformation simulation. We will compare these with experimental saving percentage of calculation time of deformation simulation later on.

TABLE I

SAVING MASS NUMBER IN EVERY TYPE.

resolution	classic model	octree model		
		type 0	type 1	type 2
9	729	703	678	622
saving ratio (%)	0	3.57	7.00	14.68
17	4913	3681	3343	2915
saving ratio (%)	0	25.08	31.96	40.67
33	35937	17219	15032	12652
saving ratio (%)	0	52.09	58.17	64.79

TABLE II

SAVING ELEMENT NUMBER IN EVERY TYPE.

resolution	classic model	octree model		
		type 0	type 1	type 2
9	7748	6858	6386	5769
saving ratio (%)	0	11.49	17.58	25.54
17	56368	37400	33486	28438
saving ratio (%)	0	33.65	40.59	49.55
33	438368	176710	152971	126915
saving ratio (%)	0	59.69	65.10	71.05

III. COMPARATIVE RESULTS

In our experiment, we firstly calibrate all the uncertain physical parameters per each voxel with the same size by GA (Genetic Algorithm). For this purpose, we should prepare a real rheology object and its pushing experimental equipment. Secondly, we check shape precisions between classic and octree models whose voxel resolutions are $8\times8\times8$ and $16\times16\times16$. If the differences are small enough, our octree-based models have no problem for keeping visual reality. Thirdly, we will ascertain our main purpose whether our octree-based models can save computation cost or not against the classic model. If experimental saving ratio is approximately equivalent to theoretical saving ratio, our purpose is exactly achieved.

A. Experimental System and Evaluation Index

First of all, we make a real rheology object by mixing wheat flour and water whose ratio is 2 : 1. The weight of real rheology object is $630[g]$ and shape of that is $8.0\times8.0\times8.0[cm]$. Then, the real rheology object is pushed by a rigid body located at the tip of robotic manipulator $PA-10$ (Mitsubishi Heavy Industry Co.). The width of the rigid body is $2.0[cm]$ and also speed pushing the rheology object is $2.0[cm/second]$.

The deformation of rheology object, that is, the sequence of shapes is measured by two stereo vision camera systems *Digiclops* and software development kit *Triclops* (provided by Point Grey Research Inc, Canada). Each captures about three thousand points as shape of the real rheology object in real-time manner.

In order to evaluate the shape difference between real and virtual rheology objects, we summarize minimum distances from captured points to their nearest points around the virtual rheology object. The virtual object consists of $N_x\times N_y\times N_z$ hexahedrons which are individually deformed from initial voxels. Therefore in order to evaluate the difference, we calculate the minimum of $N_x\times N_y\times N_z$ shortest distances for each captured point to all hexahedrons by Lin-Canny closest point algorithm [14]. In succession, we calculate sum S_{shape} of all minimum distances for all captured points, which are larger than the average sensing error $0.05[cm]$ of *Digiclops*. Finally, we use the sum of five S_{shape} at five times before, during, and after the pushing operation as the evaluation index. The five time captures are done as follows:

- before the rigid body contacts the rheology object
- $1.0[sec]$ after the rigid body contacts the rheology object
- the rigid body finishes to push the rheology object
- the rigid body starts to leave the rheology object
- $2.0[sec]$ after the rigid body leaves the rheology object

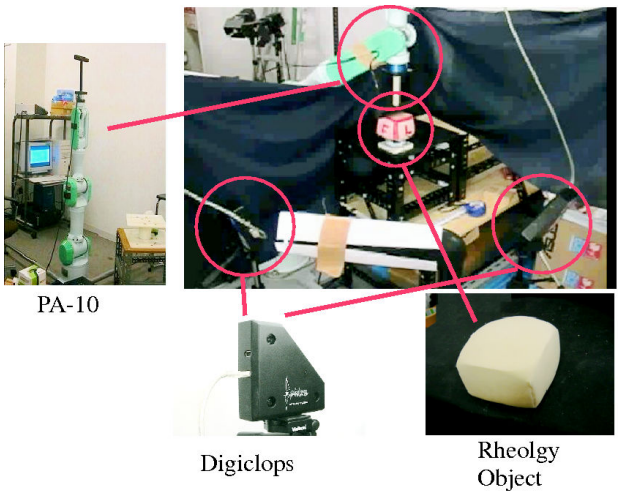

Fig. 12. Experimental view.

B. Parameter Calibration by GA

In this section, we compare two resolution octree-based models whose voxel resolutions are $8\times8\times8$ and $16\times16\times16$. In general, as the smaller the size of cube is, the smaller the weight of mass is. The weight of real rheology object is $630[g]$ and shape of that is $8.0\times8.0\times8.0[cm]$. Therefore, the mass weight is $5.04[g]$ and voxel size is $2.0[cm]$ in $4\times4\times4$ voxel resolution. Also, the mass weight is $0.864[g]$ and voxel size is $1.0[cm]$ in $8\times8\times8$ voxel resolution. In succession, the mass weight is $0.128[g]$ and voxel size is $0.5[cm]$ in $16\times16\times16$ voxel resolution. Finally, as mentioned in the previous section (Fig.10), if the mass contacts voxels with different scales, we allocate the weight of smallest voxel into the mass.

TABLE III

CALIBRATED SET OF PHYSICAL UNCERTAIN PARAMETERS ($9 \times 9 \times 9$ MASS RESOLUTION).

Physical parameters	Classic model	Octree model		
		type 0	type 1	type 2
$K^{1st}[gf/cm^3]$	76.8	158.9	96.2	97.9
${C_1}^{1st}[gfs/cm^3]$	302.6	20.7	43.1	43.8
${C_2}^{1st}[gfs/cm^3]$	12.9	7.2	8.2	8.3
a^{1st}	0.53	0.59	0.62	0.64
$K^{2nd}[gf/cm^3]$		8.4	79.8	85.1
${C_1}^{2nd}[gfs/cm^3]$		13.4	167.5	171.0
${C_2}^{2nd}[gfs/cm^3]$		283.5	7.9	8.8
a^{2nd}		0.56	0.59	0.54

TABLE IV

CALIBRATED SET OF PHYSICAL UNCERTAIN PARAMETERS ($17 \times 17 \times 17$ MASS RESOLUTION).

Physical parameters	Classic model	Octree model		
		type 0	type 1	type 2
$K^{1st}[gf/cm^3]$	17.3	23.8	12.9	8.4
${C_1}^{1st}[gfs/cm^3]$	44.3	10.1	10.5	25.2
${C_2}^{1st}[gfs/cm^3]$	4.4	4.9	5.9	7.7
a^{1st}	0.56	0.69	0.73	0.62
$K^{2nd}[gf/cm^3]$		26.8	14.2	57.4
${C_1}^{2nd}[gfs/cm^3]$		3.2	0.9	15.8
${C_2}^{2nd}[gfs/cm^3]$		3.1	2.7	4.5
a^{2nd}		0.64	0.63	0.63
$K^{3rd}[gf/cm^3]$		24.6	1.8	8.7
${C_1}^{3rd}[gfs/cm^3]$		10.7	13.0	56.6
${C_2}^{3rd}[gfs/cm^3]$		14.2	13.9	1.8
a^{3rd}		0.62	0.52	0.33

In our comparison, we prepare classic and octree-based voxel/lattice virtual rheology object whose surrounding voxel sizes are the same. Moreover, in each octree model, we individually calibrate the basic element per each voxel whose size is different. For example, we calibrate two sets K^{1st}, ${C_1}^{1st}$, ${C_2}^{1st}$, a^{1st} and K^{2nd}, ${C_1}^{2nd}$, ${C_2}^{2nd}$, a^{2nd} for $8 \times 8 \times 8$ voxel resolution. Also, we calibrate three sets K^{1st}, ${C_1}^{1st}$, ${C_2}^{1st}$, a^{1st}, and K^{2nd}, ${C_1}^{2nd}$, ${C_2}^{2nd}$, a^{2nd}, and K^{3rd}, ${C_1}^{3rd}$, ${C_2}^{3rd}$, a^{3rd} for $16 \times 16 \times 16$ voxel resolution. By GA (Genetic Algorithm) [8], we calibrated such parameters as shown in Table III and IV. The evaluation index is the sum of five S_{shape}, that is, five differences between virtual and real shapes of rheology objects.

C. Comparative Results

Shape deformation of virtual rheology object is simulated as the following four steps. The time step solving the differential equation is denoted as $0.002[sec]$. If and only if any external force is not added, the step 1 can be skipped.

1) External operation of surrounding point
2) Calculation of all basic MSD elements
3) Calculation of all mass points
4) Indication of whole shape

The calculation time is evaluated during $5.0[sec]$ from start pushing to $2.0[sec]$ after leaving. In our simulation, we use the following PC and software. CPU: Intel Pentiam4 3.0 GHz, Memory: 1.0 Gbyte, Video: nVIDIA GeForce FX 5700, OS: Windows, Graphics Software: OpenGL.

TABLE V

EVALUATING SHAPE DIFFERENCE ($9 \times 9 \times 9$ MASS RESOLUTION).

Trial	Classic model	Octree model		
		type 0	type 1	type 2
1st $[m]$	11.58	11.78	11.83	11.80
ave.$[mm]$	4.75	4.83	4.85	4.83
2nd $[m]$	10.73	10.41	10.92	10.83
ave.$[mm]$	4.62	0.44812	0.46968	0.46589
3rd $[m]$	9.06	8.27	8.69	8.59
ave.$[mm]$	3.82	3.48	3.66	3.62
4th $[m]$	9.10	8.21	8.65	8.55
ave.$[mm]$	3.87	3.42	3.62	3.57
5th $[m]$	9.31	8.24	8.70	8.59
ave.$[mm]$	4.17	3.93	4.09	4.05
sum $[m]$	49.78	46.92	48.79	48.36
ave.$[mm]$	4.25	4.03	4.18	4.15

TABLE VI

EVALUATING SHAPE DIFFERENCE ($17 \times 17 \times 17$ MASS RESOLUTION).

Trial	Classic model	Octree model		
		type 0	type 1	type 2
1st $[m]$	11.87	12.10	12.15	11.91
ave.$[mm]$	4.86	4.96	4.98	4.88
2nd $[m]$	10.88	10.43	11.09	10.50
ave.$[mm]$	4.68	4.49	4.77	4.52
3rd $[m]$	8.39	8.07	8.07	8.92
ave.$[mm]$	3.53	3.40	3.40	3.76
4th $[m]$	8.31	7.97	7.98	8.80
ave.$[mm]$	3.48	3.34	3.35	3.69
5th $[m]$	8.37	8.03	8.08	8.83
ave.$[mm]$	3.48	3.33	3.36	3.67
sum $[m]$	47.82	46.61	47.36	48.96
ave.$[mm]$	4.01	3.91	3.97	4.10

In this section, we firstly describe all the calibrated physical parameters in Table III and Table IV. In spite of a few differences, we can understand that almost all the tendencies are the same. In these results, we can see that our calibrations during about one month by GA minimizing the sum of five S_{shape} are meaningful. Secondly, we evaluate shape differences between real object and virtual classic and octree-based MSD objects by the sum of five S_{shape} in Table V and Table VI. The sum is for about 3000×5 captured points, and therefore distance error average for each captured point is bounded by a small value 5 [mm]. All results are completely equivalent. Moreover, we illustrate deformed shapes of classic and octree-based MSD models in figures 13 and 14. In these figures 13 and 14, all orange points mean positions whose differences of virtual and real objects are larger than 2.5[mm]. We can see that all the shapes are quite similar, and consequently the octree-based models have same performances against the classic model concerning to shape precision.

Finally, we compare practical calculation time of total, mass point, and basic element in the classic and octree-based MSD rheology models as shown in Table VII and

VIII. In every case, total calculation time is always larger than calculation time for processing mass point and basic element. The reason is that total calculation needs control, memory, function procedures and so on. All the results in Table VII are less than 33 [ms] and therefore they are fast enough for watching shape deformation by CRT display or Liquid Crystal Display. On the other hand, all the results in Table VIII are 8 times slower in the classic model but 5 times slower in the hierarchical model. In general, the latter speed is sometimes acceptable since deformation of rheology object is not so fast.

As compared with theoretical evaluations in Table I and Table II, experimental results shown in Table VII and VIII are similar. Especially, computation cost of the classic model experimentally and theoretically increases 8 times larger as long as the resolution level increments, on the other hand, computation cost of our octree-based hierarchical model experimentally and theoretically increases 5 times larger as long as the resolution level increments. As a result, we can ascertain our main purpose that using the octree as rheology model efficiently saves computation cost. Note that **saving ratio** is calculated by ((calculation time of the classic model)-(calculation time of each octree-based model)/(calculation time of the classic model) $\times$ 100).

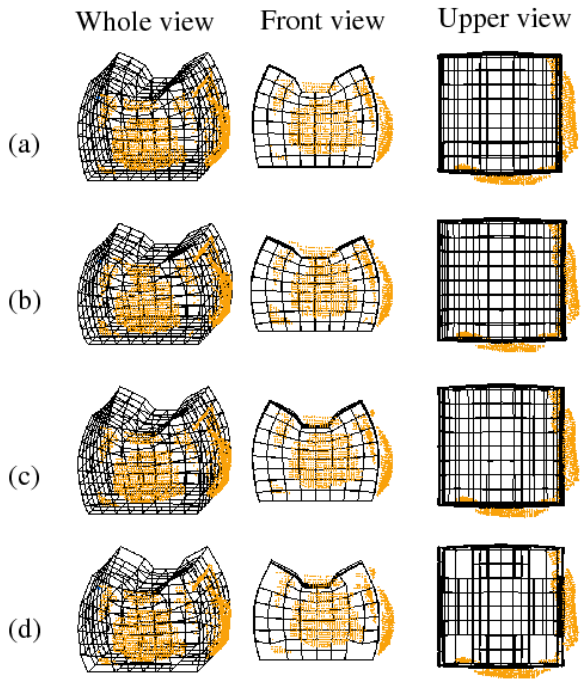

Fig. 13. Shape descriptions of $9 \times 9 \times 9$ mass resolution. (a) Classic model, (b) Octree model (type 0), (c) Octree model (type 1), and (d) Octree model (type 2).

As illustrated in Table IX and X, we compare practical memory storage of total, mass point, and basic element in the classic and octree-based MSD rheology models. In every case, practical memory storage of mass point and basic element are similar to theoretical memory storage of mass point and basic element. However, practical total memory

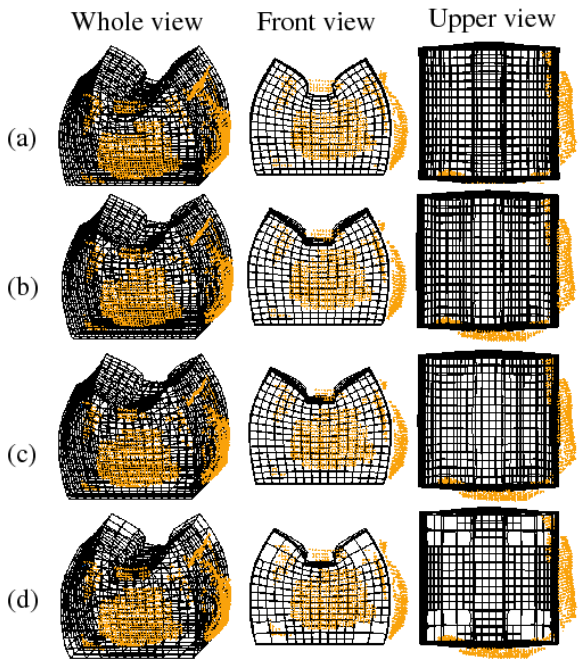

Fig. 14. Shape descriptions of $17 \times 17 \times 17$ mass resolution. (a) Classic model, (b) Octree model (type 0), (c) Octree model (type 1), and (d) Octree model (type 2).

TABLE VII
SAVING PRACTICAL CALCULATION TIME ($9 \times 9 \times 9$ MASS RESOLUTION).

Time	Classic model	Octree model		
		type 0	type 1	type 2
total [*msec*]	31.9	29.7	29.4	25.5
saving ratio (%)	-	7.0	7.8	20.2
mass point [*msec*]	1.06	1.03	0.97	0.89
saving ratio (%)	-	2.9	8.7	16.2
basic element [*msec*]	28.5	26.4	24.8	22.1
saving ratio (%)	-	7.1	12.9	22.3

TABLE VIII
SAVING PRACTICAL CALCULATION TIME ($17 \times 17 \times 17$ MASS RESOLUTION).

Time	Classic model	Octree model		
		type 0	type 1	type 2
total [*msec*]	251.2	150.0	135.6	122.0
saving ratio (%)	-	40.3	46.0	51.4
mass point [*msec*]	12.0	9.8	8.8	8.2
saving ratio (%)	-	24.4	32.1	36.8
basic element [*msec*]	195.4	130.9	117.7	1056.0
saving ratio (%)	-	33.0	39.7	46.3

storage extremely differs from theoretical total memory storage. The differences cannot be absorbed in the storage area of all other variables. This is mainly due to our compiler Visual C++. As a result, we cannot ascertain our associate purpose that using the octree as rheology model efficiently saves memory storage. Note that **saving ratio** is calculated by ((memory storage of the classic model)-(memory storage of each octree-based model)/(memory storage of the classic model) $\times$ 100).

TABLE IX
SAVING PRACTICAL MEMORY STORAGE ($9 \times 9 \times 9$ MASS RESOLUTION).

Memory	Classic model	Octree model		
		type 0	type 1	type 2
total $[KByte]$	9964	9980	9828	9716
saving ratio (%)	-	0.84	1.37	2.49
mass point $[KByte]$	84.6	81.7	78.9	72.6
saving ratio (%)	-	3.44	6.75	14.17
basic element $[KByte]$	1012.9	932.7	883.6	784.9
saving ratio (%)	-	7.92	12.77	22.52

TABLE X
SAVING PRACTICAL MEMORY STORAGE ($17 \times 17 \times 17$ MASS RESOLUTION).

Memory	Classic model	Octree model		
		type 0	type 1	type 2
total $[KByte]$	62528	59648	59048	58272
saving ratio (%)	-	4.61	5.57	6.81
mass point $[KByte]$	569.9	431.9	394.1	346.1
saving ratio (%)	-	24.21	30.85	39.27
basic element $[KByte]$	7666.1	5086.4	4554.1	3867.6
saving ratio (%)	-	33.65	40.60	49.55

IV. CONCLUSIONS

In this paper, we proposed an octree-based hierarchical MSD structure for representing an arbitrary rheology object. Based on many kinds of comparative and experimental results, we can see that shape consistency of proposed octree-based voxel/lattics structure is better than or equal to that of the classic one. Nevertheless even in a low resolution, we can see that calculation time of proposed octree-based hierarchical structure is two times faster than that of the classic voxel/lattics structure. Under many theoretical and experimental results, we can understand this tendency exponentially accelerates as the resolution of octree becomes higher. That is, computation cost of the classic model experimentally and theoretically increases 8 times larger as long as the resolution level increments, on the other hand, computation cost of our octree-based hierarchical model experimentally and theoretically increases 5 times larger as long as the resolution level increments. As a result, our octree-based MSD voxel/lattics model is quite useful for not only maintaining deformation precision but also speeding up simulation time.

REFERENCES

[1] D.Bourguignon, M.P.Cani. Controlling anisotropy in mass-spring systems. In *Proc. of the 11th Eurographics Workshop on Computer Animation and Simulation*, pp.113-123, 2000.

[2] X.Wu., M.Downes, T.Goktekin, F.Tendick. Adaptive nonlinear finite elements for deformable body simulation using dynamic progressive meshes. In *Proc. Eurographics '01*, pp.349-358, 2001.

[3] G.Debunne, M.Desbrun, M. P.Cani., A.Barr. Dynamic real-time deformations using space and time adaptive sampling. In *Proc. SIGGRAPH '01*, pp.31-36, 2001.

[4] J.Berkley. Haptic rendering of deformable bodies using real-time finite element analysis: an application to surgical simulation. In *Doctoral Thesis, University of Washington*, pp.49-54, 2002.

[5] M.Muller, J.Dorsey, L.McMillan, R.Jagnow, B.Cutler. Stable real-time deformations. In *Proc. of ACM SIGGRAPH Symposium on Computer Animation*, pp.49-54, 2002.

[6] S.Tokumoto, Y.Fujita, S.Hirai. Deformation modeling of visco-elastic objects for their shape control. In *Proc. of the IEEE Int. Conf. on Robotics and Automation*, pp.1050-1057, 1999.

[7] M.Kimura, Y.Sugiyama, S.Tomokuni, S.Hirai. Constructing rheologically deformable virtual objects. evolutionary techniques. In *Proc. of the IEEE Int. Conf. on Robotics and Automation*, pp.3737-3743, 2003.

[8] R.Nogami, F.Ujibe, H.Fujii and H.Noborio. Precise deformation of rheologic object under MSD models with many voxels and calibrating parameters In *Proc. of the IEEE Int. Conf. on Robotics and Automation*, pp.1919-1926, 2004.

[9] C.L.Jackins and S.L.Tanimoto. Octtrees and their use in representing three-dimensional objects. In *Computer Vision, Graphics, Image Processing*, pp.249-270, 1980.

[10] H.Noborio, S.Fukuda, S.Arimoto. Construction of the octree approximating three-dimensional objects by using multiple views. In *IEEE Trans. on Pattern Analysis and Machine Intelligence*, pp.769-782, 1988.

[11] H.Noborio, S.Fukuda, S.Arimoto. Fast interference check method using octree representation. In *Journal of Advanced Robotics*, pp.193-212, 1989.

[12] D.Gilles and D.Mathieu and B.Alan H. and C.Marie-Paule. Interactive multiresolution animation of deformable models In *Proc. of the Workshop on Computer Animation and Simulation*, pp.133-144, 1999.

[13] F.Ganovelli, P.Cignoni, R.Scopigno Introducing multiresolution representation in deformable object modeling In *SCCG '99 Conference Proceedings*, April 28th-May 1st, Budmerice (Slovakia), pp.149-158, 1999.

[14] M.C.Lin and J.F.Canny. A fast algorithm for incremental distance calculation. In *Proc. of the IEEE Int. Conf. on Robotics and Automation*, pp.1008-1014, 1991.

Force/Shape Reappearance of MSD Rheology Model Calibrated by Force/Shape Sequence

Haruyuki Yoshida, Fumiaki Ujibe and Hiroshi Noborio
Osaka Electro-Communication University, Hatsu-Cho 18-8, Neyagawa, Osaka 572-8530 , Japan
nobori@noblab.osakac.ac.jp

Abstract

In this paper, we firstly push or pull real and virtual rheology objects by the same displacement or force sequence. Then by minimizing the difference between shape or force sequences of real and virtual objects, we calibrate many parameters of rheology MSD (Mass-Spring-damper) model, pull-off force model and friction force model between a rigid object and its pushing or pulling rheology one. The calibration is done by a probabilistic search (Genetic Algorithm). In a few years, we have deeply investigated "pushed, calibrated, and evaluated by shape sequence" and also "pushed, calibrated, and evaluated by force sequence". In this paper, we completely compare all the eight possibilities. Consequently, we get the best visual reality under push and calibration by shape sequence, and also the wonderful tactile reality under push and calibration by force sequence. Moreover, we ascertain reappearance of force or shape sequence when sensing data (pusing operation) in calibration differ from sensing data (pushing operation) in evaluation. Finally, we find a practical defective point for us to manipulate a virtual deformable object in a 3-D CG environment. A human operator cannot push or pull a rheology object by a rigid body via force sequence because any force sensor is not equipped in his hand. To overcome this problem in future, we should build some collision model between rigid and rheology objects, which always transforms pushing displacement and velocity into pushing force in the 3-D CG environment.

Keywords: Rheology Object, Dynamic Simulation, Haptics

1. Introduction

In order to express models of elastic and visco-elastic objects, many researchers have tried the following four approaches, i.e., mass-spring-damper (MSD) method [7] finite difference method (FDM) [3], boundary element method (BEM) [2], and finite element method (FEM) [4]. However, considering the history, we notice that a few researches deal with calibration of physical uncertain parameters from experimental sensing data [1]. Furthermore, few researches focus on a rheology object although it is quite popular material in our living life, e.g., food materials such as several kinds of noodles, human bodies such as organs and muscles, and an article of clothing. To overcome these drawbacks in a couple of years, we have modeled an arbitrary rheology object by MSD [11], and then have calibrated their uncertain physical parameters by many kinds of sensing data such as total shape sequence or local force sequence [5]∼ [6]. The reason using MSD method is to speed up calculation, to keep the stability, and also to control residual replacement. Note that the residual replacement is the main difference of rheology object against elastic or visco-elastic object. First of all, we completely compare eight possibilities multiplying two (displacement and force) pushes, two (shape and force) calibrations, and two (shape and force) evaluations. In results, in order to maintain visual reality, we should select the combination of displacement push and shape calibration. As contrasted with this, so as to keep tactile reality, we should select the combination of force push and force calibration. Secondly, we check force and shape reappearances of MSD rheology model calibrated by force and shape sequences, respectively. For this purpose, we use two kinds of pushing operations.

First of all, we evaluate the difference between shape sequences of our MSD model pushed by the second operation, whose physical parameters are calibrated by the first and second operations. In other words, we evaluate the difference when calibration data equal to or differ from evaluation data. Consequently, since the difference is small enough, we can see that the shape reappearance is maintained. Secondly, we evaluate the difference between force sequences of our MSD model pushed by the second operation, whose physical parameters are calibrated by the first and second operations. In other words, we evaluate the difference when calibration data equal to or differ from evaluation data. Consequently, since the difference is small enough, we can see that the force reappearance is kept. As a result, we maintain reappearance of our MSD model for several kinds of pushing operations.

The section 2 describes our voxel/lattice structure with many basic MSD elements which consist of Voigt and damper parts. In addition, we explain how to calculate force propagation in the structure. They are calculated by solving dynamic equation. Moreover, we model two kinds of forces, that is, pull-off force model and friction force model. Section 3 explains how to start to deform a virtual rheology object by displacement or force sequence. In section 4, we explain how to evaluate differences between experimental real and calibrated virtual objects by shapes or forces. Moreover in section 5, we give several kinds of comparative real and virtual results to investigate the best MSD model and its physical properties. Finally in section 6, we give a few conclusions and ongoing remarks. In this research, we tested two starting up methods such as displacement and force pushing operations. Needless to say, the displacement pushing is more useful than the force pushing because a human hand does not equip any force sensor in a 3-D CG environment. However, since there is no model for a rigid body to collide with a rheology object, a virtual force distribution during a pushing period is not good for the displacement pushing (the distribution is wonderful for the force pushing). In order to overcome this drawback, we should build a smart collision model between rigid and rheology objects. The model's role is to transform a swept

volume of a rheology object by a rigid body into a force per each sampling time in a virtual 3-D CG environment.

2. Modeling of A Virtual Rheology Object Based on The Mass-Spring-Damper Elements

In this section, we firstly introduce our basic MSD element with two neighbor masses, two dampers and one spring. Secondly, we explain how to give external forces at some surface masses and then show how to propagate internal forces between neighbor masses. In succession, we explain our basic voxel/lattice MSD model which all basic elements are allocated.

2.1. Voigt and the Other Parts in Our Basic Element

As illustrated in Fig.1, we introduce our MSD element which consists of Voigt part and damper part serially. We briefly introduce properties generated from three coefficients. The larger the coefficient K is, the stronger the elasticity is. K controls displacement of deformation behavior. Moreover, the larger the coefficient C_1 is, the stronger the viscosity is. C_1 controls speed of the behavior. Furthermore, the larger the coefficient C_2 is, the larger the residual displacement is. If C_2 is small enough, the object appears elastic or visco-elastic property. On the other hand, if C_2 is large enough, the object appears plastic property. In addition, length ratio of Voigt and the other parts is denoted as a: $1-a$ (Fig.1). By changing the ratio, all the above properties are differently condensed.

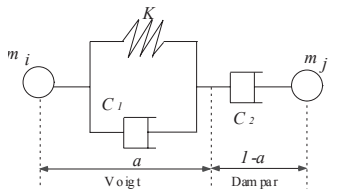

Figure 1: Our basic element with two dampers and one spring

2.2. A Voxel/Lattice Structure

A real rheology object is located on in a 3-D environment. In this research, as shown in Fig.2, we firstly represent the real object by the set of voxels with same size. This is the virtual voxel model of real rheology object. Secondly, we allocate mass points at all the corners of voxels. Finally, we connect each mass to all the neighbor masses by the basic MSD elements. In general, each mass has at most 26 neighbor masses, and therefore we connect them by 26 basic elements with three kinds of distances along X, Y, Z, XY, XZ, YZ, XYZ distances.

This is the virtual voxel/lattice model of real rheology object. This model can express several kinds of deformation shapes flexibly by changing physical parameters of basic MSD elements. The elements are inserted between neighboring mass points as illustrated in Fig.2(b). The virtual rheology object is deformed by expanding and contracting the elements. Let $P_{i,j,k}$ be position vector corresponding

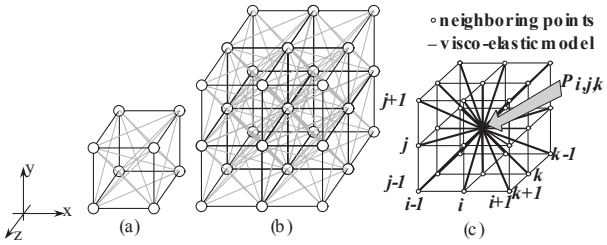

Figure 2: A voxel/lattice model of rheology object

to mass point (i,j,k) (i,j,k are integers, $1 \le i \le N_x$, $1 \le j \le N_y$ and $1 \le k \le N_z$, N_x, N_y, N_z: numbers of masses along X, Y, Z axes, respectively). Let us derive quadratic differential equation of each mass at $P_{i,j,k}$. Each internal force acting on $P_{i,j,k}$ by the element between $P_{i,j,k}$ and its neighbor $P_{i+\alpha,j+\beta,k+\gamma}$ is denoted by $F_{i,j,k}^{\alpha,\beta,\gamma}$. For each mass, 6 shorter elements whose distance is denoted as l, 12 normal elements whose distance is denoted as $\sqrt{2}l$, and 8 longer elements whose distance is denoted as $\sqrt{3}l$ are located. As a result, the unit length l is defined as $5/(N_x-1)$ [cm] for a virtual rheology object.

Therefore, total internal force $F_{i,j,k}^{int}$ acting on $P_{i,j,k}$ is given by the sum of $26(=6+12+8)$ internal forces $F_{i,j,k}^{\alpha,\beta,\gamma}$. Moreover, if the sum of active external forces at $P_{i,j,k}$ is denoted by $F_{i,j,k}^{ext}$, we obtain the following quadratic differential equation. This summation requires small calculation time.

$$M\ddot{P}_{i,j,k} = F_{i,j,k}^{int} + F_{i,j,k}^{ext} \tag{1}$$

In order to calculate next position $P_{i,j,k}$ ($1 \le i \le N_x$, $1 \le j \le N_y$ and $1 \le k \le N_z$) at each mass, we should solve the above differential equation. In this research, we select the *Euler* method as an efficient method while keeping shape stability. But, the calculation is mostly expensive.

$$F_{i,j,k}^{int} = \sum_{\substack{\alpha,\beta,\gamma \in \{-1,0,1\} \\ (\alpha,\beta,\gamma) \neq (0,0,0)}} F_{i,j,k}^{\alpha,\beta,\gamma} \tag{2}$$

Finally, in our recent work [10], we suppose that force propagations around surface and core areas of real rheology object differ from each other. For this purpose, we firstly distinguish and calibrate each basic MSD element in surface and core areas of virtual rheology object (Fig.3). That is, we prepare one set of K^{surf}, C_1^{surf}, C_2^{surf}, a^{surf}, m^{surf} in the surface area of MSD models, and also prepare another set K^{core}, C_1^{core}, C_2^{core}, a^{core}, m^{core} in the core area of that. Furthermore, all elements are classified into three for giving different sets of K, C_1, C_2, a. Firstly, we allocate a set of K^{short}, C_1^{short}, C_2^{short}, a^{short} for the length $l[cm]$. Secondly, we allocate another set of K^{normal}, C_1^{normal}, C_2^{normal}, a^{normal} for the length $\sqrt{2}l[cm]$. Finally, we allocate the other set of K^{long}, C_1^{long}, C_2^{long}, a^{long} for the length $\sqrt{3}l[cm]$.

2.3. Model of Pull-off Force

In this paragraph, we explain how to generate a 3 DOF pull-off force F_p. In our pull-off model, we assume the Voigt

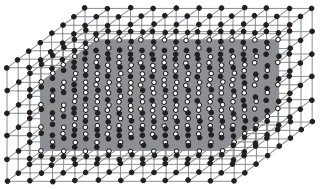

Figure 3: Surface and core areas of virtual rheology object. Black and white mass points are located on the surface and core areas, respectively. Gray voxel and dotted line are among the core area. This model has $10 \times 5 \times 7$ resolutions.

model at each mass point between rigid and rheology objects (Fig.4(a)). By adding relative displacement and velocity between rigid and rheology objects into the Voigt model at each mass, we always control elastic and viscous forces to pull off. This method is regarded as a kind of penalty method [9].

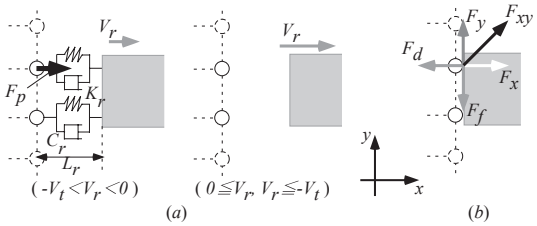

Figure 4: (a) Model of pull-off force, (b) Model of friction force

In the following, we focus on push-on or pull-off behavior along the X-axis. The behavior along Y or Z-axis is also the same. If and only if a rigid object is slowly left from a rheology object, we artificially add pull-off forces to mass points around the rheology object. The mass points are defined as a set of points where a rigid object was already met with a rheology object. That is, if a relative velocity V_r between rigid and rheology objects is smaller than its threshold V_t, the elastic force is calculated by relative displacement L_r and its coefficient K_r, and also the viscous force is done by relative velocity V_r and its coefficient C_r in the equation 3.

$$F_p = \begin{cases} K_r L_r + C_r V_r & (-V_t < V_r < 0) \\ 0 & (0 \leq V_r \ or \ V_r \leq -V_t) \end{cases} \tag{3}$$

2.4. Model of Friction Forces

In this paragraph, we consider a friction force F_f between rigid and rheology objects. In general, the Amonton-Coulomb force is classified into static and kinetic frictions (Fig.4(b)). First of all, at each mass encountered by rheology and rigid objects, we divide the internal force F_{xy} into vertical and horizontal forces, i.e., F_x and F_y.

Secondly, we calculate the maximum static friction force by $\mu_s F_d$ ($F_d = -F_x$). In succession, if $\mu_s F_d$ is larger than F_y, rheology and rigid objects are sticking and consequently the static friction force F_y acts at the mass point. Otherwise, both are sliding and therefore the kinetic friction force $\mu_k F_d$ acts at the mass point. The direction of static friction is equal to that of internal force F_y. As contrasted with this, the direction of kinetic friction is opposite to that of internal force F_y

$$F_f = \begin{cases} \mu_k F_d & (\mu_s F_d < F_y) \\ F_y & (\mu_s F_d \geq F_y) \end{cases} \tag{4}$$

Here, F_f appears a friction force at each mass point between encountered rheology and rigid objects. μ_k and μ_s are defined as coefficients of kinetic and static friction. In succession, F_d is the vertical force of rheology object at each mass point from rigid floor or pushing objects, F_x is an internal force of rheology object at each mass point. As uncertain parameters, we calibrate the static friction coefficient μ_s and the kinetic friction coefficient μ_k. The intervals are given as $0.01 < \mu_s \leq 0.99$ and $0.01 \leq \mu_k < 0.99$ under the condition that $\mu_k < \mu_s$.

3. Digital Force/Displacement Transformation

First of all, we explain how to transform displacements or forces between discrete rheology and rigid objects encountered each other. The advantage of MSD model is to calculate force propagation and shape deformation efficiently. For this reason, we do not like to prepare an enormous number of force/displacement transformation points within encountered area. The reason is as follows: As the number of voxels of rheology object and also the number of pixels around rigid body increase, calculation time of deformation increases exponentially. To overcome this explosion, we propose a smart digital/analog transformation at a few points within an encountered area between rheology and rigid objects.

As mentioned in the section 2, we already explain how to digitalize a virtual rheology object. Therefore in this section, we explain how to digitalize surface of a virtual rigid body. First of all, we uniformly divide the surface encountered by rigid and rheology objects into a set of pixels (Fig.5(a)). Secondly, we exchange displacements or forces between discrete points P_i^d of rigid body and mass points P_j^m of rheology object. For this purpose, we develop a smart analog/digital transformation method as follows: An active force f^* at P_i^d usually hits inside a pixel around the virtual rheology object. Therefore, a major force f^* should be distributed into four forces f_a, f_b, f_c and f_d at four mass points (cell vertices) P_j^m around the rheology object (Fig.5(b)). Moreover, magnitudes of four forces f_a, f_b, f_c and f_d are determined as follows: First of all, the total force measured by the 6 DOF force sensor is equally divided into each force f^* at each discrete point P_i^d. Secondly, we divide each pixel into four areas A, B, C and D centered at P_i^d. Thirdly, we determine $f_a = s \times t$ [area A] if $0.25 \times l \leq s$ and $0.25 \times l \leq t$, we regard $f_b = (l - s) \times t$ [area B] if $s \leq 0.75 \times l$ and $0.25 \times l \leq t$, we select $f_c = (l - s) \times (l - t)$ [area C] if $s \leq 0.75 \times l$ and $t \leq 0.75 \times l$, and finally we find $f_d = s \times (l - t)$ [area D] if $0.25 \times l \leq s$ and $t \leq 0.75 \times l$. Overall, magnitudes of four forces linearly correspond to their opposite areas. For example, magnitudes of f_a, f_b, f_c and f_d are linearly determined as areas A, B, C and D (Fig.5(b)), cf. equation 5).

$$\begin{aligned} f_a &= f^* \times s \times t (0.25 \times l \leq s, 0.25 \times l \leq t) \\ f_b &= f^* \times (l - s) \times t (s \leq 0.75 \times l, 0.25 \times l \leq t) \\ f_c &= f^* \times (l - s) \times (l - t) (s \leq 0.75 \times l, t \leq 0.75 \times l) \\ f_d &= f^* \times s \times (l - t) (0.25 \times l \leq s, t \leq 0.75 \times l) \end{aligned} \tag{5}$$

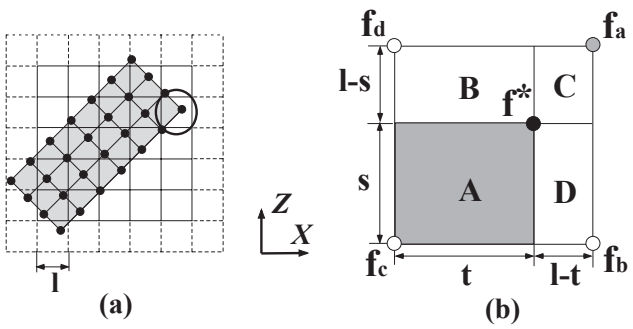

Figure 5: (a) A cell-based relationship between encountered surfaces of rheology and rigid objects. (b) An original force f^* is distributed into four forces f_a, f_b, f_c and f_d.

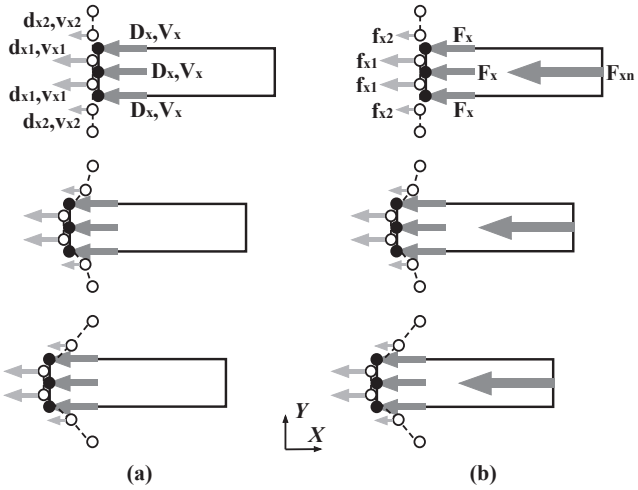

Figure 6: A smart transformation on the X-axis. (a) displacement and velocity pushing. (b) force pushing.

In the following, we explain how to push and pull a virtual rheology object by a virtual rigid body via sequence of displacement and velocity or force sequence. Based on the bilinear approximation transformation explained above, a set of encountered masses is transformed by sequence of displacement and velocity or force sequence. For the evaluation, we keep deformations of virtual and real rheology objects are the same. In Fig.6, we describe some behavior on the XY 2-D plane. Also, we prepare same behaviors on the YZ and ZX 2-D planes.

3.1. Displacement and Velocity Pushing

First of all, this pushing or pulling is quite wonderful for us to use in the 3-D CG virtual world. The reason is a human operator does not have any force sensor on his hand. In a virtual 3-D world, both of displacements and velocities can be automatically calculated. In Fig.6(a), displacement D_x and velocity V_x of rigid body can be always calculated in the 3-D CG world. Consequently, all the displacements or velocities of discrete points (dotted by black) within the contact area are given. Based on the analog/digital transformation, displacement d_x and velocity v_x around a rheology object at their neighboring masses (dotted by white) are calculated. In this case, larger displacements d_{x1} and v_{x1} and smaller displacements d_{x2} and $v_{x2}$are distributed.

3.2. Force Pushing

First of all, this pushing or pulling is so not good. The reason is that an operator does not equip any force sensor in order to manipulate a virtual rheology object by a virtual rigid body. In a 3-D CG world, each force cannot be detected, and therefore the force should be completely measured by 6 DOF force sensor as F_{xn} in advance. In Fig.6(b), the total merged force F_{xn} is distributed into F_x at mass points around a virtual rheology object according to equation $F_x = F_{xn}/n$ (n: the number of discrete points where rigid and rheology objects encounter). Using the analog/digital transmission method, external forces f_{x1} and f_{x2} at mass points around a virtual rheology object are calculated.

4. Evaluation of Virtual Rheology Object by Shape and Force Sequences

In this section, we explain how to evaluate a calibrated virtual rheology object. For this purpose, we prepare two kinds of differences against its experimental real rheology object. One is the shape difference, and the other is the force difference.

4.1. How to Calculate Shape Difference between Real and Virtual Objects

A rheology object is experimentally and precisely pushed by two rigid bodies located at tips of two machines (Fig.10). The deformation, that is, the sequence of shapes is measured by two stereo vision camera systems *Digiclops* and its software development kit (SDK) *Triclops* (provided by Point Grey Research Inc, Canada). Each captures about three or more thousand points as shape of real rheology object in the real-time manner.

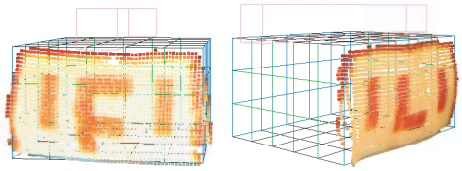

Figure 7: The real and virtual coordinate systems are coincident with each other by matching their vertices and color landmarks

In order to evaluate a shape difference between real and virtual rheology objects, we summarize minimum distances (s_n) from captured points to their nearest surfaces around a virtual rheology object (Fig.7). A virtual object consists of $N_x \times N_y \times N_z$ hexahedrons which are individually deformed from initial voxels. Therefore in order to evaluate the difference, we calculate the minimum of $N_x \times N_y \times N_z$ shortest distances for each captured point to all hexahedrons by Lin-Canny closest point algorithm [8]. In succession, we

calculate the sum S_{shape} of 0all minimum distances for all captured points N_s, which are smaller than the average error 0.05[cm] of *Digiclops*. Finally, in the present study, we use sum of S_{shape} captured at $M(=5)$ times during and after each pushing for the evaluation (Fig.9(a)).

$$S_{shape} = \sum_{m=1}^{M} \sum_{n=1}^{N_s} |s_n| \tag{6}$$

4.2. How to Calculate Force Difference between Real and Virtual Rheology Objects

In order to evaluate a force difference between real and virtual rheology objects, we summarize reactive forces from them under the Newton's 3rd (action-reaction) law. During the period B ($t_0 \sim t_n$) in Fig.8, we summarize the difference of calculated virtual and experimental real forces under the sampling time 2 [msec]. Each F_{mea} of two real sequences is directly measured by two force sensors mounted in two machines. On the other hand, each F_{calc} of two virtual sequences of forces is indirectly calculated at their positions of force sensors. The F_{calc} is calculated by summarizing all the reactive forces at the discrete points around the rigid body by the smart analog/digital transformation.

$$S_{force} = \sum |F_{mea}(t) - F_{calc}(t)| \tag{7}$$

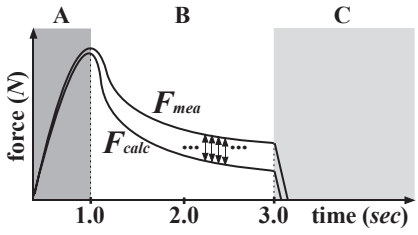

Figure 8: The total difference S_{force} between experiment internal forces F_{mea} and calculated internal forces F_{calc} in the time step Δt (= 2.0[msec])

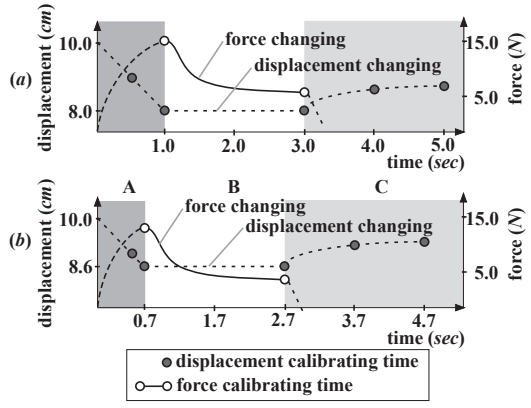

Figure 9: Pushing, keeping and releasing operations between rheology and rigid objects (a) first pushing. (b) second pushing.

5. Experimental Results

In our experiment, a real rheology object is built by mixing wheat flour and water. The weight of rheology object is 510.0[g] and the scales of that are 10.0[cm] × 5.0[cm] × 7.0[cm] along X, Y and Z axes. Then, the real rheology object is pushed by a rigid body located at the tip of the robotic manipulator $PA-10$ (Mitsubishi Heavy Industry Co.). Especially so as to investigate reappearance of our MSD rheology object, we prepare two kinds of pushing operations described in the Fig.9. The deformation of rheology object, that is, the sequence of shapes is measured by two stereo vision camera systems *Digiclops* and software development kit (SDK) *Triclops* (provided by Point Grey Research Inc, Canada). Each captures about three thousand points as shape of real rheology object in real-time manner. Then, we calibrate all the sets of physical parameters by GA (Genetic Algorithm).

Figure 10: Our experimental system.

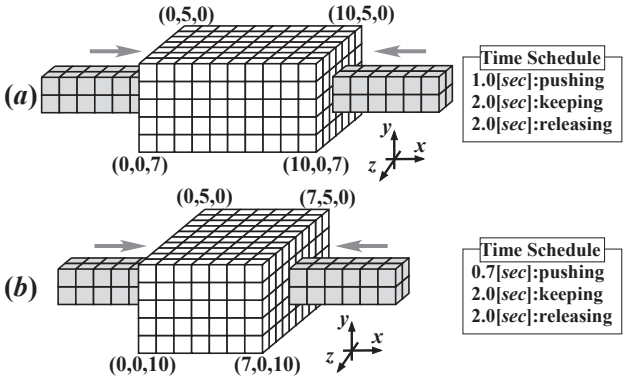

Figure 11: (a) first pushing operation. (b) second pushing operation.

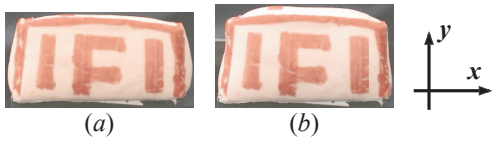

Figure 12: (a) before deformation. (b) after deformation.

In this research, we compare four combinations by two evaluations. Four combinations are as follows:

(**a**) starting by displacement sequence - calibrating by shape sequence (S_{shape})

(**b**) starting by displacement sequence - calibrating by force sequence (S_{force})

(**c**) starting by force sequence - calibrating by shape sequence (S_{shape})

(**d**) starting by force sequence - calibrating by force sequence (S_{force})

For each of four combinations, we evaluate the sum of shape or force differences between real and virtual objects. In Table 1, we describe all shape errors captured by the stereo visions. The captured points are 2821, 2795, 2815, 2815, 2811 at 1st, 2nd, 3rd, 4th, 5th trials, respectively, and consequently total ones are 14317. In addition, calculated final shapes are described in Fig.13. Note that orange points in Fig.13 means virtual surface points whose errors are larger than or equal to 0.25cm. On the other hand, calculated and measured force distributions are illustrated in Fig.14.

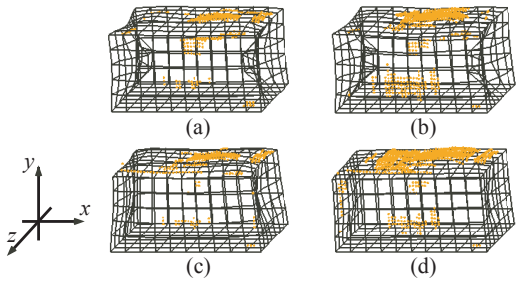

Figure 13: Four types of shape evaluations. (a) displacement push captured by the first pushing - calibration by shape differences captured by the first pushing - evaluated by shape differences captured by the first pushing. (b) displacement push captured by the first pushing - calibration by force differences captured by the first pushing - evaluated by shape differences captured by the first pushing. (c) force push captured by the first pushing - calibration by shape differences captured by the first pushing - evaluated by shape differences captured by the first pushing. (d) force push captured by the first pushing - calibration by force differences captured by the first pushing - evaluated by shape differences captured by the first pushing.

According to the above results, we can understand the following facts:

- In order to get a visual reality, we should select the combination (a). The reason is as follows: the S_{shape} and the number of large error points are the smallest (Table1). Two concave shapes around pushing sides and four convex shapes around no pushing sides are to be accurate (Fig.13).
- In order to get a tactile reality, we should select the combination (d). The reason is as follows: each and total force errors of (b) are better than those of (d) slightly (Fig.14). However, force sequence around pushing period is not accurate. This reduced to the tactile reality.

According to the results mentioned above, we should use twin calibration sets (a) and (d) for making visual and tactile realities in a 3-D CG environment.

Table 1: Force and shape evaluating four combinations.

	categories	(a)	(b)	(c)	(d)
	push operation	disp.	disp.	force	force
	calibration index	shape	force	shape	force
shape error per [cm] all points	$1st$	419.45	425.79	435.25	429.89
	$2nd$	432.93	481.01	497.36	464.33
	$3rd$	360.42	458.16	375.70	449.01
	$4th$	347.64	442.07	328.92	484.61
	$5th$	353.06	444.74	323.50	510.67
	total	1912.5	2251.8	1960.7	2338.5
shape error per [cm] each point	$1st$	0.15	0.15	0.15	0.15
	$2nd$	0.15	0.17	0.18	0.17
	$3rd$	0.12	0.15	0.12	0.15
	$4th$	0.12	0.16	0.12	0.17
	$5th$	0.13	0.16	0.12	0.18
	total	0.13	0.16	0.14	0.16
large error point ($\geq$ 0.25[cm]) number	$1st$	480	505	565	533
	$2nd$	550	752	752	607
	$3rd$	338	667	385	734
	$4th$	367	645	320	795
	$5th$	352	624	333	882
	total	2087	3193	2355	3551
large error point ($\geq$ 0.25[cm]) percentage	$1st$	17.02	17.9	20.03	18.89
	$2nd$	19.68	26.91	26.91	21.72
	$3rd$	10.99	21.69	12.52	23.87
	$4th$	13.04	22.91	11.37	28.24
	$5th$	12.52	22.2	11.85	31.38
	total	15.58	22.30	16.45	24.80

5.1. Comparative Evaluation of Parameter Reappearance

As the comparative study of different pushing operations, we evaluate force and shape sequences of rheology MSD models by the second pushing operation, which are calibrated by the first and second pushing ones. Both pushing operations are explained in Fig.11 and Fig.9. The difference between them is as follows: the pushing side is $10.0[cm] \times 7.0[cm]$, and pushing time is $0.7[sec]$.

In the previous paragraph, we can see the same kinds of combinations such as displacement pushing, shape calibrating, shape evaluating or force pushing, force calibrating, force evaluating are better than the other combinations. For this reason, we evaluate the following combination for the second pushing operation.

(**e**) displacement push captured by the second operation - calibration by the sum S_{shape} captured by the second operation.

(**f**) force push captured by the second operation - calibration by the sum S_{force} captured by the second operation.

(**g**) displacement push captured by the second operation - calibration by the sum S_{shape} captured by the first operation.

(**h**) force push captured by the second operation - calibration by the sum S_{force} captured by the first operation.

For each of four combinations, we evaluate the sum of

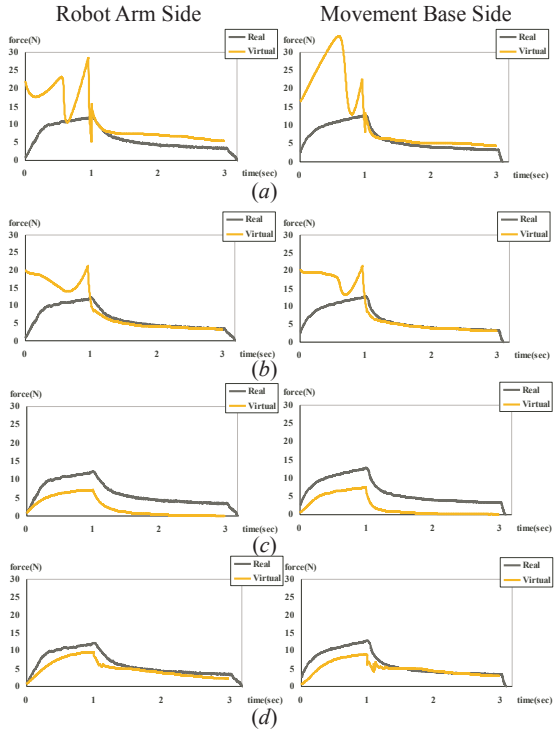

Figure 14: Four types of force evaluations. (a) total error sum: 3803.6[N], each sampling error: 2.54[N], displacement push captured by the first pushing - calibration by shape differences captured by the first pushing - evaluated by force differences captured by the first pushing. (b) total error sum: 538.7[N], each sampling error: 0.36[N], displacement push captured by the first pushing - calibration by force differences captured by the first pushing - evaluated by force differences captured by the first pushing. (c) total error sum: 7448.3[N], each sampling error: 4.97[N], force push captured by the first pushing - calibration by shape differences captured by the first pushing - evaluated by force differences captured by the first pushing. (d) total error sum: 979.5[N], each sampling error: 0.65[N], force push captured by the first pushing - calibration by force differences captured by the first pushing - evaluated by force differences captured by the first pushing.

shape or force differences between real and virtual objects. In Table 2, we describe all shape errors captured by the stereo visions. The captured points are 2255, 2168, 2213, 2201, 2165 at 1st, 2nd, 3rd, 4th, 5th trials, respectively, and consequently total ones are 11029. In addition, calculated final shapes are described in Fig.15. Note that orange points in Fig.15 means virtual surface points whose errors are larger than or equal to 0.25cm. On the other hand, calculated and measured force distributions are illustrated in Fig.16.

According to the above results, we can understand the following facts:

- As shown in Fig.15, comparing shape sequences (e) and (g) calibrated by shape differences along first and second operations, we obtain the similar set of shapes. That is, we evaluate total difference by about 200$[cm]$ (each difference is about 0.02$[cm]$).

Table 2: Force and shape evaluating four combinations.

	categories	(e)	(f)	(g)	(h)
	appearance	same data	same data	different data	different data
	push operation	disp.	force	disp.	force
	calibration index	shape	force	shape	force
shape error per $[cm]$ all points	$1st$	445.24	525.72	492.30	525.52
	$2nd$	382.42	522.09	462.06	506.37
	$3rd$	402.07	638.01	437.84	627.37
	$4th$	376.91	648.86	405.80	649.12
	$5th$	358.24	657.62	385.31	665.96
	total	1964.9	2992.3	2183.3	2974.3
shape error per $[cm]$ each point	$1st$	0.20	0.23	0.22	0.23
	$2nd$	0.17	0.24	0.21	0.23
	$3rd$	0.18	0.29	0.20	0.28
	$4th$	0.17	0.29	0.18	0.29
	$5th$	0.17	0.30	0.18	0.31
	total	0.18	0.27	0.20	0.27
large error point ($\geq$ 0.25[cm]) number	$1st$	707	1024	857	1017
	$2nd$	616	989	830	941
	$3rd$	620	1349	758	1334
	$4th$	553	1347	697	1399
	$5th$	529	1381	657	1503
	total	3025	6090	3799	6194
large error point ($\geq$ 0.25[cm]) percentage	$1st$	31.35	45.41	38.00	45.10
	$2nd$	28.02	45.06	37.81	42.87
	$3rd$	28.02	60.96	34.25	60.28
	$4th$	25.12	61.20	31.67	63.56
	$5th$	24.43	63.79	30.35	69.42
	total	27.43	55.22	34.45	56.16

- As described in Fig.16, comparing force sequences (f) and (h) calibrated by force differences along first and second operations, we obtain the similar set of forces. That is, we evaluate total difference by 100$[N]$ (each difference is about 0.06$[N]$).

According to the results mentioned above, we should use twin sets (e) and (f) calibrated by the second operation or g and h calibrated by the first operation for making visual and tactile realities in a 3-D CG environment.

6. Conclusions and ongoing remarks

In this paper, we compared eight combinations of displacement and force pushes, shape and force calibrations, and shape and force evaluations. Consequently, we selected two wonderful combinations such as displacement push - shape calibration - shape evaluation and force push - force calibration - force evaluation. As a result, in order to maintain visual and tactile realities of virtual rheology object, we use the dual system based on the first and second sets of calibrated parameters.

Furthermore, we checked whether each set calibrated by one pushing operation is straightforwardly applied for another pushing operation. For this purpose, we compared shape and force errors under all the parameters calibrated by the first pushing operation with those under all the parameters calibrated by the second pushing operation. As a result, we can see our twin sets have reappearance concerning to shapes and forces even though calibrated data differ from evaluation data.

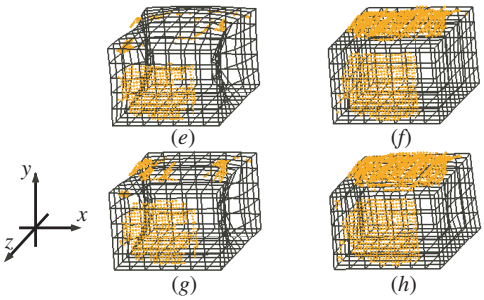

Figure 15: Four types of shape evaluations. (e) displacement push captured by the second pushing - calibration by shape differences captured by the second pushing - evaluated by shape differences captured by the second pushing. (f) force push captured by the second pushing - calibration by force differences captured by the second pushing - evaluated by shape differences captured by the second pushing. (g) displacement push captured by the second pushing - calibration by shape differences captured by the second pushing - evaluated by shape differences captured by the first pushing. (h) force push captured by the second pushing - calibration by force differences captured by the second pushing - evaluated by shape differences captured by the first pushing.

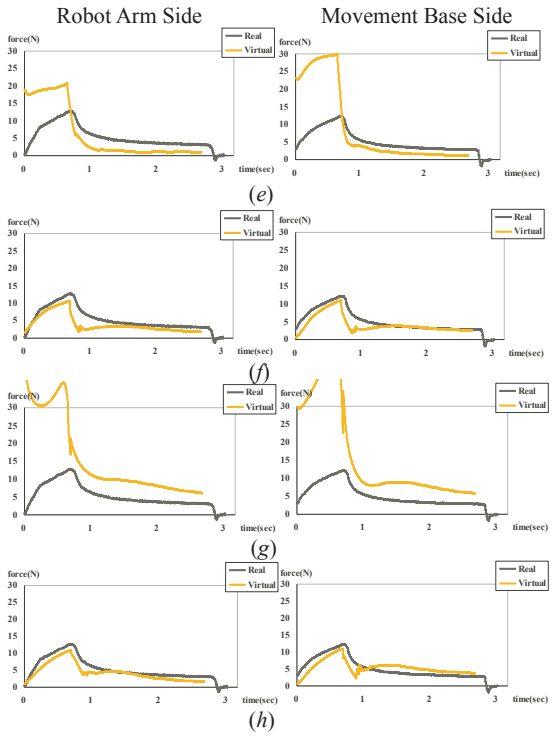

Figure 16: Four types of force evaluations. All are evaluated by the second pushing operation. (e) displacement push captured by the second operation, calibration by shape sum captured by the second operation. (f) force push captured by the second operation, calibration by force sum captured by the second operation. (g) displacement push captured by the second operation, calibration by shape sum captured by the first operation. (h) force push captured by the second operation, calibration by force sum captured by the first operation.

Finally, the displacement pushing operation is useful in order for us to use in a virtual 3-D CG world because the displacement can be always calculated in the environment. However, when we observe our comparative evaluations, force distributions especially during the pushing period are not good. Consequently in future, we should prepare and calibrate some collision model between rigid and rheology objects for translating a set of displacements and velocities into its set of forces.

References

[1] C.Laugier. A.Joukhadar, F.Garat. Parameter identification for dynamic simulation. In *Proc. of the IEEE Int. Conf. on Robotics and Automation*, pages pp.1928–1933, 1997.

[2] D.K.Pai. D.James. Artdefo: accurate real time deformable objects. In *Proc. of the SIGGRAPH '99*, pages pp.65–72, 1999.

[3] A.Barr K.Fleischer. D.Terzopoulos, J.Platt. Elastically deformable models. In *Proc. of the SIGGRAPH '87*, pages pp.205–214, 1987.

[4] K.Fleisher. D.Terzopoulos D. Modeling inelastic deformation: viscoelasticity, plasticity, fracture. In *Proc. of the SIGGRAPH '99*, pages pp.269–278, 1988.

[5] S.Nishimoto T.Tanemura. H.Noborio, R.Enoki. On the calibration of deformation model of rheology object by a modified randomized algorithm. In *Proc. of the IEEE Int. Conf. on Robotics and Automation*, pages pp.3729–3736, 2003.

[6] Y.Murata H.Yoshida and H.Noborio. A smart rheologic msd model pushed/calibrated/evaluated by experimental impulses. In *Proc. of the IEEE/RSJ Int. Conf. Intelligent Robots and Systems*, pages pp.1614–1621, 2005.

[7] K.Waters. A muscle model for animating three-dimensional facial expression. In *Proc. of the SIGGRAPH '87*, pages pp.17–24, 1987.

[8] M.C.Lin and J.F.Canny. A fast algorithm for incremental distance calculation. In *Proc. of the IEEE Int. Conf. on Robotics and Automation*, pages pp.1008–1014, 1991.

[9] J.Wilhelms. M.Moore. Collsion detection and response for computer animation. *Computer Graphics*, pages pp.289–298, 1988.

[10] H.Fujii H.Noborio. R.Nogami, F.Ujibe. Precise deformation of rheologic object under msd models with many voxels and calibrating parameters. In *Proc. of the IEEE Int. Conf. on Robotics and Automation*, pages pp.1919–1926, 2004.

[11] S.Hirai. S.Tokumoto, Y.Fujita. Deformation modeling of visco-elastic objects for their shape control. In *Proc. of the IEEE Int. Conf. on Robotics and Automation*, pages pp.1050–1057, 1999.

基礎論文

力/形状でキャリブレーションしたMSDレオロジーモデルの力/形状の再現性について

吉田晴行　氏部史章　登尾啓史

VR医学
Japanese Journal for Medical Virtual Reality

2007
Vol. 5　No. 1　通巻5号

別刷

日本VR医学会
Japanese Society for Medical Virtual Reality
http://www.jsmvr.umin.ne.jp

力/形状でキャリブレーションしたMSDレオロジーモデルの力/形状の再現性について

吉田 晴行 *，氏部 史章 **，登尾 啓史 **
* 制御機械工学専攻, ** 情報工学専攻
大阪電気通信大学 大学院工学研究科

On the Force/Shape Reappearance of MSD Rheology Model Calibrated by Force/Shape Sequence

Haruyuki Yoshida*, Fumiaki Ujibe**, Hiroshi Noborio**
*Division of Mechanical and Control Engineering, **Division of Information and Computer Science, Graduate School of Engineering,
Osaka Electro-Communication University

Abstract: In this paper, we firstly push or pull real and virtual rheology objects by the same sequence of displacements or forces. Then by minimizing the sum of differences between shape or force sequences of real and virtual objects, we calibrate many parameters of rheology MSD (Mass-Spring-Damper) model, pull-off force model and friction force model between a rigid object and its pushed or pulled rheology object. The calibration is processed by a near-optimal probabilistic search (genetic algorithm). In this paper, we firstly consider eight combinations which rheology objects are pushed, calibrated, evaluated by shape sequence, and pushed, calibrated, evaluated by force sequence. After completely comparing all the possibilities, we get the best visual reality under push and calibration by shape sequence, and also the wonderful tactile reality under push and calibration by force sequence. Moreover, we ascertain reappearance of force or shape sequence even though sensing data (pushing operation) in calibration differs from sensing data (pushing operation) in evaluation.
Keyword: Rheology object, Mass-Spring-Damper(MSD) model, Parameter identification.

1 はじめに

近年，3 次元 CG が創り出す仮想環境において，人工物体を操作する研究が盛んである．例えば，人工物体の変形アニメーションを創出したり，触覚フィードバックデバイスを介して接触力や衝突力を体感する試みが注目されている．これまで，剛体，弾性体，塑性体のモデルは数多く提案されてきた [1],[2],[3],[4]．しかし，実際と仮想の振る舞いを合致させるようにモデルパラメータを同定する研究は少ない [5],[6]．また，食品，衣類，人体などを構成するレオロジー物体モデルの提案もほとんどない [9],[10]．このため我々は，運動方程式が高速かつ安定に解ける MSD(Mass-Spring-Damper) の格子構造モデルを仮想レオロジー物体のモデルとして採用し，その未知パラメータを同定してきた [7],[8]．

本論文では，変位と力で変形を起動し，形状と力で未知パラメータを同定し，形状と力で実物体と仮想物体の合致を評価する．また，異なる 2 種類の押し方を適用し，一方の押し方で同定されたモデルパラメータの組を持つ仮想物体に対して，他方の押し方が与えられた際の変形応答挙動を評価し，同定パラメータの汎用性を考察する．

本論文では，第 2 章でレオロジー物体の力学変形特性を表現する MSD(Mass-Spring-Damper) 要素モデル，および 3 次元仮想物体を構築する 3 次元格子構造モデルについて，その詳細を述べる．第 3 章では，リアルな挙動を再現するために導入した凝着力と摩擦力のモデルを説明する．第 4 章では，実物体と仮想物体の押し方を説明する．第 5 章では，形状と力の 2 種類の指標より未知パラメータの同定手法を述べ，第 6 章ではそれらを評価する．そして第 7 章では，本取り組みにより得られた知見をまとめ, 結論とする．

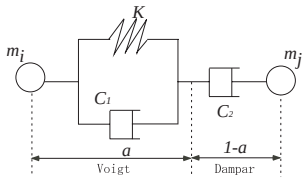

Figure 1 : 我々の 3 要素モデル　Our three element model to represent rheological properties.

2 レオロジー物体のモデル化手法

レオロジー物体とは，弾性体と塑性体の中間的な力学変形特性を有する物体の総称とされる．レオロジー物体は，外力を作用させると変形するが，外力を解放したあとその形状は初期形状まで戻らない．ここで，外力解放前後の形状差を“ 戻り変位 ”，初期形状と外力解放後の形状との差を“ 残留変位 ”という．弾性体や塑性体では，それぞれ戻り変位と残留変位しか見受けられないが，レオ

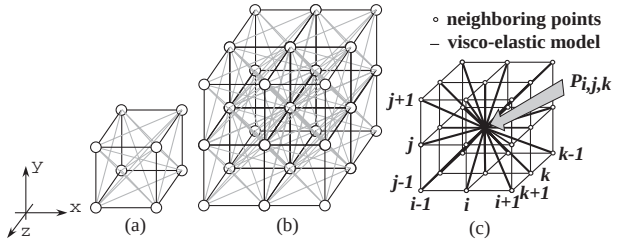

Figure 2 : 格子構造モデル　A voxel/lattice model

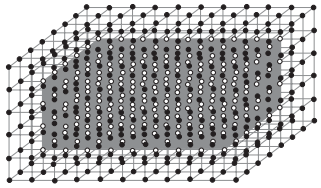

Figure 3 : 仮想レオロジー物体の表面領域と内部領域　Surface and core areas of virtual rheology object.

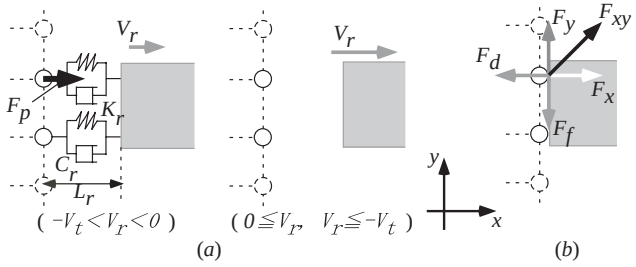

Figure 4 : 仮想レオロジー物体 (破線で表現) と仮想剛体 (灰色で表現) の接触. A rheology object is expressed by a set of dotted lines and a rigid body is represented by the gray object. (a) 凝着力モデル　Pull-off force model. (b) 摩擦力モデル Friction force model.

ロジー物体では両方とも見受けられる．このような力学変形特性を持つ例としては，パン生地やゼリー等の食品類，臓器や血管等の生体組織等がある．本章では，レオロジー物体の変形特性を記述する力学モデルを提案する．

2.1　力学 3 要素モデル (MSD モデル)

本研究では，レオロジー物体の変形特性を表現するため，MSD(Mass-Spring-Damper) モデルを用いる (**Fig.1**)．このマス (質量)，スプリング (弾性要素)，ダンパ (粘性要素) より構成されたモデルは，レオロジー特性を容易に表現できるとともに安定かつ高速に解ける運動方程式を導出する特徴がある [9] [10]．ここで，戻り変位と残留変位は，それぞれこのモデルのフォークト部 (Fig.1 の左部) とダンパ部 (Fig.1 の右部) で表現される．ここで，フォークト部の弾性パラメータを K，粘性パラメータを C_1，ダンパ部の粘性パラメータを C_2 とする．また，フォークト部とダンパ部の長さの比率を $a : 1-a$ とする．

次に，3 次元仮想レオロジー物体の構築手法 [10] を述べる．上述の力学 3 要素モデルを 3 次元格子構造に配置する (**Fig.2**)．まず，単位長を設定し，それに合わせて x，y，z の各軸方向を分割する．各線分の交点に質点を配置し，各線分に 3 要素モデルを配置する．また，形状を保つため，斜め方向にも 3 要素モデルを配置する (Figs.2(a),(b))．これより，1 辺の長さを l_{voxel} とすると，3 要素モデルの長さは l_{voxel},$\sqrt{2}l_{voxel}$,$\sqrt{3}l_{voxel}$ の 3 種類となる．すなわち，長さ l_{voxel} の要素の係数 K^{short}, C_1^{short}, C_2^{short}, a^{short}, 長さ $\sqrt{2}l_{voxel}$ の要素の係数 K^{normal}, C_1^{normal}, C_2^{normal}, a^{normal}, 長さ $\sqrt{3}l_{voxel}$ の要素の係数 K^{long}, C_1^{long}, C_2^{long}, a^{long} を同定対象とする．

次に，格子数 $N_x \times N_y \times N_z$ 個で構成された 3 次元格子構造の力学関係を考える．質点数は，$(N_x+1)\times(N_y+1)\times(N_z+1)$ 個となる (Fig.2(c))．ここで，質点 $P_{i,j,k}(i,j,k$ は整数, $1 \le i \le N_x+1$, $1 \le j \le N_y+1$, $1 \le k \le N_z+1)$ とその隣接点 $P_{i+\alpha,j+\beta,k+\gamma}$ 間の要素に働く力を $F_{i,j,k}^{\alpha,\beta,\gamma}$ とすると，質点 $P_{i,j,k}$ に作用する内力 $F_{i,j,k}^{int}$ は $F_{i,j,k}^{\alpha,\beta,\gamma}$ の総和となる．

$$F_{i,j,k}^{int} = \sum_{\substack{\alpha,\beta,\gamma\in\{-1,0,1\} \\ (\alpha,\beta,\gamma)\neq(0,0,0)}} F_{i,j,k}^{\alpha,\beta,\gamma} \tag{1}$$

さらに，質点 $P_{i,j,k}$ に作用する外力の総和を $F_{i,j,k}^{ext}$ とするとニュートンの運動第二法則より，質点 $P_{i,j,k}$ の運動方程式は以下のように表現される．

$$m\ddot{P}_{i,j,k} = F_{i,j,k}^{int} + F_{i,j,k}^{ext} \tag{2}$$

ここで，質点 $P_{i,j,k}$ の質量 m は，実物体の総質量を総質点数 $(N_x+1)\times(N_y+1)\times(N_z+1)$ で割ることで得られる．この運動方程式 (式 (2)) を数値積分 (例えばルンゲ・クッタ法) で解くと，各時刻における各質点の変位が求まり，仮想レオロジー物体の変形挙動が決定される．なお，床面に接する質点は，作用反作用の法則 (ニュートンの運動第三法則) より等価な反力を与えて固定する．

我々は，表面領域と内部領域で力伝播が異なるモデルを考える．すなわち，表面領域の係数 K^{surf}, C_1^{surf}, C_2^{surf}, a^{surf} と内部領域の係数 K^{core}, C_1^{core}, C_2^{core}, a^{core} を独立に同定する．解像度 $10\times5\times7$ の仮想レオロジー物体を **Fig.3** に示す．黒と白の質点はそれぞれ，表面と内部の領域にあり，灰色のボクセルは内部領域に相当する．

3　物体表面に働く力のモデル

本研究の目的は，実物体の変形挙動を仮想物体に再現させることである．そのため，実レオロジー物体が他の物体と接する際に生ずる凝着力と摩擦力をモデル化し，実空間における力学現象のリアリティーを向上させる (**Fig.4**)．

3.1　凝着力モデル

レオロジー物体は，他の物体と凝着する特性を持つ．本研究では，ペナルティ法としてケルビン・フォークトモデル (弾性係数を K_r，粘性係数を C_r とする) を採用し，凝着力 F_p を表現する (式 (3)) [11] [12] [13]．この凝着力は，それらがある速度以下で遠ざかるときのみ接触面上の質点に発生する．ここで，物体間の相対変位を L_r，相対速度とその閾値を V_r および V_t とする．

$$F_p = \begin{cases} K_r L_r + C_r V_r \ (-V_t < V_r < 0) \\ 0 \ (0 \le V_r \ or \ V_r \le -V_t) \end{cases} \tag{3}$$

3.2　摩擦力モデル

一般に，接触する物体の間には摩擦が生ずる．本研究では，レオロジー物体とそれを押したり引いたりする剛体との間，およびレオロジー物体と床面との間に摩擦が生じる．ここでは，アモントン-クーロンの摩擦法則に従って静止摩擦力および動摩擦力を導入する．今回の変形実験では，レオロジー物体と剛体が x 軸を垂線方向として接触することから yz 平面に摩擦力が生ずる．一方，レオロジー物体と床面は y 軸を垂線方向として接触することより xz 平面に摩擦力が生ずる．

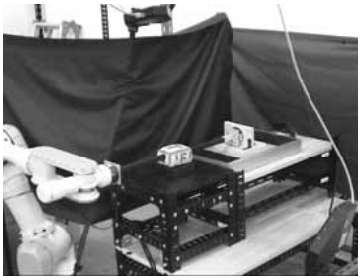

Figure 5 : 実験計測システム． An experimental measurement system.

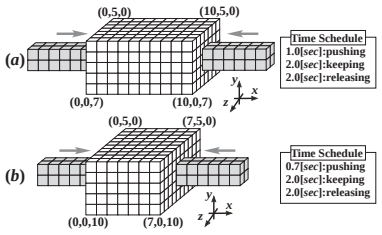

Figure 6 : (a) 第 1 の押し方 First pushing operation. (b) 第 2 の押し方 Second pushing operation.

まず，剛体が働きかける力 F_{xy} を x 方向と y 方向に分ける (Fig.4(b))．ここで，x 方向に作用する F_x の反力を垂直抗力 F_d とし，それに最大静止摩擦係数 μ_s を掛けると最大静止摩擦力 $\mu_s F_d$ が得られる．これと y 方向に作用する力 F_y を比較し，F_y の方が大きければ動摩擦力 $\mu_k F_d$，そうでなければ静止摩擦力 F_y を摩擦力 F_f を発生させる (式 (4))．

$$F_f = \begin{cases} \mu_k F_d (\mu_s F_d < F_y) \\ F_y \ (\mu_s F_d \geq F_y) \end{cases} \tag{4}$$

4 物体の押し方について

ここでは，現実と仮想のレオロジー物体の押し方について考察する．

4.1 実物体の押し方について

まず，小麦粉と水を 2 : 1 の割合で混ぜ合わせた物体 (総質量 510[g]) を $10.0[cm] \times 5.0[cm] \times 7.0[cm]$ に成型する．次に，ロボットアーム (三菱重工業製 $PA10$) の先端に取り付けた剛体でそれを正確に押し付ける (**Fig.5**)．本論文では，**Fig.6** に示すような 2 種類の加重実験を行う．1 つ目では，$5.0[cm] \times 7.0[cm]$ の両面を $2.0[cm/sec]$ の速度で $1.0[sec]$ の間加重し，その状態を $2.0[sec]$ 保持し，そして除重する (Fig.6(a))．2 つ目では，$5.0[cm] \times 10.0[cm]$ の両面を $2.0[cm/sec]$ の速度で $0.7[sec]$ の間加重し，その状態を $2.0[sec]$ 保持し，そして除重する (Fig.6(b))．

4.2 仮想物体の押し方について

本節では，位置変位と力による仮想物体への 2 種類の押し方を説明する (**Fig.7**)．

4.2.1 位置変位での押し

これは，仮想レオロジー物体の表面質点に強制的に変位を与え，外力を間接的に与える方法である．まず，仮想レオロジー物体と同様に，仮想剛体の表面を格子状に分割し質点を配置する．次に，仮想剛体の質点が仮想レオロジー物体の質点と接すればそのまま変位を受け渡し，そうでなければ仮想レオロジー物体の 4 つの隣接質点に変位を分配して受け渡す (Fig.7(a))．ここで，仮想剛体の

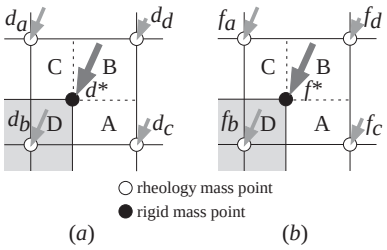

Figure 7 : 外力は近隣の 4 質点に分配される． External force is distributed into four forces at neighbor masses. (a) 変位押し displacement pushing operation. (b) 力押し force pushing operation.

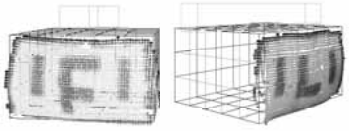

Figure 8 : 現実と仮想の座標系は頂点とカラーランドマークで一致させる． Real and virtual coordinate systems are coinsident with each other by matching their vertices and color landmarks.

質点 (黒い点で表示) の変位を d^*，仮想レオロジー物体の質点 (白い点で表示) の変位を各々 d_a, d_b, d_c, d_d とする．この変位 d^* は予め定めたロボットアームや移動台の手先速度に時間を掛けたものである．ここでは，4 つの領域 A,B,C,D の面積比率に d^* を掛けることで，4 つの位置変位 d_a, d_b, d_c, d_d を算出する．例えば，d_a は領域 A の面積比率を掛けて算出する．この双一次補間という手法より，剛体の質点の変位から仮想レオロジー物体の質点の変位を計算する．

4.2.2 力での押し

これは，仮想レオロジー物体の表面質点に外力を直接与える方法である．この外力は，ロボットアームと移動台の手先に取り付けた力覚センサでリアルタイムに計測されたものを用いる．まず，前節と同様に剛体の表面を格子状に分割し質点を配置する．次に，計測反力を仮想レオロジー物体と接する剛体表面の質点数で割り，各々の外力 f^* を算出する．最後に，前節の双一次補間より，各々の外力 f^* を隣接 4 質点に力 f_a, f_b, f_c, f_d として分配する (Fig.7(b))．

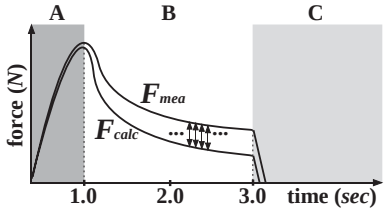

Figure 9 : 時刻 t_0(=1.0[sec]) から時刻 t_n(=3.0 [sec]) までのサンプリングタイム Δt(= 2.0[$msec$]) 毎の現実の力 F_{mea} と計算の力 F_{calc} の差の総合計 S_{force}． The total difference S_{force} between experiment real forces F_{mea} and calculted virtual forces F_{calc} from t_0 (=1.0[sec]) to t_n (=3.0 [sec]) per Δt (=2.0[msec]).

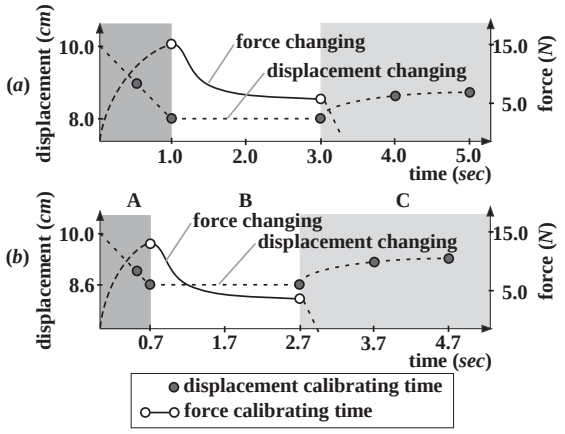

Figure 10 : 押し，維持，解放オペレーション　Pushing, keeping and releasing operations between rheology and rigid objects. **(a)** 第一の押し First pushing operation whose $t_0 = 1.0$ and $t_n = 3.0$. **(b)** 第二の押し Second pushing operation whose $t_0 = 0.7$ and $t_n = 2.7$.

5　形状と力を用いたパラメータ同定法

ここでは，遺伝アルゴリズム（準最適確率手法の一種）で形状または力の誤差を最小化させ，3 つのモデルの未知パラメータを同定する．なお，仮想レオロジー物体が変形する際のサンプリングタイムは 2.0[$msec$] としている．

5.1　形状によるパラメータ同定

まず, 実レオロジー物体の変形を 3 次元ステレオビジョンカメラ Digiclops® とソフトウェア Triclops(Point Grey Research 社製) で計測する．これより, 物体表面の 3 次元位置座標をリアルタイムで 1000 点ほど計測できる (**Fig.8**)．この計測は, 実験開始時から除重後 2.0[sec] まで実施する．そして，各計測点から仮想レオロジー物体の表面までの最小距離 s_n を Lin-Canny Algorithm [14] で求める．すべての計測点 (ここでは，その総数を N_s とする) についての合計 S を，変形の特徴が現れる 5 つの時刻 ($M = 5$) で合計し評価指標 S_{shape} を求める．その 5 つの時刻とは, 1 つ目の加重実験であれば実物体を押し始めから 0.5, 1.0, 3.0, 4.0, 5.0[sec] 後，2 つ目の加重実験であれば 0.5, 0.7, 2.7, 3.7, 4.7[sec] 後である (式 (5), **Fig.10**)．

$$S_{shape} = \sum_{m=1}^{M} \sum_{n=1}^{N_s} |s_n| \tag{5}$$

5.2　力によるパラメータ同定

まず, ロボットアームと移動台の先端部に取り付けた剛体にかかる反力を 6 軸力覚センサ (ニッタ (株) 社製) で計測する．次に, この力覚センサで取得した力 F_{mea} および仮想レオロジー物体から仮想剛体にかかる力の合力 F_{calc} の差の合計を力誤差評価の指標とする (**Fig.9**)．このとき，剛体がレオロジー物体から離れると力覚センサで力を計測できない．したがって, 剛体がレオロジー物体を押し切った時刻 t_0 からその状態を維持した時刻 t_n までが計測区間 (計測回数 n は約 1000 回) となり, 各時刻の力誤差の絶対値の和 S_{force} が評価指標となる (式 (6), Fig.10)．

$$S_{force} = \sum_{i=0}^{n} |F_{mea}(t_i) - F_{calc}(t_i)| \tag{6}$$

6　2 種類の評価について

この章では 2 種類の評価を行う．1 つ目は，加重手法と同定手法を組み合わせ的に変化させて，形状や力を評価するものである．2 つ目は，パラメータを同定する際の加重方法と形状や力を評価する際の加重方法を異なるものにし，同定パラメータにどの程度の再現性があるかを評価するものである．

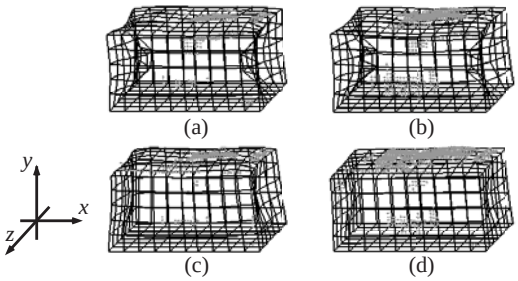

Figure 11 : 変位起動/形状同定，変位起動/力同定，力起動/形状同定，力起動/力同定による最終形状．　Final shapes by displacement/force pushing and shape/force calibrations.

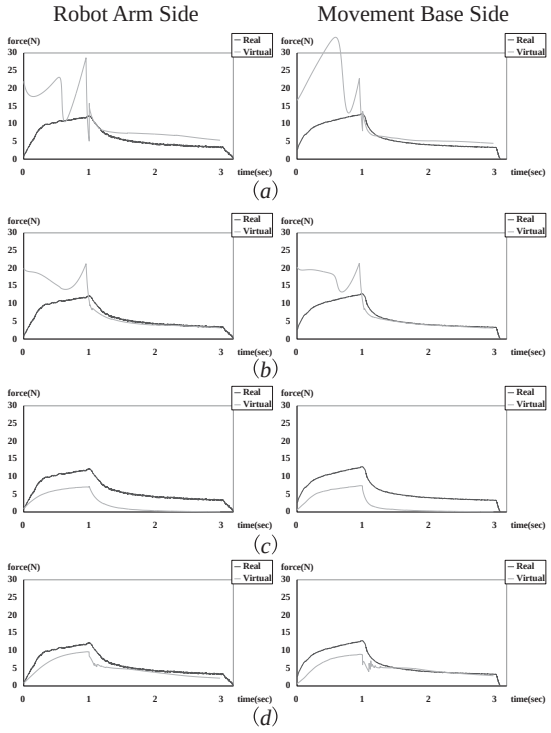

Figure 12 : 変位起動/形状同定，変位起動/力同定，力起動/形状同定，力起動/力同定による力波形．　Force waves by displacement/force pushing and shape/force calibrations.

6.1　4 パターンについての評価

まず, 10.0[cm] × 5.0[cm] × 7.0[cm] に成型したレオロジー物体の左右 5.0[cm] × 7.0[cm] の面に加重する変形実験をした (Fig.6(a), Fig.10(a))．そして，2 つの加重方法と 2 つのパラメータ同定法の組み合わせである 4 パターンそれぞれについて, 形状と力を評価する．

- (**a**) 変位押しによる起動 - 形状誤差 S_{shape} によるパラメータ同定
- (**b**) 変位押しによる起動 - 力誤差 S_{force} によるパラメータ同定
- (**c**) 力押しによる起動 - 形状誤差 S_{shape} によるパラメータ同定
- (**d**) 力押しによる起動 - 力誤差 S_{force} によるパラメータ同定

上記 4 パターンについて形状と力の誤差を評価する．ここで，形状誤差 S_{shape} と力誤差 S_{force} を **Table 1** に示す．また，最終形状を **Fig.11**, また力波形を **Fig.12** に示

Table 1 : 変位起動/形状同定，変位起動/力同定，力起動/形状同定，力起動/力同定による形状のリアリティ． Shape realities by displacement/force pushing and shape/force calibration.

	categories	(*a*)	(*b*)	(*c*)	(*d*)
	push operation	disp.	disp.	force	force
	calibration index	shape	force	shape	force
shape error per $[cm]$ all points	$1st$	419.45	425.79	435.25	429.89
	$2nd$	432.93	481.01	497.36	464.33
	$3rd$	360.42	458.16	375.70	449.01
	$4th$	347.64	442.07	328.92	484.61
	$5th$	353.06	444.74	323.50	510.67
	total	1913.5	2251.8	1960.7	2338.5
shape error per $[cm]$ each point	$1st$	0.15	0.15	0.15	0.15
	$2nd$	0.15	0.17	0.18	0.17
	$3rd$	0.12	0.15	0.12	0.15
	$4th$	0.12	0.16	0.12	0.17
	$5th$	0.13	0.16	0.12	0.18
	total	0.13	0.16	0.14	0.16
large error point (≥ 0.25[cm]) number	$1st$	480	505	565	533
	$2nd$	550	752	752	607
	$3rd$	338	667	385	734
	$4th$	367	645	320	795
	$5th$	352	624	333	882
	total	2087	3193	2355	3551
large error point (≥ 0.25[cm]) percentage	$1st$	17.02	17.9	20.03	18.89
	$2nd$	19.68	26.91	26.91	21.72
	$3rd$	10.99	21.69	12.52	23.87
	$4th$	13.04	22.91	11.37	28.24
	$5th$	12.52	22.2	11.85	31.38
	total	15.58	22.30	16.45	24.80

す．なお，2 箇所のステレオビジョンカメラで計測した表面点数は，各々2821, 2795, 2815, 2815, 2811 であり，全体のそれは 14317 であった．

まず，(**a**) における力誤差合計は 3803.6$[N]$ であり，サンプリングタイムごとの力誤差平均は 3.80$[N]$ である．一方，(**b**) における力誤差合計は 538.7$[N]$ であり，サンプリングタイムごとの力誤差平均は 0.54$[N]$ である．また，(**c**) における力誤差合計は 7448.3$[N]$ であり，サンプリングタイムごとの力誤差平均は 7.45$[N]$ である．一方，**(d)** における力誤差合計は 979.5$[N]$ であり，サンプリングタイムごとの力誤差平均は 0.98$[N]$ である．最後に，Fig.11 において，距離誤差が 0.25$[cm]$ 以上であった点を灰色で示す. これらの結果から以下の事項がわかる．

- 視覚のリアリティを獲得するにはパターン **(a)** が最良である. 何故なら，形状誤差 S_{shape} および悪点数が最小であり (Table 1)，押した側面の 2 つのへこみ形状と押されてない側面の 4 つのふくらみ形状が正確であるからである (Fig.11).
- 触覚のリアリティを獲得するにはパターン **(d)** が最良である．何故なら，**(b)** の力誤差の平均と総計が **(d)** のそれらよりも良好だからである (Fig.12). しかし, 押しているときの力波形が少々不正確なことが問題として残る．

以上より, 形状を合わせるには **(a)**，力を合わせるには **(d)** の物理パラメータを利用するのが望ましい．

6.2 再現性についての評価

ここでは，2 つの異なる押し方より，同定した物理パラメータの汎用性を評価する．そのため，10.0$[cm]$ × 7.0$[cm]$ の側面を 0.7$[sec]$ の間押す新しい押し方を採用する (Fig.6(b), Fig.10(b))．なお，前節の比較実験において，同系統のパターンが良い結果を得ていたので，ここでは以下の 4 パターンに絞って評価する．

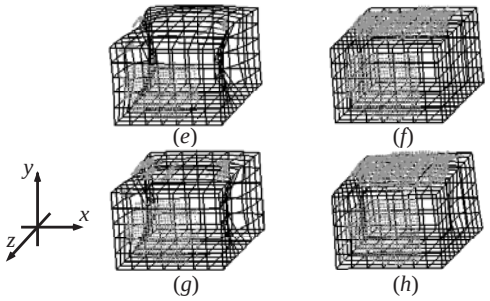

Figure 13 : 再現性に関する 4 パターンの最終形状． Concerning to reappearance, we compare four kinds of final shapes.

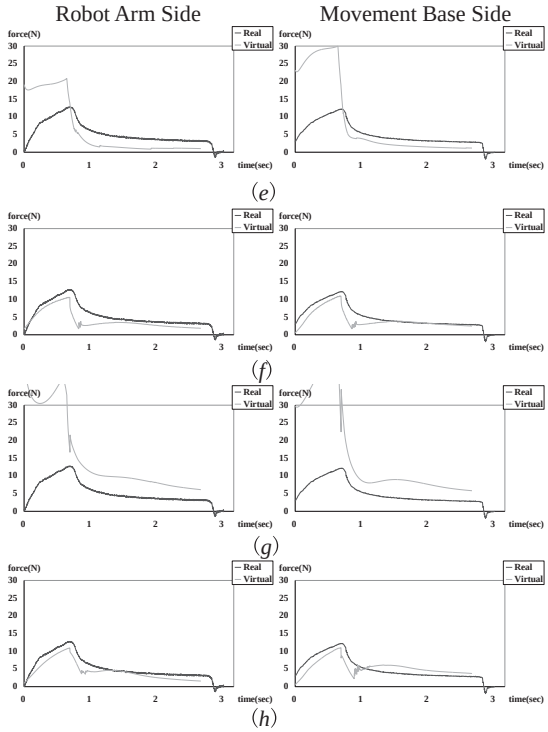

Figure 14 : 再現性に関する 4 パターンの力波形. Concerning to reappearance, we compare four kinds of force distributions.

(**e**) 新しい押し方で変位押し/新しい押し方の形状誤差 S_{shape} でパラメータ同定
(**f**) 新しい押し方で力押し/新しい押し方の力誤差 S_{force} でパラメータ同定
(**g**) 新しい押し方で変位押し/以前の押し方の形状誤差 S_{shape} でパラメータ同定
(**h**) 新しい押し方で力押し/以前の押し方の力誤差 S_{force} でパラメータ同定

上記 4 パターンを形状および力の誤差で評価した．まず, **Table 2** では, 2 箇所のステレオビジョンカメラから計測した点についての誤差を評価した．各々の計測点数は, 2255, 2168, 2213, 2201, 2165 であり，全体の計測点数は 11029 である．また, 最終形状を **Fig.13**, 力波形を **Fig.14** に示す．ここで，誤差が 0.25$[cm]$ 以上の点を灰色で示す. これらの結果から以下の事項がわかる．

- Fig.13 において，パターン **(e)** と **(g)** の形状を比較した．その結果，上部の膨らみに若干の違いはあるものの，距離の差は 200$[cm]$ 程度（各点の距離の差は 0.02$[cm]$ 程度）と十分に再現性のある結果が

Table 2 : 2 種類の押し方に関する形状の再現性. Shape reappearances calibrated by two kinds of pushing operations.

	categories	(e)	(f)	(g)	(h)
	appearance	same data	same data	different data	different data
	push operation	disp.	force	disp.	force
	calibration index	shape	force	shape	force
shape error per $[cm]$ all points	$1st$	445.24	525.72	492.30	525.52
	$2nd$	382.42	522.09	462.06	506.37
	$3rd$	402.07	638.01	437.84	627.37
	$4th$	376.91	648.86	405.80	649.12
	$5th$	358.24	657.62	385.31	665.96
	total	1964.9	2992.3	2183.3	2974.3
shape error per $[cm]$ each point	$1st$	0.20	0.23	0.22	0.23
	$2nd$	0.17	0.24	0.21	0.23
	$3rd$	0.18	0.29	0.20	0.28
	$4th$	0.17	0.29	0.18	0.29
	$5th$	0.17	0.30	0.18	0.31
	total	0.18	0.27	0.20	0.27
large error point (≥ 0.25[cm]) number	$1st$	707	1024	857	1017
	$2nd$	616	989	830	941
	$3rd$	620	1349	758	1334
	$4th$	553	1347	697	1399
	$5th$	529	1381	657	1503
	total	3025	6090	3799	6194
large error point (≥ 0.25[cm]) percentage	$1st$	31.35	45.41	38.00	45.10
	$2nd$	28.02	45.06	37.81	42.87
	$3rd$	28.02	60.96	34.25	60.28
	$4th$	25.12	61.20	31.67	63.56
	$5th$	24.43	63.79	30.35	69.42
	total	27.43	55.22	34.45	56.16

得られた.

- Fig.14 において，パターン **(f)** と **(h)** を力で比較した．その結果，ほぼ同等の力波形が得られ，その力の差も 100$[N]$ 程度 (各々の力の差は 0.1$[N]$ 程度) と十分に再現性のある結果が得られた.

以上の結果より，同じ側面押しであれば，多少加重方法を変更しても，同程度の再現性が期待できることがわかった.

7 まとめ

本論文では，まず変位と力で変形を起動し，次に形状と力でパラメータを同定し，最後に形状と力でモデルを評価する 8 パターンについて比較した．その結果，変位起動/形状同定が形状を合致させるのに良く，力起動/力同定が力を合致させるのに良いことがわかった．これより，これら 2 種類の物理パラメータの集合を併用することで，形状と力のリアリティを両立させられることがわかった.

次に，異なる 2 種類の押し方を用いて物理パラメータ集合の汎用性を確かめた．すなわち，一方の押し方で同定したパラメータのモデルを他方の押し方で評価した．その結果，異なる押し方のあいだの形状と力の差は十分に小さいことから，1 つの押し方で取得した物理パラメータ集合には一定の汎用性のあることが確認された.

References

[1] K.Waters, "A muscle model for animating three-dimensional facial expression", Proc. SIGGRAPH '87, pp.17-24, 1987.

[2] D.Terzopoulos and K.Fleisher, "Modeling inelastic deformation: viscoelasticity, plasticity, fracture", Proc. SIGGRAPH '99, pp.269-278, 1988.

[3] D.James and D.K.Pai, "Artdefo: accurate real time deformable objects", Proc. SIGGRAPH '99, pp.65-72, 1999.

[4] D.Bourguignon and P.M.Cani, "Controlling anisotropy in mass-spring systems", Proc. of the 11th Eurographics Workshop on Computer Animation and Simulation, pp.113-123, 2000.

[5] A.Joukhadar, F.Garat and C.Laugier,"Parameter identification for dynamic simulation", Proc. of the IEEE Int. Conf. on Robotics and Automation, pp.1928-1933, 1997.

[6] A.Joukhadar and C.Laugier, "Dynamic simulation: Model, basic algorithms, and optimization", Proc. of the Workshop on the Algorithmic Foundations of Robotics, pp.273-286, 1996.

[7] R.Nogami, F.Ujibe, H.Fujii and H.Noborio, "Precise deformation of rheologic object under MSD models with many voxels and calibrating parameters", Proc. of the IEEE Int. Conf. on Robotics and Automation, pp.1919-1926, 2004.

[8] H.Yoshida, Y.Murata and H.Noborio, "A smart rheologic MSD model pushed/calibrated/evaluated by experimental impulses", Proc. of the IEEE/RSJ Int. Conf. Intelligent Robots and Systems, pp.1614-1621, 2005.

[9] S.Tokumoto, Y.Fujita and S.Hirai, "Deformation modeling of viscoelastic objects for their shape control", Proc. of the IEEE Int. Conf. on Robotics and Automation, pp.1050-1057, 1999.

[10] S.Tokumoto, S.Hirai and H.Tanaka, "Constructing virtual rheological objects", Proc. World Multiconference on Systemics Cybernetics and Infomatics, pp.106-111, 2001.

[11] W.Goldsmith, "Impact: The theory and physical behavior of colliding solids", Edward Alrnold, London, 1960.

[12] K.H.Hunt, F.R.E.Crossley, "Coefficient of restitution interpreted as damping in vibroimpact", Journal of Applied Mechanics, pp.440-445, 1975.

[13] M.Moore, J.Wilhelms, "Collsion detection and response for computer animation", Computer Graphics, vol.22, pp.289-298, 1988.

[14] M.C.Lin and J.F.Canny, "A fast algorithm for incremental distance calculation", Proc. of the IEEE Int. Conf. on Robotics and Automation, pp.1008-1014, 1991.

4.4　アダプティブ切断モデル

191

Computer Assisted Radiology and Surgery (CARS), pp. 150-154, June 2006

A Virtual surface cutting operation using mesh refinement method

Huynh Quang Huy Viet, Takahiro Kamada, Yasufumi Takama, Hiromi T. Tanaka

Department of Human and Computer Intelligence
Ritsumeikan University

Abstract. The cutting operation of 3D surface meshes plays an important role in surgery simulators. One of the important requirements for surgical simulators is the visual reality. We propose a new strategy for cutting on surface mesh: refinement and separate strategy consisting of the refinement followed by the separation of the refined mesh element. Because of the advantage of the low computational complexity, the longest-edge refinement method is utilized for the refinement process. The proposed strategy gives the faithful representation of interaction paths of a surgical tool.

Keywords: surgery simulation; cutting simulation; virtual sculpting; haptic interfac; deformable object; adaptive mesh refinement

---

1. Introduction

Surgical simulators have been developed to create environments to help train physicians in learning skills of surgical operations at many research centers. The virtual cutting operation plays an important role in surgery simulators. The virtual cutting methods can be divided into two categories: (i) volume cutting method that consists of cutting methods on a tetrahedral mesh and (ii) surface cutting method that consists of cutting methods on a 3D surface mesh. One of the important requirements for cutting methods is the issue of accuracy representation of the interaction path of a surgical tool.

In addition the cutting techniques may also be classified into two major categories based on the implementation of a cutting operation; those that remove intersected meshes[7] and those that re-mesh intersected meshes[1,3,4,5,10,11]. The methods of the first category simply dismiss mesh elements that intersect the cutting tool; the methods of the second category recreate the path passed over by the tool through the intersected mesh elements by way of re-meshing them. The methods of the second category have the disadvantage of the supplemental cost for computing the intersection path but provide a good visual representation of the path passed over by the cutting tool. In order to have the accuracy representation of the intersection path without considerably scarifying the cost of computation of deformation, there is a strategy proposed and implemented on tetrahedral meshes: refinement and remove strategy [12]. This strategy composes of the refinement followed by the elimination of the mesh elements (tetrahedral) on the surface cut. Despite the fact that the sizes of removed mesh elements are small due to the previous mesh refinement process, the approach still has the drawback of creating non-smooth cuts, and hence are still not appropriate for a realistic simulator.

We propose a new strategy for cutting on surface mesh: refinement and separate strategy consisting of the refinement followed by the separation of the refined mesh element. Since the advantage of the low computational cost (linear time complexity comparing to O(NlogN) time complexity of Delaunay refinement methods), the longest-

edge refinement method [6] is utilized for the refinement process. The proposed strategy gives the faithful representation of the interaction path in comparing with the conventional methods.

This paper is organized as follows. Section 2 introduces the longest-edge refinement method which is the base for constructing the proposed method for virtual cutting. Section 3 and 4 detail the data structure and algorithm. Section 5 shows the experimental results. Section 6 is devoted for conclusions and future works.

2. Backward longest-size refinement algorithm

As a preliminary for presenting the proposed method, we introduce the backward longest-size refinement algorithm of Rivara [6] for triangular mesh refinement. The method only bisects along the longest-edge of a triangle; this guarantees the construction of non-degenerate and smooth irregular triangulations whose geometrical properties only depend on the initial mesh. In order to maintain a conforming mesh, the local refinement of a given triangle involves refinement of the triangle itself and refinement of its longest edge neighbors.

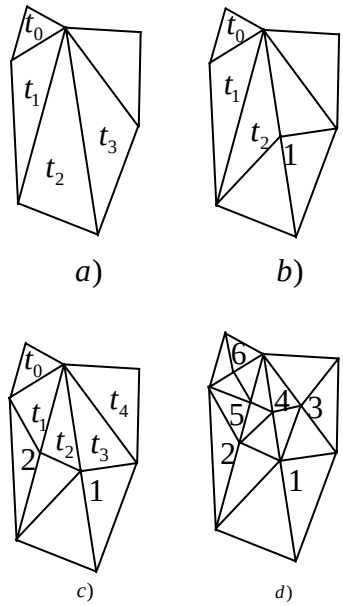

Fig. 1. Backward longest-side bisection of triangle t_0.

Longest-side propagation path is a concept utilized in the backward longest-size refinement algorithm. It is defined as follows: For any triangle t_0 of any conforming triangulation T, the longest-side propagation path of t_0 will be the ordered list of all the triangles $\{t_0,t_1,\ldots t_n\}$, such that t_i is the neighbor triangle of t_{i-1}, by the longest-size of t_{i-1}, for i=1,2,…,n. The longest-side propagation path pf triangle t_0 is denoted as LSPP(t_0).

The following is the backward longest-size refinement algorithm[6]:

Backward Longest-Size Bisection (T,t)
While t remains without being bisected do
Find the LSPP(t)
If t^*, the last triangle of the LSPP(t), is a terminal boundary triangle, bisect t^*
Else bisect the (last) pair of terminal triangles of the LSPP(t)

Figure 1 explains the backward longest-size refinement algorithm: Fig. 1a gives the initial triangulation; Fig. 1b gives the first step of the process; Fig. 1c gives the second step in the process and Fig. 1d gives the final triangulation.

3. Data structure of 3D surface mass-spring mesh

The objects of the surgical simulation are represented by 3D surface meshes. The surface mesh of the object is taken from laser scanner. The VRML output file of a laser scanner is used in a data structure based on winged-edge data structure, which includes the physical parameters of a damped mass-spring model. The data which is stored at each vertices are their 3D coordinates, the value of mass and the information of an edge adjacent to vertex, the data which is stored at each edge are the start of node, the end of node of vertex, the parameters of a damper and a spring, the previous edge for left face, the next edge for left face. This data structure allows quick computation of finding the adjacent triangles for cutting algorithm, and performing of deformation.

4. Cutting algorithm

There are different approaches for changing the topology of an object such as destroying the mesh elements or dividing them. In our proposed method, to yield accuracy representation of cutting paths, instead of simple dividing the triangles (the mesh elements), we refine them by subdividing into smaller triangles using the longest-edge refinement algorithm mentioned in the previous section. The virtual cut is performed on separating the smaller triangles.

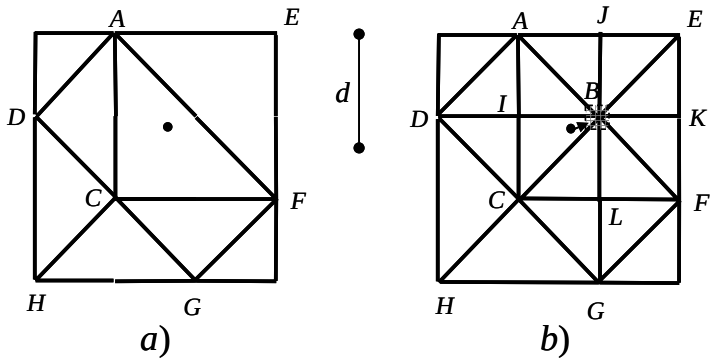

Fig. 2. The initial interacting point.

At first the triangle that is collided by the surgical tool is refined by using the backward longest-edge refinement algorithm mentioned in previous section, as showed in the Fig.2. The vertex that is nearest the colliding point is considered as the initial vertex for performing cutting.

Suppose that a virtual cut is being carried out at a vertex, we call this vertex as the reference vertex, the cut is performed by repetition of the following steps:

1. Finding the next vertex in cutting path: The next vertex is the vertex which is adjacent to the reference vertex and has the closest distance toward the direction of the motion of a surgical. The edge linking the reference vertex to the next vertex is called reference edge. Figure 3a shows how to choose the next vertex.

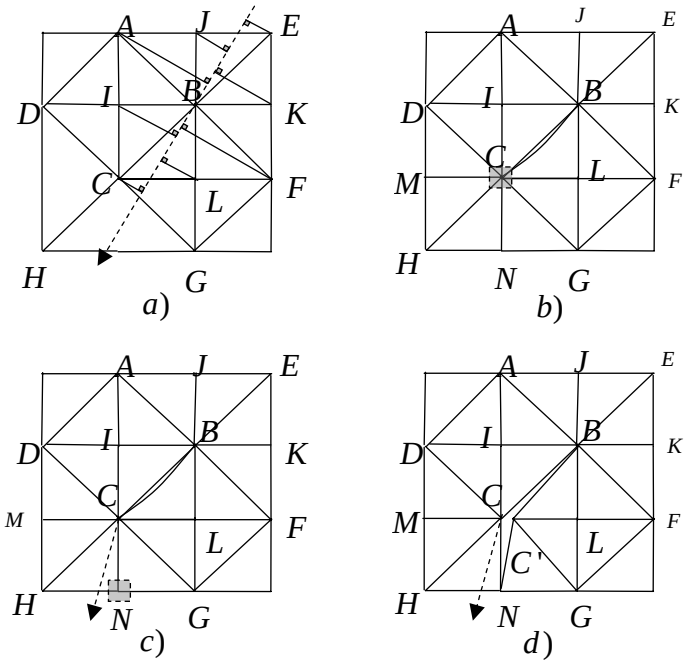

Fig. 3. Re-meshing and making new points in a cutting process.

2. Changing the topology: The triangles sharing the next vertex from the reference vertex in cutting path are refined by the longest-edge refinement algorithm until the longest-edge l of the subdivided smaller triangles is satisfied the requirement of $d/2<l<d$, where d is a predefined distance. Notice that the requirement of $l>d/2$ is to assure the termination for a refinement process. Figure 3b.gives an illustration a process of refinement of the triangles sharing the next vertex.

3. Changing the adjacent information of two triangles along the cutting path: The reference vertex is duplicated and the adjacent information of two triangles sharing the reference vertex is updated as not adjacent. Figure 3c and 3d clarifies this step when considering the vertex C as a reference vertex.

5. Experimental results

We build the system as showed in Fig. 4a to implement the proposed method. The handling of the virtual object in 3D virtual space is performed by using the haptic interface device Phantom. The visual result is represented realistically in the X3D display screen.

In Fig. 4b, the cutting path appears delicately; the very small shakes of the hand handling the Phantom arm are captured and expressed faithfully in zigzags. This shows the effectiveness of the proposed method in accuracy representation of the trajectory of motion of the surgical tool.

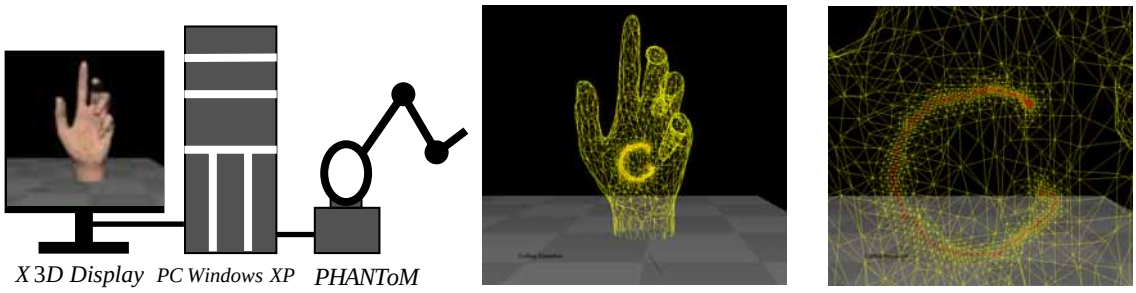

a) System diagram b) Virtual cutting c) The enlargement image

Fig. 4. System diagram and experimental results.

6. Conclusions

The paper introduces a new virtual cutting method for accuracy representation of the motion of a surgical tool. The main contribution of the work is a real-time 3D surface cutting algorithm that cooperates with the longest-edge based local refinement algorithm for unstructured meshes of triangle. The experiment results show the performance of the approach. Our closest goal of future work is to render deformation and haptic of highly deformable virtual objects under a virtual cutting.

References

[1] C. Basdogan. Simulation of instrument-tissue interactions and system integration. In *Medicine Meets Virtual Reality*.

[2] C. Bruyns, S. Senger, A. Menon, K. Montgomery, S. Wildermuth, and R. Boyle. A survey of interactive mesh-cutting techniques and a new method for implementing generalized interactive mesh cutting using virtual tools. *Journal of Visualization and Computer Animation*, 13(1):21–42, 2002.

[3] C. D. Bruyns and S. Senger. Interactive cutting of 3d surface meshes. *Computers & Graphics*, 25:635–642, 2001.

[4] C. Mendoza and C. Laugier. Simulating soft tissue cutting using finite element models. In *Proc. of the IEEE Int. Conf. on Robotics and Automation*, pages 1109–1114, Taipei, Taiwan, 2003.

[5] H. Nienhuys and A. Stappen. A surgery simulation supporting cuts and finite element deformation. In *Proc. Fourth Int. Conf. on Med. Image Comput. and Computer-Assisted Intervention (MICCAI 2001)*, pages 145–152, Utrecht, The Netherlands, 2001.

[6] M.C. Rivara. New mathematical tools and techniques for the refinementand/or improvement of unstructured triangulations. In *5th International Meshing Roundtable*, pages 77–86, 1996.

[7] S. Cotin, H. Delingette, and N. Ayache. A hybrid elastic model for real-time cutting, deformations, and force feedback for surgery training and simulation. *The Visual Computer*, 16(7):437–452, 2000.

[8] S. Payandeh, J. Dill, J. Zhang. A study of level-of -detail in haptic rendering. ACM Transactions on Applied Perception, 2(1): 15-34, 2005.

[9] S. Cotin, H. Delingette, and N. Ayache. A Hybrid Elastic Model allowing Real-Time Cutting, Deformations and Force-Feedback for Surgery Training and Simulation**.** *The Visual Computer*, 16(8):437-452, 2000.

[10] F. Ganovelli, P. Cignoni, C. Montani, R. Scopigno. Enabling Cuts on Multiresolution Representation. The Visual Computer, Springer International,. Vol. 17 (5), 274-286, 2001.

[11] M. Harders, D. Steinemann, M. Gross, G. Szekely, "A Hybrid Cutting Approach for Hysteroscopy Simulation", Conference on Medical Image Computing and Computer-Assisted Intervention (MICCAI'05), pp. 567-574, 2005.

[12] C. Forest., H. Delingette, N. Ayache. Removing Tetrahedra from manifold tetrahedralisation : application to real-time surgical simulation, Medical Image Analysis, April 2005, vol. 9, no 2, p. 113–122.

An Adaptive 3D Surface Mesh Cutting Algorithm for Deformable Objects

Huynh QUANG HUY VIET†, Takahiro KAMADA†, Yasufumi TAKAMA†, and Hiromi T.TANAKA†

† Department of Human and Computer Intelligence
College of Information Science and Engineering
Ritsumeikan University

Abstract Surgical simulators have been developed to create environments to help train physicians in learning skills of surgical operations at many research centers. The cutting operation of 3D surface meshes plays an important role in surgery simulators. One of the important requirements for surgical simulator is the issue of accuracy representation of the interaction path of a surgical tool. For getting the faithful representation of interacting paths without sacrificing the computation cost for deformation modeling, it is necessary to refine a mesh element which being intersected by a surgical tool. We propose a new strategy consisting of the refinement followed by a separation of the mesh elements being in collision with a surgical tool. The proposed algorithm gives the faithful representation of the interaction path in comparing with the conventional methods.

Key words surgery simulation; cutting simulation; virtual sculpting; haptic interface; deformable object; adaptive mesh refinement

1. Introduction

Surgical simulators have been developed to create environments to help train physicians in learning skills of surgical operations at many research centers. The virtual cutting operation plays an important role in surgery simulators. The virtual cutting methods can be divided into two categories: (i) volume cutting method that consists of cutting methods on a tetrahedral mesh and (ii) surface cutting method that consists of cutting methods on a 3D surface mesh. One of the important requirements for cutting methods is the issue of accuracy representation of the interaction path of a surgical tool.

In addition the cutting techniques may also be classified into two major categories based on the implementation of a cutting operation; those that remove intersected meshes [1] and those that re-mesh intersected meshes [2]〜[8]. The methods of the first category simply dismiss mesh elements that intersect the cutting tool; the methods of the second category recreate the path passed over by the tool through the intersected mesh elements by way of re-meshing them. The methods of the second category have the disadvantage of the supplemental cost for computing the intersection path but provide a good visual representation of the path passed over by the cutting tool. In order to have the accuracy representation of the intersection path without considerably scarifying the cost of computation of deformation, there is a strategy proposed and implemented on tetrahedral meshes: refinement and remove strategy [9]. This strategy composes of the refinement followed by the elimination of the mesh elements (tetrahedral) on the surface cut. Despite the fact that the sizes of removed mesh elements are small due to the previous mesh refinement process, the approach still has the drawback of creating non-smooth cuts, and hence are still not appropriate for a realistic simulator. Moreover, there are not the implementations of this strategy on surface meshes.

We propose a new strategy for cutting on surface mesh: refinement and separate strategy consisting of the refinement followed by the separation of the refined mesh element. Since the advantage of the low computational cost (linear time complexity comparing to $O(NlogN)$ time complexity of Delaunay refinement methods), the longest-edge refinement method [10] is utilized for the refinement process. The proposed strategy gives the faithful representation of the interaction path in comparing with the conventional methods.

This paper is organized as follows: Section 2 introduces the longest-edge refinement method which is the base for constructing the proposed method. Section 3 details the data

structure and the cutting algorithm. Section 4 gives the experiment results. Section 5 is devoted for conclusions and future works.

2. Backward Longest-Edge Refinement Algorithm

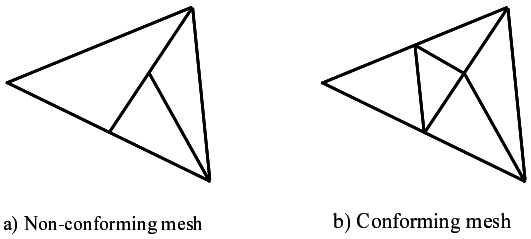

a) Non-conforming mesh b) Conforming mesh

Fig. 1 Non-conforming mesh and conforming mesh

As a preliminary for presenting the proposed method, in this section we introduce the backward longest-edge refinement algorithm of Rivara [10] for triangular mesh refinement. The requirement of a refinement of a mesh is to satisfy the main properties: conforming, well shaped and smooth. A conforming mesh is a mesh without any "T-junctions". T junction is a non-conforming point which is defined as an interior point of an edge of one triangle and common vertex of two other adjoin triangles. Rivara proposed the backward longest-edge bisection refinement algorithm. The method only bisects along the longest-edge of a triangle; this guarantees the construction of non-degenerate and smooth irregular triangulations whose geometrical properties only depend on the initial mesh. In order to maintain a conforming mesh, the local refinement of a given triangle involves refinement of the triangle itself and refinement of its longest edge neighbors.

Longest-side propagation path is a concept utilized in the backward longest-edge refinement algorithm. It is defined as follows: For any triangle t_0 of any conforming triangulation T, the longest-edge propagation path of t_0 will be the ordered list of all the triangles $t_0, t_1, t_2, ...t_{n-1}, t_n$, such that t_i is the neighbor triangle of t_{i-1}, by the longest-edge of t_{i-1}, for $i = 1, 2, ..n$. The longest-edge propagation path pf triangle t_0 is denoted as $LSPP(t_0)$.

Figure 2 explains the backward longest-edge refinement algorithm: Fig. 2a gives the initial triangulation; Fig. 2b gives the first step of the process; Fig. 2c gives the second step in the process and Fig. 2d gives the final triangulation.

Figure 3 shows the backward longest-edge refinement algorithm. We utilize this algorithm to develop an algorithm for cutting on 3D surface mesh.

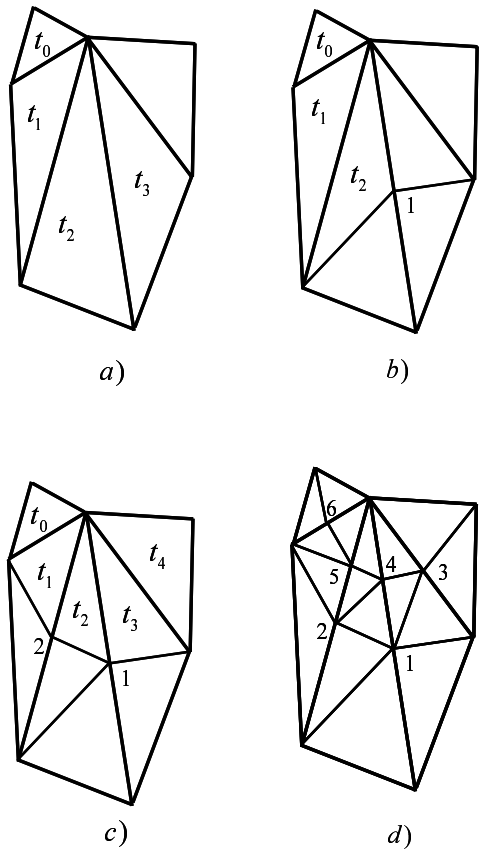

Fig. 2 Backward longest-edge bisection of triangle t_0

- **Backward-longest-edge-refinement** (T)
  - Sign all triangles which have unacceptable size and add them to T_0
  - i=0
  - **White** T_i is not empty **Do**
    - Run BackwardLongestEdgeBisection(t) for all triangles t in T_i
    - i=i+1
    - Sign all triangles which have unacceptable size and add them to T_i
- **Backward-longest-size-bisection** (t)
  - **While** t remains without being bisected **Do**
    - Find the LSPP(t)
    - **If** t', the last triangle of the **LSPP**(t) , is a terminal boundary triangle **Then** bisect t*
    - **Else** bisect the (last) pair of terminal triangles of the LSPP(t)
- **LEPP**(t)
  - L=**null**
  - i=1
  - L[i]=t
  - **If** t has a neighbor t_{nb} on its longest edge **Then**
    - L[i]= t_{nb}
    - WHILE L[i] has a longest edge neighbor different from L[i-1] Do
      - Let t_{nb} be the longest edge neighbor of L[i-1]
      - i=i+1
      - L[i]= t_{nb}
  - **Return** L

Fig. 3 Backward longest-edge refinement algorithm

3. Data Structure and Cutting Algorithm

The objects of the surgical simulation are represented by 3D surface meshes. The surface mesh of the object can be taken from laser scanner. The VRML output file of a laser scanner is used in a data structure based on winged-edge data structure, which includes the physical parameters of a damped mass-spring model. The data which is stored at each

vertices are their 3D coordinates, the value of mass and the information of an edge adjacent to vertex, the data which is stored at each edge are the start of node, the end of node of vertex, the parameters of a damper and a spring, the previous edge for left face, the next edge for left face. This data structure allows quick computation of finding the adjacent triangles for cutting algorithm, and performing of deformation.

There are different approaches for changing the topology of an object such as destroying the mesh elements or dividing them. In our proposed method, to yield accuracy representation of cutting paths, instead of simple dividing the triangles (the mesh elements), we refine them by subdividing into smaller triangles using the longest-edge refinement algorithm mentioned in the previous section. The virtual cut is performed by way of separating the subdivided smaller triangles.

At first the triangle that is collided by the surgical tool is refined by using the backward longest-edge refinement algorithm mentioned in previous section, as showed in the Fig. 4b. The vertex that is nearest the colliding point is considered as the initial vertex for performing cutting.

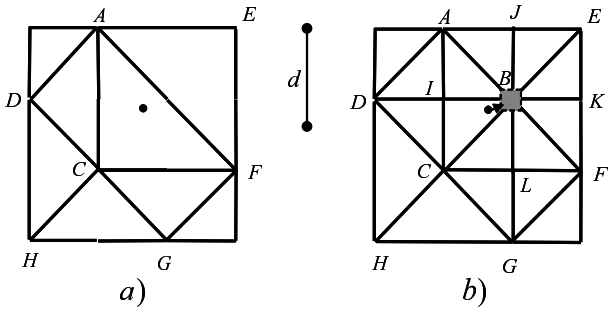

Fig. 4 Initial interacting point.

Suppose that a virtual cut is being carried out at a vertex, we call this vertex as the reference vertex, the cut is performed by repetition of the following steps:

1. Finding the next vertex in cutting path: The next vertex is the neighboring vertex which has the closest distance toward the direction of the motion of a surgical tool. The neighboring vertex is a vertex adjacent to the reference vertex, or is the vertex of a triangle sharing the common edge with the triangle of the reference vertex; and do not lie on the common edge. The edge linking the reference vertex to the next vertex is called reference edge. Figure 5a shows how to choose the next vertex.

2. Changing the topology: The triangles sharing the next vertex from the reference vertex in cutting path are refined by the longest-edge refinement algorithm until the longest-edge l of the subdivided smaller triangles is satisfied the requirement of $d/2 < l < d$, where d is a predefined distance. Notice that the requirement of $l > d/2$ is to assure the termination for a refinement process. Figure 5b. gives an illustration a process of refinement of the triangles sharing the next vertex.

3. Changing the adjacent information of two triangles along the cutting path: The reference vertex is duplicated and the adjacent information of two triangles sharing the reference vertex is updated as not adjacent. Figure 5c and d clarifies this step when considering the vertex C as a reference vertex.

In the case that the next vertex is not belong the same triangle of the reference vertex and the edge which is shared by the two triangles is the longest edge as shown Fig. 6a, this edge is swapped so as the next vertex is connected with the reference vertex by an edge, and the cutting process is continued as described in Step 2 and Step 3 (see Fig. 6b).

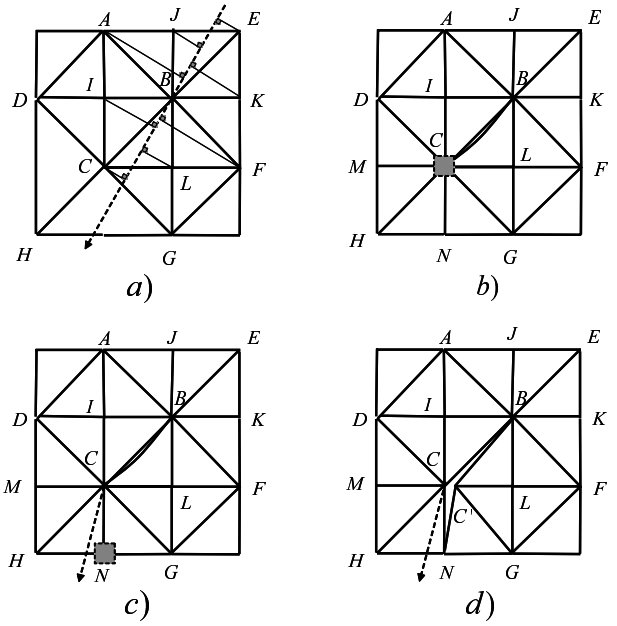

Fig. 5 Remeshing and making new point in a cutting process.

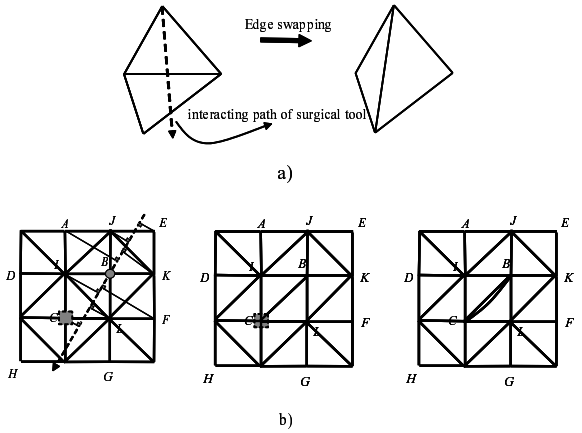

Fig. 6 Swapping an edge in a cutting process.

We calculate the mass, spring stiffness and spring damping of new vertices and edges by utilizing the formations

proposed in the multiresolution modeling methods for soft objects [11]∼[13].The mass is calculated as follows:

$$m_i = \frac{D\sum_j S_j}{3} \tag{1}$$

here S_j is the area of the adjacent triangles and D is the material density. Let E be the material elastic modulus, l be the length of the spring at rest, and S_j is the area of the adjacent triangles, then the spring stiffness is calculated as follows:

$$k = \frac{E\sum_j S_j}{l^2} \tag{2}$$

the spring damping for the edge linking the masses m_1 and m_2, whose spring stiffness is calculate by the above formula, is as follows:

$$c = \frac{2\sqrt{k(m_1+m_2)}}{l} \tag{3}$$

l is the length of the spring at rest.

It is necessary to have an algorithm for generating the groove of a cutting path. As shown in Fig. 7, when the triangles ABC and BCD are divided and the vertices B_1, B_2, C_1, C_2 are created, the bottom of the groove is generated at the tip positions of the cutting tool G_1 and G_2.

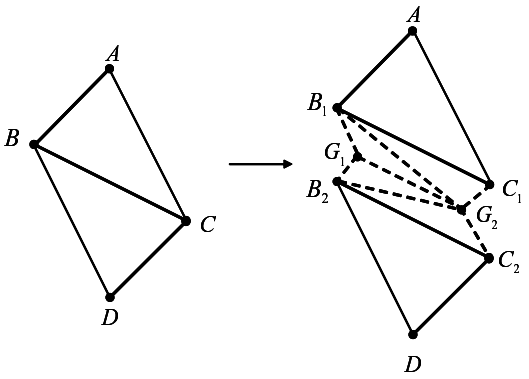

Fig. 7 Groove Generation

4. Experimental Results

We build the system as showed in Fig. 8 to implement the proposed method. The handling of the virtual object in 3D virtual space is performed by using the haptic interface device Phantom. The visual result is represented realistically in the X3D display screen.

Figure 9 shows the wireframe representation of a virtual cutting of a hand which is model by the 3D surface triangle mesh: Fig.9a gives the original representation of the hand and Fig.9b gives the result of the virtual cutting.

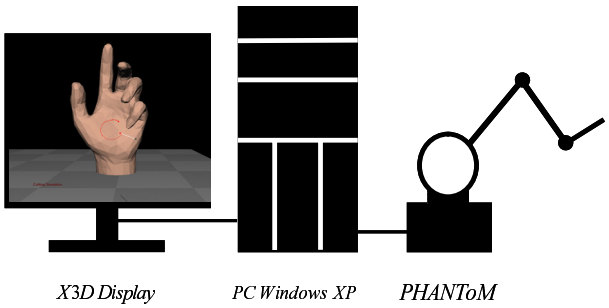

Fig. 8 System diagram.

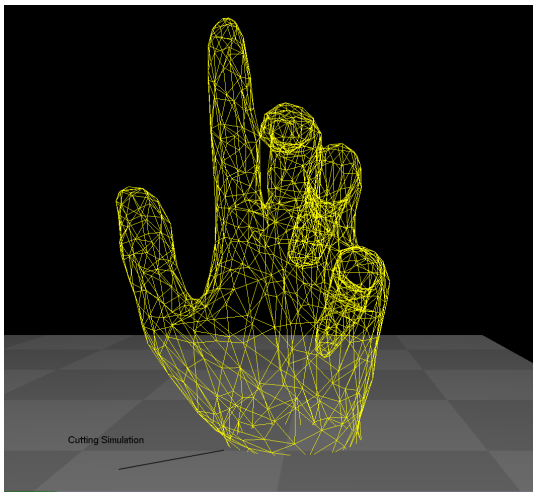

(a) Original 3D hand

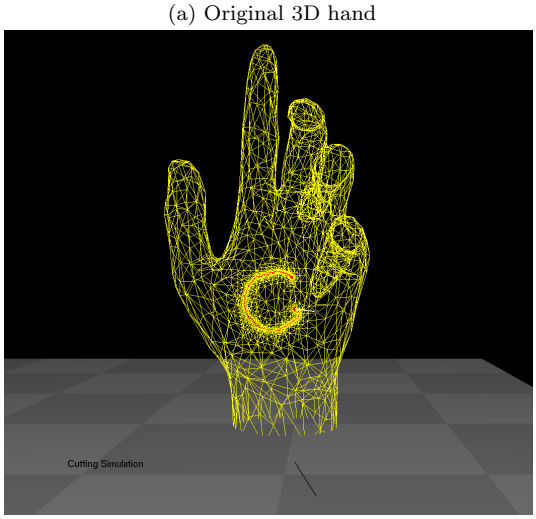

(b) A virtual cutting

Fig. 9 Wireframe representation.

Fig.10a show the enlargement of the result, the cutting path appears delicately; the very small shakes of the hand handling the Phantom arm are captured and expressed faithfully in zigzags. This show the effectiveness of the proposed method in accurate representation of the motion of the surgical tool. In fact if the friction force in hand surface is considered, the real motion of hand, which handles the Phantom arm, will become smooth. However, this does not affect the effectiveness of the proposed algorithm.

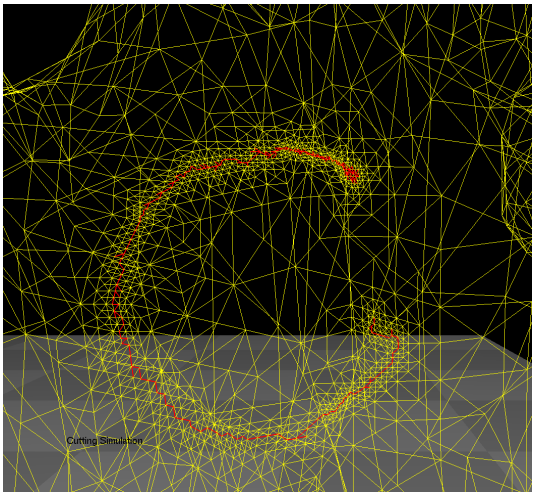

(a) Cutting with mesh refinement

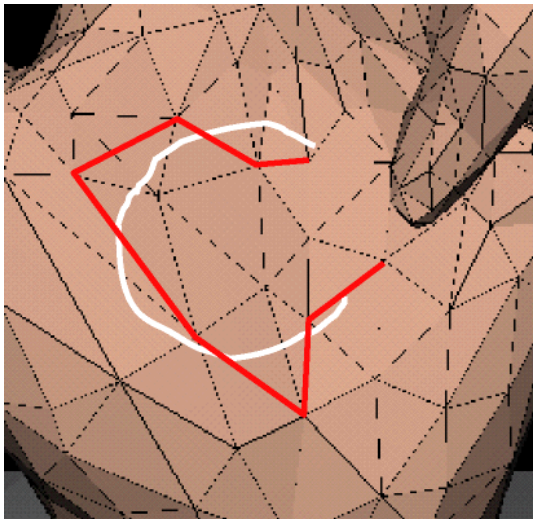

(b) Cutting without mesh refinement

Fig. 10 Comparison of the algorithm with and without mesh refinement.

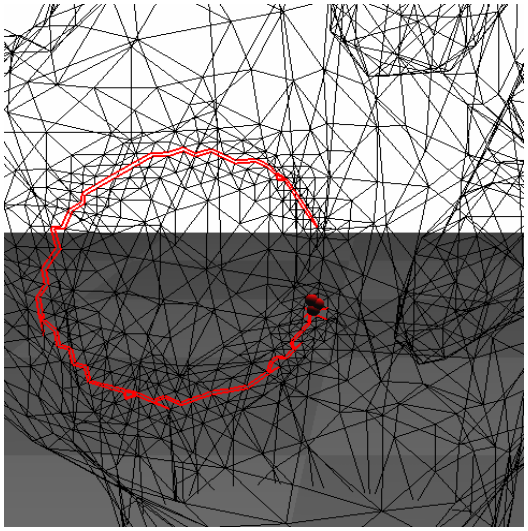

Fig. 11 A cutting path in surface with tension.

Fig.10b shows the result without using mesh refinement algorithm for the same motion of cutting tool of the previous experiment, the cutting path is far different from the motion of cutting tool.

In addition, in Fig.11 we show a crevice of cutting path in a hand surface with tension.

In Fig.12, we show a result of cutting with groove generation.

5. Conclusions

The paper introduces a new virtual cutting method for accuracy representation of the motion of a surgical tool. The main contribution of the work is a real-time 3D surface cutting algorithm that cooperates with the longest-edge based local refinement algorithm for unstructured meshes of triangle. The experiment results show the performance of the approach. Our closest goal of future work is to render deformation and haptic of highly deformable virtual objects under a virtual cutting.

References

[1] S. Cotin, H. Delingette and N. Ayache: "A hybrid elastic model for real-time cutting, deformations, and force feedback for surgery training and simulation.", The Visual Computer, **16**, 7, pp. 437–452 (2000).

[2] C. D. Bruyns and S. Senger: "Interactive cutting of 3d surface meshes", Computers & Graphics, **25**, pp. 635–642 (2001).

[3] H.-W. Nienhuys and A. F. van der Stappen: "A surgery simulation supporting cuts and finite element deformation", Medical Image Computing and Computer-Assisted Intervention, Utrecht, The Netherlands, pp. 153–160 (2001).

[4] C. Basdogan: "Simulation of instrument-tissue interactions and system integration", Medicine Meets Virtual Reality 2001 (2001).

[5] D. Bielser, P. Glardon, M. Teschner and M. Gross: "A state machine for real-time cutting of tetrahedral meshes", Journal of Graphical Models, **66**, 6, pp. 398–417 (2004).

[6] M. Harders, D. Steinemann, M. Gross and G. Szekely: "A hybrid cutting approach for hysteroscopy simulation", Conference on Medical Image Computing and Computer-Assisted Intervention, Palm Springs, USA (2005).

[7] F. Ganovelli, P. Cignoni, C. Montani and R. Scopigno: "Enabling cuts on multiresolution representation", The Visual

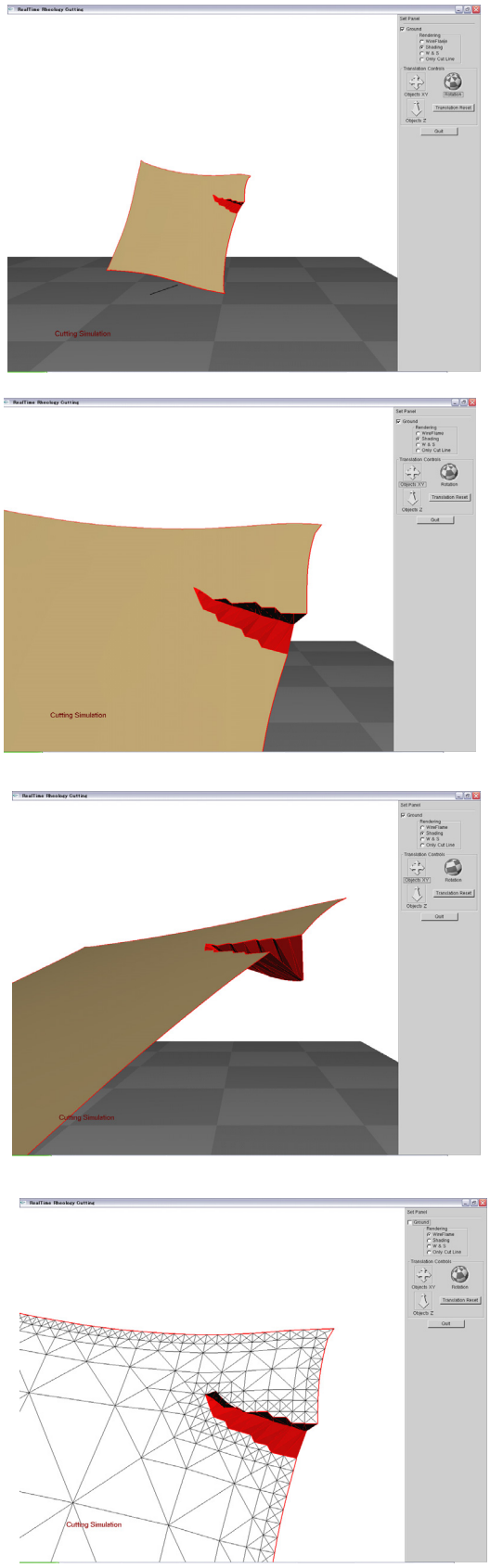

Fig. 12 Cut a groove on a surface

Computer, **17**, 5, pp. 274–286 (2001).

[8] C. Mendoza and C. Laugier: "Simulating soft tissue cutting using finite element models", Proc. of the IEEE Int. Conf. on Robotics and Automation, Taipei, Taiwan, pp. 1109–1114 (2003).

[9] C. Forest., H. Delingette and N. Ayache: "Removing tetrahedra from manifold tetrahedralisation : application to real-time surgical simulation", Medical Image Analysis, **9**, 2, pp. 113–122 (2005).

[10] M.-C. Rivara: "New mathematical tools and techniques for the refinementand/or improvement of unstructured triangulations", 5th International Meshing Roundtable, pp. 77–86 (1996).

[11] C. Paloc, F. Bello, R. Kitney and A. Darzi: "Online multiresolution volumetric mass spring model for real time soft tissue deformation", Proceedings of the 5th International Conference on Medical Image Computing and Computer-Assisted Intervention, pp. 219–226 (2002).

[12] F. Ganovelli, P. Cignoni, C. Montani and R. Scopigno: "A multiresolution model for soft objects supporting interactive cuts and lacerations.", Computer Graphics Forum, **19**, 3, pp. 271–282 (2000).

[13] A. V. Gelder: "Approximate simulation of elastic membranes by triangulated spring meshes", Journal of Graphics Tools, **3**, 2, pp. 21–42 (1998).

[14] C. Bruyns, S. Senger, A. Menon, K. Montgomery, S. Wildermuth and R. Boyle: "A survey of interactive mesh-cutting techniques and a new method for implementing generalized interactive mesh cutting using virtual tools.", Journal of Visualization and Computer Animation, **13**, 1, pp. 21–42 (2002).

[15] S. Payandeh, J. Dill and J. Zhang: "A study of level-ofdetail in haptic rendering", ACM Transactions on Applied Perceptions, **2**, 1, pp. 15–34 (2005).

[16] A. Liu, F. Tendick, K. Cleary and C. Kaufmann: "A survey of surgical simulation: applications, technology, and education", Presence: Teleoperators and Virtual Environments, **12**, 6, pp. 599–614 (2003).

[17] D. Serby, M. Harders and G. Szekely: "A new approach to cutting into finite element models", Proceedings of the 4th International Conference on Medical Image Computing and Computer-Assisted Intervention, pp. 425–433 (2001).

[18] C. Forest, H. Delingette and N. Ayache: "Cutting simulation of manifold volumetric meshes", Medical Image Computing and ComputerAssisted Intervention, pp. 235–244 (2002).

[19] F. Boux de Casson and C. Laugier: "Simulating 2d tearing phenomena for interactive medical surgery simulators", Proceedings of Computer Animation, Philadelphia, PA (US) (2000).

[20] J. Suarez, A. Plaza and G. Carey: "Propagation path properties in iterative longest-edge refinement", Proceedings of 12th International Meshing Roundtable, pp. 79–90 (2003).

[21] H. T.Tanaka and F. Kishino: "Adaptive mesh generation for surface reconstruction: Parallel hierarchical triangulation without discontinuities", Proc. IEEE Conf. Computer Vision Pattern Recognition (CVPR93), New York City, pp. 88–94 (1993).

4.5 結言

本章では適応的なモデリング手法について述べた．アダプティブメッシュモデル，階層的メッシュモデルともに，モデルの精度と計算時間を両立させることが可能である．力学パラメータの設定法に関して，今後の研究が望まれる．

203

第5章　アクティブ虚血ダイナミクスとマンモグラフィーへの応用

5.1　緒言

近年，手術シミュレーションにおける生体軟組織のモデリング，デジタルヒューマンに代表される筋骨格モデリング，食品工学における食品素材のモデリング等において，複雑な力学的特性を有する柔軟物のモデリングが必要とされている．現在，超音波装置および MRI を用いた柔軟物内部の変形計測が行われおり，力学的特性の同定方法に関する研究が進められている [47, 48].

組織の活性度や病巣の有無を評価する方法として，金子らは虚血ダイナミクスに着目している [49]．虚血とは，臓器などに外力を加えたときに一時的に血流量が低下し，臓器の色が変化することである．金子らは空気圧による変形と虚血面積をそれぞれ観測することによって，虚血ダイナミクスを調べることを提案している．そこで本章では，アクティブ虚血ダイナミクスを粘弾性FE モデルを用いてシミュレーションすることを目的とする．

5.2　FE モデルを用いた動的変形のシミュレーション

本節では，一次元FE モデルの計算法を述べる．一次元FE モデルでは，物体を線形要素の集合として表す．これによって，全体の変形を線形要素の変形の和として表現することができる．そこで一次元FE モデルとして，長さを h，断面積を A，質量を M，密度を ρ としたときの線形物体の変形を式に表す．Fig.5.1 に示すように物体を線形の集合で表し，線形要素の一つを T_p と表す．さらに T_p の頂点を左から順に P_i，P_j とする．節点 P_i の初期座標を $x = \xi_i$ で表す．また，P_i の初期座標からの変位を u_i で表す．線形要素 T_p の変形は節点の変位 u_i，u_j で表すことができる．節点 P_0 から P_4 までの変位を縦にならべたものを縦ベクトル $\boldsymbol{u} = [u_0, u_1, u_2, u_3, u_4]^T$ で表す．線形要素 T_p の変形により P_i に生じる内力を f_i^p で表す．Fig.5.2 に一次元FE モデルの概要を示す．ノード数を 5 として，それに囲まれる要素数を 4，節点 P_0 を

204

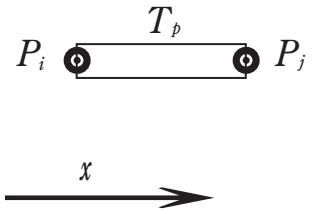

図 5.1: 1D rectangular element

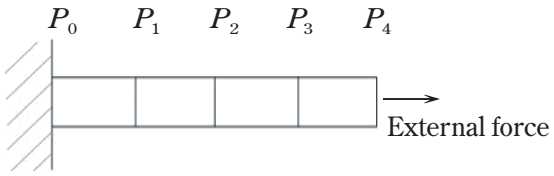

図 5.2: 1D finite element model

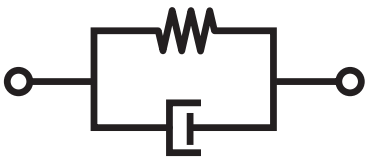

図 5.3: Voigt model

固定し，節点 P_4 に外力を印加する．

粘弾性物体の一次元 FE モデルを述べる．粘弾性モデルには Fig.5.3 に示す，バネとダンパーが並列に繋がる Voigt モデルが挙げられる．線形 T_p の変形により各節点に生じる粘弾性力は，ヤング率 E と粘性率 C を用いて，

$$F^{\mathrm{1D}}_{\mathrm{viscoelastic}} = E\boldsymbol{J}\boldsymbol{u}_N + C\boldsymbol{J}\dot{\boldsymbol{u}}_N \tag{5.1}$$

と表すことができる．ここで $\boldsymbol{J}$ は接続行列であり，今回のモデルでは以下のように表すことができる．

$$\boldsymbol{J} = \frac{A}{h}\begin{bmatrix} 1 & -1 & & & \\ -1 & 2 & -1 & & \\ & -1 & 2 & -1 & \\ & & -1 & 2 & -1 \\ & & & -1 & 1 \end{bmatrix}. \tag{5.2}$$

節点 P_i に作用する粘弾性力を f_i と表すと，f_i は節点 P_i を含む線形要素により発生

205

する力の総和に一致するので，

$$f_i = \sum f_i^p \tag{5.3}$$

と表すことができる．また，質量が線形要素の各頂点に集中していると仮定すると，全体の慣性行列 $\boldsymbol{M}$ は以下のように表すことができる．

$$\boldsymbol{M} = \frac{\rho h A}{6}\begin{bmatrix} 2 & 1 & & & \\ 1 & 4 & 1 & & \\ & 1 & 4 & 1 & \\ & & 1 & 4 & 1 \\ & & & 1 & 2 \end{bmatrix}. \tag{5.4}$$

今回のモデルでは，左端が固定された状態を想定しているので，離れないように拘束する必要がある．ここでは制約安定化法 (Constraint Stablization Method:CSM) を用いて拘束する．固定の為の拘束式を $\boldsymbol{a}^T\boldsymbol{u}_n = 0$ とする．行列 $\boldsymbol{a} = [1,0,0,0,0]^T$ は拘束する節点を表す行列である．また ω を各周波数とする．以上を用いて，固定されている節点の運動方程式を以下のように表すことができる．

$$\boldsymbol{a}^T\ddot{\boldsymbol{u}}_N + \boldsymbol{a}^T(2\omega\dot{\boldsymbol{u}}_N + M\boldsymbol{u}_N) = 0 \tag{5.5}$$

ただし，$\boldsymbol{f}$ は各節点に加わる外力 $\boldsymbol{f} = [0,0,0,0,f(t)]^T$ であり，$f(t)$ は時刻 t における外力である．ここで，拘束力としてラグランジュの未定乗数 λ を導入すると物体の各節点の運動方程式は以下のように表すことができる．

$$-(E\boldsymbol{J}\boldsymbol{u}_N + C\boldsymbol{J}\dot{\boldsymbol{u}}_N) + \boldsymbol{f} + \boldsymbol{a}\lambda - M\ddot{\boldsymbol{u}}_N = 0. \tag{5.6}$$

ここで $\dot{\boldsymbol{u}}_N = \boldsymbol{v}$ を含めてまとめると

$$\begin{bmatrix} I & & \\ & M & -\boldsymbol{a} \\ & \boldsymbol{a}^T & \end{bmatrix}\begin{bmatrix} \dot{\boldsymbol{u}}_N \\ \dot{\boldsymbol{v}}_N \\ \lambda \end{bmatrix} = \begin{bmatrix} \boldsymbol{v}_N \\ -(E\boldsymbol{J}\boldsymbol{u}_N + C\boldsymbol{J}\dot{\boldsymbol{u}}_N) + \boldsymbol{f} \\ \boldsymbol{a}^T(2w\boldsymbol{v}_N + w^2\boldsymbol{u}_N) \end{bmatrix}. \tag{5.7}$$

状態変数 $\boldsymbol{u}_N$，$\boldsymbol{v}_N$ の値を与えると，左辺の係数行列と右辺を求めることができる．左辺の係数行列は正則なので，$\dot{\boldsymbol{u}}_N$，$\dot{\boldsymbol{v}}_N$ を求められ，Runge-Kutta 法や Runge-Kutta Fehlberg 法などの数値積分を用いると各節点の変位と変位速度を計算することができ，最終的に物体の変形を求めることができる．

粘塑性物体の一次元 FE モデルを述べる．粘弾性モデルには図 5.4 に示す，バネとダンパーが直列に繋がる Maxwell モデルが挙げられる．粘塑性物体に発生する応力 σ とひずみ ε は，

$$\sigma = E\varepsilon^{ela}, \sigma = C\dot{\varepsilon}^{ela}, \tag{5.8}$$

$$\varepsilon = \varepsilon^{ela} + \varepsilon^{vis} \tag{5.9}$$

図 5.4: Maxwell model

である．ここで，ε^{ela} と ε^{vis} はそれぞれ弾性要素と粘性要素のひずみである．これをまとめると，

$$\dot{\sigma} + \frac{E}{C}\sigma = E\dot{\varepsilon} \tag{5.10}$$

となる．これを $\sigma(t)$ について畳み込みで解くと，

$$\sigma(t) = \int_0^t E e^{-\frac{E}{C}(t-t')}\dot{\varepsilon}(t')\mathrm{d}t' \tag{5.11}$$

となる．以上の応力とひずみの関係から，粘塑性物体の変形により生じる力は以下のように示すことができる．

$$F^{\mathrm{1D}}_{\mathrm{viscoplastic}} = E\boldsymbol{J}\boldsymbol{w} \tag{5.12}$$

ここで

$$\boldsymbol{w} = \int_0^t e^{-\frac{E}{C}(t-t')}\dot{\boldsymbol{u}}_N(t')\mathrm{d}t' \tag{5.13}$$

である．したがって物体の各節点の運動方程式は以下のように表すことができる．

$$-E\boldsymbol{J}\boldsymbol{w} + \boldsymbol{f} + \boldsymbol{a}\lambda - M\ddot{\boldsymbol{u}}_N = 0. \tag{5.14}$$

結果として次式の微分方程式が得られるので，粘塑性物体の変形を求めることができる．

$$\begin{bmatrix} I & & \\ & M & -\boldsymbol{a} \\ & \boldsymbol{a}^T & \end{bmatrix} \begin{bmatrix} \dot{\boldsymbol{u}}_N \\ \dot{\boldsymbol{v}}_N \\ \lambda \end{bmatrix} = \begin{bmatrix} \boldsymbol{v}_N \\ -E\boldsymbol{J}\boldsymbol{w} + \boldsymbol{f} \\ \boldsymbol{a}^T(2w\boldsymbol{v}_N + w^2\boldsymbol{u}_N) \end{bmatrix}. \tag{5.15}$$

二次元 FE モデルの計算法を述べる．二次元 FE モデルでは，物体を三角形要素の集合として表す．三角形要素の厚さを d，三角形要素の一つを T_p と表す．また，T_p の頂点を反時計回りに P_i，P_j，P_k とする．頂点 P_i の初期座標を $(x, y) = (\xi_i, \eta_i)$ で表し，初期状態のときの T_p の面積を S_p とする．P_i の初期位置からの変位を $\boldsymbol{u}_i$ で表す．三角形要素 T_p の変形は頂点の変位 $\boldsymbol{u}_i, \boldsymbol{u}_j, \boldsymbol{u}_k$ で表すことができる．

207

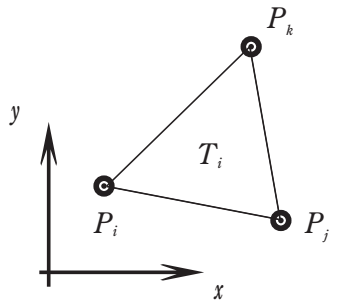

図 5.5: 2D triangular element

ここで，Fig.5.5 に示す三角形要素のひずみを考える．三角形要素の任意の点を $P(\xi,\eta)$ とおいて，形状関数 $N_{ijk}(\xi,\eta)$ を以下のように定義する．

$$N_{ijk}(\xi,\eta)=\frac{\Delta PP_jP_k}{\Delta P_iP_jP_k}=\frac{(\xi\eta_j-\eta\xi_j)+(\xi_j\eta_k-\eta_j\xi_k)+(\xi_k\eta-\eta_k\xi)}{2\Delta P_iP_jP_k}. \tag{5.16}$$

すると，P の位置は以下のように表すことができる．

$$\boldsymbol{u}(\xi,\eta)=\boldsymbol{u}_iN_{ijk}(\xi,\eta)+\boldsymbol{u}_jN_{jki}(\xi,\eta)+\boldsymbol{u}_kN_{kij}(\xi,\eta). \tag{5.17}$$

次に x 方向のひずみ，y 方向のひずみ，および $x-y$ 平面におけるせん断ひずみをそれぞれ $\varepsilon_{\xi\xi},\varepsilon_{\eta\eta},\varepsilon_{\xi\eta}$ で表し，ひずみ行列 $\boldsymbol{\varepsilon}$ をそれらの縦行列と定義する．また，$x-y$ 平面における変位を $\boldsymbol{u}=[u_x,u_y]^T$ とすると，ひずみ行列は，

$$\boldsymbol{\varepsilon}=\begin{bmatrix}\varepsilon_{\xi\xi}\\ \varepsilon_{\eta\eta}\\ \varepsilon_{\xi\eta}\end{bmatrix}=\begin{bmatrix}\dfrac{\partial}{\partial\xi}u_x\\ \dfrac{\partial}{\partial\eta}u_y\\ \dfrac{\partial}{\partial\xi}u_y+\dfrac{\partial}{\partial\eta}u_x\end{bmatrix}=\boldsymbol{L}\boldsymbol{u} \tag{5.18}$$

で表すことができる．ただし $\boldsymbol{L}$ は，

$$\boldsymbol{L}=\begin{bmatrix}\dfrac{\partial}{\partial\xi} & 0\\ 0 & \dfrac{\partial}{\partial\eta}\\ \dfrac{\partial}{\partial\eta} & \dfrac{\partial}{\partial\xi}\end{bmatrix}. \tag{5.19}$$

208

また，三角形要素 T_p にかかる応力行列 $\boldsymbol{\sigma}$ をひずみと同様にして，以下のように定義する．

$$\boldsymbol{\sigma} = \begin{bmatrix} \sigma_{\xi\xi} \\ \sigma_{\eta\eta} \\ \sigma_{\xi\eta} \end{bmatrix}. \tag{5.20}$$

このとき，応力とひずみの関係を以下のように表すことができる．

$$\boldsymbol{\sigma} = \boldsymbol{D} \cdot \boldsymbol{\varepsilon}. \tag{5.21}$$

ここで $\boldsymbol{D}$ は以下のような弾性行列である．

$$\boldsymbol{D} = \begin{bmatrix} \lambda + 2\mu & \lambda & \\ \lambda & \lambda + 2\mu & \\ & & \mu \end{bmatrix} \tag{5.22}$$

ただし，λ，μ はラーメの定数である．ラーメの定数は，二次元物体の弾性が一様で等方であると仮定したときにヤング率 E とポアソン比 ν で表すことができる．

$$\lambda = \frac{\nu E}{(1+\nu)(1-2\nu)}, \quad \mu = \frac{E}{2(1+\nu)}. \tag{5.23}$$

弾性要素においてこの定数を，λ^{ela}，μ^{ela} とおく．粘性においても λ^{vis}，μ^{vis} とおくことができる．また，一次元のときの T_p における部分接続行列 $\boldsymbol{J}_p$ は二次元において，$\boldsymbol{J}_p^{\lambda}$，$\boldsymbol{J}_p^{\mu}$ として以下のように表すことができる．

$$\boldsymbol{J}_p^{\lambda} = \frac{h}{4S_p} \begin{bmatrix} \boldsymbol{A}_{j,k;j,k} & \boldsymbol{A}_{j,k;k,i} & \boldsymbol{A}_{j,k;i,j} \\ \boldsymbol{A}_{k,i;j,k} & \boldsymbol{A}_{k,i;k,i} & \boldsymbol{A}_{k,i;i,j} \\ \boldsymbol{A}_{i,j;j,k} & \boldsymbol{A}_{i,j;k,i} & \boldsymbol{A}_{i,j;i,j} \end{bmatrix}, \tag{5.24}$$

$$\boldsymbol{J}_p^{\mu} = \frac{h}{4S_p} \begin{bmatrix} 2\boldsymbol{B}_{j,k;j,k} & 2\boldsymbol{B}_{j,k;k,i} & 2\boldsymbol{B}_{j,k;i,j} \\ 2\boldsymbol{B}_{k,i;j,k} & 2\boldsymbol{B}_{k,i;k,i} & 2\boldsymbol{B}_{k,i;i,j} \\ 2\boldsymbol{B}_{i,j;j,k} & 2\boldsymbol{B}_{i,j;k,i} & 2\boldsymbol{B}_{i,j;i,j} \end{bmatrix} + \begin{bmatrix} \boldsymbol{C}_{j,k;j,k} & \boldsymbol{C}_{j,k;k,i} & \boldsymbol{C}_{j,k;i,j} \\ \boldsymbol{C}_{k,i;j,k} & \boldsymbol{C}_{k,i;k,i} & \boldsymbol{C}_{k,i;i,j} \\ \boldsymbol{C}_{i,j;j,k} & \boldsymbol{C}_{i,j;k,i} & \boldsymbol{C}_{i,j;i,j} \end{bmatrix} \tag{5.25}$$

ただし

$$\boldsymbol{A}_{i,j;l,m} = \begin{bmatrix} (\eta_i - \eta_j)(\eta_l - \eta_m) & -(\eta_i - \eta_j)(\xi_l - \xi_m) \\ -(\xi_i - \xi_j)(\eta_l - \eta_m) & (\xi_i - \xi_j)(\xi_l - \xi_m) \end{bmatrix}, \tag{5.26}$$

$$\boldsymbol{B}_{i,j;l,m} = \begin{bmatrix} (\eta_i - \eta_j)(\eta_l - \eta_m) & 0 \\ 0 & (\xi_i - \xi_j)(\xi_l - \xi_m) \end{bmatrix}, \tag{5.27}$$

$$\boldsymbol{C}_{i,j;l,m} = \begin{bmatrix} (\xi_i - \xi_j)(\xi_l - \xi_m) & -(\xi_i - \xi_j)(\eta_l - \eta_m) \\ -(\eta_i - \eta_j)(\xi_l - \xi_m) & (\eta_i - \eta_j)(\eta_l - \eta_m) \end{bmatrix}. \tag{5.28}$$

209

二次元粘弾性物体では，三角形要素 T_p の変形により各節点に生じる粘弾性力は次式のように表すことができる．

$$F^{\mathrm{2D}}_{\mathrm{viscoelastic}} = (\lambda^{ela}\boldsymbol{J}_\lambda + \mu^{ela}\boldsymbol{J}_\mu)\boldsymbol{u}_N + (\lambda^{vis}\boldsymbol{J}_\lambda + \mu^{vis}\boldsymbol{J}_\mu)\dot{\boldsymbol{u}}_N. \tag{5.29}$$

以降は一次元のときと同様に微分方程式を求めることができ，これを数値的に計算すると 2 次元物体全体の変形を求めることができる．

二次元粘塑性物体では，三角形要素 T_p の変形により各節点に生じる粘塑性力は次式のように表すことができる．

$$F^{\mathrm{2D}}_{\mathrm{viscoplastic}} = \lambda^{ela}\boldsymbol{J}_\lambda\boldsymbol{w}_\lambda + \mu^{ela}\boldsymbol{J}_\mu\boldsymbol{w}_\mu \tag{5.30}$$

ただし

$$\boldsymbol{w}_\lambda = \int_0^t e^{-\frac{\lambda^{ela}}{\lambda^{vis}}(t-t')}\dot{\boldsymbol{u}}_N(t')\mathrm{d}t', \tag{5.31}$$

$$\boldsymbol{w}_\mu = \int_0^t e^{-\frac{\mu^{ela}}{\mu^{vis}}(t-t')}\dot{\boldsymbol{u}}_N(t')\mathrm{d}t'. \tag{5.32}$$

同様にして微分方程式は，

$$\begin{bmatrix} I & & & & \\ & M & -\boldsymbol{a} & & \\ & \boldsymbol{a}^T & & & \\ & & & I & \\ & & & & I \end{bmatrix} \begin{bmatrix} \dot{\boldsymbol{u}}_N \\ \dot{\boldsymbol{v}}_N \\ \lambda \\ \dot{\boldsymbol{w}}_\lambda \\ \dot{\boldsymbol{w}}_\mu \end{bmatrix} = \begin{bmatrix} \boldsymbol{v}_N \\ -\lambda^{ela}\boldsymbol{J}_\lambda\boldsymbol{w}_\lambda - \lambda^{ela}\boldsymbol{J}_\mu\boldsymbol{w}_\mu + \boldsymbol{f} \\ \boldsymbol{a}^T(2w\boldsymbol{v}_N + w^2\boldsymbol{u}_N) \\ -(\lambda^{ela}/\lambda^{vis})\boldsymbol{w}_\lambda + \boldsymbol{v}_N \\ -(\lambda^{mu}/\mu^{vis})\boldsymbol{w}_\mu + \boldsymbol{v}_N \end{bmatrix} \tag{5.33}$$

となり，これを数値的に計算することで全体の変形を求めることができる．

5.3 アクティブ虚血ダイナミクスの FE シミュレーション

肌表面などの赤みを帯びた部分に力を加えたときに，白色に変化する．これは血管が外力により圧迫され，血流量が一時的に低下するためである．この状態から外力を除去すると再び血流が正常となり，最終的に元の色に戻る．これを虚血といい，肌表面に限らず，臓器においても観測されうる．能動的に力を印加・除去した際の虚血ダイナミクスのことを，アクティブ虚血ダイナミクスと呼ぶ．ダイナミクスの評価指標として，虚血部面積の立ち上がり時定数・立下り時定数に着目する方法と周波数応答に着目する方法がある．金子らは，前者に注目し，圧力を加えた空気を

210

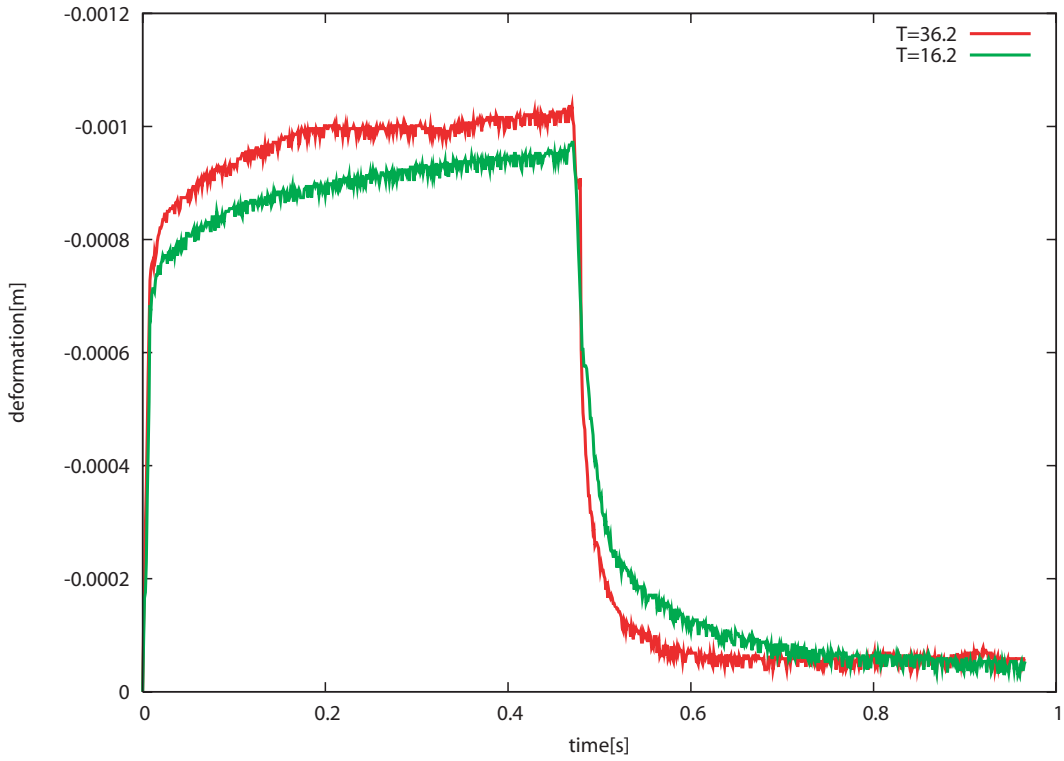

図 5.6: Experimental result of deformation [49]

211

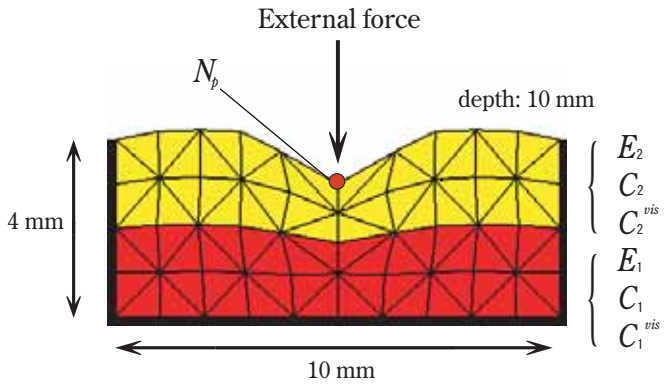

図 5.7: Simulation model

肌表面に与えてダイナミクスの指標としている [49]．本節では金子らによる観測結果 [49] と FE シミュレーションの結果を比較する．

シミュレーションには Fig.5.7 のようなモデルを用いた．4×10 の格子を用いて，三角形要素を交互に配置した．格子の横幅を 0.001 m，高さを 0.0001 m，奥行きを 0.001 m とした．密度を 1200 kg/m^3，ポアソン比を 0.49 として，人肌に近い理想的な等方性物体と同じように設定した．また，三要素モデルの下層のパラメータを E_1，C_1，C_1^{vis}，上層のパラメータを E_2，C_2，C_2^{vis} とした．最上部中心の節点 N_p に外力 0.05 N を 0.47 s の間印加してから開放し，この節点の変位量を調べた．

下層と上層が同じパラメータを有する場合のシミュレーションを行った．このとき，三要素モデルのフォークト部の粘性率を $C_1 = C_2 = 30\,\mathrm{N/(m^2/s)}$ とした場合と $C_1 = C_2 = 80\,\mathrm{N/(m^2/s)}$ とした場合を比較した．ただし，三要素モデルのパラメータを $E_1 = E_2 = 3800\,\mathrm{N/m^2}$，$C_1^{vis} = C_2^{vis} = 30000\,\mathrm{N/(m^2/s)}$ とした．それぞれのシミュレーション結果と金子らによる実験データを Fig.5.8 に示す．変位の立ち上がりのときには，$C_1 = C_2 = 30\,\mathrm{N/(m^2/s)}$ の場合のほうが再現性が高いことがわかる．変位の立ち下がりのときには，$C_1 = C_2 = 80\,\mathrm{N/(m^2/s)}$ の場合のほうが再現性が高いことがいえる．これより空気圧が時間的に一定でない，もしくは指表面の粘弾性が線形でないことが考えられる．空気圧が一定でない場合，立ち下がりのときに残留し，そのまま指表面に圧力を加えつづけている可能性がある．指表面の粘弾性が線形でない場合，立ち上がりのときよりも立ち下がりのときのほうが粘性が大きい可能性がある．フォークト部と粘性部の力がつりあうまでの局所的な区間において，再現性が低い．フォークト部と粘性部の力がつりあっている 0.1 s から 0.5 s 付近では，実験データでは曲線的に変形している．しかし，どちらのパラメータの場合も直線的に変形していることがわかる．これは下層の粘弾性が影響していると考えられる．これには，下層と上層のパラメータを変化させてシミュレーションを行うことによっ

212

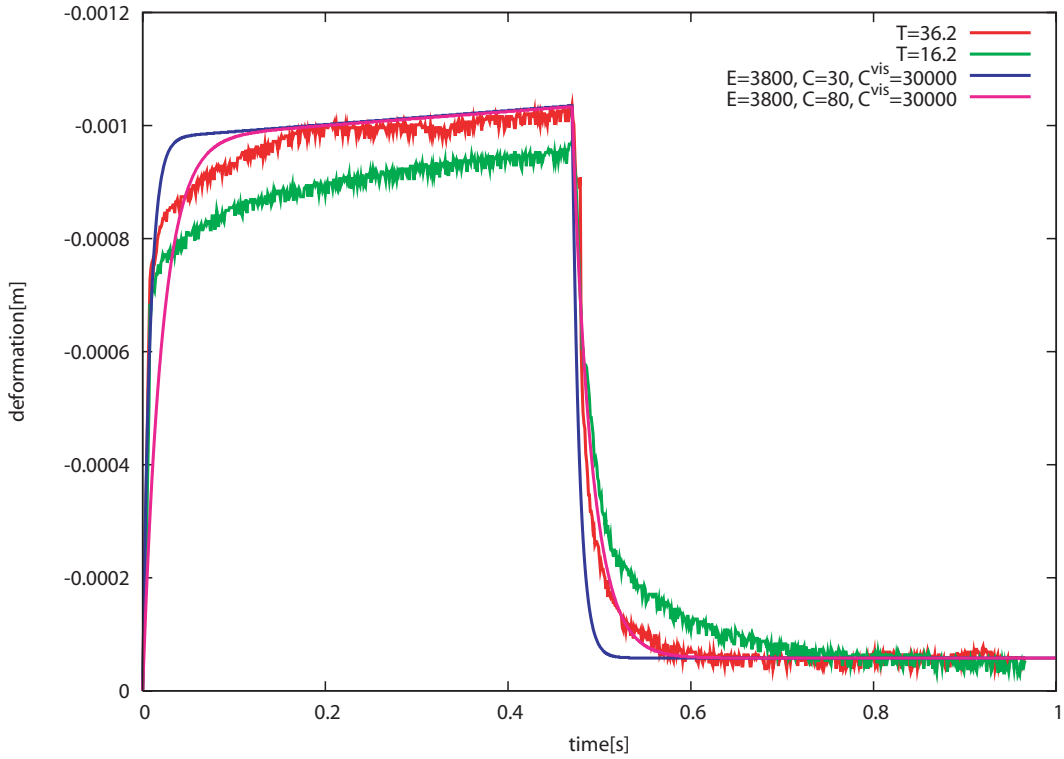

図 5.8: Comparison graph between experiment data and simulation using same parameters

213

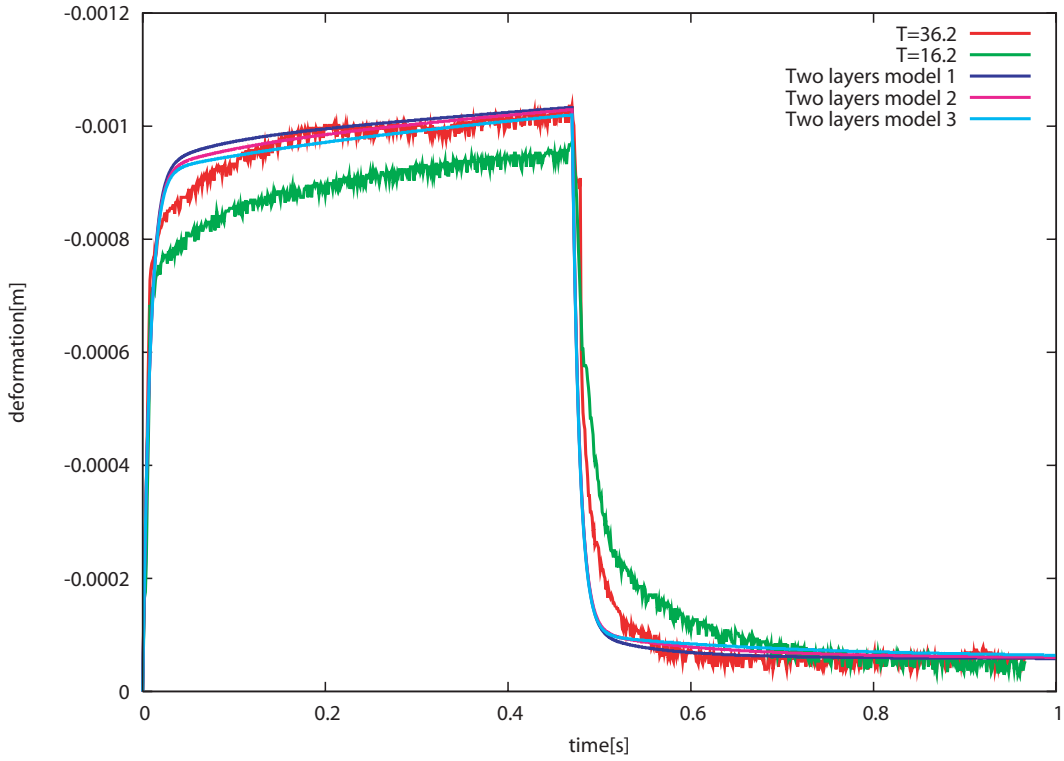

図 5.9: Comparison graph between experiment data and simulation using different parameters

て対応する．残留変位は実験データと一致することがわかる．これは C^{vis} が影響を及ぼす変位なので，C^{vis} の値の設定が正確であることを示している．

下層と上層が異なるパラメータをもつときのシミュレーションを行った．このとき，下層の三要素モデルのフォークト部の粘性率を，モデル 1 で $C_1 = 500\,\mathrm{N/(m^2/s)}$，モデル 2 で $C_1 = 1000\,\mathrm{N/(m^2/s)}$，モデル 3 で $C_1 = 2000\,\mathrm{N/(m^2/s)}$ とした場合で比較した．ただし，三要素モデルの上層のパラメータを $E_2 = 3800\,\mathrm{N/m^2}$，$C_2 = 30\,\mathrm{N/(m^2/s)}$，$C_2^{vis} = 30000\,\mathrm{N/(m^2/s)}$，下層のパラメータを $E_1 = 500\,\mathrm{N/m^2}$，$C_1^{vis}\,\mathrm{N/(m^2/s)}$ とした．それぞれのシミュレーション結果と金子らによる実験データを Fig.5.9 に示す．どのモデルにおいても，変位の立ち上がりのときの再現性は高いことがわかる．しかし，フォークト部と粘性部の力がつりあうまでの局所的な区間において，再現性が低い．フォークト部と粘性部の力がつりあう 0.1 s から 0.5 s 付近では，どちらのパラメータの場合も曲線的に変形しており，このときの再現性は高い．

214

5.4　マンモグラフィーのための力学モデル

本節では，パーティクルベースモデルのマンモグラフィーへの応用に関して述べる．マンモグラフィーとパーティクルモデルによる計算結果とを比較し，評価する．さらに，ファントムの撮影結果との比較を通して，パーティクルモデルの精度を検証する

215

On Compression Model for Integrative Analysis of Different View Breast Xrays

Yasuyo Kita, Shinichi Tokumoto, and Shinichi Hirai

Abstract— **The breast deformation during medical procedures makes it difficult to analyze different breast images integratively. The simulation of the breast deformation is effective to compensate the difference of the breast shape among the images. However, realistic simulation is very difficult since the actual deformation is quite complicated and the detailed conditions about the deformation are hardly known mainly because of the large individual variations in both geometry and tissue organizations. For a CAD system for integratively analyzing different view mammograms (breast Xrays) [1], a simplified model to simulate the breast compression, which is derived base on several approximations about the deformation is used. Although it contributes to derive valuable results, the precision of the results is desired to improve. In this paper, we discussed about a breast compression model aiming at more accurate solutions. Two trials for better understanding on the breast deformation under the compression are shown: simulation of mammographic compression using a mechanical model and inspection of internal deformation using a devised phantom. These experimental results gave us some clues for better simulation.**

I. INTRODUCTION

Breast cancer is one of the most serious disease for women. Recently, several types of medical images are used for screening programs to detect breast cancer in its early stages with less oversight. Especially, mammograms, MRI and Ultrasound are well used because of their good balance in trade-off between specificity/sensitivity and cost. It is effective to integrate the information obtained from different images, as each modality has its merits and demerits. However, it is not easy because a breast deformed into very different shapes during the procedures. For mammograms, a breast is strongly compressed into flattened shape primarily to reduce x-ray dosage. For taking MRI, the breast is pendulous in specially designed breast coil as the patient lies on her front in the magnet; the gravity pulled down the breast so as to get it away from her chest wall. On the other hand, since women lie on the bed with her face up during the ultrasound process, the breast shape is pulled toward the chest wall by the gravity.

It is a natural and sensible strategy to simulate the deformation of the breast to compensate the difference in the shapes among the images. At first, deformable models which deform so as that image features of the two different images coincide each other were used to compensate relatively small deformation, such as pre-post contrast MRI[2][3] [4]. Later, to decrease deformations inconsistent to the physics, constraints based on volume conservation principle were introduced[5][6].

For larger deformation as like seen in compression procedures, finite element models (FEM) of breast have been intensively studied recently aiming at accurate simulation[7][8][9][10][11][12][13]. However, FEM models can simulate accurate deformation only when all internal end external factors, such as geometry and biomechanics of the breast, forces exerted to the breast, and boundary conditions are given correctly. Unfortunately, in most of practical cases, it is quite difficult to grasp these information: geometry of the breast varies largely according to individuals; organization of internal soft tissues are also different among the individuals; both strength of compression and boundary condition at the connection of chest wall are very complicated.

Especially, in the case of integrative analysis of different view mammograms (breast Xrays), the input is only two projective images of differently deformed breast. To simulate the breast compression process for building a CAD (Computer Aided Diagnosis) system under such situation, Kita et al [1] introduced a simplified compression model based on several approximations. For appropriate simplification, it is important to understand the principle and tendency of the breast deformation under compression. Actually, the compression model was derived based on several clinical studies[14],[15]. Especially, Novak[15] studied deformations of the breast surface during compression by observing the movements of marks made on the skin of volunteers' breast. However, such observations only give information about skin movement, and do not strictly give information about movements of tissue internal to the breast. To improve the model, we need more investigations about the internal deformation caused by the compression.

In this paper, we showed some preliminary trials for better understanding of the breast deformation including its internal deformation to improve the compression model used in the CAD system. In Section II, we briefly explain the scheme of the CAD system and the compression model used in the current system. In Section III, the breast deformation by compression is investigated by comparing a mammogram and a MRI of the same breast through the intermediary of a mechanical model. In Section IV, the internal deformation by compression is investigated by observing a phantom in a industrial CT scanner, which is devised to have 286 points of

Y. Kita is with Information Technology Research Institute, National Institute of Advanced Industrial Science and Technology, 1-1-1 Umezono,Tsukuba 305-8568, Japan y.kit@aist.go.jp

S. Tokumoto is with System Division, Industrial Technology Center of Wakayama Prefecture, Ogura 60, Wakayama city, Wakayama pref., 649-6261, Japan tokumoto@wakayama-kg.go.jp

S. Hirai is with Dept. Robotics, Ritsumeikan Univ. Kusatsu, Shiga 525-8577, Japan hirai@se.ritsumei.ac.jp

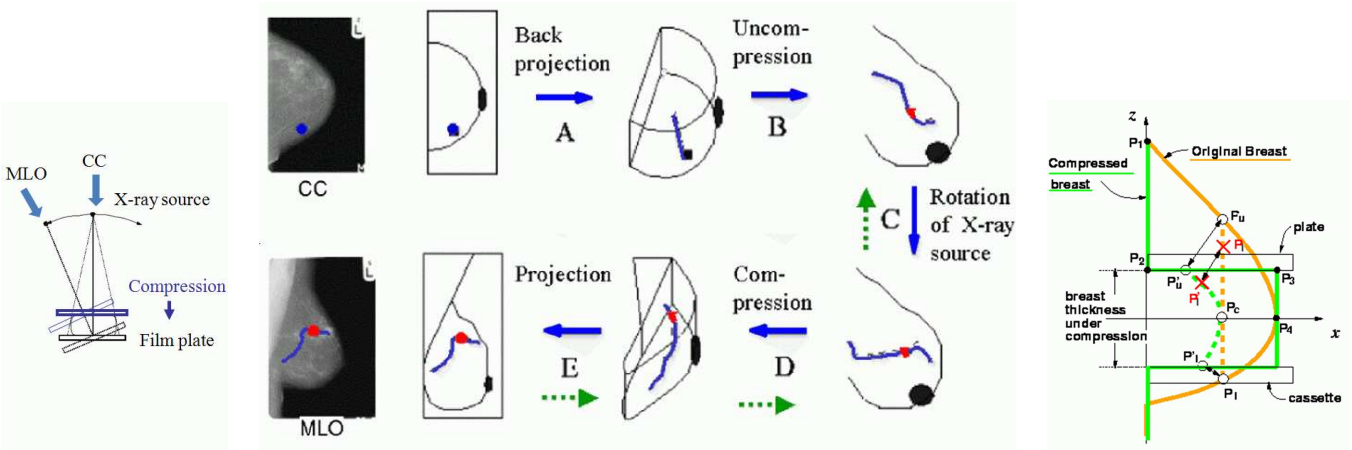

(a) (b) (c)

Fig. 1. Strategy for determining 3D position from two mammographic views.

marks inside of it. Finally, we discuss and clarify the matters to improve in Section V.

II. Scheme of the CAD system [1]

Recently, performing two different views of the breast, the medio-lateral oblique (MLO) and cranio-caudal (CC), is spread in screening programs, since it may greatly improve sensitivity and specificity. When a mammogram is performed the breast is compressed between the film cassette and compression plate in the direction of the x-ray source: "head to toe" for the CC view and "over the shoulder diagonally to the hip" for the MLO view, as shown in Fig. 1(a). Unfortunately, radiologists find it difficult to relate points in the CC view to those in the MLO view because the breast is largely deformed in the different directions. To help their diagnosis, a CAD (Computer Aided Diagnosis) system which simulates the breast deformation during mammogram performance and suggests the corresponding position between different viewed mammograms has been developed[1]. The method calculates the epipolar curve, that is the locus of possible corresponding positions of the point in the other image by simulating the five steps of the process: A: back projection → B: uncompression → C: rotation → D: compression → E: projection as shown by the solid arrows as shown in Fig. 1(b). As a result, the line in the MLO image is calculated.

This physics-based approach have another merit: it also can help to estimate the 3D position of a lesion in the uncompressed breast, despite the fact that the breast is never imaged in the uncompressed state in mammography. This technique works after finding the corresponding point along the epipolar curve and then back-tracking the movement of the point during the simulation of the processes as shown by the dashed arrows in Fig. 1(b). Fig. 2 shows an example of the resultant 3D position obtained by the system. Here, the 3D shape of the individual breast shown in the right-hand two windows is automatically reconstructed from the breast outlines in CC and MLO images. This localization is very important to guide biopsies and/or fusion of multi-modal data

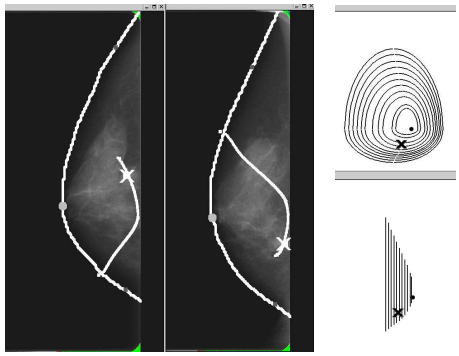

Fig. 2. 3D position of legion obtained by the CAD system

of the breast.

The breast deformation caused by compression and uncompression is simulated using the simplified geometrical compression model proposed in [16], This model enables the calculation of the position of any point of the breast under compression from its original position in the uncompressed state, and vice versa as shown in Fig. 1(c). The model was derived based on some approximations on the breast deformation under the compression as like:

Approximation 1(A1). The cross-section for compression of the breast is deformed only in the plane by compression. Here, "the cross-section for compression" means the cross-section cut by the plane which is parallel to the compression direction and perpendicular to the chest wall.

Approximation 2(A2). In the mid-plane between the plate and the cassette, there is no deformation.

Through experiments using about 50 pairs of CC and MLO images of both English and Japanese women [16][1], average error, which is distance from the actual corresponding point to the predicted curve, is less than 7 mm. It overcomes the current radiologists predictions, average error of which is about 10 mm. The accuracy can be improved by replacing

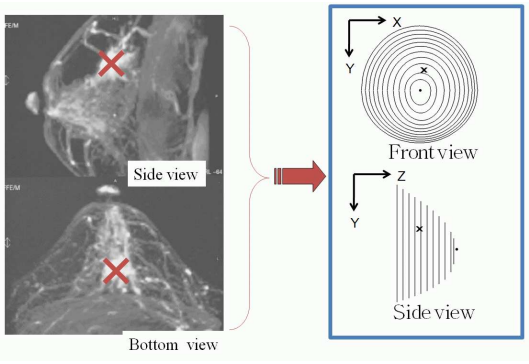

Fig. 3. 3D model reconstructed from MR MIP data

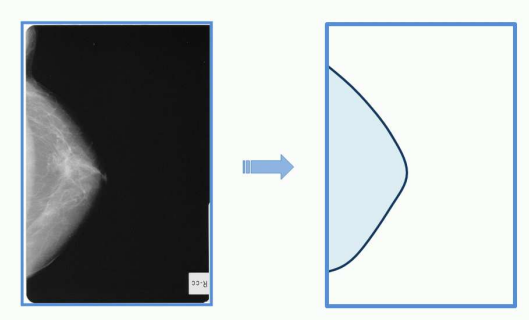

Fig. 4. CC data of the breast of the MR data in Fig.3

the compression model with a richer compression model, Actually, Zhang et al[13] uses a breast FEM model which is reconstructed from MRI data of the same breast to calculate the similar corresponding lines. The accuracy of the experimental results using six patients was reported as about 2.2 mm. However, it should be noticed the former method has merits of working only with the two view mammograms in real time, while the latter requires MRI of the same breast and takes much longer time. This characteristics is important for a handy and easy-to-use CAD system for aiding the diagnosis of mass screening with mammograms only.

Therefore, the improvement of the simplified compression model only with the input images is also desirable. Yam et al [17] improved the compression model by introducing some variable parameters into the model and by adjusting the values based on the correspondences of prominent features (micro-calcifications) on the images. However, mammographic views do not always have enough numbers of corresponding pairs of prominent features.

One direction is to build a more sophisticated geometrical compression model by understanding the breast deformation by compression in more details.

III. Simulation of CC Mammographic Compression using a Mechanical Model

To understand better the breast deformation by compression, we simulated CC mammographic compression of breast using a mechanical model reconstructed from MR data and compared the results with actual CC image. We use the

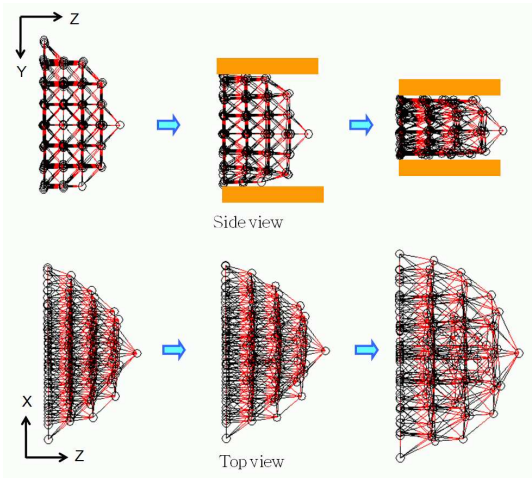

Fig. 5. Compression simulation 1

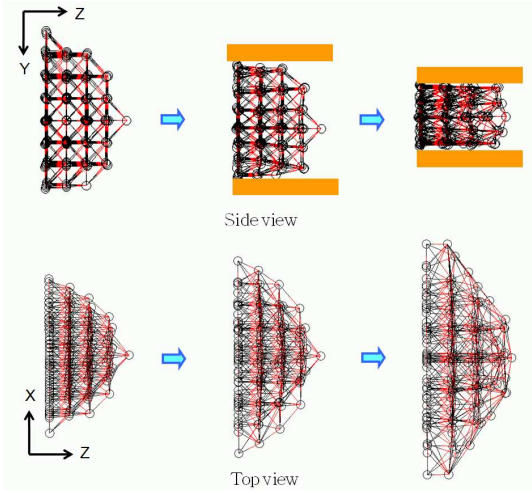

Fig. 6. Compression simulation 2

rheological model developed by Kimura et al.[18], which can simulate the deformation of elastic, viscoelastic. and plastic objects in almost real time. Although the parameters of this model are not directly related with actual biomechnical parameters like Young's modulus, these can be adjusted relatively intuitively. The 3D geometry of the model is reconstructed from outlines in MRI MIP (Maximum Intensity Projection) images as shown in Fig.3. For simulating compression by two plates, Dirichlet boundary conditions (displacement-controlled conditions) are applied to the nodes touched to the plates which move gradually towards each other until the distance between the plates becomes the width at taking the CC image. At the connection to the fixed chest wall, only the z coodinates of the nodes at the chest wall is fixed. Fig. 5 shows a top and side viewsof a simulation result. Although several simulations were tried while manually adjusting the parameters of the viscoelasticity of the model, the outline of the deformed breast did not get close to the one observed in the actual CC image in Fig. 4. The biggest difference is the tendency of elongation in the X

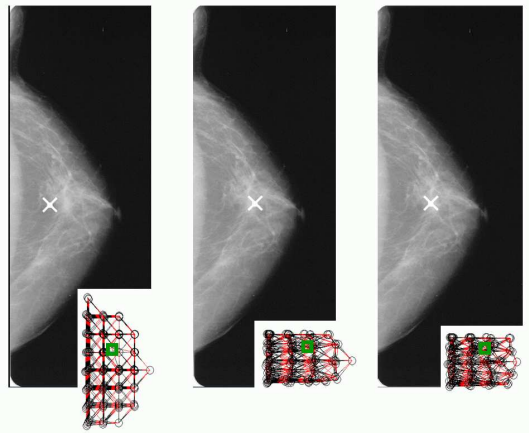

Fig. 7. Projected positions of a lesion detected in MR data

direction, which is perpendicular to the compression and along the chest wall. Although there are also some studies simulating the CC compression[10][13], the consistency of the simulated shape with the actual observation has not been sufficiently investigated. As far as we review, such tendency does not seen in any simulation results. We infer that this is mainly because both the connection with the chest wall and the compression action are fairly complicated and are not well implemented in the simulations. Actually, it is hard to represent this complicated boundary conditions. Instead of sticking to that, we add one more Dirichlet boundary conditions for the nodes on the horizontal plane through the nipple, so as to the outline of the shape after the simulation coincides with the one observed in actual CC image. Concretely, the nodes are forced to move to the position which produce the outline of CC. Fig. 6 shows the deformation of the breast using this condition.

To examine the effects of this modification on the internal deformation, we check the consistency of projected position of a lesion. In Fig. 7, white crosses illustrate three projections of a lesion which is detected in MRI (crosses in Fig. 3): from left to right, the projection of the location at original MRI shape, that after the compression simulation shown in Fig. 5 and that after the compression simulation shown in Fig. 6. As you see, the last one gives best coincidence. This result encourages us to make good use of the features observed in images to specify the deformation.

This observation also gives a clue to the improvement of the geometric compression model used in the CAD system: the modification realizing this tendency of elongation along the chest wall should be added.

IV. Observation of internal deformation using devised phantom

In order to grasp internal deformation of flexible objects in details, Tokumoto et al.[19] has devised gel phantoms in which small metallic elements arranged with regular intervals and measured the movements of the elements using an industrial CT scanner, TOSCANER-24200AV. Fig.8 shows one example of the experimental results using a semi-ellipsoid phantom made of human-skin gel. The size of the phantom is 130 (major axis) $\times$ 110 (minor axis) $\times$ 70 (height) mm. 286 metallic elements are arranged inside of the phantom. To observe the internal deformation, the movement of the elements were observed by the CT scanner at three times: with no compression, under compression to the width of 100 mm, and under compression to the width of 80 mm. In Fig. 8(a), white, red and blue colors illustrate the position of the elements at each state respectively.

To observe more clearly, the movement of the metallic elements which on a horizontal plane at the initial state is picked up in Fig. 8(b). The movement in the compression direction (in the Y direction) is big at the part which are pressed directly by the plates (at the part of $X = 60 \sim 100$ in Fig.8(b)). On the other hand, at the remaining outer part, the movement in the X direction, which is perpendicular to the compression direction is stronger. One more noteworthy point is that the former part obviously got denser than the latter part under the compression. This gives us a valuable lesson that too strong volume conservation constraints could cause removal from reality.

This observation suggested some amendments to the compression model used in the CAD system.

1) On Approximation 1:
   In the current system, for simplification, we ignore the movement perpendicular to the cross-section and consider the deformation only within each cross-section. However, cross-sections tend to bend outward with the biggest displacement at the mid-plane between the plates.
2) On Approximation 2:
   In the mid-plane between the plates, deformation in the compression direction can by ignored. However, the displacements in the other directions should be considered.
3) On 3D reconstruction from the outlines of mammograms:
   In the current system, individual 3D breast shape is reconstructed on the assumption that its horizontal and vertical outlines can be approximated with 10-percent scale-downed outlines of CC and MLO images respectively[1]. However, it looks better to take into consideration the distortion of the outlines during the compression rather than assuming the change as similar transformation.

V. Conclusions

In this paper, we discussed about the model which can simulates breast compression for practical medical applications. To shed light upon the physical deformation of breast under mammographic compression, we have done two-types of experiments: simulation of mammographic compression using a mechanical model and inspection of internal deformation using a devised phantom. Based on the experimental results, Some key issues to improve the compression model used currently in the CAD system[1] were specified in Section IV.

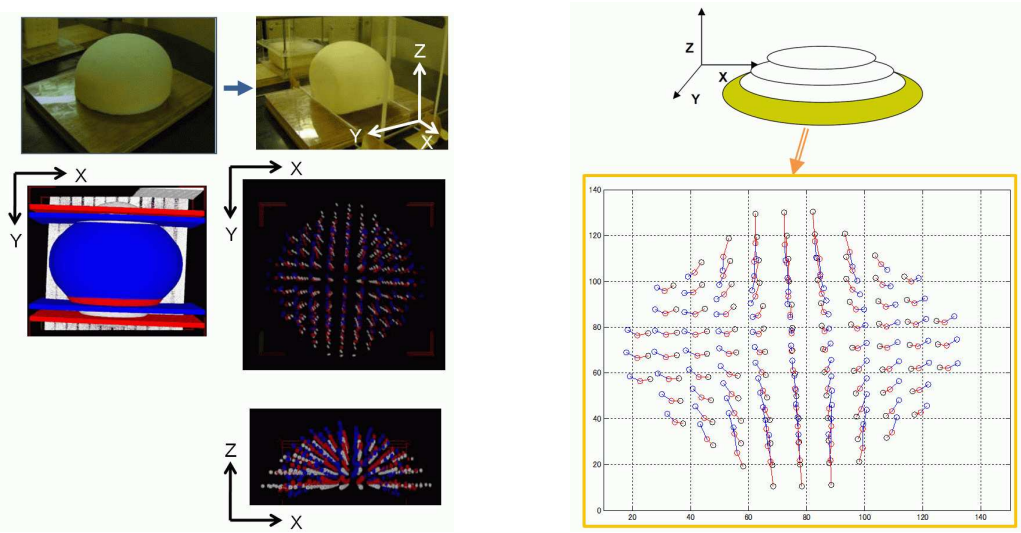

(a) (b)

Fig. 8. Inspection results of internal deformation of a phantom with metallic elements inside

Our future work will focus on:
1. Further investigation of the breast deformation under mammographic compression by increasing the number of the experiments in-line with ones shown in this paper.
2. Development of more sophisticated compression model for the CAD system based on the facts obtained from the experiments above.

Acknowledgements

The authors gratefully acknowledge discussions in Medical Vision laboratory, University of Oxford, which has inspired the basic idea of this paper. This research was supported by Grant in Aid for Scientific Research (17206024) by the Ministry of Education, Culture, Sports, Science and Technology of Japan.

REFERENCES

[1] Y. Kita, E. Tohno, R. P. Highnam and J. M. Brady:"A CAD system for the 3D location of lesions in mammograms", *Medical Image Analysis*, Vol. 6, pp. 267–273, 2002.

[2] Rueckert, D. and Sonoda, L.I. and Hayes, C. and Hill, D.L.G. and Leach, M.O. and Hawkes, D.J.:"Nonrigid registration using free-form deformations: Application to breast MR images", *IEEE Trans. on Medical Imaging*, Vol. 18, No. 8, pp. 712–721, 1999.

[3] F.J.P. Richard and L.D. Cohen,:"A New Image Registration Technique with Free Boundary Constraints: Application to Mammography", *Computer Vision and Image Understanding*, Vol. 89, No.2-3, pp. 166–196, 2003.

[4] C. P. Behrenbruch, K. Marias, P. A. Armitage, M. Yam, N. Moore, R. E. English, J. Clarke, and J. M. Brady: "Fusion of contrast-enhanced breast MR and mammographic imaging data", *Medical Image Analysis*, Vol. 7, pp. 311–340, 2003.

[5] C. Tanner, J.A. Schnabel, A. Degenhard, A.D. Castellano-Smith, C. Hayes, M.O. Leach, D.R. Hose, D.L.G. Hill and D.J. Hawkes: "Validation of Volume-Preserving Non-Rigid Registration: Application to Contrast-Enhanced MR-Mammography", In *Proc. of 5th International Conference on Medical Image Computing and Computer-Assisted Intervention*, pp. 307–314, 2002.

[6] Rohlfing, T. and Maurer, Jr., C.R. and Bluemke, D.A. and Jacobs, M.A.: "Volume-preserving nonrigid registration of MR breast images using free-form deformation with an incompressibility constraint", *IEEE Trans. on Medical Imaging*, Vol. 22, No. 6, pp. 730–741, 2003.

[7] A. Samani, J. Bishop, M. J. Yaffe, and D. B. Plewes:"Biomechanical 3-D Finite Element Modeling of the Human Breast Using MRI Data", *IEEE Trans. on Medical Imaging*, Vol. 20, No. 4, pp. 271–279, 2001.

[8] F.S. Azar, D.N. Metaxas,and M.D. Schnall: "Methods for modeling and predicting mechanical deformations of the breast under external perturbations", *Medical Image Analysis*, Vol. 6, No. 1, pp. 1–27, 2002.

[9] Y. Liu, A. E. Kerdok, and R. D. Howe: "A nonlinear finite element model of soft tissue indentation", In *Proc. of Second International Symposium on Medical Simulation*, pp. 67–76, 2004.

[10] P. Pathmanathan, D. Gavaghan, J. Whiteley, M. Brady, M. Nash, P. Nielsen, V. Rajagopal: "Predicting Tumour Location by Simulating Large Deformations of the Breast Using a 3D Finite Element Model and Nonlinear Elasticity", In *Proc. of Medical Image Computing and Computer-Assisted Intervention (MICCAI) 2004*, pp. 217–224, 2004.

[11] T.J. Carter, C. Tanner, W.R. Crum, and D.J. Hawkes:"Biomechanical Model Initialized Non-rigid Registration for Image-Guided Breast Surgery", In *Proc. of MICCAI 2006 Workshop on Computatonal Biomechnics for Medicine*, pp. 104–112, 2006.

[12] V. Rajagopal, J.H. Chung, R Warren, R. Highnam, M. Nash, and P. Nielsen:"Finite Element Modelling of Breast Biomechanics: Predicting the Effects of Gravity", In *Proc. of MICCAI 2006 Workshop on Computatonal Biomechnics for Medicine*, pp. 94–103, 2006.

[13] Y. Zang, Y. Qiu, D. B. Goldgof, S. Sarkar, and L. Li: "3D Finite Element Modeling of Nonrigid Breast Deformation for Feature Registration in X-ray and MR Images", In *Proc. of IEEE Workshop on Applications of Computer Vision*, pp. 38–43, 2007.

[14] E. Roebuck: *"Clinical radiology of the breast"*, Heinemann medical books, Oxford, 1990.

[15] R. Novak: *"The transformation of the female breast during compression at mammography with special reference to the importance for localization of a lesion"*, ACTA radiologica supplement 371 Stockholm, 1989.

[16] Y. Kita, R.Highnam and M. Brady:"Correspondence between different view breast X rays using curved epipolar lines", *Computer Vision and Image Understanding*, Vol. 83, pp. 38–55, 2001.

[17] M. Yam, M. Brady, R. Highnam, C. Behrenbruch, R. English, and Y. Kita:"Three-dimensional reconstruction of microcalcification clusters from two mammographic views", *IEEE Trans. Medical Imaging*, vol. 20 no. 6, pp. 479–489, 2001.

[18] M. Kimura, Y. Sugiyama, S. Tomokuni, and S. Hirai: "Constructing Rheologically Deformable Virtual Objects", In *Proc. IEEE Int. Conf. on Robotics and Automation (ICRA2003)*, pp. 3737–3743, 2003.

[19] S. Tokumoto and S. Hirai: "Internal Deformation Measurements of Flexible Objects for Identification of Paprameters by CT Scanner", In *Proc. of SICE SI2006*, pp. 73–74, 2006 [In Japanese].

5.5　結言

本章では，粘弾性FEモデルによるアクティブ虚血ダイナミクスのシミュレーションを実行した．アクティブ虚血ダイナミクスのFEシミュレーションでは，評価指標として外力印加時の変位の立ち上がり時定数，立ち下がり時定数に着目した．立ち上がり時定数，立ち下がり時定数は粘弾性の影響を受けず，外力印加時間に依存することを示した．また，マンモグラフィーのためにパーティクルモデルによる変形推定を用い，精度の良い変形形状推定が可能であることを示した．

221

第6章　マイクロフォースセンサによる内部力計測

6.1　緒言

本章では，中実で半球形状の柔軟指先の底辺中央に，マイクロフォースセンサを埋め込み，マイクロフォースセンサによる内部力の計測を実験的に評価する．

6.2　センサ埋め込み型柔軟指先の構造

本研究で製作するマイクロフォースセンサ埋め込み型柔軟指先を TES(Tactile Sensor-Embedded Soft Fingertip) と略称し，TES の構造について記述する．

図 6.1 が本研究で製作した TES と種々の信号処理回路を組合わせた全体図である．直径 40mm のポリウレタンゴム（商品名：人肌ゲル）に内蔵されたタクタイルセンサから伸びたフレキシブルケーブルが入力回路に接続されており，次段のオフセットカット回路，増幅回路を介して安定的な出力信号を計測できる．TES は 3 重構造となっており，環境と接触するゴム部分は中実構造になっている．TES の内部構造の模式図を図 6.2-(a) に，内蔵されているタクタイルセンサデバイスを図 6.2-(b) に示す．

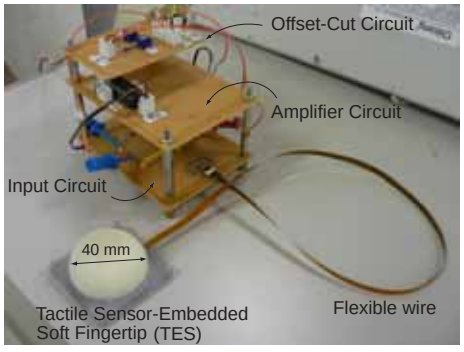

図 6.1: TES and its measurement circuit system

222

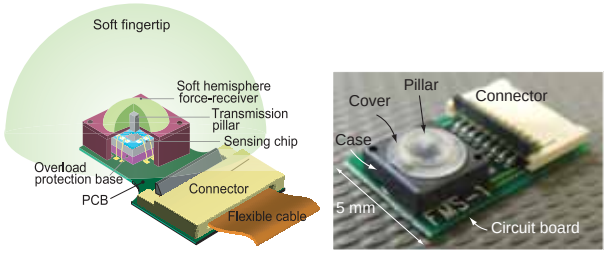

(a) inner structure (b) tactile sensor

図 6.2: A novel tactile sensor packaged for sensing slight change of force and moment.

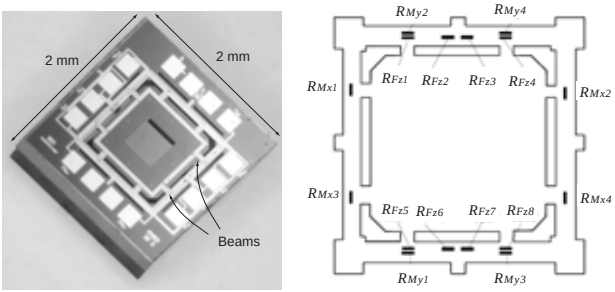

(a) sensing chip (b) piezoresistors layout

図 6.3: An enhanced six-axes micro-force/moment sensing chip.

表 6.1: Specification of the sensor.

Strength	Force	Moment
	5000 [mN]	800 [N·μm]
Sensitivity	S_{Fz}	S_{Mx}, S_{My}
	0.2 [mV/mN]	2.83 [mV/(N·μm)]

さらに，タクタイルセンサ内部には力伝達用ピラーと共に，6 軸マイクロフォースセンサチップ (図 6.3-(a)) が薄い透明ゴム被膜を介して設置されている．また，チップ上のピエゾ抵抗素子の配置図を図 6.3-(b) に示す．

本センサは，最大 3 軸の力と 3 軸のモーメントを計測可能であるが，本稿では 3 軸 (F_z, M_x, M_y) のみを計測対象としている．よって，3 軸それぞれの感度を強度と共に表 6.1 に示す．

223

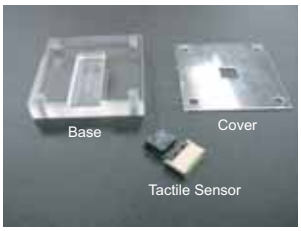

(a) all components

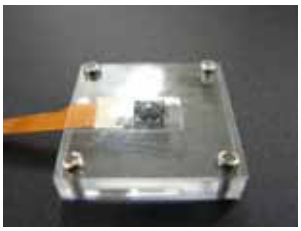

(b) sensor base

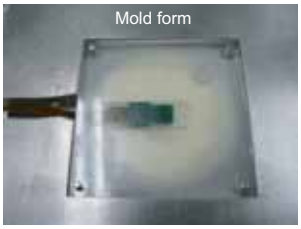

(c) backside of the TES

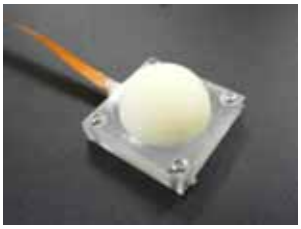

(d) completion

図 6.4: Fabrication process of the TES.

6.3 TESの製作工程

マイクロフォースセンサは，ロボットハンドに取り付けた上での利用を想定している．本章では直径 20mm の TES に関する製作工程を以下に示す．この大きさは，柔軟指先の弾性モデルと圧縮実験結果との比較により得られた知見に基づいている [55, 57].

6.3.1 指先材料と製作方法

本デバイスの指先材料には，フィギア製作等に多用される「人肌ゲル」(エクシールコーポレーション) を用いる．同材料の線形ヤング率は，力学パラメータ同定試験により約 0.20MPa〜0.24MPa を得ている [55, 57]．本商品の特徴として，同程度のヤング率の指先を製作する限り同梱されている定量の樹脂溶剤と硬化剤を混合するだけでよく，混合割合を求め調合する必要がないため製作が容易である．また，内部の気泡の発生がほとんどなく，アクリル系材料の型枠との剥離が容易なため，センサの埋め込み作業を含んだ製作工程に適している．

図 6.4 は TES の製作手順でありその完成図を図 6.5 に示す．図 6.4-(a) にアクリル材料で加工したセンサ用ベースとカバーを示す．それぞれの寸法は，ベースが 26mm 四方で厚み 5mm，カバーが厚み 0.4mm になっている．ベースにはタクタイルセンサとフレキシケーブルが通る溝が加工されている．それらを組み合わせてセンサベー

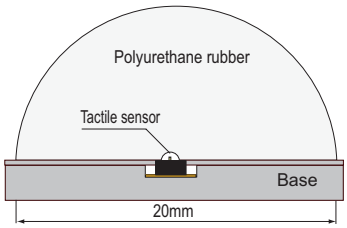

図 6.5: Illustration of the TES

スとし (図 6.4-(b))，タクタイルセンサを中央に配置する．次に，あらかじめ混合した「人肌ゲル」を直径 20mm の半球形状型枠に注入し，センサベースを逆向きに挿入する (図 6.4-(c))．硬化後，センサベースを剥離すると TES が完成する (図 6.4-(d))．

6.3.2　オフセット電圧調整回路と増幅回路

本センサ単体での出力電圧は，数 mV〜数十 mV のオーダーであるため，ロボットハンドの触覚デバイスとしての用途を考慮すると，増幅回路を組み込む必要がある．また，各 3 軸出力値 (F_z, M_x, M_y) には無負荷状態で最大出力に対して 10% 程度のオフセット電圧が発生するため，増幅前段においてオフセットカット回路を組み込む必要がある．さらに，柔軟材料で覆われたセンサの繰り返し使用によってオフセット電圧値が常に変動するため，センサ電源投入後，毎回手動で調整する必要がある．したがって，センサ内部に形成されているピエゾ抵抗素子によるホイートストンブリッジを利用して並列に可変抵抗器を取り付け，オフセット電圧を調整する．図 6.6-(a) がオフセット電圧調整回路であり，図 6.6-(b) に (F_z, M_x, M_y) それぞれの実際の電子回路を示す．また，出力電圧に対する増幅率を F_z で 2000 倍，M_x, M_y で 500 倍としている．差を与えた理由は，表 1 に示したように，F_z に比べて M_x, M_y の方が，感度が大きいためである．

6.4　TES の圧縮実験とその評価

本節では，完成したタクタイルセンサ埋め込み型柔軟指に対して静的な圧縮試験を行うことで，本触覚デバイスの有効性を検証する．

225

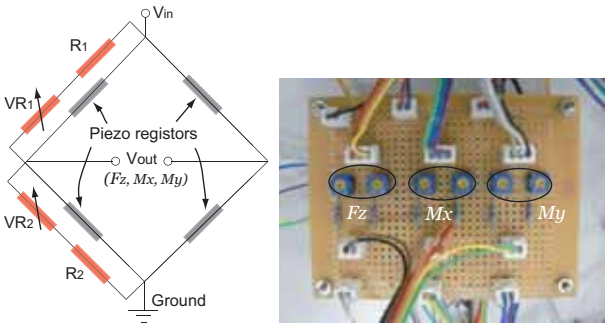

(a) bridge circuit　　(b) offset-cut circuit

図 6.6: An offset-cut bridge circuit and its electronic circuit board.

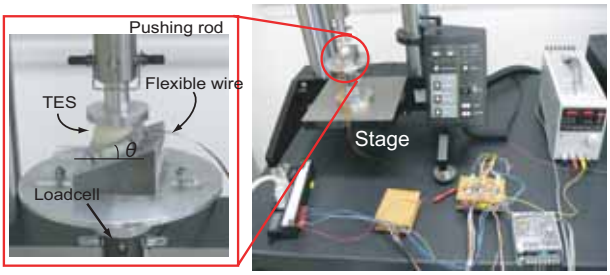

図 6.7: Apparatus for compression test.

6.4.1　実験装置と方法

TES に所望の荷重を加えるために，INSTRON 社製マイクロテスター (5848 型) を使用する．実験装置の構成図を図 6.7 に示す．マイクロテスターは垂直降下するロッド部，対象物体に加えた荷重を計測するロードセル部，ロッドが対象物体に加える力や移動速度などを制御するコントロール部から構成されている．出力電圧の計測には，CONTEC 社製のアナログ入力ボード (AD12-16(PCI)EV) を使用する．

実験方法としては，3 軸力成分 (F_z, M_x, M_y) の出力電圧を計測するために，まず図 6.8-(a)，(b) に示すように，θ の傾斜を持つ治具の上に TES を設置し，次に，接触方位角 ϕ を持つ方向に治具を固定する．この配置により任意の方向からの圧縮実験を可能にする．本実験では，傾斜角 θ が 5° から 30° までの 5° 刻みの 6 種類の傾斜治具を用意し実験を行う．また，方位角 ϕ に関しては，0°，90°，180°，270° と変化させて圧縮方向に荷重を加えた．本試験ではロッドの下降速度を 3.0mm/min とし，ステージ下部にあるロードセルの読みが目標の 3N に到達するまで荷重を加えて，同時にセンサ出力電圧を計測する．図 6.9 にロードセルによる印加荷重-時間のグラフを示す．これは，センサ値ではないことに注意されたい．図内の数値は，6 種類の傾斜

226

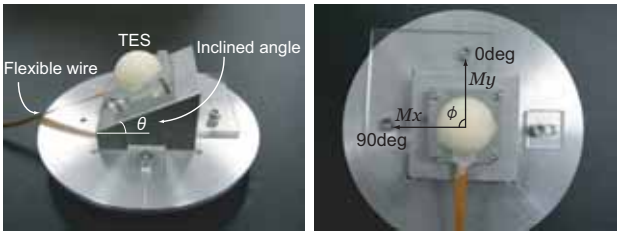

(a) relation of θ (b) relation of ϕ

図 6.8: Compression test and setting of the TES.

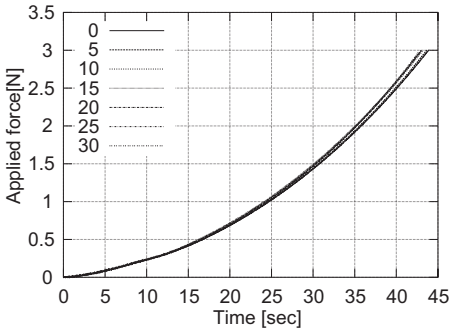

図 6.9: Input pattern of the applied force which is measured by the loadcell in a basic experiment.

角における実験結果と垂直接触結果 ($\theta = 0°$) を示す．図から分かるように，傾斜角に関わらず印加荷重は時間に対してほぼ等しい曲線を描く．

6.4.2 センサノイズとディジタルフィルタ処理

TES 圧縮の本試験の前に実施した基礎実験において，センサ出力には図 6.10-(a) に示すように F_z で幅が最大約 0.37V，M_x, M_y で最大約 0.1V のノイズが生じた．そこで，このセンサ出力のノイズを除去するためにディジタルフィルタ処理を施して平滑化しセンサ出力値を得る．フィルタには時間関数として式 (6.1) に示す IIR (Infinite Impulse Response) 型を用いた．

$$V(t) = rU(t) + (1 - r)V(t - 1) \tag{6.1}$$

上式において $U(t)$ がセンサ計測値で，$V(t-1)$ が一段前の平滑化した値である．ここで，$r = 0.1$ として処理を行った．図 6.10-(b) にフィルタ処理後の計測結果を示す．

227

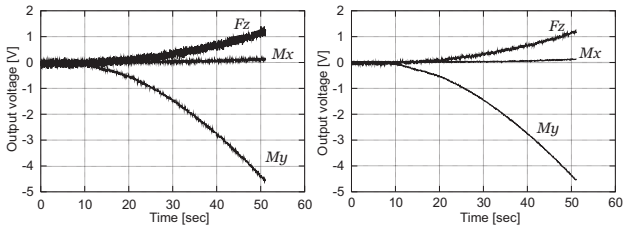

(a) before filtering　　(b) after filtering

図 6.10: Digital filtering process of sensor measurements.

フィルタ処理を行うことによってノイズが大きく軽減されていることが確認できる．以降の試験結果ではフィルタ処理を行った計測結果を示す．

6.4.3　実験結果

本圧縮実験では θ を $5°, 10°, 15°, 20°, 25°, 30°$ で，ϕ を $0°, 90°, 180°, 270°$ で変化させているため，最終的に 24 通りの実験データを取得している．取得データ量が膨大であるため，その特徴を示すために $\phi = 90°$ のときの実験結果を図 6.11 に図示する．横軸に時間軸，縦軸にセンサの出力電圧を示す．3 章で述べたように，F_z が 2000 倍に，M_x, M_y が 500 倍に増幅されている．また，図 6.11 の (a) から (f) までの図は，傾斜角 θ を変化させたときの結果である．

この結果から分かるように，θ が増加するにしたがって M_y も同様に増加しているが，逆に M_x は変化していない．この現象は図 6.8-(b) のモーメントの位置関係 $(\phi = 90°)$ からも理解できる．また，F_z がほとんど変化していないことが分かる．これは図 6.7 にあるように，ロッドを通して TES に加わる荷重の方向が指先半球形状の中心を向いているためである．逆言すると，接触外力が TES に対して求心方向を向いている限り，どの角度から圧縮しても F_z は変化しないことを意味する．仮に，荷重方向が TES の傾斜面に垂直である場合，理論と実験の両観察から傾斜角 $\theta = 0°$ のときに F_z が極小を持つことが知られている [55]．また，図 6.11-(c)，(d)，(f) において，M_x がわずかに上昇していることが分かる．この理由として，それらの傾斜治具の取り付け精度が挙げられる．つまり，$\phi = 90°$ になるように治具の取り付けを行っているが，実際にはわずかな誤差があったと考えられる．その結果，特に感度が良いモーメント出力 (ここでは M_x) がわずかに検出され，増幅されることによって M_x が増加したと推察される．

次に，モーメントの軌跡をさらに観察するために，M_x, M_y をまとめた結果を図 6.12 に示す．第 1 象限にプロットした点列が $\phi = 90°$ の M_y データに相当し，第 3 象

228

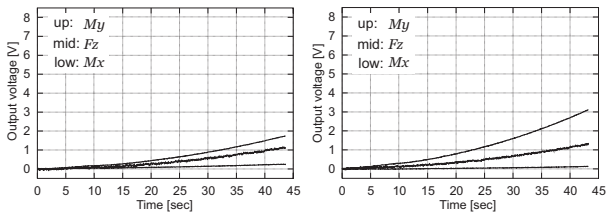

(a) $\theta = 5°$ (b) $\theta = 10°$

(c) $\theta = 15°$ (d) $\theta = 20°$

(e) $\theta = 25°$ (f) $\theta = 30°$

図 6.11: Results of compression test when $\phi = 90°$.

229

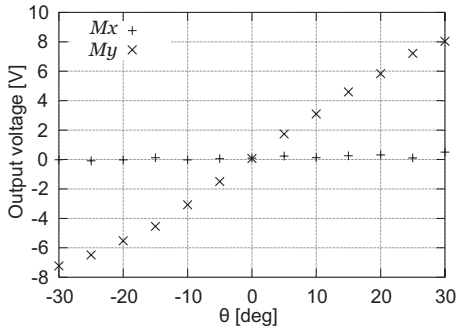

図 6.12: Relationship between M_x and M_y.

限のそれが $\phi = 270°$ の M_y データに相当する．図から分かるように，M_x と M_y 間のクロストーク（他軸への不必要な信号の漏れ）がほとんどなく独立に計測できることを示している．また，M_y の軌跡ではわずかに S 字カーブが見受けられる．この現象は，指先柔軟材料の幾何学的，材料学的非線形性に起因すると考えられ，数理モデルとして明確化するためにはさらなる実験的検証が必要である．

6.5 結言

本章では，MEMS 技術で設計し開発されたマイクロフォースセンサを埋め込んだ柔軟指先 (TES) を製作し，その基本性能ならびに，製作工程を記述した．また，本触覚デバイスへの圧縮実験を行うことで，クロストークなく 3 軸の出力値それぞれが独立に計測できていることが分かった．これらの基礎実験を通して，今回製作した触覚デバイス（TES）の基本特性を明らかにした．

230

マイクロフォース・モーメントセンサ内蔵ソフトフィンガの開発と接触実験

○藤井 郁夫　井上 貴浩　Dzung Viet Dao　杉山 進　平井 慎一　(立命館大学)

Development of Soft Finger with Micro Force/Moment Sensor and Its Contact Experments

Ikuo Fujii, Takahiro Inoue, Dzung Viet Dao, Susumu Sugiyama, and Shinichi Hirai

Graduate School of Science and Engineering, Ritsumeikan Univ.,
1-1-1 Noji-Higashi, Kusatsu, Shiga 525-8577, Japan
E-mail: rr010015@se.ritsumei.ac.jp

Abstract— In this paper, we show a novel tactile sensor fabricated by embedding a Micro-Force/Moment Sensor inside a hemispherical soft fingertip, which is applicable to the object manipulation using robotic hands. This sensor is produced by MEMS technology, designed to detect one force component (Fz) and two moment components (Mx, My). We show the high sensitivity and performance of the sensor, its strucure, and detection principle. Finally, we show that Fz, Mx, and My measured by the electrical potential difference on each terminal have high accuracy and keep low fluctuation in compression test of the soft fingertips.

Key Words: Micro-Force/Moment Sensor, Soft Fingertip, Manipulation

1. はじめに

ロボットハンドによる物体操作に関する研究は，近年様々な手法により行われている．安定して物体を把持するためには，指先は剛体ではなく人間のように柔らかい物質であることが好ましい．また，物体の把持・操作において指先の力覚は，最も重要な情報の一つと考えられ，特に柔軟指においては指先のセンシング能力が重要である．

本稿では，指先のセンシングの手段として，柔軟指に直接力センサを埋め込む方法を用いる．これは，直接力センサを埋め込むことによって，視覚などを用いて間接的にセンシングを行うのに比べて精度の高いセンシングが可能であると考えたためである．柔軟指に埋め込むセンサとして新たに MEMS 技術により製作されたマイクロフォース・モーメントセンサ [1] を用いる．このセンサのチップは，小型 ($2 \times 2[\mathrm{mm}^2]$) で 1 軸方向の力 ($Fz$) と 2 軸回りのモーメント ($Mx, My$) が検出可能であり，これらにより指先の押し込み量や接触方向を検出することが可能である．

本稿では，このセンサを半球型ソフトフィンガに埋め込み，ロボットハンドの指先への応用を目的とした触覚デバイスを製作した．Fig.2-(a) に示したこの触覚デバイスを TES(tactile sensor-embedded soft fingertip) と略して呼ぶ．製作した TES を用いて動的な接触試験を行う．接触時に半球内部に発生する力とモーメント (Fz, Mx, My) をセンサの出力電圧から検出し，ロボットハンドの物体操作への応用に適したセンサの高い感度と応答性を確認する．

2. センサの構造と検出原理

Fig.1-(a) にソフトフィンガ内部に埋め込むセンサを示す．センサはセンシングエリアとコネクタから構成される．センシングエリアは，Fig.2-(b) に示すセンサチップ，力伝達用ピラー，柔軟な半球状接触部で構成されている．

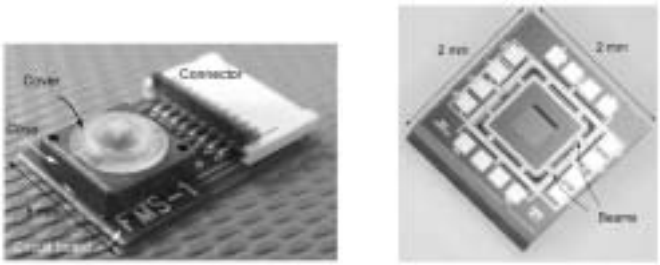

(a) schematic of the sensor　(b) sensing chip

Fig.1 A novel tactile sensor

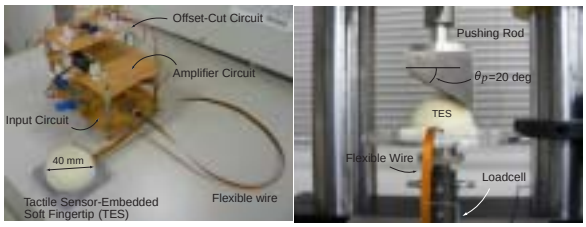

(a) overall view of TES　(b) compression test

Fig.2 Setup of tactile sensor-embedded soft fingertip (TES).

物体の接触により，半球状接触部に力やモーメントが加わるとそれらは力伝達用ピラーを介してセンシングチップに伝達する．センシングチップは，検出素子としてピエゾ抵抗素子を用いており，加わった力やモーメントを電圧の変化量に変換する．本センサはその電圧の変化量から加わった力やモーメントの大きさ及び方向を検出することが出来る．

3. 接触実験

Fig.1-(a) で示したセンサを直径 40mm の半球型ソフトフィンガに埋め込み，その性能を検証するために接

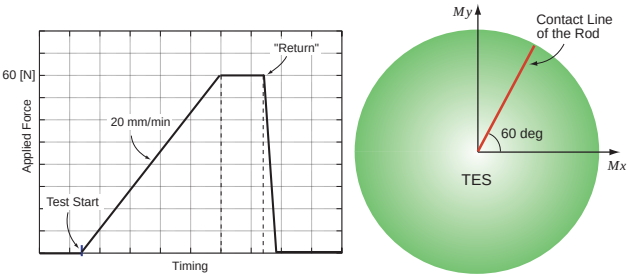

(a) motion of the rod (b) contacting angle

Fig.3 Motion manner of the pushing rod of the compression machine.

触実験を行った．Fig.2-(a) に TES の全体図を示す．今回の実験では，出力電圧を予め 3000 倍に増幅して検出した．

Fig.2-(b) のように圧縮試験機にソフトフィンガを設置する．上部に加重用のロッドがあり，このロッド部が垂直に降下することによりソフトフィンガに加重し変形させる．試験機の下部にはロードセルが設置されており，ソフトフィンガに与えた加重を計測できる．Fig.2-(b) に示すように今回はロッド接触部を半球に対して 20deg 傾け，Fig.4-(b) に示すように，ロッドの接触方向は半球の x 軸に対して 60deg の方向に設定して加重した．Fig.3-(a) にロッド動作を示す．ロッドを 20mm/min の一定速度で降下させソフトフィンガに 60N まで加重し，60N 到達後にロッドを初期位置に急速に戻すという動作を行った．実験結果を Fig.4 と Fig.5 に示す．比較対象として，Fig.4-(a) にはロッド接触部が 0deg の時の Fz の実験結果を示す．各実験では，実験開始時刻が一致していない．これは 1 回の実験で 3 軸同時に計測したのではなく，1 回に 1 軸ずつ計測したためである．Fig.4, Fig.5 から，各出力電圧ともロッドが線形的に降下しているのに対して出力電圧は非線形の結果を示していることが分かる．これは弾性体の変形特性の影響を受けたためと考えられる．また，Fig.4-(a) から，θp=20deg の方が θp=0deg より出力電圧が大きいことが分かる．これは半球上で剛体対象物が接触することによって生じる弾性ポテンシャルエネルギーが極小値を持つ (LMEE)[2] ことから妥当な結果であると考えられる．

次に，荷重 60N 到達後にロッドが急速に初期位置に戻る動作について検証する．Fig.3-(a) と Fig.4 からロッドが急速に初期位置に戻るのと同期して，出力電圧が初期値に戻っていることが確認できる．また，一旦急速に出力が下がった後，約 35〜36 秒の時点からは徐々に初期値に戻っていることが確認できる．これは急速なロッドの移動に半球の形状変化がついていかず徐々に元の形状に変形しためと考えられる．

さらに，Fig.5 を見ると，Mx の値が My より大きいことが確認できる．これは，ロッドの接触面がセンサの x 軸に対して 60deg 傾いており，x 軸周りのモーメントが大きくなったためと考えられる．また，どちらの出力電圧結果ともロッドが初期位置に急速に戻った後，一度初期の値を越えてから徐々に戻っていることが確認できた．

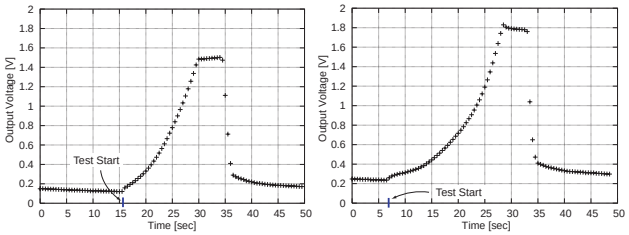

(a) Fz in $\theta_p = 0$ deg (b) Fz in $\theta_p = 20$ deg

Fig.4 The results of Fz when the force is wholly applied to the fingertip up to 60 N.

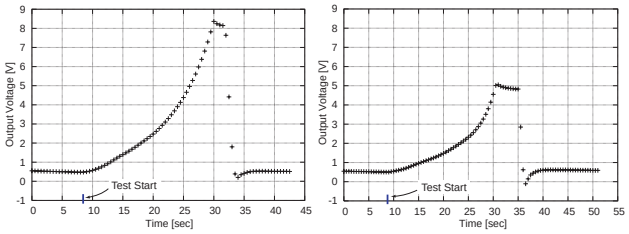

(a) Mx in $\theta_p = 20$ deg (b) My in $\theta_p = 20$ deg

Fig.5 The results of Mx and My.

4. おわりに

本論文では，ロボットハンドによる物体操作に応用可能な TES システムを製作し，接触実験を行った．センサチップは，MEMS 技術を用いて製作されており，小型で多軸力覚を検出することが可能である．センサを埋め込んだソフトフィンガを用いて接触実験を行い，3 軸の力とモーメント (Fz, Mx, My) を検出しその高い感度と応答性を確認できた．

これらの結果からこのシステムがロボットハンドの指先に装着し，その触覚能力を用いた物体操作を行うのに適してると考える．

今後は，Fig.5 に示す 2 リンクロボットに TES システムを装着し，ソフトフィンガ内部の力覚情報による 2 リンクロボットの制御を目指す．

参考文献

1) Dzung Viet Dao: ”Study on Silicon Piezoresistive Six-Degree of Freedom Micro Force-Moment Sensors and Application to Fluid Mechanics”, *Doctoral thesis in Ritsumeikan University*, 2003.
2) 井上，平井: ”ロボットハンドによる物体操作のための半球型柔軟指の静的弾性モデル”, 日本機械学会論文集 C 編, Vol.72, No.715, pp.872-878, 2006.

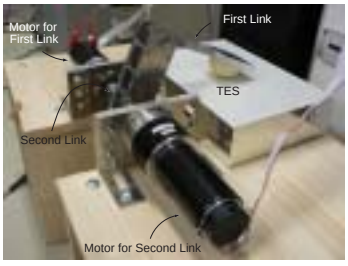

Fig.6 2 link robot equipped with a TES system.

Tactile Perception using Micro Force/Moment Sensor Embedded in Soft Fingertip

Ikuo Fujii, Takahiro Inoue, Dzung Viet Dao, Susumu Sugiyama, and Shinichi Hirai
Department of Robotics, Ritsumeikan Univ.,
1-1-1 Noji-Higashi, Kusatsu, Shiga 525-8577, Japan
rr010015@se.ritsumei.ac.jp

***Abstract*— In this paper, we show a novel tactile sensor fabricated by embedding a Micro-Force/Moment Sensor inside a hemispherical soft fingertip, which is applicable to the object manipulation using robotic hands. This sensor is produced by MEMS technology, designed to detect one force component (*Fz*) and two moment components (*Mx,My*). The structure is composed of a central square-block and four crisscross beams across the block, and its dimension is 9 mm^2 for a single sensing chip. We designed two types piezoresistors on the beams. One is a conventional two-terminal piezoresistor capable to measure a longitudinal strain, and the other is a four-terminal square-shaped piezoresistor capable to measure a transverse strain. We also applied a structural analysis to the chip to evaluate stress distribution on it. Finally, we show that *Fz,Mx*, and *My* measured by the electrical potential difference on each terminal have high accuracy and keep low fluctuation in compression test of the soft fingertip.**

***Index Terms*— Tactile sensor, Grasping, Manipulation, MEMS, Piezoresistor, Force/moment sensor, Soft fingertip.**

I. Introduction

Soft-fingered manipulation has much potential to simplify the explanation of secure grasping mechanism in human and the design of control system of robotic hands with soft fingers.

Inoue *et al.* [1], [2] have proposed a quasi-static manipulation method based on the concept of "*local minimum of elastic potential energy* (LMEE)" on a hemispherical soft fingertip. Their study clarified that the object position and posture grasped by two rotational soft fingers are determined uniquely without any control input because the grasped object consistently comes to rest stably at an LMEE. This invaluable secure grasping comes from the softness of a full rubber and solid fingertip structure, not from a rubber coating structure on a rigid fingertip. In order to make full use of the characteristics of the solid-rubber fingertip, we need to microminiaturize an individual sensor used for being embedded into the soft fingertip.

This study shows a novel micro-force/moment sensor produced by using MEMS technology, which is able to detect six forces and moments [3]. Furthermore, we present a tactile sensor-embedded soft fingertip (TES) using a type of three-axes force/moment sensing chip that is improved for the use of application of tactile perception. The conventional sensing chip is composed of cross-shaped four beams that is designed by linear elastic theory and FEM analysis [3]. Additionally, eighteen piezoresistors are placed on the beams in an uniform rule, which are able to measure the longitudinal and shear stresses externally applied. Finally, we conduct a static compression test for the TES, and demonstrate that the sensor can detect the subtle force and moment and has an outstanding sensitivity to recognize the forces.

II. Design of Micro Force/Moment Sensor

We describe the design of a six-degree of freedom force/moment micro sensing chip using the piezoresistance effect in silicon. The sensing chip is designed to be able to simultaneously detect three components of force and three components of moment in three orthogonal directions.

The sensing chip is a single crystalline crossbeam with piezoresistors diffused on the surface of the four suspended-beams. Forces and moments applied to the sensing chip, shown in Fig.1 and Fig.2, deform the four beams and change the resistance of the piezoresistors, which leads to a change in output of corresponding measurement circuits. The beam's dimension, piezoresistance coefficients and the positions of piezoresistors on the sensing chip are the main factors determining the sensitivity of the sensor.

In this section, we describe the structural analysis of the sensing chip, which is based on classical elasticity theory

A. The case when F_z is applied to the sensing chip

The sensing chip is composed of four beams and a central block as shown in Fig.1. Let us consider a force F_z is applied to the central point *O*. The stress states in the four beams are similar because of symmetry of the model. The problem can be simplified to the case of a beam that is fixed at one end, and free but guided to *z* axis at the other with load $F_z/4$, as shown in Fig.3-(a). The cross-sectional plane at the free end is always vertical, therefore, there is no angular deformation. The general equation for longitudinal stress at any point can be written by

$$\sigma_L(x) = \frac{F_z}{4Z_Y}\left(\frac{L}{2} - x\right), \tag{1}$$

$$Z_Y = \frac{I_Y}{t/2} = \frac{wt^2}{6}, \tag{2}$$

where I_Y, Z_Y are the moment of inertia of the cross-sectional area with respect to the *Y* axis and corresponding section modulus, respectively. The longitudinal stress σ_L

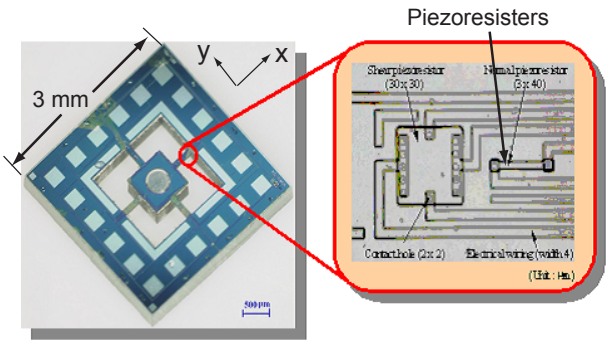

Fig. 1. Sensing chip fabricated by using MEMS technology

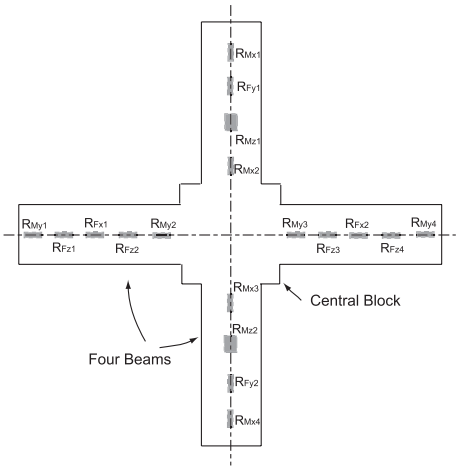

Fig. 2. Design of 18 piezoresistors

on the beam's surface reaches maximum at both ends of the beam and zero at the center, as shown in Fig.3-(b). The deflection at any point can be represented as

$$\delta z = \frac{F_z \cdot x^2}{48 E_X I_Y}(3L - 2x), \tag{3}$$

$$\delta z_{max} = \frac{F_z \cdot L^3}{48 E_X I_Y}, \tag{4}$$

where E_X is the Young's modulus of single crystal silicon in X direction.

B. The case when $M_x(M_y)$ is applied to the sensing chip

When a moment M_y around the Y axis is applied to the central block of the sensing chip, the beams A and B are bent, while the beams C and D are purely twisted. By symmetry, we need only to consider the stress states in the beams A and D. The stresses in the beams B and C are equal in magnitude but opposite in sign with those of the beams A and D, respectively. Fig.4 shows the reaction forces and moments acting on each member (beam A, beam D, and central block).

The displacement in Z direction, δz, and slope angle, θ, of the free end of the beam A due to moment M_{RY} and

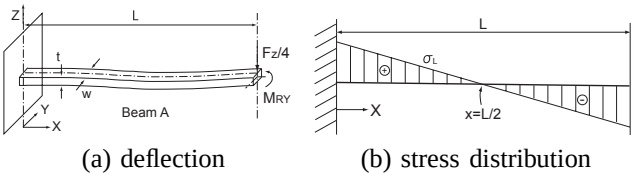

(a) deflection (b) stress distribution

Fig. 3. Analytical model of a beam in F_z

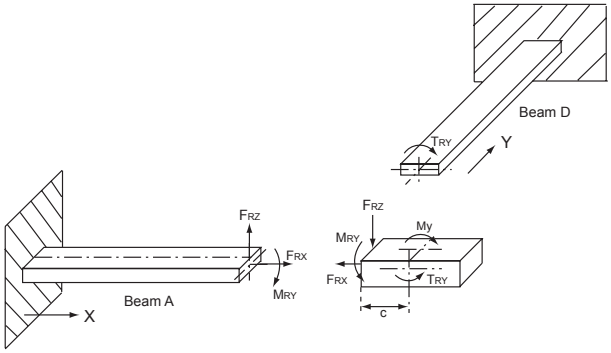

Fig. 4. Analytical model of a beam in $M_x(M_y)$

force F_{RZ} can be written by

$$\delta z = \frac{F_{RZ} \cdot L^3}{3E_X I_Y} - \frac{M_{RY} \cdot L^2}{2E_x I_Y}, \tag{5}$$

$$\theta = \frac{M_{RY} \cdot L}{E_X I_Y} - \frac{F_{RZ} \cdot L^2}{2E_x I_Y}, \tag{6}$$

The central block is also rotated around the original point O by the angle θ, therefore, the displacements of the free end can be expressed as

$$\delta z \simeq c\theta, \tag{7}$$

$$\delta x \simeq c\theta^2. \tag{8}$$

Substituting Eqs. (7) and (8) into Eqs. (5) and (6), the force F_{RZ} and moment M_{RY} can be written by

$$F_{RZ} = \frac{12 E_X I_Y}{L^3}\left(c + \frac{L}{2}\right)\theta, \tag{9}$$

$$M_{RY} = \frac{12 E_X I_Y}{L^2}\left(\frac{c}{2} + \frac{L}{3}\right)\theta, \tag{10}$$

$$F_{RX} = \frac{wtE_X}{L} c\theta^2. \tag{11}$$

Note that the free end of the beam D is also rotated by angle θ (equal to the rotation angle of the central block around the$Y$ axis). The stress state in this beam is equivalent to the case in which a square-cross-sectional surface with one end is fixed , and be purely twisted at the free end by a torque moment T_{RY}. The value of torque moment T_{RY} applied at the free end of the beam D can be represented as [4]

$$T_{RY} = \frac{KG}{L}\theta, \tag{12}$$

where G is shear modulus, and K is the geometric factor of the beam, which is determined by the experimental

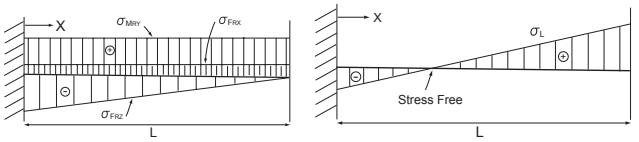

(a) individual stress (b) total stress σ_L

Fig. 5. Stress distribution when the $M_x(M_y)$ is applied to the central block

formula:

$$K = \frac{wt^3}{16}\left\{\frac{16}{3} - 3.36\frac{t}{w}\left(1 - \frac{t^4}{12w^4}\right)\right\}. \quad (13)$$

Now, the moment equilibrium of the central block can be expressed as

$$M_y = 2(M_{RY} + T_{RY} + F_{RZ}\cdot c). \quad (14)$$

Substituting Eqs. (9), (10), and (12) into Eq. (14), the deformed angle θ can be calculated as

$$\theta = \frac{1}{2}\cdot\frac{M_y}{\frac{12E_XI_Yc}{L^3}\left(c+\frac{L}{2}\right) + \frac{12E_XI_Y}{L^2}\left(\frac{c}{2}+\frac{L}{3}\right) + \frac{KG}{L}}. \quad (15)$$

Finally, the equation of the longitudinal stresses on the surface of the beam A induced by moment M_{RY}, forces F_{RZ}, and F_{RX} can be respectively written by

$$\sigma_{M_{RY}}(x) = \frac{M_{RY}t}{2I_Y} = \frac{6E_Xt\theta}{L^2}\left(\frac{c}{2}+\frac{L}{3}\right), \quad (16)$$

$$\sigma_{F_{RZ}}(x) = -\frac{F_{RZ}(L-x)t}{2I_Y} = -\frac{6E_Xt\theta}{L^3}(c+\frac{L}{2})(L-x), \quad (17)$$

$$\sigma_{F_{RX}}(x) = \frac{F_{RX}}{wt} = \frac{E_Xc\theta^2}{L} \geq 0. \quad (18)$$

By applying the superposition method, the total longitudinal stress on the surface of the beam A is then represented as follows:

$$\sigma_L(x) = \sigma_{M_{RY}}(x) + \sigma_{F_{RZ}}(x) + \sigma_{F_{RX}}(x). \quad (19)$$

Fig. 5-(a) shows the distributions of the longitudinal stresses $\sigma_{M_{RY}}, \sigma_{F_{RZ}}, \sigma_{F_{RX}}$, and Fig. 5-(b) shows the total longitudinal stress σ_L represented in Eq. (19).

The stresses at the fixed end $(x=0)$ and free end $(x=L)$ can be expressed as

$$\sigma_L(0) = -\frac{6E_Xt\theta}{L^2}\left(\frac{L}{6}+\frac{c}{2}\right) + \frac{E_Xc\theta^2}{L}, \quad (20)$$

$$\sigma_L(L) = \frac{6E_Xt\theta}{L^2}\left(\frac{L}{3}+\frac{c}{2}\right) + \frac{E_Xc\theta^2}{L}. \quad (21)$$

The stress-free point can be found by solving Eq. (19), $\sigma_L(x) = 0$.

$$x_{\sigma=0} = \frac{L}{2c+L}\left(\frac{L+3c}{3} + \frac{Lc\theta}{3t}\right). \quad (22)$$

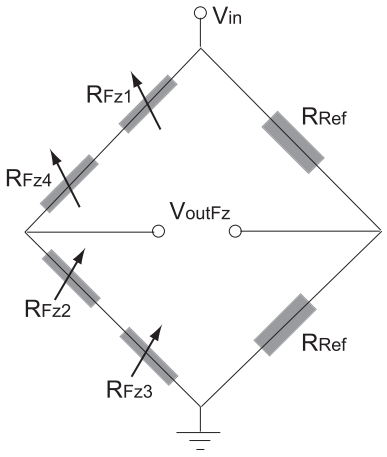

Fig. 6. Wheatstone bridge to measure the force F_z

III. Detection Principle

As shown in Fig.2, eighteen piezoresistors are designed on the surface of all beams, which are distinguished into two types of piezoresistors; one detects longitudinal stresses and the other does shear stresses. Furthermore, input/output terminals for measuring the forces and moments $(F_x, F_y, F_z, M_x, M_y, M_z)$ are arranged on the outer frame of the sensing chip, as shown in Fig.1. As an example, we explain a detection principle of F_z that can be independently measured from the other signals.

Fig.6 shows a wheatstone bridge to measure the force F_z. Since two reference resistors R_{Ref} are identical and constant and all the piezoresistors R_{Fzi} are designed to be identical, this is a half bridge and be balanced at stress-free state. When the resistances of piezoresistors $R_{F_{zi}}$ are changed due to stress, the output voltage of F_z-bridge is expressed by

$$V_{outFz} = \frac{r}{(1+r)^2}\left(\frac{\Delta R_{F_{z1}} + \Delta R_{F_{z4}}}{R_{F_{z1}} + R_{F_{z4}}} - \frac{\Delta R_{F_{z2}} + \Delta R_{F_{z3}}}{R_{F_{z2}} + R_{F_{z3}}}\right)V_{in}, \quad (23)$$

where

$$r = \frac{R_{F_{z1}} + R_{F_{z4}}}{R_{F_{z2}} + R_{F_{z3}}} = 1. \quad (24)$$

When a vertical force F_z is applied to the sensing chip, the longitudinal stresses in the four piezoresistors of the F_z-bridge can be written from Eq. (1) as follows:

$$\sigma_{R_{Fz1}} = \sigma_{R_{Fz4}} = -\sigma_{R_{Fz2}} = -\sigma_{R_{Fz3}}, \quad (25)$$

where $\sigma_{R_{Fzi}}$ is the longitudinal stress at piezoresistors $R_{F_{zi}}(i = 1-4)$. Therefore, the following relationship is satisfied.

$$\Delta R_{F_{z1}} = \Delta R_{F_{z4}} = -\Delta R_{F_{z2}} = -\Delta R_{F_{z3}}. \quad (26)$$

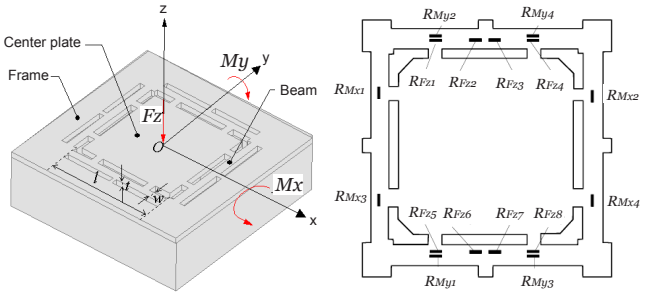

(a) structure (b) layout of piezoresistors

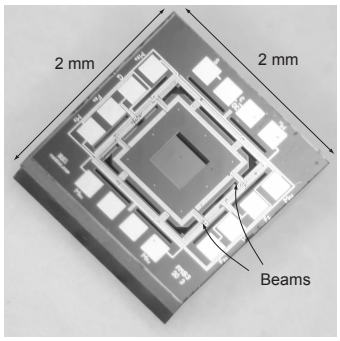

(c) sensing chip

Fig. 7. Improved new micro force/moment sensor.

TABLE I
MAXIMUM FORCE AND MOMENT.

Strength	Force [mN]	Moment [N·μm]
	5000	800
Sensitivity	S_{Fz} [mV/mN]	S_{Mx}, S_{My} [mV/(N·μm)]
	0.2	2.83

Consequently, the F_z-bridge is unbalanced, and the output response appears. For the F_z-bridge, the output voltage represented in Eq. (23) can finally be expressed by

$$V_{outFz} = \frac{1}{2}\frac{\Delta R_{F_{z1}}}{R_{F_{z1}}} V_{in}. \tag{27}$$

IV. IMPROVED MICRO FORCE/MOMENT SENSOR AND ITS PACKAGING

For the application by means of a robotic hand equipped with tactile sensors, we have to redesign a refined sensor having high sensitivity and increase the intensity of the sensor. In the present section, we show an improved micro force/moment sensor that has high sensitivity and strength, as shown in Fig.7 and Table I.

In this sensor the piezoresistors are placed as shown in Fig.7-(b), and the potential difference that is generated by applying force to the sensor can be measured by the corresponding bridge circuit designed within the sensing chip. As shown in Fig.7-(c), a set of power electrode and the electrodes for measuring (Fz, Mx, My) are laid out around the sensing chip.

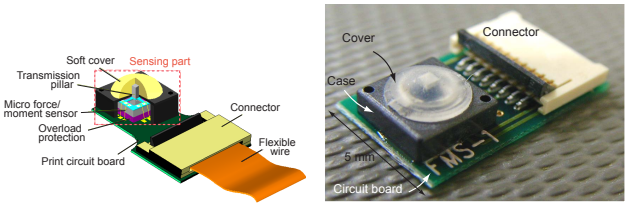

(a) schematic of the sensor (b) tactile sensor

Fig. 8. A novel tactile sensor packaged for sensing slight change of force and moment.

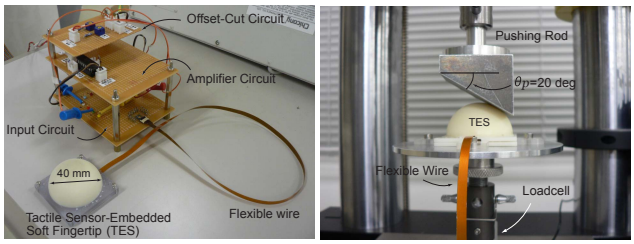

(a) overall view of TES (b) compression test

Fig. 9. Setup of tactile sensor-embedded soft fingertip (TES).

In addition, as shown in Fig.8 we show a tactile sensor packaged for the use of applications, for example: measuring the slight force in contact with some sort of object and the inner force/pressure within soft materials, etc. This tactile sensor is able to detect the external force applied through a soft and thin rubber covered the sensing chip. The detecting mechanism is that the applied force first transmits to a pillar through the soft rubber, as shown in Fig.8-(a). Continuously, the pillar placed on the central stage of the sensing chip shown in Fig.7-(c) yields the combined bending and tortional deflections on each beam.

V. TACTILE SENSOR-EMBEDDED SOFT FINGERTIP (TES)

A. Structure and Setup

This study provides a novel *T*actile sensor-*E*mbedded *S*oft fingertip that is abbreviated as TES, which is necessary for the tactile feedback required for the acquirement of human-like manipulation ability using a robotic soft-fingered hand.

Fig.9-(a) shows a TES system that consists of an input circuit, a amplifier circuit, an offset-cut circuit, and the TES itself. The voltage gain of the amplifier circuit is approximately 3000-fold.

B. Compression Test

We conduct the compression test of a TES as shown in Fig.9-(b), and demonstrate the high performance and excellent dynamic response of the sensor. In this test, a pushing rod that inclines by 20 deg makes contact with the TES, and we increase the applied force until the loadcell placed on the compression machine marks 60 N, as shown in Table II and Fig.10-(a). Furthermore, the rod is in contact

TABLE II

INPUT MANNER OF THE APPLIED FORCE IN COMPRESSION

Timing	Motion manner of pushing rod
Test start	20 mm/min compression
Max force (60 N)	0 mm/min (Test stops)
Up to push "Return"	0 mm/min (Stopping)
After push "Return"	The rod returns rapidly to initial position

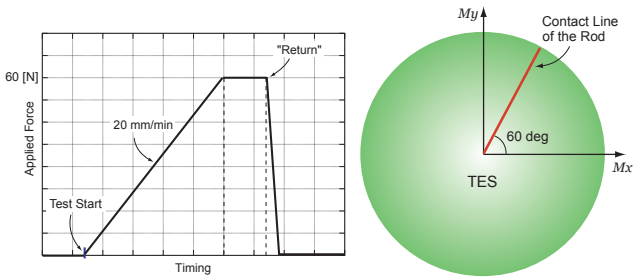

(a) motion of the rod (b) contacting angle

Fig. 10. Motion manner of the pushing rod of the compression machine.

with the soft fingertip keeping 60 deg from the x-axis, as illustrated in Fig.10-(b). The results of (Fz, Mx, My) measured by the TES are plotted in Fig.11 and Fig.12, and Fz in the contact of $\theta_p = 0$ is also depicted in Fig.11-(a) for comparison. Note that the starting point of the compression is not consistent in every figure because it is difficult to synchronize the onset of compression and electrical measurement of the output voltage of TES. In addition, the output voltage in the figures is previously amplified by 3000 times.

As shown in Fig.11 and Fig.12, each output voltage increases with a certain power law against the linearly-applied force. The Fz voltage when $\theta_p = 20$ deg is larger than that in $\theta_p = 0$. This result comes from the fact that the local minimum of elastic potential energy (LMEE) on hemispherical soft fingertip exists [1], [2]. While the speed of response is good enough to follows the rod's return, the the voltage gradually decreases to the initial value when the time is approximately 36 sec and 35 sec in Fig.11-(a) and Fig.11-(b), respectively. This means that the shape variation of soft fingertip cannot follow the rapid rod's return.

As shown in Fig.12, the voltage of Mx is larger than that of My. It is because that the contacting rod is placed at the position inclined by 60 deg from the x-axis, as illustrated in Fig.10-(b). In addition, we find in both figures that the voltage passes across the initial value, and then restitutes to the initial value.

VI. CONCLUDING REMARKS

This paper has presented a novel tactile sensor-embedded soft fingertip (TES) where a micro force/moment sensing chip is used. This sensing chip is fabricated by using MEMS technology, and its strength is designed by FE analysis. We have shown the high sensitivity and performance of the sensor, and demonstrated that the response

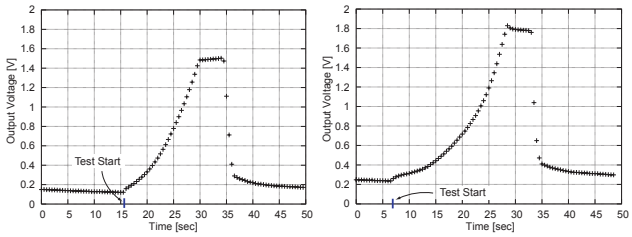

(a) Fz in $\theta_p = 0$ deg (b) Fz in $\theta_p = 20$ deg

Fig. 11. The results of Fz when the force is wholly applied to the fingertip up to 60 N.

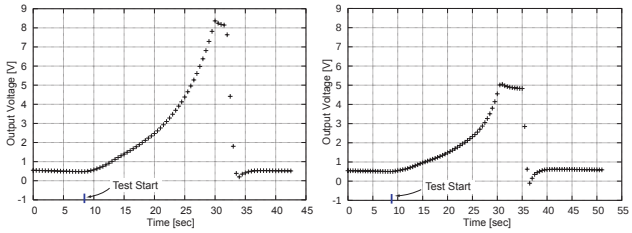

(a) Mx in $\theta_p = 20$ deg (b) My in $\theta_p = 20$ deg

Fig. 12. The results of Mx and My.

characteristics is superior in the dynamic sense. Finally, we have clarified that TES system is absolutely useful for robotic fingertips that is able to play as the perception like human fingers.

In future works, we are going to use the TES system to soft-fingered robotic hand, and achieve the dextrous manipulation with human-like tactile perception.

ACKNOWLEDGMENT

This research was supported in part by the Ritsumeikan University 21st Century COE program "Micro Nanoscience Integrated Systems".

REFERENCES

[1] T.Inoue and S.Hirai, "Local Minimum of Elastic Potential Energy on Hemispherical Soft Fingertip", *Proc. IEEE Int. Conf. on Robotics and Automation*, pp.2319-2324, 2005.

[2] T.Inoue and S.Hirai, "Study on Hemispherical Soft-Fingered Handling for Fine Manipulation by Minimum D.O.F. Robotic Hand", *Proc. IEEE Int. Conf. on Robotics and Automation*, which will be presented in Orlando, USA, 2006.

[3] Dzung Viet Dao, "Study on Silicon Piezoresistive Six-Degree of Freedom Micro Force-Moment Sensors and Application to Fluid Mechanics", *Doctoral thesis in Ritsumeikan University*, 2003.

[4] R.J.Roark, "Formulas for stress and strain", 4th Ed., *McGraw-Hill*, 1965.

参考文献

[1] Fung, Y. C. and Tong, P., *Classical and Computational Solid Mechanics*, World Scientific Publishing, 2001.

[2] Crandall, S. H., Karnopp, D. C., Kurts, E. F., and Pridmore-Brown, D. C., *Dynamics of Mechanical and Electromechanical Systems*, McGraw-Hill, 1968.

[3] Riederer, S. J., *Current technical development of magnetic resonance imaging*, SIAM J. IEEE Engineering in Medicine and Biology, Vol. 19, pp.34–41, 2000.

[4] Matuszewski, B. J., Shen, J. K. and Shark, L. K., *Estimation of Internal Body Deformations Using an Elastic Registration Technique*, International Conference on Medical Information Visualisation-BioMedical Visualisation, pp.15–20, 2006.

[5] Cho, J. and Benkeser, P. J., *Elastically deformable model-based motion-tracking of left ventricle*, The 26th Annual International Conference of the IEEE EMBS, Vol. 1, pp.1925–1928, 2004.

[6] Papademetris, X., Sinusas, A. J., Dione. D. P., Constable, R. T., and Duncan, J. S., *Estimation of 3-D left ventricular deformation from medical images using biomechanical models*, IEEE Transactions on Medical Imaging, Vol. 21, pp.786–800, 2002.

[7] Chenoune, Y., Delechelle, E., Petit, E., Goissen, T., Garot, J., and Rahmouni, A., *Segmentation of cardiac cine-MR images and myocardial deformation assessment using level set methods*, Computerized Medical Imaging and Graphics, Vol. 29, pp.607–616, 2005.

[8] Lang, J., Pai, D. K., and Woodham, R. J., *Robotic acquisition of deformable models*, IEEE International Conference on Robotics and Automation, Vol. 1, pp.933–938, 2002.

[9] Caselles, V., Catte, F., Coll, T., and Dibos, F., *A geometric model for active contours in image processing*, Numerische Mathematik, Vol. 66, No. 1, pp.1–31, 1993.

[10] Malladi, R., Sethian, J. A., and Vemuri, B. C., *Shape modeling with front propagation: a level set approach*, IEEE Transactions on Pattern Analysis and Machine Intelligence, Vol. 17, No. 2, pp.158–175, 1995.

[11] Caselles, V., *Geometric models for active contours*, International Conference on Image Processing, Vol. 3, pp.9–12, 1995.

[12] Huang, F. Z. and Su, J. B., *Face Contour Detection Using Geometric Active Contours*, Proceedings of the 4th World Congress on Intelligent Control and Automation, Vol. 3, pp.2090–2093, 2002.

[13] Kass, M. and Witkin. A., *Snakes: active contours models*, IJOCV, Vol.1, No.4, pp.321–331, 1987.

[14] Xu, C. Y., Pham, D. L., and Prince, J. L., *Image segmentation using deformable models*, Handbook of Medical Imaging, pp.129–174, 2000.

[15] Harris, C. and Stephens, M., *A combined corner and edge detector*, Proceedings of The Fourth Alvey Vision Conference, Vol. 1, No. 4, pp.147–151, 1988.

[16] Horn, B. K. P., *Closed Form Solution of Absolute Orientation using Unit Quaternions*, Optical Society of America A: Optics, Image Science and Vision, Vol. 4, pp.629–642, 1987.

[17] Zhang, P. L., Hirai, S., Endo, K. and Morikawa, S., *Local Deformation Measurement of Bilogoical Tissues Based on Feature Tracking of 3D MR Volumetric Images*, IEEE/ICME International Conference on Complex Medical Engineering, pp.711–716, 2007.

[18] Zhang, Y. F. and Doermann, D., *Scene Labeling by Relaxation Operations*, IEEE Transactions on Pattern Analysis and Machine Intelligence, Vol. 28, pp.643–649, 2006.

[19] Chen, G. Q., *Robust Point Feature Matching in Projective Space*, Proceedings of the 2001 IEEE Computer Society Conference on Computer Vision and Pattern Recognition, Vol .1, pp.717–722, 2001.

[20] Zhang, Z. Y., Deriche, R., Faugeras, O., and Luong, Q.-T., *A robust technique for matching two uncalibrated images through the recovery of the unknown epipolar geometry*, Artificial Intelligence Journal, pp.87–119, 1995.

[21] Xu, R. and Chen, Y. W., *Wavelet-Based Multiresolution Medical Image Registration Strategy Combining Mutual Information with Spatial Information*, International Journal of Innovative Computing, Information and Control, Vol. 3, No. 2, pp.285–296, 2007.

[22] Rogelj, P., Kovacic, S., and Gee, J. C., *Validation of a Non-rigid Registration Algorithm for Multi-modal Data*, ipmi02, pp.299–307, 2002.

[23] 友國誠至, 杉山勇太, 平井慎一, 実時間計算可能な仮想レオロジー物体の構築, 日本バーチャルリアリティ学会論文誌, Vol. 8，No. 3，pp.247–254, 2003.

[24] Naoki Ueda, Shinichi Hirai, and Hiromi T. Tanaka, *Extracting Rheological Properties of Deformable Objects with Haptic Vision*, Proc. IEEE Int. Conf. on Robotics and Automation, pp.3902–3907, New Orleans, April, 2004.

[25] 伊藤正安, 望月剛, 超音波診断装置, コロナ社, 2002.

[26] 日本磁器共鳴医学会 教育委員会 編, 基礎から学ぶMRI, インナービジョン, 2001.

[27] 大城 理, 菅 幹生, 湊 小太郎, 千原 國宏, MRIを用いた生体組織の力学特性計測, 日本機械学会2002年度年次大会講演論文集, pp.123–124, 2002.

[28] 岡 久雄, 植田 俊之, 横加振法による生体力学特性の計測, 信学技法, Vol. 93, No. 13, pp.33–40, 1993.

[29] 西村 洋祐, 朱 志光, 小林 英津子, 陳 献, 久田 俊明, 稲田 紘, 佐久間 一郎, 臓器シミュレーションへの応用を目的とした肝臓物性値測定, 第11回日本コンピュータ外科学会大会合同論文集, pp.151–152, 2002.

[30] 西村 直樹, 山田 昇, 超音波による生体組織の粘弾性計測, 日本音響学会講演論文集, pp.1137–1138, 1997.

[31] 黒岩 正貴, 山田 昇一郎, 回折トモグラフィ法による生体の減衰率分布の画像化, 日本音響学会講演論文集, pp.1139–1140, 1997.

[32] 道下 和昭, 長谷川 英之, 金井 浩, 音響放射圧を用いた低周波加振による粘弾性特性計測, 日本音響学会講演論文集, pp.1163–1164, 2003.

[33] 岩井 喜典, 斉藤 雄督, 今里 悠一, 医用画像診断装置, コロナ社, 2003.

[34] 喜多 泰代, Ralph Highnam, Michael Brady, 対象の変形を考慮した乳部ステレオX線像間の対応手法, 情報処理学会論文誌, Vol. 37, No. 6, pp.1234–1243, 1996.

[35] 伊藤 正安, 望月 剛, 超音波診断装置, コロナ社, 2002.

[36] 植野 映, 東野 英利子, 椎名 毅, 山川 誠, 伊藤 吾子, 新しい手法ーエラストグラフィ, 日本乳癌検診学会誌, Vol. 14, No. 2, pp.190–195, 2005.

[37] 岡部 哲夫, 藤田 広志, 医用画像工学, 医師薬出版株式会社, 2006.

[38] 徳田 淳一, 平野 勝也, 塚元 鉄二, 土肥 健純, 波多 伸彦, 誘導手術のためのリアルタイム臓器トラッキング/高速画像レジストレーションに関する研究, 電子情報通信学会論文誌, Vol. J87–D–II, No. 1, pp.339–347, 2004.

[39] Mayoran Rajendra, Akio Yamamoto, Toshiaki Oda, Hideo Yokata, Ryutaro Himeno, Toshiro Higuchi, *Application of Force Sensor made of Shielded Strain Gauges in MR-related Biomechanical Measurements*, 計測自動制御学会第 8 回システムインテグレーション部門講演会, 2007.

[40] Yamamoto, A., Rajendra, M., Hirano, Y., Kataoka, H., Yokota, H., Himeno, R., Higuchi, T., *Motion Generation in MRI Using an Electronic Linear Motor for Visualizing Internal Deformation of Soft Objects by tagged cine-MRI*, Proc. IEEE/ISIE, pp.2741–2746, 2007.

[41] Chaouis,D., Gassert, R., Sache, L., and Bleuler, H., *Design of a Simple MRI/fMRI Compatible Force/TorqueSensor*, Proc. IEEE/RSJ IROS, pp.2593–2599, 2007.

[42] Tada, M., Sasaki, S., Ogasawara, T., *Development of an Optical 2-axis Force Sensore Usable in MRI Environments*, Proc. IEEE Sensors, pp.984–989, 2002.

[43] 下田 陽久, ディジタル画像処理, CG-ARTS 協会, 1990.

[44] 徐 剛, 辻 三郎, 3 次元ビジョン, 共立出版, 1998.

[45] 守野 雅也, 大坪 豊佳, 吉田 晴行, 登尾 啓史, 力学変形特性に基づくレオロジー物体の未知パラメータ推定手法, ロボティクス・メカトロニクス講演会, 2007.

[46] Nogami, R., Ujibe, F., Fujii, H., and Noborio, H., *Precise Deformation of Rheologic Object under MSD Models with Many Voxels and Calibrating Parameters*, Proc. of the IEEE Int. Conf. on Robotics and Automation, pp.1919–1926, 2004.

[47] 遠藤 和美, 張 鵬林, 平井 慎一, 柔軟物の内部変形計測による FE モデルの力学パラメータ同定, 計測自動制御学会第 8 回システムインテグレーション部門講演会予稿集, 2007.

[48] 活田 崇至, 村松 潤治, 早見 信一郎, 森川 茂廣, 平井 慎一, 超音波画像と MRI を用いた内部計測による柔軟物の FE モデルの検証, ロボティクスシンポジア予稿集, 2006.

[49] 金子 真, 水田 知宏, 柴田 暁秀, 東森 充, アクティブ虚血ダイナミクスと医療診断への応用, 計測自動制御学会第 8 回システムインテグレーション部門講演会予稿集, 2007.

[50] 渡辺 篤志, 小林 博子, 奥田 知規, 川澄 岩雄, 嶋津 秀昭, 体表組織弾性特性の非接触計測の原理的検討とシステム開発, 生体医工学, Vol. 43, No. 1, pp. 109–116, 2005.

[51] Yamada,D. et. al., *Development of Elastic Robot Finger having Rides which can Detect a Distribution of Contact Condition*, Transactions of the Japan Society of Mechanical Engineers, Series C, Vol. 70, No. 690, pp.236–242, 2004.

[52] Chang, L. Y. and Matsuoka, Y., *A Kinematic Thumb Model for the ACT Hand*, Proceedings of the IEEE Int. Conf. on Robotics and Automation, pp.1000–1005, 2006.

[53] Murakami, K. and Hasegawa, T., *Tactile Sensing of Edge Direction of an Object using a Robotic Fingertip with Soft Skin*, Journal of the Robotics Society of Japan (RSJ), Vol. 24, No. 2, pp.240–247, 2006.

[54] Tada, Y. et. al., *Anthropomorphic Soft Fingertip with Tactile Receptors in the Skin*, Journal of the Robotics Society of Japan (RSJ), Vol. 23, No. 4, pp.482–487, 2005.

[55] Inoue, T. and Hirai, S., *Elastic Model of Deformable Fingertip for Soft-Fingered Manipulation*, Transactions of the IEEE on Robotics and Automation, Vol. 22, No. 6, pp.1273–1279, 2006.

[56] Wang, Q. et. al., *Development of a Soft Fingertip Sensor Utilizing MEMS-based Multi-axis Force Sensor*, Proceedings of Int. Symp. on Flexible Automation, pp.128–131, 2006.

[57] Inoue, T. and Hirai, S., *Elastic Force Models of Hemispherical Soft Fingertip with Geometric and Material Nonlinearities for Fine Soft-fingered Manipulation*, Journal of the Robotics Society of Japan (RSJ), Vol. 25, No. 2, pp.221–230, 2007.

論文

[1] Penglin Zhang, Shinichi Hirai, and Kazumi Endo, *A Feature Matching-based Approach to Deformation Fields Measurement from MR Images of Non-rigid Object*, Int. J. of Innovative Computing, Information and Control, acceptted for publication, 2008.

[2] 井川 武思, 登尾 啓史, "階層レオロジー MSD モデルの形状精度と計算時間について", VR 医学, Vol. 6, No. 1, 修正後掲載予定, 2008.

[3] 井上 貴浩, 藤井 郁夫, 平井 慎一, Qiang Wang, Dzung Viet Dao, 杉山 進, "マイクロフォース・モーメントセンサ埋め込み型柔軟指先の製作と圧縮実験による評価", 日本機械学会論文誌 C 編, Vol. 73, No. 736, pp.3228–3233, 2007.

[4] Penglin Zhang, Shinichi Hirai, Kazumi Endo, and Shigerhiro Morikawa, *Local Deformation Measurement of Biological Tissues Based on Feature Tracking of 3D MR Volumetric Images*, 2007 IEEE/ICME Int. Conf. on Complex Medical Engineering (CME2007), Beijing, May 23–25, 2007.

[5] Penglin Zhang, Shinichi Hirai, and Kazumi Endo, *A Method for Non-rigid 3D Deformation Fields Measurement: Application to Human Calf MR Volumetric Images*, Workshop on Modeling, Identification, and Control of Deformable Soft Objects, IEEE/RSJ Int. Conf. on Intelligent Robots and Systems, San Diego, U.S.A., November, 2007.

[6] Yasuyo Kita, Shinichi Tokumoto, and Shinichi Hirai, *On Compression Model for Integrative Analysis of Different View Breast Xrays*, Workshop on Modeling, Identification, and Control of Deformable Soft Objects, IEEE/RSJ Int. Conf. on Intelligent Robots and Systems, San Diego, U.S.A., November, 2007.

[7] Takeshi Ikawa and Hiroshi Noborio, *On the Precision and Efficiency of Hierarchical Rheology MSD Model*, Proc. of the IEEE/RSJ International Conference on Intelligent Robots and Systems, pp.376–383, 2007.

[8] Haruyuki Yoshida, Fumiaki Ujibe, Hiroshi Noborio, *Force/Shape Reappearance of MSD Rheology Model Calibrated by Force/Shape Sequence*, Proc. of the 17th Int. Conf. on Artificial Reality and Telexistence, pp.121–128, 2007.

[9] Huynh Quang Huy Viet, Takahiro Kamada, Yasufumi Takama, and Hiromi T. Tanaka, *An Adaptive 3D Surface Mesh Cutting Algorithm for Deformable Objects*, 情報処理学会「画像の認識・理解シンポジウム (MIRU'06)」論文集, pp.1359–1364, July, 2006.

[10] Huynh Quang Huy Viet, Takahiro Kamada, Yasufumi Takama, and Hiromi T. Tanaka, *A Virtual Surface Cutting Operation Using Mesh Refinement Method*, Proc. 20th Int. Congress and Exhibition Osaka, International Jornal of Conputer Assisted Radiology and Surgery (CARS06), pp.150–152, June, 2006.

[11] Ikuo Fujii, Takahiro Inoue, Dzung Viet Dao, Susumu Sugiyama, and Shinichi Hirai, *Tactile Perception Using Micro Force/Moment Sensor Embedded in Soft Fingertip*, Proc. IEEE Sensors, pp.558–562, Daegu, Korea, October, 2006.

[12] Junji Muramatsu, Takashi Ikuta, Shinichi Hirai, and Shigehiro Morikawa, *Validation of FE Deformation Models using Ultrasonic and MR Images*, Proc. 9th IEEE Int. Conf. on Control, Automation, Robotics and Vision, pp.1091–1096, Singapore, December, 2006.

[13] Hiromi T. Tanaka, Yoshinori Tsujino, Takahiro Kamada, and Hyung Quang Huy Viet, *Bisection Refiniment Based Real-Time Adaptive Mesh Model for Deformation and Cutting of Soft Object*, Proc. 9th IEEE Int. Conf. on Control, Automation, Robotics and Vision, pp.1103–1110, Singapore, December, 2006.

[14] Takahiro Inoue and Shinichi Hirai, *Local Minimum of Elastic Potential Energy on Hemispherical Soft Fingertip*, Proc. IEEE Int. Conf. on Robotics and Automation, pp.2319–2324, Barcelona, April, 2005.

[15] Mizuho Shibata and Shinichi Hirai, *Stability Analysis for Dynamic Control on Contact with Soft Interface in Continuous-discrete Time System*, Proc. IEEE/RSJ Int. Conf. on Intelligent Robots and Systems, pp.1628–1633, Edmonton, Canada, August, 2005.

口頭発表

[1] 遠藤和美, 村松潤治, 平井慎一, 柔軟物の内部変形計測による FE モデルの力学パラメータ同定, ロボティクス・メカトロニクス'07 講演会予稿集 CD-ROM, 2007.

[2] Penglin Zhang, Shinichi Hirai, and Kazumi Endo, *A Feature Tracking-based Approach for Local Deformation Fields Measurement of Biological Tissue from MR Volumes*, 3rd Joint Workshop on Machine Perception and Robotics (MPR2007), Kusatsu, November, 2007.

[3] Kazumi Endo, Penglin Zhang, Shinichi Hirai, and Shinichi Tokumoto, *Identification of Nonuniform Physical Parameters through Measurement of Inner Deformation*, 3rd Joint Workshop on Machine Perception and Robotics (MPR2007), Kusatsu, November, 2007

[4] 遠藤和美, 張鵬林, 平井慎一, 徳本真一, 柔軟物の内部変形計測による非一様 FE モデルのパラメータ同定法の検証, 計測自動制御学会システムインテグレーション部門学術講演会, pp.1170–1171, 2007.

[5] 活田崇至, 村松潤治, 早見信一郎, 森川茂廣, 平井慎一, 田中弘美, 超音波画像と MRI を用いた内部計測による柔軟物の FE モデルの検証, ロボティクスシンポジア予稿集, pp.544–549, 2006.

[6] 藤井郁夫, 井上貴浩, 平井慎一, Dzung Viet Dao, 杉山進, MEMS フォースセンサを用いたソフトフィンガ型触覚デバイスの開発と接触実験, ロボティクス・メカトロニクス'06 講演会予稿集 CD-ROM, 2006.

[7] 徳本真一, 平井慎一, CT スキャナを用いたパラメータ同定のための柔軟物の内部変形計測, 計測自動制御学会システムインテグレーション部門学術講演会, pp.73–74, 2006.

[8] 藤井郁夫, 井上貴浩, Dzung Viet Dao, 杉山進, 平井慎一, マイクロフォース・モーメントセンサ内蔵ソフトフィンガの開発と接触実験, 計測自動制御学会システムインテグレーション部門学術講演会, pp.488–489, 2006.

[9] 遠藤和美, 張鵬林, 村松潤治, 平井慎一, 森川茂廣, MRI ボリュームデータにおける 3 次元ブロックマッチングを用いた FE モデルパラメータの同定, 計測自動制御学会システムインテグレーション部門学術講演会, pp.1036–1037, 2006.

[10] Yoshinori Tsujino, Huynh Quang Huy Viet, and Hiromi T. Tanaka, *A Real-Time Dynamic Adaptive Deformable Mesh Model for Soft Objects Based on Bisection Refinement and Binary Simplification Algoritms*, 2nd Joint Workshop on Machine Perception and Robotics, Fukuoka, November 2006.

[11] 藤井郁夫, 井上貴浩, Dzung Viet Dao, 杉山進, 平井慎一, マイクロフォース・モーメントセンサを内蔵した半球型ソフトフィンガの静的接触実験, 計測自動制御学会システムインテグレーション部門学術講演会, pp.1123–1124, 2005.